Synthetic Polypeptides for Biomedical and Bioactive Applications

by

Steven Josef Shirbin

BSc. (Hons)

Submitted in total fulfilment of the requirements of the degree of Doctor of Philosophy

October 2016

Department of Chemical and Biomolecular Engineering

The University of Melbourne

Abstract

Synthetic polypeptides are bioinspired mimics of natural polypeptides, readily prepared through controlled synthetic polymerization processes. Their use has offered chemists and biologists around the world the ability to precisely control the synthesis, scale-up, modification and engineering of polypeptides with properties similar to those seen in the natural world. The plethora of possible functionality gives synthetic polypeptides an array of properties shown to be highly useful in the biomedical and antimicrobial (bioactive) fields. Despite this, significant deficiencies surrounding the application of synthetic polypeptide materials in these fields remain. This thesis reports on the fabrication and testing of novel synthetic polypeptide and synthetic polypeptide-based materials to address deficiencies related to the application of synthetic polypeptides in nanoparticle drug delivery, cellular scaffolds for tissue engineering and antimicrobial materials for water treatment.

For drug delivery, investigations into the use of synthetic polypeptide-based nanoparticles for cisplatin delivery have traditionally focused on micelle assemblies. Different synthetic polypeptide-based self-assemblies such as vesicles offers the prospect of introducing a new biocompatible and biodegradable architecture for cisplatin delivery. In this study, the preparation of novel cancer-targeting synthetic polypeptide-based vesicles for cisplatin drug delivery is described. The vesicles were prepared through a novel drug-induced self-assembly process. Folic acid was conjugated to the vesicle corona to form an active targeting drug delivery system. *In vitro* studies on these targeted vesicles showed significantly higher cellular binding/uptake and dose-dependent cytotoxicity toward cancerous cells (HeLa) compared to non-cancerous cells (NIH-3T3). Next, preliminary studies into the preparation of aptamer (advanced targeting ligands composed of single strand nucleotides) targeted synthetic poly(L-glutamic acid)-based drug delivery systems was investigated. Poly(L-glutamic acid) or PLG, has

been utilized in a range of synthetic polypeptide-based drug delivery systems owing to its biocompatibility and favorable enzymatic biodegradability profiles. Whilst aptamers have been used as advanced targeting ligands in a wide range of polymeric nanoparticle drug delivery systems, they have yet to be investigated in delivery systems composed of PLG. Conjugation of a model single stranded DNA (ssDNA) aptamer to poly(ethylene glycol)-*b*-poly(L-glutamic acid) (PEG-*b*-PLG) block copolymers, common synthetic PLG-based nanoparticle precursors, was achieved through thiol-maleimide coupling chemistries and the conjugates successfully isolated through preparative gel electrophoresis. The DNA-polymer conjugation and isolation protocols established in this work offer potential use in future studies employing aptamer-targeting of PLG-based delivery systems.

For tissue engineering, the biocompatible, biodegradable and cell adhesive properties of synthetic polypeptides makes them useful materials for the fabrication of 3D polymeric hydrogels with macroporous morphologies ideally suited for cell in-growth. Traditionally, synthetic polypeptides have been used as partial components of these gel networks, and often require side-chain modifications to allow for cross-linking to take place, thus hindering the effective study of these materials as cellular scaffolds. In this study, macroporous hydrogels composed entirely of synthetic polypeptides were prepared through direct cross-linking of a single poly(L-glutamic acid)-*b*-poly(L-lysine) (PLG-*b*-PLL) polypeptide component under cryogelation conditions. Tuning the relative ratios of the amino acid constituents could result in cryogels with very different pore structures, swelling, and mechanical properties, suitable for a range of soft tissue engineering applications. These cryogels were shown to be enzymatically biodegradable and demonstrated excellent biocompatibility, cell attachment and cell proliferation profiles with mammalian fibroblast (NIH-3T3) cells.

The inherent antimicrobial (bioactive) properties of peptides are utilized in this study through the preparation of synthetic polypeptide-based cryogels with inherent antimicrobial (bioactive) properties, for potential water purification applications. Traditionally, the effective bioactive properties of antimicrobial

cryogels come from the incorporation of known antimicrobial agents to the gel structure rather than from the polymer itself. The leaching of these toxic agents is commonly reported in these systems, leading to potential toxicity issues. Cryogels composed of a polycationic poly(L-lysine) and hydrophobic poly(D,L-valine) copolymer were prepared with the gels displaying high swelling, and inherent antimicrobial activity against *E. coli* after brief 1 h exposure, with no toxic leaching. Compared to a conventional 'nanoporous' hydrogel, the cryogel macropores and their integrity were found to be crucial for bactericidal activity where they allow for effective uptake of bacteria into the gels, and provide a confined environment and increased surface area for contact of the bacteria with the antimicrobial polymer walls.

The materials prepared in this thesis and the study of their properties, demonstrate an advancement in the scientific understanding and applicability of synthetic polypeptides in the relevant biomedical and bioactive fields.

Declaration

This is to certify that

(i) this thesis comprises only my original work towards the PhD except where indicated in the Preface;

(ii) due acknowledgement has been made in the text to all other material used;

(iii) the thesis is less than 100,000 words in length, exclusive of tables, maps, bibliographies and appendices.

Steven Josef Shirbin

October 2016

Preface

Assistance with *in vitro* cell studies was given by Ms Fatemeh Karimi in **Chapter 4** and by Ms Shu Lam in **Chapter 5**

Acknowledgements

Completing my PhD and this thesis has been an incredibly challenging and rewarding experience. It goes without saying that the work presented in this thesis only describes a portion of my PhD journey. It fails to acknowledge the challenges, the sacrifices and most importantly, the support of the many people around me who have made the completion of this journey possible.

First and foremost, I would like to express my sincere gratitude to my supervisor, Professor Greg Qiao and acknowledge the guidance and support he has given me over my PhD journey; from his invaluable ideas on project direction, to getting me to see my work with a clear and rational mind. I would also like to thank him for his personal support and enthusiasm towards the completion of this thesis and for his help in improving my scientific communication skills throughout my PhD.

I would like to thank various members of the Polymer Science Group who have played a very supportive role through my PhD journey. To Dr. Adrian Sulistio, for his patience and unconditional support in teaching me the ropes of synthetic polypeptides and setting me on my way. To Dr. Paul Gurr, for the banter, the laughs and always helping to make things feel not-so-serious. To Dr. Qiang Fu, Prof. Mehmet Ozmen, Dr. Katharina Ladewig, Ms Shu Lam, Ms Fatemeh Karimi and Mr Nicholas Chan for all your collaboration, helpful advice and contribution to this work.

I would like to acknowledge the help and scholarship support of Dr. Xiaoqing Zhang from CSIRO, and the assistance of Prof. Wei Duan and Dr. Tao Wang from Deakin University for their help on projects that often did not work out, but kept on trying.

I am very grateful for receiving the generous financial support from the following agencies: The University of Melbourne Scholarship Office for the Australian Postgraduate Award; the CSIRO for the Postgraduate Studentship Award and scholarship top-up; the Melbourne School of Engineering for the Melbourne Abroad Travel Scholarship (MATS) which helped to support my travel to Macro 2016 (World Polymer Congress, Istanbul); and to the DAAD Germany International Exchange Service, for their generous financial support in my short visit and study at the University of Bayreuth.

Last but not least, I would like to thank my friends and family, whose love and support has been unbounded throughout my PhD. To my friends, for their mateship and their understanding through my somewhat inconsistent and inattentive presence over the duration of my studies. To my siblings, for their constant positivity and encouragement surrounding my work, and to my parents, for providing me with plentiful opportunities and for your endless support and generosity which cannot be sufficiently acknowledged in these words.

Publications

Peer-reviewed Journal Articles

Chapter 2

"Cisplatin induced formation of biocompatible and biodegradable polypeptide-based vesicles for targeted anticancer drug delivery"

Steven J. Shirbin, Katharina Ladewig, Qiang Fu, Molly Klimak, Xiaoqing Zhang, Wei Duan and Greg G. Qiao

Biomacromolecules, **2015,** 16, (8), 2463-2474.

Chapter 3

"Conjugation and isolation of a model DNA aptamer to poly(L-glutamic acid) -based delivery systems"

Steven J. Shirbin, Tao Wang, Wei Duan and Greg G. Qiao

Macromolecular Bioscience, **2016**. In Preparation.

Chapter 4

"Macroporous hydrogels composed entirely of synthetic polypeptides: biocompatible and enzyme biodegradable 3D cellular scaffolds"

Steven J. Shirbin, Fatemeh Karimi, Nicholas Jun-An Chan, Daniel E. Heath, and Greg G. Qiao

Biomacromolecules, **2016**, *17* (9), 2981-2991. (**Cover Article**)

Chapter 5

"Polypeptide-based macroporous cryogels with inherent antimicrobial properties: the importance of a macroporous structure"

Steven J. Shirbin, Shu J. Lam, Nicholas Jun-An Chan, Mehmet M. Ozmen, Qiang Fu, Neil O'Brien-Simpson, Eric C. Reynolds and Greg G. Qiao

ACS Macro Letters, **2016**, 5, (5) 552-557.

Chapter 4 Cover Art

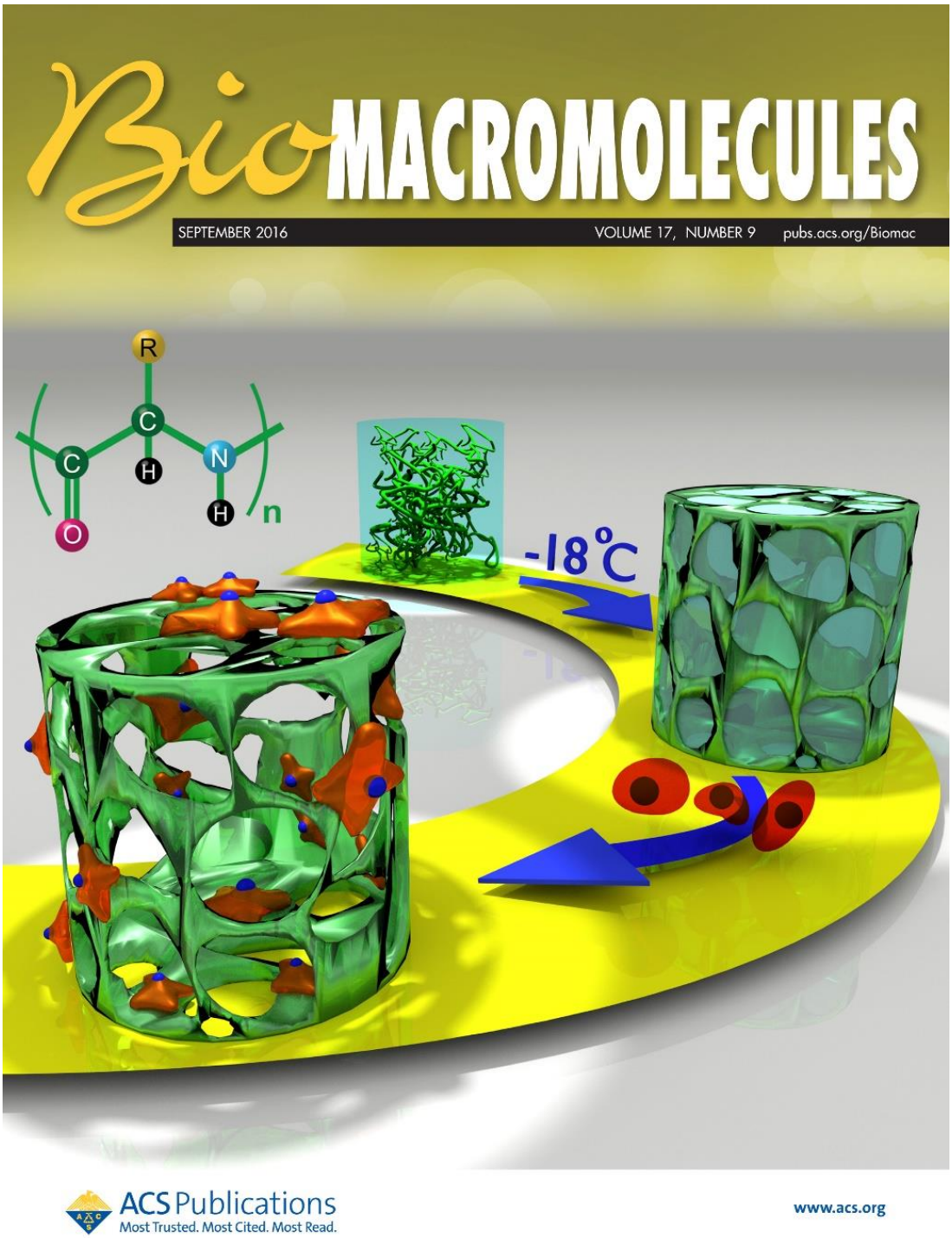

Conference Proceedings

"Amino acid-based star polymers for cancer therapy"

Steven Josef Shirbin, Adrian Sulistio, Anton Blencowe, Xiaoqing Zhang, Wei Duan, and Greg G. Qiao

- 34th Australasian Polymer Symposium Conference, (Darwin, Northern Territory, Australia), 7th – 10th July 2013 (Poster).

"Polypeptide-based block copolymer scaffold for targeted drug delivery"

Steven Josef Shirbin, Katharina Ladewig, Xiaoqing Zhang, Wei Duan, and Greg G. Qiao

- 35th Australasian Polymer Symposium Conference, (Gold Coast, Queensland, Australia), 12th-15th July 2015 (Oral).

"Macroporous hydrogels composed entirely of synthetic polypeptides: biocompatible and enzyme biodegradable 3D cellular scaffolds"

Steven Josef Shirbin, Fatemeh Karimi, Nicholas Jun-An Chan, Daniel E. Heath, and Greg G. Qiao

- 46th IUPAC World Polymer Congress (Macro 2016), (Istanbul, Turkey), 17th-21st July 2016 (Poster).

"Preparation and Antimicrobial Properties of Macroporous Polypeptide-based Cryogels"

Steven Josef Shirbin, Shu J. Lam, Nicholas Jun-An Chan, Mehmet M. Ozmen, Qiang Fu, Neil O'Brien-Simpson, Eric C. Reynolds and Greg G. Qiao

- 46th IUPAC World Polymer Congress (Macro 2016), (Istanbul, Turkey), 17th-21st July 2016 (Oral).

Table of Contents

List of Figures

Chapter 1

Figure 1.9. Poly(L-glutamic acid) dendrimer hybrid star polymer using 8-arm PAMAM dendrimer as initiator.

Figure 1.10. Structures of various active targeting ligands (A) folic acid (B) RGD peptide sequence (C) RNA aptamer (D) antibody.

Figure 1.11. Cell uptake and cytotoxicity of FA-conjugated vesicles. CLSM images of HeLa cells incubated with (A) FA-free (B) FA-conjugated Dox-loaded vesicles (C) free Dox. (D) Cytotoxicity of free Dox, FA-free and FA-conjugated Dox-loaded vesicles against HeLa cells at different Dox concentrations.

Figure 1.12. (A) Conjugation site of RGD to maleimide functionalities of PLG-*g*-PEG polymer. (B) *In vivo* tests showing metabolism of free drug (CDDP), RGD-free and RGD-conjugated nanoparticles into tumor tissue, with increased nanoparticle retention when conjugated to RGD-targeting ligand. Vitamin E conjugation used as hydrophobic segment to induce self-assembly.

Figure 1.13. Examples of cross-linking strategies used for macroporous hydrogel formation.

Figure 1.14. SEM micrographs of 3D macroporous hydrogels prepared from different porogens. (A) salt (NaCl) (B) gelatin.

Figure 1.15. (A) Agarose/alginate cryogels prepared from different polymer concentrations showing different pore sizes. (B) Water-saturated chitosan/gelatin cryogels showing elastic compression.

Figure 1.16. Fabrication of biodegradable macroporous gelatin cryogels for tissue engineering. (A) Synthesis of methacrylated gelatin followed by free radical polymerization to form cross-linked gels (B) *In vitro* enzymatic degradation in the presence of collagenase type II (C) SEM colored image of 3T3 mammalian fibroblast (red) cells on cryogel surface (grey) (scale bar= 10 μm).

Figure 1.17. (A) Formation of poly(L-lysine) incorporated macroporous hydrogels through use of porous salt-leached PLGA sponge as scaffold (B) Cross-section of hydrogel scaffold stained with FITC following reaction with poly(L-lysine) amine side chain. Scale bar = 100 μm (C) Intravital images of new vascular growth inside of hydrogels following *in vivo* studies. Scale bar = 50 μm.

Figure 1.18. (A) Pore size distribution of PLG/CS physically cross-linked gels with different freezing temperature (B) Proliferation curve of adipose-derived stem cells (ASCs) on scaffolds containing different PLG/CS molar ratios determined by DNA content (C,D) SEM images of gel cross-sections showing macropores.

Figure 1.19. (A) Typical structure of a methacrylated PLG used for radical polymerization cross-linking (B) Schematic representation of the radical copolymerization cross-linking of methacrylated synthetic PLG with HEMA (hydroxylethyl methacrylate) to form gels (C) SEM cross-section of cryogels prepared from different polymer concentrations.

Figure 1.20. Antibacterial peptide Polymyxin B structure, showing 5 amino groups (blue) from 2,4-diaminobutyric acid (Dab) amino acid residues as sites of cationic charge, with phenylalanine, leucine residues and a hydrocarbon tail (red) as the hydrophobic units.

Figure 1.21. (A) α-helical conformation of LL-37. (B) Schematic wheel plot showing amino acid distribution of cathelicidin LL-37 in α-helical structure. Most positively charged amino acids are localized to one side of the molecule, with hydrophobic amino acids located on the opposite side (amphipathicity).

Figure 1.22. Schematic of cell membrane structure in (A) Gram-negative and (B) Gram-positive bacteria.

Figure 1.23. Attachment and insertion of antimicrobial peptides into membrane bilayers to form pores by a 'barrel-stave' mechanism.

Chapter 2

Figure 2.8. (A) Cytotoxicity of CDDP-loaded vesicles towards HeLa cells incubated for 72 h. (B) IC_{50} values for free drug and CDDP-loaded vesicles. Data shown represents mean ± standard error.

Figure 2.9. Normalized UV-vis absorbance of FA- conjugated vesicles and FA-free vesicles (DI water).

Figure 2.10. (A) Cytotoxicity of CDDP-loaded, FA-conjugated vesicles towards HeLa (squares) and NIH-3T3 cells (circles) incubated for 72 h. X-axis normalized to Pt concentration. Lines show results of non-linear fit [log(inhibitor) vs. normalized response]. (B) Comparison of the IC_{50} values of the FA-conjugated vesicles in NIH-3T3 cells vs HeLa cells. (C) Control experiment comparing the IC_{50} values of free CDDP in the two cell lines. Data shown represents mean ± standard error.

Figure 2.11. Flow cytometry cell binding data of FITC-labeled CDDP-loaded FA-free and FA-conjugated vesicles to HeLa and NIH-3T3 cells after 24 h incubation. (A) Flow cytometry HeLa cell binding data (B) FITC mean fluorescence intensity (MFI) of HeLa and NIH-3T3 cells. Untreated cells used as controls. Δ represents change in MFI. Data shown represents mean ± standard error.

Figure 2.12. Confocal laser scanning microscopy (CLSM) images of HeLa (A-C) and NIH-3T3 cells (D-F) incubated with FA-free and FA-conjugated vesicle for 24 h (37 ^{o}C, 400, 000 cells/mL). Untreated cells used as controls. The vesicles were tagged with FITC (green), cell membrane was stained with CellMask Deep Red (red) and the cell nucleus with DAPI (blue) in all images. Scale bar = 10 μm.

Chapter 3

Figure 3.1. Agarose (2%) gels of DNA-polymer conjugations using the relevant FITC-labeled polypeptide-based copolymer. (A) **P4** (B) **P5**. Blue and red arrows indicate conjugate bands. ^{a} molar excess of polymer relative to DNA. RT = room temperature.

Figure 3.2. Top. Portion of preparative anionic exchange chromatogram of conjugation reaction mixture of thiol DNA and **P4**-FITC showing potential peaks of interest. Bottom. Agarose (2%) gel electrophoresis of anionic exchange peak fractions. DNA (L) = 100 bp DNA ladder.

Figure 3.3. Agarose (1%) gel electrophoresis of isolated DNA-polymer conjugates.

Figure 3.4. UV-Vis absorbance spectra of (A) DNA-**P4**-FITC and (B) DNA-**P5**-FITC isolated conjugates (DI water). Note: absorbance spectra not normalized for better identification of conjugate λ_{max} DNA absorbance at 260 nm.

Chapter 4

Figure 4.1. FT-IR spectra of cryogel A, copolymer A, EDCI and sulfo-NHS cross-linking agents. Note: amide I stretch in cryogel corresponding to both copolymer backbone and side chain (amide) cross-links.

Figure 4.2. FT-IR spectra of cryogel B, copolymer B, EDCI and sulfo-NHS cross-linking agents. Note: amide I stretch in cryogel corresponding to both copolymer backbone and side chain (amide) cross-links.

Figure 4.3. ESEM and CLSM images showing pore morphologies of non-labelled and FITC-labelled cryogels respectively. Images are of cross-sections in the x-y plane. ESEM images are of swollen cryogels (PBS) under low vacuum. CLSM images of cryogels swollen in PBS and z-stacked.

Figure 4.4. Pore size and pore wall thickness distributions of cryogel A and cryogel B obtained by analysis of CLSM images by ImageJ software.

Figure 4.5. Swelling and mechanical properties of cryogels; (a) Images of cryogels swollen to equilibrium in PBS (left cryogel A, right cryogel B), (b) equilibrium mass swelling ratios, (c) stress vs strain curves from compression tests and (d) Young's

Figure 5.2. (a) Reduction of excess glutaraldehyde cross-linker with 0.1 % w/v sodium borohydride. (b) ATR FT-IR of cryogel C washed in sodium borohydride showing absence of aldehyde peak.

Figure 5.3. ESEM characterization on the cross-sectional morphology of (i) cryogel A (ii) cryogel C (iii) cryogel D and (iv) control hydrogel.

Figure 5.4. Comparison of physical properties of cryogels and conventional hydrogel. (a) Mass swelling kinetics of dried cryogel and hydrogel in water (b) Stress vs. strain curve of gels subjected to compression tests. Note the purple arrow shows the point at which hydrogel started to fail/deform.

Figure 5.5. Photographs of control hydrogel (i-iii) and cryogel C (iv-vi) during mechanical testing.

Figure 5.6. Cytotoxicity evaluation of cryogel-conditioned medium using NIH-3T3 fibroblast cells. Error bars represent the standard deviation from the mean (n = 4).

Figure 5.7. (a) Schematic of method used to investigate the antimicrobial efficacy of polypeptide gels. (b) Log reduction and % kill of *E. coli* on polypeptide cryogels A, B, C and D, and the control hydrogel. Error bars represent the standard deviation from the mean ($n \geq 4$).

Figure 5.8. (a) Representative ESEM images of cryogel C after incubation with *E. coli* for 1 h, followed by vigorous flushing and agitation with saline buffer (0.9% NaCl solution). Note the red arrows indicate the *E. coli* cells (b) Viability of *E. coli* cells found in the 'supernatant' or saline buffer used to flush the gels (black bars) and cells entrapped in the gel (red bars) relative to the positive growth control. Cell viability was measured in terms of the absorbance at 490 nm using an MTS-based assay. Error bars represent the standard deviation from the mean (n = 4).

Chapter 6

Appendices

List of Schemes

Chapter 1

Chapter 2

Chapter 3

Chapter 4

Scheme 4.2. (a) Synthesis of PLG-*r*-PLL random copolypeptides and (b) their fabrication into synthetic polypeptide cryogels; (i) Random copolypeptide dissolved in DI H_2O, followed by addition of EDCI/sulfo-NHS then frozen at -18 °C for 24 h; (ii) gel is thawed at RT and washed thoroughly in DI water and PBS (pH= 7.4).

Chapter 5

Scheme 5.1. (a) Synthesis of PLL-*b*-PDLV block copolypeptide (**P1**), and (b) its fabrication into cryogels: (i) Block copolypeptide (**P1**) and glutaraldehyde cross-linker (CL) dissolved in PBS, then frozen at -18 ˚C for 24 h (ii) Gel is thawed at RT and washed thoroughly in DI water, $NaBH_4$ 0.1% w/v PBS (pH= 9.4), and PBS (pH= 7.4).

List of Tables

Chapter 1

Chapter 2

Chapter 3

Chapter 4

Chapter 5

List of Abbreviations

3D	three-dimensional
AANCA	amino acid *N*-carboxyanhydride
AFM	atomic force microscopy
AMM	activated monomer mechanism
AMP	antimicrobial peptide
ATR FT-IR	attenuated total reflectance fourier transform infrared
Bz	benzyl
CBz/Z	carboxybenzyl
CCS	core cross-linked star
CDDP	cisplatin
CFU	colony forming units
CL	cross-linker
CLSM	confocal laser scanning microscopy
CMC	critical micelle concentration
CS	chitosan
DA	Diels-Alder
DAPI	4′,6-diamidino-2 phenylindole
DCC	*N*,*N*′-dicyclohexylcarbodiimide
DCM	dichloromethane
DD	degree of degradation
DI	deionized water
DLC	drug loading content
DLE	drug loading efficiency
DLS	dynamic light scattering
DMAP	4-(dimethylamino)pyridine
DMEM	Dulbecco's modified eagle medium
DMF	*N*,*N*-dimethylformamide
DMSO	dimethyl sulfoxide

DNA	deoxyribonucleic acid
Dox	doxorubicin
DP	degree of polymerization
DTT	dithiothreitol
DVB	divinylbenzene
ECM	extracellular matrix
EDC/EDCI	*N*-(3-(dimethylamino)propyl)-*N*'-ethylcarbodiimide
EDTA	ethylenediaminetetraacetic acid
EGFR	epidermal growth factor receptor
EPR	enhanced permeability and retention
ESEM	environmental scanning electron microscope
FA	folic acid/facial amphiphilicity
FBS	fetal bovine serum
FITC	fluorescein isothiocyanate
Fmoc	fluorenylmethyloxycarbonyl
FR	folic acid receptor
FT-IR	fourier transform-infrared
Glu	glutamic acid
GPC	gel permeation chromatography
GSH	glutathione
HEMA	hydroxyethyl methacrylate
HCl	hydrochloric acid
HMDS	hexamethyldisilazane
ICP-OES	inductively coupled plasma-optical emission spectroscopy
kDa	kilodalton
kPa	kilopascal
Lys	lysine
Mal	maleimide
MFI	mean fluorescence intensity
MHz	megahertz
MI	macroinitiator
MIC	minimum inhibitory concentration

MWCO	molecular weight cut-off
NaCl	sodium chloride
NaOH	sodium hydroxide
NCA	*N*-carboxyanhydride
NHS	*N*-hydroxysuccinimide
NMR	nuclear magnetic resonance
NP	nanoparticle
PAsp	poly(aspartic acid)
PAMAM	poly(amido amine)
PBLG	poly(γ-benzyl-L-glutamate)
PBS	phosphate buffer saline
PEG	poly(ethylene glycol)
PDI	polydispersity index
PDA	phenylenediamine
PG-TXL	polyglutamic acid-paclitaxel drug conjugate
Phosgene	carbonyl dichloride
PLA	poly(lactic acid)
PLC	poly(L-cystine)
PLGA	poly(lactic-*co*-glycolic acid)
PLG	poly(L-glutamic acid)
PLL	poly(L-lysine)
PVA	poly(vinyl alcohol)
PZLL	poly(ε-carboxybenzyl-L-lysine)
RA	radial amphiphilicity
Retro DA	retro Diels-Alder
RGD	arginylglycylaspartic acid peptide
RM	reaction mixture
RNA	ribonucleic acid
ROP	ring-opening polymerization
RT	room temperate
SCM	side chain modified
SEC	size exclusion chromatography

SEM	scanning electron microscope
Sulfo-NHS	*N*-hydroxysulfosuccinimide sodium salt
ssDNA	single-stranded deoxyribonucleic acid
tBu	*tert*-butyl
TCEP	*tris*(2-carboxyethyl)phosphine
TEA	triethylamine
TEM	transition electron microscope
TFA	trifluoroacetic acid
TGA	thermogravimetric analysis
THF	tetrahydrofuran
TMS	trimethylsilyl
Triphosgene	*bis*(trichloromethyl) carbonate
TXL	paclitaxel
UV-Vis	ultraviolet-visible

List of Notations

b	block copolymer
brs	broad singlet (NMR)
co	copolymer
c_p	polymer concentration
d	doublet (NMR)
dd	doublet of doublet (NMR)
D_h	hydrodynamic diameter
Đ	polydispersity
E	Young's/elastic modulus (compressive)
ε	extinction coefficient (UV-Vis)
f	arm number
g	graft polymer
M_n	number-average molecular weight
m	multiplet (NMR)
P	porosity
Q_M	mass swelling ratio
Q_V	volume swelling ratio
r	random copolymer
s	singlet (NMR)
ss	single strand
t	triplet (NMR)
tert	tertiary
W_g	gel fraction
Z	carboxybenzyl (CBz)

1

Synthetic Polypeptides for Biomedical and Bioactive Applications

1.1 Background

Natural peptides and polypeptides (proteins) are copolymers of α-amino acids linked together through amide (peptide) bonds (**Figure 1.1**). The diverse (R group) functionality and ability to self-assemble into complex, highly ordered structures is responsible for their selective enzyme activity, bioactivity, and wide ranging signaling and mechanical properties inside of biological systems.[1-4] Their ability to biodegrade through proteolytic (enzymatic) processes plays an essential role in regulating various biological process including the immune response, metabolism and new tissue growth.[5-8] These remarkable polypeptide materials ultimately derive their properties from the precisely controlled sequences and compositions of their constituent amino acid monomers. Over the years, synthetic mimics of these polypeptides, known as synthetic polypeptides, have offered chemists and biologists around the world the ability to precisely control the synthesis, scale-up, modification and engineering of polypeptides with properties similar to those seen in the natural world.[9] The plethora of natural and modified amino acids available offers an endless array of chemical functionality, and the potential to build diverse synthetic polypeptide architectures for many applications.

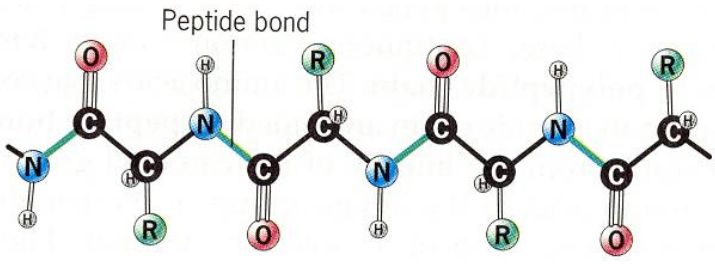

Figure 1.1 General structure of polypeptides.

It is for these reasons, that synthetic polypeptides have been utilized in fields such as drug delivery, as cellular scaffolds in tissue engineering and as bioactive materials for antimicrobial applications. With an ever increasing need for new, inexpensive and effective functional biomaterials for specified applications, the interest in the use of synthetic polypeptide materials in these fields are continually on the rise.

1.2 Synthetic Polypeptide Synthesis

In order to prepare synthetic polypeptide materials with complex and precise architectures, well-defined polypeptides of sufficiently large chain length and narrow chain length polydispersity (PDI) must be synthesized, thus requiring a controlled polymerization approach.[10-11] To enable sufficient use and analysis of such materials in a cost-effective way, a polymerization approach which offers 'scale up' capabilities is also desired. Compared to the lengthy and expensive solid phase peptide synthesis (SPPS) protocols, synthetic polypeptides (>30 amino acid residues) have traditionally been synthesized through the controlled and efficient ring-opening polymerization (ROP) of α-amino acid *N*-carboxyanhydrides (AANCA) monomers (**Figure 1.2**).[10, 12] AANCAs were first discovered by Leuchs in the early 1900s[13] with the polymerization of these monomers some years later lacking the control required to generate defined polypeptides. Deming in 1997 published the first well-controlled and living AANCA ROP using Nickel catalysts.[14] Since then, further significant improvements have allowed for the living polymerization of polypeptides with predicted MWs, narrow PDIs and in multi-gram scale.

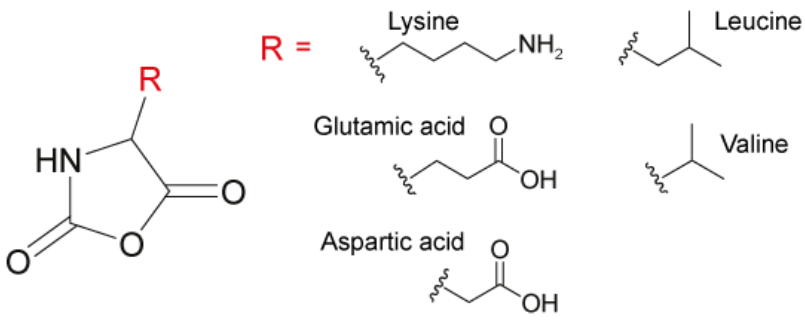

Figure 1.2 General chemical structure of α-amino acid *N*-carboxyanhydrides (AANCA) alongside some α-amino acid examples.

The benefit of using α-amino acid NCAs is two-fold: it blocks the amino group from reacting (thereby avoiding any side reactions with other NCA molecules) and the simultaneous activation of the carbonyl group to acylation, even at room temperature.[12] The popularity of ROP is attributed to the fact that it is not a radical-based technique and is consequently not sensitive to the presence of radical scavengers such as oxygen. It involves simple reagents and is able to prepare high molecular weight polymers in good yields and large quantities without racemization at the chiral centre.[10] Still to this day, NCA ROP remains the most common and reliable method of polypeptide synthesis. Whilst a number of synthetic polypeptides have been prepared using alternative approaches such as SPPS, references relating to synthetic polypeptides in this chapter almost exclusively refer to those polypeptides synthesized through NCA ROP.

1.2.1 α-amino acid *N*-Carboxyanhydride (AANCA) synthesis

Following the accidental discovery of α-amino acid NCAs by Leuchs, a preferred route to their synthesis was developed by Fuchs[15] and Farthing[16] known as the Fuchs-Farthing method which involved direct addition of phosgene gas (that acts as a carbonyl source) to α-amino acid solutions, transforming them directly into their NCA derivatives. However, this synthetic route is hampered by several problems. Besides the toxicity of the gas itself, phosgene is hard to handle which leads to complications in maintaining a balanced stoichiometric ratio. More often than not, phosgene is added in large excess which could possibly lead to the formation of undesired side reactions, affecting the subsequent ROP of AANCAs. As a result, phosgene derivatives such as triphosgene are now used instead. Triphosgene is available in a stable, crystalline solid form which overcomes the handling problems associated with phosgene gas. When added to α-amino acid solutions, triphosgene dissociates into three phosgene equivalents, which enables efficient synthesis of AANCAs (**Scheme 1.1A**).[17]

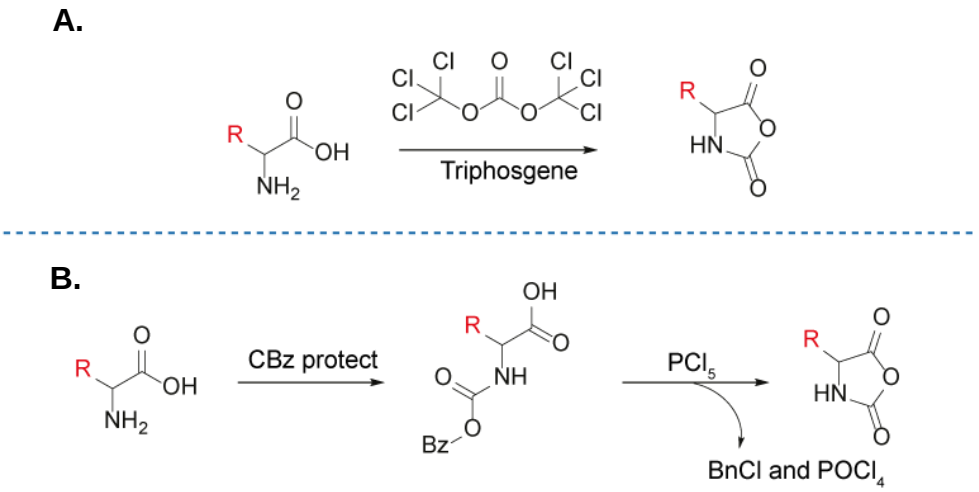

Scheme 1.1. Synthesis of AANCAs from their respective amino acids using (A) triphosgene and (B) phosphorus pentachloride (PCl_5).

Other synthetic pathways for the synthesis of AANCAs that avoid the use of phosgene have since been developed, and include the use of *bis*(2,4-dinitrophenyl)carbonate,[18] carbamoylation and nitrosation,[19-20] and the use of phosphorus halides such as phosphorus pentachloride (PCl_5) following amine protection with carboxybenzyl (CBz, Z) group. (**Scheme 1.1B**).[21-22]

Aside from the preparation and use of unmodified NCA monomers derived from conventional natural amino acid precursors (e.g. lysine, glutamic acid, cysteine), there has been a growing trend in the use of side chain modified (SCM) NCAs, which has greatly increased the range of NCA monomers and subsequent polypeptide side chain functionality.[23] For instance, a large range of saccharide (sugar)-modified NCA derivatives have been synthesized (**Figure 1.3A**) to prepare glycopolypeptides.[24-26] As well, a range of NCA monomers with alkene[27-29], alkyne [30-31] and halogen functionality [32-33] (**Figure 1.3**) have also been developed in recent years to enable efficient post polymerization modifications to the synthetic polypeptide side chain.

A notable disadvantage to the use of NCAs is their relatively high sensitivity to water, hindering the long term storage of these precursors and often requiring fresh batch synthesis before each ROP.[12, 34]

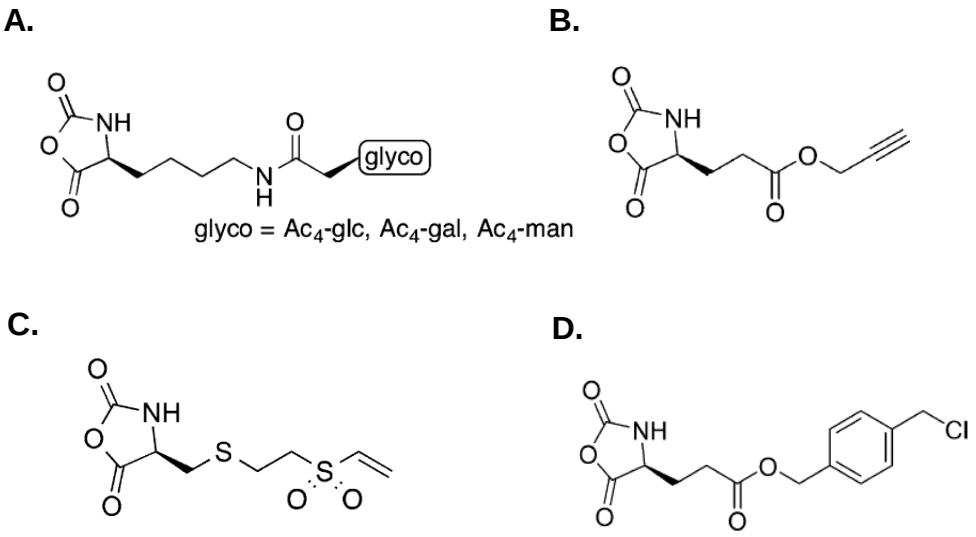

Figure 1.3. Structures of some side chain modified NCAs (A) saccharide (glyco) modified[26] (B) alkyne modified[30] (C) alkene modified [29] (D) halogen modified.[33]

1.2.2 Ring Opening Polymerization (ROP) of AANCAs

The controlled synthesis of polypeptides through the ROP of AANCAs occurs, as with other polymerization mechanisms, when the initiation step is faster relative to the subsequent propagation steps.[12] Selecting an appropriate initiator that promotes this fast initiation ensures that all growing chains are formed simultaneously and that a narrow distribution of polypeptide chain molecular weight is achieved.

In 1997, Deming reported on the first controlled living ROP of AANCAs using transition metal catalysts, overcoming commonly reported termination reactions and giving rise to well-defined synthetic polypeptides with narrow molecular weight distributions.[14] Prior to this work, the most widely used initiators for the ROP of NCAs were either nucleophilic (aliphatic primary amines) or basic (triethylamine or sodium methoxide) initiators, with primary amine initiators considered to give the best MW control at the time.[12, 34] Mechanistic studies on the use of amine initiators for ROP of AANCAs concluded on two competing mechanisms; namely the normal amine mechanism (NAM) and the activated monomer mechanism (AMM).[34] In the NAM mechanism, the initiation step

commences with nucleophilic attack of the initiator to the carbonyl of the NCA. Ring-opening of the AANCA, followed by decarboxylation, provides a free amino group on the ring-opened AANCA which promotes propagation (**Scheme 1.2A**). On the other hand, the AMM involves the deprotonation of an AANCA monomer by an amine initiator to generate an anion (**Scheme 1.2B)**. This results in a much faster propagation rate, and hence a lower rate ratio of initiation to propagation compared to the NAM, resulting in high molecular weight and broad PDI polypeptides.[34] Both mechanisms are thought to compete at various time points in any given reaction, subsequently hampering the controlled polymerization process.

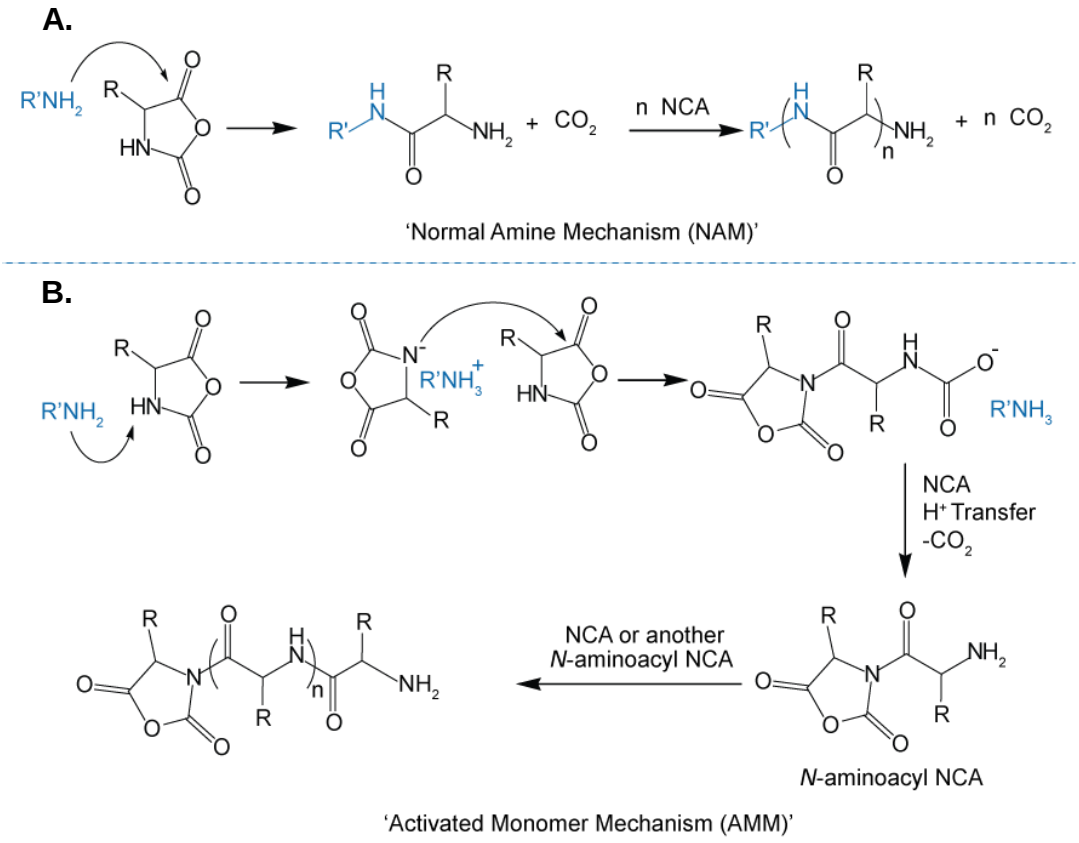

Scheme 1.2. Initiation and propagation of the ROP of AANCAs initiated by primary amines via (A) the normal amine mechanism (NAM) and (B) the activated monomer mechanism (AMM).

The difficulties in obtaining controlled polypeptides with low PDIs from primary amine initiators was overcome in the early 2000s, when Schlaad and coworkers

utilized simple amine hydrochloride salts as initiators.[35] The presence of the acidic hydrochloride reduces the chance of NCA anion formation in the system, hence avoiding the AMM mechanism (**Scheme 1.3**). The less nucleophilic "dormant" amine hydrochloride chain ends exist in a favored state of equilibrium with the free propagating amine, resulting in short lifetimes of reactive amine species. Increasing the temperature has been shown to increase the equilibrium concentration of the free reactive amine species,[34, 36] and therefore longer reaction times and higher temperatures are often required with this procedure.

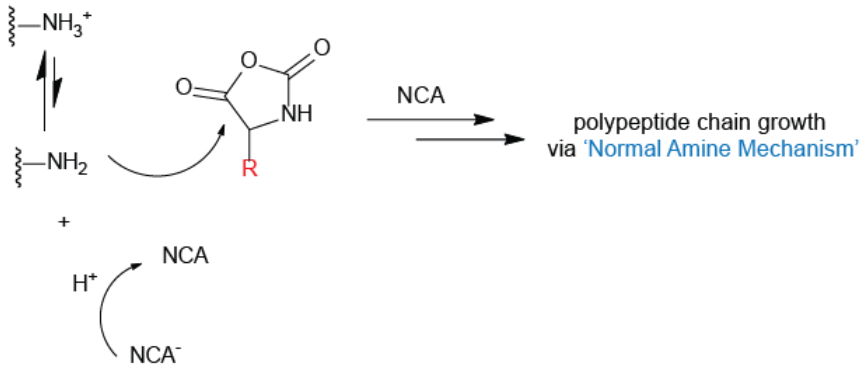

Scheme 1.3. Mechanism of ROP of AANCAs initiated by primary amine-hydrochlorides.

Other strategies for controlling NCA ROP using primary amine initiators have since been developed,[37] from extensive purification of reagents using high vacuum techniques,[38] to low reaction temperatures,[20] ammonium salts with non-nucleophilic tetrafluoroborate anions,[39] and use of N_2 flow in the reaction mixture.[40] In 2007, Lu and Cheng reported on the use of organosilicon amine (silazane) initiators for NCA ROP.[41-42] Using secondary amines hexamethyldisilazane (HMDS) and *N*-trimethylsilyl amine as initiators (**Scheme 1.4**), the controlled ROP of γ-benzyl-$_L$-glutamate NCA monomer into poly(γ-benzyl-$_L$-glutamate) (PBLG) was obtained at room temperature with expected MWs and low PDIs.[41-42] The study found that polymerization proceeded via a unique, trimethylsilyl carbamate propagating group through a single group transfer mechanism. This helped to eliminate the competing mechanisms that had previously hampered control using

primary amine initiators. The method was extended further to include a variety of TMS-derivatized primary amine initiators bearing different functional groups[42] and has recently been coupled with organocatalysts to accelerate the polymerization of less reactive NCA monomers.[43]

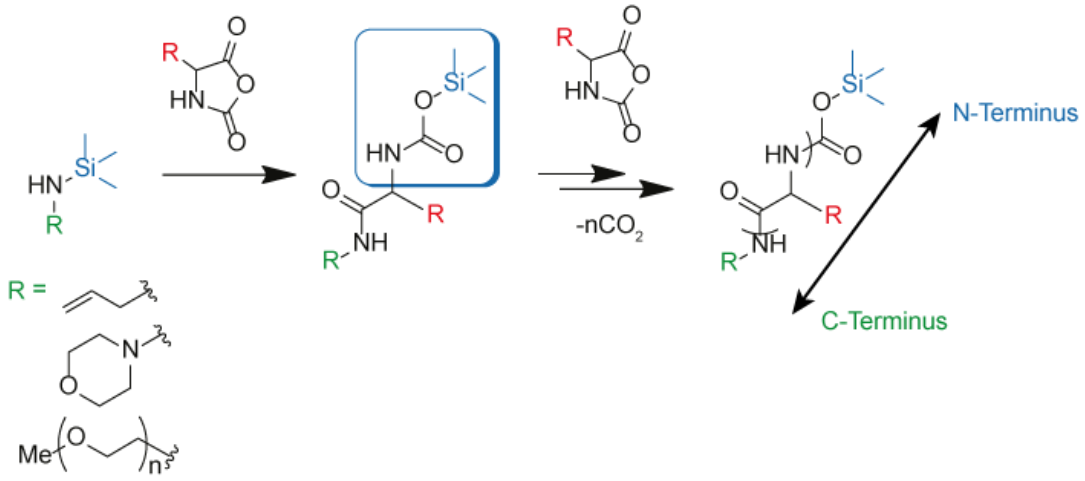

Scheme 1.4. *N*-trimethylsilyl amine initiated ROP of AANCAs through a TMS carbamate intermediate.

1.3 Synthetic Polypeptide Nanoparticles for Cancer Drug Delivery

Synthetic polypeptides have shown enormous potential in the drug delivery field, owing to their well reported biocompatibility and biodegradability properties. The wide range of potential chemical functionality instilled from their constituent amino acid monomers can result in their self-assembly into ordered nanostructures, and provide specific sites for direct attachment or charged-induced interactions with different drugs and biomolecules.[44-47]

Research into synthetic polypeptide-drug nanoparticles for cancer therapeutic drug delivery applications fundamentally follows from the general understanding around the benefits of polymer-drug conjugates over conventional free drug treatments. Conventional low molecular weight hydrophobic anticancer drug molecules, (e.g. doxorubicin, paclitaxel, cisplatin), have traditionally shown low accumulation of

drug inside tumor cells due to their non-selective uptake into solid tumors and their relatively quick clearance out of the body by the kidneys.[48] This results in commonly reported widespread toxicities and ineffective treatment regimens when in use.[49-51] Nanosized carriers, or nanoparticles (NPs) such as micelles, vesicles and star-shaped polymers, offer the prospect of improving small molecule drug delivery by exploiting a particular property of tumors of what is known as the EPR (enhanced permeability and retention) effect.[52-55] Tumors are typically in a state of leaky vasculature, due to large gaps in the endothelial cells of tumor blood vessels (fenestration). Accompanied by the poor the lymphatic drainage around tumor sites, the resulting pressure difference across the tumors allows for macromolecules >20 kDa ranging in size from 10 nm to 200 nm to preferentially accumulate and be retained in the tumors (**Figure 1.4**).[48, 53, 56-57]

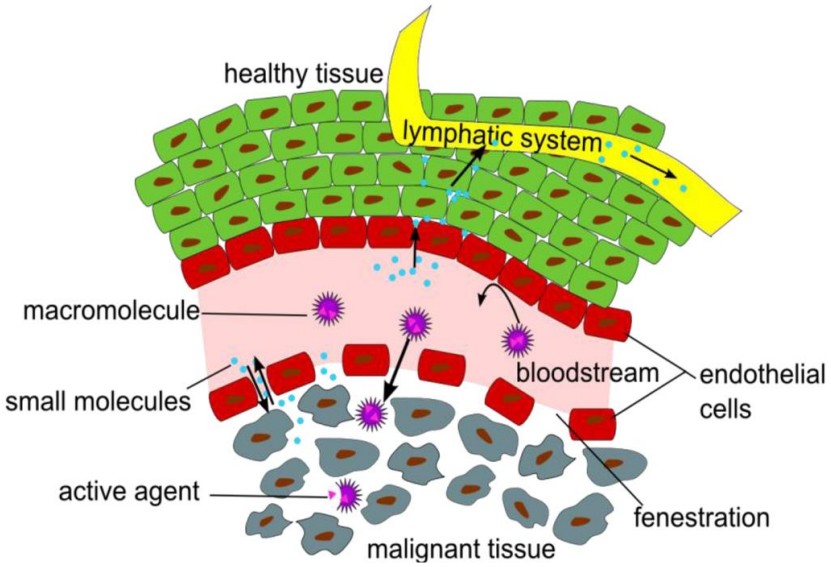

Figure 1.4. Illustration of the Enhanced Permeation and Retention (EPR) effect of macromolecular structures as drug delivery systems in malignant tissue.[58]

This EPR effect is essentially a passive targeting system for accumulation of nanoparticles into the tumor mass, and has been attributed to reduced systemic toxicities compared to the free drug.[55, 59] Nanoparticles are able to achieve an optimal EPR effect if they can evade the immune response, avoid widespread organ uptake, and remain highly stable in the blood stream until reaching the tumor site.[48,

[60] These biological barriers are seen to be best overcome using nanoparticles around 100 nm in size and neutral or slightly anionic in surface charge.[48, 61] To help avoid uptake of nanoparticle by macrophages, particularly in the liver, surface functionalization of nanoparticles with components such as poly(ethylene glycol) (PEG) is commonly employed. This 'PEGylation' strategy forms a hydrating layer that in turn hinders protein adsorption and subsequent recognition by macrophages of the mononuclear phagocyte system (MPS).[62-63]

The most successful of the polypeptide-drug conjugates used thus far have been in the form of linear and block copolymers, the last of which can result in self-assembly of the polypeptide into micelle and vesicle spherical nanoparticles.[64] More recently, nanoparticles comprised of synthetic polypeptides and of higher architectural complexity have been prepared in the hope of improving on these existing systems. They include layer-by-layer nanocapsules incorporating polypeptide layers,[65-66] highly branched macromolecular architectures including dendrimer-based hybrid star polymers[67-68] and more recently, polypeptide-based core cross-linked star polymers.[69]

1.3.1 Linear systems

It is not surprising that the initial focus on synthetic polypeptide-drug conjugates focused on the simple linear homopolypeptide systems. In the early 1980s, Zunino and coworkers developed poly(L-aspartic acid) (PAsp) conjugates of daunorubicin and doxorubicin, demonstrating significantly reduced toxicities and a greater therapeutic effect than free drug.[70-72] Some years later, poly(L-glutamic acid) (PLG) came to be investigated in a range of highly promising polymer-drug conjugate systems.[73-74] The highly biocompatible and effective biodegradable profiles of PLG have been utilized in the formation of paclitaxel poliglumex (PG-TXL, PPX),[75] (**Figure 1.5**) otherwise known as Xyotax, the first biodegradable drug conjugate to make it to clinical trials. PG-TXL, a 39 kDa covalent conjugate of linear poly(L-glutamic acid) and the commonly used chemotherapeutic drug paclitaxel, has undergone phase 3 clinical trials for the treatment of lung and ovarian cancers and

has been considered one of the most successful drug–polymer conjugate to date.[57, 76-78] The drug is conjugated via an ester bond to the carboxylic acid side chain of PLG (**Figure 1.5**). Recently, it has been designated as an orphan drug in combination with radiotherapy for the treatment of glioblastoma multiforme (GBM).[79] The biocompatible properties of PG-TXL and its ideal molecular weight and size for exploiting the EPR effect gives it a recommended drug equivalents dosage almost twice as that of free paclitaxel.[57] Cathepsin B, a lysosomal protease, plays a key role in the lysosomal degradation of PLG, and has shown to be directly involved in the release of paclitaxel from the conjugate.[76, 80-81] The upregulation of cathepsin B in certain malignant tumors offers the prospect of selective polymer degradation and drug release from the conjugate near the tumor site.[82-83] The use of linear PLG in a range of other polymer-drug conjugates has been reported and have shown promising results.[84-85]

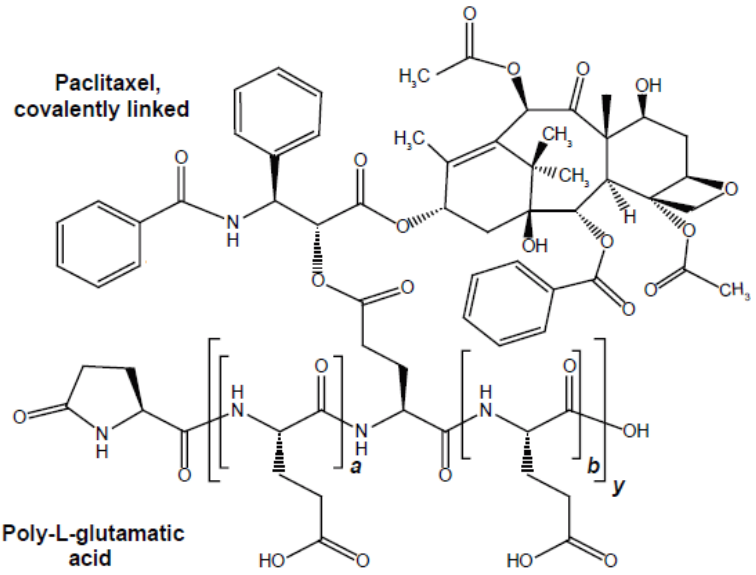

Figure 1.5. Structure of paclitaxel poliglumex (PG-TXL). Paclitaxel is conjugated by ester linkage to the *γ*-carboxylic acid side chains of poly(L-glutamic acid). Conjugated paclitaxel represents approximately 36% by weight of PPX, equivalent to about one paclitaxel ester linkage per 11 glutamic acid units.[76]

1.3.2 Micelle/vesicle systems

The self-assembly of amphiphilic block copolymers composed entirely or partially of synthetic polypeptides into defined nanoparticle assemblies such as micelles and vesicles **(Figure 1.6**), has been studied considerably in the drug delivery field.[64, 86]

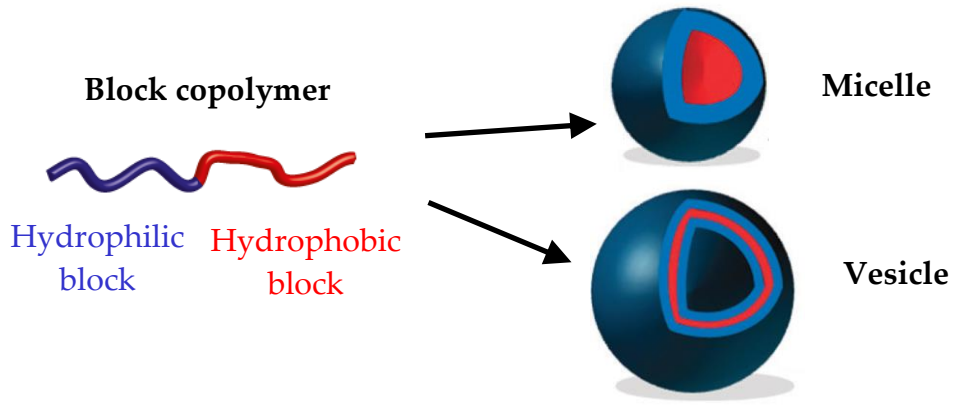

Figure 1.6. Self-assembly of block copolymers into micelle and vesicle, adapted from Fuks *et al*.[64]

Micelles are the simplest form of nanoparticle assemblies created by the self-assembly of amphiphilic block copolymers into spherical nanoparticles with hydrodynamic diameters generally between 10-100 nm.[87-88] During self-assembly, the non-soluble segments of the block copolymer associate together into a core suitable for hydrophobic drug loading and stabilized by a surrounding shell of soluble segments. Vesicles are another form of block copolymer self-assembly that consist of a hydrophobic polymeric layer (membrane) surrounding a reservoir or cavity, with both regions suitable for drug encapsulation.[89-90] Vesicles are typically in the size range of 100-300 nm and due to their larger structure can encapsulate a larger amount of drug compared to micelles, thus reducing the amount of delivery vehicles required while achieving similar drug dosages.[90] The self-assembly of block copolymers composed entirely out of polypeptides into vesicles has been reported by Deming and co-workers. Using charged poly(L-lysine), poly(L-arginine) or poly(L-glutamic acid) as the hydrophilic block and poly(L-leucine) as the hydrophobic block, vesicle formation could be achieved (**Figure 1.7**).[91-92] It was found that the

use of a large hydrophilic block relative to a short α-helical hydrophobic block could favor the formation of these vesicles. Lecommandoux and co-workers have also demonstrated the successful preparation of vesicles from zwitterionic poly(L-glutamic acid)-*b*-poly(L-lysine) block copolymers, with pH responsive assembly.[93]

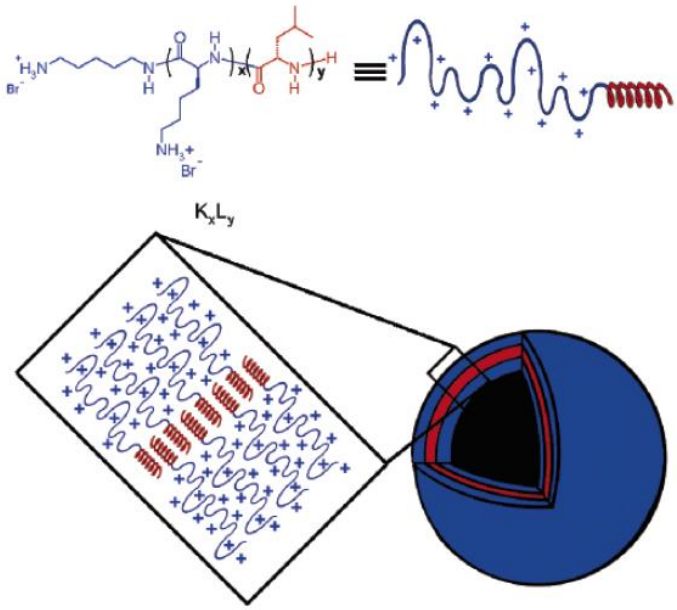

Figure 1.7. The proposed self-assembly of poly(L-lysine)$_{60}$-*b*-poly(L-leucine)$_{20}$ block copolymers into vesicles.[91]

However, a large number of synthetic polypeptide nanoparticle delivery systems in the literature have been prepared from polypeptide-based copolymers, containing synthetic hydrophobic polypeptide blocks, such as side-chain protected poly(L-aspartic acid), poly(L-glutamic acid) or poly(L-leucine) and non-polypeptide hydrophilic blocks, such as PEG.[46, 94] For example, Deming and co-workers demonstrated the successful vesicle formation of PEG-modified poly(L-lysine) (hydrophilic) and poly(L-leucine) (hydrophobic) block copolymers.[95] Early works by Kataoka *et al*. report on the formation of micelles from poly(γ-benzyl-L-aspartate) (PBLA) coupled to PEG for drug delivery applications.[96] The PBLA, acting as a biodegradable hydrophobic segment, could result in self- assembly of the copolymer and encapsulate drug in the hydrophobic core. Ding[97] and Hua[98] have reported on

the use of poly(L-leucine)-*b*-PEG-*b*-poly(L-leucine) triblock copolymer micelles respectively as drug delivery vehicles.

The conjugation/coordination of drug to a polypeptide block can itself result in sufficient copolymer amphiphilicity and therefore self-assembly to take place. This effective drug-induced self-assembly was pioneered by Kataoka and co-workers who used block copolymers consisting of PEG and poly(L-glutamic acid) or poly(L-aspartic acid) that self-assemble into micelles after conjugation or coordination of hydrophobic anticancer drugs such as doxorubicin and platinum-based cisplatin (or CDDP) to the polypeptide carboxylate side chains (**Figure 1.8**).[46, 99-102]

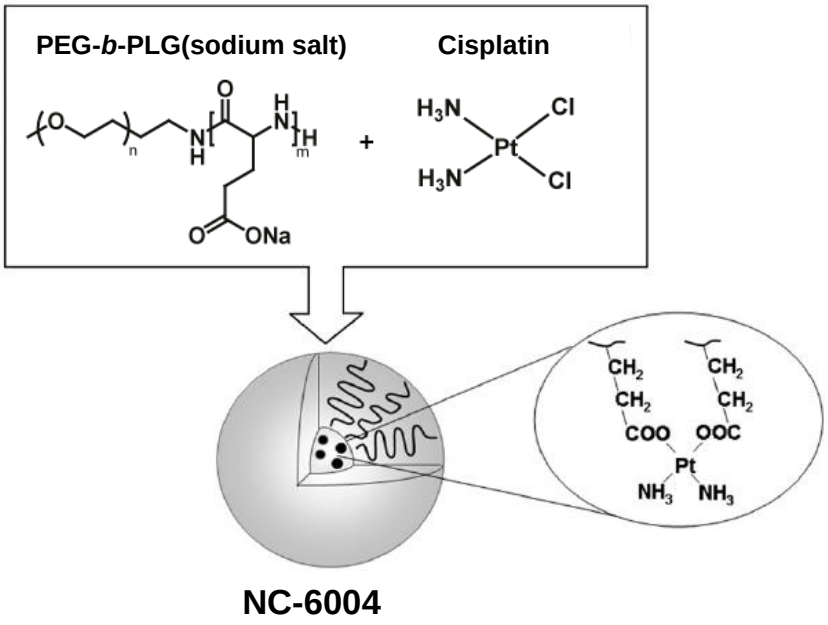

Figure 1.8. Chemical structures of PEG-*b*-poly(sodium-L-glutamate) block copolymer and CDDP, and resulting micellar structures after coordination of CDDP to the polypeptide side chain (NC-6004). Adapted from Kataoka *et al*.[101]

Several of these platinum-based anticancer drug nanoparticle delivery systems have shown very promising *in vivo* results, in particular NC-6004, a micellar nanoparticles system composed of PEG-*b*-poly(L-glutamic acid) block copolymer with cisplatin coordinated to the poly(L-glutamic acid) carboxylate side chains

(**Figure 1.8**). NC-6004 has displayed significantly reduced neurotoxicity and nephrotoxicity compared to free drug and is currently in wide- spread clinical trials for pancreatic, head and neck, and lung cancers.[46, 103-104]

1.3.2.1 Nanoparticle bio-stability and drug release

The bio-stability of self-assembled nanoparticles is an important requirement to ensure sufficient blood circulation of the nanoparticles and sufficient therapeutic effects. The use of a PEG hydrophilic block to induce self-assembly of copolymers ensures that it is located on the periphery of the nanoparticle to perform its role as a stealth layer to macrophage uptake, and therefore improve the blood circulation time of the nanoparticle, as discussed previously.[48] However, for micelles and vesicles that are susceptible to dissociation under sheer or dilution below the critical micelle concentration (CMC), the bio-stability of the nanoparticle must be thoroughly considered.[45] For instances where hydrophobic drug loading is performed through encapsulated to the hydrophobic regions of the nanoparticle via physical interactions, uncontrolled dissociation of the nanoparticle can result in burst release of drug payloads to non-targeted areas. A range of cross-linking strategies have been devised when using polypeptide-based micelles and vesicles, to prevent these self-assemblies from uncontrolled dissociation. For micelles, cross-linking can take place either in the shell or core whereas for vesicles, cross-linking of the polymeric membrane commonly takes place.[45, 105-107] Deming[108] and Sulistio[109] reported separately on the preparation of vesicles containing DOPA residues on diblock copolypeptides which could effectively undergo vesicle membrane cross-linking under oxidative conditions, resulting in increased nanoparticle stability.

The introduction of stimuli-responsive cross-linking strategies has allowed these stabilized-assemblies to cleave under conditions representative of the intracellular environment, to result in triggered release of drug payloads at the tumor site.[45, 107] For instance, Lee and coworkers prepared robust polymer micelles composed of PEG-*b*-poly(L-aspartic acid)-*b*-poly(L-phenylalanine) with reaction of acid-labile

ketal-containing cross-linkers with the aspartate residues. Encapsulated doxorubicin (Dox) showed rapid endosomal release at endosomal pH (pH 5) compared to physiological pH (pH 7.4) (**Scheme 1.5**).[110]

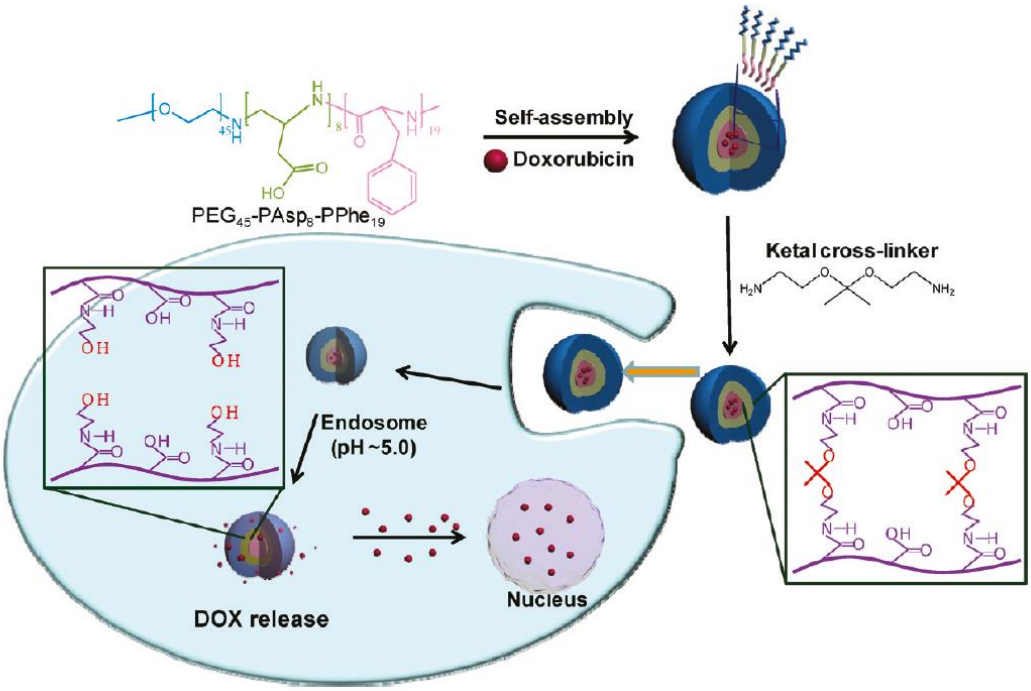

Scheme 1.5. Illustration of shell cross-linking of doxorubicin-loaded polymer micelles with a pH-labile ketal cross-linker and intracellular release triggered by endosomal pH.[110]

Ren *et al.* have reported on 'sheddable micelles' using a reduction-sensitive cystamine-conjugated PEG, to initiate the ROP of leucine NCA. The micelle shells can detach in a reductive environment, representative of intracellular conditions, resulting in accelerated release of encapsulated doxorubicin.[111] Recently, stable polypeptide micelle systems have been developed without cross-linking, utilizing pH charge reversal capabilities to exploit the effect of charge on nanoparticle stability and delivery.[112-113] Using modified synthetic polypeptides, the charge of the micelle can reverse from an initial negative charge of the micelle in the blood stream (to avoid nanoparticle-protein interactions) to a positive charge near or inside the acidic cellular environment to result in improved nanoparticle delivery and uptake.

A range of other micelle/vesicle cross-linking strategies including photo-responsive cross-linking have been employed to enhance their biostability and control drug release.[45]

The conjugation/coordination of drug to polypeptide-based nanoparticles offers another level of control over the drug release process. This strategy reduces the risk of systemic burst drug release compared to the drug encapsulation strategies described earlier and has an obvious benefit over conventional drug therapies by achieving vastly greater drug loads on a per molecule basis. Due to the large range of functionalities that can be obtained with a polypeptide block, the attachment of drugs onto the polypeptide side chain can be made through direct covalent conjugation, or through stimuli responsive linkers (e.g. acid-labile hydrazone) for selective intracellular drug release.[114-116] As mentioned previously, covalent conjugation of paclitaxel to poly(L-glutamic acid) through ester linkages was used in the preparation of PG-TXL in the late 1990s, a promising drug delivery candidate.[75-76] Although this ester linkage is somewhat acid labile, drug release is strongly mediated through enzymatic degradation of the polypeptide by endosomal lysozymes which are upregulated in cancer cells.[77, 80-81] The attachment of drugs or bioactive compounds to linear poly(L-glutamic acid) via acid-labile hydrazone linkages by Hurwitz[117] in 1980 then Hashida[118-119] in the late 1990s, demonstrated good therapeutic profiles due to controlled cargo release. In 2008, Guan and co-workers reported on the synthesis of a PEGylated peptide-targeted poly(L-glutamic acid) copolymer (15 amino acid residues) with doxorubicin conjugated to the polymer side chain through hydrazone linkages. Payloads of four doxorubicin molecules per polymer unit were achieved and the drug shown to release effectively in intracellular acidic conditions whilst remaining stable under systemically neutral conditions.[115] Mentioned previously, the coordination of cisplatin drugs to block copolymers composed of PEG and carboxylate-containing synthetic polypeptides have been used to prepare effective micelle drug delivery systems (**Figure 1.8**).[46, 101] Sustained and controlled drug release profiles from the micelles is observed in these systems due to controlled ligand exchange of the platinum-polymer (carboxylate) complexes with chloride ions present in physiological medium.[101, 120-

[123] An additional benefit of cisplatin coordination to poly(L-glutamic acid) side chains is the suspected interpolymer cross-linking that can occur due to the two coordination sites of cisplatin, thereby increasing the micelle stability.[104]

1.3.3 Star-shaped systems

Star-shaped polymers are macromolecular structures, typically of nanoscale size consisting of several linear chains linked to a central core, forming 3D globular structures.[69] They can be tuned to a variety of size regimes by varying the core density and arm length, and can be functionalized at any point of the architecture (core, inner arms, arm periphery).[124-126] They can also combine the advantages of polymeric micelles by providing enhanced encapsulation capabilities for hydrophobic drugs in the core[127-129] whilst avoiding issues associated with the sudden dissociation below the critical micelle concentration (CMC) of polymeric micelles.[130-131] As a result, star-shaped polymers have gained significant attention in the polymer therapeutic field as potential drug delivery vehicles.

There are three prevalent methods for constructing star-shaped polymers: grafting-from (core-first), grafting-to, and grafting-to/from (arm-first) approaches. Both the core-first and arm-first approaches (**Scheme 1.6**), [132] will be discussed below.

1.3.3.1 Core-first approach

The 'core-first' (grafting-from) approach involves the use of multifunctional initiators as the core to initiate the polymerization of monomers to form the star-like arms (**Scheme 1.6A**). This method allows for the preparation of star polymers with a precise number of arms, in high yields and ease of isolation from the crude reaction material.

The first successful synthesis of functionalized polypeptide-based star polymers from primary amine-terminated multifunctional initiators was reported by Inoue *et al*. who reported the synthesis of six-armed stars, poly(γ-benzyl-L-aspartate) and poly(γ-benzyl-L-glutamate) using 6 arm amino functionalized initiators.[133] Recently,

Duro-Castano and coworkers developed 3-arm star-shaped poly(L-glutamic acid) (PLG) stars from a range of central core initiators.[134] The star polymers were shown to effectively degrade enzymatically by cathepsin B and demonstrated a 3-fold increase in cell uptake of the star compared to linear PLG with similar MW. The star shaped polymers also demonstrated longer retention times and greater distributions *in vivo* compared with linear PLG.[134]

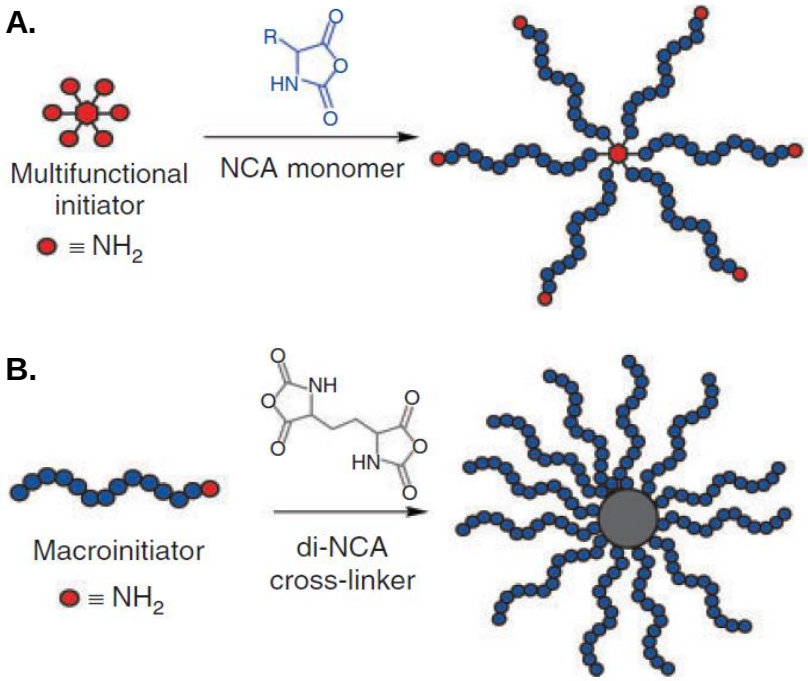

Scheme 1.6. Synthetic approaches for the preparation of polypeptide-based star polymers via (A) core-first and (B) arm-first approaches, adapted from Blencowe *et al.*[132]

The use of branched primary amine-terminated initiators known as dendrimer initiators, has allowed for the preparation stars with more than 20 arms These dendrimer initiators have been shown to initiate the ROP of AANCA monomers to form polypeptide-based star polymers with a dendrimer core known as 'dendrimer hybrid star polymers' **(Figure 1.9)**.[68, 135-136] The highly branched structure and the presence of successive generations provide a higher molecular weight core and a higher number of arms than stars synthesized from conventional 'core-first'

multifunctional initiators. Poly(amido amine) (PAMAM) dendrimers are a commonly employed initiator, and have been used to prepare a raft of well-defined hybrid star polypeptides by ROP initiation of *γ*-benzyl-L-glutamate NCAs.[135, 137-138] Tansey and coworkers have synthesized biodegradable branched poly(L-glutamic acid) centered around a PAMAM dendrimer core **(Figure 1.9**). The star polymers

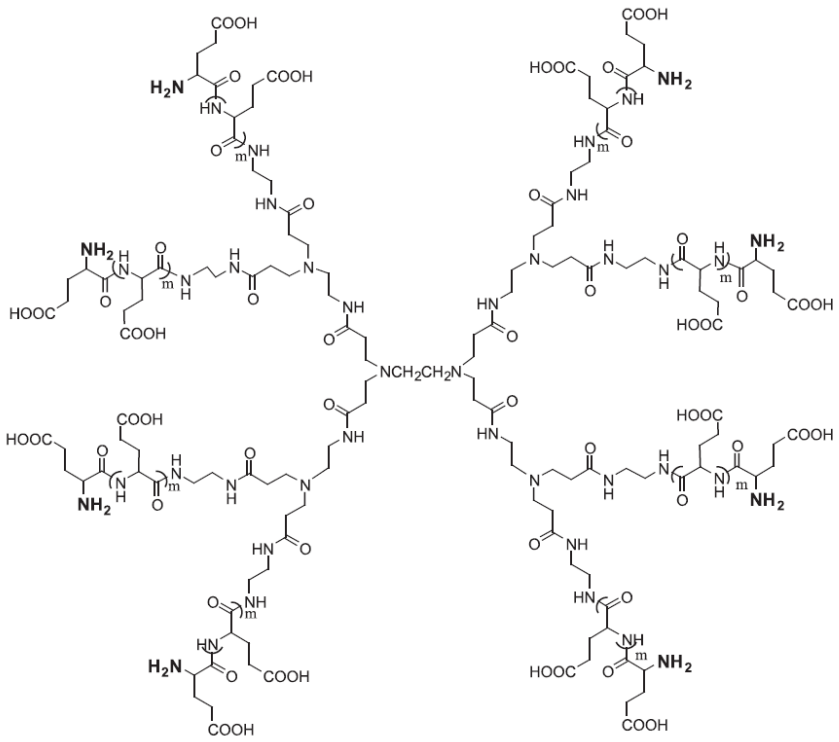

Figure 1.9. Poly(L-glutamic acid) dendrimer hybrid star polymer using 8-arm PAMAM dendrimer as initiator.[135]

were shown to successfully degrade in the presence of lysosomal enzyme cathepsin B. Folic acid, a tumor targeting ligand, was conjugated to the periphery of these stars, and dye conjugated to the glutamic acid side chains, with *in vitro* analysis showing selective uptake of the stars into tumor cells.[135] Covalent drug loading to these hybrid star polymers was demonstrated by Kono and coworkers in 2008 with the conjugation of doxorubicin to a single L-glutamic acid residue residing in-between the dendrimer core and PEG grafts on each star arm. Drug was conjugated to the glutamic side chain through an acid-labile hydrazone linker and demonstrated selective drug release under endosomal acidic (pH 5.5) conditions.[67]

1.3.3.2 Arm-first approach (CCS)

Both the 'core-first' and 'grafting-to' approaches render stars with limited core sizes which can impact the potential of drug encapsulation in the star core. This problem of limited core size can be overcome by using an 'arm-first' approach, through use of a macroinitiator (arm) to initiate the polymerization of a cross-linkable monomer, forming a densely cross-linked star core (**Scheme 1.6B)**. These polymer architectures are generally referred to as 'core cross-linked star' (CCS) polymers.

CCS polymers synthesized by the 'arm-first' approach (**Scheme 1.6B)** were first reported by Zilliox *et al*. in 1968[139] and involved the use of anionic polymerization of polystyrene (PSt) with divinylbenzene (DVB). CCS polymers composed entirely of synthetic polypeptides via an arm-first approach was reported by Sulistio *et al.* in 2011 (**Scheme 1.7**).[140] Using a one pot-strategy, an amine *N*-TMS initiator was added to a NCA monomer solution to generate a polypeptide macroinitiator (MI). The MI was then used to polymerize L-cystine, a di-NCA cross-linker, to generate the densely cross-linked CCS polymers. These star polymers were composed of poly(L-lysine) (PLL) or poly(γ-benzyl-L-glutamate) arms radiating from a reductive-labile poly(L-cystine) (PLC) core. The CCS could be core-functionalized via reaction with primary amines bearing different functional groups (e.g., pyrene, alkyne), and deprotection of the side-chains yielding water soluble, biocompatible, and biodegradable star polymers (**Scheme 1.7**).[140-141] The stars were also capable of sequestering hydrophobic drugs, such as the anti-cancer drug pirarubicin through physical interactions (e.g. π– π stacking) with a pyrene-functionalized core.[140]

The potential to conjugate molecules/drugs to the CCS arms via acid-labile linkers was also demonstrated, with deprotection of the PBLG arms by hydrazine generating hydrazide functionalities suitable for the conjugation of drugs through acid-labile hydrazone bonds. However, the loading and release of drugs to these hydrazide functionalities were not tested.[141]

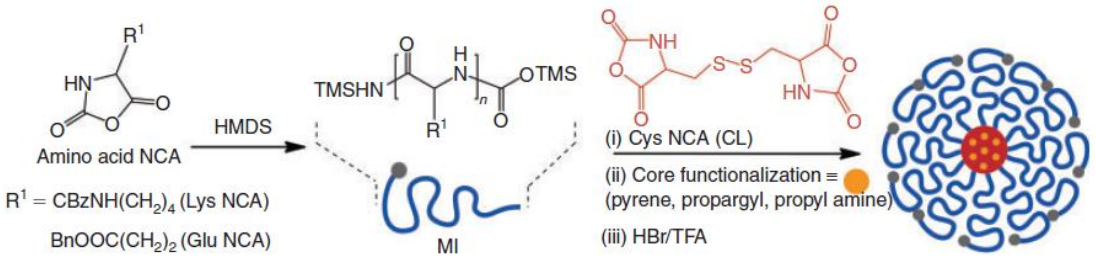

Scheme 1.7. Synthesis of CCS polymers composed entirely of synthetic polypeptides. Adapted from Sulistio *et al.*[140]

Shortly after, Xing *et al*. synthesized polypeptide-based CCS nanogels via ROP of PBLG and L-cystine NCA monomers using PEG-NH_2 as macroinitiator (**Scheme 1.8)**.[142] The CCS consisted of PEG arms and a densely packed core containing PBLG cross-linked with poly(L-cystine). The stars demonstrated high drug loading through core encapsulation of drug indomethacin, and the release of drug enhanced through cleavage of the core disulfide bonds by glutathione (GSH) reducing agent.[142] *In vitro* studies showed that the stars were biocompatible, however no *in vitro* studies of the drug-loaded nanogels were performed.

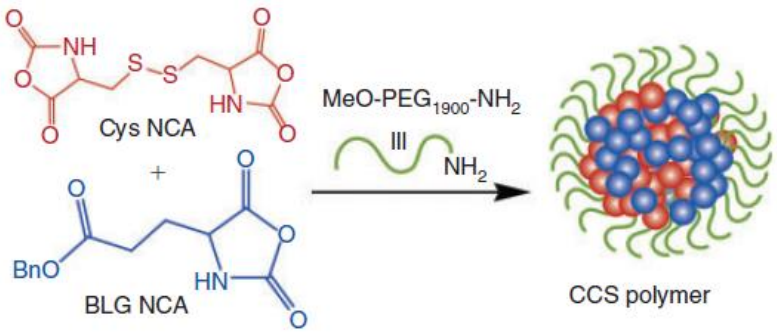

Scheme 1.8. Synthesis of CCS polymers (or nanogels) via ROP of L-cystine and γ-benzyl-L-glutamate NCA derivatives using PEG-NH_2 as macroinitiator. Adapted from Xing *et al.*[142]

1.3.4 Active targeting of polypeptide-based drug delivery systems

The majority of the drug delivery systems discussed thus far, are designed to preferentially accumulate in tumor tissues through passive targeting, namely via the

EPR effect as discussed above. The ability to actively target these delivery systems to cancerous cells specifically, offers the prospect of improved drug delivery efficiencies and a further reduction in side effects. Active targeting involves the incorporation of ligands to the delivery system. These ligands have specific recognition for a target substrate, commonly an overexpressed receptor or antigen on the surface of diseased cancerous cells, resulting in internalization of the delivery system often through receptor mediated endocytosis.[143-146]

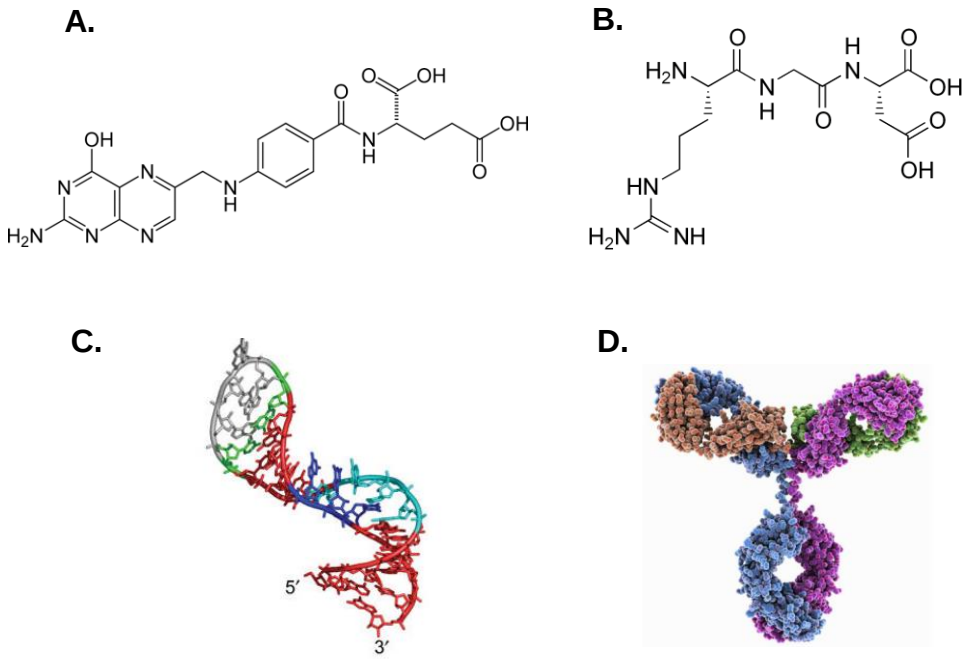

Figure 1.10. Structures of various active targeting ligands (A) folic acid (B) RGD peptide sequence (C) RNA aptamer (D) antibody

Examples of active targeting ligands include small molecules such as sugars, and vitamins (e.g. folic acid), to highly selective targeting ligands such as peptides (e.g. RGD sequence), antibodies and DNA/RNA aptamers (**Figure 1.10**). [144]

The use of these ligands to actively targeted NPs has long been envisaged as a promising complementary strategy to the passive EPR effect, and to further

augment the efficiencies of cancer nanomedicines. This strategy has been employed in a number of polypeptide-based drug delivery systems.

One of the most extensively studied small molecule targeting moieties for polypeptide-based delivery systems is folic acid (FA).[135, 147-150] The receptor for folic acid constitutes a useful target primarily because of the upregulation of this receptor in many human cancers, and increased receptor density as the cancer worsens.[145, 151] Its widespread use can also be attributed to its relatively cheap cost, and useful chemical functionality for facile conjugation to polymers.

Sulistio and coworkers demonstrated the diverse functionality of their polypeptide CCS polymers (mentioned above) by conjugating FA-PEG to the peripheral allyl functionalities on poly(L-lysine) CCS arms through thiol-ene click chemistry (**Scheme 1.9**).[147] After 3 h incubation with a breast cancer cell line (MDA-MB-231), only 13% of cells incubated with non-folic acid conjugated CCS were associated with these particles compared to 55% for cells incubated with the folic acid conjugated CCS. However, no *in vitro* cell studies were performed on drug-loaded CCS to determine whether this increased uptake would lead to increased cancer cell death.

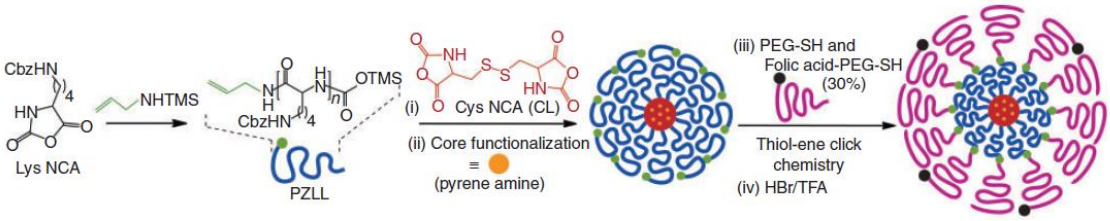

Scheme 1.9. Synthesis of synthetic polypeptide CCS polymer via an allylamine *N*-TMS initiator, followed by conjugation of FA-PEG to star periphery, adapted from Sulistio *et al.*[147]

Yang and coworkers demonstrated the increased cytotoxicity of FA-conjugated drug-loaded polypeptide-based vesicles in cancer cells.[149] Thiol-FA molecules were conjugated to the peripheral maleimide functionalities on PEG-*b*-PLG-*b*-PEG triblock copolymer vesicles containing anticancer drug doxorubicin. Results from

flow cytometry and confocal laser scanning microscopy (CLSM) analysis showed that FA-conjugated vesicles exhibited higher cellular uptake in HeLa cancer cells than FA-free vesicles, leading to higher cancer cell cytotoxicity (**Figure 1.11**).[149]

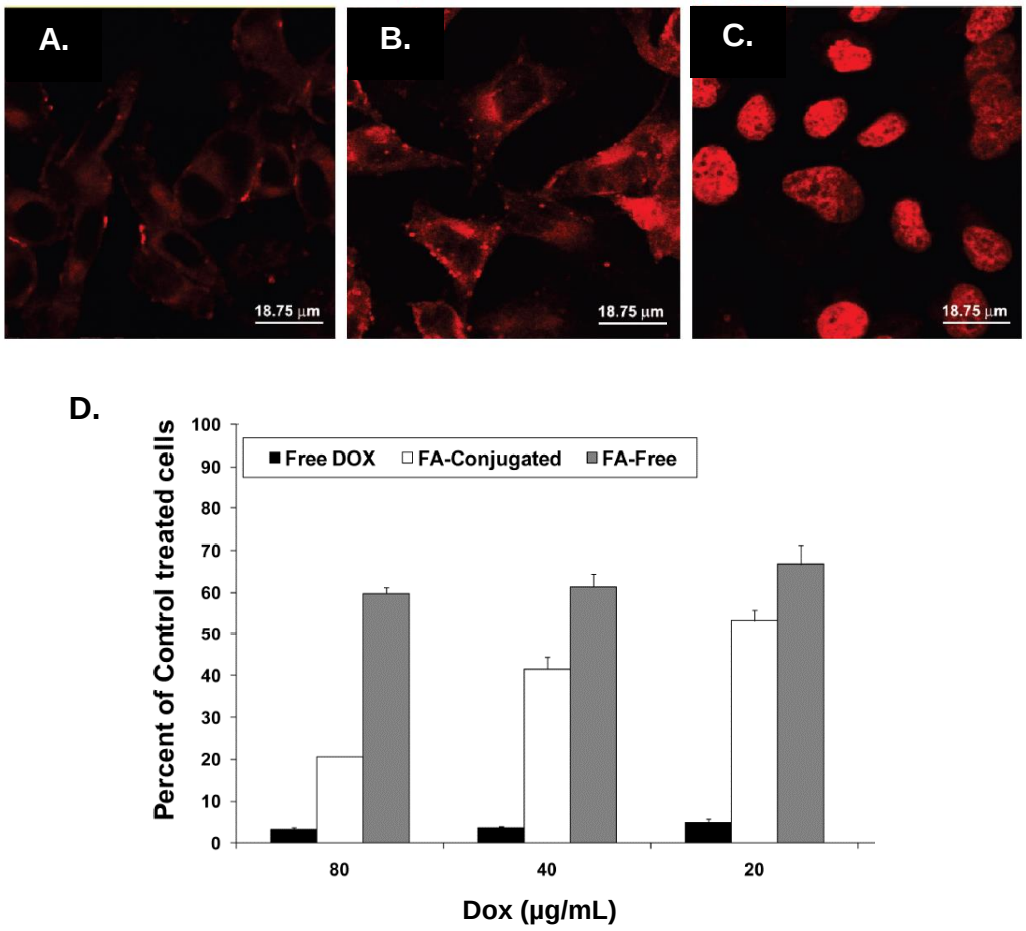

Figure 1.11. Cell uptake and cytotoxicity of FA-conjugated vesicles. CLSM images of HeLa cells incubated with (A) FA-free (B) FA-conjugated Dox-loaded vesicles (C) free Dox. (D) Cytotoxicity of free Dox, FA-free and FA-conjugated Dox-loaded vesicles against HeLa cells at different Dox concentrations.[149]

Conjugation of highly selective targeting ligands such as peptides and antibodies have also been performed on polypeptide-based drug delivery systems. Tumor-penetrating peptides which bind to upregulated integrin receptors on tumor cells has become a popular active targeting approach.[85, 115, 152-153] RGD, a peptide sequence which binds to $\alpha_V\beta_3$ integrins, commonly overexpressed in tumors, has

been conjugated to both linear [85] and micelle drug loaded polypeptide-based vehicles[153-154] to improve their cellular uptake. Song and coworkers conjugated thiol-functionalized RGD sequences to a cisplatin (CDDP)-loaded micelle composed of PLG polymer and maleimide PEG grafts (**Figure 1.12A**). Compared to micelles without the RGD sequence, the targeted micelle showed enhanced internalization rates in mouse melanoma (B16F1) cells and higher retention in tumor tissues (**Figure 1.12B**).[153]

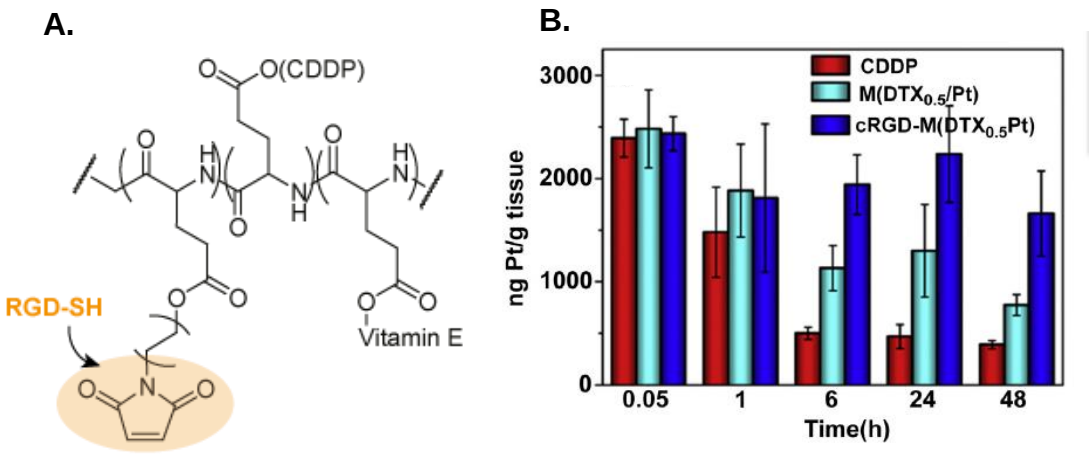

Figure 1.12. (A) Conjugation site of RGD to maleimide functionalities of PLG-*g*-PEG polymer. (B) *In vivo* tests showing metabolism of free drug (CDDP), RGD-free and RGD-conjugated nanoparticles into tumor tissue, with increased nanoparticle retention when conjugated to RGD-targeting ligand.[153] Vitamin E conjugation used as hydrophobic segment to induce self-assembly.

The conjugation of antibodies to polypeptide-based delivery vehicles has also been demonstrated.[155-156] In 2003, Vega and coworkers conjugated a monoclonal antibody with specific binding to epithelial growth factors receptors (EGFR), (also commonly overexpressed in tumor cells) to a doxorubicin loaded PEG-PLG copolymer.[155] Tests showed rapid cellular uptake (less than 5 minutes) of the drug loaded conjugate to carcinoma cells compared to the non-targeted conjugates, which required up to 24 h before any detection of cell uptake. As well, the targeted conjugates showed a higher potency than free doxorubicin in inhibiting the growth

of carcinoma cells after a 6 h exposure period. Binding of the antibody conjugate to EGFR on the cancerous cells was experimentally confirmed. The study also showed that binding of the targeted nanoparticle to the cancer cells could be blocked completely by pre-treatment of the cell with the antibody, demonstrating the highly specific targeting capabilities of the system. Despite the high specificity of these advanced targeting ligands, their use in the active targeting of polypeptide-based drug delivery systems is limited, likely due to their high cost and lengthy, delicate purification protocols required post-conjugation.

1.4 Macroporous Hydrogels for Tissue Engineering Applications

Tissue engineering is an interdisciplinary field that aims to restore, maintain, or improve tissue functions that are defective or have been lost due to acute injury or chronic disease. Due to a worldwide under-supply of organ donations, and serious issues of infection and immune rejection following tissue transplantation, the development or growth of new functional biological tissue from patient cells has become a focus of researchers worldwide.[157] In order to achieve this, biological substitutes, or scaffolds have been investigated, which can assist the growth, restoration or maintenance of tissue from living cells. The most common approach involves *in vitro* cell seeding of a porous scaffold by cells isolated from the patient. The scaffold, providing an effective platform for cell attachment, growth and differentiation, is then implanted or injected into the body (**Scheme 1.10**).[158-160]

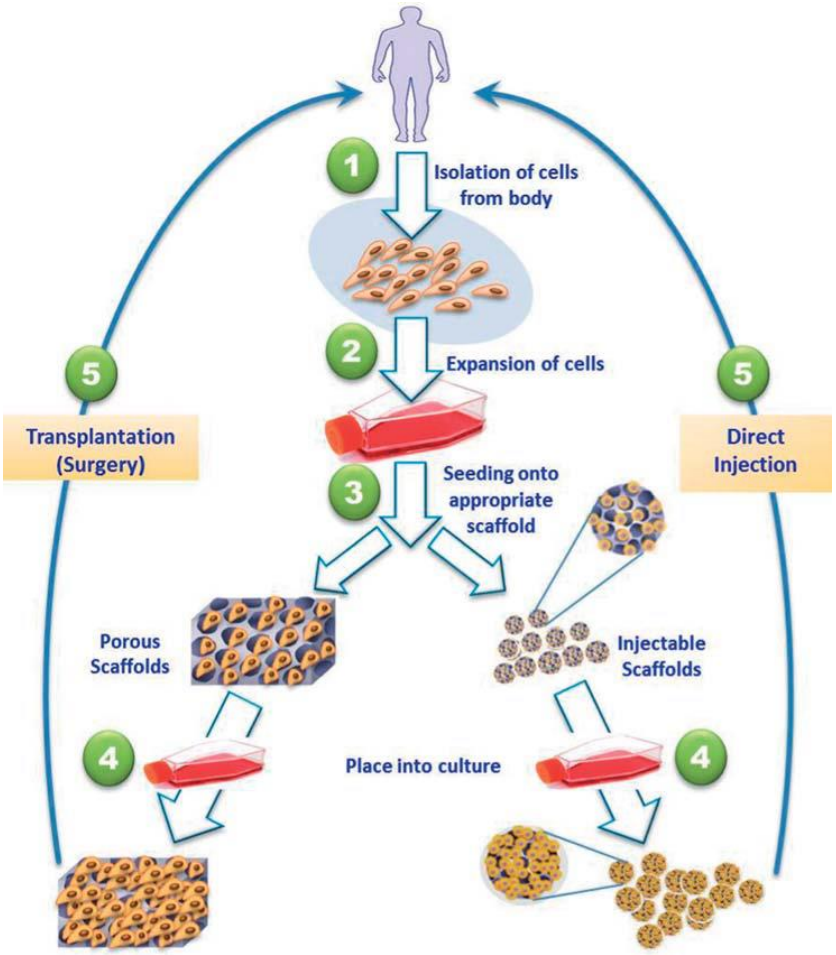

Scheme 1.10. Schematic illustration of the most common tissue engineering approaches using supportive scaffolds for cell seeding and tissue growth, followed by transplantation or injection into the body.[160]

Three dimensional (3D) porous polymeric hydrogels (cross-linked macromolecular networks formed by hydrophilic polymers swollen in water or biological fluids[161]) have been investigated extensively in this field as they closely mimic the physical and in some cases the chemical properties of the extracellular matrix (ECM).[160, 162-164] The ability of these scaffolds to permit cell-biomaterial interactions, the sufficient transport of gases and nutrients required for cell growth, support pre-vascularization (blood-vessel) growth and display a minimal inflammatory response all define the success of the scaffold.[159, 165-166] The porosities and pore sizes of these hydrogels have shown to play a large role on the effectiveness of cell migration and vascularization of new tissue growth in the scaffold.[167-169]

Conventional hydrogels, often characterized as 'nanoporous' with pores <1 μm, have shown to suffer from low cell migration, and blood vessel in-growth due to their small pore sizes and often require degradation of cross-links to allow for cell migration.[167, 170-171] 'Macroporous' hydrogels on the other hand, with pore sizes >10 μm,[162, 172] and commonly consisting of pores around or greater than 100 μm, closely mimic the ECM architecture and have shown improved cell growth and vasculature formation into their gel structures.[166-167, 173-174]

1.4.1 Preparation of macroporous hydrogels

The formation of macroporous hydrogels requires two fundamental processes to take place: cross-linking/gelation of a monomer/polymer precursor and the formation of macropores. Depending on the system, these processes can be designed to take place either separately or simultaneously. These two processes are described separately below.

1.4.1.1 Cross-linking

Like conventional hydrogels, macroporous hydrogels can be formed through chemical or physical cross-linking processes (**Figure 1.13**):

Physical cross-linking

Physically cross-linked gels can be formed through ionic, hydrogen bonding or hydrophobic interactions between polymers and is an effective process to form hydrogels without the requirement of chemical cross-linkers. Physically cross-linked macroporous hydrogels are generally developed through a freeze-thaw process (described later), and have been utilized in the preparation of porous hydrogels composed of polyelectrolyte synthetic and natural peptides[175-176] as well as poly(vinyl alcohol)(PVA) gels through hydrogen bonding (**Figure 1.13**). [177-178] However, due to the relatively weak bonding in these gel networks, they are often prone to pore collapse and small pore sizes unless chemically cross-linked.[166, 179-182]

Chemical cross-linking

For hydrogels in general, chemical cross-linking is the most commonly used method for gel formation. The introduction of covalent bonds in the gel network results in extra stability and strength compared to physically cross-linked gel networks.[166, 183] Polymerization cross-linking, a widely used method for cross-linking/gelation, typically involves the free-radical copolymerization of vinyl functionalized macromers/monomers sometimes in the presence of a divinyl monomer cross-linker (**Figure 1.13**).[184-185] A range of acrylates, acrylamide and other vinyl monomers can be employed in these systems[185-186] along with a wide variety of visible, ultraviolet, and red-ox initiators for radical generation. [181, 187-188] An ionic comonomer is also commonly included in the mixture to increase the swelling capacity of the gel in aqueous environments.[184]

The use of bi or multifunctional chemical cross-linkers is also a commonly employed method for chemical cross-linking.[183] Hydrogels, being hydrophilic in nature, typically use polymer precursors containing hydrophilic (e.g. amine, hydroxide, or acid) functional groups thereby allowing for complementary reactivity with these cross-linkers using standard coupling procedures. For instance, glutaraldehyde (a dialdehyde) has been used to conjugate a large range of natural polymers containing amine functionalities including chitosan and gelatin gels,[189-191] resulting in Schiff-base formation (**Figure 1.13**).

EDC/NHS coupling agents have also been used to cross-link amine and acid functionalities between polymers[172, 192] as well as promote direct cross-links between polymer chains in natural polymers which contain both acid and amine functionalities in their polymer structures (**Figure 1.13**).[181, 193] The use of EDC/NHS coupling is known as "zero-length" cross-linking, as it avoids the typical incorporation of cross-linkers into the polymer gel network.

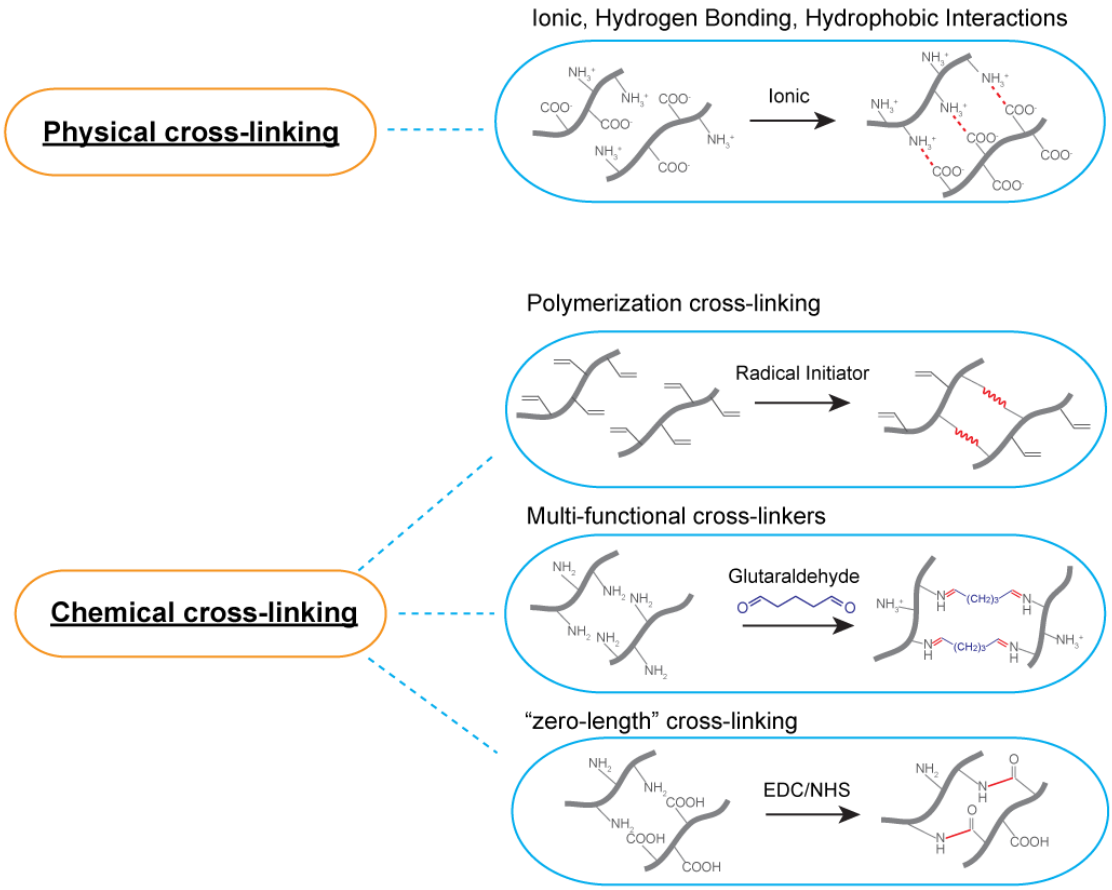

Figure 1.13. Examples of cross-linking strategies used for macroporous hydrogel formation.

1.4.1.2 Macropore formation

Several methods are employed to generate macroporous morphologies in hydrogels, the most common of which rely on physical interruptions in the hydrogel-forming solution, known as porogens, that are then removed after gelation (**Table 1.1**). For each macropore forming strategy described below, a wide array of cross-linking strategies such as those described above, have been utilized.

Macropore method	Porogen	Pros/Cons
Particle leaching	Salts, sugars, bacteria, paraffins	Pros: Tuneable pore size and porosity through changes in particle size and concentration Cons: Difficulty with porogen removal, use of organic solvents leads to potential toxicity issues. Difficulty controlling pore orientation
Gas foaming	Gas from chemical reaction, nucleation or bubbling e.g. CO_2	Pros: Gases generally non-toxic to cells. No organic solvent required Cons: Often display reduced pore interconnectivity
Cryogelation	Ice crystals	Pros: Non-toxic porogen. Ease of porogen removal. Generates highly interconnected porous structures. Control over porosity and pore orientation
Freeze-drying	Ice crystals	Pros: Non-toxic porogen. Ease of porogen removal. Control over porosity and pore orientation Cons: Often low structural stability, reduced pore interconnectivity. Energy intensive. Long processing times

Table 1.1. Common macropore forming methods used in the preparation of macroporous hydrogels.

Particle -leaching

Particle casting–leaching can be considered as the simplest technique for developing porous scaffolds with almost uniform pore size.[163, 194-195] The procedure includes the casting or dispersion of a porogen with controlled particle size into an organic

polymer solution containing cross-linker. The appropriate cross-linking technique is used to solidify or cross-link the polymer, to produce a polymer–porogen network. The solvent is then evaporated/washed out along with the removal of the entrapped porogens by use of a selective solvent to reveal the macroporous polymer network (**Scheme 1.11**). [162]

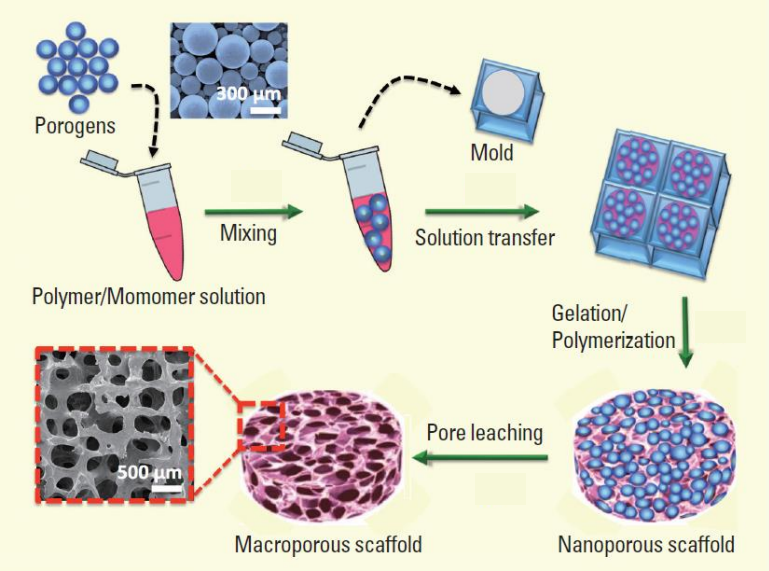

Scheme 1.11. Fabrication of macroporous hydrogels using particle (porogen) leaching.[162]

A range of porogens have been used in this method including sugar,[196] salt,[197] live bacteria,[198] parrafin,[199] and gelatin (**Figure 1.14**).[199]

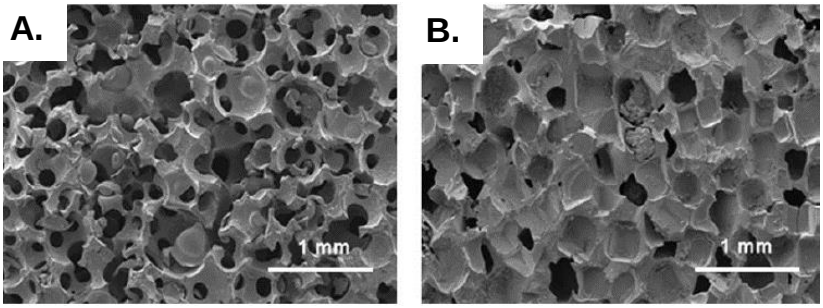

Figure 1.14. SEM micrographs of 3D macroporous hydrogels prepared from different porogens. (A) salt (NaCl) (B) gelatin.[200]

However, traditional limitations to this method are the incomplete removal of porogens or organic solvent from the gel networks thus posing potential cytotoxicity issues. Using this method therefore requires extensive washing for porogen removal.[163, 201]

Gas foaming/leaching

This method utilizes the nucleation and growth of gas bubbles dispersed throughout a polymer solution to generate a porous structure.[202-205] Typically, an effervescent salt is employed as a gas foaming agent to release a gas (porogen) upon chemical reaction, thereby creating pores inside a solidifying/cross-linking polymer solution. The most commonly used foaming agent for fabricating porous hydrogels is sodium bicarbonate owing to its ability to generate CO_2 in mildly acidic solutions.[206-207] Gas bubbles can also be formed by release from a pre-saturated gas (e.g. supercritical CO_2)-polymer mixture following a reduction in pressure.[202, 204] The gas foaming method is generally inexpensive, with the porogens employed (e.g. CO_2,) displaying reduced toxicity profiles over porogens used in particle leaching, and can be conducted without the use of organic solvent.[163]

Cryogelation

Cryoglelation is a process that uses frozen ice crystals in aqueous solutions as porogens to prepare gels with large, highly interconnected pores, and high porosities.[166, 184, 208-209] Developed more than 30 thirty years ago,[210-211] this technique typically involves the freezing of an aqueous solution containing polymer and cross-linker. As the solvent freezes, a concentrated liquid (unfrozen) microphase develops around the ice crystals containing the polymer and cross-linker, resulting in effective polymer cross-linking/ gelation. Thawing of the frozen solution removes the non-toxic ice water crystals to leave behind the macroporous hydrogel structure, commonly referred to as a 'cryogel' (**Scheme 1.12**). A modified cryogelation approach using free-thaw cycles, to generate repetitive phase separations between the polymer and water phases has been used to fabricate physically cross-linked gels of poly(vinyl alcohol) (PVA).[178, 212-213]

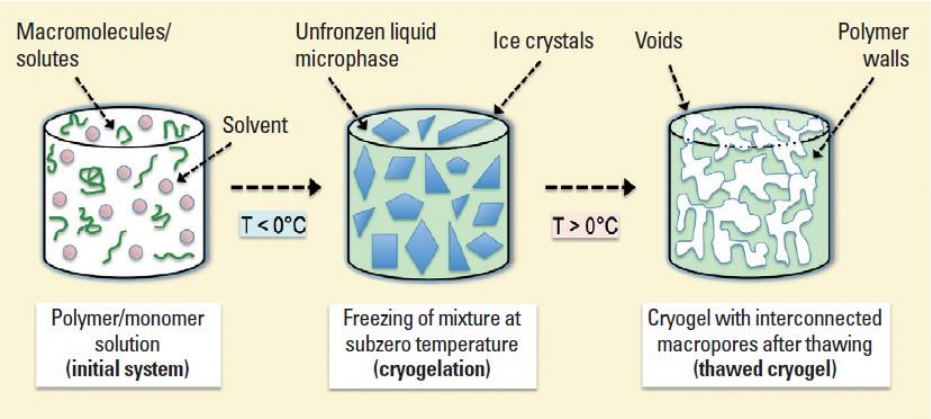

Scheme 1.12. The cryogelation process to generate macroporous hydrogels (cryogels).[162]

The cryogel pore sizes, and pore morphologies can be modulated through changes in gelation conditions including polymer concentration, freezing temperatures, direction of freezing etc. (**Figure 1.15A**).[214-217] Due to the high concentration of polymer and cross-linker in the liquid microphase, the cryogel often contains thick and densely cross-linked pore walls, typically resulting in strong porous hydrogels with higher mechanical strength and a larger resistance to deformation (high elasticity) compared to other pore forming strategies (**Figure 1.15B**).[166, 184]

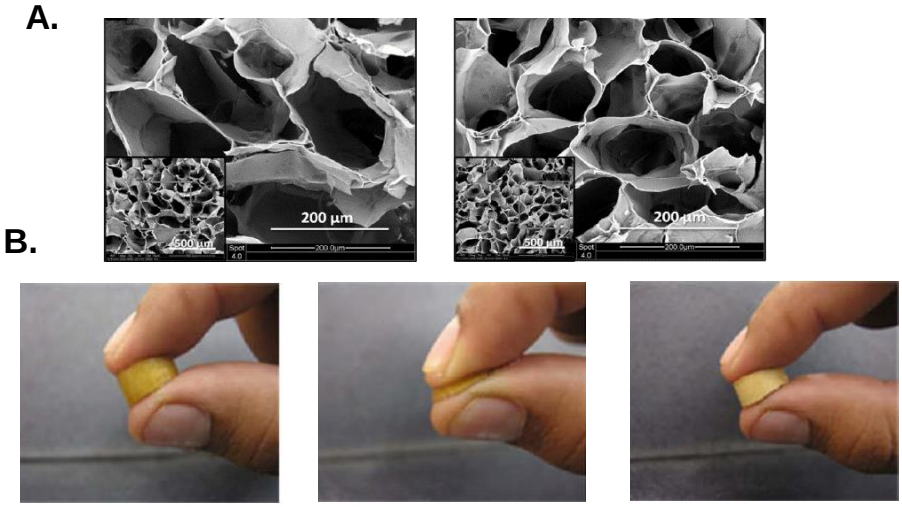

Figure 1.15. (A) Agarose/alginate cryogels prepared from different polymer concentrations showing different pore sizes.[218] (B) Water-saturated chitosan/gelatin cryogels showing elastic compression.[189]

The other added benefit to cryogelation over most other pore forming strategies is it avoids the use of potentially cytotoxic porogens and the ease of porogen removal (water ice) by simple warming.[162, 166]

Freeze-drying/Lyophilization

Freeze-drying, also known as lyophilization, has been widely used in the fabrication of macroporous hydrogels for tissue engineering.[175, 191, 219-220] This method uses rapid cooling to produce thermodynamic instability, resulting in phase separation in a cross-linked polymer solution. The solvent is then removed by sublimation under vacuum to create pores in the dried structure. This method can also be used to prepare physically cross-linked gels, however to improve the physical properties of such gels chemical cross-linking of the gels is often performed before or after freeze-drying to give greater strength and pore integrity to the gel structures.[181, 191, 221-222] In addition, freeze-drying is largely energy intensive and requires long drying times to ensure complete removal of solvent (water).[163]

1.4.2 Properties of macroporous scaffolds for tissue engineering

The success of scaffolds for tissue engineering purposes relies on a number of physiochemical properties to be thoroughly considered so that the fabricated gels can closely mimic the ECM and provide a suitable environment for cell and tissue growth. These include scaffold surface properties, porosity and pore size, cell biocompatibility, biodegradation and mechanical strength.

Surface properties

The surface properties of macroporous scaffolds, as with all scaffolds used for tissue engineering application, play a large role in the cell attachment capabilities of the gel.[157, 159-160]As most cells in engineered tissues are anchorage- dependent, the scaffolds should ultimately contain properties that favor this attachment. The high porosities and large pore sizes of macroporous cryogels allow for a large accessible surface area for the cells to interact with the gels. The presence of charged (ionic) groups, in particular high cationic charge densities, have shown to promote cellular

attachment to surfaces including hydrogels through direct physico-chemical interactions, or via adsorption of serum proteins to the gels. [223-227] The incorporation or immobilization of natural polymers into the hydrogel structure such as heparin,[172, 228] fibronectin[229] and gelatin[230-231] as well as attachment of specific cell adhesion ligands (e.g. RGD peptide sequences),[232-233] and growth factors (eg. EGF)[234] are all commonly performed to generate hydrogel surface properties suitable for cell adhesion.

Porosity and pore size

Typically, high gel porosities (corresponding to a high overall pore volume relative to the total volume of the gel scaffold) of >80-90% encourages cell ingrowth, the mass transfer of nutrients and oxygen, and uniform cell distributions.[231, 235-236] The large pore sizes generated in macroporous hydrogels (approx. >100 μm) have been shown to further enhance these effects, as well as encourage new blood vessel growth (neovascularization) into the hydrogel matrix.[166-167, 174] However, the ideal macropore sizes required for cell growth is not fully understood and is also likely to be cell dependent. For instance, an optimum pore size of 5–15 μm has been suggested for fibroblast ingrowth, 20–125 μm for regeneration of adult mammalian skin, 100–350 μm for regeneration of bone, 40–100 μm for osteoid ingrowth, and 20–125 μm for regeneration of adult mammalian skin.[159]

Mechanical properties

During tissue regeneration, the gel scaffold provides physical support for the growth and protection of cells and tissue in the presence of internal or external applied forces. Therefore, the biostability of many scaffolds depend on factors such as its strength and elasticity (resistance to failure or breakage) and stiffness (deformation under a given load). These mechanical properties can vary both on the cross-linking strategy (physical vs chemical discussed above) and the method of macroporous gel formation. For instance, cryogels typically display large strength and elasticity due to their dense highly interconnected polymer walls.[166, 184] There is strong evidence showing that soft tissue response is dependent upon the mechanical properties of

the implanted material,[237-240] with cells likely to respond better in an environment that mimics the mechanical properties of the tissues in their native state.[238, 240] Therefore the specific mechanical properties of the gel must be considered for the type of tissue engineering application in mind. The major factors affecting the mechanical properties and structural integrity of a macroporous scaffold are often related to its porosity, including pore volume, size, shape, orientation, and connectivity.[159, 172, 241]

Biocompatibility/Biodegradability

Hydrogels used for tissue engineering applications must show no or very limited toxicities and adverse immunological responses to mammalian cells. For macroporous hydrogels, the toxicities of the monomer, polymer, initiator, solvent, cross-linker, porogen etc. must all be considered, particularly in the case of non-quantitative reaction conversions and ineffective gel purifications. For instance, thorough washing protocols must be employed to remove organic solvents used during salt leaching methods,[163] as well as the potential high osmolarity effects on cells from salt porogen leaching.[200] Glutaraldehyde, an effective and widely used polymer cross-linker has reported cytotoxicites and therefore requires thorough neutralization and washing out in order to reduce the potential toxic effects owing to these gels.[190, 242] The hydrogel must also ideally undergo controlled degradation, at a rate best suited to support, and yet not hinder, effective cell proliferation and tissue growth. Therefore a range of natural polymers with inherent biodegradability properties (e.g. collagen, chitosan),[243] and synthetic biodegradable polymers (e.g. poly(lactic acid), poly (ε-caprolactone)) have been utilized for gel fabrication, as well as the incorporation of stimuli cleavable (e.g. disulfide bond) cross-linkers into the hydrogel networks.[243 244]

1.4.3 Polymers for macroporous hydrogels

A variety of natural and synthetic polymers have been used to prepare macroporous hydrogels:

Natural polymers

The two main classes of natural polymer used in macroporous hydrogel preparation for tissue engineering applications are polysaccharides (e.g. chitosan, alginate, hyaluronic acid and collagen) and fibrous proteins (e.g. collagen and gelatin), owing to their biocompatibility, inherent biodegradability and critical biological recognition properties which often closely mimic those found in the natural ECM. For instance, collagen, and its related gelatin are commonly employed in the preparation of macroporous hydrogels for tissue engineering applications. Their tensile strength, suitable biocompatibility, (enzyme) biodegradability profiles and the presence of cell attachment moieties in their structure (e.g. RGD peptide sequences) have made them popular materials as cellular scaffolds. (**Figure 1.16**).[190, 230, 245-246]

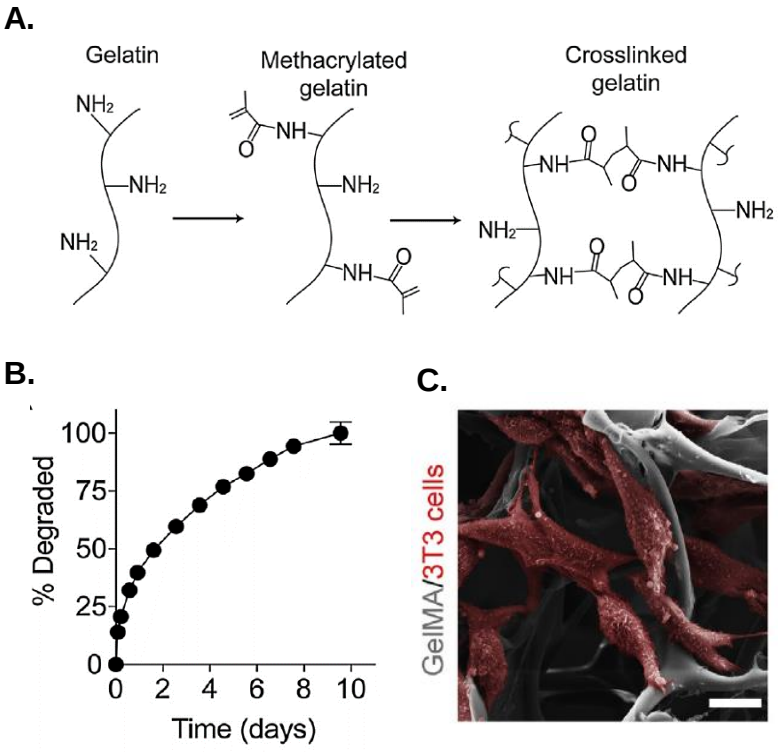

Figure 1.16. Fabrication of biodegradable macroporous gelatin cryogels for tissue engineering. (A) Synthesis of methacrylated gelatin followed by free radical polymerization to form cross-linked gels (B) *In vitro* enzymatic degradation in the presence of collagenase type II (C) SEM colored image of 3T3 mammalian fibroblast (red) cells on cryogel surface (grey) (scale bar= 10 μm).[230]

Often these natural polymers are modified with functional groups such as acrylamides for radical polymerization cross-linking strategies[232, 243-244, 247] and their amine functionalities have been used for reaction with chemical cross-linkers such as glutaraldehyde.[189, 191, 242] However, the use of natural polymer-based hydrogels has shown some drawbacks, including purification difficulties, immunogenicity and pathogen transmission.[244, 248-249]

Synthetic polymers

Compared to natural polymers, synthetic polymers have the potential for more controllable and reproducible chemical and physical properties allowing preparation of a large range of hydrogel materials with specific properties.[186, 244, 250] However, processing steps to instill cell–material interaction and biodegradability properties have to be taken into account when using such polymers for gel fabrication.

The most common synthetic non-biodegradable polymer used to prepare macroporous gels is PEG, with gelation commonly formed through photo-induced radical polymerization of PEG acrylates.[186, 207, 244] The use of PEG, although biocompatible, generally requires the incorporation of natural polymers, cell adhesion ligands or stimuli responsive bonds to the gel to allow for effective cell attachment and biodegradation profiles.[167, 172, 251-252] To avoid the use of natural polymers, yet still display sufficient biodegradability profiles, macroporous hydrogels have been composed of synthetic biodegradable polyesters including poly(lactic acid) (PLA),[253] poly(lactic-*co*-glycolic acid) (PLGA)[254] and poly(ε-caprolactone).[255] Synthetic polypeptides are another class of biodegradable material which have recently been investigated for the fabrication of macroporous hydrogels for tissue engineering applications. Their use also offers the prospect of avoiding the scale up, batch variability and potentially immunogenic responses associated with the use of natural polymers. Aside from their well-established biocompatibility, and enzyme biodegradability properties described earlier, synthetic polypeptides also display effective cell attachment capabilities, with

preparation of polyelectrolyte multilayer coatings (PEM) composed of charged synthetic polypeptides such as poly(L-glutamic acid) (PLG) and poly(L-lysine) (PLL) shown to enhance the cell adhesion properties of surfaces.[227, 256-257] Reports pertaining to the fabrication and performance of synthetic polypeptides as materials for three dimensional macroporous cellular scaffolds is to be discussed below.

1.4.4 Macroporous hydrogels composed of synthetic polypeptides

The fabrication of synthetic polypeptides into three-dimensional macroporous hydrogels for tissue engineering applications was first reported by Lavik *et al*. in 2006.[174] The hydrogel was prepared through the cross-linking of an amine-reactive four-arm PEG with poly(L-lysine) around a porous salt-leached poly(lactic-*co*-glycolic acid) (PLGA) scaffold (**Figure 1.17**).

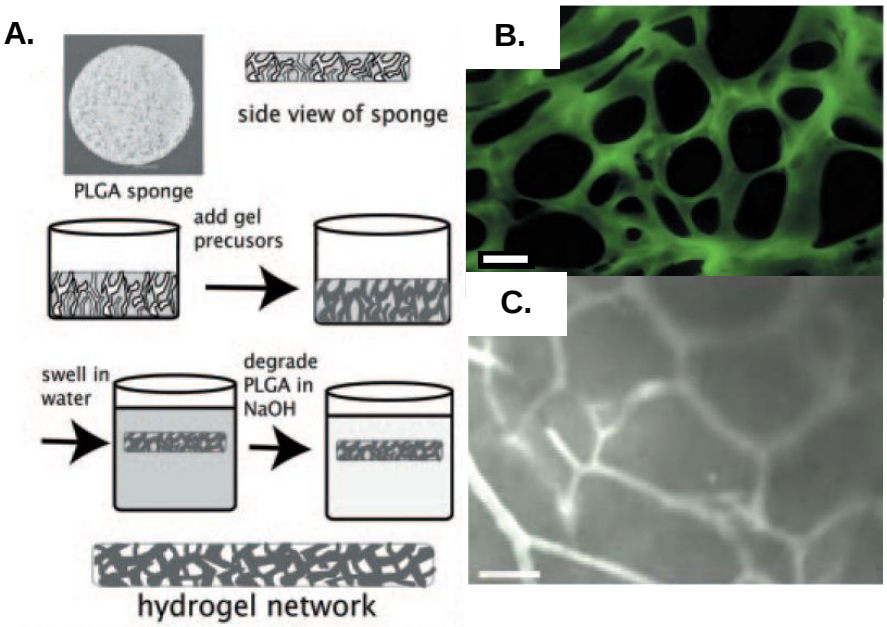

Figure 1.17. (A) Formation of poly(L-lysine) incorporated macroporous hydrogels through use of porous salt-leached PLGA sponge as scaffold (B) Cross-section of hydrogel scaffold stained with FITC following reaction with poly(L-lysine) amine side chain. Scale bar = 100 μm (C) Intravital images of new vascular growth inside of hydrogels following *in vivo* studies. Scale bar = 50 μm.[174]

After degradation of the PLGA scaffold, a macroporous polypeptide-based gel was isolated with large pore sizes ranging from 250-500 μm (**Figure 1.17A and B**). The scaffolds were highly biocompatible and were able to support the growth of microvessels after implantation into mice, with blood flow established after 2 weeks (**Figure 1.17C**). The presence of the polypeptide also ensured the gels were enzymatically biodegradable.[174]

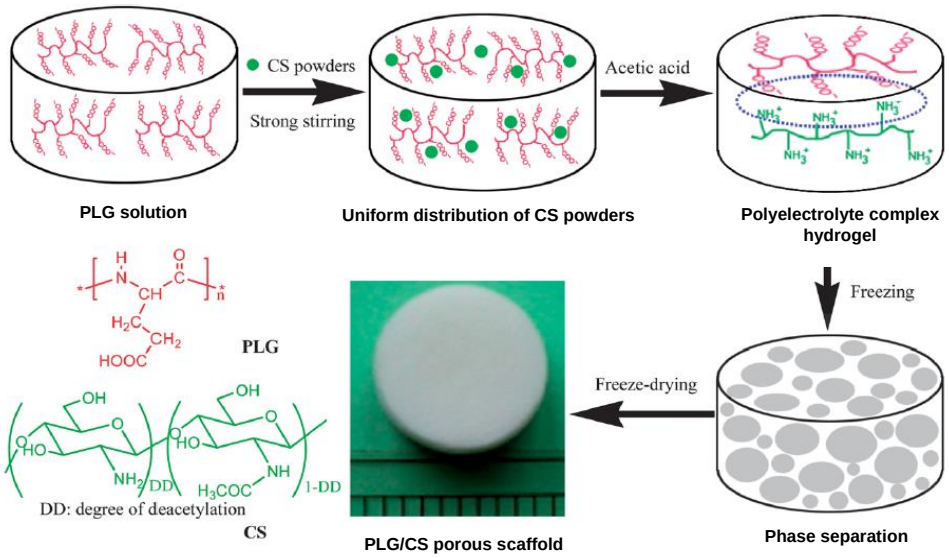

Scheme 1.13. Fabrication of physically cross-linked PLG/CS macroporous hydrogel scaffolds.[175]

Lin and coworkers generated macroporous hydrogels composed of poly(L-glutamic acid) (PLG) and chitosan (CS) using physical (ionic) cross-linking (**Scheme 1.13**).[175] Macroporous hydrogels containing pore sizes up to 150 μm were fabricated using a freeze-drying protocol (**Scheme 1.13, Figure 1.18C and D**), with pore sizes significantly reducing upon decrease of freezing temperature (**Figure 1.18A**). The gels were shown to be enzymatically biodegradable, with a degradation rate dependent on the proportion of PLG and chitosan used in the gels. Similar properties and observations were observed for PLG and chitosan macroporous cryogels chemically cross-linked through EDCI zero-length cross-linking methods.[258] For freeze-dried physically cross-linked PLG and chitosan hydrogels, gels with the

highest pore sizes showed better cell growth than gels with smaller pore size. Cell proliferation was also shown to increase with PLG content, this being attributed to the high biocompatibility of the PLG block and the negative (ionic) surface charge of PLG suitable for cell attachment (**Figure 1.18B**).[175]

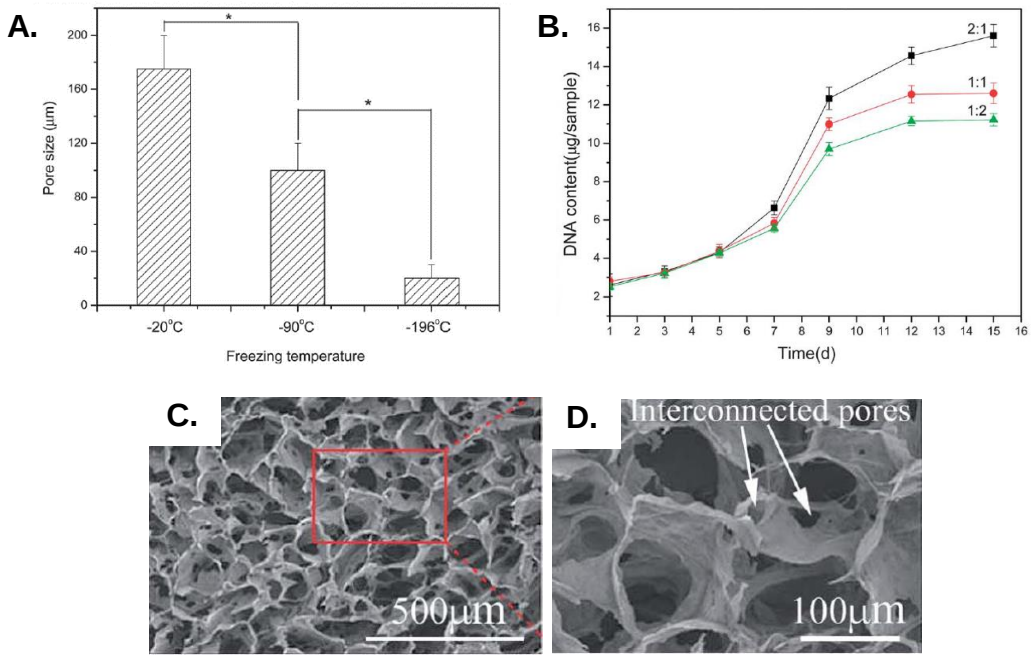

Figure 1.18. (A) Pore size distribution of PLG/CS physically cross-linked gels with different freezing temperature (B) Proliferation curve of adipose-derived stem cells (ASCs) on scaffolds containing different PLG/CS molar ratios determined by DNA content (C,D) SEM images of gel cross-sections showing macropores. [175]

Macroporous hydrogels have also been prepared through radical polymerization of methacrylated synthetic polypeptides (**Figure 1.19**). Jing and coworkers prepared freeze-dried biodegradable and pH-sensitive macroporous gels through the cross-linking of methacrylated PLG and a temperature sensitive acrylate modified cellulose.[259] Rypacek and coworkers also developed macroporous hydrogels through copolymerization of a methacrylated linear poly(L-glutamic), poly(L-alanine) and poly(L-lysine) statistical copolymer with HEMA (hydroxyethyl methacrylate) to improve the mechanical properties of the gel.[233] Copolymerization with methacroylated RGD ligands was also performed to incorporate RGD into the

gel structure for improved cell adhesive properties. However, as no general macropore forming strategy was employed, pore sizes were limited to 5-20 μm, thereby potentially limiting their effective use as tissue engineering scaffolds. Pore sizes were improved some years later in the preparation of cryogels through radical copolymerization of methacrylated PLG and HEMA (**Figure 1.19**).[215] The gels prepared contained high porosities (>90%), and large pore sizes ~80 μm, with the pore morphologies shown to change from polyhedral (or spongy) to lamellae upon increasing the polymer concentration (**Figure 1.19C**). The gels demonstrated enzyme biodegradable capabilities and could be biofunctionalized through click chemistry. However, no cell studies were performed on these gels, therefore their suitability as cellular scaffolds for tissue engineering applications could not be determined.

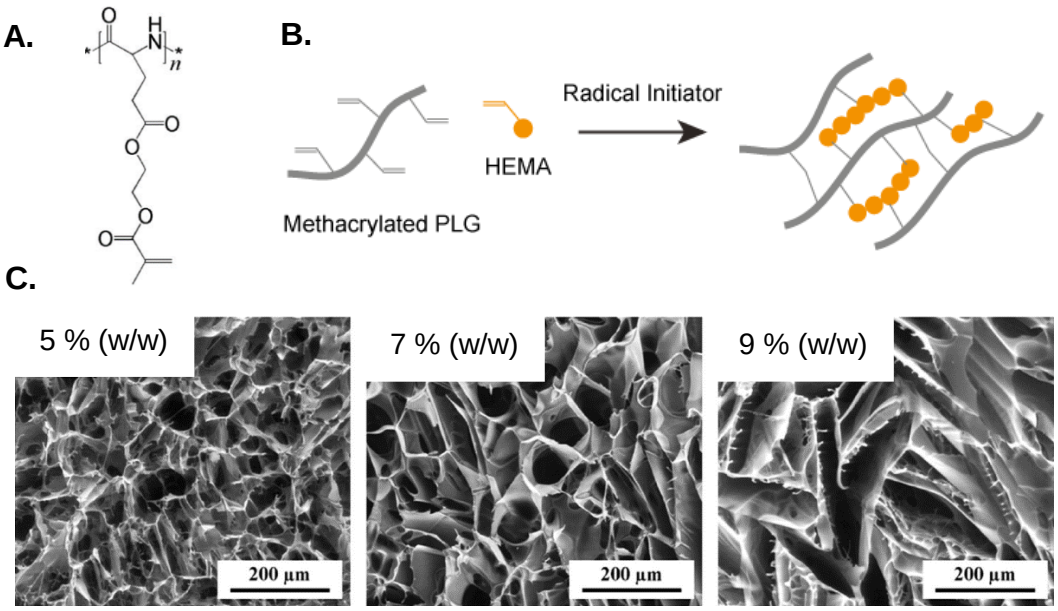

Figure 1.19. (A) Typical structure of a methacrylated PLG used for radical polymerization cross-linking (B) Schematic representation of the radical copolymerization cross-linking of methacrylated synthetic PLG with HEMA (hydroxylethyl methacrylate) to form gels (C) SEM cross-section of cryogels prepared from different polymer concentrations.[215]

1.5 Synthetic Polypeptides for Antimicrobial Applications

Antimicrobial resistance has become a growing concern in recent years as difficult to treat infections develop in our hospitals and our wider community. The emergence of drug-resistant strains to conventional antimicrobial treatments has resulted in a shift in focus to non-traditional antimicrobial agents such as polymers and peptides with bioactive properties. The success of innate defense peptides known as antimicrobial peptides (AMPs), has translated to the use of simpler, readily prepared synthetic polypeptides with similar properties to AMPs.

1.5.1 Antimicrobial peptides (AMPs)

In the natural world, nearly all organisms possess innate defense peptides with broad ranging antimicrobial activities[260-262] known as antimicrobial peptides (AMPs). AMPs such as defensins, cathedlicins, polymyxins to name a few, typically contain ~20–60 amino acids, consisting of specific sequences of both cationic and hydrophobic amino acids (**Figure 1.20**).[263-264]

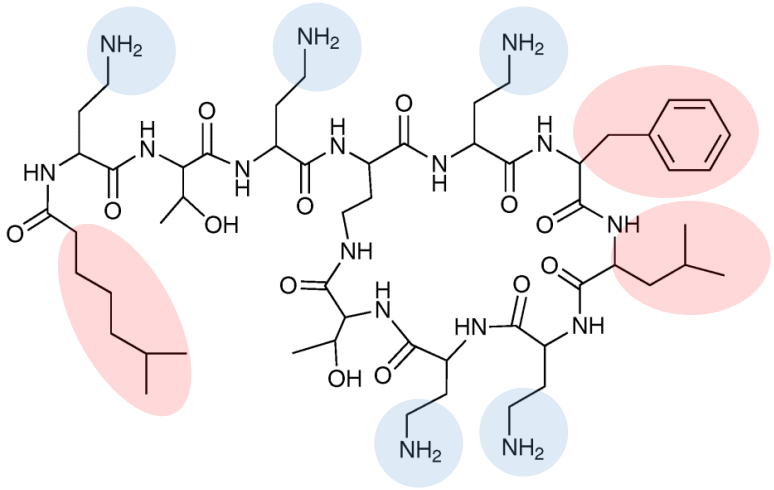

Figure 1.20. Antibacterial peptide Polymyxin B structure, showing 5 amino groups (blue) from 2,4-diaminobutyric acid (Dab) amino acid residues as sites of cationic charge, with phenylalanine, leucine residues and a hydrocarbon tail (red) as the hydrophobic units.

AMPs adopt various secondary structures (e.g., α-helix, β-sheet) (**Figure 1.21A**) that are crucial for their antimicrobial activities against a broad range of bacteria, yeasts, fungi and viruses including highly resistant pathogens.[262, 265-266]

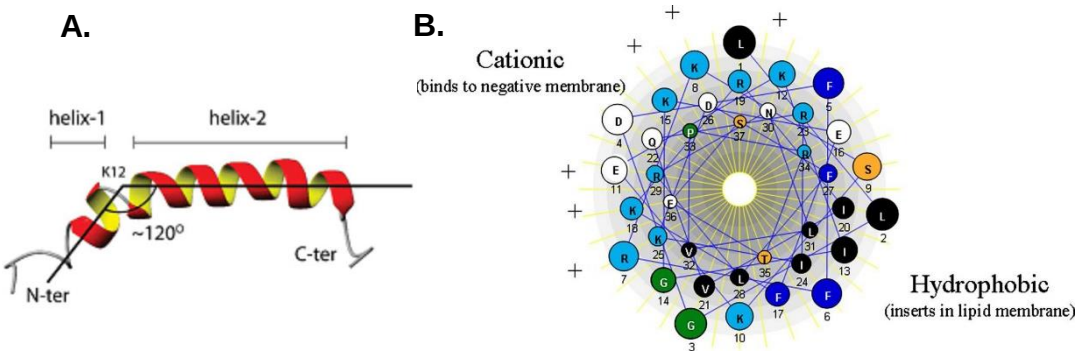

Figure 1.21. (A) α-helical conformation of LL-37. [267] (B) Schematic wheel plot showing amino acid distribution of cathelicidin LL-37 in α-helical structure. Most positively charged amino acids are localized to one side of the molecule, with hydrophobic amino acids located on the opposite side (amphipathicity). [262]

Antibacterial AMPs are the most studied AMPs to date. A common attribute of antibacterial AMPs, and AMPs in general, is their amphipathic (or facial amphiphilic) organization whereby the cationic (e.g. lysine) and hydrophobic (e.g. leucine) regions of the peptide are localized on separate faces (**Figure 1.21B**).[263, 268] This amphipathicity allows for binding an insertion into the bacterial cell wall, which for the majority of antibacterial AMPs, described as membrane-active, results in bacterial membrane disruption, and cell death.[263, 269]

Bacteria can be classed into two categories, gram-negative and gram-positive, depending on their cell wall compositions (**Figure 1.22**). Gram-negative bacteria (e.g. *E. coli, P. aeruginosa*) have two lipid-rich hydrophobic membranes and a thin peptidoglycan layer present in the periplasmic space with negatively charged lipopolysaccharides located on the outer membrane (**Figure 1.22A**). Gram- positive bacteria (e.g. S. *aureus*) contain a single lipid rich membrane with a thick outer peptidoglycan layer (**Figure 1.22B**). Negative charged teichoic and lipoteichoic acids are present in the outer peptidoglycan layer.

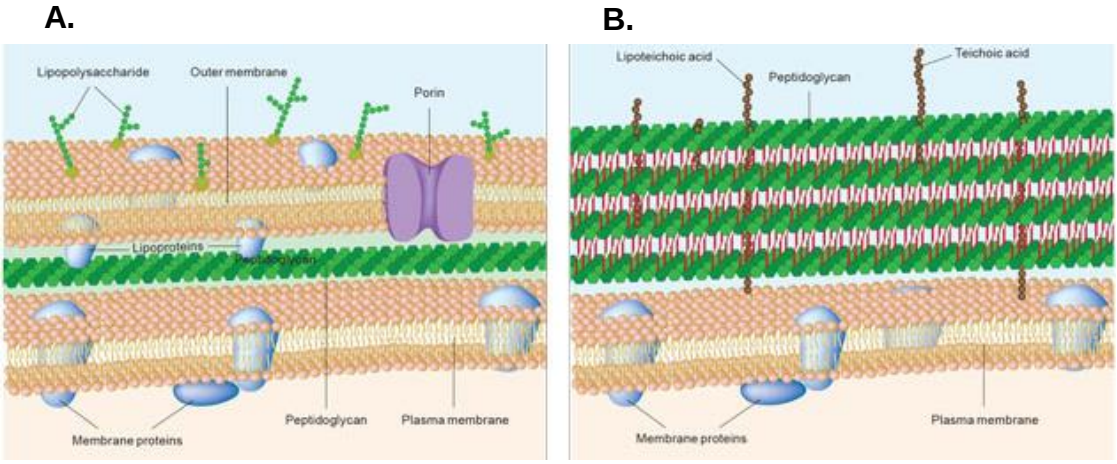

Figure 1.22. Schematic of cell membrane structure in (A) Gram-negative and (B) Gram-positive bacteria. © Shutterstock

Since both bacteria categories contain negatively charged species on the periphery of their cells walls and inner hydrophobic regions, the amphipathicity of AMPs results in their initial electrostatic interaction with the negatively charged cell walls followed by entering and insertion into the lipid-rich hydrophobic membranes of cells. [263, 270-275] In one particular mode of action, described as the 'barrel-stave model', the insertion of the AMP creates pores in the membrane, disrupting the membrane and resulting in cell lysis and death (**Figure 1.23**).[269-270] Due to the high level of cholesterol, lower lipid content and low anionic charge in mammalian cell membranes, there is a general selectivity of AMPs to antimicrobial cell walls rather than mammalian cells.[269]

The antibacterial activity of cationic peptides can be modulated through alteration of the peptide's hydrophobicity or net charge. Studies have shown that low hydrophobicity can reduce antimicrobial activity,[276] whilst high levels of hydrophobicity can decrease selectivity between the desired bacterial targets and host cells.[277-280] Similarly an increase in surface charge above a certain maximum (varying with each peptide) has been shown not to lead to an increase in activity,[268] and in some cases, leads to higher toxicities. For example, increasing positive net charge of AMP V13K from +8 to +9 resulted in a sharp increase in hemolytic (blood

toxicity) activity, while decreasing the net charge to lower than +4 resulted in negligible activity against *P. aeruginosa*.[281] Thus, this balance of charge and hydrophobicity can be delicate and must be empirically determined for each series of peptides.[269]

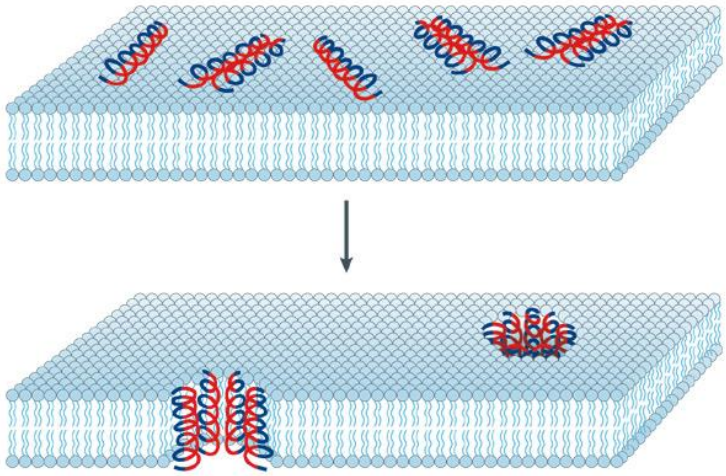

Figure 1.23. Attachment and insertion of antimicrobial peptides into membrane bilayers to form pores by a 'barrel-stave' mechanism.[270]

However, the actions of AMPs often do not stop after the initial interaction with the antimicrobial membrane. Despite controversy remaining as to their exact mode or modes of action, evidence has shown that AMPs can also kill cells by inhibiting proteins, DNA and RNA synthesis, or by interacting with certain intracellular targets.[263, 270, 282-283] Even if intracellular targets are involved, an initial cell membrane interaction with peptides is required for the antimicrobial activities of AMPs.[284]

Unlike antibiotics, which target specific cellular activities (e.g. synthesis of DNA, protein, or cell wall), the targeting of the lipid-rich cell membrane which are generic and necessary components of microbe cells, results in limited resistance to these peptides. The targeted organisms have to adapt their whole membrane chemistry in order to survive, as opposed to modifying just receptor interactions or enzymatic processes as is the case for some of the most commonly used antibiotics.[285-286]

Because of this feature, AMPs have attracted significant attention as potentially clinical antimicrobial agents.

Despite these advantages of AMPs, their commercial development has been limited.[274] For instance, they have shown to induce high hemolytic activity and other toxicities in mammalian cells at their large therapeutic dosages,[287-291] and due to their naturally derived structure, they are prone to recognition by the immune system resulting in fast proteolytic degradation.[292-293] Formulation of synthetic peptides can get around these issues by insertion of functional groups that modulate amphiphilicity, altering the net charge to reduce hemolytic activity (blood toxicity), or incorporation of unnatural or D-amino acids to protect against proteolytic degradation.[263] However, synthesis of these AMPs in general is often difficult to achieve due to their precise sequencing. This requires controlled peptide synthesis (e.g. solid phase peptide synthesis) procedures that are expensive and inefficient, resulting in high production costs and limiting their wide-spread use.[274, 288] Therefore the preparation of simple polymeric peptide analogues with similar properties to natural AMPs via cost-effective, efficient, and scalable processes is currently being investigated by researchers.

1.5.2 Synthetic AMPs prepared through NCA ROP

As mentioned previously, NCA ROP is an effective and convenient way to synthesize polypeptides on a large scale. Studies on the membrane activity of synthetic polypeptides, prepared by the ring-opening polymerization of NCA monomers, date back to the late 1950s.[294] While these studies showed that amphiphilic synthetic polypeptides (e.g. poly(L-lysine)) and copolypeptides (e.g. poly (L-lysine) and poly(L-leucine) random copolymers) were bioactive and able to bind to and disrupt cellular membranes, the lack of control of the polymerization process prevented identification of any structure-functional relationship.[11] Therefore, it was only until the development of synthetic polypeptides with suitable control in the late 1990s by Deming[14] that interest arose in the use of polypeptides for antimicrobial therapies.

Deming and his coworkers in 2001 used this controlled NCA ROP method to synthesis approximately 500 membrane active amphiphilic copolypeptides, with narrowly defined length and interchain composition.[295] These ''random'' copolypeptides were composed of hydrophilic, cationic L-lysine residues plus one of the following hydrophobic amino acids: L-leucine, L-phenylalanine, L-isoleucine, L-valine, or L-alanine to mimic the amphiphilicity of AMPs. Parameters such as chain length and hydrophobic content were varied between polymers. By employing an optical assay, they screened these polymers to study the effect of side chain conformation on polypeptide-membrane interactions. Due to the controlled nature of these polymerizations, within each sample, chain length and interchain composition were narrowly defined.[295] They concluded that polypeptides containing amino acids favoring α-helical secondary structures (e.g. alanine, phenylalanine, and leucine) are generally much stronger membrane disruption agents compared with those containing amino acids favoring β-sheet secondary structures (e.g. iso-leucine and valine).[295] Antimicrobial tests on a small sample of these copolymers with *S. aureus*, *E. coli*, and *P. aeruginosa* showed potent antimicrobial activity, the best of which was the copolypeptide combination of lysine and alanine.[11]

In recent years, the readable synthesis of AMP mimics using NCA ROP has resulted in some interesting new antimicrobial materials. Utilizing a new strategy to synthesize polypeptides with potentially broad range side chain functionalities, Hammond and coworkers synthesized a library of novel synthetic polypeptides through NCA ROP of *γ*-propargyl-Glu-NCA.[296] Polypeptides were prepared in varying molecular weights (30 to 140 repeat units) with click chemistry then used to graft primary, secondary and tertiary amines with hydrophobic hydrocarbon chains to the side chains of the polypeptide. MIC values (defined as the minimum inhibitory concentration of an antimicrobial that can inhibit the growth of bacteria) showed that the polypeptides, particularly those containing quaternary amines exhibited broad-spectrum antimicrobial properties against both Gram positive (*S. aureus*) and Gram negative (*E. coli*) bacteria. The polypeptides also displayed low

hemolytic activity and were shown to be useful as surface coatings to prevent bacterial attachment to glass.[296]

Using controlled synthetic procedures, synthetic polypeptides can also be prepared with novel secondary structures to improve on existing limitations associated with AMP use. As mentioned previously, AMPs can display poor biostability due to interactions with proteases, and also result in blood (hemolytic) and other toxicities. This has been attributed to the common amphipathic or facially amphiphilic (FA) secondary structure of AMPs (**Figure 1.24A**). This secondary conformation reveals an exposed peptide backbone vulnerable to enzymatic degradation and the hydrophobic face of AMPs promotes non-specific interactions with mammalian blood proteins resulting in high hemolytic activities.[263, 292, 297] In fact, high hemolytic activities have been reported for synthetic polypeptide AMPs despite having potent antimicrobial properties.[298] To address this issue, Xiong *at al.* developed novel secondary structures of synthetic polypeptide AMPs. Using NCA ROP, the authors synthesized homopolypeptides of poly(γ-hexyl-L-glutamate) with cationic side chain end groups (PHLG-BIm) (**Figure 1.24C**). The polypeptide was shown to self-assemble into a hydrophobic helical core covered with cationic groups in all radial directions of the helix, known as radial amphiphilicity (RA) (**Figure 1.24B**).[299]

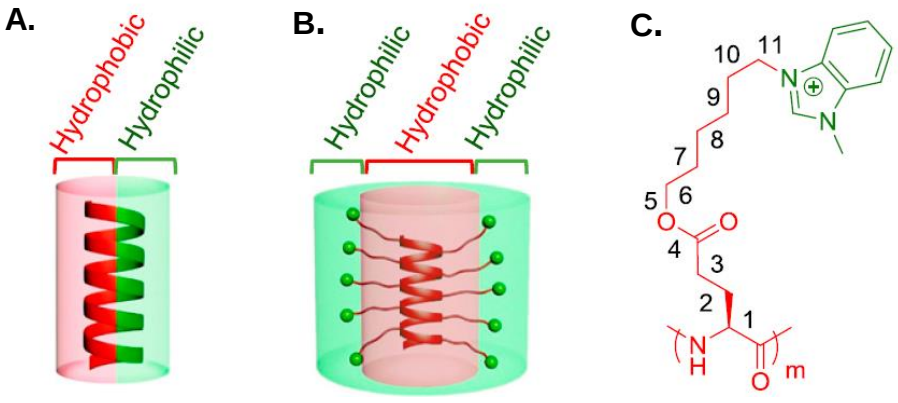

Figure 1.24. Illustrations showing (A) Typical amphipathic secondary structure of AMPs with facial amphiphilicity (FA) (B) Radial amphiphilicity (RA) of AMPs (C) Chemical structure of PHLG-BIm.[299]

Despite only preliminary mechanistic studies into the effect of this new architecture, the polymers displayed broad antimicrobial activities, and shielding of the hydrophobic core by the charged exterior shell was shown to result in low hemolytic activity and a protection from proteolytic degradation.[299]

It is important to note that in some studies, secondary structures traditionally attributed to natural antimicrobial peptides (α-helix, β-sheet) have not been observed in synthetic polypeptide AMPs, despite their potent and broad ranging antimicrobial properties.[298, 300] In fact, dual drug delivery/antimicrobial polypeptides which self- assemble into vesicles structures[148] and nanocapsules[301] have all shown effective antimicrobial efficacies. Therefore, the antimicrobial efficacies observed in these cases appears less stringent on the traditional secondary structure seen in native AMPs.

The grafting of synthetic polypeptides to a range of different non-peptide polymers has been studied to not only improve the antimicrobial properties and functions of these materials but also to generate different polymer architectures for different applications. Chan Park and coworkers in 2012 prepared cationic peptidopolysaccharides, copolymers of chitosan and polylysine as a bacterial cell wall peptidoglycan mimic to facilitate the penetration of the polymer into the bacterial cell wall (**Figure 1.25**).[300] Utilizing a chitosan backbone, polypeptide sidechains made of polylysine were grafted via NCA ROP. The peptidopolysacharides demonstrated effective broad spectrum antimicrobial activity and low MIC values against clinically significant bacteria and fungi with a high selectivity for these pathogens over mammalian red blood cells (low hemolytic activity). Mechanistic studies determined that the peptidopolysaccharide killed the bacteria and fungi through membrane disruption, and was attributed to the close resemblance between the peptidopolysaccharides and the peptidoglycan layer present in the bacterial cells walls (**Figure 1.25**). The authors also prepared poly(lysine)-*r*-poly(phenylalanine) random copolymer grafts and found that the addition of the hydrophobic phenylalanine residues resulted in lower antimicrobial activity (higher MIC) values than using just polylysine.[300]

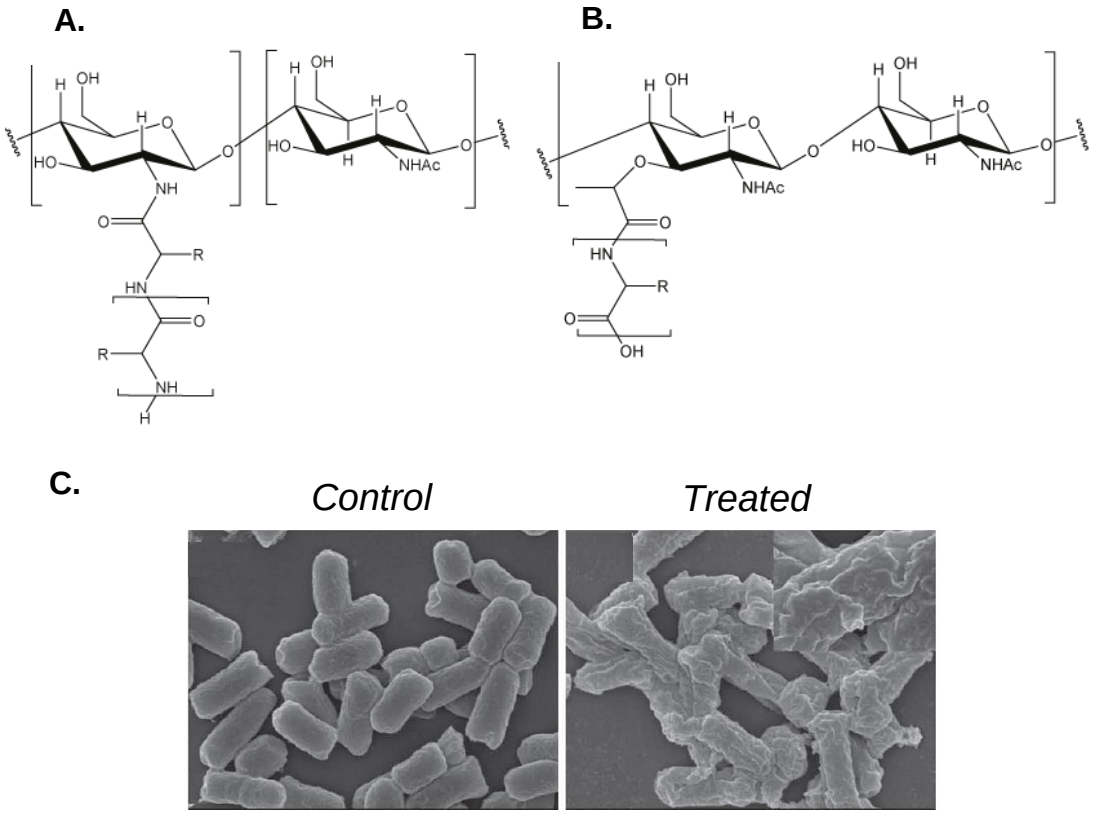

Figure 1.25. (A) Chemical structure of peptidopolysaccharide (chitosan-*g*-polypeptide)(R = Lys) and (B) Bacterial cell wall peptidoglycan (C) Morphology of *E. coli* cells before (control) and after (treatment) with peptidopolysaccharide (chitosan-*g*-poly(L-lysine)). [300]

Cell-adhesive conventional 'nanoporous' peptide/polypeptide hydrogels with inherent antibacterial activity have recently been synthesized for potential wound healing/tissue regeneration scaffolds.[302-306] The most common approach to antimicrobial hydrogels is to load, often non-covalently, known antimicrobial agents e.g. antibiotics, heavy metals onto scaffolds.[302] A hydrogel with innate antimicrobial properties means that the addition of these antimicrobial agents is not required, and avoids the potential of these agents leaching into the surrounding environment.[302, 306] Schneider and coworkers 10 years ago developed hydrogel scaffolds composed of short synthetic peptides (MAX1[304, 307] (**Figure 1.26**) and MARG1[305]) containing lysine (cationic) and valine (hydrophobic) residues. Hydrogels formed by the self-assembly of the amphiphilic peptide were shown to be 'contact active', whereby

bacteria undergo cell membrane disruption and resulting cell death upon contact of the bacteria with the gel. The gels exhibited broad bactericidal activity, including against highly resistance bacteria[305] with selective toxicity toward bacterial cells compared mammalian cells.[304-305] The peptides in this case were synthesized through the time-consuming and high cost solid-phase peptide synthesis protocol.

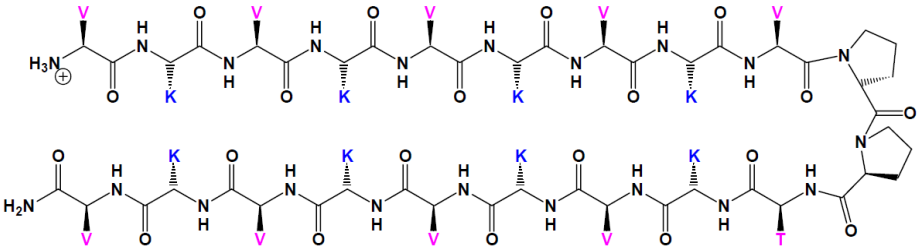

Figure 1.26. MAX1 peptide and its amphiphilic β-hairpin structure showing alternating cationic lysine (K) and hydrophobic valine (V) residues.[307]

In recent years, Christman and coworkers developed synthetic polypeptide hydrogels for similar applications using NCA ROP synthesis. Random polypeptides consisting of poly(L-lysine) and poly(L-alanine) were synthesized through NCA ROP and cross-linked with 6-arm polyethylene glycol (PEG)-amide succinimidyl glutarate (ASG) to form hydrogels (**Figure 1.27**).[308] The hydrogels showed suitable cell attachment and proliferation of mammalian cells and demonstrated significant antimicrobial activity against *E. coli* and *S. aureus* bacteria, suspected to be due to bacteria cell membrane disruption upon contact with the gel.

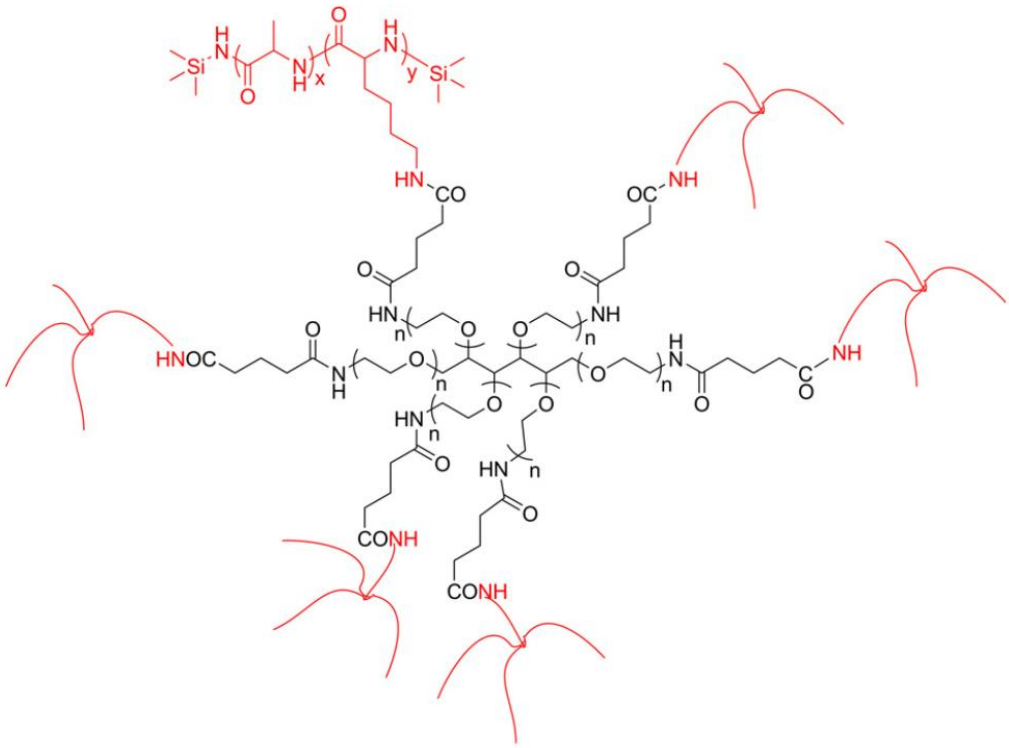

Figure 1.27. Antimicrobial poly(L-lysine)-*r*-poly(L-alanine) copolypeptides/6-arm PEG-ASG hydrogels.[308]

The utilization of synthetic polypeptides in the above biomedical and bioactive applications is indicative of the versatility and wide ranging functional capabilities of these materials. Despite these promising perspectives, research into the use of synthetic polypeptides in these fields is still in its infancy, particularly when considering the complex structural and functional capabilities of their natural biological counterparts. Therefore, there will remain for some time, a significant level of interest in the potential applicability and function of synthetic polypeptide materials in the biomedical and bioactive fields.

1.6 Thesis Objective

The biomimetic properties of synthetic polypeptides and their readable, cost-effective preparation have made them attractive materials for chemists and biologists in the biomedical and antimicrobial (bioactive) fields. Despite this, significant deficiencies remain surrounding the application of synthetic polypeptide materials in these fields:

For instance, in drug delivery, investigations into the use of synthetic polypeptide-based nanoparticles for anticancer cisplatin (CDDP) delivery have traditionally focused on micelle architectures. The development of different synthetic polypeptide-based architectures such as vesicles for cisplatin delivery provides an alternative and potentially useful approach for CDDP delivery. Extending the active targeting of these synthetic polypeptide-based drug delivery nanoparticles such as those containing poly(L-glutamic acid) (PLG) requires the use of more specific active targeting ligands, such as aptamers. Aptamers, selected nucleotide sequences with high antigen specificity, have been used as active targeting ligands in a wide range of polymer drug delivery systems; but have yet to be investigated in synthetic PLG-based delivery systems.

In the field of tissue engineering, the use of synthetic polypeptide materials to generate macroporous hydrogels often requires chemical modification and has thus far been limited to partial components of these gel networks. To effectively study the suitability of synthetic polypeptides as a material for 3D cell culture applications and to better utilize the beneficial properties owing to these materials, the preparation of macroporous hydrogels composed entirely of synthetic polypeptides is desirable.

In the antimicrobial (bioactive) field, polymeric cryogels with antimicrobial properties have demonstrated to be suitable candidates for water treatment applications. However the antimicrobial activity of these cryogels have traditionally come from the incorporation of known antimicrobial agents to the gel structure

rather than from the polymer gel itself, leading to leaching of these agents and subsequent toxicity issues. The antimicrobial (bioactive) properties of synthetic polypeptides presents the possibility of preparing cryogels with inherent antimicrobial properties, thus avoiding toxic leaching issues.

Thus, the objective of this thesis is to fabricate and test novel synthetic polypeptide and synthetic polypeptide-based materials to address the above deficiencies and in the process, advance the scientific understanding and applicability of synthetic polypeptides in the relevant biomedical and bioactive fields (**Figure 1.28**). All synthetic polypeptides described in this thesis were prepared using the scalable and cost-effective NCA ROP procedure.

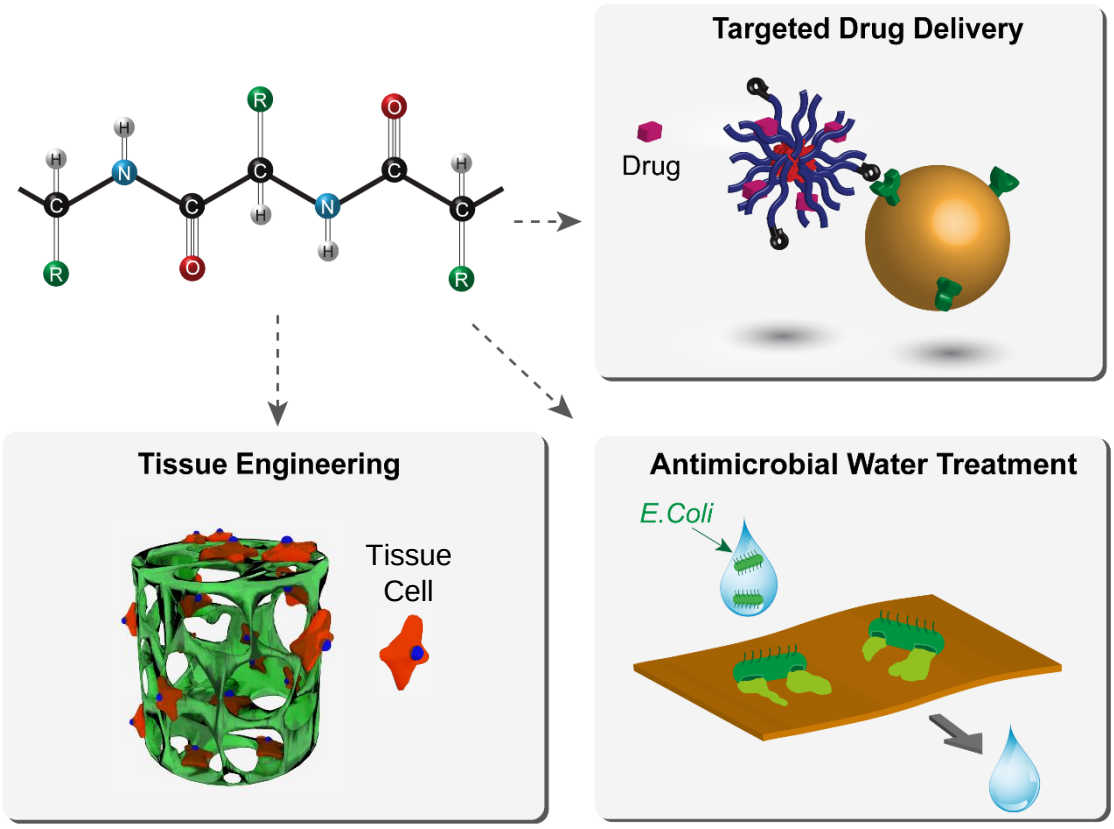

Figure 1.28. *Research themes of this thesis*: Synthetic polypeptides for biomedical and bioactive applications.

1.7 Thesis outline

Chapter 2 outlines the preparation of cisplatin(CDDP)-loaded, poly(L-glutamic acid) (PLG)-based vesicles as a novel, biocompatible, and biodegradable architecture for targeted CDDP delivery. The chapter also outlines a new approach to the preparation of vesicle structures along with their active targeting to cancer cells. Conjugation of hydrophobic CDDP drug to a maleimide(Mal)-PEG-*b*-PLG block copolymer containing short polypeptide block, generated a short, rigid, cross-linked hydrophobic segment resulting in self-assembly of the block polymer into hollow vesicle structures. The morphologies of these hollow vesicle structures were analyzed using a number of analytical techniques including TEM and AFM, with drug loading content and drug loading efficiencies also determined. Drug release studies were performed to determine the release profiles in conditions representative of the intracellular and extracellular environment. Finally, folic acid (FA) was conjugated to the maleimide moieties on the periphery of the vesicles to generate active targeting drug-loaded vesicles. Cell viability assays, confocal laser scanning microscopy (CLSM) and flow cytometry were performed on cancerous (HeLa) and non-cancerous (NIH-3T3) cells incubated with the FA-conjugated vesicles, to determine the selective targeting capabilities and cytotoxicities of these vesicles to cancerous cells compared to non-cancerous cells.

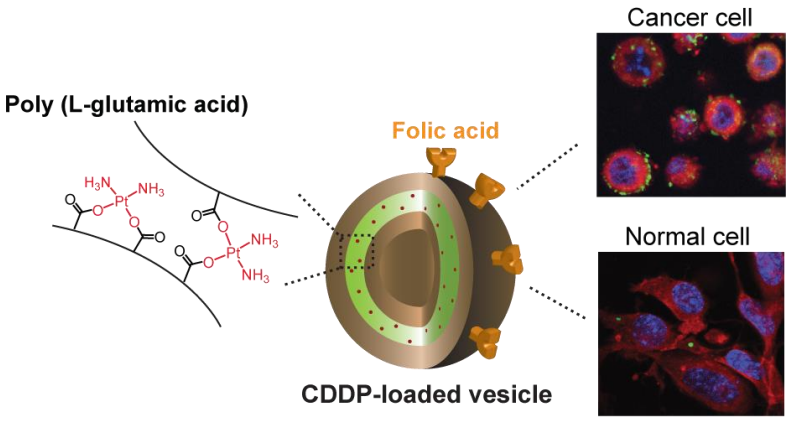

Figure 1.29. *Chapter 2*: Cisplatin-induced formation of biocompatible and biodegradable polypeptide-based vesicles for targeted anticancer drug delivery.

Chapter 3 looks at extending the targeting capabilities of synthetic poly(L-glutamic acid)(PLG)-based drug delivery systems, such as the vesicles studied in **Chapter 2**, by presenting preliminary studies into the preparation of DNA aptamer-targeted PLG-based delivery systems. A thiol-functionalized model single-stranded DNA (ssDNA) aptamer was conjugated to PEG-*b*-PLG block copolymers; common PLG-based nanoparticle precursors used for drug delivery applications. DNA was conjugated to Mal-PEG-*b*-PLG-NH_2 and Mal-PEG-*b*-(PLG-*r*-PLL)-NH_2 block copolymers using thiol-maleimide coupling chemistry, with conjugations monitored through gel electrophoresis, and a range of conjugation conditions studied. A reliable method for the isolation of the conjugates was then investigated using preparative anionic exchange chromatography and preparative gel electrophoresis procedures. Confirmation of conjugate isolation was performed through UV-Vis analysis.

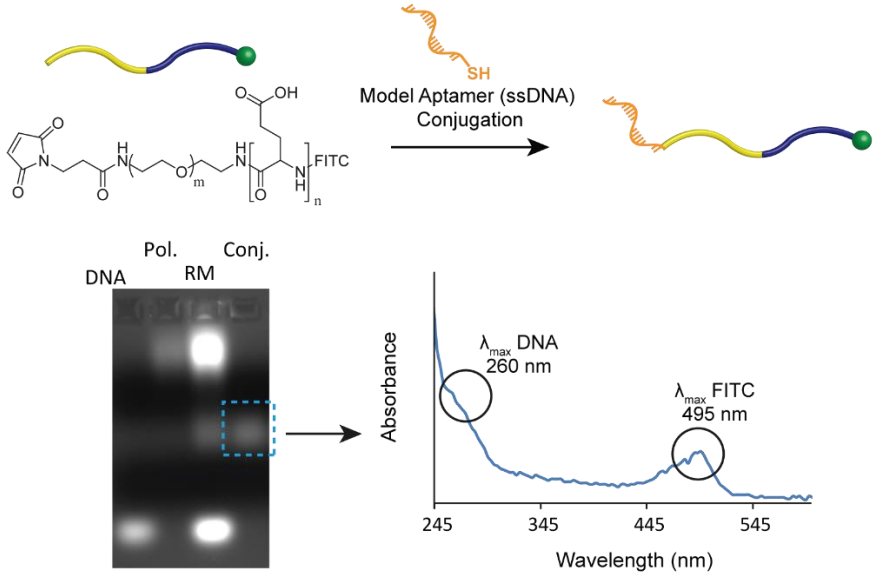

Figure 1.30. *Chapter 3*: Conjugation and purification of a model DNA aptamer to poly(L-glutamic acid)-based delivery systems.

Chapter 4 presents the preparation of the first macroporous hydrogels composed entirely of synthetic polypeptides, and their potential suitability as 3D cellular scaffolds for tissue engineering applications. Under cryoconditions, macroporous

hydrogels in the form of macroporous cryogels were prepared using a single copolymer component through direct EDC/sulfo-NHS zero-length cross-linking between poly(L-glutamic acid) (PLG) and poly(L-lysine) (PLL) residues on a PLG-*r*-PLL random copolypeptide chain. The relative ratios of the polypeptide were varied to determine its effect on the pore structure, swelling and mechanical properties of the gels. The macroporous morphologies of the gels were analyzed using confocal laser scanning microscopy (CLSM) and environmental SEM (ESEM). To demonstrate the potential use of these cryogels as 3D cellular scaffolds, enzymatic biodegradability, cell viability, cell attachment, and cell proliferation tests using mammalian fibroblast (NIH-3T3) cells were performed.

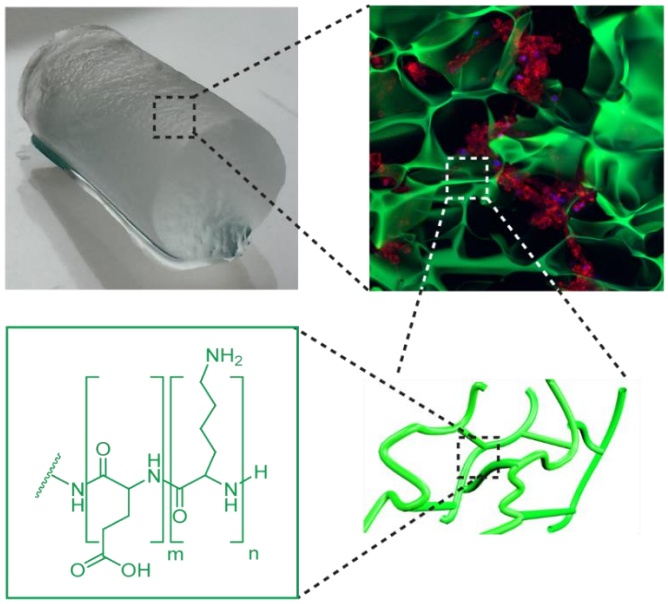

Figure 1.31. *Chapter 4*: Macroporous hydrogels composed entirely of synthetic polypeptides: biocompatible and enzyme biodegradable 3D cellular scaffolds.

Chapter 5 details the preparation of synthetic polypeptide-based macroporous cryogels with inherent antimicrobial properties for potential water purification applications. This is the first reported case of macroporous hydrogels with inherent antimicrobial properties. Gels were chemically cross-linked through the amine residue of a polycationic and hydrophobic poly(L-lysine)-*b*-poly(L,D-valine) block copolymer using glutaraldehyde as cross-linker under cryogenic conditions. The

porosity of the gels were analyzed using ESEM analysis and swelling and mechanical properties of the gels were obtained. The absence of toxic leachate or contaminant was verified through viability tests on mammalian NIH-3T3 cells. The antibacterial performance of the gels was evaluated based on *E. coli* viability after brief incubation of a bacteria solution with the gels. The effect of macroporosity on the antimicrobial performance of the gels was also analyzed with comparative antimicrobial tests performed on conventional nanoporous hydrogels.

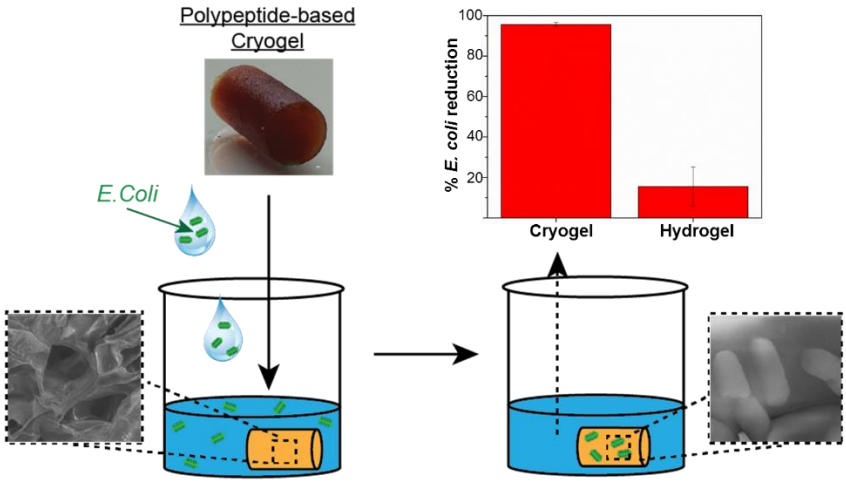

Figure 1.32. *Chapter 5*: Polypeptide-based macroporous cryogels with inherent antimicrobial properties: the importance of a macroporous structure.

In **Chapter 6**, concluding remarks from each chapter are presented along with some proposed future directions for the work outlined in this thesis. **Chapter 7** describes the characterization methods and detailed experimental procedures for all the work presented in this thesis.

1.8 References

(1) Alberts, B.; Johnson, A.; Lewis, J.; Morgan, D.; Raff, M.; Roberts, K.; Walter, P., *Molecular Biology of the Cell, Sixth Edition*. 2015; p 1-1342.

(2) Meroz, Y.; Horn, D., *Proteins-Structure Function and Bioinformatics* **2008,** *72* (2), 606-612.

(3) Branden, C. T., J., *Introduction to Protein Structure*. Garland: New York, 1991.

(4) Ganz, T., *Integr. Comp. Biol.* **2003,** *43* (2), 300-304.

(5) Neurath, H.; Walsh, K. A., *Proc. Natl. Acad. Sci. U.S.A.* **1976,** *73* (11), 3825-3832.

(6) Ciechanover, A.; Orian, A.; Schwartz, A. L., *J. Cell. Biochem.* **2000**, 40-51.

(7) Bingol, B.; Shang, M., *Neuron* **2011,** *69* (1), 22-32.

(8) Bell, R. A. V.; Al-Khalaf, M.; Megeney, L. A., *Skeletal Muscle* **2016,** *6*.

(9) Katchalski-Katzir, E., *Acta Biochim. Pol.* **1996,** *43* (1), 217-226.

(10) Deming, T. J., *J. Polym. Sci., Part A* **2000,** *38* (17), 3011-3018.

(11) Deming, T. J., *Prog. Polym. Sci.* **2007,** *32* (8-9), 858-875.

(12) Kricheldorf, H. R., *Angewandte Chemie-International Edition* **2006,** *45* (35), 5752-5784.

(13) Leuchs, H.; Geiger, W., *Berichte Der Deutschen Chemischen Gesellschaft* **1908,** *41*, 1721-1726.

(14) Deming, T. J., *Nature* **1997,** *390* (6658), 386-389.

(15) Fuchs, F., *Berichte Der Deutschen Chemischen Gesellschaft* **1922,** *55*, 2943-2943.

(16) Farthing, A. C.; Reynolds, R. J. W., *Nature* **1950,** *165* (4199), 647-647.

(17) Daly, W. H.; Poche, D., *Tetrahedron Lett.* **1988,** *29* (46), 5859-5862.

(18) Fujita, Y.; Koga, K.; Kim, H.-K.; Wang, X.-S.; Sudo, A.; Nishida, H.; Endo, T., *J. Polym. Sci. A Polym. Chem.* **2007,** *45* (22), 5365-5370.

(19) Collet, H.; Bied, C.; Mion, L.; Taillades, J.; Commeyras, A., *Tetrahedron Lett.* **1996,** *37* (50), 9043-9046.

(20) Vayaboury, W.; Giani, O.; Cottet, H.; Deratani, A.; Schue, F., *Macromol. Rapid Commun.* **2004,** *25* (13), 1221-1224.

(21) Hemmi, K.; Takeno, H.; Okada, S.; Nakaguchi, O.; Kitaura, Y.; Hashimoto, M., *J. Am. Chem. Soc.* **1981,** *103* (23), 7026-7028.

(22) Yuki, H., *Nippon Kagaku Zasshi* **1956,** *77*, 44-51.

(23) Deming, T. J., *Chem. Rev.* **2016,** *116* (3), 786-808.

(24) Rude, E.; Meyerdel.M, *Carbohydr. Res.* **1968,** *8* (2), 219-&.

(25) Gibson, M. I.; Hunt, G. J.; Cameron, N. R., *Organic & Biomolecular Chemistry* **2007,** *5* (17), 2756-2757.

(26) Kramer, J. R.; Deming, T. J., *J. Am. Chem. Soc.* **2010,** *132* (42), 15068-15071.

(27) Sun, J.; Schlaad, H., *Macromolecules* **2010,** *43* (10), 4445-4448.

(28) Krannig, K. S.; Sun, J.; Schlaad, H., *Biomacromolecules* **2014,** *15* (3), 978-984.

(29) Zhou, J. R.; Chen, P. P.; Deng, C.; Meng, F. H.; Cheng, R.; Zhong, Z. Y., *Macromolecules* **2013,** *46* (17), 6723-6730.

(30) Engler, A. C.; Lee, H. I.; Hammond, P. T., *Angewandte Chemie-International Edition* **2009,** *48* (49), 9334-9338.

(31) Zhang, R. J.; Zheng, N.; Song, Z. Y.; Yin, L. C.; Cheng, J. J., *Biomaterials* **2014,** *35* (10), 3443-3454.

(32) Song, Z. Y.; Zheng, N.; Ba, X. C.; Yin, L. C.; Zhang, R. J.; Ma, L.; Cheng, J. J., *Biomacromolecules* **2014,** *15* (4), 1491-1497.

(33) Deng, Y.; Xu, Y. Z.; Wang, X.; Yuan, Q. L.; Ling, Y.; Tang, H. Y., *Macromol. Rapid Commun.* **2015,** *36* (5), 453-458.

(34) Hadjichristidis, N.; Iatrou, H.; Pitsikalis, M.; Sakellariou, G., *Chem. Rev.* **2009,** *109* (11), 5528-5578.

(35) Dimitrov, I.; Schlaad, H., *Chem. Commun.* **2003,** (23), 2944-2945.

(36) Knobler, Y.; Bittner, S.; Virov, D.; Frankel, M., *Journal of the Chemical Society C-Organic* **1969,** (14), 1821-&.

(37) Cheng, J. J.; Deming, T. J., Synthesis of Polypeptides by Ring-Opening Polymerization of alpha-Amino Acid N-Carboxyanhydrides. In *Peptide-Based Materials*, Deming, T., Ed. Springer-Verlag Berlin: Berlin, 2012; Vol. 310, pp 1-26.

(38) Aliferis, T.; Iatrou, H.; Hadjichristidis, N., *Biomacromolecules* **2004,** *5* (5), 1653-1656.

(39) Conejos-Sanchez, I.; Duro-Castano, A.; Birke, A.; Barz, M.; Vicent, M. J., *Polymer Chemistry* **2013,** *4* (11), 3182-3186.

(40) Zou, J.; Fan, J.; He, X.; Zhang, S.; Wang, H.; Wooley, K. L., *Macromolecules* **2013,** *46* (10), 4223-4226.

(41) Lu, H.; Cheng, J. J., *J. Am. Chem. Soc.* **2007,** *129* (46), 14114-+.

(42) Lu, H.; Cheng, J. J., *J. Am. Chem. Soc.* **2008,** *130* (38), 12562-12563.

(43) Lu, H.; Bai, Y.; Wang, J.; Gabrielson, N. P.; Wang, F.; Lin, Y.; Cheng, J., *Macromolecules* **2011,** *44* (16), 6237-6240.

(44) Duro-Castano, A.; Conejos-Sanchez, I.; Vicent, M. J., *Polymers* **2014,** *6* (2), 515-551.

(45) Hehir, S.; Cameron, N. R., *Polym. Int.* **2014,** *63* (6), 943-954.

(46) Matsumura, Y., *Adv. Drug Del. Rev.* **2008,** *60* (8), 899-914.

(47) Lu, H.; Wang, J.; Song, Z.; Yin, L.; Zhang, Y.; Tang, H.; Tu, C.; Lin, Y.; Cheng, J., *Chem. Commun.* **2014**.

(48) Blanco, E.; Shen, H.; Ferrari, M., *Nat. Biotechnol.* **2015,** *33* (9), 941-951.

(49) Elting, L. S.; Cooksley, C.; Chambers, M.; Cantor, S. B., *Cancer* **2003,** *98* (7), 1531-1539.

(50) Curigliano, G.; Mayer, E. L.; Burstein, H. J.; Winer, E. P.; Goldhirsch, A., *Progress in Cardiovascular Diseases* **2010,** *53* (2), 94-104.

(51) Kamb, A., *Nat. Rev. Drug Discov.* **2005,** *4* (2), 161-165.

(52) Matsumura, Y.; Maeda, H., *Cancer Res.* **1986,** *46* (12), 6387-6392.

(53) Maeda, H.; Greish, K.; Fang, J., The EPR effect and polymeric drugs: A paradigm shift for cancer chemotherapy in the 21st century. In *Polymer Therapeutics Ii: Polymers as Drugs, Conjugates and Gene Delivery Systems*, SatchiFainaro, R.; Duncan, R., Eds. 2006; Vol. 193, pp 103-121.

(54) Maeda, H.; Nakamura, H.; Fang, J., *Adv. Drug Del. Rev.* **2013,** *65* (1), 71-79.

(55) Safra, T.; Muggia, F.; Jeffers, S.; Tsao-Wei, D. D.; Groshen, S.; Lyass, O.; Henderson, R.; Berry, G.; Gabizon, A., *Ann. Oncol.* **2000,** *11* (8), 1029-1033.

(56) Duncan, R., *Nature Reviews Cancer* **2006,** *6* (9), 688-701.

(57) Haag, R.; Kratz, F., *Angewandte Chemie-International Edition* **2006,** *45* (8), 1198-1215.

(58) Stockhofe, K.; Postema, J. M.; Schieferstein, H.; Ross, T. L., *Pharmaceuticals (Basel, Switzerland)* **2014,** *7* (4), 392-418.

(59) Ranganathan, R.; Madanmohan, S.; Kesavan, A.; Baskar, G.; Krishnamoorthy, Y. R.; Santosham, R.; Ponraju, D.; Rayala, S. K.; Venkatraman, G., *International Journal of Nanomedicine* **2012,** *7*, 1043-1060.

(60) Wilhelm, S.; Tavares, A. J.; Dai, Q.; Ohta, S.; Audet, J.; Dvorak, H. F.; Chan, W. C. W., *Nature Reviews Materials* **2016,** *1*, 16014.

(61) Boulaiz, H.; Alvarez, P. J.; Ramirez, A.; Marchal, J. A.; Prados, J.; Rodriguez-Serrano, F.; Peran, M.; Melguizo, C.; Aranega, A., *Int. J. Mol. Sci.* **2011,** *12* (5), 3303-3321.

(62) Greenwald, R. B.; Choe, Y. H.; McGuire, J.; Conover, C. D., *Adv. Drug Del. Rev.* **2003,** *55* (2), 217-250.

(63) Harris, J. M.; Chess, R. B., *Nature Reviews Drug Discovery* **2003,** *2* (3), 214-221.

(64) Fuks, G.; Talom, R. M.; Gauffre, F., *Chem. Soc. Rev.* **2011,** *40* (5), 2475-2493.

(65) Ochs, C. J.; Such, G. K.; Caruso, F., *Langmuir* **2011,** *27* (4), 1275-1280.

(66) Yan, S. F.; Zhu, J.; Wang, Z. C.; Yin, J. B.; Zheng, Y. Z.; Chen, X. S., *European Journal of Pharmaceutics and Biopharmaceutics* **2011,** *78* (3), 336-345.

(67) Kono, K.; Kojima, C.; Hayashi, N.; Nishisaka, E.; Kiura, K.; Wataral, S.; Harada, A., *Biomaterials* **2008,** *29* (11), 1664-1675.

(68) Byrne, M.; Thornton, P. D.; Cryan, S.-A.; Heise, A., *Polymer Chemistry* **2012,** *3* (10), 2825-2831.

(69) Sulistio, A.; Gurr, P. A.; Blencowe, A.; Qiao, G. G., *Aust. J. Chem.* **2012,** *65* (8), 978-984.

(70) Pratesi, G.; Savi, G.; Pezzoni, G.; Bellini, O.; Penco, S.; Tinelli, S.; Zunino, F., *Br. J. Cancer* **1985,** *52* (6), 841-848.

(71) Zunino, F.; Giuliani, F.; Savi, G.; Dasdia, T.; Gambetta, R., *Int. J. Cancer* **1982,** *30* (4), 465-470.

(72) Zunino, F.; Savi, G.; Giuliani, F.; Gambetta, R.; Supino, R.; Tinelli, S.; Pezzoni, G., *European Journal of Cancer & Clinical Oncology* **1984,** *20* (3), 421-425.

(73) Li, C., *Adv. Drug Del. Rev.* **2002,** *54* (5), 695-713.

(74) Duncan, R.; Vicent, M. J., *Adv. Drug Del. Rev.* **2013,** *65* (1), 60-70.

(75) Li, C.; Yu, D. F.; Newman, R. A.; Cabral, F.; Stephens, L. C.; Hunter, N.; Milas, L.; Wallace, S., *Cancer Res.* **1998,** *58* (11), 2404-2409.

(76) Chipman, S. D.; Oldham, F. B.; Pezzoni, G.; Singer, J. W., *International Journal of Nanomedicine* **2006,** *1* (4), 375-383.

(77) Singer, J. W.; Shaffer, S.; Baker, B.; Bernareggi, A.; Stromatt, S.; Nienstedt, D.; Besman, M., *Anti-Cancer Drugs* **2005,** *16* (3), 243-254.

(78) Li, C.; Wallace, S., *Adv. Drug Del. Rev.* **2008,** *60* (8), 886-898.

(79) Galic, V. L.; Herzog, T. J.; Wright, J. D.; Lewin, S. N., *Expert Opinion on Investigational Drugs* **2011,** *20* (6), 813-821.

(80) Shaffer, S. A.; Baker Lee, C.; Kumar, A.; Singer, J. W., *Eur. J. Cancer* **2002,** *38*, S129-S129.

(81) Shaffer, S. A.; Baker-Lee, C.; Kennedy, J.; Lai, M. S.; de Vries, P.; Buhler, K.; Singer, J. W., *Cancer Chemotherapy and Pharmacology* **2007,** *59* (4), 537-548.

(82) Podgorski, I.; Sloane, B. F., *Biochem. Soc. Symp.* **2003,** (70), 263-76.

(83) Aggarwal, N.; Sloane, B. F., *Proteomics Clinical Applications* **2014,** *8* (5-6), 427-437.

(84) Springett, G. M.; Takimoto, C.; McNamara, M.; Doroshow, J. H.; Syed, S.; Eastham, E.; Spriggs, D.; Pezzulli, S.; Michelson, G.; Dupont, J., *Journal of Clinical Oncology* **2004,** *22* (14), 226S-226S.

(85) Eldar-Boock, A.; Miller, K.; Sanchis, J.; Lupu, R.; Vicent, M. J.; Satchi-Fainaro, R., *Biomaterials* **2011,** *32* (15), 3862-3874.

(86) Tian, B.; Tao, X.; Ren, T.; Weng, Y.; Lin, X.; Zhang, Y.; Tang, X., *J. Mater. Chem.* **2012,** *22* (34), 17404-17414.

(87) Croy, S. R.; Kwon, G. S., *Curr. Pharm. Des.* **2006,** *12* (36), 4669-4684.

(88) Letchford, K.; Burt, H., *European Journal of Pharmaceutics and Biopharmaceutics* **2007,** *65* (3), 259-269.

(89) Discher, D. E.; Eisenberg, A., *Science* **2002,** *297* (5583), 967-973.

(90) Soussan, E.; Cassel, S.; Blanzat, M.; Rico-Lattes, I., *Angewandte Chemie-International Edition* **2009,** *48* (2), 274-288.

(91) Holowka, E. P.; Pochan, D. J.; Deming, T. J., *J. Am. Chem. Soc.* **2005,** *127* (35), 12423-12428.

(92) Holowka, E. P.; Sun, V. Z.; Kamei, D. T.; Deming, T. J., *Nat. Mater.* **2007,** *6* (1), 52-57.

(93) Rodriguez-Hernandez, J.; Lecommandoux, S., *J. Am. Chem. Soc.* **2005,** *127* (7), 2026-2027.

(94) Lavasanifar, A.; Samuel, J.; Kwon, G. S., *Adv. Drug Del. Rev.* **2002,** *54* (2), 169-190.

(95) Bellomo, E. G.; Wyrsta, M. D.; Pakstis, L.; Pochan, D. J.; Deming, T. J., *Nat. Mater.* **2004,** *3* (4), 244-248.

(96) Kwon, G.; Naito, M.; Yokoyama, M.; Okano, T.; Sakurai, Y.; Kataoka, K., *J. Controlled Release* **1997,** *48* (2-3), 195-201.

(97) Ding, J.; Li, C.; Zhang, Y.; Xu, W.; Wang, J.; Chen, X., *Acta Biomater.* **2015,** *11*, 346-355.

(98) Hua, S.-H.; Li, Y.-Y.; Liu, Y.; Xiao, W.; Li, C.; Huang, F.-W.; Zhang, X.-Z.; Zhuo, R.-X., *Macromol. Rapid Commun.* **2010,** *31* (1), 81-86.

(99) Yokoyama, M.; Okano, T.; Sakurai, Y.; Kataoka, K., *J. Controlled Release* **1994,** *32* (3), 269-277.

(100) Nakanishi, T.; Fukushima, S.; Okamoto, K.; Suzuki, M.; Matsumura, Y.; Yokoyama, M.; Okano, T.; Sakurai, Y.; Kataoka, K., *J. Controlled Release* **2001,** *74* (1-3), 295-302.

(101) Nishiyama, N.; Okazaki, S.; Cabral, H.; Miyamoto, M.; Kato, Y.; Sugiyama, Y.; Nishio, K.; Matsumura, Y.; Kataoka, K., *Cancer Res.* **2003,** *63* (24), 8977-8983.

(102) Yokoyama, M.; Miyauchi, M.; Yamada, N.; Okano, T.; Sakurai, Y.; Kataoka, K.; Inoue, S., *Cancer Res.* **1990,** *50* (6), 1693-1700.

(103) Matsumura, Y., *Jap. J. Clin. Oncol.* **2008,** *38* (12), 793-802.

(104) Uchino, H.; Matsumura, Y.; Negishi, T.; Koizumi, F.; Hayashi, T.; Honda, T.; Nishiyama, N.; Kataoka, K.; Naito, S.; Kakizoe, T., *Br. J. Cancer* **2005,** *93* (6), 678-687.

(105) Thurmond, K. B.; Kowalewski, T.; Wooley, K. L., *J. Am. Chem. Soc.* **1996,** *118* (30), 7239-7240.

(106) O'Reilly, R. K.; Hawker, C. J.; Wooley, K. L., *Chem. Soc. Rev.* **2006,** *35* (11), 1068-1083.

(107) van Nostrum, C. F., *Soft Matter* **2011,** *7* (7), 3246-3259.

(108) Holowka, E. P.; Deming, T. J., *Macromol. Biosci.* **2010,** *10* (5), 496-502.

(109) Sulistio, A.; Blencowe, A.; Wang, J.; Bryant, G.; Zhang, X.; Qiao, G. G., *Macromol. Biosci.* **2012,** *12* (9), 1220-1231.

(110) Lee, S. J.; Min, K. H.; Lee, H. J.; Koo, A. N.; Rim, H. P.; Jeon, B. J.; Jeong, S. Y.; Heo, J. S.; Lee, S. C., *Biomacromolecules* **2011,** *12* (4), 1224-1233.

(111) Ren, T. B.; Feng, Y.; Dong, H. Q.; Li, L.; Li, Y. Y., *Progress in Chemistry* **2011,** *23* (1), 213-220.

(112) Lee, Y.; Ishii, T.; Cabral, H.; Kim, H. J.; Seo, J.-H.; Nishiyama, N.; Oshima, H.; Osada, K.; Kataoka, K., *Angewandte Chemie-International Edition* **2009,** *48* (29), 5309-5312.

(113) Han, S.-S.; Li, Z.-Y.; Zhu, J.-Y.; Han, K.; Zeng, Z.-Y.; Hong, W.; Li, W.-X.; Jia, H.-Z.; Liu, Y.; Zhuo, R.-X.; Zhang, X.-Z., *Small* **2015,** *11* (21), 2543-2554.

(114) Bae, Y.; Nishiyama, N.; Fukushima, S.; Koyama, H.; Yasuhiro, M.; Kataoka, K., *Bioconjugate Chem.* **2005,** *16* (1), 122-130.

(115) Guan, H.; McGuire, M. J.; Li, S.; Brown, K. C., *Bioconjugate Chem.* **2008,** *19* (9), 1813-1821.

(116) Sui, B.; Xu, H.; Jin, J.; Gou, J.; Liu, J.; Tang, X.; Zhang, Y.; Xu, J.; Zhang, H.; Jin, X., *Molecules* **2014,** *19* (8), 11915-11932.

(117) E. Hurwitz, M. W., J. Pitha, *Journal of Applied Biochemistry* **1980,** *2*, 25-35.

(118) Hashida, M.; Akamatsu, K.; Nishikawa, M.; Yamashita, F.; Takakura, Y., *J. Controlled Release* **1999,** *62* (1-2), 253-262.

(119) Akamatsu, K.; Yamasaki, Y.; Nishikawa, M.; Takakura, Y.; Hashida, M., *Biochem. Pharmacol.* **2001,** *62* (11), 1531-1536.

(120) Huynh, V. T.; Chen, G. J.; de Souza, P.; Stenzel, M. H., *Biomacromolecules* **2011,** *12* (5), 1738-1751.

(121) Yan, X. L.; Gemeinhart, R. A., *J. Controlled Release* **2005,** *106* (1-2), 198-208.

(122) Nishiyama, N.; Yokoyama, M.; Aoyagi, T.; Okano, T.; Sakurai, Y.; Kataoka, K., *Langmuir* **1999,** *15* (2), 377-383.

(123) Huynh, V. T.; de Souza, P.; Stenzel, M. H., *Macromolecules* **2011,** *44* (20), 7888-7900.

(124) Yang, K. M.; Liang, H.; Lu, J., *J. Mater. Chem.* **2011,** *21* (28), 10390-10398.

(125) Wiltshire, J. T.; Qiao, G. G., *Aust. J. Chem.* **2007,** *60* (10), 699-705.

(126) Gao, H. F.; Matyjaszewski, K., *Macromolecules* **2007,** *40* (3), 399-401.

(127) Jiang, G. H.; Ren, J. B., *Des. Monomers Polym.* **2010,** *13* (5), 427-436.

(128) Terashima, T.; Ouchi, M.; Ando, T.; Kamigaito, M.; Sawamoto, M., *J. Polym. Sci., Part A* **2006,** *44* (17), 4966-4980.

(129) Schramm, O. G.; Meier, M. A. R.; Hoogenboom, R.; van Erp, H. P.; Gohy, J. F.; Schubert, U. S., *Soft Matter* **2009,** *5* (8), 1662-1667.

(130) Johnston, A. P. R.; Cortez, C.; Angelatos, A. S.; Caruso, F., *Current Opinion in Colloid & Interface Science* **2006,** *11* (4), 203-209.

(131) Kojima, C.; Kono, K.; Maruyama, K.; Takagishi, T., *Bioconjugate Chem.* **2000,** *11* (6), 910-917.

(132) Blencowe, A.; Tan, J. F.; Goh, T. K.; Qiao, G. G., *Polymer* **2009,** *50* (1), 5-32.

(133) Inoue, K.; Sakai, H.; Ochi, S.; Itaya, T.; Tanigaki, T., *J. Am. Chem. Soc.* **1994,** *116* (23), 10783-10784.

(134) Duro-Castano, A.; England, R. M.; Razola, D.; Romero, E.; Oteo-Vives, M.; Angel Morcillo, M.; Vicent, M. J., *Mol. Pharm.* **2015,** *12* (10), 3639-3649.

(135) Tansey, W.; Ke, S.; Cao, X. Y.; Pasuelo, M. J.; Wallace, S.; Li, C., *J. Controlled Release* **2004,** *94* (1), 39-51.

(136) Junnila, S.; Houbenov, N.; Hanski, S.; Iatrou, H.; Hirao, A.; Hadjichristidis, N.; Ikkala, O., *Macromolecules* **2010,** *43* (21), 9071-9076.

(137) Higashi, N.; Koga, T.; Niwa, M., *ChemBioChem* **2002,** *3* (5), 448-454.

(138) Qiu, S.; Huang, H.; Dong, C. M., *Chin. J. Polym. Sci.* **2009,** *27* (6), 797-805.

(139) Worsfold, D. J.; Zilliox, J. G.; Rempp, P., *Can. J. Chem.* **1969,** *47* (18), 3379-&.

(140) Sulistio, A.; Widjaya, A.; Blencowe, A.; Zhang, X. Q.; Qiao, G., *Chem. Commun.* **2011,** *47* (4), 1151-1153.

(141) Sulistio, A.; Blencowe, A.; Widjaya, A.; Zhang, X. Q.; Qiao, G., *Polymer Chemistry* **2012,** *3* (1), 224-234.

(142) Xing, T.; Lai, B.; Ye, X. D.; Yan, L. F., *Macromol. Biosci.* **2011,** *11* (7), 962-969.

(143) Chou, L. Y. T.; Ming, K.; Chan, W. C. W., *Chem. Soc. Rev.* **2011,** *40* (1), 233-245.

(144) Kamaly, N.; Xiao, Z. Y.; Valencia, P. M.; Radovic-Moreno, A. F.; Farokhzad, O. C., *Chem. Soc. Rev.* **2012,** *41* (7), 2971-3010.

(145) Lu, Y. J.; Low, P. S., *Adv. Drug Del. Rev.* **2002,** *54* (5), 675-693.

(146) Vlahov, I. R.; Leamon, C. P., *Bioconjugate Chem.* **2012,** *23* (7), 1357-1369.

(147) Sulistio, A.; Lowenthal, J.; Blencowe, A.; Bongiovanni, M. N.; Ong, L.; Gras, S. L.; Zhang, X. Q.; Qiao, G. G., *Biomacromolecules* **2011,** *12* (10), 3469-3477.

(148) Wang, M.; Zhou, C.; Chen, J.; Xiao, Y.; Du, J., *Bioconjugate Chem.* **2015,** *26* (4), 725-34.

(149) Yang, X.; Grailer, J. J.; Rowland, I. J.; Javadi, A.; Hurley, S. A.; Matson, V. Z.; Steeber, D. A.; Gong, S., *Acs Nano* **2010,** *4* (11), 6805-6817.

(150) Lee, Y. K., *Macromolecular Research* **2006,** *14* (3), 387-393.

(151) Leamon, C. P., *Current Opinion in Investigational Drugs* **2008,** *9* (12), 1277-1286.

(152) Song, W. T.; Li, M. Q.; Tang, Z. H.; Li, Q. S.; Yang, Y.; Liu, H. Y.; Duan, T. C.; Hong, H.; Chen, X. S., *Macromol. Biosci.* **2012,** *12* (11), 1514-1523.

(153) Song, W. T.; Tang, Z. H.; Zhang, D. W.; Zhang, Y.; Yu, H. Y.; Li, M. Q.; Lv, S. X.; Sun, H.; Deng, M. X.; Chen, X. S., *Biomaterials* **2014,** *35* (9), 3005-3014.

(154) Miura, Y.; Takenaka, T.; Toh, K.; Wu, S.; Nishihara, H.; Kano, M. R.; Ino, Y.; Nomoto, T.; Matsumoto, Y.; Koyama, H.; Cabral, H.; Nishiyama, N.; Kataoka, K., *Acs Nano* **2013,** *7* (10), 8583-8592.

(155) Vega, J.; Ke, S.; Fan, Z.; Wallace, S.; Charsangavej, C.; Li, C., *Pharm. Res.* **2003,** *20* (5), 826-832.

(156) Kato, Y.; Umemoto, N.; Kayama, Y.; Fukushima, H.; Takeda, Y.; Hara, T.; Tsukada, Y., *J. Med. Chem.* **1984,** *27* (12), 1602-1607.

(157) O'Brien, F. J., *Mater. Today* **2011,** *14* (3), 88-95.

(158) Lee, K. Y.; Mooney, D. J., *Chem. Rev.* **2001,** *101* (7), 1869-1879.

(159) Dhandayuthapani, B.; Yoshida, Y.; Maekawa, T.; Kumar, D. S., *International Journal of Polymer Science* **2011**.

(160) El-Sherbiny, I. M.; Yacoub, M. H., *Global Cardiology Science & Practice* **2013,** *2013* (3), 316-342.

(161) Ahmed, E. M., *Journal of Advanced Research* **2015,** *6* (2), 105-121.

(162) Bencherif, S. A.; Braschler, T. M.; Renaud, P., *Journal of Periodontal and Implant Science* **2013,** *43* (6), 251-261.

(163) Annabi, N.; Nichol, J. W.; Zhong, X.; Ji, C. D.; Koshy, S.; Khademhosseini, A.; Dehghani, F., *Tissue Engineering Part B-Reviews* **2010,** *16* (4), 371-383.

(164) Tibbitt, M. W.; Anseth, K. S., *Biotechnol. Bioeng.* **2009,** *103* (4), 655-663.

(165) Langer, R.; Tirrell, D. A., *Nature* **2004,** *428* (6982), 487-492.

(166) Henderson, T. M. A.; Ladewig, K.; Haylock, D. N.; McLean, K. M.; O'Connor, A. J., *J. Mater. Chem. B* **2013,** *1* (21), 2682-2695.

(167) Chiu, Y.-C.; Cheng, M.-H.; Engel, H.; Kao, S.-W.; Larson, J. C.; Gupta, S.; Brey, E. M., *Biomaterials* **2011,** *32* (26), 6045-6051.

(168) Mandal, B. B.; Kundu, S. C., *Biomaterials* **2009,** *30* (15), 2956-2965.

(169) Lien, S. M.; Ko, L. Y.; Huang, T. J., *Acta Biomater.* **2009,** *5* (2), 670-679.

(170) Freudenberg, U.; Hermann, A.; Welzel, P. B.; Stirl, K.; Schwarz, S. C.; Grimmer, M.; Zieris, A.; Panyanuwat, W.; Zschoche, S.; Meinhold, D.; Storch, A.; Werner, C., *Biomaterials* **2009,** *30* (28), 5049-5060.

(171) Tsurkan, M. V.; Levental, K. R.; Freudenberg, U.; Werner, C., *Chem. Commun.* **2010,** *46* (7), 1141-1143.

(172) Welzel, P. B.; Grimmer, M.; Renneberg, C.; Naujox, L.; Zschoche, S.; Freudenberg, U.; Werner, C., *Biomacromolecules* **2012,** *13* (8), 2349-2358.

(173) Wake, M. C.; Patrick, C. W.; Mikos, A. G., *Cell Transplantation* **1994,** *3* (4), 339-343.

(174) Ford, M. C.; Bertram, J. P.; Hynes, S. R.; Michaud, M.; Li, Q.; Young, M.; Segal, S. S.; Madri, J. A.; Lavik, E. B., *Proc. Natl. Acad. Sci. U.S.A.* **2006,** *103* (8), 2512-2517.

(175) Yan, S.; Zhang, K.; Liu, Z.; Zhang, X.; Gan, L.; Cao, B.; Chen, X.; Cui, L.; Yin, J., *J. Mater. Chem. B* **2013,** *1* (11), 1541-1551.

(176) Berger, J.; Reist, M.; Mayer, J. M.; Felt, O.; Peppas, N. A.; Gurny, R., *European Journal of Pharmaceutics and Biopharmaceutics* **2004,** *57* (1), 19-34.

(177) Zhang, Y. B.; Ye, L.; Cui, M.; Yang, B. G.; Li, J. J.; Sun, H.; Yao, F. L., *Rsc Advances* **2015,** *5* (95), 78180-78191.

(178) Holloway, J. L.; Lowman, A. M.; Palmese, G. R., *Soft Matter* **2013,** *9* (3), 826-833.

(179) Lee, S. B.; Kim, Y. H.; Chong, M. S.; Hong, S. H.; Lee, Y. M., *Biomaterials* **2005,** *26* (14), 1961-1968.

(180) Kudo, K.; Ishida, J.; Syuu, G.; Sekine, Y.; Ikeda-Fukazawa, T., *J. Chem. Phys.* **2014,** *140* (4).

(181) Van Vlierberghe, S., *J. Mater. Sci* **2016,** *51* (9), 4349-4357.

(182) Zhao, X.; Kim, J.; Cezar, C. A.; Huebsch, N.; Lee, K.; Bouhadir, K.; Mooney, D. J., *Proc. Natl. Acad. Sci. U.S.A.* **2011,** *108* (1), 67-72.

(183) Hunt, J. A.; Chen, R.; van Veen, T.; Bryan, N., *J. Mater. Chem. B* **2014,** *2* (33), 5319-5338.

(184) Okay, O.; Lozinsky, V. I., Synthesis and Structure–Property Relationships of Cryogels. In *Polymeric Cryogels: Macroporous Gels with Remarkable Properties*, Okay, O., Ed. Springer International Publishing: Cham, 2014; pp 103-157.

(185) Okay, O., *Prog. Polym. Sci.* **2000,** *25* (6), 711-779.

(186) Guarino, V.; Gloria, A.; Raucci, M. G.; Ambrosio, L., *Polymers* **2012,** *4* (3), 1590-1612.

(187) Kahveci, M. U.; Beyazkilic, Z.; Yagci, Y., *J. Polym. Sci., Part A* **2010,** *48* (22), 4989-4994.

(188) Hennink, W. E.; van Nostrum, C. F., *Adv. Drug Del. Rev.* **2012,** *64*, 223-236.

(189) Kathuria, N.; Tripathi, A.; Kar, K. K.; Kumar, A., *Acta Biomater.* **2009,** *5* (1), 406-418.

(190) Dainiak, M. B.; Allan, I. U.; Savina, I. N.; Cornelio, L.; James, E. S.; James, S. L.; Mikhalovsky, S. V.; Jungvid, H.; Galaev, I. Y., *Biomaterials* **2010,** *31* (1), 67-76.

(191) Wu, X. M.; Black, L.; Santacana-Laffitte, G.; Patrick, C. W., *J. Biomed. Mater. Res. A* **2007,** *81A* (1), 59-65.

(192) Eiselt, P.; Lee, K. Y.; Mooney, D. J., *Macromolecules* **1999,** *32* (17), 5561-5566.

(193) Henderson, T. M. A.; Ladewig, K.; Haylock, D. N.; McLean, K. M.; O'Connor, A. J., *J. Biomater. Sci., Polym. Ed.* **2015,** *26* (13), 881-897.

(194) Chiu, Y. C.; Larson, J. C.; Isom, A.; Brey, E. M., *Tissue Engineering Part C-Methods* **2010,** *16* (5), 905-912.

(195) Murphy, W. L.; Dennis, R. G.; Kileny, J. L.; Mooney, D. J., *Tissue Eng.* **2002,** *8* (1), 43-52.

(196) Wei, G. B.; Ma, P. X., *Biomaterials* **2009,** *30* (32), 6426-6434.

(197) Park, J. S.; Woo, D. G.; Sun, B. K.; Chung, H. M.; Im, S. J.; Choi, Y. M.; Park, K.; Huh, K. M.; Park, K. H., *J. Controlled Release* **2007,** *124* (1-2), 51-59.

(198) Xu, F.; Sridharan, B.; Durmus, N. G.; Wang, S. Q.; Yavuz, A. S.; Gurkan, U. A.; Demirci, U., *Plos One* **2011,** *6* (4).

(199) Draghi, L.; Resta, S.; Pirozzolo, M. G.; Tanzi, M. C., *Journal of Materials Science-Materials in Medicine* **2005,** *16* (12), 1093-1097.

(200) Kim, J.; Yaszemski, M. J.; Lu, L. C., *Tissue Engineering Part C-Methods* **2009,** *15* (4), 583-594.

(201) Hamid, Z. A. A.; Blencowe, A.; Ozcelik, B.; Palmer, J. A.; Stevens, G. W.; Abberton, K. M.; Morrison, W. A.; Penington, A. J.; Qiao, G. G., *Biomaterials* **2010,** *31* (25), 6454-6467.

(202) Lips, P. A. M.; Velthoen, I. W.; Dijkstra, P. J.; Wessling, M.; Feijen, J., *Polymer* **2005,** *46* (22), 9396-9403.

(203) Ma, P. X.; Choi, J. W., *Tissue Eng.* **2001,** *7* (1), 23-33.

(204) Dehghani, F.; Annabi, N., *Curr. Opin. Biotechnol.* **2011,** *22* (5), 661-666.

(205) Ozcelik, B.; Blencowe, A.; Palmer, J.; Ladewig, K.; Stevens, G. W.; Abberton, K. M.; Morrison, W. A.; Qiao, G. G., *Acta Biomater.* **2014,** *10* (6), 2769-2780.

(206) Huh, K. M.; Baek, N.; Park, K., *J. Bioact. Compatible Polym.* **2005,** *20* (3), 231-243.

(207) Keskar, V.; Marion, N. W.; Mao, J. J.; Gemeinhart, R. A., *Tissue Engineering Part A* **2009,** *15* (7), 1695-1707.

(208) Savina, I. N.; Ingavle, G. C.; Cundy, A. B.; Mikhalovsky, S. V., *Scientific Reports* **2016,** *6*.

(209) Plieva, F. M.; Karlsson, M.; Aguilar, M. R.; Gomez, D.; Mikhalovsky, S.; Galaev, I. Y., *Soft Matter* **2005,** *1* (4), 303-309.

(210) Lozinsky, V. I.; Vainerman, E. S.; Korotaeva, G. F.; Rogozhin, S. V., *Colloid. Polym. Sci.* **1984,** *262* (8), 617-622.

(211) Vainerman, E. S.; Lozinsky, V. I.; Rogozhin, S. V., *Colloid. Polym. Sci.* **1981,** *259* (12), 1198-1201.

(212) Liu, Y.; Vrana, N. E.; Cahill, P. A.; McGuinness, G. B., *Journal of Biomedical Materials Research Part B-Applied Biomaterials* **2009,** *90B* (2), 492-502.

(213) Ricciardi, R.; D'Errico, G.; Auriemma, F.; Ducouret, G.; Tedeschi, A. M.; De Rosa, C.; Laupretre, F.; Lafuma, F., *Macromolecules* **2005,** *38* (15), 6629-6639.

(214) Strom, A.; Larsson, A.; Okay, O., *J. Appl. Polym. Sci.* **2015,** *132* (29), 42194.

(215) Sedlacik, T.; Proks, V.; Slouf, M.; Duskova-Smrckova, M.; Studenovska, H.; Rypacek, F., *Biomacromolecules* **2015,** *16* (11), 3455-65.

(216) Stokols, S.; Tuszynski, M. H., *Biomaterials* **2004,** *25* (27), 5839-5846.

(217) Chau, M.; De France, K. J.; Kopera, B.; Machado, V. R.; Rosenfeldt, S.; Reyes, L.; Chan, K. J. W.; Förster, S.; Cranston, E. D.; Hoare, T.; Kumacheva, E., *Chem. Mater.* **2016**, DOI: 10.1021/acs.chemmater.6b00792. Published Online: April 14, 2016.

(218) Tripathi, A.; Kumar, A., *Macromol. Biosci.* **2011,** *11* (1), 22-35.

(219) Lv, Q.; Feng, Q. L., *Journal of Materials Science-Materials in Medicine* **2006,** *17* (12), 1349-1356.

(220) Ohya, Y.; Matsunami, H.; Ouchi, T., *J. Biomater. Sci., Polym. Ed.* **2004,** *15* (1), 111-123.

(221) Kang, H. W.; Tabata, Y.; Ikada, Y., *J. Bioact. Compatible Polym.* **1999,** *14* (4), 331-343.

(222) Ma, L.; Gao, C. Y.; Mao, Z. W.; Zhou, J.; Shen, J. C.; Hu, X. Q.; Han, C. M., *Biomaterials* **2003,** *24* (26), 4833-4841.

(223) Schneider, G. B.; English, A.; Abraham, M.; Zaharias, R.; Stanford, C.; Keller, J., *Biomaterials* **2004,** *25* (15), 3023-3028.

(224) Qiu, Q.; Sayer, M.; Kawaja, M.; Shen, X.; Davies, J. E., *Journal of Biomedical Materials Research* **1998,** *42* (1), 117-127.

(225) Lee, J. H.; Jung, H. W.; Kang, I. K.; Lee, H. B., *Biomaterials* **1994,** *15* (9), 705-711.

(226) Omrani, M. M.; Kiaie, N.; Ansari, M.; Kordestani, S. S., *Journal of Macromolecular Science Part B-Physics* **2016,** *55* (6), 617-626.

(227) Cao, B.; Yan, S.; Zhang, K.; Song, Z.; Cao, T.; Chen, X.; Cui, L.; Yin, J., *Macromol. Biosci.* **2011,** *11* (7), 970-977.

(228) Camci-Unal, G.; Nichol, J. W.; Bae, H.; Tekin, H.; Bischoff, J.; Khademhosseini, A., *J Tissue Eng Regen Med* **2013,** *7* (5), 337-347.

(229) Seidlits, S. K.; Drinnan, C. T.; Petersen, R. R.; Shear, J. B.; Suggs, L. J.; Schmidt, C. E., *Acta Biomater.* **2011,** *7* (6), 2401-2409.

(230) Koshy, S. T.; Ferrante, T. C.; Lewin, S. A.; Mooney, D. J., *Biomaterials* **2014,** *35* (8), 2477-2487.

(231) Tripathi, A.; Kathuria, N.; Kumar, A., *J. Biomed. Mater. Res. A* **2009,** *90A* (3), 680-694.

(232) Bencherif, S. A.; Sands, R. W.; Bhatta, D.; Arany, P.; Verbeke, C. S.; Edwards, D. A.; Mooney, D. J., *Proc. Natl. Acad. Sci. U.S.A.* **2012,** *109* (48), 19590-19595.

(233) Studenovska, H.; Vodicka, P.; Proks, V.; Hlucilova, J.; Motlik, J.; Rypacek, F., *J Tissue Eng Regen Med* **2010,** *4* (6), 454-463.

(234) Gobin, A. S.; West, J. L., *Biotechnol. Progr.* **2003,** *19* (6), 1781-1785.

(235) Drury, J. L.; Mooney, D. J., *Biomaterials* **2003,** *24* (24), 4337-4351.

(236) Hwang, C. M.; Sant, S.; Masaeli, M.; Kachouie, N. N.; Zamanian, B.; Lee, S. H.; Khademhosseini, A., *Biofabrication* **2010,** *2* (3).

(237) Discher, D. E.; Janmey, P.; Wang, Y. L., *Science* **2005,** *310* (5751), 1139-1143.

(238) Liu, J.; Zheng, H.; Poh, P. S. P.; Machens, H.-G.; Schilling, A. F., *Int. J. Mol. Sci.* **2015,** *16* (7), 15997-16016.

(239) Geckil, H.; Xu, F.; Zhang, X. H.; Moon, S.; Demirci, U., *Nanomedicine* **2010,** *5* (3), 469-484.

(240) Sartori, S.; Chiono, V.; Tonda-Turo, C.; Mattu, C.; Gianluca, C., *J. Mater. Chem. B* **2014,** *2* (32), 5128-5144.

(241) Savina, I. N.; Cnudde, V.; D'Hollander, S.; Van Hoorebeke, L.; Mattiasson, B.; Galaev, I. Y.; Du Prez, F., *Soft Matter* **2007,** *3* (9), 1176-1184.

(242) Jurga, M.; Dainiak, M. B.; Sarnowska, A.; Jablonska, A.; Tripathi, A.; Plieva, F. M.; Savina, I. N.; Strojek, L.; Jungvid, H.; Kumar, A.; Lukomska, B.; Domanska-Janik, K.; Forraz, N.; McGuckin, C. P., *Biomaterials* **2011,** *32* (13), 3423-3434.

(243) Van Vlierberghe, S.; Dubruel, P.; Schacht, E., *Biomacromolecules* **2011,** *12* (5), 1387-1408.

(244) Zhu, J. M.; Marchant, R. E., *Expert Review of Medical Devices* **2011,** *8* (5), 607-626.

(245) Bhat, S.; Tripathi, A.; Kumar, A., *Journal of the Royal Society Interface* **2011,** *8* (57), 540-554.

(246) Tan, H. P.; Marra, K. G., *Materials* **2010,** *3* (3), 1746-1767.

(247) Van Vlierberghe, S.; Dubruel, P.; Lippens, E.; Cornelissen, M.; Schacht, E., *J. Biomater. Sci., Polym. Ed.* **2009,** *20* (10), 1417-1438.

(248) Brandl, F.; Sommer, F.; Goepferich, A., *Biomaterials* **2007,** *28* (2), 134-146.

(249) Varghese, S.; Elisseeff, J. H., Hydrogels for musculoskeletal tissue engineering. In *Polymers for Regenerative Medicine*, Werner, C.; Eisseeff, J. H.; Fischbach, C.; Freier, T.; Garcia, A. J.; Mooney, D. J.; Pompe, T.; Salchert, K.; Varghese, S.; Werner, C.; Zhang, S.; Zhao, X., Eds. 2006; pp 95-144.

(250) Tessmar, J. K.; Gopferich, A. M., *Macromol. Biosci.* **2007,** *7* (1), 23-39.

(251) Deshmukh, M.; Singh, Y.; Gunaseelan, S.; Gao, D. Y.; Stein, S.; Sinko, P. J., *Biomaterials* **2010,** *31* (26), 6675-6684.

(252) Hudalla, G. A.; Eng, T. S.; Murphy, W. L., *Biomacromolecules* **2008,** *9* (3), 842-849.

(253) Gong, Y. H.; Zhou, Q. L.; Gao, C. Y.; Shen, J. C., *Acta Biomater.* **2007,** *3* (4), 531-540.

(254) Gentile, P.; Chiono, V.; Carmagnola, I.; Hatton, P. V., *Int. J. Mol. Sci.* **2014,** *15* (3), 3640-3659.

(255) Koupaei, N.; Karkhaneh, A., *Tissue Engineering and Regenerative Medicine* **2016,** *13* (3), 251-260.

(256) Richert, L.; Arntz, Y.; Schaaf, P.; Voegel, J. C.; Picart, C., *Surf. Sci.* **2004,** *570* (1-2), 13-29.

(257) Richert, L.; Lavalle, P.; Vautier, D.; Senger, B.; Stoltz, J. F.; Schaaf, P.; Voegel, J. C.; Picart, C., *Biomacromolecules* **2002,** *3* (6), 1170-1178.

(258) Cao, B.; Yin, J.; Yan, S.; Cui, L.; Chen, X.; Xie, Y., *Macromol. Biosci.* **2011,** *11* (3), 427-434.

(259) Zhang, Z.; Chen, L.; Deng, M.; Bai, Y.; Chen, X.; Jing, X., *J. Polym. Sci., Part A* **2011,** *49* (13), 2941-2951.

(260) Ganz, T., *J. Leukocyte Biol.* **2004,** *75* (1), 34-38.

(261) Martin, E.; Ganz, T.; Lehrer, R. I., *J. Leukocyte Biol.* **1995,** *58* (2), 128-136.

(262) Izadpanah, A.; Gallo, R. L., *Journal of the American Academy of Dermatology* **2005,** *52* (3), 381-392.

(263) Bahar, A. A.; Ren, D., *Pharmaceuticals (Basel, Switzerland)* **2013,** *6* (12), 1543-75.

(264) Sitaram, N., *Curr. Med. Chem.* **2006,** *13* (6), 679-696.

(265) Hancock, R. E. W.; Falla, T. J., *Clin. Microbiol. Infect.* **1996,** *1* (4), 226-229.

(266) Cole, A. M.; Cole, A. L., *Am. J. Reprod. Immunol.* **2008,** *59* (1), 27-34.

(267) Porcelli, F.; Verardi, R.; Shi, L.; Henzler-Wildman, K. A.; Ramamoorthy, A.; Veglia, G., *Biochemistry* **2008,** *47* (20), 5565-5572.

(268) Dathe, M.; Wieprecht, T., *Biochimica Et Biophysica Acta-Biomembranes* **1999,** *1462* (1-2), 71-87.

(269) Jenssen, H.; Hamill, P.; Hancock, R. E. W., *Clin. Microbiol. Rev.* **2006,** *19* (3), 491-+.

(270) Brogden, K. A., *Nature Reviews Microbiology* **2005,** *3* (3), 238-250.

(271) Yang, L.; Gordon, V. D.; Trinkle, D. R.; Schmidt, N. W.; Davis, M. A.; DeVries, C.; Som, A.; Cronan, J. E., Jr.; Tew, G. N.; Wong, G. C. L., *Proc. Natl. Acad. Sci. U.S.A.* **2008,** *105* (52), 20595-20600.

(272) Shai, Y., *Biopolymers* **2002,** *66* (4), 236-248.

(273) Zhang, L. J.; Rozek, A.; Hancock, R. E. W., *J. Biol. Chem.* **2001,** *276* (38), 35714-35722.

(274) Hancock, R. E. W.; Sahl, H.-G., *Nat. Biotechnol.* **2006,** *24* (12), 1551-1557.

(275) Oren, Z.; Shai, Y., *Peptide Science* **1998,** *47* (6), 451-463.

(276) Lee, D. G.; Kim, H. N.; Park, Y.; Kim, H. K.; Choi, B. H.; Choi, C.-H.; Hahm, K.-S., *Biochim. Biophys. Acta* **2002,** *1598* (1–2), 185-194.

(277) Kustanovich, I.; Shalev, D. E.; Mikhlin, M.; Gaidukov, L.; Mor, A., *J. Biol. Chem.* **2002,** *277* (19), 16941-16951.

(278) Zelezetsky, I.; Pag, U.; Sahl, H. G.; Tossi, A., *Peptides* **2005,** *26* (12), 2368-2376.

(279) Al-Badri, Z. M.; Som, A.; Lyon, S.; Nelson, C. F.; Nusslein, K.; Tew, G. N., *Biomacromolecules* **2008,** *9* (10), 2805-2810.

(280) Colak, S.; Nelson, C. F.; Nusslein, K.; Tew, G. N., *Biomacromolecules* **2009,** *10* (2), 353-359.

(281) Jiang, Z.; Vasil, A. I.; Hale, J. D.; Hancock, R. E. W.; Vasil, M. L.; Hodges, R. S., *Biopolymers* **2008,** *90* (3), 369-383.

(282) de Lucca, A. J.; Walsh, T. J., *Antimicrob. Agents Chemother.* **1999,** *43* (1), 1-11.

(283) Otvos, L., *J. Pept. Sci.* **2005,** *11* (11), 697-706.

(284) He, K.; Ludtke, S. J.; Worcester, D. L.; Huang, H. W., *Biophys. J.* **1996,** *70* (6), 2659-2666.

(285) Guilhelmelli, F.; Vilela, N.; Albuquerque, P.; Derengowski, L. d. S.; Silva-Pereira, I.; Kyaw, C. M., *Frontiers in Microbiology* **2013,** *4*.

(286) Yeaman, M. R.; Yount, N. Y., *Pharmacol. Rev.* **2003,** *55* (1), 27-55.

(287) Shukla, A.; Fleming, K. E.; Chuang, H. F.; Chau, T. M.; Loose, C. R.; Stephanopoulos, G. N.; Hammond, P. T., *Biomaterials* **2010,** *31* (8), 2348-2357.

(288) Marr, A. K.; Gooderham, W. J.; Hancock, R. E. W., *Curr. Opin. Pharmacol.* **2006,** *6* (5), 468-472.

(289) Matsuzaki, K., *Biochimica Et Biophysica Acta-Biomembranes* **2009,** *1788* (8), 1687-1692.

(290) Pacor, S.; Giangaspero, A.; Bacac, M.; Sava, G.; Tossi, A., *J. Antimicrob. Chemother.* **2002,** *50* (3), 339-348.

(291) Bacalum, M.; Radu, M., *International Journal of Peptide Research and Therapeutics* **2015,** *21* (1), 47-55.

(292) Stroemstedt, A. A.; Pasupuleti, M.; Schmidtchen, A.; Malmsten, M., *Antimicrob. Agents Chemother.* **2009,** *53* (2), 593-602.

(293) Sieprawska-Lupa, M.; Mydel, P.; Krawczyk, K.; Wojcik, K.; Puklo, M.; Lupa, B.; Suder, P.; Silberring, J.; Silberring, J.; Reed, M.; Pohl, J.; Shafer, W.; McAleese, F.; Foster, T.; Travis, J.; Potempa, J., *Antimicrob. Agents Chemother.* **2004,** *48* (12), 4673-4679.

(294) Sela, M.; Katchalski, E., Biological Properties of Poly-α- Amino Acids. In *Adv. Protein Chem.*, C.B. Anfinsen, M. L. A. K. B.; John, T. E., Eds. Academic Press: 1959; Vol. Volume 14, pp 391-478.

(295) Wyrsta, M. D.; Cogen, A. L.; Deming, T. J., *J. Am. Chem. Soc.* **2001,** *123* (51), 12919-12920.

(296) Engler, A. C.; Shukla, A.; Puranam, S.; Buss, H. G.; Jreige, N.; Hammond, P. T., *Biomacromolecules* **2011,** *12* (5), 1666-1674.

(297) Chen, Y. X.; Mant, C. T.; Farmer, S. W.; Hancock, R. E. W.; Vasil, M. L.; Hodges, R. S., *J. Biol. Chem.* **2005,** *280* (13), 12316-12329.

(298) Zhou, C.; Qi, X.; Li, P.; Chen, W. N.; Mouad, L.; Chang, M. W.; Leong, S. S. J.; Chan-Park, M. B., *Biomacromolecules* **2010,** *11* (1), 60-67.

(299) Xiong, M.; Lee, M. W.; Mansbach, R. A.; Song, Z.; Bao, Y.; Peek, R. M., Jr.; Yao, C.; Chen, L.-F.; Ferguson, A. L.; Wong, G. C. L.; Cheng, J., *Proc. Natl. Acad. Sci. U.S.A.* **2015,** *112* (43), 13155-13160.

(300) Li, P.; Zhou, C.; Rayatpisheh, S.; Ye, K.; Poon, Y. F.; Hammond, P. T.; Duan, H.; Chan-Park, M. B., *Adv. Mater.* **2012,** *24* (30), 4130-4137.

(301) Zhou, C.; Wang, M.; Zou, K.; Chen, J.; Zhu, Y.; Du, J., *ACS Macro Lett.* **2013,** *2* (11), 1021-1025.

(302) Veiga, A. S.; Schneider, J. P., *Biopolymers* **2013,** *100* (6), 637-644.

(303) Jiang, L.; Xu, D.; Sellati, T. J.; Dong, H., *Nanoscale* **2015,** *7* (45), 19160-19169.

(304) Salick, D. A.; Kretsinger, J. K.; Pochan, D. J.; Schneider, J. P., *J. Am. Chem. Soc.* **2007,** *129* (47), 14793-14799.

(305) Salick, D. A.; Pochan, D. J.; Schneider, J. P., *Adv. Mater.* **2009,** *21* (41), 4120-4123.

(306) Ng, V. W. L.; Chan, J. M. W.; Sardon, H.; Ono, R. J.; Garcia, J. M.; Yang, Y. Y.; Hedrick, J. L., *Adv. Drug Del. Rev.* **2014,** *78*, 46-62.

(307) Kretsinger, J. K.; Haines, L. A.; Ozbas, B.; Pochan, D. J.; Schneider, J. P., *Biomaterials* **2005,** *26* (25), 5177-5186.

(308) Song, A.; Rane, A. A.; Christman, K. L., *Acta Biomater.* **2012,** *8* (1), 41-50.

2

Cisplatin-Induced Formation of Biocompatible and Biodegradable Polypeptide-Based Vesicles for Targeted Anticancer Drug Delivery

2.1 Chapter Perspective

Investigations into the use of synthetic polypeptide-based nanoparticles for anticancer cisplatin (CDDP) delivery have traditionally focused on micelle architectures. The development of different synthetic polypeptide-based architectures for cisplatin delivery provides an alternative and potentially useful approach for CDDP delivery. In this chapter, synthetic polypeptide-based vesicles were prepared as a novel, biocompatible, and biodegradable architecture for cisplatin delivery. Vesicles were formed from maleimide-poly(ethylene oxide)-*b*-poly(L-glutamic acid) block copolymers upon conjugation with the drug itself. Drug release studies demonstrated a low and sustained drug release profile in systemic conditions with a higher "burst-like" release rate being observed under late endosomal/lysosomal conditions. Peripheral functionalization of the vesicles with folic acid (FA) generated targeting vesicles which exhibited significantly higher cellular binding/uptake into and dose-dependent cytotoxicity toward cancer cells (HeLa) compared to noncancerous cells (NIH-3T3).

2.2 Introduction

Cisplatin (CDDP), a hydrophobic chemotherapeutic agent used extensively to treat a wide range of cancers,[1-2] has for many years had limited efficacy due to solubility and toxicity issues that have affected its cancer therapy effect.[3-4] Its incorporation into polymer nanoparticles has been studied for many years as a means to improve its poor water solubility, alleviate the systemic cytotoxicity associated with the free drug, and improve drug loading at the tumor site.[5] Nanoscale assemblies for CDDP delivery has for many years largely involved matrix (micelle) systems, demonstrating effective delivery profiles and reduced CDDP associated toxicity.[6-8] In recent times, there has been a focus on the use of biodegradable and biocompatible polymers as precursors to these delivery systems.[9-14] Most notable has been the widespread use of self-assembling poly(ethylene glycol)-*b*-poly(L-glutamic acid) (PEG-*b*-PLG) block copolymers into micellar delivery systems upon conjugation with platinum drugs.[15-19] Poly(ethylene glycol), a hydrophilic biocompatible polymer, acts as a stealth coating that improves the circulation time of the nanoparticles in the bloodstream.[20-21] Poly(L-glutamic acid), possesses unique biodegradability properties,[22-23] and a free acid moiety that allows for effective conjugation of the platinum drug to the γ-COOH group of the polypeptide side chain, rendering the polypeptide block hydrophobic and leading to drug-induced self-assembly.[16] Cisplatin, with its two coordination sites, is typically able to bind to two carboxylate residues, often leading to intra/inter polymer cross-linking (similar in principle to its antitumor mechanism of disrupting the DNA structure in cell nuclei through the formation of intra- and interstrand cross-links[24]), which can help stabilize the core of these CDDP-loaded micellar assemblies.[17, 25]

Vesicles, large bioinspired nanoscale assemblies,[26] have been of interest in CDDP delivery systems mainly in the form of drug-loaded, self-assembling, lipid-based vesicles (liposomes).[27-29] In contrast to micelles, vesicles contain a hydrophobic membrane and an aqueous cavity that allow for versatile drug transport properties and-due to their larger structure–encapsulation of a larger amount of drugs

compared to micelles, thus allowing for smaller amounts of drug delivery vehicles to be administered while achieving similar drug dosages.[30]

Vesicles, like other nanoparticle systems, are able to passively target tumor cells by exploiting the leaky vasculature at tumor sites, commonly known as the enhanced permeability retention (EPR) effect.[31-32] Cell uptake can be further enhanced by modifying the surface of the vesicle with active targeting ligands such as antibodies, aptamers, or folic acid (FA) that bind to cell receptors that are overexpressed in tumor cells; thus allowing for more localized drug release profiles at the tumor sites.[33-35]

We recently developed a vesicle system for CDDP drug delivery via the use of self-assembling synthetic polymers.[36-37] Although, we-similarly to others-demonstrated high drug loading and effective cancer toxicity in this work, the lack of biodegradability limits the practicality of applying such materials clinically. It would thus be desirable to establish a CDDP-loaded vesicle delivery system using naturally occurring precursors in order to further improve on these existing delivery systems.

In the early 2000s, Lecommandoux *et al.*[38] and Deming *et al.*[39-41] reported on the successful preparation of vesicles from self-assembling, amphiphilic, polypeptide-based block copolymers. Vesicle formation was attributed to the presence of small, rigid (α-helical), hydrophobic peptide blocks that favor the formation of a densely packed, hydrophobic membrane. The stability of the secondary conformation requires that the hydrophilic segment be sufficiently large to sterically stabilize as well as solubilize these dense, hydrophobic domains.[41-42] Deming and co-workers demonstrated that successful vesicle formation of a poly(ethylene glycol)-modified polypeptide (hydrophilic) and poly(L-leucine) (hydrophobic) block copolymer required a hydrophilic block range of 100−150 repeating units with a hydrophobic segment of ∼20 repeat units (∼10−20 mol %).[39] Other reported works have demonstrated the use of long, hydrophilic and short, rigid, hydrophobic segments to promote tight packing of the polymers into spherical vesicles.[43-44]

In the above cases, vesicle formation can be attributed to the hydrophobic segment of the polymer itself. However, herein we postulate that the formation of polypeptide-based (PEG-*b*-PLG) block copolymer vesicles may also be directed by the drug itself, whereby the intrinsic cross-linking capabilities of cisplatin are used to form a short, rigid, cross-linked hydrophobic segment, which subsequently induces self-assembly.

This chapter describes the facile preparation of cisplatin (CDDP)-loaded vesicles composed of a biocompatible and biodegradable poly(ethylene oxide)$_{114}$-*b*-poly(L-glutamic acid)$_{12}$ block copolymer. The rationally designed block copolymer consists of a hydrophilic PEG block of 114 repeat units with a short PLG block of 12 repeat units to achieve a hydrophobic component of ~10 mol %. The copolymer itself exists in a unimolecular state in aqueous, physiological environments. CDDP conjugation to the polypeptide block induces the self-assembly of the copolymer into vesicles in water through the formation of a dense, cross-linked, hydrophobic domain. Maleimide functionalities on the vesicle surface/outer corona allow for conjugation of thiol-functionalized folic acid (FA), resulting in presentation of this cancer targeting ligand on the vesicle periphery. HeLa (cervical cancer cells) and NIH-3T3 (noncancerous fibroblasts) cell lines with respectively high and low FA receptor (FR) expression are used for *in vitro* cytotoxicity and cellular uptake studies to demonstrate the specificity of the cancer targeting capabilities of the resulting drug delivery vehicle.

2.3 Results and Discussion

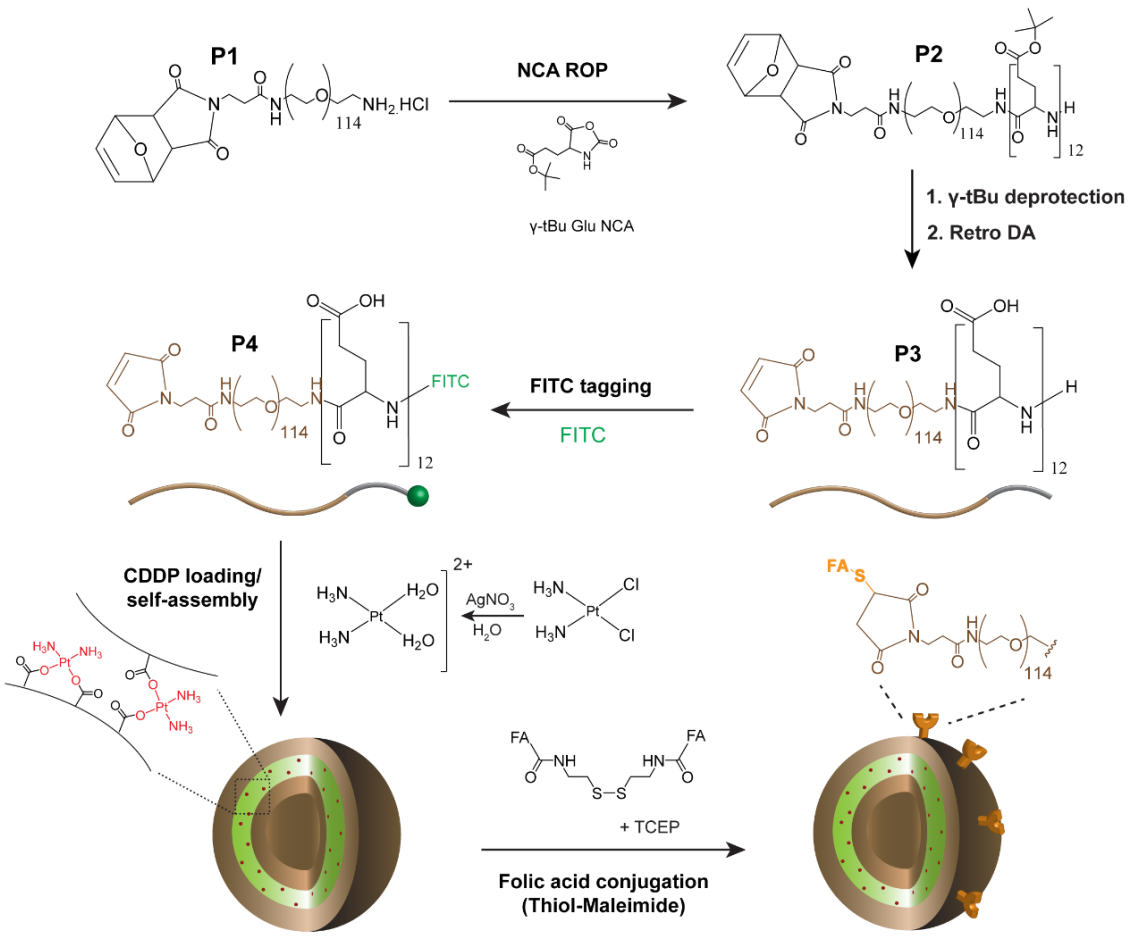

Scheme 2.1. Synthetic scheme of folic acid-conjugated CDDP-loaded Mal-PEG-*b*-PLG-FITC vesicles.

2.3.1 Synthesis of Block Copolymer

The preparation of polypeptide-based vesicles suitable for targeted drug delivery to cancer cells began with the synthesis of maleimide functional PEG-*b*-PLG-NH_2 (Mal-PEG-*b*-PLG-NH_2) **P3** block copolymer by controlled ring-opening polymerization (ROP) of *γ-tert*-butyl-L-glutamate *N*-carboxyanhydride (*γ*-tBu Glu NCA) monomer using furan protected Mal-PEG(5 kDa)-NH_2HCl (**P1)** as macroinitiator (MI) (**Scheme 2.1**). The maleimide group is susceptible to nucleophilic attack by amines.[45] Preliminary NMR and GPC analysis after polymerization using unprotected MI confirmed the presence of higher molecular weight species and a

noticeable reduction in maleimide vinyl proton intensities as a result of self-coupling between the terminal maleimide and the amine of the living block copolymer chain. This observation was particularly obvious after repetitive isolation and concentration of the unprotected MI copolymer. A thermally reversible Diels–Alder (DA) reaction between furan and maleimide MI was therefore adopted for the protection of the reactive maleimide double bond in **P1** (~95 mol % protection based on maleimide vinyl proton integration δ_H = 7.00 ppm, ^{1}H NMR d_6-DMSO) throughout the polymer synthetic process.[46-49]

The use of an amine hydrochloride salt initiator allows for the controlled polymerization of *γ*-tBu Glu NCA monomer by ensuring a controlled concentration of reactive free amine species in an associate-dissociate equilibrium.[50] For block copolymer synthesis a monomer to macroinitiator ratio ([M]: [I]) of 11 was used to obtain a future hydrophobic (drug conjugated) glutamic acid block of ~10 mol %, with ^{1}H NMR analysis used to confirm block copolymer synthesis with a degree of polymerization (DP) of 12 (**Figure 2.1B**, see **Appendix Figure A2.3** for polypeptide block ^{1}H integration).^{1}H NMR analysis of the block copolymer **P2** in **Figure 2.1A** shows the characteristic signals of the poly(L-glutamic acid) side chain methylene protons (c and c', CH–C**H**$_2$–C**H**$_2$–CO–O–tBu) at δ_H = 1.7–2.3 ppm with the *γ-tert*-butyl protecting group (d, CH–CH_2–CH_2–CO–O–**tBu**) proton resonances at δ_H = 1.4 ppm. Resonances from δ_H = 5.0–6.5 ppm were assigned to the protected maleimide DA cycloadduct which exists as both endo/exo stereoisomers as reported in literature (see **Appendix Figure A2.2**).[49, 51]

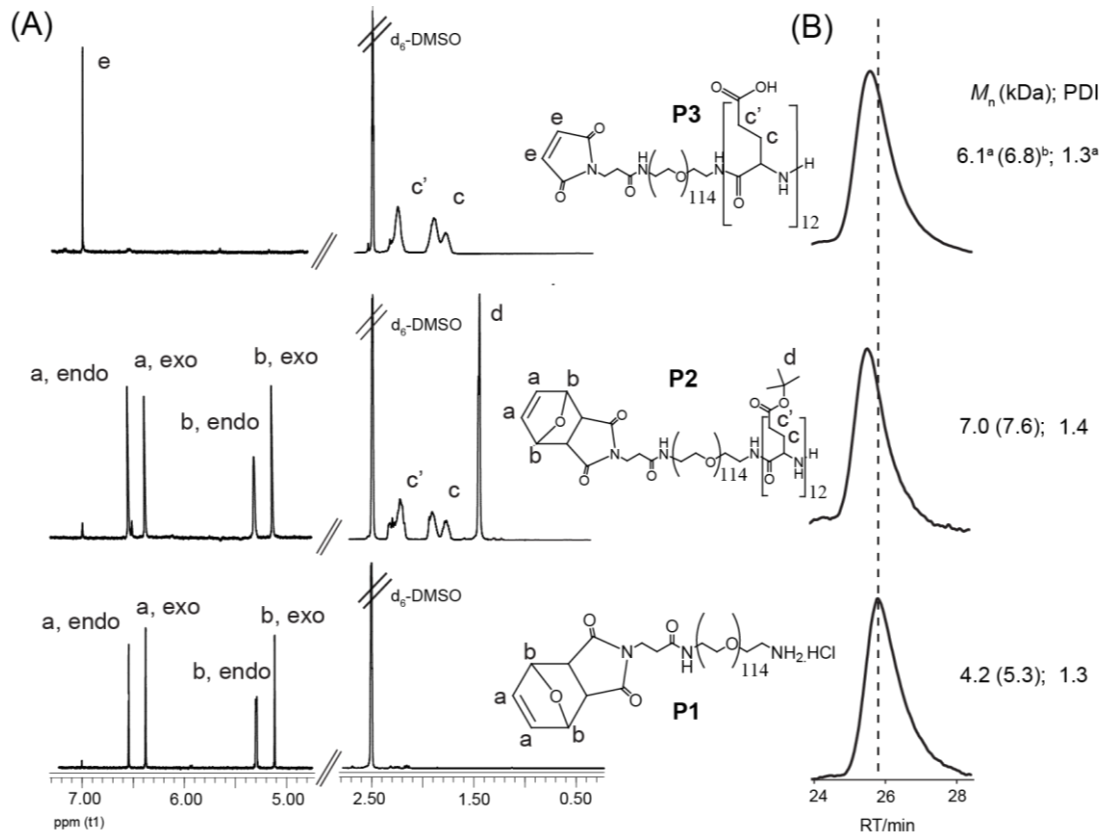

Figure 2.1. (A) ^{1}H NMR (d_6-DMSO) spectra and (B) GPC (DMF) RI chromatograms of polymers **P1**-**P3.** [a] M_n and PDI determined by GPC using MeO-PEG-OH standards, [b] M_n determined by ^{1}H NMR analysis using PEG (C**H**$_2$-C**H**$_2$-O) proton integrations as reference.

Traditionally, γ-benzyl protected L-glutamic acid NCA has been employed for the ROP synthesis of PLG. Subsequent deprotection conditions typically involve strong acid (HBr) or bases (NaOH), which have been found to cause both poly(ethylene glycol) and polypeptide backbone chain cleavage.[52] Strong acids have also been found to promote retro DA at low temperatures[53] and readily react with the resulting free maleimide. To avoid any unwanted chain cleavage or maleimide hydrolysis, γ-tBu Glu NCA monomer was employed with the protecting group readily removed under mild conditions (TFA in DCM) after polymerization. Retro DA was performed under reflux to afford the free maleimide copolymer (**P3**) with ^{1}H NMR analysis in **Figure 2.1A** confirming the disappearance of the t-butyl and DA cycloadduct protons, with an increase in the free maleimide double bond vinyl

protons at (δ_H = 7.00 ppm ^{1}H, d_6-DMSO) to ~97 mol % integrity as calculated by ^{1}H NMR integration. SEC analysis in **Figure 2.1B** shows a unimodal distribution with a relatively narrow polydispersity (~1.3) maintained throughout the polymerization and deprotection of the block copolymer, indicating the absence of any unwanted higher MW self-coupled block copolymer or cleaved species.

The resulting block copolymer **P3** contains a terminal maleimide and amine group suitable for conjugation of a thiol targeting ligand and fluorescent FITC tag, respectively. Conjugation of the FITC tag was performed through a conventional amine-isothiocyanate coupling procedure (**Scheme 2.1**) using triethylamine as catalyst to prepare block copolymer **P4**. FITC tagging efficiency was determined to be ~50 mol % through UV–Vis (494 nm, ε = 85200 Lmol^{-1}cm^{-1}) and ^{1}H NMR analysis.

2.3.2 CDDP Loading of Block Copolymer/Vesicle Formation

Cisplatin was conjugated to the carboxylic acid side chain of the PLG block via a *cis*-diaminediaqua platinum(II) complex using previously reported procedures[7] (**Scheme 2.1**). Conjugation of platinum to the carboxylic acid side chain was verified through FT-IR (**Figure 2.2**).

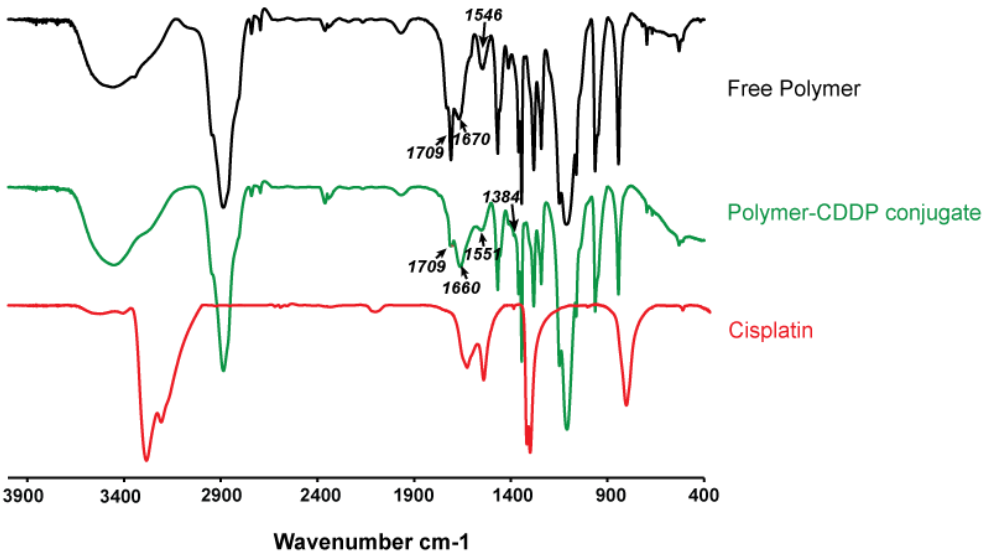

Figure 2.2. FT-IR spectra of free polymer, polymer-CDDP complex and CDDP. Spectra ran in transmittance mode.

A reduction in absorbance of the carbonyl (C=O) stretch of COOH at 1709 cm^{-1} and the presence of new COO–Pt stretch at 1384 cm^{-1} is consistent with reports of Pt binding to PLG acid groups.[54-55] Additionally, small shifts in the amide I (1670–1660 cm^{-1}) and amide II (1546–1551 cm^{-1}) frequencies indicate a secondary conformation change of the polypeptide block after CDDP conjugation, possibly due to cross-linking by the drug.

ICP-OES was used to determine a drug loading content (DLC) of 7.4 wt % (see **Appendix 2** for comparative DLC based on TGA). Assuming that each platinum drug is bound to two carboxylate groups, this DLC value was used to determine a drug conjugation efficiency (DCE) of 50% (see **Appendix 2 for DCE calculations**), indicating a strong drug loading capacity where half of the carboxylate side chains of the polymer are complexed with drug. **Table 2.1** summarizes the Pt (II) loading properties of vesicles, all of which are lipid-based (liposomes) where the Pt(II) drug is encapsulated through physical interactions, currently in clinical trials.[27] The drug loading capacity in this work is comparable, and even higher than SPI-077 and Aroplatin liposomal systems.

Compound	**Pt (II)**	**Carrier**	**DLC (wt %)**	**Ref**
Lipoplatin	cisplatin	liposome	10	[56]
Lipoxal	oxaliplatin	liposome	10	[57]
SPI-077	cisplatin	liposome	6.7	[58]
Aroplatin	oxaliplatin	liposome	6	[59]
PEG-*b*-PLG	cisplatin	polypeptide-based vesicle	7.4	This work

Table 2.1. Platinum(II)- loaded vesical (liposomal) nanocarriers currently in clinical trials.[27]

The added benefit of a biodegradable polypeptide component in this work is also likely to have an improved toxicity and drug release profile to these Pt (II)-loaded

liposomes. The drug loading also compares well with cisplatin-conjugated nonbiodegradable synthetic polymer (HPMA) micelles (AP5280) currently in clinical trials (8.5 wt %).[60] In the case of polypeptide-based PEG-*b*-PLG micelles (NC-6004) currently in clinical trials, with CDDP also conjugated to the PLG backbone, the drug loading is much higher (39 wt %).[15, 19] In NC-6004, the PLG block consists of ~40 repeat units[15] and so the lower DLC in this work is expected due to the shorter peptide segment employed (DP = 12) and therefore lower number of L-glutamic acid units available for metal conjugation. However, due to the much larger size of vesicles compared to these micelles, far fewer delivery vectors can be administered for the same therapeutic dose.[30]

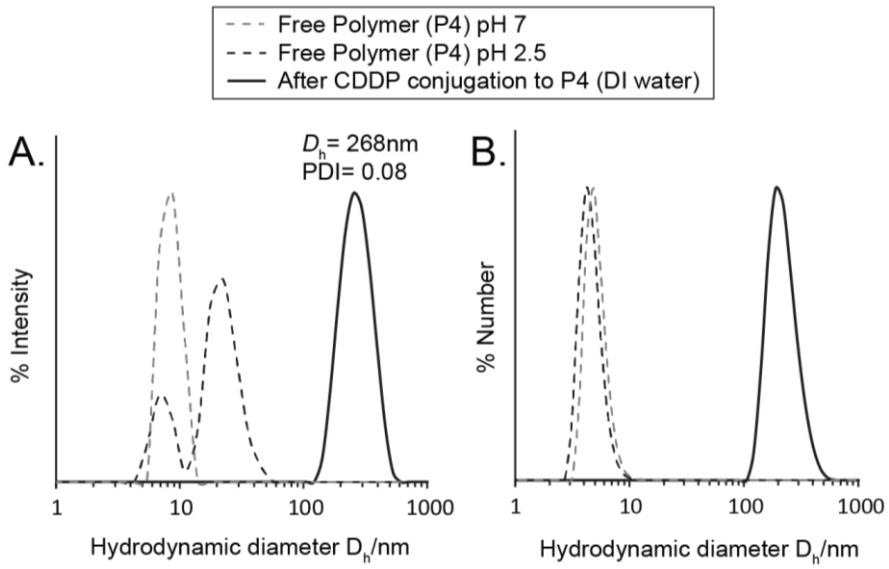

Figure 2.3. DLS hydrodynamic diameter analysis of free polymer (**P4**) at different pH and free polymer after CDDP conjugation (A) %Intensity profile (B) % Number profile. Polymer concentration 1 mg mL^{-1}. Average standard deviation of D_h across all data (three x sample measurements) = ± 2.7 nm.

Analysis of the nanoparticle size and structure was conducted by DLS, TEM, and AFM. DLS data in **Figure 2.3** reveals an average hydrodynamic diameter (D_h) of 268 nm (intensity) after CDDP conjugation, well within the size range of vesicle assemblies. A low PDI of 0.08 was recorded, with number distribution data in **Figure 2.3B** indicating an absence of any smaller sized assemblies, e.g., micelles.

To determine whether these vesicle size assemblies could be achieved without CDDP conjugation, self-assembly analysis was performed on the free polymer (**P4**) before CDDP conjugation at pH 7 and at pH 2.5 (**Figure 2.3**). As expected no self-assembly of **P4** at pH 7 is observed, with only unimolecular species (<10 nm) present due to the charged (hydrophilic) PLG block. The pKa of poly(L-glutamic acid) is reported to lie between 4 and 5,[61-62] and at pH values <4, PLG groups are predominantly neutralized to form hydrophobic α-helical segments.[63-64] DLS intensity distribution data of neutralized **P4** at pH 2.5 also shows no vesicle size formation, with only small assemblies (~25 nm) and unimolecular species (<10 nm) observed and number distribution data showing entirely unimolecular species. The data indicates that in this case, hydrophobicity of the polypeptide block alone is not enough to form vesicle size assemblies. The formation of well-defined vesicle size assemblies is due to the CDDP conjugation/self-assembly process. We suspect that it involves the conjugation of CDDP to the polymer chains, with intrachain cross-linking forming a short rigid block that self-assembles into tight regularly packed vesicle structures.

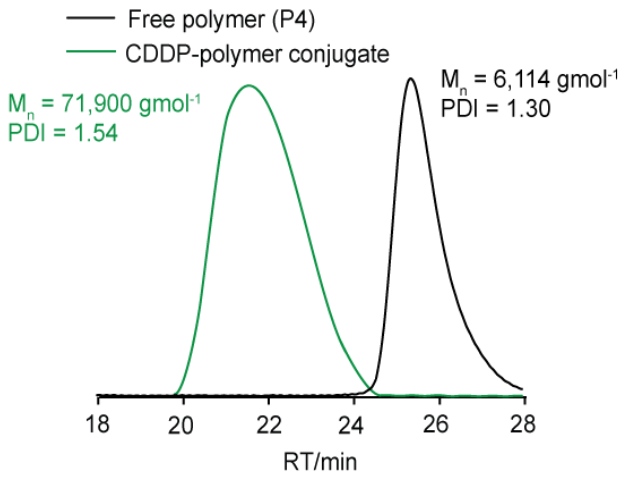

Figure 2.4. GPC (DMF) SEC chromatograms of free polymer (**P4**) before and after CDDP conjugation. M_n and PDI determined by GPC using MeO-PEG-OH standards.

To determine whether any interstrand crosslinking of the assembled vesicles by CDDP takes place due to the close proximity of the polymer chains in the tightly

packed vesicle membrane, SEC analysis of the CDDP conjugated block copolymer was performed in DMF, a good solvent for both PEG and CDDP conjugated PLG blocks. **Figure 2.4** shows a large shift in retention time of the polymer after CDDP conjugation corresponding to a MW increase to ~72 kDa. Such a large increase in MW strongly indicates the presence of interchain cross-linking of polymer chains by CDDP within the vesicle membrane.

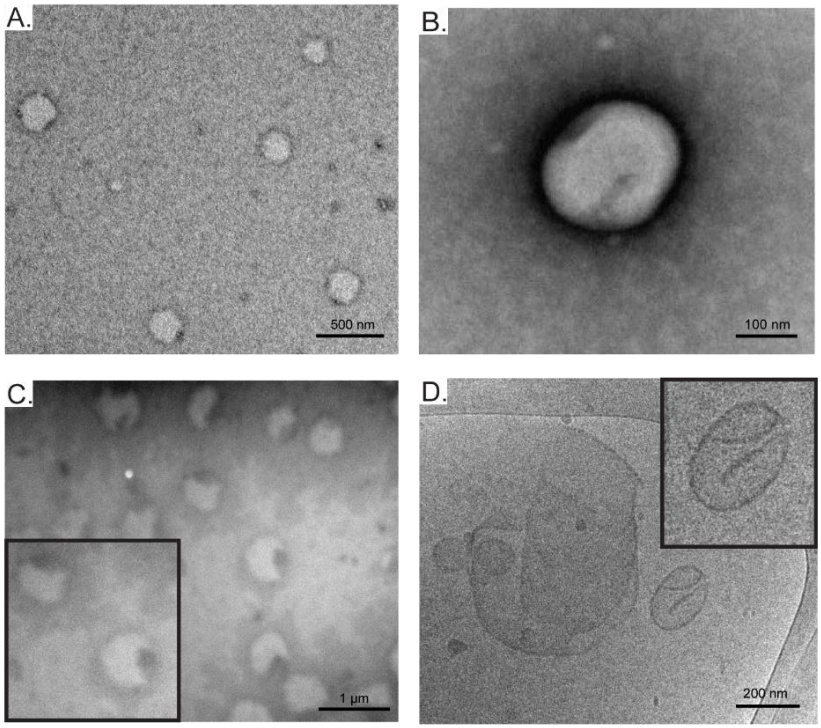

Figure 2.5. TEM analysis of CDDP-loaded block copolymer vesicles. (A, B) Negative stain, air-dried sample (C) No stain, vacuum-dried sample. (D) Cryo-TEM sample. Samples at 1 mg mL^{-1} polymer concentration.

In order to observe the physical morphology of the resulting vesicle self-assemblies, TEM and AFM analysis was performed. TEM analysis is shown in **Figure 2.5**. Under standard TEM and cryo-TEM conditions**, Figure 2.5A, B and D** shows spherical structures with thin membranes and diameters of around 250 nm, in good agreement with the DLS data. Slight structural deformations/indentations are observed on the membranes of the assemblies, typical of vesicles, and is suggestive of a hollow vesicle assembly, e.g., **Figure 2.5D**.

Vesicles, unlike micelles, are prone to partial core collapse and membrane deformations due to their intrinsic hollow structure.[65-67] Drying of TEM samples cast onto copper grids by freeze-drying or under direct vacuum has been reported to promote these deformations.[67] Using this method as an aid in further determining whether the self-assembly structures were indeed hollow structures suggestive of vesicles, TEM image of vacuum-dried samples is presented in **Figure 2.5C**. The particles show what are suspected to be a ruptured vesicle wall exposing a hollow core. The increase in observed particle size (~500 nm) is due to the flattening of the ruptured vesicle when absorbed onto the TEM grid. Also, it has been reported that vacuum drying of vesicles on TEM grid can result in a 2-fold increase in vesicle wall thickness,[67] which could be another cause for the larger observed size in **Figure 2.5C**. Therefore, despite **Figure 2.5C** not being representative of the true size of the vesicle, it clearly shows the presence of hollow vesicle structures. The air-dried samples in **Figure 2.5A, B** shows only minor shrinkage/core collapse of the vesicle structures after air drying, and still maintain vesicle wall integrity, with sizes (~250 nm) slightly lower than those obtained in DLS where the vesicles are in a hydrated state, a commonly reported observation.[68-69] The vacuum-dried sample in **Figure 2.5C** was analyzed without staining so that any dense platinum regions could be visualized. The dense (darker) holes in the structures, suggests an exposure of a platinum packed membrane, consistent with the proposed vesicle structure in **Figure 2.6A**. It is important to note that a small number of vesicles of roughly the same size with an anomalous shape were also observed under TEM analysis. Incomplete vesicle assembly in these cases can be explained by the cross-linking of the polypeptide chains inhibiting the regular packing of polymer chains into a uniform vesicle structure.

The formation of hollow vesicle structures is further supported by the AFM data in **Figure 2.6B**. The 3D AFM image shows a partial collapse of the particles with z-profile analysis showing a clear indentation in the structure where the collapse occurred predominantly during AFM tapping mode. The cross-sectional diameter of the structure of 260 nm is in good agreement with the other air-dried samples used in TEM analysis (**Figure 2.5A, B**) and DLS data.

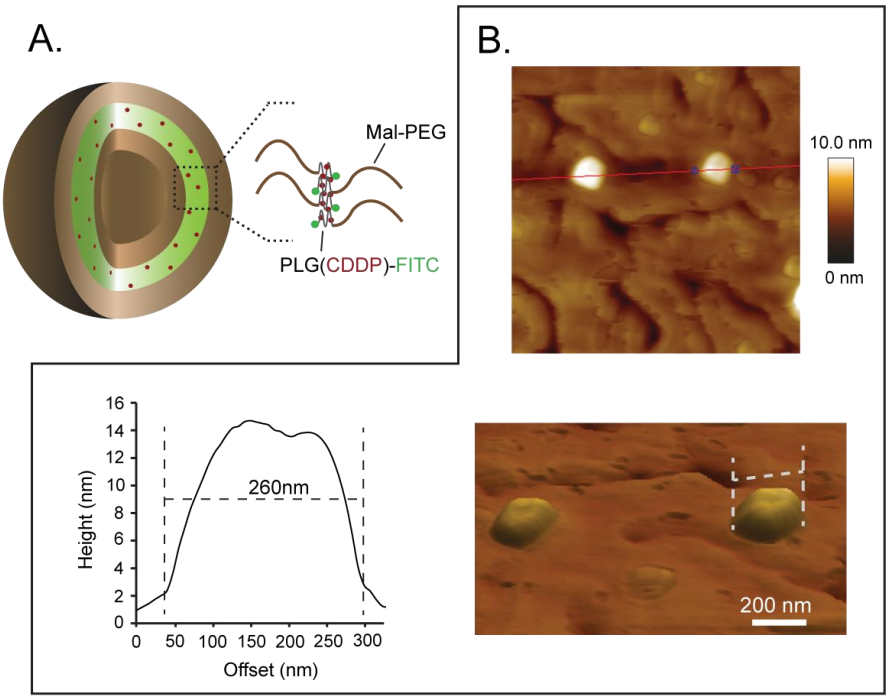

Figure 2.6. (A) The proposed self-assembly vesicle structure with PEG assemblies on the outer vesicle surface/corona and inner core with dense CDDP cross-linked PLG forming the hydrophobic membrane. (B) AFM analysis of vesicles on silicon wafer (polymer concentrations 0.5 mg mL^{-1}) including 3D AFM image and z-profile analysis showing cross-sectional diameter of vesicle structure marked with white dashed line.

Zeta potential of the vesicle was measured to be −3.93 ± 0.5 mV, relatively low due to the conjugation of the carboxylate anion with the Pt metal of CDDP. The slight negative charge is likely to be due to the remaining unconjugated carboxylate groups, and is quite suitable for *in vivo* use, which can effectively reduce protein absorbance during blood circulation.[70]

2.3.3 Cisplatin (CDDP) Release

In vitro release of the CDDP incorporated vesicles was performed using the *o*-phenylenediamine colorimetric assay (*o*-PDA) carried out according to a previously published protocol.[7, 71] The release of cisplatin is initiated in the presence of chloride

ions, which results in a ligand exchange from the metal–polymer back to its original metal–chloride complex (**Figure 2.7A**).[7, 15] To mimic the pH/chloride concentrations in the plasma and late endosomal/lysosomal environment, release was performed in PBS (pH = 7.4, [Cl^-] = 140 mM) and in sodium acetate buffer (pH = 5.2, [Cl^-] = 35 mM), respectively (**Figure 2.7B**).

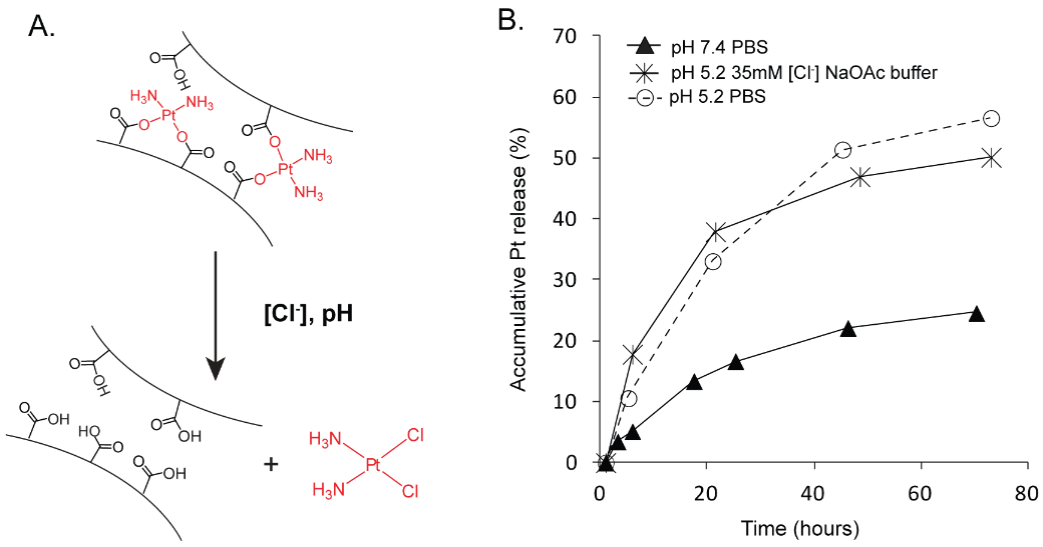

Figure 2.7. (A) Release mechanism of CDDP from drug-loaded vesicles. (B) Release profile of cisplatin from drug-loaded vesicles. Average error for release ± 1.2%. Release measurements performed in duplicates.

It is commonly misreported that a release in PBS/0.9% NaCl ([Cl^-] = ~137–150 mM) at pH 5 is representative of the intracellular environment. Rather, the intracellular chloride concentration is reported to lie between 4 and 60 mM, with an average of around 35–40 mM.[72-73] While release at pH 5/([Cl^-] = ~137–150 mM) often has the result of an improved drug release profile over standard PBS due to the protonation of the carboxylic acid after drug removal to promote its release, it is not representative of the intracellular chloride concentration.

CDDP release data in **Figure 2.7B** shows that in pH 7.4 PBS, a slow and sustained release profile is observed with no burst release of drug. This controlled release of CDDP from the vesicles in pH 7.4 PBS is considerably slower than other cisplatin

drug delivery systems in the literature[16, 36, 71] and presents an opportunity for alleviating the systemic drug release/acute toxicity issues that have hampered the use of high cisplatin dosages in cancer therapy.[74] The slow release of drug is likely to be explained by stable secondary structures/CDDP cross-linking in the vesicle membrane which is helping to stabilize the vesicle structure and slow the rate of metal–ligand exchange.[25, 75] In fact, this vesicle stability was further supported by DLS analysis, which showed that vesicle size was maintained even after 6 days of release. Release in pH 5.2/35 mM [Cl−], representative of the late endosomal/lysosomal environment, is twice as fast (~35% over 24 h), which is suggestive of a faster "burst-like" release profile of the drug from the vesicles once inside the target cancer cell. It is important to note that accelerated intracellular CDDP release is likely to occur inside malignant cells due to overexpression of lysosomal proteases such as cathepsin B (known for its high activity in metabolizing PLG acid resides), which will promote breakdown of the vesicle structure;[76-77] however, this will be the subject of further study. Drug release from the vesicles in pH 5.2 at the higher chloride concentrations of PBS shows a similar release profile to the 35 mM [Cl^-] sample with a slightly higher total release after 76 h. This indicates that chloride concentrations above those present intracellularly only have a marginal effect on the release rate from the vesicles. In this case, pH appears to dominate the rate of drug release.

2.3.4 Cytotoxicity Studies In Vitro

The *in vitro* cytotoxicity of the CDDP-loaded vesicles was assessed using an alamarBlue assay on cervical cancer-originating (HeLa) cells following incubation for 72 h. Free block copolymer precursor and free CDDP were employed as controls. As **Figure 2.8** shows, the free polymer (**P4**) demonstrates good biocompatibility, with no cytotoxicity observed over the concentrations tested, supporting its potential as an effective precursor to these drug delivery vesicles. The CDDP-loaded vesicles show a dose dependent inhibition of HeLa cell proliferation (IC_{50} = 0.60 mmol/L). The viability difference of the free CDDP (IC_{50} = 0.065 mmol/L) and that of the CDDP-loaded vesicles at equivalent drug dosages is a commonly reported

observation in nanoparticle delivery of CDDP,[8, 17, 78] and can be attributed to the different drug formats. CDDP is only toxic once dissociated from the vesicle, thus the CDDP-incorporated vesicles with a controlled CDDP release profile would take a longer time to reach similar cytotoxicity than the free CDDP. This reduced toxicity would allow for higher drug dosages to be applied for a more sustained drug effect. As well, any passive and active targeting capabilities of these vesicles is likely to improve cisplatin delivery to the cancer cell and reduce acute cisplatin toxicities very commonly reported with free cisplatin therapy.[5]

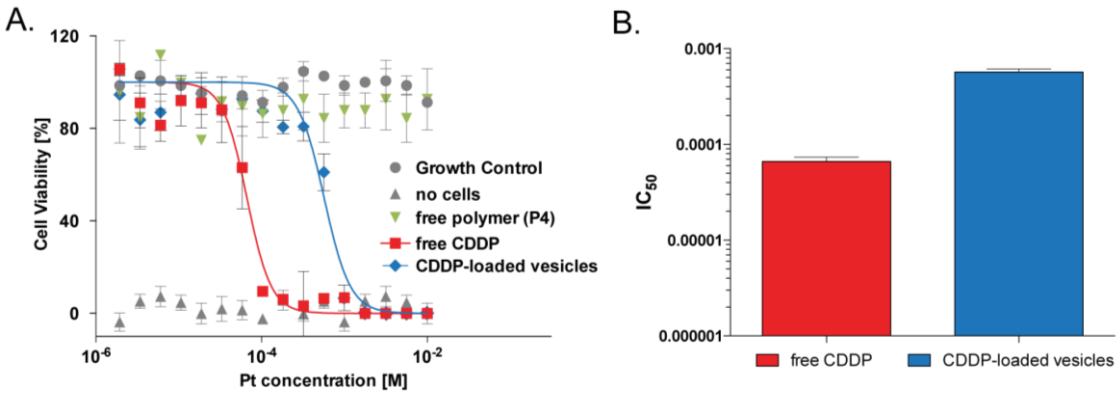

Figure 2.8. (A) Cytotoxicity of CDDP-loaded vesicles towards HeLa cells incubated for 72 h. (B) IC_{50} values for free drug and CDDP-loaded vesicles. Data shown represents mean ± standard error.

The exposed maleimide groups on the vesicle corona present an opportunity to conjugate thiol targeting ligands to form active targeting vesicles. The conjugation of a thiol-functionalized folic acid (FA) targeting ligand to the vesicle would be expected to facilitate the active targeting of the vesicle to cancerous cells through folate receptor-mediated endocytosis.[79] To determine whether this would result in a higher toxicity to cancer cells compared to noncancerous cells, HeLa cells and NIH-3T3 were selected as cancerous and noncancerous cells, respectively. NIH-3T3 cells lack overexpressed folic acid receptors (FR),[80] while HeLa cells, typical of many cancer cells, greatly overexpress FR.[81]

Folic acid was conjugated to the maleimide moieties on the corona of the FITC-labeled CDDP-loaded vesicle through thiol-maleimide coupling (**Scheme 2.1**). A novel FA precursor using cystamine as a disulfide linker was synthesized through standard EDCI/DMAP coupling procedures and confirmed through ^{1}H NMR analysis (see **Appendix Figure A2.5**). The precursor was then reduced *in situ* in the presence of TCEP to reveal the free reactive thiol for coupling to the vesicle. Normalized UV–vis spectra of the folic acid-decorated vesicle (FA-conj. vesicle) in **Figure 2.9**, reveals an absorbance profile matching that of free FA. The absorbance peak at λ = 495 nm corresponds to the FITC-tag absorbance which appears to decrease in intensity after FA conjugation, possibly due to some FITC degradation under aqueous dialysis. Based on ^{1}H NMR analysis determining a polymer maleimide double bond proton intensity of 60% before FA conjugation (see **Appendix Figure A2.3**) and its subsequent disappearance after FA conjugation to the vesicle (see **Appendix Figure A2.6**), the extent of FA decoration on the vesicle surface was deemed to be ~60% (of surface polymers). The zeta potential of the resulting FA conjugated vesicle decreased from an initial value before FA conjugation (−3.93 ± 0.5 mV) to −5.88 ± 0.5 mV, as a result of the contributed negative charge from the free acid group of FA.

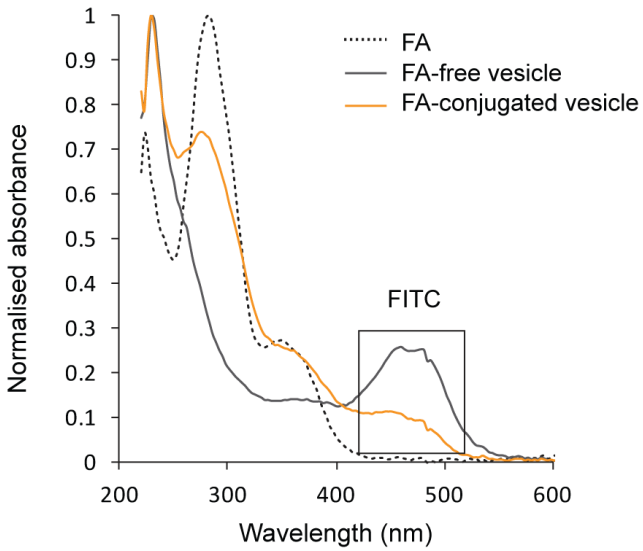

Figure 2.9. Normalized UV-vis absorbance of FA- conjugated vesicles and FA-free vesicles (DI water).

Cytotoxicity studies in **Figure 2.10** show that the FA-conjugated, CDDP-loaded vesicles are statistically significantly more toxic to HeLa than NIH-3T3 cells (**Figure 2.10A, B**) with IC_{50} values of 0.28 mmol/L and 1.3 mmol/L, respectively. The free drug showed no difference in IC_{50} values for the two cell lines used (**Figure 2.10C**), indicating that the higher toxicity of the FA vesicles to HeLa cells is due to the enhanced cellular uptake attributed to folate receptor-mediated endocytosis.[82] It is also worthy to mention the increased HeLa cell toxicity of the FA-conjugated vesicles (IC_{50}= 0.28 mmol/L) compared to FA-free vesicles (**Figure 2.8**, IC_{50} = 0.60 mmol/L) further suggesting an increased uptake of vesicles into the cancer cells due to the conjugated FA targeting ligand.

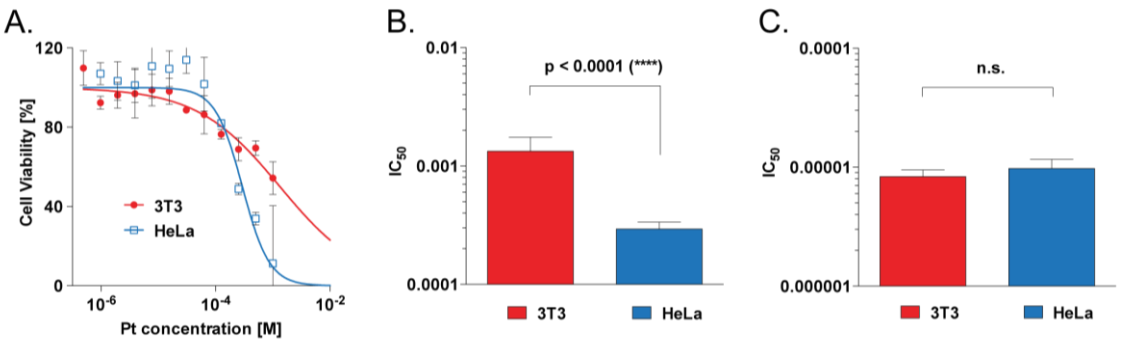

Figure 2.10. (A) Cytotoxicity of CDDP-loaded, FA-conjugated vesicles towards HeLa (squares) and NIH-3T3 cells (circles) incubated for 72 h. X-axis normalized to Pt concentration. Lines show results of non-linear fit [log(inhibitor) vs. normalized response]. (B) Comparison of the IC_{50} values of the FA-conjugated vesicles in NIH-3T3 cells vs HeLa cells. (C) Control experiment comparing the IC_{50} values of free CDDP in the two cell lines. Data shown represents mean ± standard error.

2.3.5 Cell Binding/Uptake Studies In Vitro

To determine whether the FA targeting ligand improves cell binding and uptake of the vesicles to cancer cells relative to noncancerous cells, both flow cytometry and confocal microscopy analysis were conducted using HeLa and NIH-3T3 cells after incubation with CDDP-loaded vesicles with and without FA for 24 h. **Figure 2.11B** shows the mean fluorescence intensity (MFI) of HeLa and NIH-3T3 cells incubated

with FA-free and FA-conjugated vesicles bearing FITC-tags, as measured by flow cytometry. The flow cytometry analysis clearly demonstrates a far greater enhancement of vesicle cellular binding in HeLa cells as a result of the FA targeting ligand (change in MFI of 3462) compared to the NIH-3T3 cells (change in MFI of 193) presumably facilitated by the folate receptor-mediated endocytosis process. To verify this uptake mechanism, future studies will need to be conducted involving a competitive vesicle-cell binding assay in media containing free folic acid.[83]

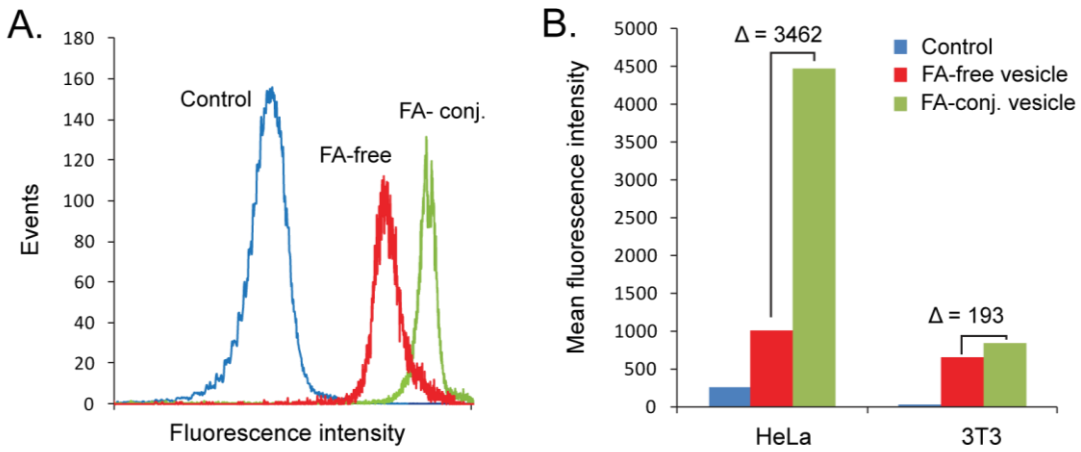

Figure 2.11. Flow cytometry cell binding data of FITC-labeled CDDP-loaded FA-free and FA-conjugated vesicles to HeLa and NIH-3T3 cells after 24 h incubation. (A) Flow cytometry HeLa cell binding data (B) FITC mean fluorescence intensity (MFI) of HeLa and NIH-3T3 cells. Untreated cells used as controls. Δ represents change in MFI. Data shown represents mean ± standard error.

Confocal microscopy analysis was then performed on the same samples. As shown in **Figure 2.12**, the FITC fluorescence intensity of HeLa cells incubated with FA-conjugated vesicles was significantly higher than cells incubated with FA-free vesicles (**Figure 2.12B, C**), which was consistent with the flow cytometry results. Large numbers of FA-conjugated vesicles are clearly seen binding to the HeLa cell membrane, and many are internalized into the cytosol, evidence from the particular patterns of green fluorescence. FITC fluorescence intensity of NIH-3T3 cells incubated with FA-conjugated vesicles was similar to FA-free vesicles (**Figure**

2.12E, F) with no observed increase in cell binding/uptake. This was again consistent with the flow cytometry results, and confirmed the enhanced binding and uptake of these FA-conjugated vesicles to cancer cells compared to noncancerous cells.

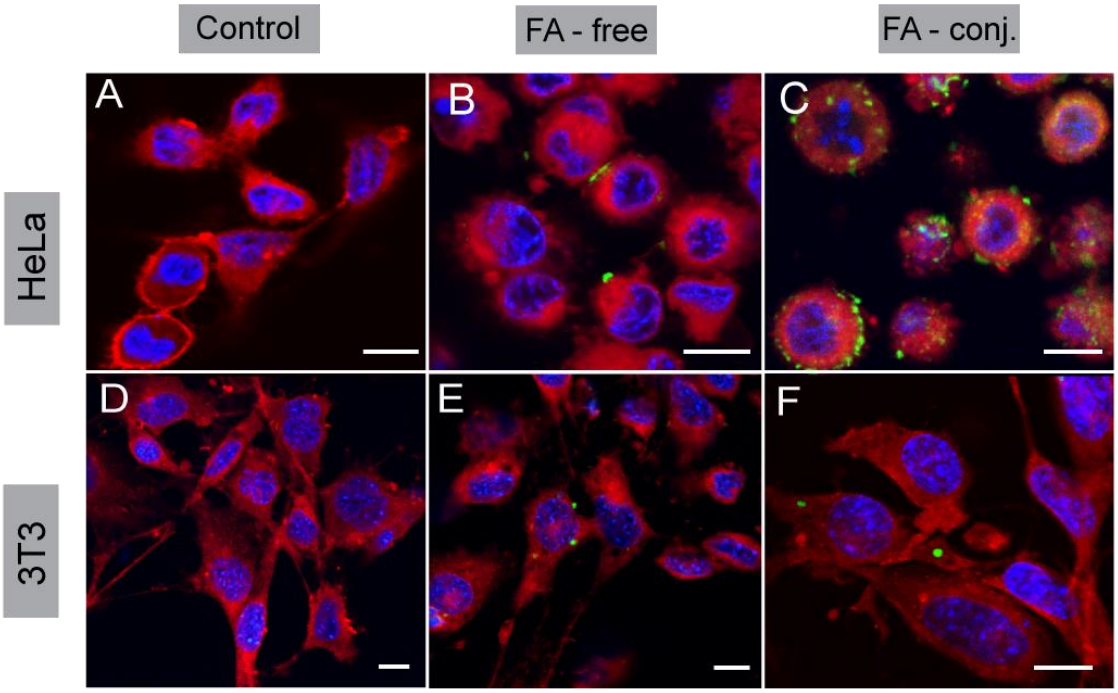

Figure 2.12. Confocal laser scanning microscopy (CLSM) images of HeLa (A-C) and NIH-3T3 cells (D-F) incubated with FA-free and FA-conjugated vesicle for 24 h (37 °C, 400, 000 cells/mL). Untreated cells used as controls. The vesicles were tagged with FITC (green), cell membrane was stained with CellMask Deep Red (red) and the cell nucleus with DAPI (blue) in all images. Scale bar = 10 μm.

2.4 Chapter Summary

In summary, CDDP-loaded, PLG-based vesicles were prepared as a novel, biocompatible, and biodegradable architecture for targeted CDDP delivery. These vesicles were formed from biocompatible Mal-PEG-*b*-PLG block copolymers with CDDP conjugation forming a short, rigid, cross-linked, drug-loaded, hydrophobic block that induced self-assembly into hollow vesicle structures with average diameters of ~270 nm. CDDP conjugation was shown to be critical to the formation of the vesicles, with both intra and interchain polymer cross-linking within the vesicle membrane by the drug suggested to occur. The morphologies of these hollow vesicle structures were analyzed and confirmed by a number of analytical techniques including TEM and AFM. Drug loading was comparable to other vesicular assemblies currently in clinical trials for Pt(II) delivery, yet possesses a distinct advantage over these in that its building block (i.e. a polypeptide-based copolymer) is biodegradable. Drug release studies demonstrated a low and controlled drug release profile in systemic conditions with significantly higher release rate observed under intracellular conditions. The exposed maleimide functionalities on the vesicle corona were conjugated to folic acid to form an active targeting delivery system that demonstrated significantly higher cellular binding/uptake and dose-dependent cytotoxicity to cancer cells compared to noncancerous cells. This demonstrates a novel approach to polypeptide-based vesicle assembly and a promising strategy for targeted, effective CDDP anticancer drug delivery.

2.5 References

(1) Galanski, M.; Jakupec, M. A.; Keppler, B. K., *Curr. Med. Chem.* **2005,** *12* (18), 2075-2094.

(2) Boulikas, T.; Vougiouka, M., *Oncol. Rep.* **2004,** *11* (3), 559-595.

(3) Stewart, D. J.; Dulberg, C. S.; Mikhael, N. Z.; Redmond, M. D.; Montpetit, V. A. J.; Goel, R., *Cancer Chemotherapy and Pharmacology* **1997,** *40* (4), 293-308.

(4) Mollman, J. E., *New Engl. J. Med.* **1990,** *322* (2), 126-127.

(5) Wang, X.; Guo, Z., *Chem. Soc. Rev.* **2013,** *42* (1), 202-224.

(6) Huynh, V. T.; Binauld, S.; de Souza, P. L.; Stenzel, M. H., *Chem. Mater.* **2012,** *24* (16), 3197-3211.

(7) Huynh, V. T.; Chen, G. J.; de Souza, P.; Stenzel, M. H., *Biomacromolecules* **2011,** *12* (5), 1738-1751.

(8) Ahmad, Z.; Tang, Z. H.; Shah, A.; Lv, S. X.; Zhang, D. W.; Zhang, Y.; Chen, X. S., *Macromol. Biosci.* **2014,** *14* (9), 1337-1345.

(9) Duncan, R.; Vicent, M. J., *Adv. Drug Del. Rev.* **2013,** *65* (1), 60-70.

(10) Croy, S. R.; Kwon, G. S., *Curr. Pharm. Des.* **2006,** *12* (36), 4669-4684.

(11) Hamley, I. W., *Biomacromolecules* **2014,** *15* (5), 1543-1559.

(12) Shi, C.; Yu, H.; Sun, D.; Ma, L.; Tang, Z.; Xiao, Q.; Chen, X., *Acta Biomater.* **2015,** *18*, 68-76.

(13) Yu, H.; Tang, Z.; Zhang, D.; Song, W.; Zhanga, Y.; Yang, Y.; Ahmad, Z.; Chen, X., *J. Controlled Release* **2015,** *205*, 89-97.

(14) Song, W. T.; Tang, Z. H.; Zhang, D. W.; Yu, H. Y.; Chen, X. S., *Small* **2015,** *11* (31), 3755-3761.

(15) Nishiyama, N.; Okazaki, S.; Cabral, H.; Miyamoto, M.; Kato, Y.; Sugiyama, Y.; Nishio, K.; Matsumura, Y.; Kataoka, K., *Cancer Res.* **2003,** *63* (24), 8977-8983.

(16) Song, W. T.; Li, M. Q.; Tang, Z. H.; Li, Q. S.; Yang, Y.; Liu, H. Y.; Duan, T. C.; Hong, H.; Chen, X. S., *Macromol. Biosci.* **2012,** *12* (11), 1514-1523.

(17) Uchino, H.; Matsumura, Y.; Negishi, T.; Koizumi, F.; Hayashi, T.; Honda, T.; Nishiyama, N.; Kataoka, K.; Naito, S.; Kakizoe, T., *Br. J. Cancer* **2005,** *93* (6), 678-687.

(18) Miura, Y.; Takenaka, T.; Toh, K.; Wu, S.; Nishihara, H.; Kano, M. R.; Ino, Y.; Nomoto, T.; Matsumoto, Y.; Koyama, H.; Cabral, H.; Nishiyama, N.; Kataoka, K., *Acs Nano* **2013,** *7* (10), 8583-8592.

(19) Plummer, R.; Wilson, R. H.; Calvert, H.; Boddy, A. V.; Griffin, M.; Sludden, J.; Tilby, M. J.; Eatock, M.; Pearson, D. G.; Ottley, C. J.; Matsumura, Y.; Kataoka, K.; Nishiya, T., *Br. J. Cancer* **2011,** *104* (4), 593-598.

(20) Roberts, M. J.; Bentley, M. D.; Harris, J. M., *Adv. Drug Del. Rev.* **2002,** *54* (4), 459-476.

(21) Duncan, R., *Nature Reviews Cancer* **2006,** *6* (9), 688-701.

(22) Richard, A.; Margaritis, A., *Crit. Rev. Biotechnol.* **2001,** *21* (4), 219-232.

(23) Li, C., *Adv. Drug Del. Rev.* **2002,** *54* (5), 695-713.

(24) Wang, D.; Lippard, S. J., *Nature Reviews Drug Discovery* **2005,** *4* (4), 307-320.

(25) Song, W. T.; Tang, Z. H.; Zhang, D. W.; Zhang, Y.; Yu, H. Y.; Li, M. Q.; Lv, S. X.; Sun, H.; Deng, M. X.; Chen, X. S., *Biomaterials* **2014,** *35* (9), 3005-3014.

(26) Discher, D. E.; Eisenberg, A., *Science* **2002,** *297* (5583), 967-973.

(27) Kieler-Ferguson, H. M.; Frechet, J. M. J.; Szoka, F. C., Jr., *Wiley Interdisciplinary Reviews-Nanomedicine and Nanobiotechnology* **2013,** *5* (2), 130-138.

(28) Guo, S.; Wang, Y.; Miao, L.; Xu, Z.; Lin, C. M.; Zhang, Y.; Huang, L., *Acs Nano* **2013,** *7* (11), 9896-9904.

(29) Khiati, S.; Luvino, D.; Oumzil, K.; Chauffert, B.; Camplo, M.; Barthelemy, P., *Acs Nano* **2011,** *5* (11), 8649-8655.

(30) Soussan, E.; Cassel, S.; Blanzat, M.; Rico-Lattes, I., *Angewandte Chemie-International Edition* **2009,** *48* (2), 274-288.

(31) Maeda, H.; Greish, K.; Fang, J., The EPR effect and polymeric drugs: A paradigm shift for cancer chemotherapy in the 21st century. In *Polymer Therapeutics Ii: Polymers as Drugs, Conjugates and Gene Delivery Systems*, SatchiFainaro, R.; Duncan, R., Eds. 2006; Vol. 193, pp 103-121.

(32) Maeda, H.; Wu, J.; Sawa, T.; Matsumura, Y.; Hori, K., *J. Controlled Release* **2000,** *65* (1-2), 271-284.

(33) Lu, Y. J.; Low, P. S., *Adv. Drug Del. Rev.* **2002,** *54* (5), 675-693.

(34) Kamaly, N.; Xiao, Z. Y.; Valencia, P. M.; Radovic-Moreno, A. F.; Farokhzad, O. C., *Chem. Soc. Rev.* **2012,** *41* (7), 2971-3010.

(35) Zhong, Y.; Meng, F.; Deng, C.; Zhong, Z., *Biomacromolecules* **2014,** *15* (6), 1955-1969.

(36) Fu, Q.; Xu, J.; Ladewig, K.; Henderson, T. M. A.; Qiao, G. G., *Polymer Chemistry* **2015,** *6* (1), 35-43.

(37) Xu, J. T.; Fu, Q.; Ren, J. M.; Bryant, G.; Qiao, G. G., *Chem. Commun.* **2013,** *49* (1), 33-35.

(38) Chécot, F.; Lecommandoux, S.; Gnanou, Y.; Klok, H.-A., *Angew. Chem. Int. Ed.* **2002,** *41* (8), 1339-1343.

(39) Bellomo, E. G.; Wyrsta, M. D.; Pakstis, L.; Pochan, D. J.; Deming, T. J., *Nat. Mater.* **2004,** *3* (4), 244-248.

(40) Holowka, E. P.; Deming, T. J., *Macromol. Biosci.* **2010,** *10* (5), 496-502.

(41) Holowka, E. P.; Pochan, D. J.; Deming, T. J., *J. Am. Chem. Soc.* **2005,** *127* (35), 12423-12428.

(42) Holowka, E. P.; Sun, V. Z.; Kamei, D. T.; Deming, T. J., *Nat. Mater.* **2007,** *6* (1), 52-57.

(43) Xu, J.; Tao, L.; Boyer, C.; Lowe, A. B.; Davis, T. P., *Macromolecules* **2011,** *44* (2), 299-312.

(44) Guo, M.; Jiang, M.; Zhang, G., *Langmuir* **2008,** *24* (19), 10583-10586.

(45) Sharpless, N. E.; Flavin, M., *Biochemistry* **1966,** *5* (9), 2963-2971.

(46) Dispinar, T.; Sanyal, R.; Sanyal, A., *J. Polym. Sci., Part A* **2007,** *45* (20), 4545-4551.

(47) Mantovani, G.; Lecolley, F.; Tao, L.; Haddleton, D. M.; Clerx, J.; Cornelissen, J.; Velonia, K., *J. Am. Chem. Soc.* **2005,** *127* (9), 2966-2973.

(48) Sanyal, A., *Macromol. Chem. Phys.* **2010,** *211* (13), 1417-1425.

(49) Sanchez, A.; Pedroso, E.; Grandas, A., *Org. Lett.* **2011,** *13* (16), 4364-4367.

(50) Dimitrov, I.; Schlaad, H., *Chem. Commun.* **2003,** (23), 2944-2945.

(51) Cooley, J. H.; Williams, R. V., *J. Chem. Educ.* **1997,** *74* (5), 582-585.

(52) Han, J. D.; Ding, J. X.; Wang, Z. C.; Yan, S. F.; Zhuang, X. L.; Chen, X. S.; Yin, J. B., *Science China-Chemistry* **2013,** *56* (6), 729-738.

(53) Bunnelle, W. H.; Shangraw, W. R., *Tetrahedron* **1987,** *43* (9), 2005-2011.

(54) Fahmy, K.; Merroun, M.; Pollmann, K.; Raff, J.; Savchuk, O.; Hennig, C.; Selenska-Pobell, S., *Biophys. J.* **2006,** *91* (3), 996-1007.

(55) Gryparis, E. C.; Mattheolabakis, G.; Bikiaris, D.; Avgoustakis, K., *Drug Deliv.* **2007,** *14* (6), 371-380.

(56) Wheate, N. J.; Walker, S.; Craig, G. E.; Oun, R., *Dalton Transactions* **2010,** *39* (35), 8113-8127.

(57) Stathopoulos, G. P.; Boulikas, T.; Kourvetaris, A.; Stathopoulos, J., *Anticancer Res.* **2006,** *26* (2B), 1489-1493.

(58) Harrington, K. J.; Lewanski, C. R.; Northcote, A. D.; Whittaker, J.; Wellbank, H.; Vile, R. G.; Peters, A. M.; Stewart, J. S. W., *Ann. Oncol.* **2001,** *12* (4), 493-496.

(59) Dragovich, T.; Mendelson, D.; Kurtin, S.; Richardson, K.; Von Hoff, D.; Hoos, A., *Cancer Chemotherapy and Pharmacology* **2006,** *58* (6), 759-764.

(60) Rademaker-Lakhai, J. M.; Terret, C.; Howell, S. B.; Baud, C. M.; de Boer, R. F.; Pluim, D.; Beijnen, J. H.; Schellens, J. H. M.; Droz, J. P., *Clin. Cancer. Res.* **2004,** *10* (10), 3386-3395.

(61) Sanson, C.; Schatz, C.; Le Meins, J. F.; Brulet, A.; Soum, A.; Lecommandoux, S., *Langmuir* **2010,** *26* (4), 2751-2760.

(62) Cheng, Y. F.; Corn, R. M., *J. Phys. Chem. B* **1999,** *103* (41), 8726-8731.

(63) Nagasawa, M.; Holtzer, A., *J. Am. Chem. Soc.* **1964,** *86* (4), 538-543.

(64) Gooding, E. A.; Sharma, S.; Petty, S. A.; Fouts, E. A.; Palmer, C. J.; Nolan, B. E.; Volk, M., *Chem. Phys.* **2013,** *422*, 115-123.

(65) Liu, F. T.; Eisenberg, A., *J. Am. Chem. Soc.* **2003,** *125* (49), 15059-15064.

(66) Wu, J.; Eisenberg, A., *J. Am. Chem. Soc.* **2006,** *128* (9), 2880-2884.

(67) Azzam, T.; Eisenberg, A., *Langmuir* **2010,** *26* (13), 10513-10523.

(68) Moughton, A. O.; O'Reilly, R. K., *Chem. Commun.* **2010,** *46* (7), 1091-1093.

(69) Sulistio, A.; Blencowe, A.; Wang, J.; Bryant, G.; Zhang, X.; Qiao, G. G., *Macromol. Biosci.* **2012,** *12* (9), 1220-1231.

(70) Xiao, K.; Li, Y. P.; Luo, J. T.; Lee, J. S.; Xiao, W. W.; Gonik, A. M.; Agarwal, R. G.; Lam, K. S., *Biomaterials* **2011,** *32* (13), 3435-3446.

(71) Yan, X. L.; Gemeinhart, R. A., *J. Controlled Release* **2005,** *106* (1-2), 198-208.

(72) Sonawane, N. D.; Verkman, A. S., *J. Cell Biol.* **2003,** *160* (7), 1129-1138.

(73) Faundez, V.; Hartzell, H. C., *Science's STKE : signal transduction knowledge environment* **2004,** *2004* (233), re8-re8.

(74) Tsang, R.; Al-Fayea, T.; Au, H.-J., *Drug Saf.* **2009,** *32* (12), 1109-1122.

(75) Mochida, Y.; Cabral, H.; Miura, Y.; Albertini, F.; Fukushima, S.; Osada, K.; Nishiyama, N.; Kataoka, K., *Acs Nano* **2014,** *8* (7), 6724-6738.

(76) Shaffer, S. A.; Baker Lee, C.; Kumar, A.; Singer, J. W., *Eur. J. Cancer* **2002,** *38*, S129-S129.

(77) Shaffer, S. A.; Baker-Lee, C.; Kennedy, J.; Lai, M. S.; de Vries, P.; Buhler, K.; Singer, J. W., *Cancer Chemotherapy and Pharmacology* **2007,** *59* (4), 537-548.

(78) Feng, Z.; Lai, Y. P.; Ye, H. F.; Huang, J.; Xi, X. G.; Wu, Z. R., *Cancer Sci.* **2010,** *101* (11), 2476-2482.

(79) Vlahov, I. R.; Leamon, C. P., *Bioconjugate Chem.* **2012,** *23* (7), 1357-1369.

(80) Bottero, F.; Tomassetti, A.; Canevari, S.; Miotti, S.; Menard, S.; Colnaghi, M. I., *Cancer Res.* **1993,** *53* (23), 5791-5796.

(81) Song, Y.; Shi, W.; Chen, W.; Li, X.; Ma, H., *J. Mater. Chem.* **2012,** *22* (25), 12568-12573.

(82) Leamon, C. P.; Low, P. S., *Biochem. J* **1993,** *291*, 855-860.

(83) Yoo, H. S.; Park, T. G., *J. Controlled Release* **2004,** *96* (2), 273-283.

3

Conjugation and Isolation of a Model DNA Aptamer to Poly(L-glutamic acid)-Based Delivery Systems

3.1 Chapter Perspective

Extending the active targeting of synthetic poly(L-glutamic acid)(PLG)-based drug delivery nanoparticles such as the vesicles described in **Chapter 2**, requires the use of more specific active targeting ligands, such as aptamers. Aptamers, selected nucleotide sequences with high antigen specificity, have been used as active targeting ligands in a wide range of polymer drug delivery systems; but have yet to be investigated in synthetic PLG-based delivery systems. In this chapter, preliminary studies into the preparation of DNA aptamer-targeted PLG-based delivery systems is investigated. A thiol-functionalized model single-stranded DNA (ssDNA) aptamer was conjugated to PEG-*b*-PLG block copolymers; common PLG-based nanoparticle precursors used for drug delivery applications. The model DNA aptamer was conjugated through thiol-maleimide coupling chemistries and the conjugates successfully isolated through preparative gel electrophoresis. The DNA-polymer conjugation and isolation protocols established in this chapter offer potential use in any future studies employing aptamer-targeting of PLG-based delivery systems.

3.2 Introduction

Polymeric delivery vehicles have long been of interest in the field of cancer drug delivery, with synthetic polypeptides a popular material used in their fabrication. Their inherent biocompatible, biodegradable properties and wide ranging side chain functionalities for drug conjugation bring attractive attributes to a drug delivery system.[1-3] For instance, poly(L-glutamic acid) or PLG, has been utilized in a range of synthetic polypeptide delivery systems,[2, 4] owing to its biocompatibility and favorable enzymatic biodegradability profiles in the presence of enzymes upregulated in certain malignant tumors (e.g. cathepsin B).[2, 5-7] Generally synthesized through the efficient *N*-carboxyanhydride ring opening polymerization (NCA ROP) process, the PLG carboxylic acid side chain can be used to covalently conjugate or coordinate drugs to the polymer.[5, 8-11] Ideally, these synthetic polypeptide-based vehicles, as with all drug delivery systems, will selectively target tumor cells but with minimal interaction with normal cells so that unwanted side effects and toxicities are minimized or eliminated. Aside from the passive targeting of these delivery systems through preferential accumulation into leaky tumor tissues, notably known as the enhanced permeability and retention (EPR) effect,[12-13] research is now turning to the use of active targeting strategies by using ligands attached to the vehicles that can recognize tumor-specific or tumor-associated antigens/receptors overexpressed on tumor cells and tissues.[14] A variety of targeting molecules have been utilized for the active targeting of PLG-based delivery systems. These including molecules such as folic acid,[7, 15-16] and peptides containing RGD sequences.[10-11, 17] However, reported cases in the use of advanced targeting ligands with higher target specificity, such as antibodies, is limited.[18] Whilst the use of antibodies presents the possibility of highly selective vehicle targeting, their use suffers from high production costs, limited biodistribution due to large size, and immunogenicity. Thus, there is a need to look at alternative advanced targeting strategies.[19-21] Aptamers,[22-24] or nucleic acid ligands, have emerged as a new class of advanced targeting ligand that rivals antibodies in their potential for therapeutic and diagnostic applications.[19, 24-25] Aptamers are single-stranded DNA (ssDNA) or RNA oligonucleotide sequences, that fold via intramolecular interactions into

unique three-dimensional structures capable of binding to target molecules with high affinity and specificity.[24, 26] Unlike traditional methods for producing antibodies which require the use of animals or cell culture, aptamers are selected chemically through an *in vitro* SELEX (systematic evolution of ligands by exponential enrichment) process without the use of animals and for this reason are sometimes termed "chemical antibodies." [22, 24] This freedom from molecular biology constraints allows for a huge advantage in the aptamer selection process compared to antibodies, from reduced production costs, and the ability to generate aptamers against a wide range of targets. Also, compared to antibodies, aptamers are much smaller in size resulting in improved cellular uptake, and are virtually non-immunogenic.[19, 24] Aptamers, however, can display a number of limitations including rapid degradation in the bloodstream due to high nuclease-sensitivity and fast renal filtration which can limit its bioavailability for *in vivo* applications.[27-28] To improve aptamer bioavailability, strategies have been developed including chemical modification and incorporation of modified nucleotides into the oligonucleotide sequence to improve aptamer resistance to nucleases;[29-30] as well as aptamer conjugation to high MW polymers (e.g. poly(ethylene glycol) (PEG)) to improve stability and increase the total molecular weight of the resultant aptamer-nanomaterial complex beyond the renal filtration threshold.[31-32]

Whilst DNA and RNA aptamers have been investigated in a range of polymeric drug delivery systems commonly comprised of poly(ethylene glycol) (PEG, a polymer shown to prolong circulation half-life[33-34]) and other synthetic polymers such as methacrylates,[35] poly(lactic acid) (PLA)[36] and poly (lactic-*co*-glycolic acid) (PLGA),[37-39] they have yet to be investigated in poly(L-glutamic acid) (PLG)-based delivery systems.

A commonly studied polymer in PLG-based drug delivery systems are PEG-*b*-PLG block copolymers. They are often utilized as precursors in the preparation of synthetic PLG-based nanoparticles for drug delivery (see also **Chapter 2**).[8-10, 15-16, 18, 40-41] Covalent conjugation/coordination of hydrophobic drugs to the PLG side chain often results in self-assembly into micelle or vesicle nanoparticle structures

with PEG outer periphery for improved nanoparticle circulation half-life and pharmacokinetic profiles (see also **Chapter 2**).[8, 10, 15-16, 18, 40-41] To investigate the potential use of aptamers with these systems, preliminary studies into aptamer conjugation to these polymers and their isolation, must first be performed.

In this chapter, a 20 nucleotide model single-stranded DNA (ssDNA) aptamer with commercial disulfide protected 5'-thiol is conjugated to maleimide-functional poly(ethylene glycol)-*b*-poly(L-glutamic acid) (Mal-PEG-*b*-PLG) and poly(ethylene glycol)-*b*-poly(L-glutamic acid-*r*-L-lysine) (Mal-PEG-*b*-(PLG-*r*-PLL)) block copolymers. The incorporation of amine functionality via a randomly dispersed PLL component offers dual functionality to the copolymer and the possibility of co-loading with additional drugs. We believe this to be the first reported case in the preparation of DNA and PLG-based block copolymer conjugates.

Model aptamer-polymer conjugations were monitored using agarose gel electrophoresis, and a range of conjugation conditions studied. A reliable method for isolation of the conjugates was then investigated using preparative gel electrophoresis. Confirmation of conjugate isolation was performed through UV-Vis analysis. The conjugation and isolation protocols offer potential use in any future studies employing aptamer-targeting of synthetic PLG-based delivery systems.

3.3. Results and Discussion

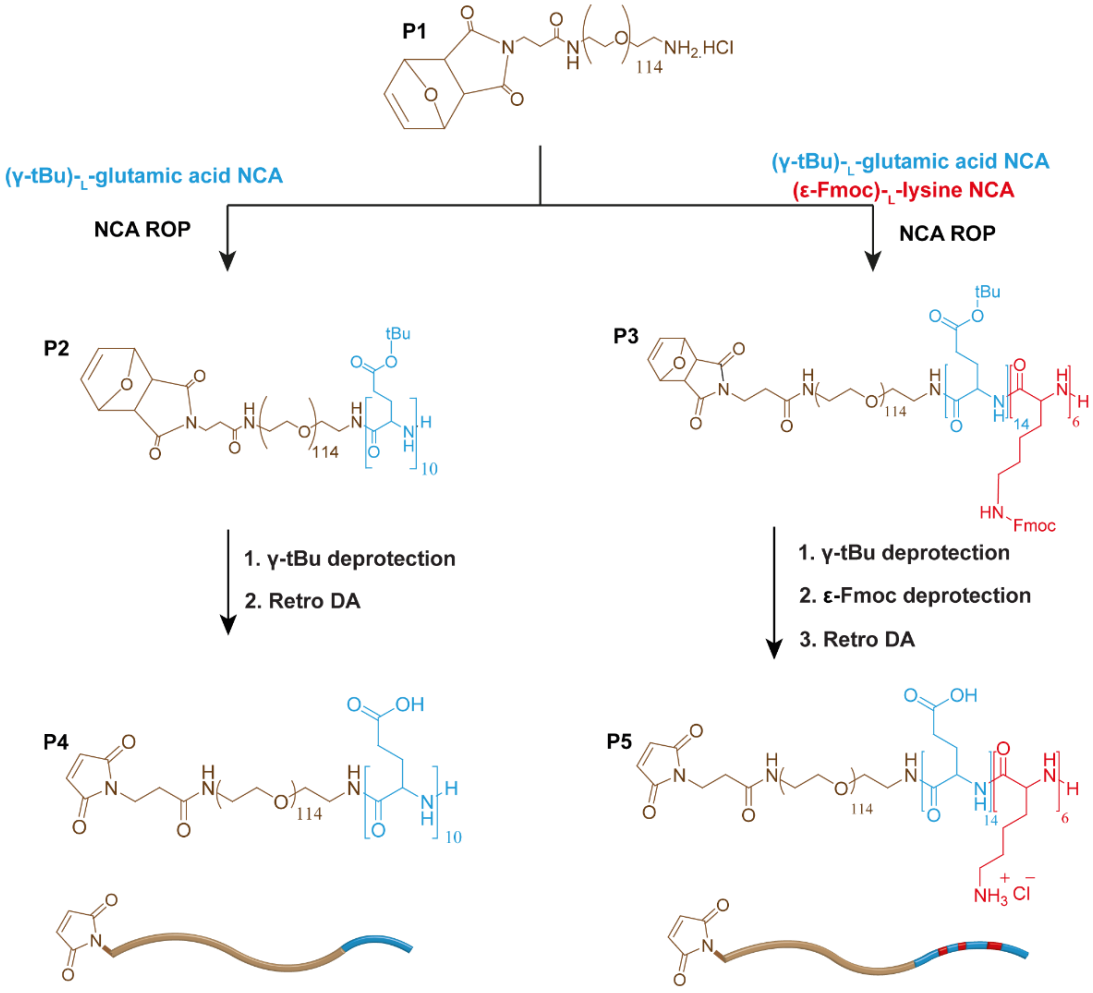

Scheme 3.1. Synthetic scheme of maleimide-functional poly(L-glutamic acid)(PLG)-based block copolymers.

3.3.1 Synthesis of Block Copolymers

The two maleimide functional copolymers Mal-PEG-*b*-PLG-NH_2 (**P4**) and Mal-PEG-*b*-(PLG-*r*-PLL)-NH_2 (**P5**) used in this chapter were synthesized through *N*-carboxyanhydride ring-opening polymerization (NCA ROP) using a furan-protected Mal-PEG (5 kDa)-NH_2 HCl as macroinitiator (**Scheme 3.1**) as per **Chapter 2**. The maleimide group is a widely used functional group in bioconjugation reactions due to its high conjugation efficiency with thiols in mild aqueous, metal-free conditions,[42-44] and has previously been used for the conjugation of thiol-

functionalized aptamers to polymers.[35, 45] As mentioned in **Chapter 2**, the maleimide group is susceptible to nucleophilic attack by amines particularly under basic conditions.[46] Its susceptibility to both acid and base hydrolysis, demands a thermally reversible Diels-Alder (DA) adduct be present to protect the maleimide double bond throughout the polymer synthetic process (**Scheme 3.1**). This adduct was formed by reaction between furan and the PEG maleimide double bond to generate macroinitiator **P1.** To reduce the chance of retro DA promotion by strong acids during the synthetic process, [47] NCA monomers were chosen which contained protecting groups readily removed under mild conditions. For the preparation of polyglutamic residues, *γ-tert*-butyl-L-glutamic acid NCA was used as monomer for effective deprotection under mild acidic conditions whilst for the preparation of polylysine residues, *ε*-Fmoc (fluorenylmethyloxycarbonyl)-L-lysine NCA was used for effective deprotection under basic conditions (**Scheme 3.1**).

Polymer	Formula	M_n (NMR)[a]	$Đ$[b]
P4	Mal-PEG (5kDa)-*b*-$(PLG)_{10}$-NH_2	6.6 kDa	1.12
P5	Mal-PEG(5kDa)-*b*-$((PLG)_{14}$-*r*-$(PLL)_6)$-NH_2	8.1 kDa	1.14

Table 3.1. Formula and molecular weight data of PLG-based block copolymers. [a] M_n determined by ^{1}H NMR analysis using PEG (CH_2-CH_2-O) proton integrations as reference; [b] PDI values calculated from GPC of the protected copolymers using MeO-PEG–OH standards.

NCA ROP generated the protected copolymers **P2**, a block copolymer consisting of PEG and a *γ-tert*-butyl-protected PLG (DP = 10) block; and **P3**, a block copolymer consisting of PEG and a random *γ-tert*-butyl-protected PLG (DP = 14) and *ε*-Fmoc -protected PLL (DP = 6) block (**Scheme 3.1**) as determined by ^{1}H NMR analysis (see **Appendix Figures A3.1** and **A3.2**). SEC analysis of the block copolymers determined a unimodal distribution of the copolymers with narrow polydispersities of 1.12 and 1.14 for **P2** and **P3** respectively (**Table 3.1**).

Polymer side chains were then deprotected using TFA for complete removal of PLG *tert*-butyl and DBU for complete removal of PLL Fmoc groups. Retro DA was then performed under reflux to afford the free maleimide copolymers (**P4** and **P5,** see **Table 3.1**) with ^{1}H NMR analysis used to confirm the disappearance of the Diels-Alder cycloadduct and generation of thiol-reactive maleimide double bond group (δ_H = 7.00 ppm ^{1}H, d_6-DMSO) with 92% and 85% integrity for **P4** and **P5** polymers respectively (see **Appendix Figures A3.3** and **A3.4**).

The fully deprotected block copolymers were then labeled with FITC on the terminal amine end groups. For polymer **P5**, FITC is also expected to react with the lysine amine side chains of the copolymer. FITC labelling efficiency was determined to be ~50 mol % (amine) through UV−Vis analysis of both copolymers.

3.3.2 Conjugation of a Model Aptamer to Copolymers

The specificity of aptamers for their target antigen resides in their unique three-dimensional folded structure owing to their specific nucleotide sequence. A demonstrated approach to the use of these 'functional' aptamers in polymer systems involves the conjugation and isolation of the non-folded aptamer sequence to the polymer, followed by its subsequent folding.[39] A model non-folded DNA aptamer was used to test for conjugation and isolation protocols with the synthetic polypeptide-based polymers.

Scheme 3.2. Conjugation of model thiol-functionalized ssDNA aptamer to polypeptide-based-FITC polymer through thiol-maleimide coupling.

DNA targeting aptamers are generally short nucleotide single strand sequences consisting of between 20-30 nucleotides,[35, 38, 48] therefore a non-folded disulfide-

protected 5' thiol-functionalized single-stranded (ssDNA) model aptamer consisting of 20 nucleotides was used for the conjugation to copolymers. The thiol-functionalized disulfide-protected ssDNA sequence was reduced before conjugation in the presence of DTT (see **experimental section 7.3**). After isolation of the reduced ssDNA sample, its conjugation to the FITC-labeled copolymers through thiol-maleimide coupling (**Scheme 3.2.**) was monitored visually by agarose gel electrophoresis (**Figure 3.1**).

A.

1 2 3 4 5 6

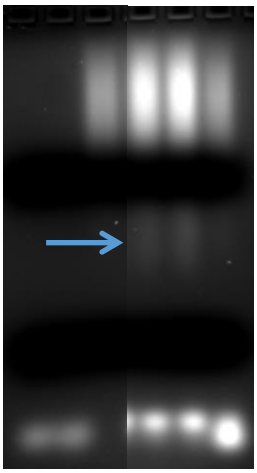

Lane	Sample	Polymer[a]	EDTA	TCEP
1	ssDNA	-	-	-
2	ssDNA/TCEP	-	-	-
3	**P4**-FITC	-	-	-
4	RT, 4 h	20	3 mM	-
5	37 °C, 2 h	20	3 mM	-
6	RT, 4 h	10	-	5 mM

B.

1 2 3 4 5 6

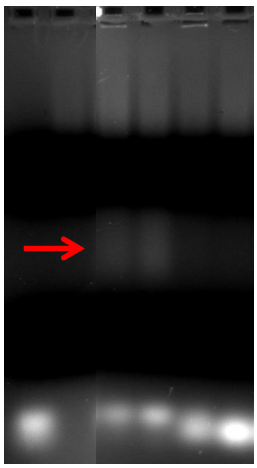

Lane	Sample	Polymer[a]	EDTA	TCEP
1	ssDNA	-	-	-
2	**P5**-FITC	-	-	-
3	RT, 4 h	20	3 mM	-
4	37 °C, 4 h	10	3 mM	-
5	RT, 4 h	10	-	1 mM
6	RT, 4 h	10	-	5 mM

Figure 3.1. Agarose (2%) gels of DNA-polymer conjugations using the relevant FITC-labeled polypeptide-based copolymer. (A) **P4** (B) **P5**. Blue and red arrows indicate conjugate bands. [a] molar excess of polymer relative to DNA. RT = room temperature.

Similarly in principle to DNA, the dominant negative charge of both copolymers from the poly-(L-glutamic acid) side chains is expected to make the polymer and any conjugate migrate down the gel towards the positive terminal of the gel electrophoresis apparatus. Any conjugate species, like their block copolymer precursors, are expected to remain in a non self-assembled state due to the charged polypeptide side chains at neutral/near neutral pH during thiol-maleimide coupling (pH 7.4) and gel electrophoresis (pH 8.5) analysis.

To prevent oxidation of the reduced DNA during the reaction process, strategies using TCEP and EDTA were tested. TCEP, as a thiol-free reducing agent, is thought to be non-competitive with thiols and can be employed to reduce disulfide bonds *in situ*.[49-50] EDTA, a metal chelating agent is also commonly employed to help prevent the reoxidation of sulfides caused by trace divalent metals.[51-52] The conjugations of reduced thiol DNA to **P4**-FITC is shown in **Figure 3.1A** and to **P5-**FITC in **Figure 3.1B**. The DNA and polymer standards show distinctly separate bands, with the DNA band running further down the gel due to its smaller size and higher charge. In all tests using TCEP, gel electrophoresis of the reaction mixture shows only bands corresponding to free DNA and polymer with no additional bands observed. Tests using EDTA all showed a new band (blue and red arrows), with its positioning relative to the free DNA and polymer consistent with the reduced migration of a high molecular weight DNA-polymer conjugate.[35, 45] A potential analytical approach to confirm the existence of conjugate band on the gel could be to use fluorescence detection where both FITC (polymer) and DNA fluorescence coincide. This approach will be tested in future aptamer-polymer conjugation studies.

Quantification of conjugate yields through analysis of band intensities could not give reliable results, due to the low conjugate yield/intensities, therefore conjugate efficiencies were interpreted visually. All reaction mixture samples separated on the gels contained DNA concentrations of ~2 μM so that comparisons could be made between the runs. Visual analysis of the conjugate bands appear to show that conjugation conditions of 37 °C, in the presence of 3 mM EDTA resulted in the highest conjugation efficiencies.

As shown in **Figure 3.1**, in all reactions containing EDTA, the band that runs furthest down the gel corresponding to unreacted DNA appear to run slower (higher molecular weight) compared to the reduced DNA standards. This suggests that despite some conjugation occurring in these reaction batches, oxidation and self-coupling of the DNA to an unreactive disulfide is taking place during the reaction, thereby reducing conjugation yields. For those reactions employing TCEP, all free DNA bands appeared to exist in their reduced state, as expected. The fact that TCEP effectively maintained the DNA in its reactive reduced state yet resulted in no noticeable conjugate suggests that the TCEP was having a detrimental effect elsewhere in the reaction. This is consistent with previous reports which have shown that TCEP can inhibit thiol-maleimide reactions by competitively reacting with the maleimide group.[53-55] The presence of TCEP has shown to result in significantly reduced thiol-maleimide reaction efficiencies compared to use of no reductant.[54] Whilst low TCEP concentrations down to 1 mM and a large excess of maleimide polymer were used in this study, even lower TCEP concentrations may be required to reduce its competitive reactivity and result in improved conjugation efficiencies.[53]

3.3.3 Isolation of DNA-Polymer Conjugates

The conjugation protocol with highest observed conjugation efficiency (37 °C, 4 h and EDTA) was then scaled up and the isolation of the DNA-polymer conjugate then attempted first through preparative anionic exchange chromatography. A range of different high resolution anionic exchange columns and solvents were tested with peaks suggestive of conjugate defined as those with UV-Vis absorbances in all three tested wavelengths; 216 nm (protein/peptide), 260 nm (DNA), 495 nm (FITC). **Figure 3.2 top** shows a typical chromatogram of the reaction mixture, showing multiple overlapping peaks with absorbance across all three wavelengths. Peaks corresponding to the polymer and/or conjugate FITC label (495 nm) are very broad and display very low resolution, possibly due to extended interactions of the material with the column or due to polymer polydispersity. These fractions were collected and ran through gel electrophoresis, with the results in **Figure 3.2 bottom**

confirming the absence of any conjugate isolation, but rather conjugate with significant amounts of either (or both) excess DNA or polymer reagent.

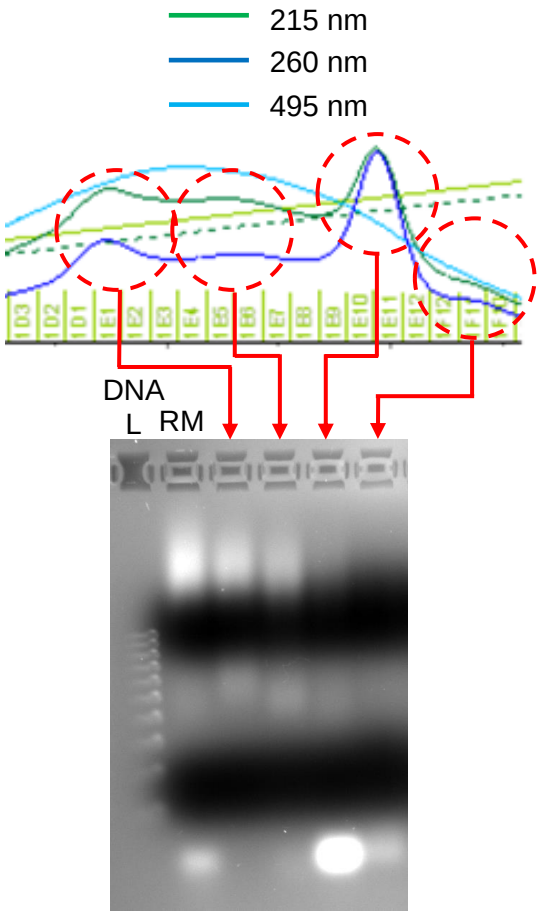

Figure 3.2. Top. Portion of preparative anionic exchange chromatogram of conjugation reaction mixture of thiol DNA and **P4**-FITC showing potential peaks of interest. Bottom. Agarose (2%) gel electrophoresis of anionic exchange peak fractions. DNA (L) = 100 bp DNA ladder.

Due to the effective separation of DNA-polymer conjugate from the free DNA and polymer as shown by gel electrophoresis (**Figure 3.1**), the isolation of the DNA-polymer conjugate was then attempted using a robust and cost-effective preparative DNA gel electrophoresis procedure (see **experimental section 7.3**). This involved running gel electrophoresis on a scaled-up DNA-polymer conjugation reaction mixture containing the highest observed conjugation efficiency (37 °C, 4 h and

EDTA, **Figure 3.1**). Then, a portion of the gel containing the DNA-polymer conjugate band of interest (**Figure 3.1** red and blue arrow) was excised, and the DNA-polymer conjugate in the removed gel slice then isolated using affinity chromatography. This involved melting and dissolving the gel slice then running through a column which binds the DNA to a silica gel membrane thus allowing the gel matrix (e.g. agarose) and impurities to be washed out. The purified DNA-polymer conjugate was then eluted out of the silica membrane using an elution solvent. The isolated conjugate samples were analyzed via gel electrophoresis (**Figure 3.3**), with only single conjugate bands observed (Lane 5) and no discernable free DNA or polymer bands indicating successful isolation of the conjugate.

Lane	Sample
1	100 bp DNA ladder
2	Reduced DNA-SH
3	Free Polymer (FITC)
4	Conjugate reaction mixture
5	Isolated conjugate

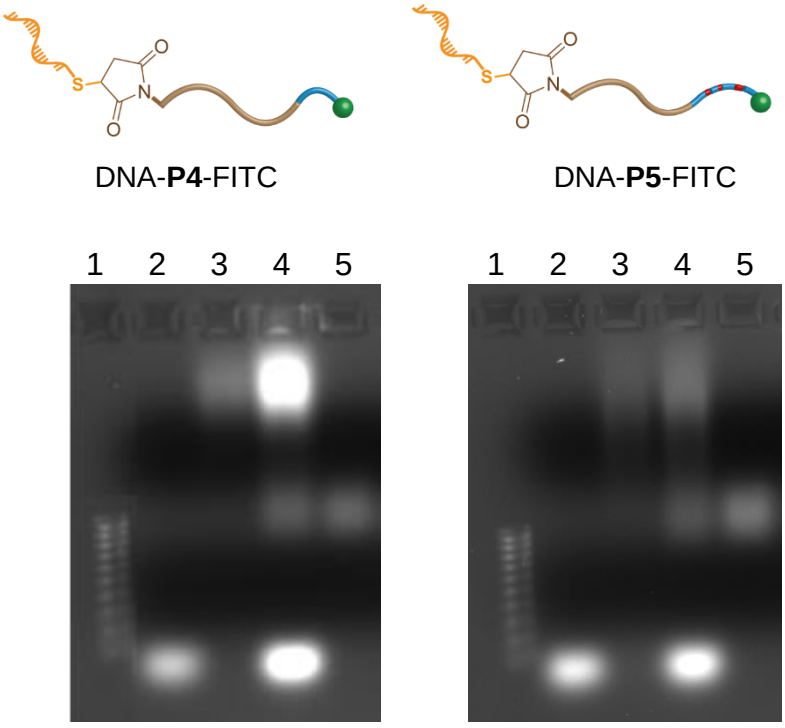

Figure 3.3. Agarose (1%) gel electrophoresis of isolated DNA-polymer conjugates.

In addition to the above analysis, further verification that these single bands were indeed DNA-polymer conjugate was performed through UV-Vis analysis of the isolated material. As shown in **Figure 3.4**, absorbance shoulders can be seen in the spectrum of both isolates at 260 nm corresponding to the λ_{max} of the ssDNA, as well as absorbance maxima at 495 nm corresponding to the λ_{max} of the polymer FITC tag. The increased absorbance maxima of FITC tag relative to DNA absorbance in **P5** conjugate compared to **P4** conjugate can be attributed to the increased FITC tagging of **P5** polymer lysine (amine) side chains (see experimental **Chapter 7**). The presence of both DNA and polymer UV-Vis absorbance profiles confirms that the isolates are indeed conjugates, and verifies the suitability of this technique in purifying and isolating PLG-based polymer-DNA conjugates.

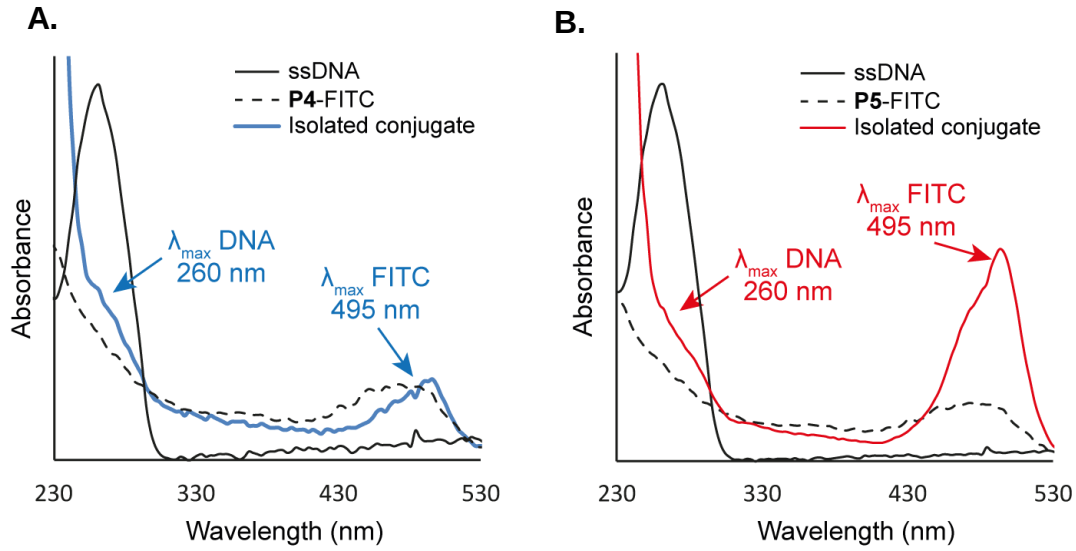

Figure 3.4. UV-Vis absorbance spectra of (A) DNA-**P4**-FITC and (B) DNA-**P5**-FITC isolated conjugates (DI water). Note: absorbance spectra not normalized for better identification of conjugate λ_{max} DNA absorbance at 260 nm.

3.4 Chapter Summary

In summary, preliminary investigations into the preparation of DNA aptamer-targeted PLG-based drug delivery systems has been explored. Thiol-reactive block copolymers composed of PEG and poly(L-glutamic acid) or poly(L-glutamic)-*r*-poly(L-lysine) blocks were first prepared and are representative of synthetic PLG-based block polymers commonly used in drug delivery applications. A thiol-functionalized model DNA aptamer was then successfully conjugated to the polymers in the presence of 3 mM EDTA, with no conjugation observed using the common *in situ* reductant TCEP, likely due its competitive reactivity with the maleimide group on the polymer. The conjugates were successfully isolated through a preparative gel electrophoresis procedure. Conjugate isolation was verified through UV-Vis analysis, with the absorbance spectra of the gel isolates containing both DNA and polymer absorbance profiles. This work details the first reported investigation into the conjugation and isolation of DNA aptamers to PLG-based delivery systems. The protocols reported in this work offer potential use in any future studies employing aptamer-targeting of synthetic PLG-based delivery systems.

3.5 References

(1) Hehir, S.; Cameron, N. R., *Polym. Int.* **2014,** *63* (6), 943-954.

(2) Duro-Castano, A.; Conejos-Sanchez, I.; Vicent, M. J., *Polymers* **2014,** *6* (2), 515-551.

(3) Lu, H.; Wang, J.; Song, Z.; Yin, L.; Zhang, Y.; Tang, H.; Tu, C.; Lin, Y.; Cheng, J., *Chem. Commun.* **2014**.

(4) Li, C., *Adv. Drug Del. Rev.* **2002,** *54* (5), 695-713.

(5) Chipman, S. D.; Oldham, F. B.; Pezzoni, G.; Singer, J. W., *Int. J. Nanomed.* **2006,** *1* (4), 375-383.

(6) Duro-Castano, A.; England, R. M.; Razola, D.; Romero, E.; Oteo-Vives, M.; Angel Morcillo, M.; Vicent, M. J., *Mol. Pharm.* **2015,** *12* (10), 3639-3649.

(7) Tansey, W.; Ke, S.; Cao, X. Y.; Pasuelo, M. J.; Wallace, S.; Li, C., *J. Controlled Release* **2004,** *94* (1), 39-51.

(8) Uchino, H.; Matsumura, Y.; Negishi, T.; Koizumi, F.; Hayashi, T.; Honda, T.; Nishiyama, N.; Kataoka, K.; Naito, S.; Kakizoe, T., *Br. J. Cancer* **2005,** *93* (6), 678-687.

(9) Guan, H.; McGuire, M. J.; Li, S.; Brown, K. C., *Bioconjugate Chem.* **2008,** *19* (9), 1813-1821.

(10) Miura, Y.; Takenaka, T.; Toh, K.; Wu, S.; Nishihara, H.; Kano, M. R.; Ino, Y.; Nomoto, T.; Matsumoto, Y.; Koyama, H.; Cabral, H.; Nishiyama, N.; Kataoka, K., *Acs Nano* **2013,** *7* (10), 8583-8592.

(11) Eldar-Boock, A.; Miller, K.; Sanchis, J.; Lupu, R.; Vicent, M. J.; Satchi-Fainaro, R., *Biomaterials* **2011,** *32* (15), 3862-3874.

(12) Maeda, H.; Greish, K.; Fang, J., The EPR effect and polymeric drugs: A paradigm shift for cancer chemotherapy in the 21st century. In *Polymer Therapeutics II: Polymers as Drugs, Conjugates and Gene Delivery Systems*, Satchi-Fainaro, R.; Duncan, R., Eds. 2006; Vol. 193, pp 103-121.

(13) Maeda, H.; Nakamura, H.; Fang, J., *Adv. Drug Del. Rev.* **2013,** *65* (1), 71-79.

(14) Kamaly, N.; Xiao, Z. Y.; Valencia, P. M.; Radovic-Moreno, A. F.; Farokhzad, O. C., *Chem. Soc. Rev.* **2012,** *41* (7), 2971-3010.

(15) Yang, X.; Grailer, J. J.; Rowland, I. J.; Javadi, A.; Hurley, S. A.; Matson, V. Z.; Steeber, D. A.; Gong, S., *Acs Nano* **2010,** *4* (11), 6805-6817.

(16) Shirbin, S. J.; Ladewig, K.; Fu, Q.; Klimak, M.; Zhang, X.; Duan, W.; Qiao, G. G., *Biomacromolecules* **2015,** *16* (8), 2463-2474.

(17) Song, W. T.; Tang, Z. H.; Zhang, D. W.; Zhang, Y.; Yu, H. Y.; Li, M. Q.; Lv, S. X.; Sun, H.; Deng, M. X.; Chen, X. S., *Biomaterials* **2014,** *35* (9), 3005-3014.

(18) Vega, J.; Ke, S.; Fan, Z.; Wallace, S.; Charsangavej, C.; Li, C., *Pharm. Res.* **2003,** *20* (5), 826-832.

(19) Keefe, A. D.; Pai, S.; Ellington, A., *Nat. Rev. Drug. Discov.* **2010,** *9* (8).

(20) Brennan, F. R.; Shaw, L.; Wing, M. G.; Robinson, C., *Mol. Biotechnol.* **2004,** *27* (1), 59-74.

(21) Weinberg, W. C.; Frazier-Jessen, M. R.; Wu, W. J.; Weir, A.; Hartsough, M.; Keegan, P.; Fuchs, C., *Cancer Metastasis Rev.* **2005,** *24* (4), 569-584.

(22) Ellington, A. D.; Szostak, J. W., *Nature* **1990,** *346* (6287), 818-822.

(23) Famulok, M.; Hartig, J. S.; Mayer, G., *Chem. Rev.* **2007,** *107* (9), 3715-3743.

(24) Sun, H. G.; Zu, Y. L., *Molecules* **2015,** *20* (7), 11959-11980.

(25) Brody, E. N.; Gold, L., *Rev. Mol. Biotechnol.* **2000,** *74* (1), 5-13.

(26) Cerchia, L.; de Franciscis, V., *Trends Biotechnol.* **2010,** *28* (10), 517-525.

(27) Osborne, S. E.; Matsumura, I.; Ellington, A. D., *Curr. Opin. Chem. Biol.* **1997,** *1* (1), 5-9.

(28) Lakhin, A. V.; Tarantul, V. Z.; Gening, L. V., *Acta Naturae* **2013,** *5* (4), 34-43.

(29) Burmeister, P. E.; Lewis, S. D.; Silva, R. F.; Preiss, J. R.; Horwitz, L. R.; Pendergrast, P. S.; McCauley, T. G.; Kurz, J. C.; Epstein, D. M.; Wilson, C.; Keefe, A. D., *Chem. Biol.* **2005,** *12* (1), 25-33.

(30) Li, N.; Nguyen, H.; Byrom, M.; Ellington, A. D., *Plos One* **2011,** *6* (6).

(31) Tan, L. H.; Neoh, K. G.; Kang, E. T.; Choe, W. S.; Su, X. D., *Macromol. Biosci.* **2011,** *11* (10), 1331-1335.

(32) Taghdisi, S. M.; Danesh, N. M.; Emrani, A. S.; Tabrizian, K.; ZandKarimi, M.; Ramezani, M.; Abnous, K., *J. Drug Targeting* **2013,** *21* (8), 739-744.

(33) Greenwald, R. B.; Choe, Y. H.; McGuire, J.; Conover, C. D., *Adv. Drug Del. Rev.* **2003,** *55* (2), 217-250.

(34) Harris, J. M.; Chess, R. B., *Nat. Rev. Drug. Discov.* **2003,** *2* (3), 214-221.

(35) Da Pieve, C.; Williams, P.; Haddleton, D. M.; Palmer, R. M. J.; Missailidis, S., *Bioconjugate Chem.* **2010,** *21* (1), 169-174.

(36) Farokhzad, O. C.; Karp, J. M.; Langer, R., *Expert Opin. Drug Deliv* **2006,** *3* (3), 311-324.

(37) Dhar, S.; Gu, F. X.; Langer, R.; Farokhzad, O. C.; Lippard, S. J., *Proc. Natl. Acad. Sci. U.S.A.* **2008,** *105* (45), 17356-17361.

(38) Guo, J. W.; Gao, X. L.; Su, L. N.; Xia, H. M.; Gu, G. Z.; Pang, Z. Q.; Jiang, X. G.; Yao, L.; Chen, J.; Chen, H. Z., *Biomaterials* **2011,** *32* (31), 8010-8020.

(39) Cheng, J.; Teply, B. A.; Sherifi, I.; Sung, J.; Luther, G.; Gu, F. X.; Levy-Nissenbaum, E.; Radovic-Moreno, A. F.; Langer, R.; Farokhzad, O. C., *Biomaterials* **2007,** *28* (5), 869-876.

(40) Nishiyama, N.; Okazaki, S.; Cabral, H.; Miyamoto, M.; Kato, Y.; Sugiyama, Y.; Nishio, K.; Matsumura, Y.; Kataoka, K., *Cancer Res.* **2003,** *63* (24), 8977-8983.

(41) Cabral, H.; Nishiyama, N.; Okazaki, S.; Koyama, H.; Kataoka, K., *J. Controlled Release* **2005,** *101* (1–3), 223-232.

(42) Narain, R., *Chemistry of Bioconjugates: Synthesis, Characterization, and Biomedical Applications*. Wiley: 2014; p 1-464.

(43) Hermanson, G. T., *Bioconjugate Techniques, 3rd Edition*. Academic Press: 2013; p 1-1146.

(44) Peng, H. J.; Chen, W. X.; Cheng, Y. F.; Hakuna, L.; Strongin, R.; Wang, B. H., *Sensors* **2012,** *12* (11), 15907-15946.

(45) Da Pieve, C.; Blackshaw, E.; Missailidis, S.; Perkins, A. C., *Bioconjugate Chem.* **2012,** *23* (7), 1377-1381.

(46) Sharpless, N. E.; Flavin, M., *Biochemistry* **1966,** *5* (9), 2963-2971.

(47) Bunnelle, W. H.; Shangraw, W. R., *Tetrahedron* **1987,** *43* (9), 2005-2011.

(48) Ferreira, C. S. M.; Matthews, C. S.; Missailidis, S., *Tumor Biol.* **2006,** *27* (6), 289-301.

(49) Maret, B.; Regnier, T.; Rossi, J. C.; Garrelly, L.; Vial, L.; Pascal, R., *Rsc Advances* **2014,** *4* (15), 7725-7728.

(50) Kirley, T. L., *Anal. Biochem.* **1989,** *180* (2), 231-236.

(51) Stevens, R.; Stevens, L.; Price, N. C., *Biochemical Education* **1983,** *11* (2), 70-70.

(52) Trivedi, M. V.; Laurence, J. S.; Siahaan, T. J., *Curr. Protein Peptide Sci.* **2009,** *10* (6), 614-625.

(53) Tyagarajan, K.; Pretzer, E.; Wiktorowicz, J. E., *Electrophoresis* **2003,** *24* (14), 2348-2358.

(54) Getz, E. B.; Xiao, M.; Chakrabarty, T.; Cooke, R.; Selvin, P. R., *Anal. Biochem.* **1999,** *273* (1), 73-80.

(55) Shafer, D. E.; Inman, J. K.; Lees, A., *Anal. Biochem.* **2000,** *282* (1), 161-164.

4

Macroporous Hydrogels Composed Entirely of Synthetic Polypeptides: Biocompatible and Enzyme Biodegradable 3D Cellular Scaffolds

4.1 Chapter Perspective

Macroporous hydrogels have demonstrated to be highly suitable cellular scaffolds in the quest to grow new patient tissue. Synthetic polypeptides have been utilized as materials to fabricate macroporous hydrogels owing to their biocompatibility, biodegradability and cell adhesive properties, however their use has thus far been limited to partial components of these gel networks. In this chapter, three-dimensional macroporous hydrogels, in the form of cryogels, composed entirely of synthetic polypeptides have been prepared to better investigate and utilise the beneficial properties of these materials in cellular scaffolds. Cryogels were prepared through direct crosslinking of a single copolypeptide composed of poly(L-glutamic acid) (PLG) and poly(L-lysine) (PLL), with optimal pore sizes. Tuning the relative ratios of the amino acid components could result in cryogels with very different pore structures, swelling, and mechanical properties. These cryogels were shown to be enzymatically biodegradable and demonstrated excellent biocompatibility, cell attachment and cell proliferation profiles with mammalian fibroblast (NIH-3T3) cells.

4.2 Introduction

Three-dimensional macroporous polymeric hydrogels have for many years received significant research attention in cell-based therapies[1-3] and tissue engineering applications[4-8] due to their macroporous structure. Compared to conventional non-macroporous hydrogels, the presence of macropores provides superior swelling and mechanical properties to the gel, generating 3D scaffolds highly suitable for *in vitro* cell culturing by mimicking the physiological function of the extracellular matrix (ECM). The open interconnected porous structure, with pore sizes ≥100 μm allows for effective cell proliferation and vascularization and facilitates the transport of nutrients and metabolites through the scaffold.[4, 9] In order to ensure the gel scaffold has suitable biocompatible and bioresponsive properties, the materials used to fabricate the gel must be carefully considered.

Synthetic polypeptides are a class of bioinspired polymers with well demonstrated biocompatibility, enzyme biodegradability, and cell adhesive properties, making them promising materials for the preparation of macroporous hydrogels as 3D cellular scaffolds. Synthetic polypeptides, such as poly(L-glutamic acid) (PLG) have been studied extensively in the drug delivery field as highly biocompatible and enzyme biodegradable drug delivery scaffolds.[10-13] Their effective cell adhesion properties have been demonstrated through the preparation of polyelectrolyte multilayer coatings (PEM) composed of charged synthetic polypeptides such as poly(L-glutamic acid) (PLG) and poly(L-lysine) (PLL) that have shown to enhance the cell adhesion properties of surfaces.[14-16] For these reasons, hydrophilic synthetic polypeptides have been used as partial components of biodegradable macroporous hydrogel scaffolds for tissue engineering applications.[17-21] In all cases, the synthetic polypeptide is one component of the gel, with additional polymers (e.g., chitosan, cellulose) and cross-linkers (e.g., 2-hydroxyethyl methacrylate, HEMA) added and incorporated into the final gel structure. However, additional synthetic steps to modify the polypeptide side-chain functionalities are often required for gelation to take place.[19-21] As well, these polypeptide-based gels make it difficult to ascertain the true effect of the synthetic polypeptide on the biocompatibility and

biodegradability properties of the gel, and their modifications are likely to alter the characteristics of the gel from their initially intended properties. Therefore, to effectively study the suitability of synthetic polypeptides as a material for 3D cell culture applications and to better utilize the beneficial properties owing to these materials, the preparation of macroporous hydrogels composed entirely of synthetic polypeptides is desirable. To achieve this, a simple, nontoxic macropore-forming approach must first be considered to fabricate hydrogels with large pore sizes (≥100 μm) suitable for the ingrowth of mammalian cells.[4] Cryogelation through chemical cross-linking is a simple approach for the introduction of large interconnected pores to a hydrogel structure and avoids the need to remove toxic solutes/gases/solvents from the scaffold,[22-25] as required in other macropore-forming approaches such as gas foaming,[26] phase separation,[18, 27] and porogen use.[28-29] In a typical aqueous cryogelation process that is commonly used to prepare cryogels for biomedical applications, an aqueous polymer solution is frozen below 0°C. Within the concentrated liquid microphase surrounding the ice crystals, gelation or cross-linking of the solution typically occurs to form the dense polymeric pore walls. Thawing of the frozen solution removes the nontoxic ice water crystals to leave behind the macroporous cryogel structure (**Scheme 4.1**).

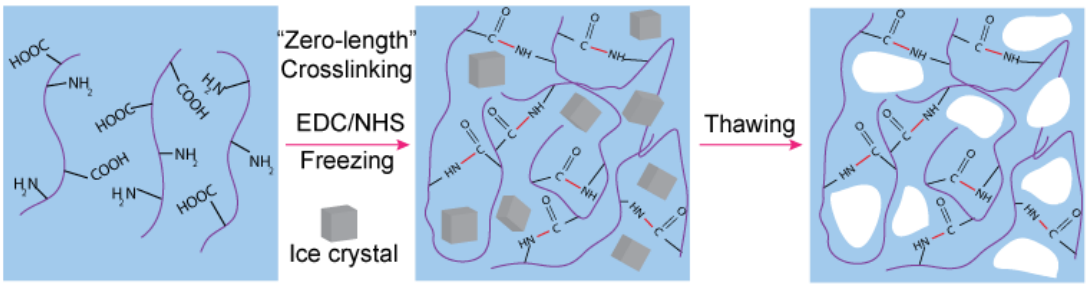

Scheme 4.1. Formation of macroporous cryogels by direct zero-length EDC/(sulfo)-NHS cross-linking of a polypeptide copolymer.

In this chapter, the facile preparation of macroporous hydrogels composed entirely of synthetic polypeptides via the cryogelation process is reported. In fact, this chapter describes the first reported case of macroporous hydrogels prepared entirely from synthetic polypeptides. These macroporous hydrogels in the form of

macroporous cryogels were prepared through a direct EDC/ sulfo-NHS zero-length cross-linking strategy[5, 8, 30-32] between the carboxylic acid (PLG) and amine (PLL) residues on a PLG-*r*-PLL random copolypeptide chain (**Scheme 4.1**). Zero-length cross-linking agents such as EDC and (sulfo)-NHS, activate the reaction of carboxylic acid groups with amines but are not themselves incorporated into the polymer gel structure and are easily removed by washing in water, thus, improving the biocompatibility prospects of the gel.[4, 30] For natural/ bioinspired polymers,[30, 32] such as polypeptides containing lysine (amine) and glutamic acid (carboxylic acid) amino acid residues, the EDC/(sulfo)-NHS reactive functional groups exist on the same polymer. This offers the prospect of preparing cryogels composed entirely of synthetic polypepides using a single copolymer component (via inter/intra molecular cross-linking) without side chain modification or incorporation of cross-linking agents/additional polymers to the cryogel network (**Scheme 4.1**).

The relative ratios of the amine to carboxylic acid (cross-linkable) components on the copolypeptide were varied to determine its effect on the cryogel pore size, pore morphology, porosity, swelling, and mechanical properties. To demonstrate the potential use of these cryogels as 3D cellular scaffolds, enzymatic biodegradability and cytocompatibility of the gels were studied through cell viability, cell attachment, and proliferation tests using mammalian fibroblast (NIH-3T3) cells.

4.3 Results and Discussion

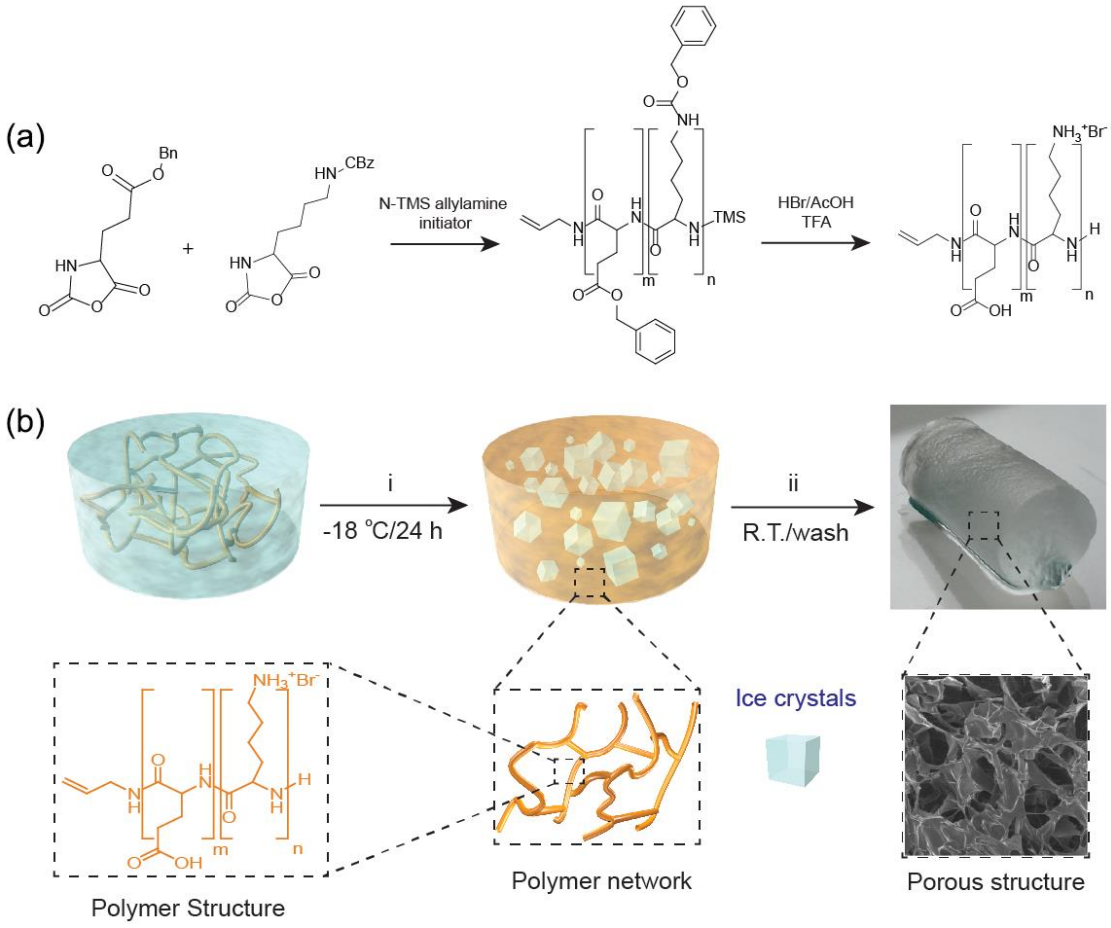

Scheme 4.2. (a) Synthesis of PLG-*r*-PLL random copolypeptides and (b) their fabrication into synthetic polypeptide cryogels; (i) Random copolypeptide dissolved in DI H_2O, followed by addition of EDCI/sulfo-NHS then frozen at -18 °C for 24 h; (ii) gel is thawed at RT and washed thoroughly in DI water and PBS (pH= 7.4).

4.3.1 Random Copolymer Synthesis

Random protected copolypeptides of *γ*-benzyl-protected poly(L-glutamic acid) (PBLG) and *ε*-carboxybenzyl-protected poly(L-lysine) (PZLL) were synthesized through α-amino acid *N*-carboxyanhydride (NCA) ring-opening polymerization (ROP) using *N*-(trimethylsilyl)-allylamine (N-TMS allylamine) as initiator (**Scheme 4.2a**). The polyglutamic and polylysine repeat units contain carboxylic acid and amine side chain functionalities respectively, thereby making it possible for

EDC/sulfo-NHS zero-length cross-linking to take place in water using a single random copolypeptide component.

In this system the polypeptide acts as both polymer and cross-linker with both inter and intra molecular cross-linking of the polypeptide expected to take place. To determine the effect of cross-linking on the cryogels, two random copolypeptides with different final molar ratios of PLG to PLL (PLG:PLL) were prepared. After subsequent side chain deprotection of the protected copolymers in hydrobromic acid (HBr), fully deprotected random copolymer A with a PLG:PLL ratio of 1:0.29 and random copolymer B with a ratio of 1:0.73 (**Table 4.1**, see **Appendix 4** for ^{1}H NMR relative ratio determination) were prepared.

Gel	**Random copolymer**	**Formula**	**NH_2/COOH (mol mol^{-1}) [a]**	**c_p % (w/v)**	***P* % (vol)**	**W_g %**	***E* (kPa)**
A	A	PLG_{24}-*r*-PLL_7	0.29	3.3	85.3 ± 1.0	88.9 ± 2.4	1.6 ± 0.3
B	B	PLG_{16}-*r*-PLL_{12}	0.73	3.3	82.4 ± 0.9	84.4 ± 1.3	65.8 ± 0.4

Table 4.1. Porosity (*P* %), gel fraction (*Wg* %) and Young's modulus (compressive; *E*) of cryogels synthesized from their corresponding random copolymers. [a] Ratio of amine (lysine) to carboxylic acid (glutamic acid) units, as determined by ^{1}H NMR; c_p, concentration of polymer. Values represent mean and standard deviation (n=3).

As can be seen from these ratios, random copolymer B has ~2.5× more cross-linkable amine groups compared to copolymer A while still remaining within the stoichiometric limits. Based on GPC and ^{1}H NMR analysis, both polypeptides had similar M_n and polydispersity ($Đ$) values (see **experimental section 7.4**). Both fully deprotected polymers demonstrated good water solubility, however this was found to be highly dependent on the solution pH.

4.3.2 Preparation of Synthetic Polypeptide Cryogels

Copolymer A was found to be fully water-soluble at pH > 4, whereas copolymer B was found to be soluble at pH values ≤ 4. These observations are consistent with the predicted high net charge (hydrophilicity) of the polypeptides at these respective pH values (calculated using copolymer ratios and side chain pKa values, not shown). The ability of these polymers to be soluble at these pH values allowed the EDC/sulfo-NHS cross-linking procedure to be performed on either copolymer within the optimum pH range for carboxylic acid/sulfo-NHS activation (pH 4.0–6.0) under cryoconditions. For the preparation of cryogel B, it was found that gelation could occur relatively quickly after addition of sulfo-NHS. Therefore, all reagents were chilled on ice before mixing to reduce the chance of cross-linking occurring before freezing. All cryogels were prepared from their corresponding random copolymer at the same polymer concentration and at a temperature of −18 °C (**Scheme 4.2**). To confirm that EDC/sulfo-NHS cross-linking agents were not incorporated into the cryogel network, and their complete removal from the system, FT-IR analysis was performed on the cryogels (**Figures 4.1 and 4.2**). Almost identical spectra can be seen for the cryogels and their corresponding random copolymer precursors, with no additional peaks in the cryogel spectrum corresponding to EDCI or sulfo-NHS cross-linking agent spectrum profiles. To confirm that these gels were not physically cross-linked gels, repeat experiments were performed in the absence of EDC/sulfo-NHS chemical cross-linking agents, with no gelation observed under identical cryogelation conditions; confirming the presence of chemical cross-linking inside the cryogels (see **Appendix Figure A4.5**).

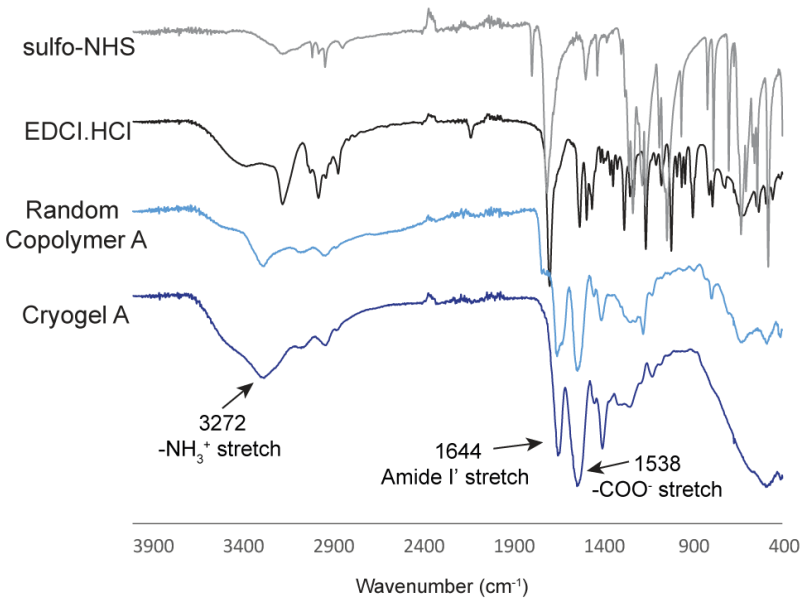

Figure 4.1. FT-IR spectra of cryogel A, copolymer A, EDCI and sulfo-NHS cross-linking agents. Note: amide I stretch in cryogel corresponding to both copolymer backbone and side chain (amide) cross-links.

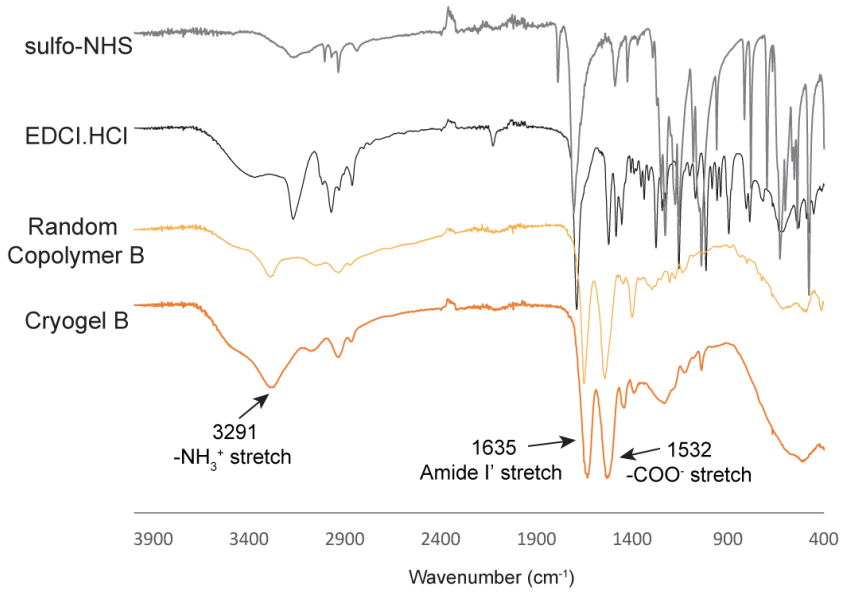

Figure 4.2. FT-IR spectra of cryogel B, copolymer B, EDCI and sulfo-NHS cross-linking agents. Note: amide I stretch in cryogel corresponding to both copolymer backbone and side chain (amide) cross-links.

4.3.3 Morphology of Cryogels

After cryogel preparation, the architecture of the cryogels was determined through ESEM and CLSM analysis on horizontal cross-sections (x-y plane) of non-labeled gels and FITC-labeled gels (**Figure 4.3**, see also **Appendix Figure A4.6**), respectively.

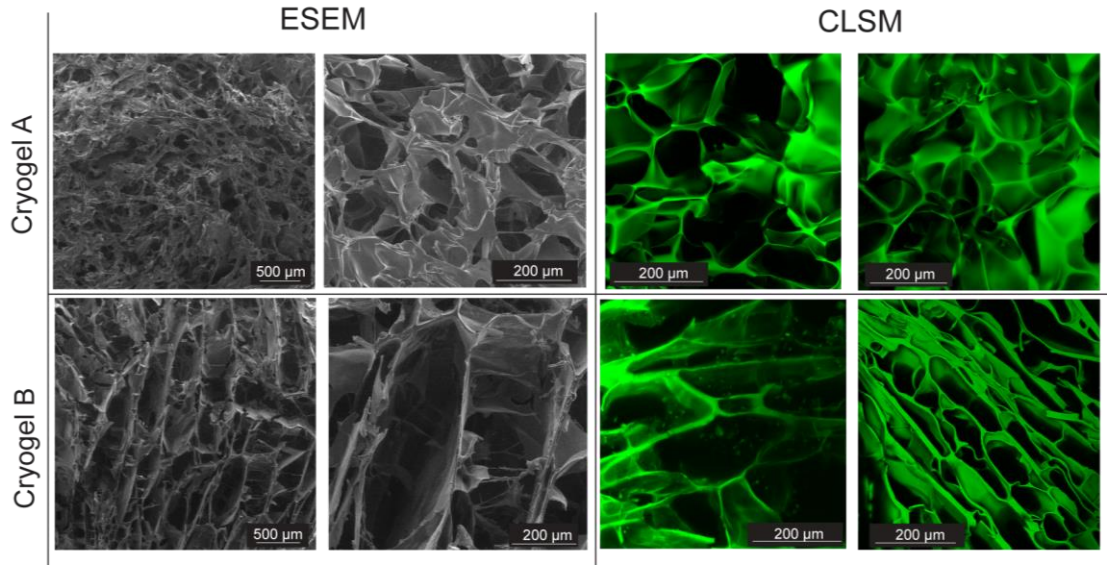

Figure 4.3. ESEM and CLSM images showing pore morphologies of non-labelled and FITC-labeled cryogels respectively. Images are of cross-sections in the x-y plane. ESEM images are of swollen cryogels (PBS) under low vacuum. CLSM images of cryogels swollen in PBS and z-stacked.

While the ESEM was performed under low vacuum, the presence of a negative atmosphere and the subsequent partial dehydration of the gels during analysis can give deformed pore structures not truly representative of the gel in the swollen state. Therefore, pore structures of FITC-labeled gels were analyzed on CLSM in their fully hydrated state (PBS). **Figure 4.3** shows both cryogels containing large interconnected pores (≥100 µm) surrounded by pore walls micrometers in thickness, characteristics highly suitable for cell and tissue growth inside hydrogels (see also **Appendix Figure A4.6).**[4, 9, 33]

The pore sizes and pore morphologies are distinctively different between the cryogels. The images of cryogel A show a sponge-like morphology with randomly

oriented pores ranging in size from 70 to 340 µm and a mean pore size of ~148 µm as calculated from ImageJ analysis (**Figure 4.4**).

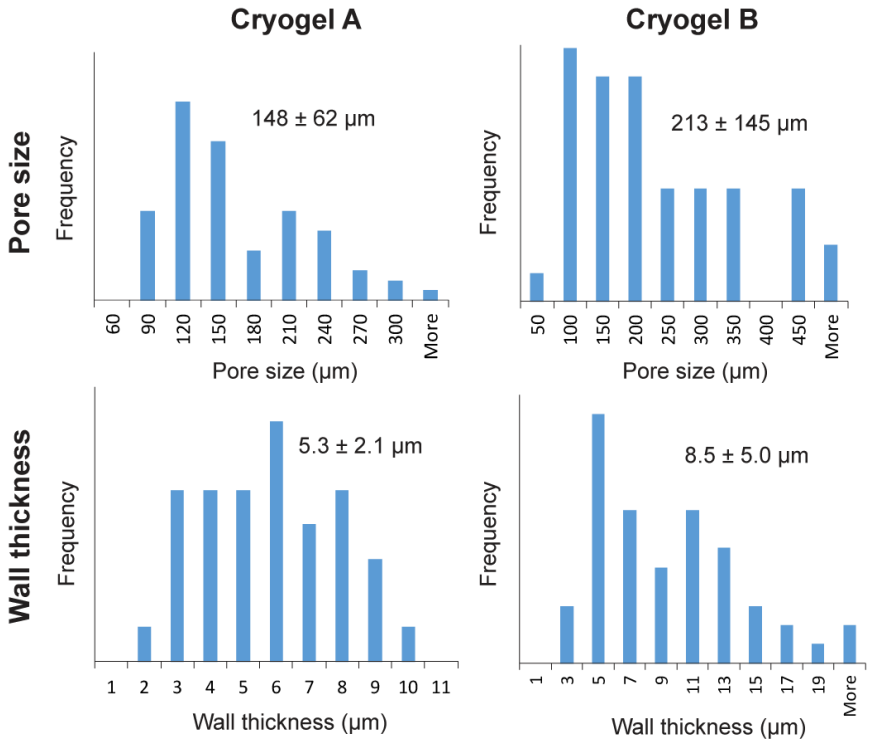

Figure 4.4. Pore size and pore wall thickness distributions of cryogel A and cryogel B obtained by analysis of CLSM images by ImageJ software.

The pore wall thickness distribution was 2–9 µm, with an average of ~5 µm. Meanwhile cryogel B have pores that appear columnar in nature[34] with large defined interconnected closed wall channels running in the z-direction of the gel. The pore sizes in cryogel B are more heterogeneous than cryogel A, ranging in size 50–650 µm with a higher average pore size of ~213 µm (longest dimension). The pore wall thickness of cryogel B also show higher size distributions to cryogel A with pore wall thicknesses up to 23 µm and a higher average pore thickness of ~8.5 µm (**Figure 4.4**) compared to cryogel A. Discrepancies in size between the ESEM and CLSM images for cryogel B are likely to be due to both vacuum/preparation defects on the gels during SEM operation and different cross-sections of the gel used for each

measurement. Nevertheless, the same large columnar-like channel structure is clearly evident in both.

Changes from sponge-like to columnar-like pore morphology in cryogels (including in polypeptide-based cryogels) have been shown to occur through increases in polymer concentration, resulting in changes to solution viscosities which can affect ice crystal growth during the freezing process.[20, 34-35] For similar reasons, the difference in pore structure between cryogel A and cryogel B may be resulting from viscosity changes that affect ice crystal growth due to the different rates of chemical cross-linking in each of the gels. As mentioned previously, gelation of random copolymer B was seen to occur relatively quickly at room temperature compared to copolymer A due to the higher quantity of cross-linkable (amine) groups (**Table 4.1**). Despite the chilling of reagents before cryogelation, a small amount of cross-linking may have occurred in cryogel B during the freezing process thereby increasing solution viscosity and affecting ice crystal growth. This increase in viscosity is also likely to affect the cross-linking reaction between the polymer chains due to their decreased diffusivities and may explain the slightly lower gel fraction (yield) observed in cryogel B compared to cryogel A (**Table 4.1**).[20, 36]

4.3.4 Swelling and Porosity of Cryogels

Due to the macroporous structure and hydrophilic nature of the gels, water can readily enter the pores and inside the pore wall (polymer) regions to effectively swell the cryogels (**Figures 4.5a** and **Appendix Figure A4.7**).

The equilibrium swelling ratios of the cryogels has been shown to be influenced by cryogel pore wall thicknesses and cross-linking degrees, with lower wall thicknesses and lower cross-linking degrees resulting in higher swelling ratios due to the flexible pores facilitating the network expansion.[4-5, 36-37] Cryogels were swollen to equilibrium in PBS and then freeze-dried, with the results in **Figure 4.5b** showing an almost 3× greater mass swelling ratio (Q_M) of cryogel A compared to cryogel B.

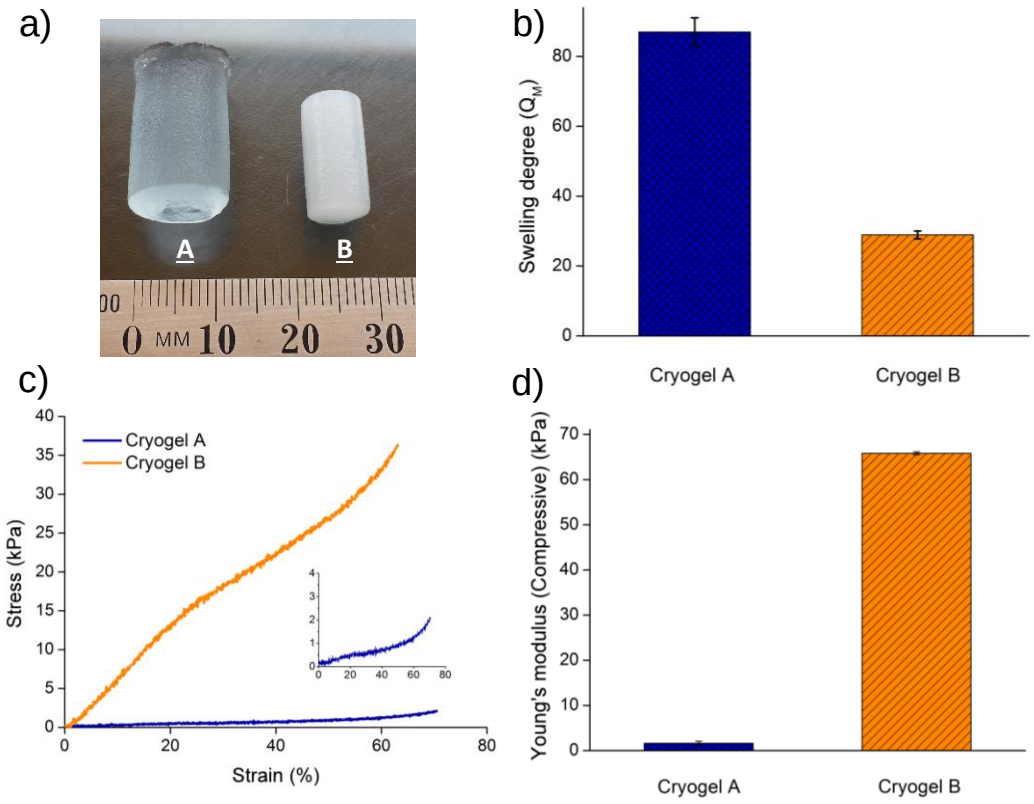

Figure 4.5. Swelling and mechanical properties of cryogels; (a) Images of cryogels swollen to equilibrium in PBS (left cryogel A, right cryogel B), (b) equilibrium mass swelling ratios, (c) stress vs strain curves from compression tests and (d) Young's moduli of gels equilibrated in PBS determined from compression tests. Values represent mean and standard deviation (n=4).

This mass swelling ratio refers to solvent in both the pores and the pore wall (polymer) regions of the gel. The volume swelling ratios (Q_V), which reflects the solvation of the polymeric walls regions only and therefore the intrinsic swelling capacity of the cryogels,[5, 38] was calculated to be 17.94 and 2.52 for cryogel A and cryogel B, respectively. The lower weight and volume swelling ratios of cryogel B compared to cryogel A are consistent with the expected higher cross-linking degree in cryogel B (denser polymeric walls) and its higher pore wall thicknesses compared to cryogel A (**Figures 4.3** and **4.4**). As well, the higher rigidity and reduced flexibility expected from a columnar channel pore morphology (cryogel B) compared to spongy pore morphology (cryogel A) may also impact the swelling nature of the gel.

Despite this, only a slight difference in porosity of both gels was determined (**Table 4.1**). Using cyclohexane uptake (a nonsolvent commonly used to calculate the pore volume of hydrophilic gels)[39] the porosity (as volume fraction %) of cryogel B (83.4% ± 0.9) was slightly lower than cryogel A (85.3% ± 1.0) suspected to be due to the thicker dense pore walls in cryogel B affecting its overall pore volume.[40] Slight differences in porosity values despite stark differences in pore morphologies and swelling ratios for cryogels has been reported previously in the literature.[32-33]

4.3.5 Mechanical Properties of Cryogels

During tissue regeneration, the gel scaffold provides physical support for the growth and protection of cells and tissue in the presence of internal or external applied forces. The most important mechanical bulk properties of biomaterial scaffolds are the elasticity and stiffness (deformation for a given load). Due to the fact that gel scaffolds as biomaterials are exclusively used in the wet state, mechanical testing was performed on the gels swollen and equilibrated in PBS. For cryogels, buffer solution can flow out from the pores under stress, acting as an efficient energy dissipation mechanism that can prevent crack formation at large deformation ratios.[41] As well, the thin but dense pore walls of the cryogels exhibit a high intrinsic mechanical strength, which provides structural support to the entire highly porous materials.[5]

Uniaxial stress−strain compression tests shown in **Figure 4.5c** demonstrate the typical compressive strength and elastic behavior of the cryogels, with compression values of up to 70% and beyond (not shown) without permanent deformation or breakage of the gels. After the release of the load, the samples reabsorb the water released during compression and regain their original shape (see **Appendix Figure A4.8**), with a faster regain observed for cryogel A. This indicates high elasticity and a reversible behavior of the gels. Despite these similarities, the cryogels demonstrated significantly different compression curves, with cryogel B showing a larger slope in the linear elastic region (0−10%) known as the Young's modulus for compression, and a steeper increase in the curve at lower strain values than cryogel

A corresponding to material densification (**Figure 4.5c**).[5] The Young's modulus of the cryogel is directly related to its bulk stiffness. For tissue engineering applications, it is generally recognized that the stiffness, or Young's modulus of the gel must closely match the tissue being engineered to allow for cells to grow in an environment representative of their natural state.[42] The Young's modulus of soft tissue ranges from <1 kPa (brain tissue) up to ~600 kPa (cartilage tissue) with strong evidence showing that soft tissue response is dependent upon the mechanical properties of the implanted material.[43-46] Therefore, for any cryogel based-system developed for soft tissue engineering applications in mind, the ability to generate gels with different mechanical properties to suit different tissue properties would be highly beneficial. Shown in **Figure 4.5d**, the Young's modulus for cryogel A was calculated to be 1.6 kPa ± 0.4, in the region of brain or skin tissues. Cryogel B on the other hand has a much larger Young's modulus of 65.8 kPa ± 0.3, with stiffness more representative of tendon tissue or nascent bone.[46-48]

An increase in cross-linking degree results in an increase in intrinsic polymer wall stiffness. While this is likely to contribute to an increase in overall (bulk) gel stiffness, the very large increase in bulk stiffness from gel A to gel B is more likely to come from their different porous morphologies discussed previously.[5, 40] It has been shown that changing from a spongy to a more closed wall columnar-like structure (including in polypeptide-based systems), can result in large increases in gel strength and stiffness.[20, 34] Whereas spongy and fibrillary pore structures consist of thin pore walls randomly distributed throughout the gel network, the columnar channel structure consists of thick polymeric walls spanning the z-axis of the gel. These channels therefore generate much more resistance to compression compared to spongy gels particularly along the z-axis where the compression tests are performed. Hence the moduli of both cryogels in this study fall within separate regions of soft tissue stiffness thereby demonstrating the ability to generate scaffolds for a range of tissue engineering applications.

4.3.6 Enzymatic Degradation of Cryogels

Bioinspired synthetic polypeptides such as poly(L-glutamic acid) can undergo effective enzymatic degradation/cleavage under physiological conditions into soluble fragments, thereby making them suitable biodegradable scaffolds for tissue engineering application.[10, 13, 15, 18, 20, 49] To test the enzyme biodegradable capabilities of the two cryogels, and to determine their relative degradability profiles, the gels were incubated in the presence of protease XIV, a model enzyme with broad specificity, with degradation measured by the loss of soluble mass (degree of degradation, DD%). Degradation results over a 14-day period in **Figure 4.6** show that the presence of the protease enzyme results in accelerated gel degradation compared to the buffer alone (PBS) due to enzymatic recognition of the polypeptide structure. There was negligible change in the shape of all samples during the degradation process.

Degradation results show a much faster degradation profile for cryogel A compared to cryogel B, with 50% degradation for cryogel A compared to ~12% degradation for cryogel B after 14 days of incubation. For effective enzymatic degradation and mass loss of the gel to take place, the enzyme must degrade the gel from the surface to the inside of the polymer walls. It must also have conformational access to the relevant inter/intra polypeptide chain cross-links within the pore walls. Compared to cryogel A, where greater pore flexibilities and reduced crosslinking densities would give improved access of the enzyme to the relevant bonds for degradation/cleavage to take place, the thicker pore walls and higher cross-linking densities of cryogel B would be expected to make this degradation process slower (**Figure 4.6**).

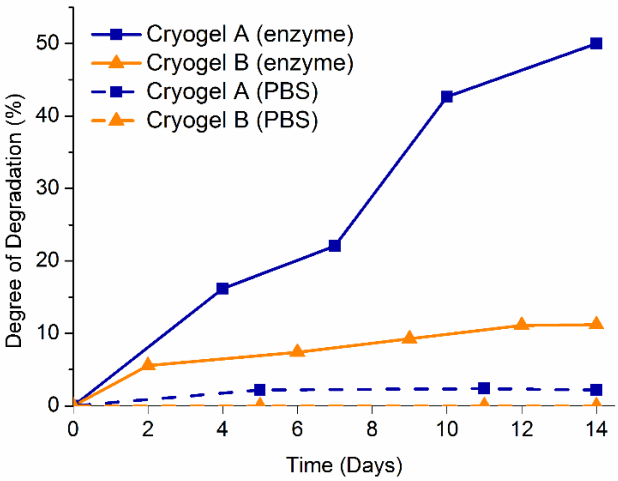

Figure 4.6. Degree of degradation of cryogels in presence of enzyme (protease XIV, 200 μg/mL) and in presence of PBS only (control, dashed line) during 14 days incubation at 37 ˚C. Degradation rate was determined by change in dry weight. Values are mean values ± (0.5-3%) (*n* =3).

4.3.7 Biocompatibility/Cytotoxicity of Cryogels In Vitro

Recently, the first cryogels partially composed of PLG were prepared for potential tissue engineering applications; however no cell/ biological studies were performed on the gels.[20] The use of lingering toxic coupling reagents (e.g. heavy metal copper) used for 'biofunctionalization' of the gels also generated potential biocompatibility issues with the gels. To determine the potential of our synthesized macroporous cryogels as scaffolds for tissue engineering applications, mammalian cell viability tests in the presence of cryogels were performed to test for any cell cytotoxicity.[50] To this end, mammalian NIH-3T3 fibroblast cells, which are commonly used for cell compatibility testing, were seeded on well-plates with cryogels disks placed on top of the culture surface. Cells cultured on the wells without gel were used as controls. The growth of cultured cells were analyzed at days 1, 3, 5, and 7 using CCK-8 assay and presented as absorbance which is proportional to the metabolic activity of the cultured cells (**Figure 4.7**). The increasing cellular metabolic activity of the cultured cells with time indicates that cell viability and growth were not hindered by the presence of either of the two cryogels inside the wells. No statistical differences in absorbance were observed between control and cryogels at each time point (P >

0.05) using student *t*-test. After 5 days of culturing, the cell viability and proliferation on the control wells and the wells containing cryogel did not increase further, suggesting the cells reached confluence inside the wells. The effective growth of fibroblast cells in the presence of the cryogels showed that the cryogels do not exert any soluble or contact cytotoxicity with cells, as the cells maintained their viability and growth in the presence of the gels.

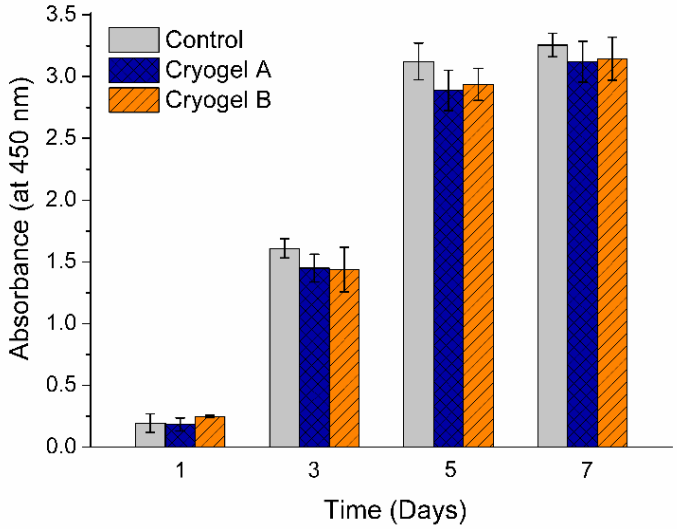

Figure 4.7. CCK-8 assay of NIH-3T3 fibroblast cells in contact with cryogels during 7 days of culture (n =4).

4.3.8 Cell Attachment and Cell Proliferation Properties of Cryogels

The presence of cationic (e.g., amine) and anionic (e.g., acid) species including PLL and PLG sequences has been shown to promote cell attachment to surfaces,[15-16, 51-52] without the requirement of biomimetic cell adhesion ligands such as RGD. Reasons for this have included the adsorption of proteins to the charged surfaces helping to mediate cell attachment[52-54] and even direct physicochemical interactions of the surface with the cells.[53-54] The presence of residual amine groups in the cryogels can be determined qualitatively through both visual/fluorescent analyses of the cryogels after conjugation to amine-reactive FITC and through FT-IR. Both cryogels show an obvious yellow/red color (**Appendix Figure A4.9**) and strong green fluorescence under CLSM (**Figure 4.3**) due to conjugated FITC, indicating the

presence of residual amine groups in the cryogels. In addition, FT-IR analysis of both cryogels (**Figures 4.1 and 4.2**) show peaks at ~3280 cm^{-1} corresponding to the N–H stretching vibrations of residual free NH_3^+ groups (lysine side chains) after washing/incubation in PBS (pH 7.4).[55-56] The spectrum of both cryogels also show a peak at ~1540 cm^{-1} characteristic of COO^- side chain stretching bands[57-59] with the absence of any typical COOH carbonyl stretches indicating that the glutamic acid side chains are deprotonated.

To determine the cell attachment and growth capabilities of these multi-charged cryogels, CLSM analysis was performed on FITC-labeled cryogels to assess the fibroblast attachment and cell growth. Suspensions of 3T3 fibroblast cells were seeded on top of the cryogel scaffolds and allowed to attach for a brief period of time. Culture medium was then added and the samples then incubated. As shown in **Figure 4.8a**, after 2 days of culture, large cell clusters can be seen inside the macroporous structure, indicative of rapid cell adhesion. Cell adhesion and growth closely follows the contours of the pores walls indicating effective cell attachment to the cryogel pore walls. Migration, penetration, and proliferation of the cells from near the site of incubation deeper into the interior of the cryogel can be observed after 4 days of culture as seen with cryogel A in **Figure 4.8b**. Despite the different relative ratios of PLL to PLG in the cryogel copolymer precursors, and therefore potentially different surface properties, the images appear to show little difference in the innate cell attachment properties of both cryogels. Determining the effect of surface morphology, protein adsorption, and charge density on the cell attachment properties of these multi-charged gels will be a focus of future studies.

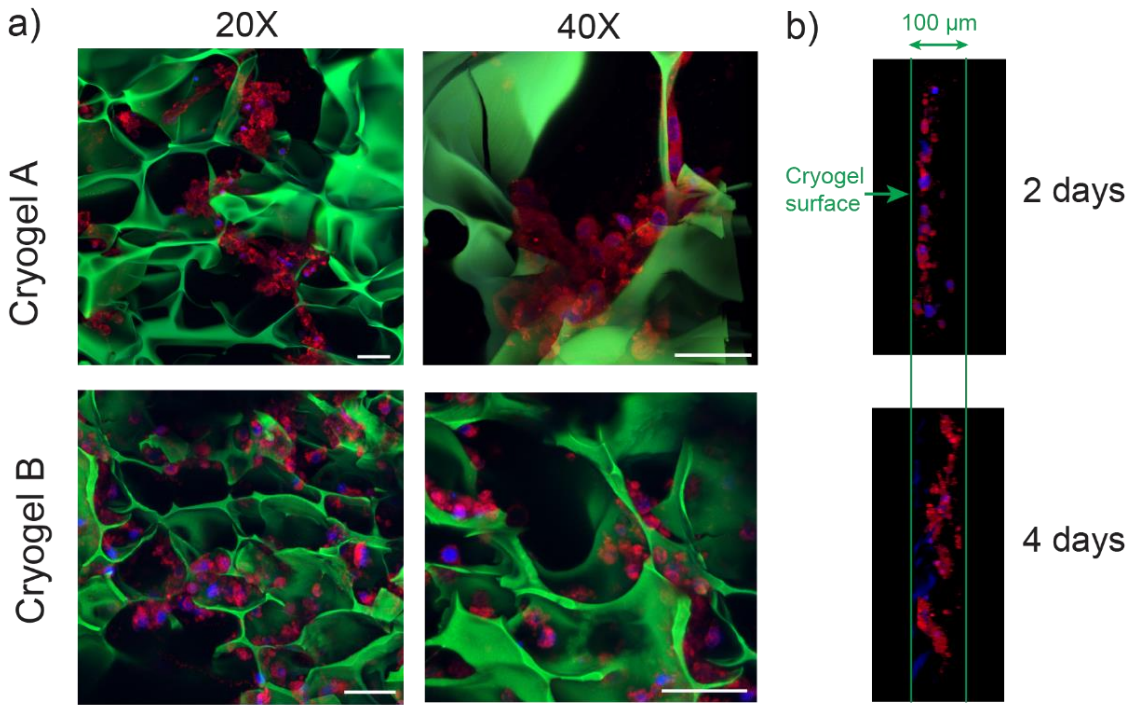

Figure 4.8. CLSM images of NIH-3T3 cells colonized on cryogels a) cross-section (x-y plane) images of cryogels after 2 days of culture. 20X and 40X microscope objectives used. Scale bars (white) represent 50 µm. Cryogels labeled with FITC (green), cell membrane stained with Deep Red plasma membrane stain (red) and cell nucleus stained with DAPI (blue). (b) z-direction image of cryogel A showing effective cell migration and growth into gel structure from direction of surface incubation (green arrow) after 4 days culture. Boundaries of the cryogel section (100 µm thickness, z-direction) indicated by green line. Fluorescent cryogel structure (green channel) removed for better visualization of cells.

To study the proliferation of cells within the gels more closely, a suspension of fibroblast cells were seeded inside the cryogel scaffolds and the cell growth and proliferation evaluated by measuring the cell metabolic activity using CCK-8 assay up to 14 days (**Figure 4.9a**). CCK-8 uses reagent WST-8, which is reduced by viable cells extracellularly to form a highly water/ media soluble colored formazen in proportion to the number of viable cells. In **Figure 4.9a**, the metabolic activity and the number of cells is seen to increase over the culture period, indicating that the cells are able to attach and proliferate inside the cryogel scaffolds. Despite the higher

pore size, pore thickness and larger heterogeneities of cryogel B compared to cryogel A, no statistical differences were observed between the two gels during the proliferation measurements. This suggests that although the different pore morphologies of these cryogels (e.g. spongy and columnar) have a large effect on their swelling and mechanical properties, they do not appear to have a large effect on cell growth. With pore sizes of both gels in the range considered optimal for cell growth (≥100 μm), any effect of pore morphology on cell growth may not be significant in this case. To determine whether there is an effect of pore morphology on the more advanced stages of tissue growth (e.g. vascularization), future studies involving vascular network growth within the cryogels will be performed.

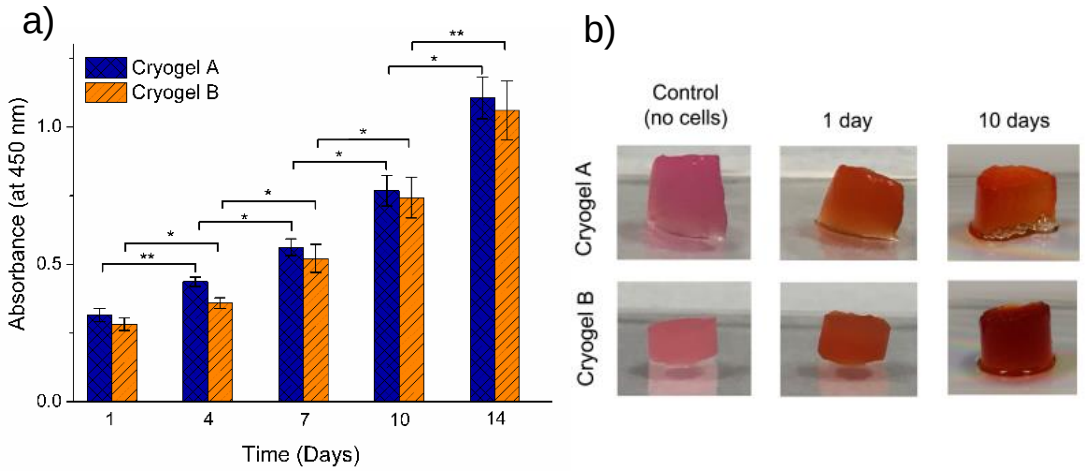

Figure 4.9. Cell growth of NIH-3T3 fibroblast cells cultured inside cryogel A and B for 14 days. (a) Cell viability determined by CCK-8 assay with absorbance of orange formazan product measured at 450 nm at different time intervals (n =3). Statistically significant differences are indicated (*P < 0.05 and **P < 0.01). (b) Images of gels after CCK-8 staining. Control gels contain CCK-8 stain without cells.

Cell proliferation can also be seen visually in **Figure 4.9b** with images of cell-cultured cryogels that sequestered the WST-8 dye from solution showing a homogeneous dark orange-red color of the generated formazen due to cell proliferation. This color is seen to darken further after 10 days of culturing as a result of increased cell growth. The cell growth rate of fibroblasts inside the cryogel

was seen to be lower than the cell culture on polystyrene well plates. This was likely due to some migration of cells from inside of the gels to the surface of the well during the experiment resulting in a loss of cells from the cryogel samples. Also, the cryogels absorbed and sequestered some of the formazen dye as shown in **Figure 4.9b**. Due to this absorption, the concentration of formazen in the solution phase was partially reduced, resulting in a decrease in the measured viability of cells growing on/inside the cryogels. Collectively, the results indicate that these macroporous cryogels provide a supportive scaffold for the attachment, survival, migration, and proliferation of cells.

4.4 Chapter Summary

In conclusion, a simple approach to the development of novel macroporous hydrogels composed entirely of biocompatible and biodegradable synthetic polypeptides has been developed. Through the use of a random copolypeptide containing both PLG and PLL, direct cross-linking of a single polymer chain through EDC/sulfo-NHS cross-linking could be achieved under cryoconditions. The resulting cryogels contain large macroporous structures with pore sizes highly suitable for tissue engineering applications (≥100 μm). By increasing the ratio of lysine relative to glutamic acid in the copolymers, gels with increased pore thicknesses and very different pore morphologies (spongey, columnar-like) could be prepared which had large effects on their swelling and mechanical stiffness properties. The stiffness (Young's modulus) of both cryogels in this study fell within separate regions of soft tissue stiffness thereby demonstrating the ability to generate scaffolds for a range of soft tissue cell culturing. These polypeptide cryogels were shown to be enzymatically biodegradable with a slower degradation profile observed for the stiff, columnar-like cryogel. Both multi-charged cryogels demonstrated excellent biocompatibility, cell attachment, and cell proliferation profiles with mammalian fibroblast (NIH-3T3) cells, demonstrating their potential as suitable cellular scaffolds.

4.5 References

(1) Tibbitt, M. W.; Anseth, K. S., *Biotechnol. Bioeng.* **2009,** *103* (4), 655-663.

(2) Zhao, X.; Kim, J.; Cezar, C. A.; Huebsch, N.; Lee, K.; Bouhadir, K.; Mooney, D. J., *Proc. Natl. Acad. Sci. U.S.A.* **2011,** *108* (1), 67-72.

(3) Bencherif, S. A.; Sands, R. W.; Ali, O. A.; Li, W. A.; Lewin, S. A.; Braschler, T. M.; Shih, T.-Y.; Verbeke, C. S.; Bhatta, D.; Dranoff, G.; Mooney, D. J., *Nat.Commun.* **2015,** *6*, 7556.

(4) Henderson, T. M. A.; Ladewig, K.; Haylock, D. N.; McLean, K. M.; O'Connor, A. J., *J. Mater. Chem. B* **2013,** *1* (21), 2682-2695.

(5) Welzel, P. B.; Grimmer, M.; Renneberg, C.; Naujox, L.; Zschoche, S.; Freudenberg, U.; Werner, C., *Biomacromolecules* **2012,** *13* (8), 2349-2358.

(6) Kumari, J.; Karande, A. A.; Kumar, A., *ACS Appl. Mater. Interfaces* **2016,** *8* (1), 264-77.

(7) Dainiak, M. B.; Allan, I. U.; Savina, I. N.; Cornelio, L.; James, E. S.; James, S. L.; Mikhalovsky, S. V.; Jungvid, H.; Galaev, I. Y., *Biomaterials* **2010,** *31* (1), 67-76.

(8) Liu, H. F.; Mao, J. S.; Yao, K. D.; Yang, G. H.; Cui, L.; Cao, Y. L., *J. Biomater. Sci., Polym. Ed.* **2004,** *15* (1), 25-40.

(9) Chiu, Y.-C.; Cheng, M.-H.; Engel, H.; Kao, S.-W.; Larson, J. C.; Gupta, S.; Brey, E. M., *Biomaterials* **2011,** *32* (26), 6045-6051.

(10) Duro-Castano, A.; Conejos-Sanchez, I.; Vicent, M. J., *Polymers* **2014,** *6* (2), 515-551.

(11) Khuphe, M.; Kazlauciunas, A.; Huscroft, M.; Thornton, P. D., *Chem. Commun.* **2015,** *51* (8), 1520-1523.

(12) Shirbin, S. J.; Ladewig, K.; Fu, Q.; Klimak, M.; Zhang, X.; Duan, W.; Qiao, G. G., *Biomacromolecules* **2015,** *16* (8), 2463-2474.

(13) Li, C., *Adv. Drug Del. Rev.* **2002,** *54* (5), 695-713.

(14) Richert, L.; Arntz, Y.; Schaaf, P.; Voegel, J. C.; Picart, C., *Surf. Sci.* **2004,** *570* (1-2), 13-29.

(15) Cao, B.; Yan, S.; Zhang, K.; Song, Z.; Cao, T.; Chen, X.; Cui, L.; Yin, J., *Macromol. Biosci.* **2011,** *11* (7), 970-977.

(16) Boura, C.; Menu, P.; Payan, E.; Picart, C.; Voegel, J. C.; Muller, S.; Stoltz, J. F., *Biomaterials* **2003,** *24* (20), 3521-3530.

(17) Yan, S.; Zhang, K.; Liu, Z.; Zhang, X.; Gan, L.; Cao, B.; Chen, X.; Cui, L.; Yin, J., *J. Mater. Chem. B* **2013,** *1* (11), 1541-1551.

(18) Cao, B.; Yin, J.; Yan, S.; Cui, L.; Chen, X.; Xie, Y., *Macromol. Biosci.* **2011,** *11* (3), 427-434.

(19) Studenovska, H.; Vodicka, P.; Proks, V.; Hlucilova, J.; Motlik, J.; Rypacek, F., *J Tissue Eng Regen Med* **2010,** *4* (6), 454-463.

(20) Sedlacik, T.; Proks, V.; Slouf, M.; Duskova-Smrckova, M.; Studenovska, H.; Rypacek, F., *Biomacromolecules* **2015,** *16* (11), 3455-65.

(21) Zhang, Z.; Chen, L.; Deng, M.; Bai, Y.; Chen, X.; Jing, X., *J. Polym. Sci., Part A* **2011,** *49* (13), 2941-2951.

(22) Lozinsky, V. I.; Okay, O., Basic Principles of Cryotropic Gelation. In *Polymeric Cryogels: Macroporous Gels with Remarkable Properties*, Okay, O., Ed. Springer: 2014; Vol. 263, pp 49-101.

(23) Lozinsky, V. I., *Russ. Chem. Bull.* **2008,** *57* (5), 1015-1032.

(24) Bencherif, S. A.; Sands, R. W.; Bhatta, D.; Arany, P.; Verbeke, C. S.; Edwards, D. A.; Mooney, D. J., *Proc. Natl. Acad. Sci. U.S.A.* **2012,** *109* (48), 19590-19595.

(25) Koshy, S. T.; Ferrante, T. C.; Lewin, S. A.; Mooney, D. J., *Biomaterials* **2014,** *35* (8), 2477-2487.

(26) Sannino, A.; Netti, P. A.; Madaghiele, M.; Coccoli, V.; Luciani, A.; Maffezzoli, A.; NicolaiS, L., *J. Biomed. Mater. Res. A* **2006,** *79A* (2), 229-236.

(27) Levesque, S. G.; Lim, R. M.; Shoichet, M. S., *Biomaterials* **2005,** *26* (35), 7436-7446.

(28) Huang, X.; Zhang, Y.; Donahue, H. J.; Lowe, T. L., *Tissue Eng.* **2007,** *13* (11), 2645-2652.

(29) Murphy, W. L.; Dennis, R. G.; Kileny, J. L.; Mooney, D. J., *Tissue Eng.* **2002,** *8* (1), 43-52.

(30) Van Vlierberghe, S., *J. Mater. Sci* **2016,** *51* (9), 4349-4357.

(31) Tripathi, A.; Kumar, A., *Macromol. Biosci.* **2011,** *11* (1), 22-35.

(32) Henderson, T. M. A.; Ladewig, K.; Haylock, D. N.; McLean, K. M.; O'Connor, A. J., *J. Biomater. Sci., Polym. Ed.* **2015,** *26* (13), 881-897.

(33) Phadke, A.; Hwang, Y.; Kim, S. H.; Kim, S. H.; Yamaguchi, T.; Masuda, K.; Varghese, S., *Eur Cell Mater* **2013,** *25*, 114-129.

(34) Chau, M.; De France, K. J.; Kopera, B.; Machado, V. R.; Rosenfeldt, S.; Reyes, L.; Chan, K. J. W.; Förster, S.; Cranston, E. D.; Hoare, T.; Kumacheva, E., *Chem. Mater.* **2016,** *28* (10), 3406-3415.

(35) Strom, A.; Larsson, A.; Okay, O., *J. Appl. Polym. Sci.* **2015,** *132* (29), 42194.

(36) Loo, S.-L.; Krantz, W. B.; Lim, T.-T.; Fane, A. G.; Hu, X., *Soft Matter* **2013,** *9* (1), 224-234.

(37) Oelschlaeger, C.; Bossler, F.; Willenbacher, N., *Biomacromolecules* **2016,** *17* (2), 580-589.

(38) Okay, O., *Prog. Polym. Sci.* **2000,** *25* (6), 711-779.

(39) Plieva, F. M.; Karlsson, M.; Aguilar, M. R.; Gomez, D.; Mikhalovsky, S.; Galaev, I. Y., *Soft Matter* **2005,** *1* (4), 303-309.

(40) Savina, I. N.; Cnudde, V.; D'Hollander, S.; Van Hoorebeke, L.; Mattiasson, B.; Galaev, I. Y.; Du Prez, F., *Soft Matter* **2007,** *3* (9), 1176-1184.

(41) Ak, F.; Oztoprak, Z.; Karakutuk, I.; Okay, O., *Biomacromolecules* **2013,** *14* (3), 719-727.

(42) Liu, J.; Zheng, H.; Poh, P. S. P.; Machens, H.-G.; Schilling, A. F., *Int. J. Mol. Sci.* **2015,** *16* (7), 15997-16016.

(43) Discher, D. E.; Janmey, P.; Wang, Y. L., *Science* **2005,** *310* (5751), 1139-1143.

(44) Wang, B. H.; Campbell, G., *Spine* **2009,** *34* (25), 2745-2753.

(45) Price, G. M.; Wong, K. H. K.; Truslow, J. G.; Leung, A. D.; Acharya, C.; Tien, J., *Biomaterials* **2010,** *31* (24), 6182-6189.

(46) Huang, G.; Wang, L.; Wang, S.; Han, Y.; Wu, J.; Zhang, Q.; Xu, F.; Lu, T. J., *Biofabrication* **2012,** *4* (4).

(47) Chen, E. J.; Novakofski, J.; Jenkins, W. K.; Obrien, W. D., *IEEE Trans. Ultrason. Ferroelect. Freq. Control* **1996,** *43* (1), 191-194.

(48) Sartori, S.; Chiono, V.; Tonda-Turo, C.; Mattu, C.; Gianluca, C., *J. Mater. Chem. B* **2014,** *2* (32), 5128-5144.

(49) Shen, Y.; Fu, X.; Fu, W.; Li, Z., *Chem. Soc. Rev.* **2015,** *44* (3), 612-622.

(50) Zhou, C.; Heath, D. E.; Sharif, A. R. M.; Rayatpisheh, S.; Oh, B. H. L.; Rong, X.; Beuerman, R.; Chan-Park, M. B., *Macromol. Biosci.* **2013,** *13* (11), 1485-1491.

(51) Lee, J. H.; Jung, H. W.; Kang, I. K.; Lee, H. B., *Biomaterials* **1994,** *15* (9), 705-711.

(52) Omrani, M. M.; Kiaie, N.; Ansari, M.; Kordestani, S. S., *Journal of Macromolecular Science Part B-Physics* **2016,** *55* (6), 617-626.

(53) Qiu, Q.; Sayer, M.; Kawaja, M.; Shen, X.; Davies, J. E., *Journal of Biomedical Materials Research* **1998,** *42* (1), 117-127.

(54) Schneider, G. B.; English, A.; Abraham, M.; Zaharias, R.; Stanford, C.; Keller, J., *Biomaterials* **2004,** *25* (15), 3023-3028.

(55) Shan, C.; Yang, H.; Han, D.; Zhang, Q.; Ivaska, A.; Niu, L., *Langmuir* **2009,** *25* (20), 12030-12033.

(56) Wu, C.; He, Q.; Zhu, A.; Li, D.; Xu, M.; Yang, H.; Liu, Y., *ACS Appl. Mater. Interfaces* **2014,** *6* (23), 21615-21623.

(57) Perry, S. L.; Leon, L.; Hoffmann, K. Q.; Kade, M. J.; Priftis, D.; Black, K. A.; Wong, D.; Klein, R. A.; Pierce, C. F., III; Margossian, K. O.; Whitmer, J. K.; Qin, J.; de Pablo, J. J.; Tirrell, M., *Nat.Commun.* **2015,** *6*.

(58) Dzwolak, W.; Marszalek, P. E., *Chem. Commun.* **2005,** (44), 5557-5559.

(59) Mendelsohn, J. D.; Yang, S. Y.; Hiller, J.; Hochbaum, A. I.; Rubner, M. F., *Biomacromolecules* **2003,** *4* (1), 96-106.

5

Polypeptide-Based Macroporous Cryogels with Inherent Antimicrobial Properties: The Importance of a Macroporous Structure

5.1 Chapter Perspective

Antimicrobial cryogels (macroporous hydrogels) display superior swelling and mechanical properties that make them suitable candidates for water purification applications. Traditionally, their antimicrobial activity comes from the incorporation of known antimicrobial agents to the gel structure rather than from the polymer gel itself, leading to leaching of these agents and subsequent toxicity issues. In this chapter, cryogels composed of synthetic polypeptides with inherent antimicrobial properties have been prepared. Gels composed of a polycationic poly(L-lysine) and hydrophobic poly(D,L-valine) copolymer were prepared through crosslinking with glutaraldehyde. The gels displayed high swelling, and inherent antimicrobial activity against *E. coli* after brief 1 h exposure with no toxic leaching. Macropores were found to be crucial for bactericidal activity where they allow for effective uptake of bacteria into the gels, and provide a confined environment and increased surface area for contact of the bacteria with the antimicrobial polymer walls.

5.2 Introduction

Peptide-based antimicrobial hydrogels have demonstrated significant potential over the years due to their inherent antimicrobial activity upon physical contact between the gel and the bacteria.[1-6] These gels often consist of a polycationic-rich surface (i.e., poly(lysine)), which is suspected to result in bacteria membrane disruption. However, their nanoporous structure and rigid physical properties, limits the applications of these 'conventional' hydrogels. Cryogels, a form of macroporous hydrogels, have for many years shown significant advantages over their conventional hydrogel counterparts through superior swelling and mechanical (e.g., elasticity, toughness) properties as a result of their interconnected macroporous structure.[7-12] Antimicrobial cryogels, an emerging and exciting field, have looked to exploit the unique mechanical and swelling properties of these systems for biomedical and water purification applications. For water purification, in particular, the presence of a large number of pores allows for faster and larger water absorption properties that are unmatched with conventional hydrogels.[13-15]

Within the limited amount of research into antimicrobial cryogels, including those for water purification, the antimicrobial activity of these gels comes from the incorporation of known antimicrobial agents rather than from the polymer itself. These include heavy metals (e.g., silver or copper),[16-17] ionic liquids,[18] or drugs.[19] Despite showing high activity, the leaching of toxic components (e.g., heavy metals, drugs) in these systems is reported, which could result in (biological and environmental) toxic components leaching into the treated water. Therefore, despite the generation of inherently antimicrobial active conventional 'nanoporous' hydrogels in the literature,[1, 6] this has yet to be demonstrated in a macroporous hydrogel (cryogel) system.

Recent studies have revealed that hydrogels consisting of both cationic and hydrophobic peptide/polypeptide components have high antimicrobial potency through suspected bacteria membrane disruption.[3-4, 20] Building upon this concept, novel polypeptide-based macroporous hydrogels in the form of cryogels were

synthesized with similar precursors in order to test for their inherent antimicrobial effect.

This chapter describes the facile preparation of a synthetic polypeptide-based cryogel with inherent antimicrobial properties for potential water purification applications. As far as aware, this appears to be the first macroporous hydrogel with inherent antimicrobial properties.

Cryogels were chemically cross-linked at subzero temperatures through the amine residue of a poly(L-lysine)-*b*-poly(D,L-valine) copolymer with glutaraldehyde as cross-linker. In comparison to a hydrogel control prepared at above zero temperatures, the presence and integrity of macropores is shown to be vital to the antimicrobial effect of the gels. A "trap and kill effect" due to the increased surface area and confinement of the bacteria to the antimicrobial gel is proposed.

5.3 Results and Discussion

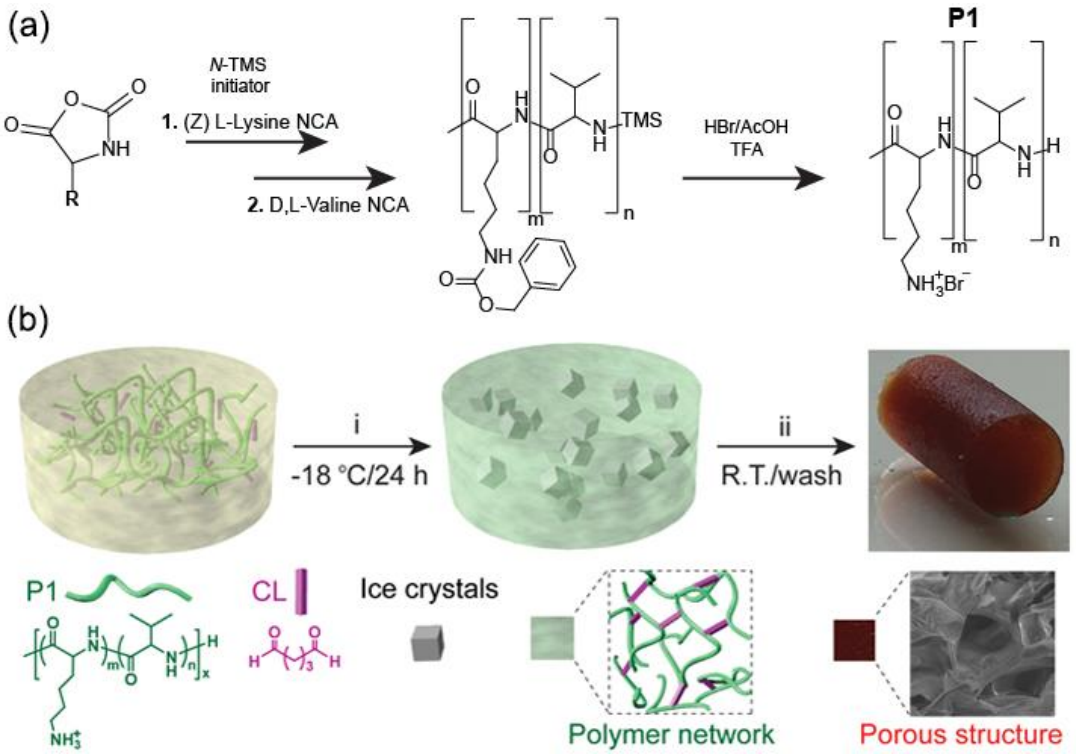

Scheme 5.1. (a) Synthesis of PLL-*b*-PDLV block copolypeptide (**P1**), and (b) its fabrication into cryogels: (i) Block copolypeptide (**P1**) and glutaraldehyde cross-linker (CL) dissolved in PBS, then frozen at -18 ˚C for 24 h (ii) Gel is thawed at RT and washed thoroughly in DI water, $NaBH_4$ 0.1% w/v PBS (pH= 9.4), and PBS (pH= 7.4).

5.3.1 Block Copolymer Synthesis

The block copolypeptide used in this study was synthesized through *N*-Carboxyanhydride ring-opening polymerization (NCA ROP) using *N*-trimethylsilylallylamine as initiator (**Scheme 5.1a**).[21] To ensure good water solubility of the final block copolypeptide, a larger polylysine block relative to hydrophobic polyvaline block was deemed appropriate. An *N*-protected CBz(Z) poly(L-lysine) block was first synthesized, followed by the shorter poly(D,L-valine) block with GPC analysis determining a M_n of 9.9 kDa with a polydispersity ($Đ$) of 1.70. Upon isolation, the protected block copolymer was insoluble in a range of

organic solvents, owing to the polyvaline block, which is known to exhibit insoluble secondary structures.[22-23] Therefore, characterization of the block copolymer (etc. relative ratios) through ^{1}H NMR analysis could only be achieved upon deprotection of the CBz-lysine side chain of the polymer. Deprotection of the copolymer poly(L-lysine) block by hydrobromic acid (HBr) generated an amphiphilic poly(L-lysine)-*b*-poly(D,L-valine) (PLL-*b*-PDLV) copolypeptide (**P1**) with the cationic poly(L-lysine) block instilling high water solubility to the copolymer. ^{1}H NMR analysis confirmed the complete deprotection of the copolymer with integration determining a poly(L-lysine) to poly(D,L-valine) ratio of 7:2 (**Figure 5.1**). Based on the M_n value above, the repeat units of PLL and PDLV were determined to be 35 and 10 units, respectively.

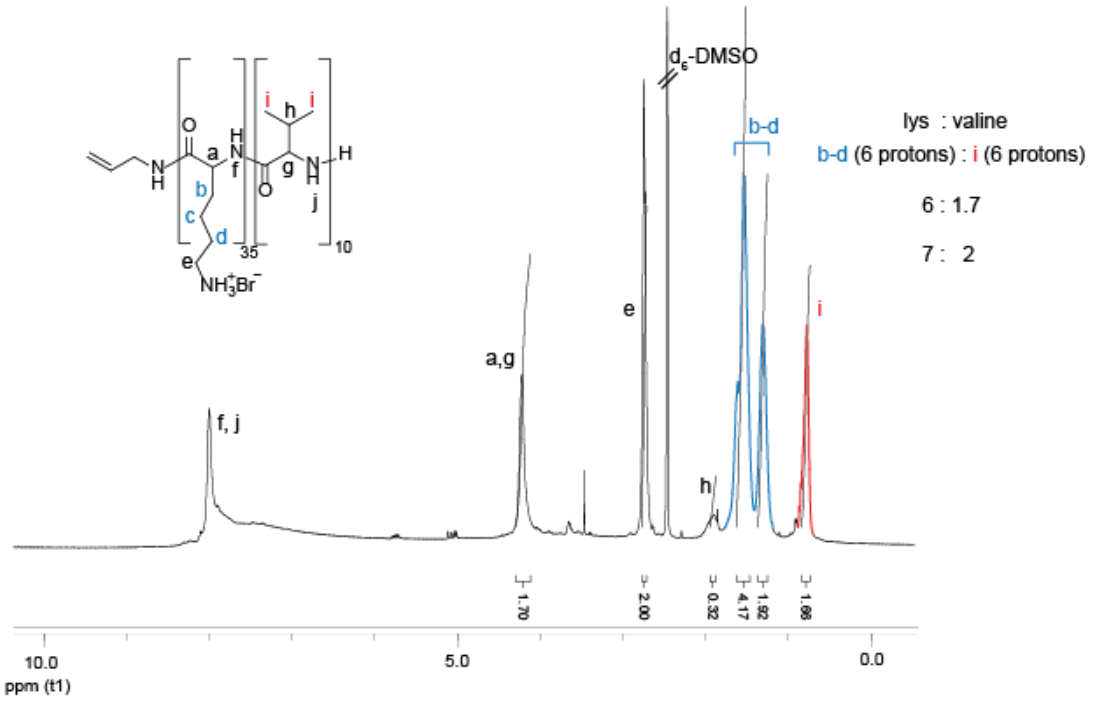

Figure 5.1. ^{1}H NMR (d_6-DMSO) spectrum of deprotected PLL-*b*-PDLV block copolymer (**P1**) including calculations of lysine:valine ratio based on the relevant integrations.

5.3.2 Preparation of Cryogels

The amine residues were chosen as the point of cross-linking with the widely used and highly amine-reactive dialdehyde cross-linker (CL), glutaraldehyde.[24-26] The

polypeptide and cross-linker in different molar ratios were dissolved in PBS (pH = 7.4) and the mixture was stored at −18 °C for 24 h. During the cryogelation process, the highly interconnected (covalent) polymeric network exists in a semi-frozen system in which the solvent (water) crystals act as porogens. Thawing of the frozen solution removes the ice crystals to leave behind the macroporous structure (**Scheme 5.1b**).

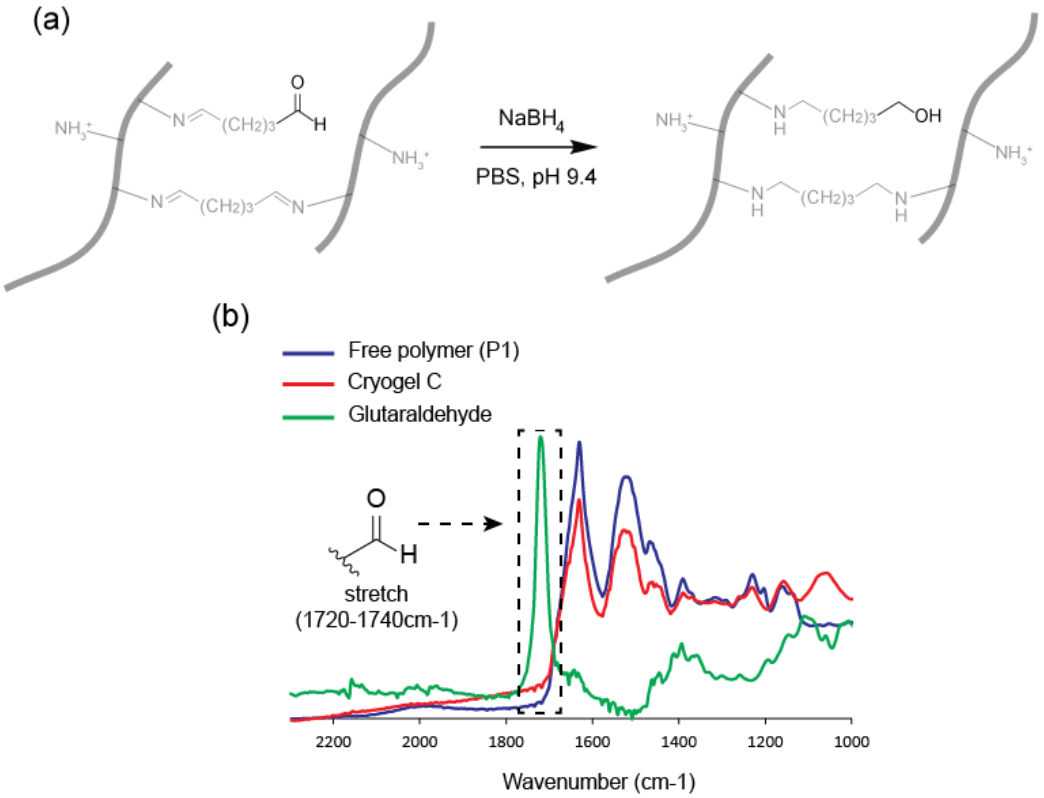

Figure 5.2. (a) Reduction of excess glutaraldehyde cross-linker with 0.1 % w/v sodium borohydride. (b) ATR FT-IR of cryogel C washed in sodium borohydride showing absence of aldehyde peak.

The gels were washed thoroughly and any remaining reactive aldehyde CL groups quenched by washing in a sodium borohydride reducing solution. The absence of residual aldehydehyde groups in the cryogels was confirmed through ATR FT-IR analysis (**Figure 5.2**).

Initial studies showed that a mass polymer concentration of 10 % with low cross-linking concentration resulted in immediate gelation of the solution before cryo storage. Therefore, a mass polymer concentration of 5 % was employed and kept constant while cross-linking amount was varied in order to study the effect on the resultant cryogel properties. **Table 5.1** shows the relative volume and molar (with respect to cross-linkable functional groups) ratios of glutaraldehyde to block polypeptide.

Gel	CL to polypeptide % (v/w)	aldehyde: NH_2	c_p % (w/v)	gelation	E^b (kPa)
A	4	0.2	5	cryo	[c]
B	8	0.4	5	cryo	1.6
C	20	1	5	cryo	12.4
D	42	2.1	5	cryo	4.4
a	67	3.3	5	hydro	21.0

Table 5.1. Cryogelation conditions and the Young's modulus (Compressive, *E*) of PLL_{35}-*b*-$PDLV_{10}$ block copolypeptide cryogels using varying amounts of glutaraldehyde cross-linker (CL). [a] Control hydrogel sample made at room temperature (25 °C), 48 h. $c_{p,}$ concentration of polymer component; [b] Mean Young's modulus (compressive) values, n = 3; [c] Data could not be obtained due to weakness of gel.

A conventional control hydrogel was synthesized at room temperature, however it required a higher CL concentration and longer storage time for gelation to occur compared to the cryogels. This reduced cross-linking efficiency during conventional gelation, as opposed to the relatively faster cryogelation process, is due to significantly higher polymer and cross-linking concentrations existing in the liquid microphase (surrounding the ice crystal porogens) in the cryogelation state.[7, 27]

5.3.3 Morphology of Cryogels

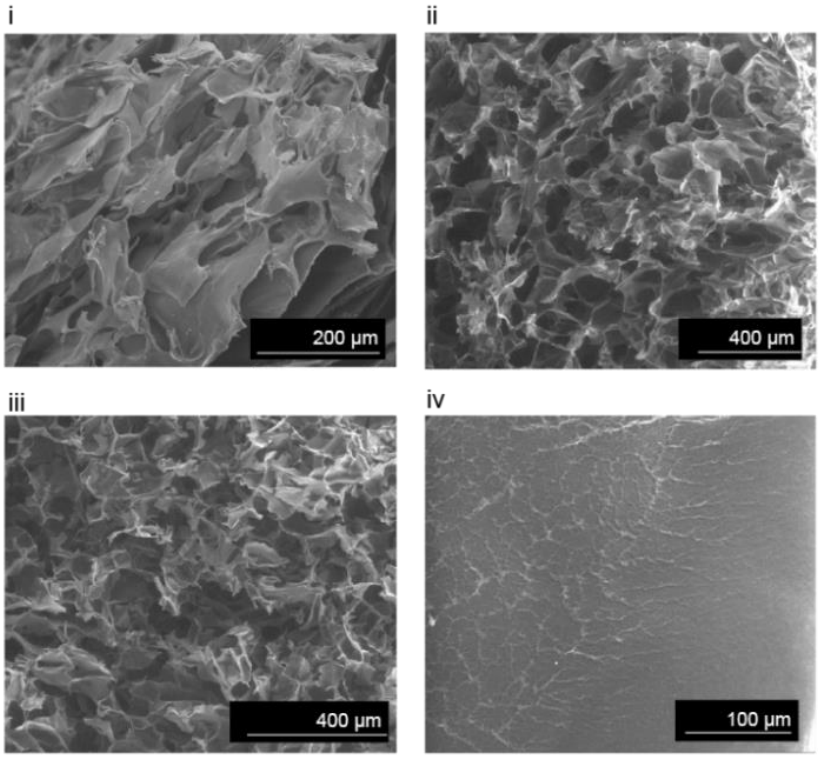

Figure 5.3. ESEM characterization on the cross-sectional morphology of (i) cryogel A (ii) cryogel C (iii) cryogel D and (iv) control hydrogel.

The internal morphologies of the cryogels and control hydrogel were investigated by environmental scanning electron microscopy (ESEM) in the wet state (**Figure 5.3**). While the hydrogel sample has a nanoporous structure, the cross-sections of all cryogels (A, C, and D) show a macroporous morphology. Comparisons of the cryogel morphologies show cryogel C (**Figure 5.3ii**) with the most intact porous structure (pore sizes between 120 and 150 µm) and cryogel A showing the least, which would be expected to be the case considering the low CL concentration used in cryogel A. Interestingly, cryogel D (**Figure 5.3iii**), with a higher CL concentration than cryogel C, displays a less regular pore structure with reduced pore integrity (see also **Appendix Figure A5.2**).

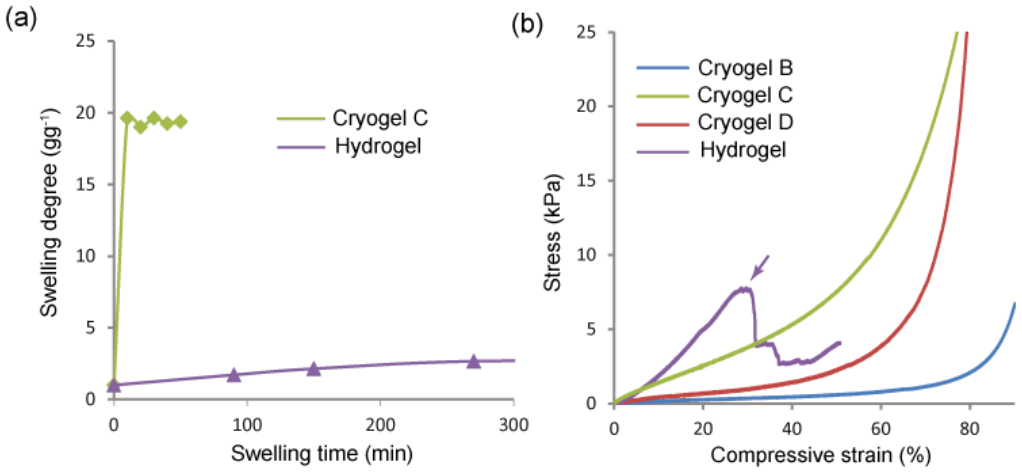

Figure 5.4. Comparison of physical properties of cryogels and conventional hydrogel. (a) Mass swelling kinetics of dried cryogel and hydrogel in water (b) Stress vs. strain curve of gels subjected to compression tests. Note the purple arrow shows the point at which hydrogel started to fail/deform.

5.3.4 Swelling and Physical Properties of Cryogels

Compared to the typically low swelling rate of the control hydrogel, cryogel C (typical of the other cryogels, data not shown), demonstrates a far superior swelling rate and degree, due to its interconnected macroporous structure. This is demonstrated by the swelling (mass) degree plotted against swelling time in **Figure 5.4a**. Uniaxial compression measurements were then performed on the gels in their swollen states. The mechanical stress–strain data in **Figure 5.4b** shows the typical compressive strength and elastic behavior of the cryogels in contrast to the brittle and fragile hydrogel. Compared to the cryogels which could be compressed beyond 80% without permanent deformation or failure, the conventional hydrogel suffers irreversible mechanical fracture at ~25% compression due to the lack of interconnected porous structure (see also **Figure 5.5.**). The lack of interconnected porous structure offers low resistance to crack propagation due to the lack of an efficient energy dissipation mechanism in the gel network. For the cryogels, water can flow out from the pore under stress, preventing crack formation at large deformation ratios, with re-swelling to its original shape after stress removal (**Figure 5.5**).[28]

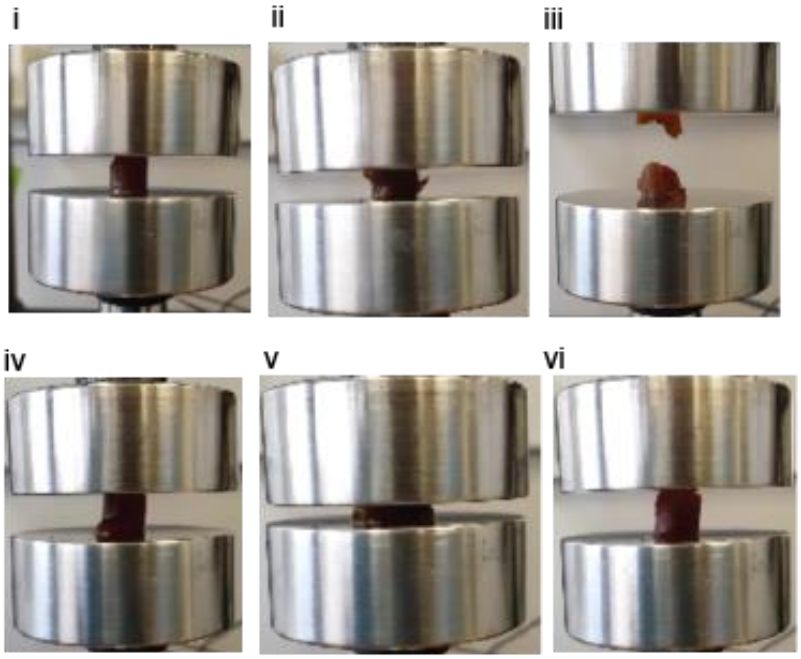

Figure 5.5. Photographs of control hydrogel (i-iii) and cryogel C (iv-vi) during mechanical testing.

Table 5.1 shows the Young's modulus (compressive) values of each of the gels, which is directly related to their bulk stiffness and is calculated from the linear elastic region of the stress–strain compression data in **Figure 5.4b**. As expected, all the cryogels exhibit a reduced Young's modulus compared to the stiff and brittle control hydrogel. For the cryogels themselves, cryogel C displayed the highest modulus, with a stress of 7.5 kPa at 50% strain compared to 2.2 and 0.60 kPa for cryogels D and B, respectively.

The higher stiffness of cryogel C compared to cryogel D, despite a lower cross-linking concentration, suggests a higher cross-linking density in cryogel C and appears consistent with the cross-section morphologies observed in the SEM data above. A possible explanation for this may come from the [aldehyde]/ [NH_2] cross-linking ratios shown in **Table 5.1**. While it is not anticipated that all cross-linking aldehyde groups will react with an equivalent of amine resides during the cryogelation stage, the amount of cross-linker employed with cryogel D may be reaching a point where oversaturation of the amine residues with just one reactive

end of glutaraldehyde is occurring. This would result in reduced cross-linking density and therefore reduced gel stiffness of cryogel D compared to cryogel C.[29]

5.3.5 Cryogel Cytotoxicity In Vitro

The absence of any toxic leachate or contaminant is a prerequisite for any material to be used for water disinfection purposes. A preliminary *in vitro* cytotoxicity study was conducted on the cryogels to evaluate if harmful products were leaching out. Cryogels C and D were selected as representative gels for this study and conditioned mediums were prepared by incubating the cryogels in cell culture medium (i.e., "complete" Dulbecco's Modified Eagle Medium (DMEM)) for 72 h. The conditioned mediums (50 vol %) were then incubated with NIH-3T3 fibroblast cells for another 72 h. Conditioned medium prepared from either cryogel C or D displayed negligible effect on fibroblast cell viability (**Figure 5.6**), indicating that the cryogels did not leach out any substances toxic to mammalian cells. Quantitative removal/ reduction of any unreacted glutaraldehyde CL which are toxic to mammalian cells was also confirmed as mentioned previously (see **Figure 5.2**).

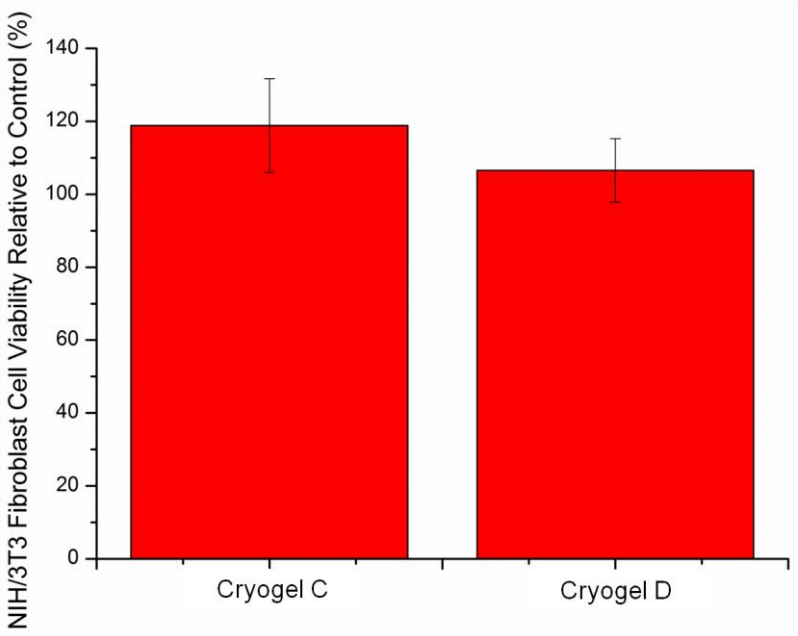

Figure 5.6. Cytotoxicity evaluation of cryogel-conditioned medium using NIH-3T3 fibroblast cells. Error bars represent the standard deviation from the mean (n = 4).

5.3.6 Antimicrobial Activity of Cryogels In Vitro

To test for antimicrobial activity, the cryogels and control hydrogel were challenged with *E. coli*, a model Gram-negative bacterial species, at an initial cell concentration of 1.2 × 10^8 CFU/mL for 1 h (**Figure 5.7a**). A saline-based buffer was then added to wash the gels and capture any remaining viable cells. The viable cell counts in the washing solution were measured and compared to the untreated control (no gel). Note that the number of cells in the untreated control increased by 0.12 log (or 31.6%; averaged for all runs) after 1 h. The cryogels exhibited antimicrobial activity but to differing extents as shown in **Figure 5.7b**.

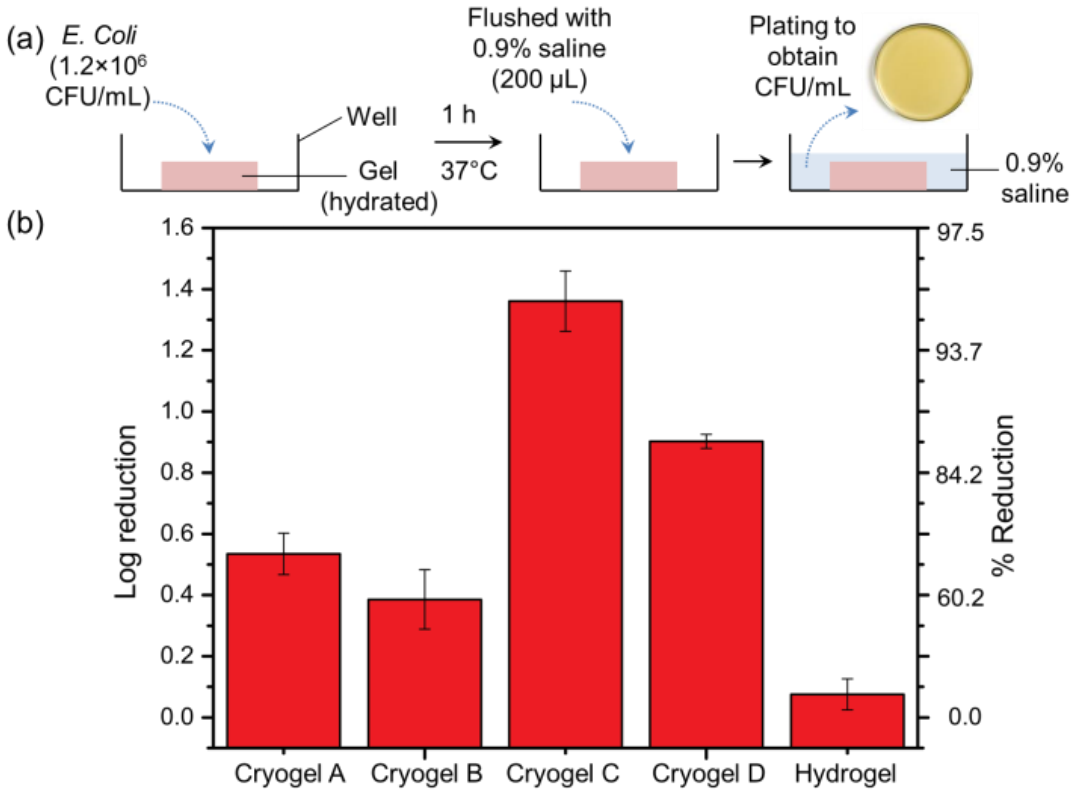

Figure 5.7. (a) Schematic of method used to investigate the antimicrobial efficacy of polypeptide gels. (b) Log reduction and % kill of *E. coli* on polypeptide cryogels A, B, C and D, and the control hydrogel. Error bars represent the standard deviation from the mean ($n \geq 4$).

Cryogel C displayed the best efficacy against *E. coli* (1.4-log reduction or 95.6% reduction in cell counts), followed by cryogel D (0.9-log reduction). Cryogels A and B showed lower antimicrobial activities compared to the other cryogels, resulting in only 0.4−0.6-log reductions in cell counts. Compared to cryogels A−D, the control hydrogel possesses negligible activity against *E. coli* (<0.1-log reduction; **Figure 5.7b**), suggesting that macropores provided through cryogelation are essential for antimicrobial activity. It is hypothesized that the presence of macropores allows for effective uptake of bacteria into the gels. As well, they provide a large surface area and confined environment (increased time of exposure) for contact with the antimicrobial polymer and effective bacterial killing. A high BET specific surface area of 627 m^2/g was indeed measured for cryogel C (see **Appendix Figure 5.4**). The possible link between pore size/surface area of gels and microbial killing efficacy has been suggested in earlier studies;[15, 30] however, to the best of our knowledge, this is the first study to elucidate the importance of macropores by comparing the antimicrobial efficacy of macroporous and non-macroporous gels.

It is noteworthy that the best-performing gel, cryogel C, exhibited the highest stiffness (as indicated by its Young's modulus, **Table 5.1**) and pore integrity (based on ESEM, **Figure 5.3**), which suggests that antimicrobial efficacy could also be linked to mechanical strength and pore structure. Cryogels with higher pore integrity, and gel stiffness (e.g. cross-linking densities) would be expected to display higher surface areas and greater confinement of bacteria within the gel pores, thereby increasing their exposure to the antimicrobial surface. The higher antimicrobial efficiency of such cryogels (e.g. cryogel C) in this study appears to support this theory.

A preliminary investigation to gain insight into the antibacterial mechanism of the cryogels was conducted. ESEM was employed to visualize the cross-sections of cryogel C after 1 h of contact with *E. coli* cells. ESEM was chosen over conventional (high vacuum) SEM to minimize possible introduction of artifacts due to more extensive sample preparation involved in the latter method.[31] Adhesion of bacterial cells (rod-shaped) within the cryogel, especially on the pore walls, was observed

(**Figures 5.8a** and **Appendix Figure 5.3**). Note that extensive washing of the gel to flush out any loosely attached bacterial cells (similar to that done in the antimicrobial test above) was performed prior to imaging.

In order to determine if the trapped bacterial cells were viable, an MTS cell viability assay was performed, where cell metabolic activity is directly proportional to the absorbance at 490 nm.[32-33] After 1 h of gel-bacteria incubation, which was followed by extensive flushing of the gel with saline, the gel was removed from the well and both the gel and the saline washing solution (hereby referred to as "supernatant") were tested for bacterial cell viability. As expected, cell viability in the supernatants of cryogel C, cryogel D, and the control hydrogel (**Figure 5.8b**) corresponds to their antimicrobial activity, as shown in **Figure 5.7b**. The supernatant of cryogel C (gel with the best antimicrobial efficacy) demonstrated the lowest absorbance at 490 nm compared to the supernatants of cryogel D and the control hydrogel. On the other hand, negligible cell viability (normalized absorbance < 0.02) was shown for all gels tested, indicating that the cells entrapped within (or on the surface of) the gels were nonviable. Based on these results, we hypothesize that cryogels are contact-active (consistent with most inherent antimicrobial gels[1, 3-4]) and exert their antimicrobial action through a "trap and kill" mechanism, where bacterial cells are trapped or confined within the macropores and subsequently killed upon contact with the PLL-*b*-PDLV copolypeptide on the pore wall. This postulated mechanism was supported by a gel reusability study, where a modest reduction in activity was observed after each use (see **Appendix Figure A5.5**). We theorize that as the cryogels are contact-active, the surface area available for bacteria adhesion would be reduced after each use, which indicates that the gel antimicrobial efficacy is surface area-dependent.

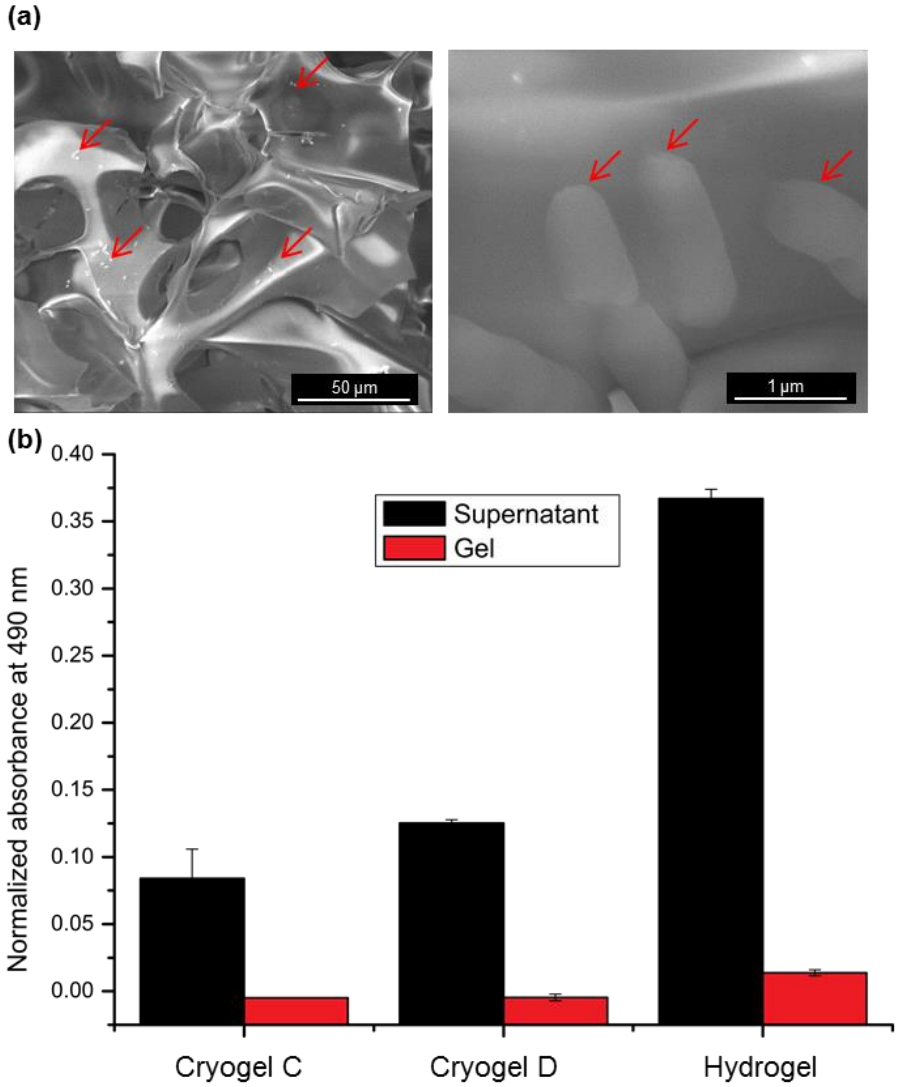

Figure 5.8. (a) Representative ESEM images of cryogel C after incubation with *E. coli* for 1 h, followed by vigorous flushing and agitation with saline buffer (0.9% NaCl solution). Note the red arrows indicate the *E. coli* cells (b) Viability of *E. coli* cells found in the 'supernatant' or saline buffer used to flush the gels (black bars) and cells entrapped in the gel (red bars) relative to the positive growth control. Cell viability was measured in terms of the absorbance at 490 nm using an MTS-based assay. Error bars represent the standard deviation from the mean (n = 4).

5.4 Chapter Summary

In summary, novel polypeptide-based cryogels (macroporous hydrogels) with inherent antimicrobial properties have been developed by cross-linking the amine residues of PLL-*b*-PDLV copolypeptides with glutaraldehyde. The cryogels exhibited superior swelling properties and mechanical strength compared to their analogous conventional hydrogel due to their macroporous structure. These cryogels displayed inherent antimicrobial activity against *E. coli* with the best performing gel causing a 95.6% reduction in viable cell counts within 1 h incubation. By comparing cryogel antimicrobial efficacy with that of the control hydrogel, macropores were found to be crucial for bactericidal activity. It is believed the presence of macropores allows for effective uptake of bacteria into the gels. ESEM imaging and cell viability tests suggest that the antimicrobial action of the cryogels involves a "trap and kill" mechanism, where macropores are believed to provide confinement and increased surface area for contact of the bacteria with the antimicrobial polymer. Mechanical strength and pore integrity of cryogels were also found to be determinants for antibacterial activity. Despite showing a reduced antimicrobial potency to existing heavy metal-incorporated cryogel systems, the inherent antimicrobial properties and lack of toxic leaching of the cryogels reported herein show potential for use in biological and environmentally friendly water purification applications.

5.5 References

(1) Ng, V. W. L.; Chan, J. M. W.; Sardon, H.; Ono, R. J.; Garcia, J. M.; Yang, Y. Y.; Hedrick, J. L., *Adv. Drug Del. Rev.* **2014,** *78*, 46-62.

(2) Irwansyah, I.; Li, Y.-Q.; Shi, W.; Qi, D.; Leow, W. R.; Tang, M. B. Y.; Li, S.; Chen, X., *Adv. Mater.* **2015,** *27* (4), 648-654.

(3) Salick, D. A.; Pochan, D. J.; Schneider, J. P., *Adv. Mater.* **2009,** *21* (41), 4120-4123.

(4) Salick, D. A.; Kretsinger, J. K.; Pochan, D. J.; Schneider, J. P., *J. Am. Chem. Soc.* **2007,** *129* (47), 14793-14799.

(5) Jiang, L.; Xu, D.; Sellati, T. J.; Dong, H., *Nanoscale* **2015,** *7* (45), 19160-19169.

(6) Veiga, A. S.; Schneider, J. P., *Biopolymers* **2013,** *100* (6), 637-644.

(7) Henderson, T. M. A.; Ladewig, K.; Haylock, D. N.; McLean, K. M.; O'Connor, A. J., *J. Mater. Chem. B* **2013,** *1* (21), 2682-2695.

(8) Ozmen, M. M.; Fu, Q.; Kim, J.; Qiao, G. G., *Chem. Commun.* **2015,** *51* (98), 17479-17482.

(9) Erturk, G.; Mattiasson, B., *J. Chromatogr. A* **2014,** *1357*, 24-35.

(10) Bencherif, S. A.; Sands, R. W.; Bhatta, D.; Arany, P.; Verbeke, C. S.; Edwards, D. A.; Mooney, D. J., *Proc. Natl. Acad. Sci. U.S.A.* **2012,** *109* (48), 19590-19595.

(11) Lozinsky, V. I.; Okay, O., Basic Principles of Cryotropic Gelation. In *Polymeric Cryogels: Macroporous Gels with Remarkable Properties*, Okay, O., Ed. Springer: 2014; Vol. 263, pp 49-101.

(12) Dinu, M. V.; Ozmen, M. M.; Dragan, E. S.; Okay, O., *Polymer* **2007,** *48* (1), 195-204.

(13) Loo, S.-L.; Krantz, W. B.; Lim, T.-T.; Fane, A. G.; Hu, X., *Soft Matter* **2013,** *9* (1), 224-234.

(14) Loo, S.-L.; Krantz, W. B.; Fane, A. G.; Gao, Y.; Lim, T.-T.; Hu, X., *Environ. Sci. Technol.* **2015,** *49* (4), 2310-2318.

(15) Loo, S.-L.; Fane, A. G.; Lim, T.-T.; Krantz, W. B.; Liang, Y.-N.; Liu, X.; Hu, X., *Environ. Sci. Technol.* **2013,** *47* (16), 9363-9371.

(16) Chaturvedi, A.; Bajpai, A. K.; Bajpai, J.; Sharma, A., *Des. Monomers Polym.* **2015,** *18* (4), 385-400.

(17) Chaturvedi, A.; Bajpai, A. K.; Bajpai, J., *Polym. Compos.* **2015,** *36* (11), 1983-1997.

(18) Patachia, S.; Damian, N., *Soft Materials* **2014,** *12* (4), 371-379.

(19) Martinez, Y. N.; Cavello, I.; Hours, R.; Cavalitto, S.; Castro, G. R., *Bioresour. Technol.* **2013,** *145*, 280-284.

(20) Song, A.; Rane, A. A.; Christman, K. L., *Acta Biomater.* **2012,** *8* (1), 41-50.

(21) Lu, H.; Cheng, J. J., *J. Am. Chem. Soc.* **2008,** *130* (38), 12562-12563.

(22) Epand, R. F.; Scheraga, H. A., *Biopolymers* **1968,** *6* (11), 1551-1571.

(23) Goh, S. L.; Platt, A. P.; Rutledge, K. E.; Lee, I., *J. Polym. Sci., Part A* **2008,** *46* (16), 5381-5389.

(24) Dainiak, M. B.; Allan, I. U.; Savina, I. N.; Cornelio, L.; James, E. S.; James, S. L.; Mikhalovsky, S. V.; Jungvid, H.; Galaev, I. Y., *Biomaterials* **2010,** *31* (1), 67-76.

(25) Kathuria, N.; Tripathi, A.; Kar, K. K.; Kumar, A., *Acta Biomater.* **2009,** *5* (1), 406-418.

(26) Jurga, M.; Dainiak, M. B.; Sarnowska, A.; Jablonska, A.; Tripathi, A.; Plieva, F. M.; Savina, I. N.; Strojek, L.; Jungvid, H.; Kumar, A.; Lukomska, B.; Domanska-Janik, K.; Forraz, N.; McGuckin, C. P., *Biomaterials* **2011,** *32* (13), 3423-3434.

(27) Lozinsky, V. I.; Plieva, F. M.; Galaev, I. Y.; Mattiasson, B., *Bioseparation* **2001,** *10* (4-5), 163-188.

(28) Ak, F.; Oztoprak, Z.; Karakutuk, I.; Okay, O., *Biomacromolecules* **2013,** *14* (3), 719-727.

(29) Murakami, S.; Aoki, N.; Matsumura, S., *Polym. J.* **2011,** *43* (9), 414-420.

(30) Li, P.; Poon, Y. F.; Li, W.; Zhu, H.-Y.; Yeap, S. H.; Cao, Y.; Qi, X.; Zhou, C.; Lamrani, M.; Beuerman, R. W.; Kang, E.-T.; Mu, Y.; Li, C. M.; Chang, M. W.; Leong, S. S. J.; Chan-Park, M. B., *Nat. Mater.* **2011,** *10* (2), 149-156.

(31) McGregor, J. E.; Staniewicz, L. T. L.; Guthrie Nee Kirk, S. E.; Donald, A. M., *Methods Mol. Biol.* **2013,** *931*, 493-516.

(32) Wang, H. W.; Cheng, H. R.; Wang, F. Q.; Wei, D. Z.; Wang, X. D., *J. Microbiol. Methods* **2010,** *82* (3), 330-333.

(33) Tsukatani, T.; Higuchi, T.; Suenaga, H.; Akao, T.; Ishiyama, M.; Ezoe, T.; Matsumoto, K., *Anal. Biochem.* **2009,** *393* (1), 117-125.

6

Conclusions and Future Perspective

6.1 Conclusions

Synthetic polypeptides, as biomimetic materials, offer an array of functionality, scalability and tunability that have allowed for their use in a diverse range of biological and bioactive applications such as drug delivery, tissue engineering and antimicrobial treatments. This thesis reports on the preparation of a range of new synthetic polypeptide materials with properties that demonstrate an advancement in the scientific understanding and applicability of synthetic polypeptides in each of these fields.

In **Chapter 2**, novel, cisplatin-loaded, synthetic polypeptide-based vesicles for the targeted delivery of cisplatin to cancer cells were prepared. These vesicles were formed from biocompatible and biodegradable Mal-PEG-*b*-poly(L-glutamic acid) block copolymers upon conjugation with the drug itself. Compared to existing vesicle assembly systems for cisplatin delivery which utilize synthetic non-biodegradable polymers, this study demonstrated preparation of synthetic biodegradable polypeptide vesicles self-assembled through a novel drug-induced process. Drug release studies demonstrated a low and sustained drug release profile in systemic conditions with a higher "burst-like" release rate being observed under late endosomal/lysosomal conditions. The peripheral maleimide functionalities on the vesicle corona were conjugated to thiol-functionalized folic acid (FA) (via *in situ* reduction of a novel bis- FA disulfide, FA-SS-FA) to form an active targeting drug delivery system. These targeting vesicles exhibited significantly higher cellular binding/uptake into and dose-dependent cytotoxicity toward cancer cells (HeLa) compared to noncancerous cells (NIH-3T3), which show high and low folic acid receptor (FR) expression, respectively. This work thus demonstrates a novel approach to polypeptide-based vesicle assembly and a promising new strategy for targeted, effective cisplatin anticancer drug delivery.

In **Chapter 3**, preliminary studies into the preparation of aptamer-targeted poly(L-glutamic acid)(PLG)-based delivery systems (e.g. vesicles in **Chapter 2**) was performed through conjugation and isolation of a model single-stranded DNA (ssDNA) aptamer to synthetic PLG-based block polymers. The study employed two maleimide-functional PEG-*b*-PLG block copolymers; Mal-PEG-*b*-PLG-NH_2 and Mal-PEG-*b*-(PLG-*r*-PLL)-NH_2, and are representative of common synthetic PLG-based nanoparticle precursors used in the drug delivery field. A thiol-functionalized ssDNA was then conjugated to the polymer through thiol-maleimide coupling chemistry and monitored through agarose gel electrophoresis. Analysis on a range of coupling conditions determined that coupling in the presence of EDTA resulted in the highest conjugation efficiencies, whereas the use of TCEP, a commonly used *in situ* reductant, resulted in no observed conjugate. Using preparative gel electrophoresis, isolation of the conjugates was achieved and verified through UV-Vis analysis. Conjugation and isolation protocols worked effectively and reproducibly with both conjugates, offering potential use in future studies employing aptamer-targeting of PLG-based delivery systems.

In **Chapter 4**, the preparation of the first three-dimensional macroporous hydrogels composed entirely of biocompatible and enzyme biodegradable synthetic polypeptides is reported. Under cryoconditions, macroporous hydrogels in the form of macroporous cryogels were prepared using a single copolymer component through direct cross-linking between poly(L-glutamic acid) (PLG) and poly(L-lysine) (PLL) residues on a PLG-*r*-PLL random copolypeptide chain. Compared to other polypeptide-based macroporous hydrogels, where the incorporation of non-synthetic polypeptide components and multi-step synthesis are required, this procedure offers a straightforward approach to prepare synthetic polypeptide hydrogels and provides an opportunity to more effectively study the suitability of synthetic polypeptide as a material for 3D cellular culture applications. The resulting macroporous cryogels were found to contain large interconnected pores (≥100 μm) suitable for cell ingrowth. Pore morphology and resulting gel stiffness could be varied, suitable for developing gels for a range of possible soft tissue engineering applications. These cryogels were shown to be enzymatically biodegradable and displayed excellent biocompatibility, cell attachment and cell proliferation profiles with mammalian fibroblast (NIH-3T3) cells, demonstrating the appeal of these novel cryogels as highly suitable cellular scaffolds.

In **Chapter 5**, the antimicrobial properties of synthetic polypeptides were utilized to prepare cryogels (macroporous hydrogels) for potential water purification applications. Existing macroporous gel systems utilize the incorporation of known antimicrobial agents into the gels rather than from the polymer itself, often resulting in toxic component leaching and thus limiting their water purification suitability. In this chapter, the first reported case of a macroporous hydrogel with inherent antimicrobial activity was reported, displaying properties highly suitable for water purification applications. Gels were chemically cross-linked through the amine residue of a polycationic and hydrophobic poly(L-lysine)-*b*-poly(D,L-valine) block copolymer with glutaraldehyde as cross-linker under cryogenic conditions. These cryogels exhibited excellent water swelling and highly compressible mechanical properties owing to their macroporous structure. The antibacterial performance was evaluated based on game-negative *E. coli* viability, with cryogels exhibiting up to 95.6% reduction in viable *E. coli* after a brief 1 h incubation. In comparison to a nanoporous hydrogel control, the presence of macropores and their integrity is shown to be vital to the antimicrobial effect of the gels. The confined environment and increased antimicrobial surface area of the macropores is believed to result in increased contact with the antimicrobial polymer through a "trap and kill" mechanism. Along with the lack of toxic leaching, these cryogels with inherent antimicrobial properties pose as potential candidates for use in biological and environmentally friendly water purification applications.

6.2 Future Perspectives

The folic-acid targeted cisplatin-loaded vesicles in **Chapter 2** demonstrated higher cellular uptake and dose dependent toxicity towards cancer cells than non-cancerous cells. Ultimately, *in vivo* studies using small animal models will reveal the true efficacy of these vesicles polymer as a targeted drug delivery vehicle for cancer treatment. The biodistribution of nanoparticles has a large effect on the performance of drug delivery carriers and is shown to be largely effected by particle size and morphology.[1] *In vivo* studies will gain important information relating to the biodistribution of these vesicles.

In **Chapter 3**, the conjugation of model DNA aptamers to synthetic polypeptides, and the isolation of these conjugates, were demonstrated to be effective approaches for

consideration in future aptamer targeted synthetic polypeptide-based drug delivery systems. However, the presence of noticeable amounts of unreacted DNA after the reaction means that significant improvements in the conjugation yields could be achieved. It was mentioned in this chapter that although the use of TCEP effectively maintains the DNA in its reduced (reactive) form, its competitive reactivity with the maleimide group of the polymer hampers any noticeable conjugation occurring. Whilst it has been shown that using very low TCEP concentrations of ≤ 1 mM may help to reduce this competitive reactivity,[2] the use of immobilized TCEP (e.g. TCEP immobilized on an agarose gel) in thiol-maleimide coupling is becoming increasingly common due to its ease of removal and apparent reduced reactivity to maleimide groups.[3-4] The use of immobilized TCEP has shown significantly higher thiol-maleimide conjugation efficiencies compared to the use of free TCEP,[3] and would be worthwhile to investigate for the conjugations studied in this chapter.

The conjugates tested in **Chapter 3** were synthetic polypeptide-based nanoparticle precursors, and therefore not drug-loaded and assumed to be linear in architecture. Whilst drug-loading and nanoparticle assembly could occur after conjugation of aptamer, future work would also look at conjugating and isolating model ssDNA aptamers to drug-loaded 3D nanoparticles, for instance the maleimide functionalized vesicles prepared in **Chapter 2** (**Figure 6.1**).

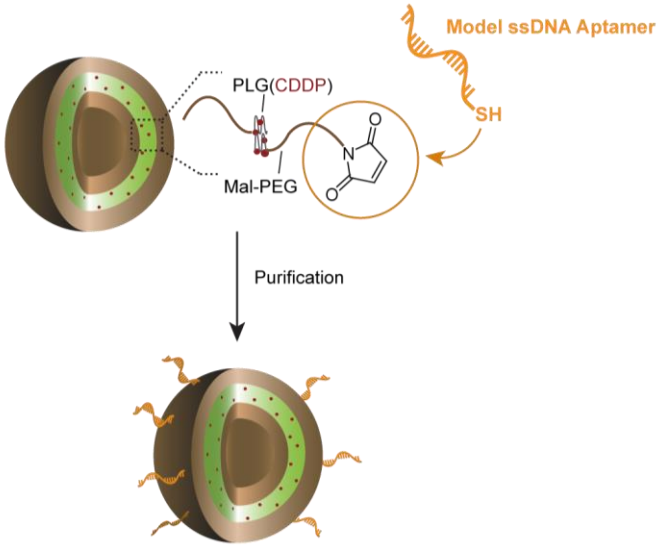

Figure 6.1. Conjugation of thiol-functionalized model ssDNA aptamer to maleimide groups on periphery of CDDP-loaded vesicle in **Chapter 2.**

Ultimately, the conjugation and purification of 'functional' aptamers (specific nucleotide sequences which can fold into the unique 3D structures required for their target recognition (**Figure 6.2**)) to synthetic polypeptide-based drug delivery systems will need to be attempted and tested for their specific targeting capabilities.

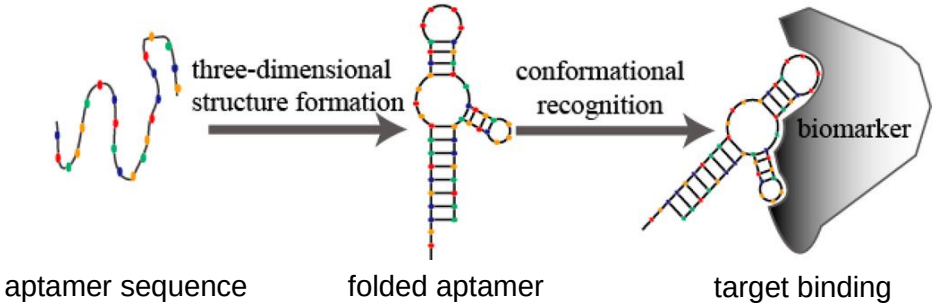

Figure 6.2. Schematic of a functional aptamer folding into its unique three-dimensional structure with specific target recognition.[5]

The synthetic polypeptide macroporous hydrogels (cryogels) described in **Chapter 4** demonstrated suitable cell adhesive and biodegradable properties as 3D cellular scaffolds. Effective cell adhesion of the scaffolds was attributed to the cationic and anionic surface charges on the scaffolds, properties shown to be favorable to cell attachment. Whilst cell attachment can occur through direct interaction the surfaces with cells, adsorption of serum proteins to these surface charges can also influence the cell adhesion to charged surfaces.[6-7] Determining the effect, if any, of protein adsorption on the cell attachment properties of these scaffolds will provide useful information toward optimizing the surface charges and therefore cell adhesive properties of these gels.

Cellular studies of the cryogels were performed on mammalian NIH-3T3 fibroblast cells to determine the suitability of the materials as cellular scaffolds. However, the gels prepared in **Chapter 4** display very different mechanical properties which may suit certain cell types depending on their stiffness (**Figure 6.3**).[8-9] Future studies would look to test these scaffolds on specific cell types which may grow optimally in either of the gels (e.g. skin or brain tissue cells for cryogel A, tendon tissue or nascent bone cells for cryogel B), so that specific tissue engineering applications can be considered for the gels.

Further to this, implantation of the materials into animal for *in vivo* studies will be necessary to determine the immunogenic response to these gels; a necessary requirement of tissue engineering scaffolds and a proposed benefit of using synthetic polypeptides over natural polymers.

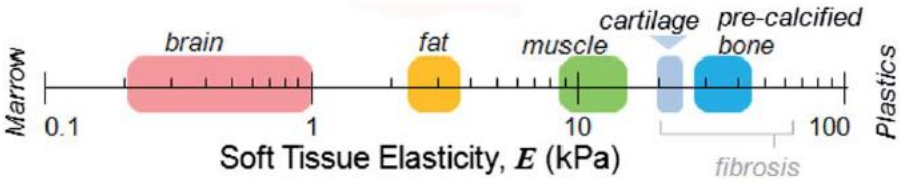

Figure 6.3 Soft tissue Young's/elastic modulus (stiffness) as a reference for the design of suitable scaffolds.[9]

In **Chapter 5**, the cryogels are described as contact-active and exert their antimicrobial action through a "trap and kill" effect, where bacterial cells are trapped or confined within the macropores and subsequently killed upon contact with the PLL-*b*-PDLV copolypeptide of the pore wall. The contact-active mechanism which results in bacteria cell death and gives the polypeptide materials its intrinsic antimicrobial properties has not been determined in this study. A range of contact-active mechanisms have been proposed for antimicrobial peptides, generally relating to the disruption of bacterial cell membranes, and include barrel-stave, carpet and toroidal models (**Figure 6.4**).[10] Studying the contact-active antimicrobial mechanism relating to these cryogels will be important for optimizing the antimicrobial efficacy of these gels. Optimization of the cryogel antimicrobial properties may come from changes to the cationic (lysine) and hydrophobic (valine) ratios of the polypeptide. It will also be worthwhile investigating the use of different hydrophobic amino acids (e.g. L-leucine or L-alanine) which studies have suggested display stronger membrane interactions and antimicrobial properties over L-valine possibly due to the formation of α-helical structures.[11] It will also be of interest to study the antimicrobial efficacy of these gels against gram-positive bacteria (e.g. *S. aureus*) to determine if they display broad ranging antimicrobial properties.

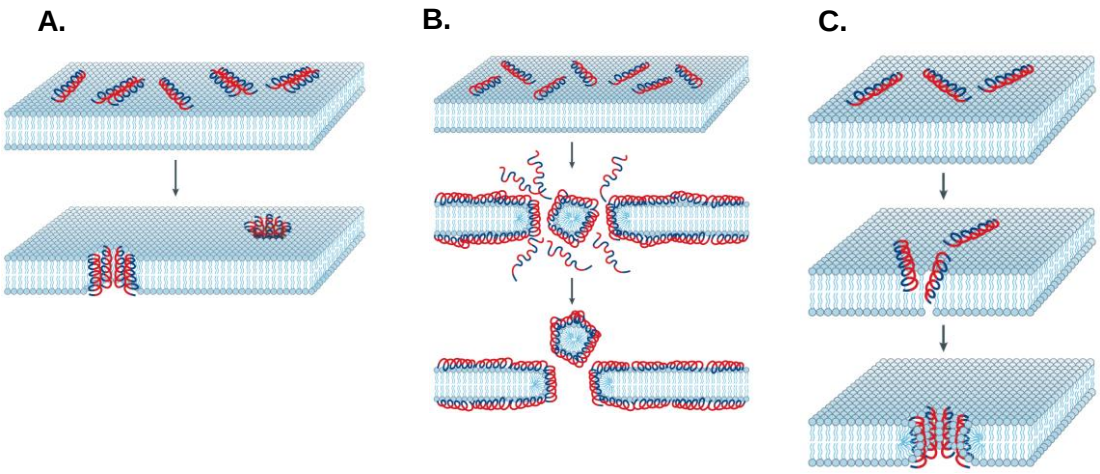

Figure 6.4. Three proposed mechanisms (models) for the contact-activity of AMPs relating to bacterial cell membrane disruption (A) barrel-stave (B) carpet (C) toroidal-pore.[10]

6.3 References

(1) Blanco, E.; Shen, H.; Ferrari, M., *Nat. Biotechnol.* **2015,** *33* (9), 941-951.

(2) Tyagarajan, K.; Pretzer, E.; Wiktorowicz, J. E., *Electrophoresis* **2003,** *24* (14), 2348-2358.

(3) Da Pieve, C.; Williams, P.; Haddleton, D. M.; Palmer, R. M. J.; Missailidis, S., *Bioconjugate Chem.* **2010,** *21* (1), 169-174.

(4) Maret, B.; Regnier, T.; Rossi, J. C.; Garrelly, L.; Vial, L.; Pascal, R., *Rsc Advances* **2014,** *4* (15), 7725-7728.

(5) Sun, H. G.; Zu, Y. L., *Molecules* **2015,** *20* (7), 11959-11980.

(6) Richert, L.; Lavalle, P.; Vautier, D.; Senger, B.; Stoltz, J. F.; Schaaf, P.; Voegel, J. C.; Picart, C., *Biomacromolecules* **2002,** *3* (6), 1170-1178.

(7) Schneider, G. B.; English, A.; Abraham, M.; Zaharias, R.; Stanford, C.; Keller, J., *Biomaterials* **2004,** *25* (15), 3023-3028.

(8) Liu, J.; Zheng, H.; Poh, P. S. P.; Machens, H.-G.; Schilling, A. F., *Int. J. Mol. Sci.* **2015,** *16* (7), 15997-16016.

(9) Sartori, S.; Chiono, V.; Tonda-Turo, C.; Mattu, C.; Gianluca, C., *J. Mater. Chem. B* **2014,** *2* (32), 5128-5144.

(10) Brogden, K. A., *Nature Reviews Microbiology* **2005,** *3* (3), 238-250.

(11) Deming, T. J., *Prog. Polym. Sci.* **2007,** *32* (8-9), 858-875.

7

Experimental

This chapter describes the various characterization methods and detailed experimental procedures utilized in all the work presented in this thesis.

7.1 Characterization Methods/Instrumentation

General characterization methods used in multiple chapters are discussed below. For details relating to methods specific to a relevant chapter, including *in vitro* culture and tests, please see relevant chapter experimental section.

Nuclear Magnetic Resonance (NMR)

^{1}H nuclear magnetic resonance (NMR) spectroscopy was used to determine the molecular structure of compounds. ^{1}H NMR analysis was performed using a Varian Unity Plus 400 MHz NMR spectrometer using the deuterated solvent as reference.

Ultraviolet-Visible (UV-Vis) Spectroscopy

Ultraviolet-visible (UV-Vis) spectroscopy was used to measure cisplatin drug loading of nanoparticles in **Chapter 2** and to qualitatively determine the conjugation of folic acid targeting ligand to vesicles in **Chapter 2**. It was also performed on DNA-polymer conjugates in **Chapter 3** to verify the presence of DNA and polymer absorbance profiles in the conjugates. UV–Vis spectrometry was performed on a Shimadzu UV-1800 spectrometer using quartz cuvettes with a 1 cm path length, and a Nanodrop 1000 Spectrophotometer (Thermo Scientific) using 2 μL samples with 1 mm path length.

Fourier-Transform Infrared (FT-IR) Spectroscopy

Fourier-transform infrared (FT-IR) spectroscopy (FT-IR) was used to determine the presence of specific functional groups in nanoparticles and hydrogels. In **Chapter 2**, FT-

IR was performed on a Bruker Tensor 27 with mid-infrared range (400−4000 cm^{-1}). The instrument was equipped with OPUS 6.5 Software. Typically, 0.1 mg of sample were ground with dry potassium bromide (KBr) at approximately 1 wt % and the resulting powder was pressed into a transparent pellet using Specac 10 ton Hydraulic Press. For each sample, 100 scans were taken in transmittance mode at a resolution of 2 cm^{-1}. In **Chapter 4**, dried cryogels and samples were analyzed by attenuated total reflectance fourier-transform infrared (ATR FT-IR), using a Bruker Tensor 27 with mid-infrared range (400−4000 cm−1). The instrument was equipped with OPUS 6.5 software. Measurements were made in transmittance mode. In **Chapter 5**, dried cryogels and samples were analyzed by ATR FT-IR using a Nexus 470 Fourier-Transform Infrared Spectrometer (Thermo Nicolet). Measurements were made in transmittance mode

Gel Permeation Chromatography (GPC)

Gel permeation chromatography (GPC) was used to characterize polymer molecular weight and polydispersity (PDI). GPC analysis was performed on a Shimadzu liquid chromatography system fitted with a PostNova Analytics MALS detector (λ = 658 nm), a Shimadzu RID-10 refractometer (λ = 633 nm), and a Shimadzu SPD-20A UV−vis detector, using three phenogel columns (Phenomenex, 5 μm) in series and HPLC grade DMF with 0.05 M LiBr as the mobile phase (1 mL/min). The oven temperature was set to 50 °C to maintain an acceptable pressure across the system, and the detectors were temperature controlled to 25 °C. Nova MALS software (PostNova) was used to determine the molecular weights and PDI using poly(ethylene glycol) standards. All GPC samples filtered through 0.45 μm filters.

Confocal Laser Scanning Microscopy (CLSM)

CLSM was used to image fluorescently stained cells, nanoparticles and hydrogels. In **Chapter 2**, CLSM images were taken using a Leica TCS SP2 AOBS confocal microscope (Leica, Germany) equipped with an argon laser (λ = 488 nm), using a 63× oil immersion objective (Leica, Germany). DAPI was excited at λ = 405 nm, FITC at λ = 488 nm, and CellMask Deep Red at λ = 633 nm. The emission filters were set at λ = 414−478 nm for DAPI, λ = 500−561 nm for FITC, and λ = 646−726 nm for CellMask Deep Red. Images were recorded at a depth of 10−20 μm from the surface of the glass coverslip. Leica confocal

software was used to acquire images of 512 × 512 pixels with images stacked in the z-direction using ImageJ software. In **Chapter 4**, CLSM images of FITC-labeled gels were taken on a Nikon A1R+ using both 20X or 40X objectives and an excitation wavelength of 488 nm. All images were generated by optical sectioning in the z-direction. Images were stacked in the z-direction and then analyzed using ImageJ software to determine the pore size and pore wall thickness of the cryogels. See relevant **Chapter 4** experimental section for imaging of gels following *in vitro* cell culture.

Environmental Scanning Electron Microscopy (ESEM)

Environmental Scanning electron microscope (ESEM) was used to image hydrogels in **Chapter 4** and **Chapter 5**. Images were acquired using a FEI Quanta 200 ESEM FEG. Gels were analyzed in their wet state under low vacuum. For **Chapter 5** ESEM images were analyzed using ImageJ analysis software to determine the pore size of cryogels (Cryogel C).

Mechanical (Compression) Tests

Mechanical (compression) tests were performed on hydrogels in **Chapter 4** and **Chapter 5.** Compression tests were performed on cylindrical hydrogels in their wet state using an Instron MicroTester (5848). For specific mechanical test protocols, see relevant chapter experimental protocols.

7.2 Experimental for Chapter 2

Materials

Furan (≥99%, Aldrich) cystamine dihydrochloride (96%, Aldrich), cis-dichlorodiamineoplatinum(II) (CDDP) (Aldrich), folic acid (≥97%, Aldrich), trifluoroacetic acid (TFA) (99%, Aldrich), fluorescein isothiocyante isomer 1 (FITC) (≥90% HPLC, Aldrich), phosphate buffered saline (PBS) (tablets, Aldrich), 4-(dimethylamino)pyridine, (DMAP) (99%, Aldrich), tris (2- carboxyethyl)phosphine hydrochloride (TCEP) (≥98%, Aldrich), 3- mercaptopropionic acid (≥99%, Aldrich), o-phenylenediamine (99.5%, Aldrich), triphosgene (98%, Aldrich), pyridine (AR, Scharlau), hydrochloric acid (37%, Scharlau), triethylamine (TEA) (99%, Ajax Fine Chemicals), *N*-

(3-(dimethylamino)propyl)-*N*′-ethylcarbodiimide hydrochloride (EDCI) (≥98%, Acros), H-Glu(OtBu)−OH (Bachem), Mal-PEG-NH_2·TFA 5 kDa (Jenkem Technology), silver nitrate (AR, Chem-Supply), sodium bicarbonate (AR, Chem-Supply), platinum standard for ICP (100 mg/L Pt in HCl, Aldrich), sodium chloride (AR, Chem-Supply), acetic acid (Glacial AR, Chem-Supply), sodium acetate (anhydrous, Chem-Supply), lithium bromide (99.9%, Aldrich), and sodium hydroxide (AR, Chem-Supply) were used as received. Pentane (anhydrous ≥99%, Aldrich), methanol (AR, Chem-Supply), chloroform (AR, Chem-Supply), dichloromethane (AR, Chem- Supply), chlorotrimetylsilane (≥99%, Aldrich), hydrogen peroxide (30%, AR, Chem-Supply), sulfuric acid (98%, ACI labscan), diethyl ether (AR, Chem-Supply), dimethylformamide (DMF) (extra dry, 99.8%, Acros), and toluene (AR, Ajax Fine Chemicals) were used as received. Tetrahydrofuran (THF) (AR, Chem-Supply) was distilled from benzophenone and sodium metal under argon. Dimethyl sulfoxide (DMSO) (≥99%, Aldrich) was stored under 3 Å molecular sieves. DMSO-d_6 (99.9%) was purchased from Cambridge Isotope Laboratories and Aldrich and stored under 3 Å molecular sieves. Dialysis tubing (Snakeskin 3.5 kDa cutoff) was purchased from ThermoScientific. Cell culture supplies (DMEM, FBS, 100 × GlutaMax, 100 × antibiotic-antimycotic), AlamarBlue(R) assay reagent, paraformaldehyde, and CellMask Deep Red Plasma Membrane Stain were purchased from Life Technologies and used as received. DAPI Fluoromount G was purchased from ProSciTech and used as received. Culture plates, microscope slides and glass coverslips were purchased from Corning.

Synthesis of Block Copolymer

*Synthesis of Furan-Protected Mal-PEG-NH_2HCl (**P1**)*

Furan-protected Mal-PEG-NH_2HCl (5.3 kDa) was synthesized through general Diels–Alder (DA) cycloaddition conditions, followed by counterion exchange of the trifluoroacetate anion with chloride anions. A mixture of Mal-PEG(5 kDa)-NH_2TFA (150 mg, 28.3 μmol), furan (2.5 mL), and deionized (DI) water (8.5 mL) was gently stirred at 35 °C for 15 h. Excess furan was removed under low vacuum followed by extraction in an ether wash (3 × 5 mL). The aqueous phase was then collected and place under low vacuum to remove excess ether. 1 M HCl (3.2 mL) was then added ($[HCl]_{final}$ = 0.2M), and the clear solution was stirred at room temperature (RT) for 6.5 h. Water was removed under high vacuum and toluene azeotrope to afford a light yellow powder, which was

then dissolved in minimal chloroform and precipitated in chilled ether. Precipitate was then centrifuged and dried under low vacuum for 48 h to obtain a white yellow powder (**P1**) (Yield: 130 mg, 86%). ^{19}F NMR was used to determine complete removal of the TFA peak at δ_F = −77 ppm after counterion exchange (see **Appendix Figure A2.1**). ^{1}H NMR (400 MHz, $CDCl_3$) δ_H (ppm): 2.35 (t, 1H, *J*= 7.2 Hz, -CH_2-CH_2-), 2.47 (t, 1H, *J*= 7.2 Hz, -CH_2-CH_2-), 2.85 (s, DA c_{exo}), 3.18 (brs, CH_2-CH_2-N*H*$_2$), 3.40 (m, 2H, -CH_2-CH_2-) 3.46 (t, 2H, *J*= 5.2 Hz, -CH_2-CH_2-), 3.63 (s, 455H, C*H*$_2$-C*H*$_2$-O-), 3.80 (t, 2H, *J*= 5.2 Hz, CH_2-C*H*$_2$-N(Mal)), 5.25 (s, DA b_{exo}), 5.30 (m, DA b_{endo}), 6.4 (s, DA a_{exo}), 6.5 (s, DA a_{endo}), 7.92 (s, CON*H*) (refer to **Appendix Figure A2.2** for DA adduct stereochemistry assignments).

*Synthesis of Furan-Protected Mal-PEG-b-PLG(γ-tBu)-NH$_2$ (**P2**)*

N-Carboxyanhydride *γ-tert*-butyl-L-glutamate (*γ*-tBu Glu NCA) was synthesized according to reported synthetic protocols on similar poly(L-glutamic acid) NCA monomers.[1-2] To an oven-dried RBF was added *γ*-tBu Glu NCA (55 mg, 0.24 mmol) under N_2 followed by anhydrous DMF (1.1 mL) and stirred to dissolve for 5 min. Furan protected Mal-PEG-NH_2HCl (**P1**) (120 mg, 22.6 μmol, M/I = 11) dissolved in anhydrous DMF (0.8 mL) was then added to the flask under N_2. The yellow-brown reaction mixture was then stirred for 3 days under N_2 at 40 °C with a needle bleed to allow for removal of HCl byproduct. Furan (0.5 mL) was then added to flask, stoppered and stirred for a further 7 h. DMF was then removed under high vacuum, with product residue dissolved up in minimal chloroform, precipitated in chilled ether and dried to afford a white-cream powder (**P2**) (Yield: 120 mg, 70%) ^{1}H NMR (400 MHz, d_6-DMSO) δ_H (ppm): 1.40 (s, *γ*-tBu), 1.73-1.90 (m, C*H*$_2$-CH_2-COO), 2.19-2.29 (m, CH_2-C*H*$_2$-COO), 2.91(s, DA c_{exo}), 3.51 (s, 455H, -C*H*$_2$-C*H*$_2$-O-), 4.24 (m, -N-C*H*-CO), 5.11 (s, DA b_{exo}), 5.30 (m, DA b_{endo}), 6.38 (s, DA a_{exo}), 6.54 (s, DA a_{endo}), 7.98 (m, CON*H*).

*Synthesis of Mal-PEG-b-PLG-NH$_2$ (**P3**)*

t-Butyl deprotection and retro DA was conducted in a one pot procedure. Protected block copolymer (**P2**) (50 mg, 78.9 μmol Glu units), DCM (3.5 mL), and TFA (3.5 mL) were stirred vigorously for 1 h, followed by the addition of toluene (8 mL). DCM and TFA were then removed under low vacuum with excess TFA removed through DCM azeotrope. The contents were then refluxed at 120 °C for 6 h, concentrated, dissolved in minimal

methanol, and precipitated in chilled ether. Precipitate was isolated and dried under vacuum to give a white powder **P3** (Yield: 45 mg, 100%). ^{1}H NMR (400 MHz, d$_6$-DMSO) δ_H (ppm): 1.75-1.90 (m, C***H*****$_2$**-CH$_2$-COO), 2.10-2.33 (m, CH$_2$-C***H*****$_2$**-COO), 3.51 (s, 456H, -C*H*$_2$-C*H*$_2$-O-), 4.21 (s, -N-C*H*-CO), 7.00 (s, mal -C*H*=C*H*-), 8.01 (m, CON*H*).

Chemical Modification of Mal-PEG-b-PLG-NH$_2$ for SEC Analysis

For better refractive index (RI) detection after GPC, carboxylic acid groups of Mal-PEG-b-PLG-NH$_2$ polymers were modified into methyl ester units using chlorotrimethylsilane as a methylating agent. Sample (3.5 mg) was dissolved in 250 µL methanol in a 2 mL eppendorf tube. Chlorotrimethylsilane (TMSCl, 9.5 µL, ~10 equiv to carboxylic acid groups) was then added, and the contents were stirred for 20 h at 21 °C. The solvent and excess TMSCl were then removed under reduced pressure, and the methylated polymer was analyzed by size exclusion chromatography (DMF).

*Fluorescent Tagging of Mal-PEG-b-PLG-NH$_2$ (**P4**)*

FITC (2.17 mg, 5.58 µmol) dissolved in anhydrous DMSO (285 µL) was added to Mal-PEG-*b*-PLG-NH$_2$ (**P3**) (30 mg, 4.41 µmol), followed by addition of triethylamine (TEA, 0.2 µL, 1.43 µmol, 0.3 equiv) as catalyst. The yellow-brown solution was stirred in the dark at 21 °C, 1050 rpm for 14 h. The reaction was then quenched with a few drops of 1 M HCl, and dialyzed against methanol over 48 h. Contents were then concentrated, precipitated in chilled ether, centrifuged, and dried to afford a light yellow solid (Yield: 25 mg, 80%). ^{1}H NMR (400 MHz, d$_6$-DMSO) δ_H (ppm): 1.75-1.90 (m, C***H*****$_2$**-CH$_2$-COO), 2.10-2.33 (m, CH$_2$-C***H*****$_2$**-COO), 3.51 (s, 455H, -C*H*$_2$-C*H*$_2$-O-), 4.20 (s, -N-C*H*-CO), 6.60 (m, FITC Ar*H*), 7.00 (s, mal -C*H*=C*H*-), 7.17 (m, FITC Ar*H*), 7.78-8.04 (m, CON*H***,** FITC Ar*H*), 10.10 (s, FITC COO*H*). UV-Vis analysis determined tagging efficiency to be ~50 mol % (494 nm (DI H$_2$O), ε = 85200 Lmol^{-1}cm^{-1}). Integrity of maleimide double bond determined to be ~60 mol % (see **Appendix Figure A2.3).**

CDDP (Cisplatin) Loading/Vesicle Formation and Cisplatin Release

Preparation of CDDP-Loaded Mal-PEG-b-PLG-FITC Vesicles

The conjugation of cis-platinum to block polymer **P4** was performed through the formation of a *cis*-diaminediaqua platinum(II) complex intermediate using modified published procedures.[3-4] CDDP (12 mg, 40 μmol) and $AgNO_3$ (13.3 mg, 80 μmol) ([$AgNO_3$]/[CDDP] = 2) was suspended in 14 mL DI water, and stirred vigorously in the dark at room temperature for 4 h. Silver chloride white precipitate was then removed by centrifuge at 4400 rpm for 1 h and the *cis*-diaminediaqua platinum(II) complex then filtered through a 0.44 μm syringe filter into an RBF containing Mal-PEG-*b*-PLG-FITC **P4** (20 mg, 34 μmol glutamic acid units, [CDDP]/[Glu] = 1.2). The contents were then left to gently stir in the dark at 37 °C for 15 h. The cloudy yellow-orange solution (indicative of self-assembly) was then dialyzed against DI water over 30 h, after which time the solution turned slightly less cloudy due to dilution effects. The dialysis contents were lyophilized to an orange powder with thermogravimetric analysis (TGA) and inductively coupled plasma optical emission spectroscopy (ICP-OES) used for quantitative determination of platinum loading. TGA was performed on a PerkinElmer Pyris-1 thermogravimetric analyzer, and the samples were heated from 30 to 700 °C at a heating rate of 10 °C/min under an atmosphere flow (20 mL/min). ICP-OES was performed on an Agilent 720-ES ICP-OES at a detected wavelength of 203.646 nm. Samples were dissolved up in 6 M HCl. A three-point standard curve was plotted between intensity versus a serial dilution of a certified Pt reference standard ranging from 1 to 10 ppm. Refer to **Appendix 2** for TGA and ICP-OES analysis, calculation of drug loading content (DLC) and drug conjugation efficiency (DCE).

In Vitro Drug Release from CDDP-Loaded Vesicles

The *in vitro* release of CDDP from the drug-loaded vesicles was evaluated by the dialysis method. The CDDP-loaded vesicles (2.4 mg) were dissolved up in the release buffer and added to 3.5 kDa dialysis tubing. The conjugate was dialyzed against the release buffer (50 mL) at 37 °C with 2 mL aliquots withdrawn at time intervals and replaced with fresh buffer. The withdrawn samples were analyzed by the *o*-phenylenediamine (*o*-PDA) colorimetric assay according to previously published procedures.[5-6] Aliquot samples (2 mL) were added to 2 mL of *o*- PDA (2 mg/mL DMF) and heated at 100 °C for 15 min. The amount of platinum in the sample was determined by measuring the UV−vis absorbance at 703 nm using cisplatin as a standard curve. The concentration of CDDP released from

the conjugate was expressed as a ratio of the amount of platinum in the released solution and that in the initial sample using the following equation:[3]

$$\%\ CDDP\ released = \frac{V_{total}(t) \times C + Y}{Z}$$

where $V_{total(t)}$ is the remaining volume in the releasing container at time t (mL); C is the concentration of platinum determined from UV−vis measurements (μg/mL); Y is the amount of platinum that has already been collected (μg); and Z is the total amount of platinum at t = 0 present in the dialysis bag (μg).

Preparation of Folic Acid-Conjugated Vesicles

Synthesis of FA-SS-FA

FA (80 mg, 0.181 mmol) was first dissolved in anhydrous DMSO (3 mL) using extensive sonication (2 h), then added to an oven-dried flask containing EDCI (84 mg, 0.44 mmol) and DMAP (4.4 mg, 36 μmol) under N_2 and stirred to dissolve. Pyridine (1.5 mL, 18.5 mmol) was then added, followed by the dropwise addition of cystamine·2HCl (21 mg, 93.2 μmol, 0.5 equiv) dissolved in anhydrous DMSO (0.5 mL). The clear solution was stirred at RT in the dark under N_2 for 3 days then precipitated in acetone (45 mL). The precipitate was subsequently washed with 1 M HCl (2 × 30 mL), DI H_2O (2 × 25 mL), acetone (3 × 20 mL) then dried under vacuum to afford a yellow solid (Yield: 55 mg, 60%). ^{1}H NMR (400 MHz, d_6-DMSO) δ_H (ppm): 1.87-2.30 (m, 8H, -C*H*$_2$-C*H*$_2$-CONH- of FA), 2.75 (m, 4H, -C*H*$_2$S-), 4.34 (m, 2H, -C*H*-), 4.48 (s, 4H, Ar-C*H*$_2$-NH-Ar), 6.63 (dd, 4H, *J*= 8.6, 1.8 Hz, -C*H*- of phenyl ring), 6.92 (br s, -N*H*-), 7.65 (dd, 4H, *J*= 8.6, 3.0 Hz -C*H*- of phenyl ring), 8.02 (m, 4H, -CON*H*-), 8.64 (s, 2H, C*H* of pyrazine), 11.4 (br s, COO*H*). (see **Appendix Figure A2.5***)*.

Synthesis of FA-Conjugated CDDP-Loaded Vesicles

Synthesis of FA-conjugated drug-loaded vesicles was performed using thiol-maleimide coupling chemistry after in situ reduction of the FA-SS-FA precursor. FA-SS-FA (1.95 mg, 3.9 μmol FA) dissolved in DMSO (750 μL) was added to a suspension containing FITC tagged vesicles (13.1 mg, 1.0 μmol maleimide groups) and degassed 20 mM $NaHCO_3$

solution (750 µL, pH 7.5). TCEP (0.1 M, 5.7 µL, 0.57 µmol) was then added and the contents sealed and stirred in the dark at 22 °C, 1200 rpm for 4 h. The reaction was quenched with 3-mercaptopropionic acid (1 µL) and stirred for an additional 3 h with the contents then transferred to a 3.5 kDa dialysis cassette and dialyzed against DI water for 24 h (3 × 1.8 L). The dialyzed product was lyophilized as a yellow powder. ^{1}H NMR (400 MHz, d_6-DMSO) δ_H (ppm): 1.75-1.90 (m, glutamic C*H*$_2$-CH$_2$-COO), 2.10-2.33 (m, glutamic CH$_2$-C*H*$_2$-COO), 3.50 (s, 455H, PEG -C*H*$_2$-C*H*$_2$-O-), 4.25 (brs, glutamic -N-C*H*-CO), 4.48 (s, Ar-C*H*$_2$-NH-Ar), 6.60 (m, FITC Ar*H*), 6.62 (m, FA -C*H*- of phenyl ring), 6.91 (m, FA -N*H*-), 7.64 (m, 4H, FA -C*H*- of phenyl ring), 8.02 (m, FA -CON*H*-), 8.63 (s, FA C*H* of pyrazine). (see **Appendix Figure A2.6***)*.

Analysis of Vesicle Size/Charge

Dynamic Light Scattering (DLS) /Zeta Potential

Dynamic light scattering (DLS) measurements were performed on a Wyatt DynaPro NanoStar fitted with a 120 mW Ga−As laser operating at 658 nm; 100 mW was delivered to the sample cell. Analysis was performed at an angle of 90° at a constant temperature of 25 ± 0.01 °C. All sample concentrations were 1 mg mL−1 and measurements were performed in triplicate. Zeta potential was performed to measure the surface charge of nanoparticles in **Chapter 2**. Zeta potential was measured on a Malvern Zetasizer Nano ZS with 4.0 mW HeNe laser operating at 632.8 nm. Analysis was performed at an angle of 173° and a constant temperature of 25 ± 0.1 °C.

Analysis of Vesicle Morphology/Structure

Transition Electron Microscopy (TEM)

TEM was performed on a Tecnai 12 Transmission Electron Microscope (FEI, Eindhoven, The Netherlands) equipped with a Gatan 626 cryoholder (Gatan,Pleasanton, CA, USA) at an operating voltage of 120 kV, and an LVEM5 Transition Electron Low Voltage Microscope (DeLonge America) operating at a voltage of 5 kV. For cryoTEM, 300-mesh copper grids coated with perforated carbon film (Lacey carbon film: ProSciTech, Qld, Australia) were first glow discharged in nitrogen to render them hydrophilic. 4 µL aliquots of the sample (1.5 mgml−1) were pipet onto each grid prior to plunging. After 30

s adsorption time grids were blotted manually using Whatman 541 filter paper, for approximately 2 s. Grids were then plunged into liquid ethane cooled by liquid nitrogen while in a laboratory-built humidity controlled vitrification system (ambient 22 °C). Frozen grids were stored in liquid nitrogen until required. For standard TEM, samples were prepared on carbon coated grids as per cryoTEM, followed by staining with 2% aqueous uranyl acetate at pH7.2 for 10 s then blotted with Whatman 541 blotting paper and air-dried for 2 min. For LVEM, samples were prepared by casting the solution (1 mgml−1) onto carbon coated copper grids for ~30 s then dried under low vacuum for 15 min. No staining was applied.

Atomic Force Microscopy (AFM)

AFM analysis was performed on 0.5 mgml−1 polymer samples drop casted (20 μL) on silicon wafers washed in piranha solution and allowed to air-dry for 48 h. Images were acquired with an MFP-3D Asylum Research instrument. Typical scans were conducted in AC (tapping) mode with ultrasharp SiN gold-coated cantilevers (MikroMasch, Bulgaria). Image processing and surface roughness analysis were performed using the Nanoscope and Igor Pro software programs, respectively.

Cytotoxicity and Uptake Studies In Vitro

Cell Culture

HeLa and NIH-3T3 cells were maintained in "complete" DMEM (supplemented with 10% FBS, 1× GlutaMAXTM, and 1× antibiotic-antimycotic) in a humidified atmosphere containing 5% CO_2 at 37 °C. Usually, cells were seeded in a T175 flask (ca. 3 × 10^6 cells/mL) and passaged twice a week prior to the performance of the subsequent cell viability or cellular uptake imaging studies.

Cell Viability Assay

Cytotoxicity of the vesicles was assessed using Invitrogen's alamarBlue cell viability reagent following the manufacturer's instructions. Briefly, cells were plated into 96 well plates at a concentration of ca. 10 000 cells/well except for the "medium blanks" in which the same amount of medium was added instead. Experimental wells received the vesicles,

free polymer and CDDP at the indicated ratios/concentrations and the plate was subsequently incubated in a humidified atmosphere containing 5% CO_2 at 37 °C. After 72 h, 10 µL of alamarBlue cell viability reagent was added to each well (except for three wells containing medium only). After 3−3.5 h of incubation under the same growth conditions, the absorbance at 570 and 600 nm of each well was measured using a Varian Cary 50 Bio UV−visible spectrophotometer. The absorbance of each well was corrected against the medium-only wells without alamarBlue reagent, and then expressed as a percentage of the growth control. Note that all experiments were conducted in triplicate, and error bars shown represent the standard error of independent experiments.

Cellular Uptake Test (Confocal Laser Scanning Microscopy CLSM)

On Day −1, sterile round glass coverslips (Φ 15 mm) were placed in the wells of a 12 well plate and HeLa and NIH-3T3 cells were seeded in "complete DMEM" medium at a cell density of 200 000 cells per well in 0.5 mL seeding volume before the plate was placed in a humidified incubator (95−100% humidity, 5% CO_2) overnight. On Day 0, the seeding medium was removed from each well and cells were gently washed with 1 mL sterile PBS. Approx. 0.5 mL of fresh "complete DMEM" medium and the FITC-labeled vesicles were added at a ratio of 500:1. The plate was returned to the incubator for 24 h. On Day 1, the medium was removed from each well, and cells were gently washed with PBS. Samples were fixed using paraformaldehyde before being stained with Deep Red Plasma stain and subsequently mounted onto microscopy slides using DAPI Fluoromount G for confocal microscope observation using a Leica TCS SP2 confocal microscope.

Cellular Uptake Test (Flow Cytometry)

Again, on Day −1 cells were seeded in "complete DMEM" at a cell density of 200 000 cells per well in 0.5 mL seeding volume before the plate was placed in a humidified incubator (95−100% humidity, 5% CO_2) overnight. On Day 0, the seeding medium was removed from each well and cells were gently washed with 1 mL sterile PBS. Approx. 0.5 mL fresh "complete DMEM" medium and the FITC-labeled vesicles were added at a mass ratio of 500:1. The plate was returned to the incubator for 24 h. On Day 1, the medium was removed from each well, and cells were gently washed with PBS, trypsinized, fixed with paraformaldehyde, and resuspended into PBS. Cell suspensions were subsequently

analyzed using an Apogee A-50 Micro Flow cytometer using a 488 laser and three light scattering detectors. At least 10000 cells were analyzed in each experiment.

7.3 Experimental for Chapter 3

Materials

Furan (≥99%, Aldrich) trifluoroacetic acid (TFA) (99%, Aldrich), fluorescein isothiocyante isomer 1 (FITC) (≥90% HPLC, Aldrich), phosphate buffered saline (PBS) (tablets, Aldrich), nuclease free water (Qiagen) tris (2- carboxyethyl)phosphine hydrochloride (TCEP) (≥98%, Aldrich), triphosgene (98%, Aldrich), D,L'-Dithiothreitol (DTT) (Aldrich), Ethylenediaminetetraacetic acid disodium salt dehydrate (EDTA, Chem-Supply), H-Lys(Fmoc)-OH (Mimotopes), pyridine (AR, Scharlau), hydrochloric acid (37%, Scharlau), triethylamine (TEA) (99%, Ajax Fine Chemicals), H-Glu(OtBu)-OH (Bachem), Mal-PEG-NH_2·TFA 5 kDa (Jenkem Technology), sodium chloride (AR, Chem-Supply), acetic acid (Glacial AR, Chem-Supply), lithium bromide (99.9%, Aldrich), and sodium hydroxide (AR, Chem-Supply) were used as received. Pentane (anhydrous ≥99%, Aldrich), methanol (AR, Chem-Supply), chloroform (AR, Chem-Supply), dichloromethane (AR, Chem- Supply), chlorotrimetylsilane (≥99%, Aldrich), diethyl ether (AR, Chem-Supply), dimethylformamide (DMF) (extra dry, 99.8%, Acros), and toluene (AR, Ajax Fine Chemicals) were used as received. Tetrahydrofuran (THF) (AR, Chem-Supply) was distilled from benzophenone and sodium metal under argon. Dimethyl sulfoxide (DMSO) (≥99%, Aldrich) was stored under 3 Å molecular sieves. DMSO-d_6 (99.9%) was purchased from Cambridge Isotope Laboratories and Aldrich and stored under 3 Å molecular sieves. Dialysis tubing (Snakeskin 3.5 kDa cutoff) was purchased from ThermoScientific. The single-stranded 20 nucleotide DNA model aptamer contained sequence 5'-GCGACTGGTTTACCCGGTCG-3' with 5' thiol modification protected as a disulfide (-S-S-C_6H_{12}-OH, 5ThioMC6-D) and was synthesized by IDT (Integrated DNA Technologies). Agarose (molecular biology certified), nucleic acid sample loading dye/sample buffer (5 x), ethidium bromide (10 mg/mL), TAE buffer (50 x), 100 bp DNA molecular ruler were all purchased from Bio-Rad and used as received. G-25 sephadex and 3 kDa nanoseparation spin columns purchased from Enzymax and Pall Corporation respectively. Gel extraction/purification performed using a nucleospin Gel and PCR clean-up kit (Machery-Nagel).

Synthesis of Block Copolymers

*Synthesis of Furan-Protected Mal-PEG-NH_2HCl (**P1**)*

As per experimental section 7.2.

$_L$-Glutamic Acid and $_L$-Lysine N-Carboxyanhydrides (NCAs).[1-2]

The amino acid (γ-*tert*-butyl)-$_L$-glutamic acid (1 g, 4.92 mmol) or (ε-Fmoc)-$_L$-lysine (1 g, 2.72 mmol) was dissolved in anhydrous THF (40 mL) in a three-necked round bottomed flask under argon. Triphosgene (glu: 0.72 g, 2.43 mmol, 1.5 equiv phosgene; lys: 0.76 g, 2.56 mmol, 2.8 equiv phosgene) was then added, and the mixture was heated at 60 °C for 2 h with continuous stirring. After cooling to room temperature, the reaction mixture was sparged with argon for 45 min into a sat. NaOH solution, then solvent removed *in vacuo*. The resulting residue was recrystallized from THF (anhydrous) and *n*-pentane (anhydrous) overnight. The resulting crystals were filtered and washed with *n*-pentane (anhydrous), dissolved in minimal THF (anhydrous) then precipitated and washed (×2) with dry *n*-pentane to afford white solids (yields: ~70%). (γ-*tert*-butyl)-$_L$-glutamic acid NCA ^{1}H NMR (400 MHz, $CDCl_3$) δ_H (ppm): 1.43 (s, 9H, γ-tBu), 2.00-2.08 (m, 1H, C*H*$_2$CH$_2$CO), 2.18-2.27 (m, 1H, C*H*$_2$CH$_2$CO), 2.44 (t, 2H, *J*= 6.6 Hz, CH$_2$C*H*$_2$CO), 4.35 (t, 1H, *J*= 6.0 Hz, ring C*H*N), 6.47 (s, 1H, ring NH)). (FMoc)-$_L$-lysine NCA ^{1}H NMR (400 MHz, $CDCl_3$): δ_H 1.41-1.89 (m, 6H, -NH-CH$_2$-C*H*$_2$-C*H*$_2$-C*H*$_2$-), 3.15 (m, 2H, -NH-C*H*$_2$-CH$_2$-CH$_2$-CH$_2$-), 4.22 (m, 2H, ring C*H*N and FMoc -CH$_2$-C*H*-), 4.41 (s, 2H, *J*= 4.8 Hz, FMoc -C*H*$_2$-CH-), 6.04 (s, 1H, NCA ring NH), 7.31 (t, 2H, *J*= 7.6 Hz, ArH), 7.41 (t, 2H, *J*= 8.0 Hz, ArH), 7.61 (d, 2H, *J*= 7.2 Hz, ArH), 7.75 (d, 2H, *J*= 7.2 Hz, ArH), 8.78 (s, 1H, -NH-C*H*$_2$-CH$_2$-CH$_2$-CH$_2$-).

Synthesis of Furan-Protected and Side-Chain Protected Block Copolymers

*Synthesis of Furan-Protected Mal-PEG-b-PLG(γ-tBu)-NH_2 (**P2**)*

As per experimental section 7.2 using the following quantities:

γ-tBu Glu NCA (20 mg, 87.2 µmol) and furan protected Mal-PEG-NH_2HCl (**P1**) (53 mg, 10 µmol, M/I = 9) dissolved in anhydrous DMF (0.3 mL). (Yield: 50 mg, 71%). M_n(GPC)= 6.4 kDa, PDI 1.12. ^{1}H NMR (400 MHz, d$_6$-DMSO) δ_H (ppm): 1.38 (s, γ-tBu), 1.72-1.87 (m, C*H*$_2$-CH$_2$-COO), 2.20-2.32 (m, CH$_2$-C*H*$_2$-COO), 2.91(s, DA c_{exo}), 3.50 (s, 455H, C*H*$_2$-C*H*$_2$-O-), 4.24 (m, -N-C*H*-CO), 5.11 (s, DA b_{exo}), 5.29 (m, DA b_{endo}), 6.37 (s, DA a_{exo}), 6.54 (s, DA a_{endo}), 7.99

(m, CON*H*). (See **Appendix Figure A3.1** and **Appendix Figure A2.2** for DA adduct stereochemistry assignments).

*Synthesis of Furan-Protected Mal-PEG-b-(PLG(γ-tBu)-r-PLL(ε-Fmoc))-NH₂ (**P3**)*

To an oven-dried RBF was added *γ*-tBu Glu NCA (10 mg, 43.6 μmol) and *ε*-Fmoc Lys NCA (13mg, 33.3 μmol) under N_2 followed by anhydrous DMF (0.4 mL) and stirred to dissolve for 5 min. Furan protected Mal-PEG-NH_2HCl (**P1**) (25 mg, 4.7 μmol, M/I = 10 Glu, 7 Lys) dissolved in anhydrous DMF (0.15 mL) was then added to the flask under N_2. Identical reaction conditions and workup used in **P2** above were performed. White-cream powder (Yield: 35 mg, 78%). M_n(GPC)= 7.2 kDa, PDI 1.14. ^{1}H NMR (400 MHz, d_6-DMSO) δ_H (ppm): 1.36 (s, Glu *γ*-tBu) 1.40-1.65 (m, Lys -NH-CH_2-C*H₂*-C*H₂*-C*H₂*-), 1.7-1.90 (m, Glu -C*H₂*-CH_2-CO-), 2.1-2.30 (m, Glu -CH_2-C*H₂*-CO-), 2.91(s, DA c_{exo}) 2.94 (s, Lys -NH-C*H₂*-CH_2-CH_2-CH_2-), 3.50 (s, 455H, -C*H₂*-C*H₂*-O-), 4.25 (m, -N-C*H*-CO), 5.11 (s, DA b_{exo}), 5.29 (m, DA b_{endo}), 6.38 (s, DA a_{exo}), 6.54 (s, DA a_{endo}), 7.23-7.86 (Lys Ar*H*). (See **Appendix Figure A3.2** and **Appendix Figure A2.2** for DA adduct stereochemistry assignments).

Synthesis of Fully Deprotected Block Copolymers

*Mal-PEG-b-PLG-NH₂ (**P4**)*

t-Butyl deprotection and retro DA was conducted in a one pot procedure. Protected block copolymer (**P2**) (25 mg, 34.8 μmol Glu units), DCM (1.4 mL), and TFA (1.2 mL) were stirred vigorously for 1 h, followed by the addition of toluene (5 mL). DCM and TFA were then removed under low vacuum with excess TFA removed through DCM azeotrope. The contents were then refluxed at 120 °C for 6 h, concentrated, dissolved in minimal methanol, and precipitated in chilled ether. Precipitate was isolated and dried under vacuum to give a white powder (**P4**) (15 mg, 65%). ^{1}H NMR (400 MHz, d_6-DMSO) δ_H (ppm): 1.75-1.90 (m, C*H₂*-CH_2-COO), 2.10-2.33 (m, CH_2-C*H₂*-COO), 3.51 (s, 456H, -C*H₂*-C*H₂*-O-), 4.21 (s, -N-C*H*-CO), 7.00 (s, mal -C*H*=C*H*-), 8.01 (m, CON*H*). (see **Appendix Figure A3.3**)

*Mal-PEG-b-(PLG-r-PLL)-NH₂ (**P5**)*

t-Butyl deprotection, Fmoc deprotection and retro DA were conducted sequentially. *t-Butyl deprotection*; Protected copolymer (**P3**) (25 mg, 34.9 μmol Glu units), DCM (1.8 mL),

and TFA (1.4 mL) were stirred vigorously for 1 h. DCM and TFA were then removed under vacuum, the contents dissolved up in minimal MeOH and precipitatated and washed in chilled ether, dried. *Fmoc deprotection*; Dried copolymer (15 mg, 9.80 μmol Lys groups), DMF (anhydrous) (0.5 mL), and DBU (5 uL, 33 μmol) stirred vigorously for 4 min, quenched with small amount of 1M HCl, then dialyzed against MeOH overnight (3 x 500 mL), concentrated and dried. *Retro DA*; To the dried contents were then added toluene (4 mL), with mixture then refluxed at 120 °C for 6 h. Contents were then concentrated, dissolved in MeOH with small amount of TFA, precipitated and washed in chilled ether to give a white solid (**P4**) (10 mg, 50%). %). ^{1}H NMR (400 MHz, d$_6$-DMSO) δ_H (ppm): 1.25-1.70 (m, Lys -NH-CH$_2$-C*H$_2$*-C*H$_2$*-C*H$_2$*-), 1.7-1.95 (m, Glu -C*H$_2$*-CH$_2$-CO-), 2.15-2.35 (m, Glu -CH$_2$-C*H$_2$*-CO-), 2.76 (s, Lys -NH-C*H$_2$*-CH$_2$-CH$_2$-CH$_2$-), 3.50 (s, 455H, -C*H$_2$*-C*H$_2$*-O-), 4.21 (m, -N-C*H*-CO), 7.00 (s, mal -C*H*=C*H*-), 8.01 (m, CON*H*) (see **Appendix Figure A3.4**)

Fluorescent Labelling of Deprotected Block Copolymers

*Mal-PEG-b-PLG-NH$_2$-FITC (**P4**-FITC)*

FITC (0.78 mg, 2.00 μmol) dissolved in anhydrous DMSO (110 μL) was added to Mal-PEG-*b*-PLG-NH$_2$ (**P4**) (10 mg, 1.52 μmol), followed by addition of triethylamine (TEA, 0.12 μL, 0.86 μmol, 0.5 equiv) as catalyst. The yellow-brown solution was stirred in the dark at 21 °C, 1050 rpm for 14 h. The reaction was then quenched with a few drops of 1 M HCl, and dialyzed against methanol over 48 h (5 x 500 mL). Contents were then concentrated, precipitated in chilled ether, centrifuged, and dried to afford a light yellow solid (Yield: 8 mg, 75%). UV-Vis analysis determined FITC conjugation of ~50 mol %.

*Mal-PEG-b-(PLG-r-PLL)-NH$_2$-FITC (**P5**-FITC)*

FITC (2.5 mg, 6.42 μmol) dissolved in anhydrous DMF (60 μL) was added to Mal-PEG-*b*-(PLG-*r*-PLL)-NH$_2$ (**P5**) (6 mg, 5.2 μmol total amine including side chains), followed by addition of pyridine (30 μL, 0.37 mmol). Anhydrous DMSO (20 μL) was then added and the yellow-brown solution stirred in the dark at 21 °C, 1050 rpm for 14 h. The reaction was then quenched with a few drops of 1 M HCl, and dialyzed against 15% DMSO 85% MeOH solution 48 h (5 x 500 mL). Contents then concentrated, dissolved up in water and freeze-dried to afford a yellow solid (Yield: 5 mg, 81%). UV-Vis analysis determined FITC conjugation of ~50 mol % relative to all NH$_2$ including side chains.

Reduction of DNA (disulfide protected) with DTT

Reduction of DTT was performed as per DNA manufacturers guidelines. In a 0.7 mL eppendorf tube was added DNA stock solution (50 μL, 16.3 nmol), TEA (1 μL) and DTT stock solution (2 μL, 4 μmol), and let to sit for 1 h. The solution was then extracted with ethyl acetate (4 x 400 μL) to remove DTT and DNA 5' thiol protecting group (5ThioMC6-D). Aqueous phase was then filtered through a G-25 mini sephadex spin column and freeze-dried to give a white solid. DNA was then dissolved in sterile PBS and analyzed for concentration using UV-Vis. DNA was reduced immediately before conjugation to polymer.

DNA Conjugation to Polypeptide-Based Polymers

In a typical conjugation procedure, reduced thiol-functionalized DNA (2 nmol) in sterile PBS was added to a 0.7 mL eppendorf tube, along with FITC-polymer (40 nmol) and EDTA (45 nmol) both in sterile PBS. Final DNA concentration ~ 140 μM. The reaction mixture was then stirred at 1050 rpm for 4 h at 37 °C. Samples were then frozen and lyophilized.

Gel Electrophoresis- Reaction Analysis

A 2% agarose gel solution was prepared (0.7 g, 35 mL TAE buffer 1X) and stained with ethidium bromide (3.5 μL). The solution was poured into gel tray, with gel comb placed into solution and allowed to set with a final gel thickness of ~0.4 cm. 200 mL TAE buffer (1X) was added to electrophoresis tray apparatus. For general sample loading into gel wells, 8 μl of sample was mixed with 2 μL DNA loading dye, mixed well, then added gently to well. Gel electrophoresis was performed on a powerpac (Bio-Rad) and a mini-sub cell GT (Bio-Rad) at 100V for ~30-40 min. Gels imaged on a Chemidoc XRS system (Bio-Rad).

Gel Electrophoresis (Preparatory)- Conjugate Isolation

For preparative gel electrophoresis, a 1% agarose gel solution (0.35 g, 35 mL TAE buffer 1X) was prepared and stained with ethidium bromide (3.5 uL). The solution was poured into tray, a taped gel comb (number of comb teeth taped depending on loading volume) placed into solution and allowed to set with final gel thickness of ~0.4 cm. 200 mL TAE buffer (1X) was added to electrophoresis tray apparatus. After loading sample, gel

electrophoresis was conducted at 60V for 35 minutes. Gels were then imaged on a Chemidoc XRS system (Bio-Rad) with conjugate band removed by scalpel. Conjugate gel band was then weighed, and the conjugate isolated from the agarose gel via use of a gel extraction/purification kit (Machery-Nagel) with some minor modifications required. Conjugate isolation was verified through gel electrophoresis (1% Agarose, 1X TAE, 60 V) and UV-Vis analysis.

Anion Exchange Chromatography Analysis and Conjugate Isolation

Conjugate analysis and isolation was performed using anion exchange liquid chromatography on a preparative AKTApurifier 100 (GE Life Sciences) using either HiTrap Q HP (7 mm, 34 µm, GE Life Sciences) or MonoQ HR5/5 columns (5 mm, 10 µm, GE Life Sciences). Simultaneous UV-Vis detection at wavelengths of 215 nm, 260 nm and 495 nm. Fractions were collected using a carousel fraction collector (Frac-950, GE Life Sciences). The solvent gradient at 1 ml/min was: 0': 100% A; 10': 50% A/50% B; 20'; 100% B, where A = 20 mM Tris pH 8.5, B = 20 mM Tris pH 8.5 + 1.25 M NaCl. Collected fractions were then desalted and concentrated using a 3 kDa mini spin column then analyzed using gel electrophoresis.

7.4 Experimental for Chapter 4

Materials

H-L-Lys(Z)-OH (Bachem), Z-Glu(OBzl)-OH (Mimotopes), triphosgene (≥98%, Aldrich), dimethylformamide (DMF) (anyhd., 99.8%, Acros), hydrobromic acid (HBr; 33% in acetic acid, Aldrich), *N*-timethylsilyl)allylamine (N-TMS allylamine; 95%, Acros), phosphate buffered saline (PBS) tablets (Aldrich), trifluoroacetic acid (TFA; Aldrich), *n*-pentane (anhydrous ≥99%, Aldrich), diethyl ether (AR, Chem-Supply), *N*-(3-(dimethylamino)propyl)-N′-ethylcarbodiimide hydrochloride (EDCI; ≥98%, Aldrich), *N*-hydroxysulfosuccinimide sodium salt (sulfo-NHS; ≥98%, Fluka), fluorescein isothiocyanate isomer 1 (FITC; ≥90%, Sigma), dimethyl sulfoxide (DMSO; AR, Ajax Finechem), methanol (MeOH; AR, Chem-Supply), ethanol (EtOH; AR, Chem-Supply), cyclohexane (AR, Ajax Finechem), protease from Streptomyces griseus Type XIV (Sigma).

Tetrahydrofuran (THF) was distilled from benzophenone and sodium metal under nitrogen.

Synthesis of Polymeric Precursors

L-Glutamic Acid and L-Lysine N-Carboxyanhydrides (NCAs).[1-2]

The amino acid (γ-OBzl)-L-glutamic acid (3 g, 12.64 mmol) or (ε-Z)-L-lysine (3 g, 10.70 mmol) was dissolved in anhydrous THF (75 mL) in a three-necked round bottomed flask under argon. Triphosgene (glu: 1.5 g, 5.05 mmol, 1.2 equiv phosgene; lys: 1.27 g, 4.28 mmol, 1.2 equiv phosgene) was then added, and the mixture was heated at 60 °C for 2 h with continuous stirring. After cooling to room temperature, the reaction mixture was sparged with argon for 45 min into a sat. NaOH solution, then solvent removed *in vacuo*. The resulting residue was recrystallized from THF (anhydrous) and *n*-pentane (anhydrous) overnight. The resulting crystals were filtered and washed with *n*-pentane (anhydrous), dissolved in minimal THF (anhydrous) then precipitated and washed (×2) with dry *n*-pentane to afford white solids (yields: ~70%). (Z)-L-lysine NCA ^{1}H NMR (400 MHz, $CDCl_3$): δ_H 1.40-1.60 (m, 4H, -NH-CH_2-CH_2-C*H*$_2$-C*H*$_2$-), 1.81-1.94 (m, 2H, -NH-CH_2-C*H*$_2$-CH_2-CH_2-), 3.18 (m, 2H, -NH-C*H*$_2$-CH_2-CH_2-CH_2-), 4.25 (t, 1H, *J*= 5.6 Hz, C*H*N), 4.97 (s, 1H, side chain NH), 5.09 (s, 2H, C*H*$_2$-ArH), 7.04 (s, 1H, ring NH), 7.3-7.4 (m, 5H, ArH). (OBzl)-L-Glutamic acid NCA ^{1}H NMR (400 MHz, $CDCl_3$): δ_H 2.09-2.30 (m, 2H, C*H*$_2$$CH_2$CO), 2.60 (t, 2H, *J*= 6.8 Hz, CH_2C*H*$_2$CO), 4.38 (t, 1H, *J*= 6.0 Hz, C*H*N), 5.14 (s, 2H, C*H*$_2$-ArH), 6.58 (s, 1H, ringNH), 7.33 -7.38 (m, 5H, ArH).

Synthesis of Protected Random Copolypeptides. Poly(OBzl-L-glutamic acid)-*r*-Poly(Z-L-lysine) (PBLG-*r*-PZLL).

Protected Random Copolymer A

To a dry 25 mL RBF was added both Glu NCA (0.8 g, 3.04 mmol) and Lys NCA (0.233 g, 0.76 mmol) under nitrogen. Dry DMF was then added and stirred to dissolve. To the stirring solution was added *N*-(trimethylsilyl)allylamine (9.12 µL, 54.3 µmol, M/I = 70), and the clear solution was stirred for 72 h under argon with bleed at room temperature. The reaction mixture was then concentrated under high vacuum, dissolved up in minimal DCM, and precipitated in chilled methanol (40 mL), washed in ether (×2), and then dried *in vacuo* to afford a clear tacky solid (0.83 g, yield: 81%). M_n (GPC)= 7.2 kDa PDI 1.70. ^{1}H

NMR (d_6-DMSO): δ_H 1.20-1.90 (m, Lys -NH-CH_2-C*H*$_2$-C*H*$_2$-C*H*$_2$-), 2.0-2.40 (m, Glu -C*H*$_2$-C*H*$_2$-CO-), 2.94 (s, Lys -NH-C*H*$_2$-CH_2-CH_2-CH_2-), 3.92 (s, C*H*-NH backbone), 4.99 (m, C*H*$_2$-ArH), 5.76 (m, CH_2=C*H*-), 7.26 (s, ArH), 8.38 (brs, CO-NH); see **Appendix Figure A4.1**. Relative ratios of the polypeptides determined from ^{1}H NMR spectra of the fully deprotected products shown in **Appendix Figure A4.3**.

Protected Random Copolymer B

Identical procedure to above random copolymer A, instead using Glu NCA (0.43 g, 1.63 mmol), Lys NCA (0.5 g, 1.63 mmol), and *N*-(trimethylsilyl)allylamine (43.84 μmol, M/I = 74). After drying, a clear tacky solid was obtained (0.61 g, Yield: 66%). M_n (GPC) = 6.7 kDa; PDI 1.80. ^{1}H NMR (d_6-DMSO): Same peak assignments as protected random copolymer A (see **Appendix Figure A4.2**). Relative ratios of the polypeptides determined from ^{1}H NMR spectra of the fully deprotected products shown in **Appendix Figure A4.4**.

Preparation of Deprotected Random Copolypeptides Poly(L-glutamic acid)-*r*-Poly(L-lysine) (PLG-*r*-PLL).

Deprotection of the OBzl and CBz (Z) protecting group was achieved through previously reported procedure[7-8] to afford the water-soluble random copolypeptides.

Random Copolymer A

To a 25 mL RBF was added the protected random copolymer A (0.83 g, (0.12 mmol) followed by trifluoroacetic acid (TFA) (5.3 mL). The solution was stirred until the polymer was dissolved, followed by addition of HBr (33% in AcOH, 5.3 mL). The resulting solution was stirred at 35 °C with thick precipitate observed soon after. The reaction mixture was stirred for a total of 2 h at 35 °C, with the suspension then transferred directly into diethyl ether, washed in ether (×2), then dried *in vacuo* overnight. The solid was then dissolved in DI H_2O and dialyzed against 2 L DI water (×3) for 24 h. The polymer precipitated in solution during the dialysis procedure, with the suspension then freeze-dried to obtain a white solid (~300 mg). ^{1}H NMR (D_2O + NaOH): δ_H 1.33-1.72 (m, Lys -NH-CH_2-C*H*$_2$-C*H*$_2$-C*H*$_2$-), 1.89-1.99 (m, Glu -C*H*$_2$-CH_2-CO-), 2.23 (m, Glu -CH_2-C*H*$_2$-CO-), 2.56 (m, Lys -NH-C*H*$_2$-CH_2-CH_2-CH_2-), 4.27 (m, C*H*-NH backbone). Using ^{1}H NMR analysis, selected glutamic acid and lysine side chain methylene protons were integrated to determine a

glutamic acid:lysine ratio of 1:0.29 (see **Appendix Figure A4.3**). Based on this ratio and the calculated M_n from GPC analysis of the protected copolymer, DP is determined to be 31 (24 glutamic, 7 lysine).

Random Copolymer B

Identical procedure to above random copolymer A. During dialysis, no precipitation of the dialysis contents is observed, with the clear solution then freeze-dried to obtain a white powder (~400 mg). ^{1}H NMR (D_2O + HCl): δ_H 1.16-1.65 (m, Lys -NH-CH_2-C*H*$_2$-C*H*$_2$-C*H*$_2$-), 1.88-2.00 (m, Glu -C*H*$_2$-CH_2-CO-), 2.25-2.40 (m, Glu -CH_2-C*H*$_2$-CO-), 2.69 (s, Lys -NH-C*H*$_2$-CH_2-CH_2-CH_2-), 3.81 (s, C*H*-NH backbone). Using ^{1}H NMR analysis, selected glutamic acid and lysine side chain methylene protons were integrated to determine a glutamic acid:lysine ratio of 1:0.73 (see **Appendix Figure A4.4**). Based on this ratio and the calculated M_n from GPC analysis of the protected copolymer, DP is determined to be 28 (16 glutamic, 12 lysine).

Preparation of Cryogels

Cryogelation reactions were conducted using an EDC/sulfo-NHS cross-linking strategy similar to reported previously.[9]

Cryogel A

A typical procedure for the preparation of cryogel A was as follows: The deprotected random copolymer A (20 mg) was suspended in DI H_2O (400 μL) followed by addition of small amounts of 2 M NaOH to achieve a pH of 5. Brief vortexing resulted in the fully dissolved polymer solution. EDCI and sulfo-NHS (molar ratio of EDCI/sulfo-NHS of 2:1) were then dissolved individually in 100 μL DI water. Based on the amount of NH_2 lysine side chain groups (calculated from the relative ratios on the deprotected polypeptide above) a 2.5-fold excess of EDCI was used. All solutions were kept on ice for 15 min. Subsequently, EDCI and sulfo-NHS solutions were added to polymer solution, mixed briefly by vortexing then withdrawn into cylindrical syringes and placed in freezer.

Cryogel B

A typical procedure for the preparation of cryogel B was as follows: The deprotected random copolymer B (20 mg) was initially suspended in DI H2O (400 μL) followed by addition of small amounts of 1 M HCl to achieve a pH of 4. Brief vortexing of the solution to dissolve polymer was followed by centrifugation to remove small amounts of insoluble material. The clear polymer solution was then cross-linked through identical EDCI/sulfo-NHS procedure described above.

All cryogelation procedures were conducted at −18 °C for 24 h at a final polymer concentration of 3.33% w/v for all samples. After completion of the cryogelation process, the resulting samples were removed and thawed at room temperature. The cryogels were then immersed in DI water and washed thoroughly with complete replacement of the solution three times (3 × 100 mL). The gels were then washed thoroughly and equilibrated in PBS before use (2 × 100 mL). Cryogels were synthesized shortly before measurements.

Characterization of Cryogels

Microstructure in the Wet State

The morphological features of the cryogel scaffolds in the wet state were examined by environmental scanning electron microscopy (ESEM) and confocal laser scanning microscopy (CLSM). ESEM (FEI Quanta 200 ESEM FEG) was performed under low vacuum setting with samples mounted on carbon tape placed on aluminum stubs. CLSM (Nikon A1R+) was performed using both 20X or 40X objectives and an excitation wavelength of 488 nm. All images were generated by optical sectioning in the z-direction. Images were stacked in the z-direction using ImageJ software. For CLSM measurements, fluorescein isothiocyanate (FITC) was covalently labeled to the cross-linked gels using a previously reported procedure.[10] Gels were incubated with FITC in 0.1 M sodium phosphate buffer (pH 9) overnight followed by extensive washing in buffer to remove unconjugated FITC. CLSM images were analyzed using ImageJ software to determine the pore size and pore wall thickness of the cryogels. Analysis was performed on at least three separate gel cross-section samples with pore size measurements representing the longest pore dimension.

Mechanical Tests

Compression tests on gels were performed using an Instron testing system (Instron 5848). Fully swollen cylindrical gels (cryogel A: ~13 mm diameter, 11 mm height; cryogel B: ~8 mm diameter, 8.5 mm height) were deformed (at constant volume) between two parallel plates, with a strain rate of 60% per minute. Engineering stresses and strains were recorded. The gel cylinders were kept hydrated in PBS solution (pH 7.4) throughout the tests. Young's moduli (compressive) were determined by the average slopes of the stress–strain compression curves over the linear elastic strain range 0–10%. Runs were performed in triplicate.

Swelling Properties and Gel Fraction of Cryogels

For equilibrium mass swelling ratios, Q_M, cryogel samples (n = 4) fully equilibrated in PBS were first weighed, then freeze-dried. Dried samples were then reweighed. The equilibrium mass swelling ratio, Q_M, was defined as the ratio of the fully swollen cryogel mass to that of its dry mass:

$$Q_M = \frac{m_s}{m_d}$$

where m_s and m_d are the weights of the swollen gel and dried gel, respectively. The swelling data was corrected by subtracting the soluble fraction of salt in PBS from the gel. Equilibrium volume swelling ratios (Q_v) were calculated as per a previously reported procedure.[11] The diameter of ethanol-dried cryogel samples (n = 3) were first measured, with samples then incubated in PBS for 2 h, followed by measurements of their swollen diameters. The volume swelling ratio was calculated by the following equation:

$$Q_V = \left(\frac{D_s}{D_d}\right)^3$$

where D_s and D_d are the diameters of the swollen gel and dried gel, respectively

The gel fraction (W_g%) of the cryogels was determined gravimetrically by weighing dried samples (m_d):

$$\text{Gel fraction, } W_g\% = \frac{m_d}{m_0} \times 100$$

where m_0 is the weight of the polymer components in the initial solution (random copolypeptide).

Porosity

The porosity of the gels was estimated by cyclohexane uptake which determines pore volume.[12-13] Porosity (*P*) was then calculated as volume fraction (%) of pores in the gel. Gel samples were first dried by gradual dehydration with ethanol (25, 50, 75, and 100%) then dried in a vacuum oven at 55 °C overnight. Pre-weighed oven-dried gels were immersed in cyclohexane for 1 h, excess liquid was removed, and the samples were weighed. Porosity was calculated as:

$$P\% = \frac{m_s - m_d}{m_d} \times 100$$

where m_s and m_d are the swollen and dry weights of the gels, respectively. Measurements were made in triplicate for each sample.

Enzymatic Degradation of Cryogels

Enzymatic degradation analysis was performed over a period of 14 days using protease (Type XIV from *Streptomyces griseus*). Cryogels were first sterilized and dried through gradual dehydration in EtOH (0−100%) then drying overnight in vacuum oven at 55 °C overnight. Cryogels (~8 mg dry weight) were then added to 2 mL eppendorf tubes, followed by addition of 1.8 mL of 200 μg/mL protease (PBS) solution, and incubated at 37 °C with gentle mixing. Control samples were prepared through an identical procedure with the addition of PBS only (no enzyme). At designated time points, gels were washed thoroughly in deionized water, sterilized, and dried in EtOH, as per above procedure, and reweighed. Fresh enzyme/buffer addition and drying procedure was used for each time point measurement. The degree of degradation DD(%) was determined by dry weight change at each time point and calculated as:

$$DD(\%) = \frac{m_i - m_t}{m_i} \times 100$$

where m_i corresponds to the initial dry weight of sample before degradation, and m_t corresponds to the dry weight of sample after time point of degradation.

Cryogels as Cell Scaffolds In Vitro

The potential of synthetic polypeptide cryogels as cell scaffolds was evaluated using mammalian fibroblast (NIH/3T3) cells. Cell Culture. NIH-3T3 fibroblast cells were obtained from American Type Culture Collection (ATCC). The cells were cultured according to standard procedure. Briefly, Dulbecco's Modified Eagle Medium (DMEM, Gibco, Invitrogen, U.S.A.) was supplemented with 10% Fetal Bovine Serum (FBS, Gibco, Invitrogen, U.S.A.), 2 mM L-glutamine (Gibco, Invitrogen, U.S.A.), 100 units/mL penicillin (Gibco, Invitrogen, U.S.A.), and 100 μg/mL streptomycin (Gibco, Invitrogen, U.S.A.). Cells were passaged every 3−4 days using 0.25% trypsin- EDTA (1×, Gibco, Invitrogen, U.S.A.) at subconfluence and incubated at 37 °C, 5% CO_2, and 90% humidity. Cell passages 5−15 were used for cell experiments.

Cryogel Biocompatibility/Cytotoxicity Studies

Swollen cryogel samples were cut into thin circular disks (cryogel A: ~6 mm diameter, ~2 mm thickness; cryogel B: ~3.5 mm diameter, ~2 mm thickness). Cryogel A disks were then cut into quarter circles and cryogel B disks into half-circles to cover approximately same interfacial surface area of a 96-well plate. Samples were sterilized in EtOH (50% 1.5 h, 75% 2 h) then thoroughly washed with sterile DI H_2O. Samples were then added to 96-well plates (Corning), washed further with sterile DI H_2O, and then equilibrated in complete DMEM in an incubator overnight (changing solution twice). Cells were first cultured in 96- well culture plates (cell density 3.125×10^3 cells cm^2) and allowed to attach. After 6 h, the medium was aspirated and the cryogel disks were placed inside the wells on top of the attached cells. The fresh culture medium was added into the wells and was changed every alternative day with fresh media during the experiments. The cell viability was probed at 1, 3, 5, and 7 days with the colorimetric CCK-8 assay (Sigma), which is based on the reduction of WST-8 to a formazan dye (orange color) by dehydrogenase activity inside the cells. In order to avoid adsorption of formazan dye by cryogels, they were transferred into another well before addition of WST-8 solution. The culture medium was changed and 10 μL WST-8 solution was added to the wells, followed

by incubation for 4 h. Then, the medium was removed and the absorbance was measured with microplate reader (TECAN M200 infinite Pro) at wavelength of 450 nm. After washing the wells with PBS, the cryogels were transferred back into the wells followed by addition of new medium. The wells were incubated and the same procedure was repeated every alternative day (at 1, 3, 5, and 7 days). At each time point, four control wells cultured without cryogels and four wells cultured in the presence of cryogel were analyzed.

Cell Attachment/Interaction Studies

Swollen FITC-labeled cryogel samples were cut into thin circular disks (cryogel A: ~6 mm diameter, ~2 mm thickness; cryogel B: ~3.5 mm diameter, ~2 mm thickness). All samples were added directly to 96-well plates and sterilized and washed as per above procedures. The gels were then saturated in complete DMEM medium overnight. The FITC-labeled cryogels were placed in 96-well tissue culture plate and 2.4×10^5 cells were seeded in 50 µL of medium on each cryogel disc. The cryogels were incubated for 4 h with saturated cell suspension to allow cell attachment. Then, 100 µL of culture medium was added and the cryogels were incubated. After 2 and 4 days, the cryogel discs were transferred into new wells and were washed two times with medium. To analyze cell growth in the cryogels, live cell staining and cell nuclear stain were performed using Deep Red and DAPI (4′,6-diamidino-2 phenylindole), respectively. Cells were incubated with Deep Red plasma membrane stain (1:1000, Invitrogen) for 20 min. The samples were then washed three times with PBS and fixed with 4% paraformaldehyde (Aldrich) at room temperature for 10 min. After rinsing the cryogels three times with PBS, the cell nuclei were stained using DAPI (1:1000, Merck Millipore) for 10 min at room temperature. The cryogels were saturated with PBS and imaged on CLSM using excitation wavelengths of 405 nm, 488 and 640 nm. The experiment was repeated at least three times. All images were generated by optical sectioning in the z direction. Images were stacked in the z-direction using ImageJ software.

Cell Proliferation Studies

Swollen cryogel samples were cut into thin circular disks (cryogel A: ~6 mm diameter, ~4 mm thickness; cryogel B: ~3.5 mm diameter, ~4 mm thickness). Cryogel A disks were

then cut into half circles, while cryogel B samples were kept as full circle to ensure comparable swollen gel sizes. Cryogels were sterilized, washed, and equilibrated in medium as per above procedure. Prior to cell seeding, the cryogels were dehydrated by a sterile filter paper for 2 min to remove and expel culture medium from the pores. This procedure facilitates the penetration of the cells into the interior of the cryogel's porous structure. The cryogels were placed into the wells of 24-well tissue culture plates and a cell suspension (105 cells in 100 μL) was seeded onto the top of each cryogel disc. The cryogels with the cell suspension were incubated in order for the cells to have time to attach to the pore walls of the cryogels. After 4 h, 500 μL of complete medium were added to each well and the well-plates were returned to the incubator. Every 2 days, the culture medium was changed and the well surfaces were checked to investigate whether migration of cells from the interior of the cryogels onto the well surfaces occurred. Once cells were observed on the well surfaces, the cryogels were carefully transferred to new wells in the well-plate and were incubated further. The step enabled only cells growing on/in the cryogel to be quantified, and not those growing on the underlying tissue culture plastic.

After 1, 4, 7, 10, and 14 days, WST-8 solution was added to each well followed by 4 h of incubation. Then a specific volume of solution was aspirated and transferred to a new well, where the absorbance was measured at 450 nm. Cells cultured on polystyrene tissue culture well-plates were used as control. Measurements were performed in triplicate.

Statistical Analysis

Data are shown as averages and standard deviations. Student's *t*-tests were used to analyze the statistical differences between samples for cytotoxicity and proliferation measurements and were considered significant at $p < 0.05$.

7.5 Experimental for Chapter 5

Materials

H-L-Lys(Z)-OH (Bachem), H-(D,L)Valine-OH (Bachem), dimethylformamide (DMF) (anyhd., 99.8%, Acros), hydrobromic acid (HBr) (33% in acetic acid, Aldrich), *N*-(trimethylsilyl)allylamine (*N*-TMS allylamine) (95%, Acros), phosphate buffered saline

(PBS) tablets (Aldrich), trifluoroacetic acid (TFA) (Aldrich), sodium borohydride ($NaBH_4$) (Ajax chemicals), *n*-pentane (anhydrous ≥99%, Aldrich), diethyl ether (AR, Chem-Supply), paraformaldehyde (Aldrich), and penicillin-streptomycin (Aldrich) were used as received. Tetrahydrofuran (THF) was distilled from benzophenone and sodium metal under nitrogen. Glutaraldehyde was supplied as a 25% aqueous solution (≥98%, Merck). Dulbecco's Modified Eagle Medium (DMEM, GIBCO Cat. No. 11995), fetal bovine serum (FBS, GIBCO Cat. No. 10099), GlutaMAX™ supplement (100x, GIBCO Cat. No. 35050), Dulbecco's Phosphate Buffered Saline (DPBS, GIBCO 14190), 0.05% trypsin-EDTA (1×, GIBCO Cat. No. 25300), SYTO® 9 green fluorescent nucleic acid stain, and propidium iodide (PI) were purchased from Invitrogen and used as received. Defibrinated horse blood (Commonwealth Serum Laboratories (CSL), Melbourne), Mueller-Hinton Broth (CM0405, Oxoid), Blood Agar Base No. 2 (CM0271, Oxoid), Yeast Extract (LP0021, Oxoid), and Bacto™ Tryptone (BD Biosciences) were used as received for bacteria culture. CellTiter 96® Aqueous Non-Radioactive Cell Proliferation assay kit was purchased from Promega and used for cell viability assays following manufacturer's instructions. 96-well cell culture plates and T175 cell culture flasks (Corning) were used for cell culture.

Synthesis of Block Copolymer

Synthesis of $_{D,L}$-Valine and (Z)-$_{L}$-Lysine N-Carboxyanhydrides (NCAs).[1-2]

The amino acid (ε-Z)-$_{L}$-Lysine (2 g, 7.14 mmol) or $_{D,L}$-Valine (1 g, 8.53 mmol)) was dissolved in anhydrous THF (50 mL) in a three-necked round bottomed flask under argon. Triphosgene (lys: 0.843 g, 2.84 mmol, 1.2 equiv. phosgene; val: 1.01 g, 3.40 mmol, 1.2 equiv. phosgene) was then added and the mixture was heated at 60 ˚C for 2 h with continuous stirring. After cooling to room temperature, the reaction mixture was sparged with argon for 45 mins into a sat. NaOH solution, then solvent removed *in vacuo*. The resulting residue was recrystallised from THF (anhydrous) and *n*-pentane (anhydrous) overnight. The resulting crystals were filtered and washed with *n*-pentane (dry), then re-precipitated and washed (x 2) with dry *n*-pentane to afford white solids (Yields: ~80 %) ^{1}H NMR ($CDCl_3$): (Z)-$_{L}$-Lysine NCA ^{1}H NMR (400 MHz, CDCl3): δ_H 1.40-1.60 (m, 4H, NH-CH_2-CH_2-C*H*$_2$-C*H*$_2$-), 1.81-1.94 (m, 2H, NH-CH_2-C*H*$_2$-CH_2-CH_2-), 3.18 (m, 2H, NH-C*H*$_2$-CH_2-CH_2-CH_2-), 4.25 (t, 1H, C*H*N), 4.97 (s, 1H, side chain NH), 5.09 (s, 2H, C*H*$_2$-ArH), 7.04 (s, 1H, ring NH), 7.3-7.4 (m, 5H, ArH). $_{D,L}$-Valine NCA ^{1}H NMR (400 MHz, $CDCl_3$): δ_H 1.02 (d,

3H, *J*= 7.0 Hz, C*H*$_3$), 1.08 (d, 3H, *J*= 7.0 Hz, C*H*$_3$), 2.25 (m, 1H, C*H*(CH$_3$)$_2$), 4.22 (d, 1H, *J* = 4.4 Hz, C*H*-NH), 6.95 (s, 1H, CO-N*H*)

Synthesis of poly (Z-L-Lysine)-b-poly(D,L-Valine) Block Copolypeptide (PZLL-b-PDLV)

To a dry 50 mL RBF was added (Z)-L- lysine NCA (1.62 g, 5.3 mmol) under argon. Dry DMF (20 mL) was then added and stirred to dissolve. To the stirring solution was added *N*-(Trimethylsilyl)allylamine (21.2 µL, 0.126 mmol, M/I = 60) and the clear solution stirred for 24 h under argon with bleed at room temperature. D,L-Valine NCA (0.325 g, 2.27 mmol) was then added to the reaction mixture and the solution stirred for a further 48 h. The reaction mixture was then concentrated under high vacuum and precipitated in diethyl ether (40 mL), washed in ether (x 2) then dried *in vacuo* to afford a white solid (0.90 g Yield: 56 %). M_n(GPC)= 9.9 kDa, PDI 1.70. Note: GPC analysis was performed on small sample of reaction mixture. NMR of the protected polypeptide could not be obtained due to the precipitated product being highly insoluble in both aqueous and organic solvents. This is due to poly(valine) typically forming insoluble secondary structures as reported previously,[14-16] rendering the block copolypeptide insoluble. See below for ^{1}H NMR of the fully soluble deprotected copolypeptide and resulting Lys : Val molar ratio calculations.

*Synthesis of poly (L-Lysine)-b-poly(D,L-Valine) Block Copolypeptide (PLL-b-PDLV) (**P1**)*

Deprotection of the lysine CBz (Z) protecting group was achieved through previously reported procedure[7-8] to afford the fully water soluble polypeptide. To a 25 mL was added the protected polypeptide (0.90 g, 9.1 µmol) followed by trifluoroacetic acid (4 mL). Brief sonication was employed to dissolve polymer, followed by addition of HBr (33% in AcOH, 4 mL). The resulting solution was stirred at 35 ˚C with thick precipitate observed soon after. The reaction mixture stirred for total of 2 h at 35 ˚C, with the suspension then transferred directly into diethyl ether, washed in ether (x 2), then dried *in vacuo* overnight. The solid was then dissolved in DI H_2O and dialyzed against 2 L DI water (x 3) for 24 h followed by freeze drying to obtain a white solid (~340 mg). ^{1}H NMR (d$_6$-DMSO): δ_H 0.78 (s, 2(C*H*)$_3$), 1.20-1.70 (m, NH-CH$_2$-C*H*$_2$-C*H*$_2$-C*H*$_2$-), 1.9 (br s, C*H*-NH valine), 2.74 (s, NH-C*H*$_2$-CH$_2$-CH$_2$-CH$_2$-), 4.22 (s, C*H*-NH backbone), 8.00 (s, CO-N*H*). Based on lysine and valine side chain protons, integration determined Lys : Val ratio to be 7:2 (see below).

Based on this ratio and the calculated M_n from GPC analysis above, DP is determined to be 45 (35 lysine, 10 valine).

Preparation of Cryogels

Cryogelation reactions were conducted at -18 ˚C. Hydrogel samples were prepared at room temperature. Deprotected copolypeptide was first dissolved in phosphate buffered saline (PBS, pH 7.4) at a polymer concentration of 5% w/v. Glutaraldehyde solution (25% Aqueous Solution, Merck) at specified cross-linking amounts to polypeptide % (v/w) was then added and vortexed briefly to dissolve. The solution was then withdrawn in plastic syringes and placed directly into freezer at -18 ˚C for 24 h. For hydrogel formation, plastic syringes containing reagents were kept at room temperature in dark and left for 48 hrs. After completion of the cryogelation process, the resulting samples were removed and thawed at room temperature. The cryogels and hydrogel were then immersed in DI water with complete replacement of the solution three times (3 x 100 mL). The gels were then immersed in a 0.1 % (w/v) sodium borohydride ($NaBH_4$) PBS solution (pH = 9.4, 100 mL) for 3 h to reduce unreacted aldehyde groups of cross-linker. Gels were then washed thoroughly and immersed in DI water (100 mL) then sterile PBS (pH = 7.4) (100 mL, x 2) with complete replacement of solution each time.

Characterization of Cryogels

Mechanical Tests

Young's modulus was determined using an Instron MicroTester (Instron 5848). Cylindrical gels (~9 mm diameter, 12 mm height) were deformed (at constant volume) between two parallel plates with a strain rate of 60% per minute. Engineering stresses and strains were recorded. The gel cylinders were kept hydrated in PBS solution (pH 7.4) throughout the tests. Young's moduli were determined by the average slopes of the stress–strain compression curves over the linear elastic strain range 0–10%. Runs were performed in triplicate.

Swelling Studies

The weight swelling degree was determined using a conventional gravimetric procedure. The gels were first dried. Cryogels were dried through freeze-drying whilst hydrogels were dried through immersion in increasing (0-100%) acetone solutions followed by vacuum oven drying at 50 ˚C overnight. Dried gels were then immersed in DI water with the water uptake measured by the cumulative mass increase at pre-determined time intervals. Excess surface water was wiped away. Mass swelling degree at time t was calculated by the following equation:

$$\text{Mass swelling degree} = \frac{m_t}{m_o}$$

Where m_t and m_o are the masses of the swollen gel at time t and dried gel, respectively

Specific Surface Area

The specific surface area of a freeze-dried sample of cryogel C was measured by a Micromeritics ASAP 2050 Xtended Pressure Sorption Analyzer with carbon dioxide (CO_2) as adsorbate at 0 ˚C. Before the measurements, the samples were degassed at 75 ˚C for 16 h. The specific surface area was obtained by the Brunauer, Emmett and Teller (BET) equation. See **Appendix Figure A5.4** for isotherm.

Antimicrobial Activity of Cryogels In Vitro

Bacterial Cell Culture

Freeze-dried cultures of *Escherichia coli* (*E. coli*, ATCC 25922) were grown aerobically and maintained by passage at ambient temperature on horse blood agar (10% v/v defibrinated horse blood, 4.4% w/v Oxoid Blood Agar Base No. 2). Overnight cultures were made from transferring a colony (*ca.* half a loop) from the agar plates to culture tubes containing sterilized Luria-Bertani broth (LB, 1% w/v Bacto™ Tryptone, 1% w/v NaCl, 0.5% w/v Oxoid Yeast Extract) (20 mL). Bacterial cultures were incubated overnight at 37 °C with aeration and without agitation. On the next day, aliquots (2 mL) were taken from the culture tubes, further diluted with LB (20 mL), and incubated for 3-4 h at 37 °C with aeration before use.

Bacterial Cell Counting

A Cell Lab Quanta SC MPL flow cytometer (Beckman Coulter) was used to count the number of bacterial cells prior to use in assays. The flow cytometer was equipped with a 100 W stabilized mercury arc lamp with wavelengths of 365, 404, and 435 nm, and a 488 nm diode laser. The fluorescence from SYTO® 9 was measured through a 525-nm band-pass filter (Fluorescent Channel 1, FL-1), and the red emission of PI was measured with a 670-nm long pass filter (Fluorescent Channel 3, FL-3). The multiparametric data were analyzed using the Cell Lab Quanta SC software.

Cells were diluted with NaCl solution (0.9%) using an appropriate dilution factor and incubated with Syto® 9 and PI (*i.e.*, 1 mL cell suspension to 1 µL of each dye). Syto® 9 stains the nucleic acids in all cells, while PI stains the nucleic acids in cells with damaged membranes. Using the Cell Lab Quanta SC software, the number of viable cells/mL (Syto® 9-positive, PI-negative) was obtained.

Antimicrobial Assay

The protocol was adapted from that reported by Chan-Park and co-workers.[17] The gels were soaked and rinsed in sterilized PBS for at least 3 days and then cut into discs of *ca*. 4 mm diameter and 3 mm height. *E. coli* cells which gave an optical density reading of *ca*. 0.7 were diluted to 1.2×10^8 cells/mL in Mueller-Hinton broth and 10 µL of bacterial suspension was spread onto each gel in a 96-well plate. The inoculated gels were incubated for 1 h at 37 °C. NaCl solution (0.9%, 0.2 mL) was then added to each well followed by vigorous agitation and flushing to recover any residual cells. An aliquot (10 µL) of the microbial suspension was then diluted with 0.9% NaCl solution using an appropriate dilution factor and plated out in LB agar (1% w/v Bacto™ Tryptone, 1% w/v NaCl, 0.5% w/v Oxoid Yeast Extract, 15 g/L Oxoid Blood Agar Base No. 2). The plates were incubated overnight at room temperature and counted for colony-forming units (CFU). Positive controls consisting of cell-only wells were used.
The results are expressed as:

$$\text{Log reduction} = \log\left(\frac{\text{CFU}}{\text{mL}}\text{ of control after 1 h}\right) - \log\left(\frac{\text{CFU}}{\text{mL}}\text{ of survivor cells on gel after 1 h}\right)$$

For the gel reusability study, cryogel C was challenged with *E. coli* cells 4 times successively, where the protocol for each cycle was as described above.

In the same experiment, the viability of the bacterial cells in the microbial suspension outside the gel (obtained through flushing with 0.9% NaCl solution) and in the gel was assessed using Promega's CellTiter 96® Aqueous Non-Radioactive Cell Proliferation assay kit. An aliquot (100 µL) was taken from the remaining microbial suspension and transferred to another 96-well plate. The gels were also transferred to a new 96-well plate and 0.9% NaCl solution (100 µL) was added. MTS/PMS solution (20 µL) was then added to each well (either containing microbial suspension or gel), followed by a 3.5 h incubation. The absorbance at 490 nm was measured with a plate reader (PerkinElmer 1420 Multilabel Counter VICTOR^3). Note that for the gel-containing wells, an aliquot (100 µL) was transferred to unused wells prior to absorbance reading.

Note that a minimum of two independent experiments of the assay were conducted and at least two technical replicates were used in each experiment for each gel type.

Bacteria Morphology Study

E. coli cells (10 µL, 1.2 × 10^8 cells/mL in Mueller-Hinton broth) was spread onto cryogel C and incubated for 1 h at 37 °C. NaCl solution (0.9%, 0.2 mL) was added which was then followed by vigorous agitation and flushing. The gel was immediately fixed with paraformaldehyde (4%) solution for 1 h and washed with PBS (1×, 10 min) and DI water (2×, 10 min). The cross-sections of the gel were observed using a FEI Quanta 200 ESEM FEG on the low-vacuum setting. Samples were pre-coated with gold using a Dynavac Mini Sputter Coater prior to imaging.

Statistical analysis

Statistical analysis was performed using a one-way classification of ANOVA and student's *t*-test (two-tailed), where differences were regarded as statistically significant with probability $P>0.05$.

Cryogel Cytotoxicity In Vitro

Mammalian Cell Culture

NIH-3T3 cells were cultivated in DMEM medium (supplemented with 10% FBS, 1× GlutaMAX™, and 1× penicillin-streptomycin) in a humidified atmosphere containing 5% CO_2 at 37 °C. Cells were seeded in a T75 flask (*ca.* 3×10^6 cells/ml) and passaged twice a week prior to performing the subsequent cell viability studies.

Mammalian Cell Viability Assay

Cytotoxicity of the cryogels was assessed using Promega's CellTiter 96® Aqueous Non-Radioactive Cell Proliferation assay kit following the manufacturer's instructions. Briefly, the cryogels were incubated in 'complete' DMEM (1 mL) at 37 °C for 72 h. The cryogels were then removed and the conditioned medium was used in subsequent cell viability assays to test for toxic compounds leaching out of the gels and/or toxic degradation products. NIH-3T3 cells were trypsinized using trypsin-EDTA, counted on a cell counter (Coulter Particle Counter Z series, Beckman Coulter), diluted with 'complete' DMEM (conditioned DMEM:fresh DMEM = 1:1), and seeded at 10 000 cells per well on 96-well plates. Subsequently, plates were incubated under standard cell maintenance conditions (37 °C, 5% CO_2). After 72 h, MTS/PMS solution (20 µL per 100 µL cells) was added to each well. Plates were further incubated for 2 h. The absorbance at 490 nm was measured with a plate reader (PerkinElmer 1420 Multilabel Counter VICTOR^3). Note that all experiments were conducted in quadruplicate, and cells that were seeded in 100% fresh and 'complete' DMEM were used as positive growth controls.

Percentage viability of cells was calculated using the following formula:

$$\% \text{ Viability} = \left(\frac{A_{490} \text{ test sample} - A_{490} \text{ background}}{A_{490} \text{ cells alone} - A_{490} \text{ background}} \right) \times 100$$

7.6 References

(1) Daly, W. H.; Poche, D., *Tetrahedron Lett.* **1988,** *29* (46), 5859-5862.

(2) Sulistio, A.; Blencowe, A.; Widjaya, A.; Zhang, X. Q.; Qiao, G., *Polymer Chemistry* **2012,** *3* (1), 224-234.

(3) Huynh, V. T.; Chen, G. J.; de Souza, P.; Stenzel, M. H., *Biomacromolecules* **2011,** *12* (5), 1738-1751.

(4) Fu, Q.; Xu, J.; Ladewig, K.; Henderson, T. M. A.; Qiao, G. G., *Polymer Chemistry* **2015,** *6* (1), 35-43.

(5) Schechter, B.; Neumann, A.; Wilchek, M.; Arnon, R., *J. Controlled Release* **1989,** *10* (1), 75-87.

(6) Gianasi, E.; Wasil, M.; Evagorou, E. G.; Keddle, A.; Wilson, G.; Duncan, R., *Eur. J. Cancer* **1999,** *35* (6), 994-1002.

(7) Sulistio, A.; Widjaya, A.; Blencowe, A.; Zhang, X. Q.; Qiao, G., *Chem. Commun.* **2011,** *47* (4), 1151-1153.

(8) Lee, J.; Lee, S. J.; Choi, J. Y.; Yoo, J. Y.; Ahn, C. H., *Eur. J. Pharm. Sci.* **2005,** *24* (5), 441-449.

(9) Welzel, P. B.; Grimmer, M.; Renneberg, C.; Naujox, L.; Zschoche, S.; Freudenberg, U.; Werner, C., *Biomacromolecules* **2012,** *13* (8), 2349-2358.

(10) Dainiak, M. B.; Allan, I. U.; Savina, I. N.; Cornelio, L.; James, E. S.; James, S. L.; Mikhalovsky, S. V.; Jungvid, H.; Galaev, I. Y., *Biomaterials* **2010,** *31* (1), 67-76.

(11) Ak, F.; Oztoprak, Z.; Karakutuk, I.; Okay, O., *Biomacromolecules* **2013,** *14* (3), 719-727.

(12) Kumari, J.; Karande, A. A.; Kumar, A., *ACS Appl. Mater. Interfaces* **2016,** *8* (1), 264-77.

(13) Kirsebom, H.; Topgaard, D.; Galaev, I. Y.; Mattiasson, B., *Langmuir* **2010,** *26* (20), 16129-16133.

(14) Epand, R. F.; Scheraga, H. A., *Biopolymers* **1968,** *6* (11), 1551-1571.

(15) Hosia, W.; Johansson, J.; Griffiths, W. J., *Mol. Cell. Proteomics* **2002,** *1* (8), 592-597.

(16) Goh, S. L.; Platt, A. P.; Rutledge, K. E.; Lee, I., *J. Polym. Sci., Part A* **2008,** *46* (16), 5381-5389.

(17) Li, P.; Poon, Y. F.; Li, W.; Zhu, H.-Y.; Yeap, S. H.; Cao, Y.; Qi, X.; Zhou, C.; Lamrani, M.; Beuerman, R. W.; Kang, E.-T.; Mu, Y.; Li, C. M.; Chang, M. W.; Leong, S. S. J.; Chan-Park, M. B., *Nat. Mater.* **2011,** *10* (2), 149-156.

Appendices

Chapter 2 Appendix

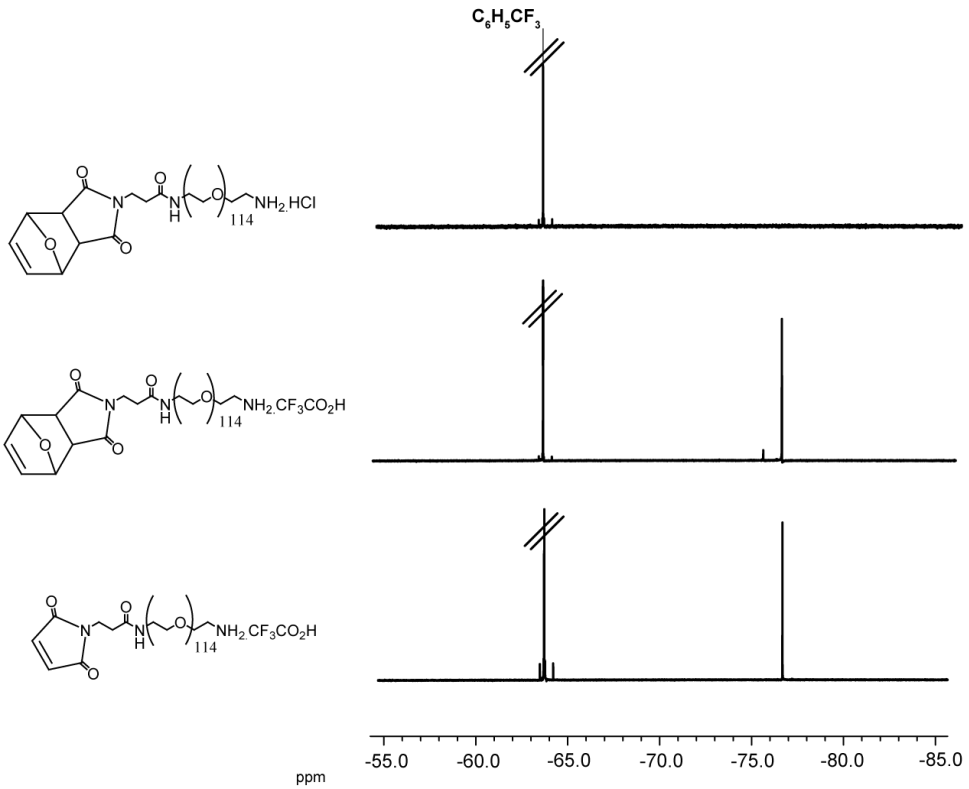

Figure A2.1. ^{19}F NMR spectra ($CDCl_3$) of furan protected Mal-PEG-NH_2TFA and furan protected Mal-PEG-NH_2HCl (**P1**) after counter ion exchange. Trifluorotoluene ($C_6H_5CF_3$) used as internal reference.

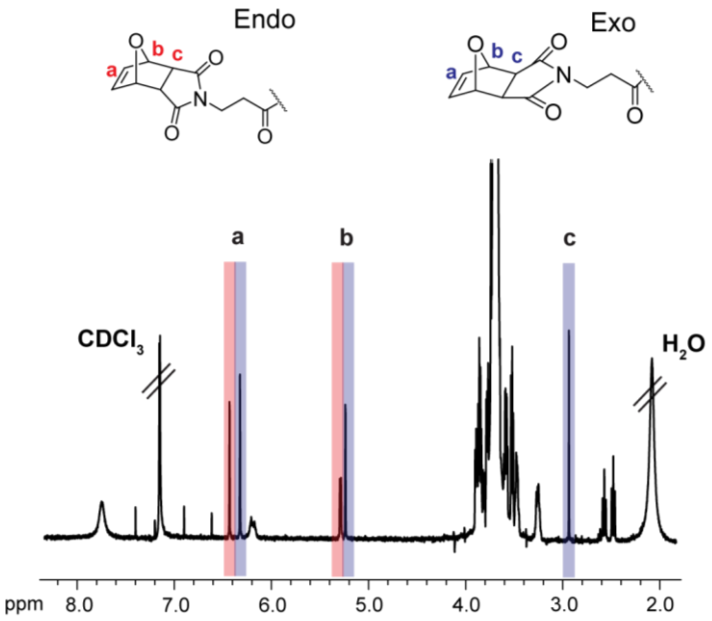

Figure A2.2. ^{1}H NMR spectra ($CDCl_3$) of **P1** following Diels Alder (DA) reaction between Mal-PEG-NH_2TFA and furan showing the endo and exo isomeric cycloadducts.

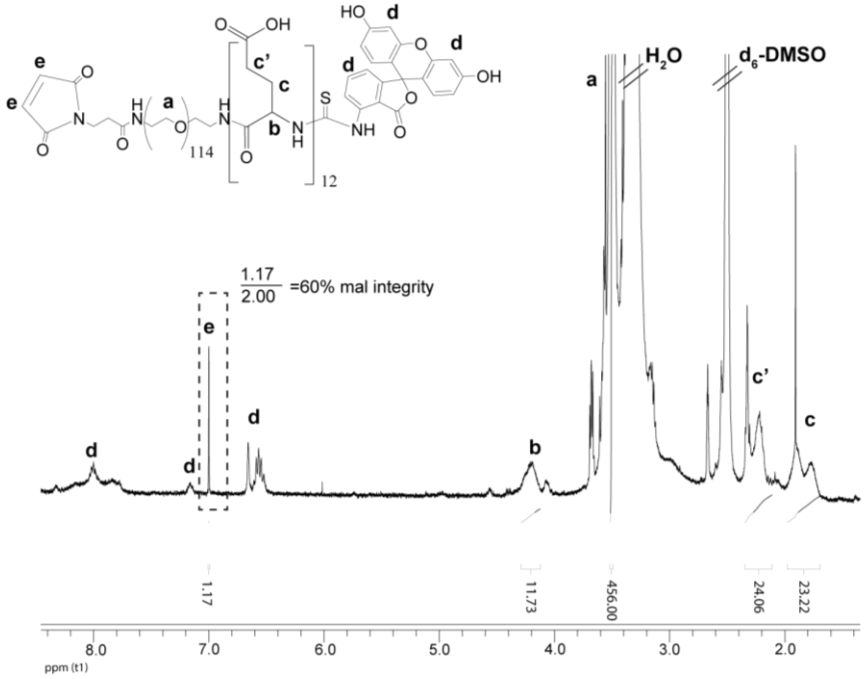

Figure A2.3. ^{1}H NMR spectra (d_6-DMSO) with integrations of FITC-tagged block copolymer (**P4**).

Calculations of Drug Loading Content and Drug Loading Efficiency:

Drug loading content (DLC):

TGA: 8.4 wt%

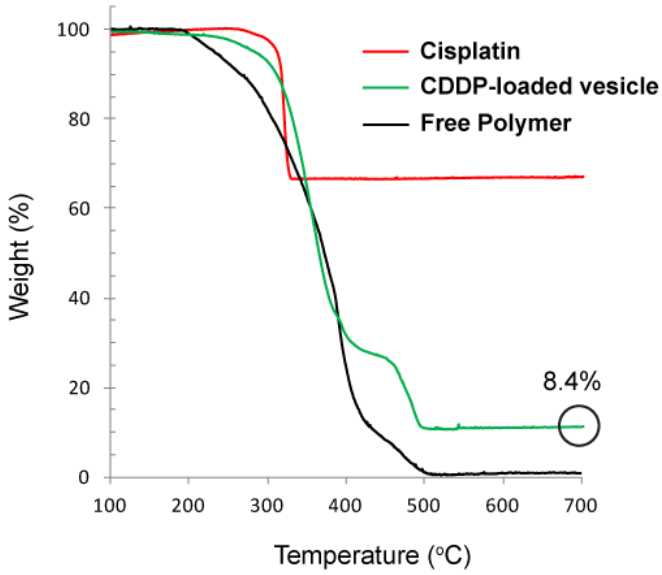

Figure A2.4. TGA traces for CDDP (red), Mal-PEG-*b*-PLG-FITC free polymer (black) and CDDP-loaded vesicles (green).

ICP-OES: 7.4 wt%

ICP-OES Pt standard curve λ = 203.646 nm:

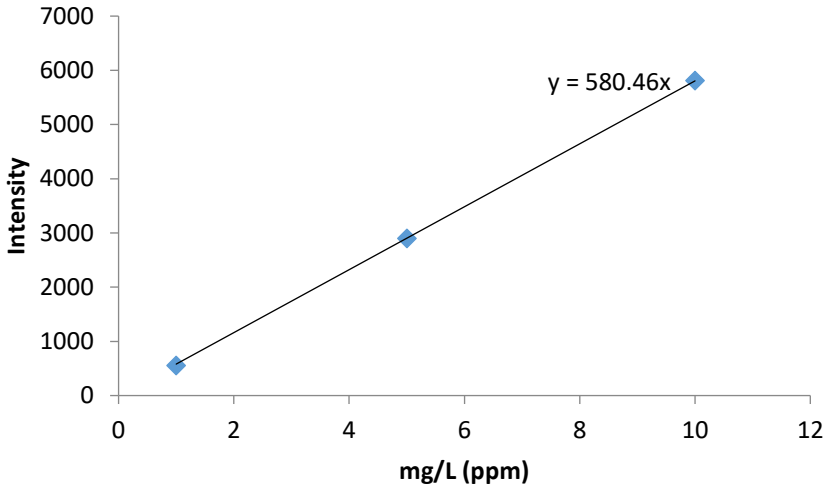

Calculation of drug conjugation efficiency (DCE) based on ICP-OES (DLC):

$$f = \frac{m_{Pt,exp}}{m_{Pt,theo}} \times 100\% = \frac{W_{Pt}/M_{Pt}}{W_{polymer}/M_{polymer}} \times 100\%$$

$$= \frac{7.4\%/195}{92.6\%/7000} \times 100\%$$

$$= 3\ Pt\ molecules\ per\ diacid\ (6)\ of\ polymer$$

$$\therefore \sim 50\%\ DCE$$

where $m_{Pt,\ exp}$: the molar amount of Pt determined by experimental data; $m_{Pt,\ theo}$: the theoretical molar amount of Pt in 100% conversion (assume that one Pt molecule forms complex with one di-acid repeating unit); W_{Pt}: weight percent of Pt measured by ICP-OES; M_{Pt}: molecular weight of Pt; $W_{polymer}$: weight percent of polymer determined from 100%-W_{Pt}; $M_{polymer}$: molecular weight of polymer.

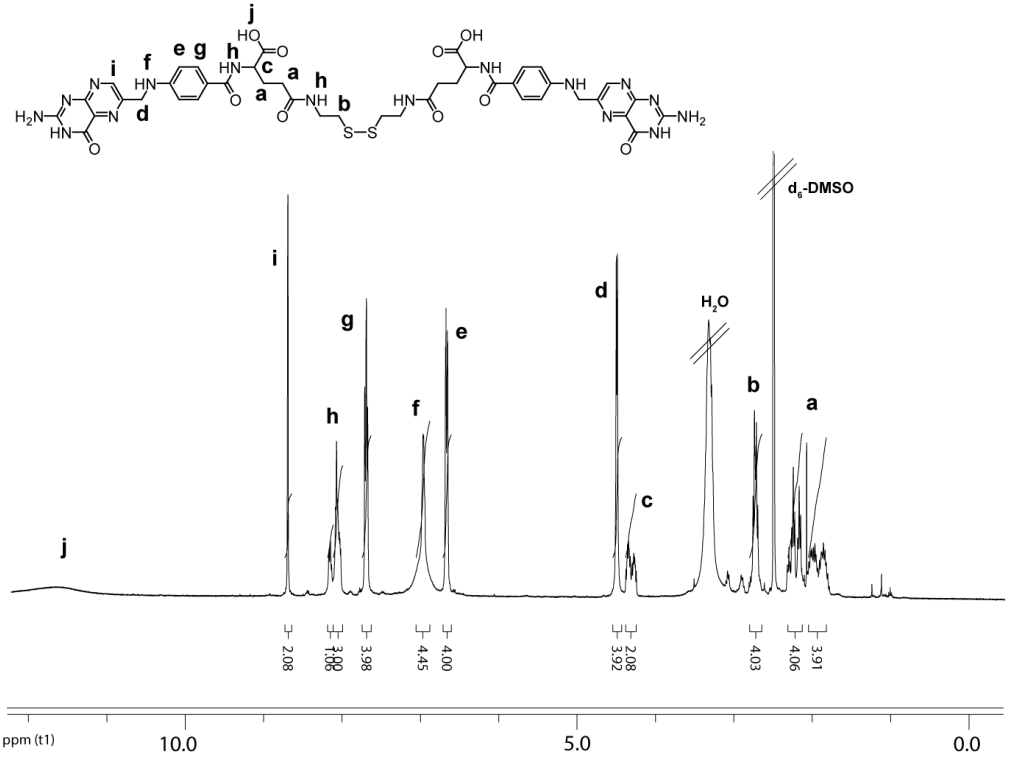

Figure A2.5. ^{1}H NMR spectra (d_6-DMSO) of FA-S-S-FA.

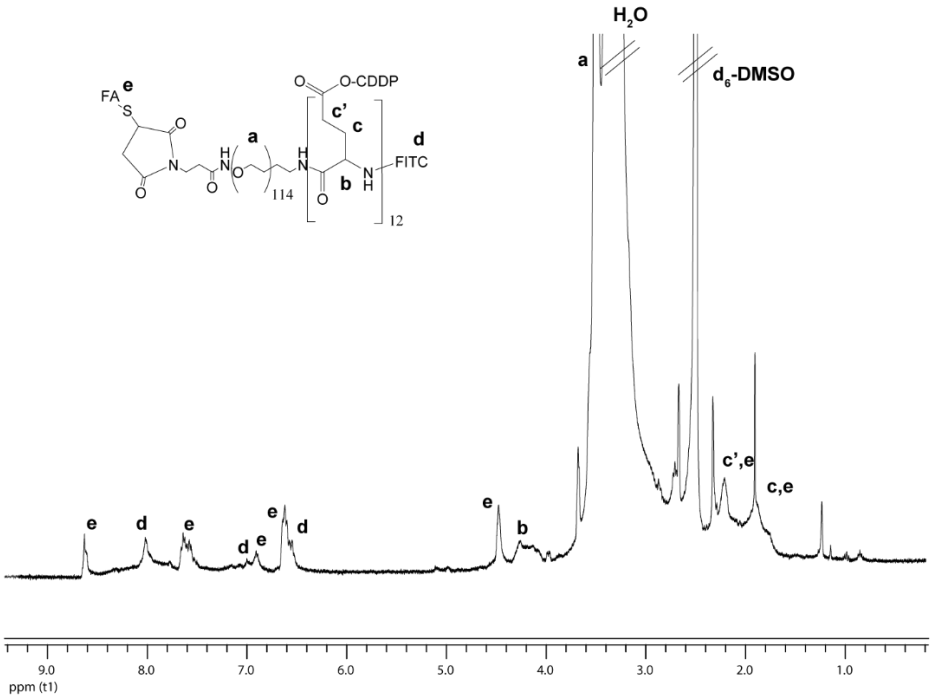

Figure A2.6. ^{1}H NMR spectra (d_6-DMSO) of FITC tagged FA-conjugated CDDP-loaded vesicles.

Chapter 3 Appendix

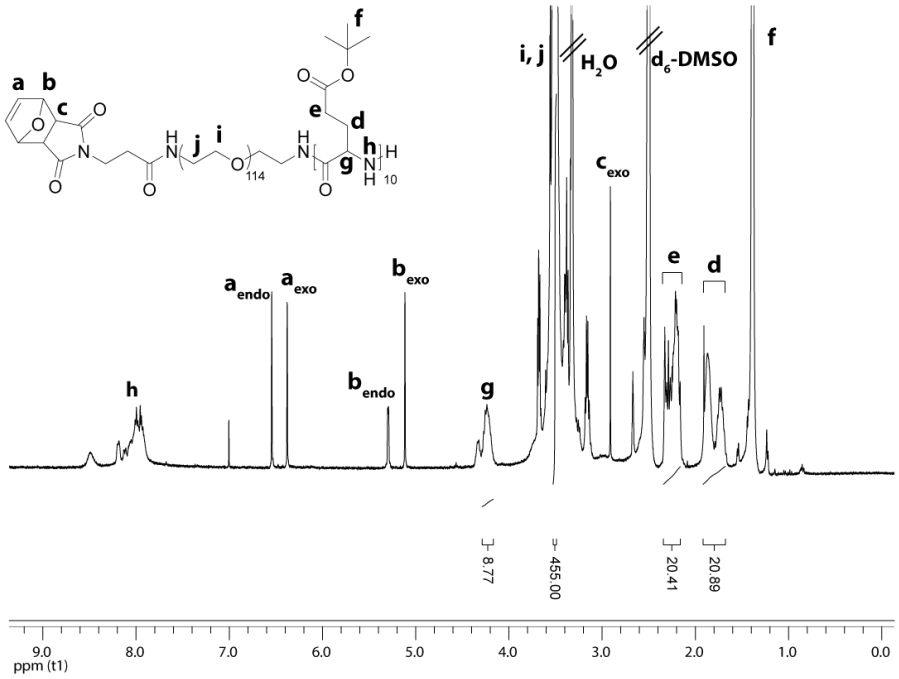

Figure A3.1. ^{1}H NMR spectra (d$_6$-DMSO) and relevant integrations of furan-protected Mal-PEG-*b*-PLG(*γ*-tBu)-NH$_2$ *(***P2**).

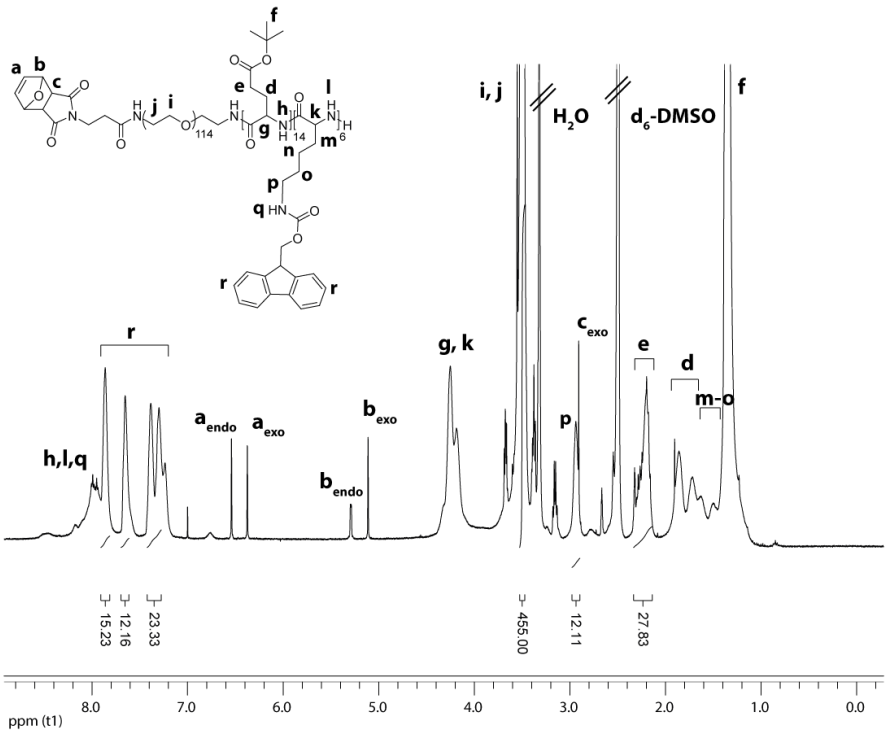

Figure A3.2. ^{1}H NMR spectra (d$_6$-DMSO) and relevant integrations of furan-protected Mal-PEG-*b*-(PLG(*γ*-tBu)-*r*-PLL(*ε*-Fmoc))-NH$_2$ (**P3**).

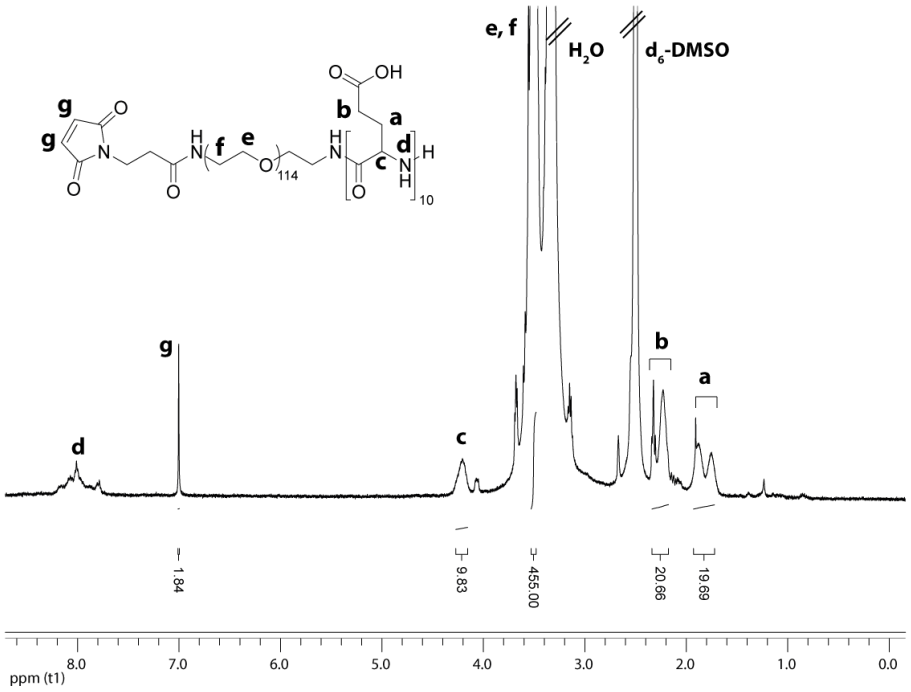

Figure A3.3. ^{1}H NMR spectra (d_6-DMSO) and relevant integrations of Mal-PEG-*b*-PLG-NH_2 (**P4**).

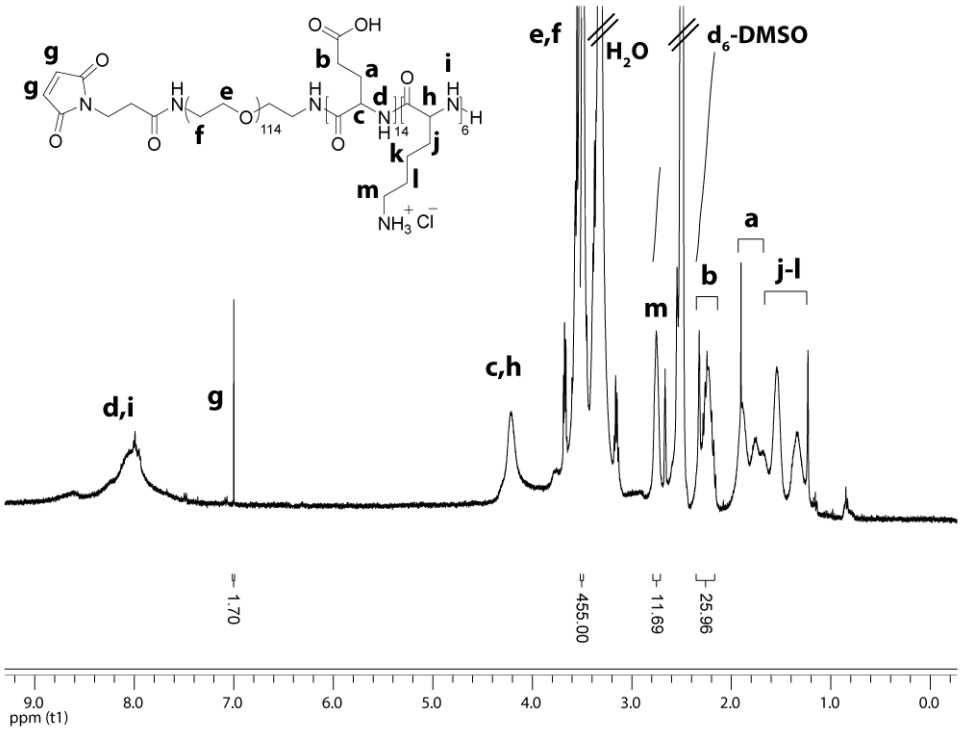

Figure A3.4. ^{1}H NMR spectra (d_6-DMSO) and relevant integrations of Mal-PEG-*b*-(PLG-*r*-PLL)-NH_2 (**P5**).

Chapter 4 Appendix

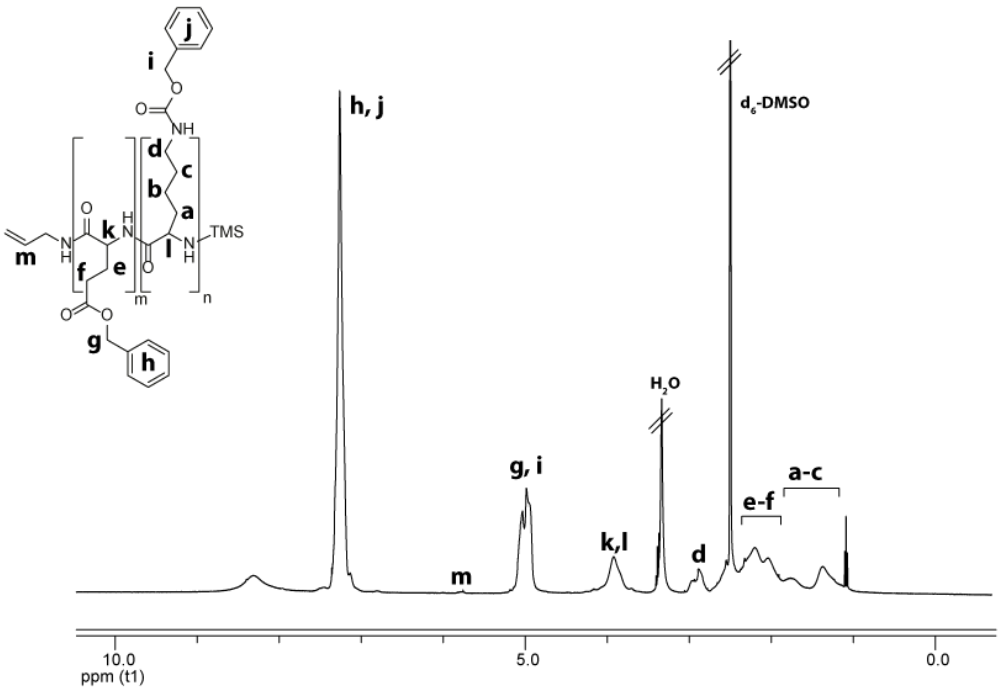

Figure A4.1. ^{1}H NMR (d_6-DMSO) spectrum of protected random copolymer A.

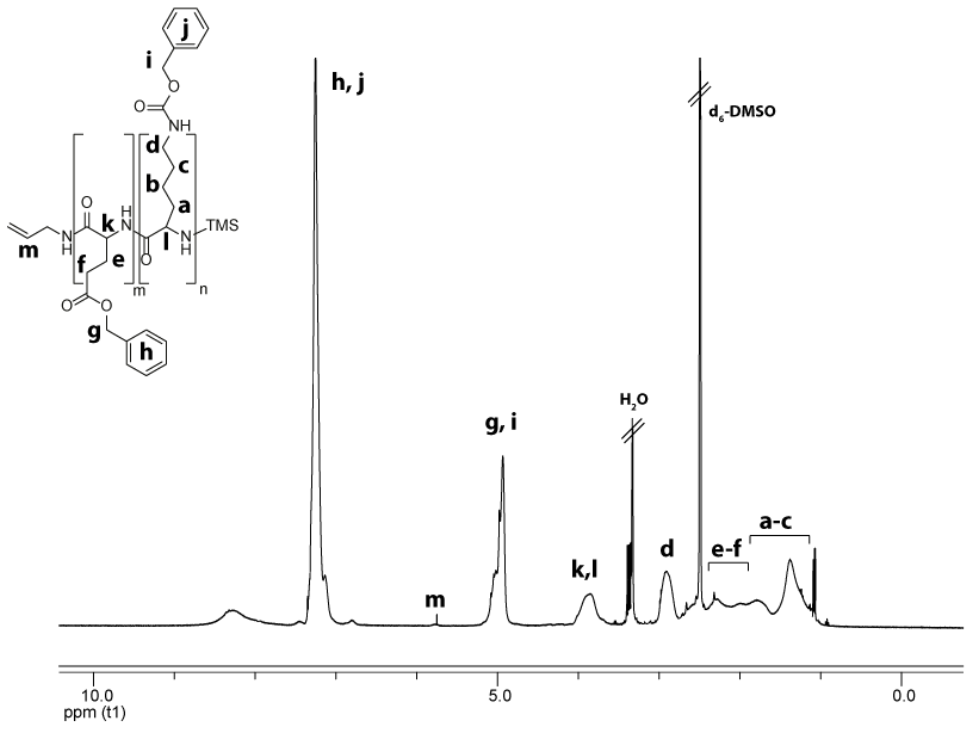

Figure A4.2. ^{1}H NMR (d_6-DMSO) spectrum of protected random copolymer B.

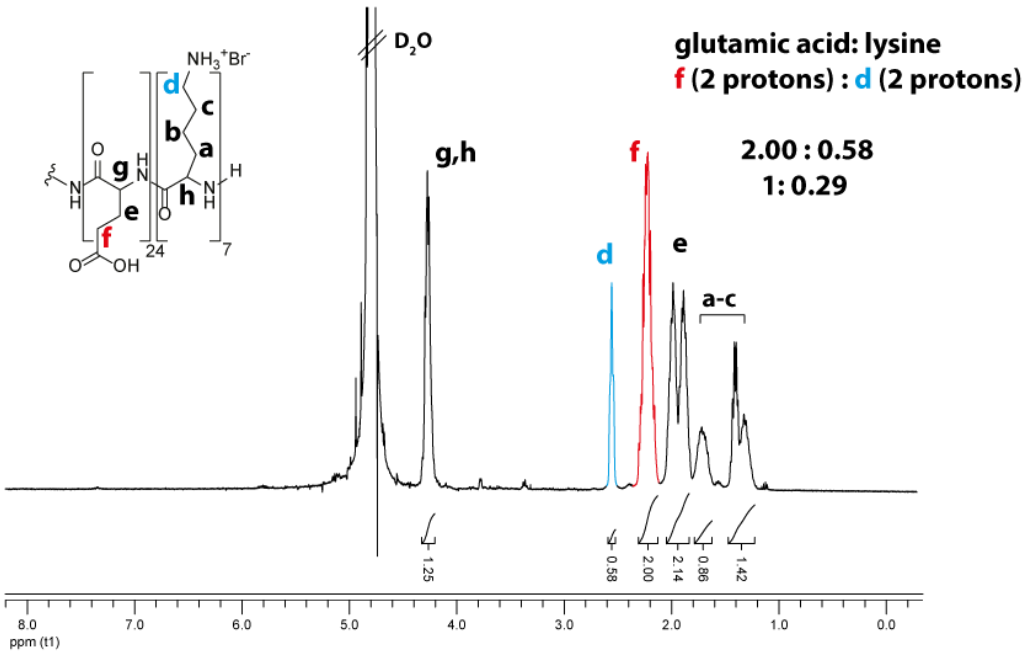

Figure A4.3. ^{1}H NMR (D_2O/NaOD) spectrum of deprotected random copolymer A including calculations of glutamic acid:lysine ratio based on the relevant integrations.

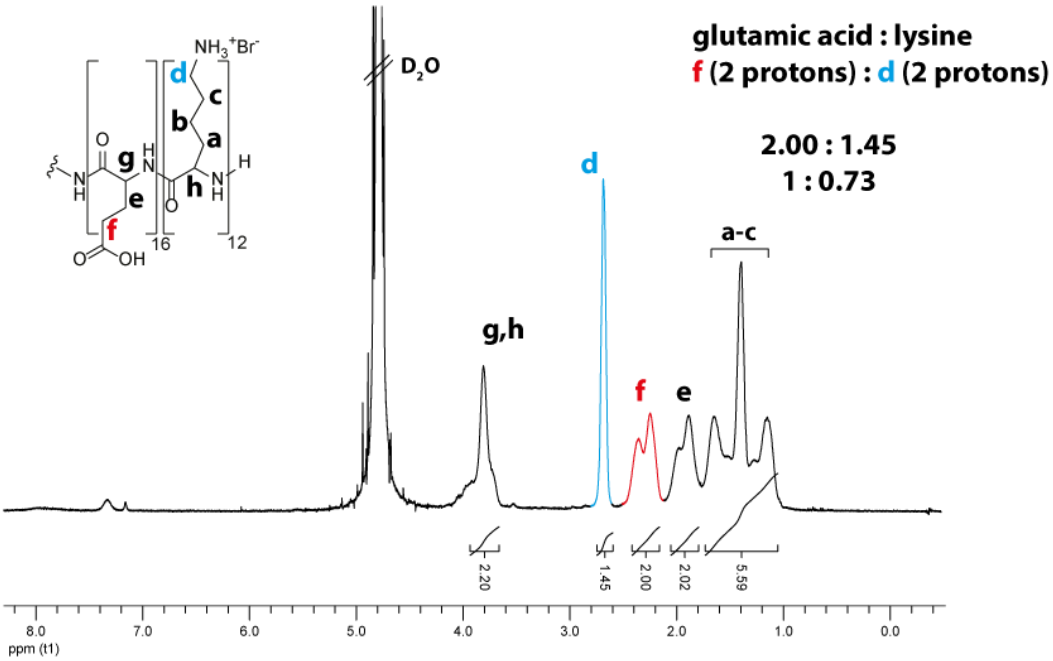

Figure A4.4 ^{1}H NMR (D_2O/DCl) spectrum of deprotected random copolymer B including calculations of glutamic acid:lysine ratio based on the relevant integrations.

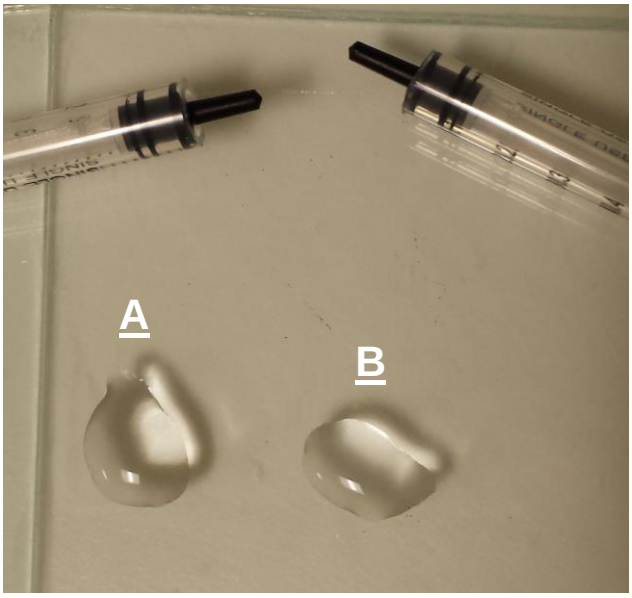

Figure A4.5. Images of polymer (random copolymer A and copolymer B) solutions showing no gel formation after freezing for 24 h in absence of EDCI/sulfo-NHS cross-linking agents. Note: Polymer concentration and solution pH values same as those used to prepare cryogels.

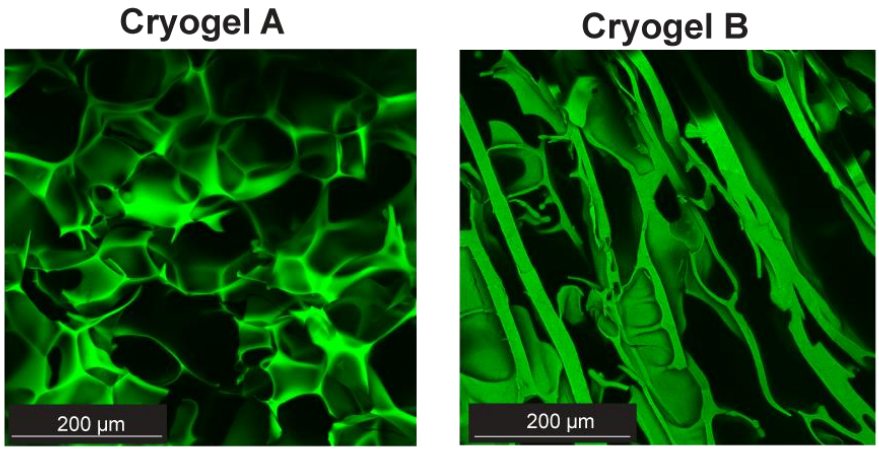

Figure A4.6. CLSM images showing pore morphologies of FITC-labeled cryogels swollen in PBS. Images are of cross-sections in the x-y plane and z-stacked.

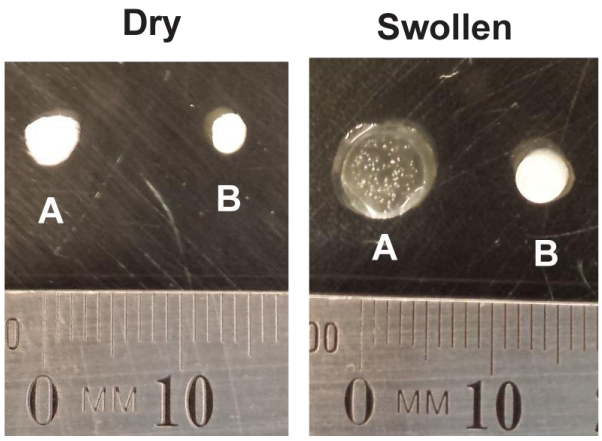

Figure A4.7. Images of dry and swollen cryogel A and B samples (PBS).

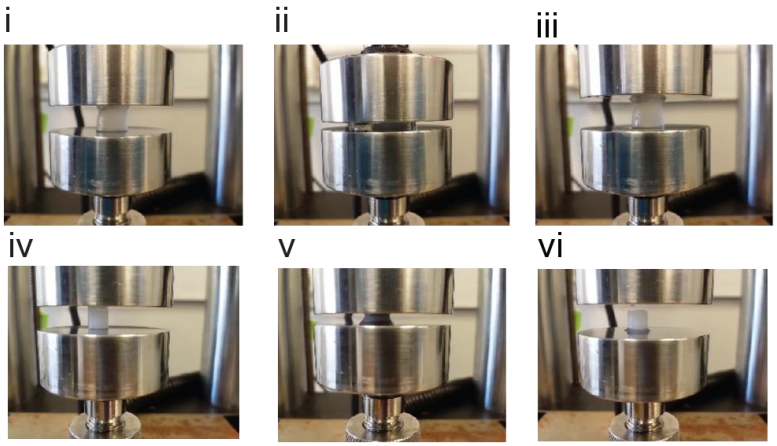

Figure A4.8. Images of cryogel A (i-iii) and cryogel B (iv-vi) during mechanical testing.

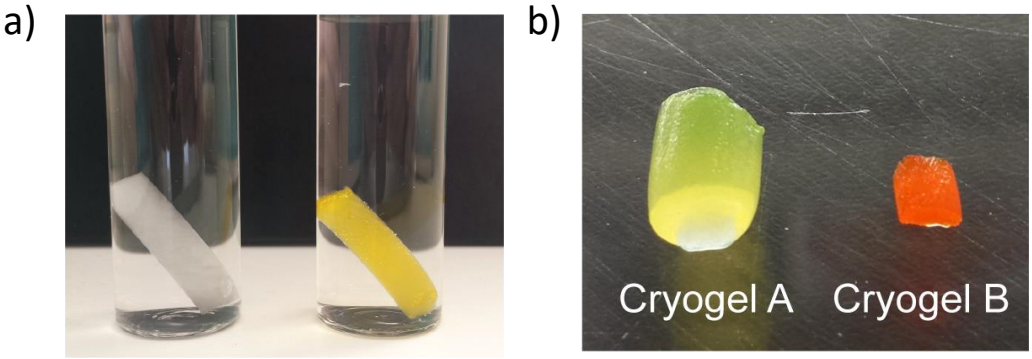

Figure A4.9. (a) Non-labeled and FITC-labeled cryogel A samples (b) FITC-labeled cryogel A and cryogel B samples.

Chapter 5 Appendix

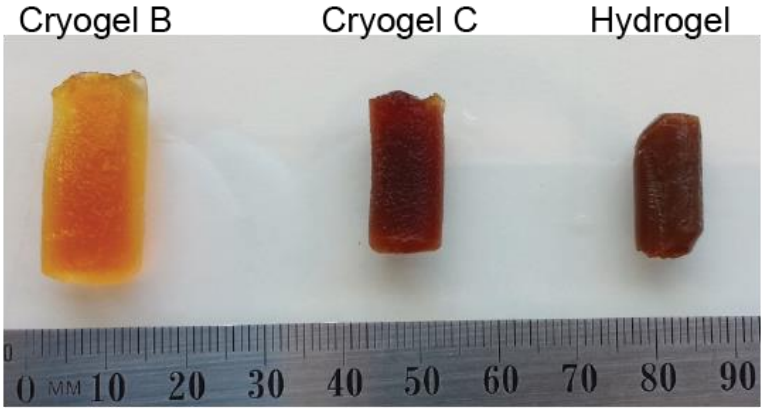

Figure A5.1. Photographs of swelled cylindrical cryogels/hydrogel made from identical batch volumes. Note increased total swelling of cryogels compared to non-macroporous hydrogel. Distinct brown colour is due to glutaraldehyde cross-linker.

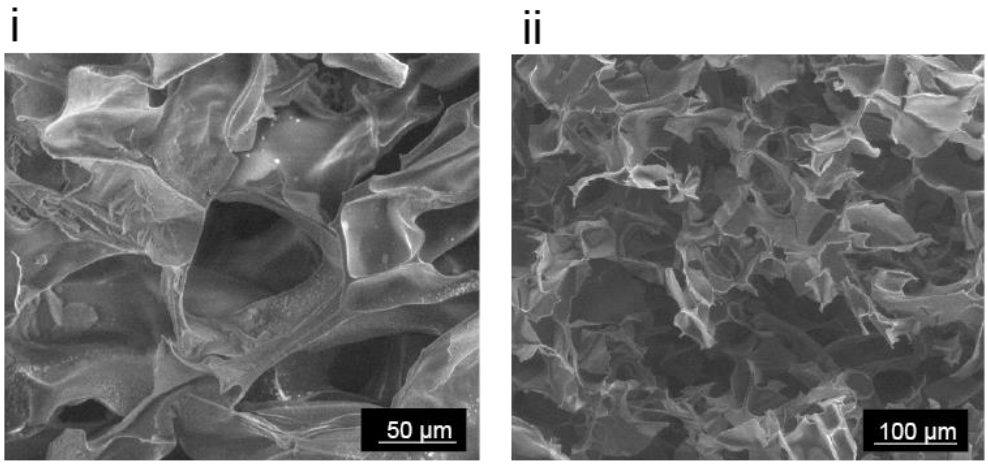

Figure A5.2. ESEM close up images on the cross-sectional morphology of (i) Cryogel C and (ii) Cryogel D.

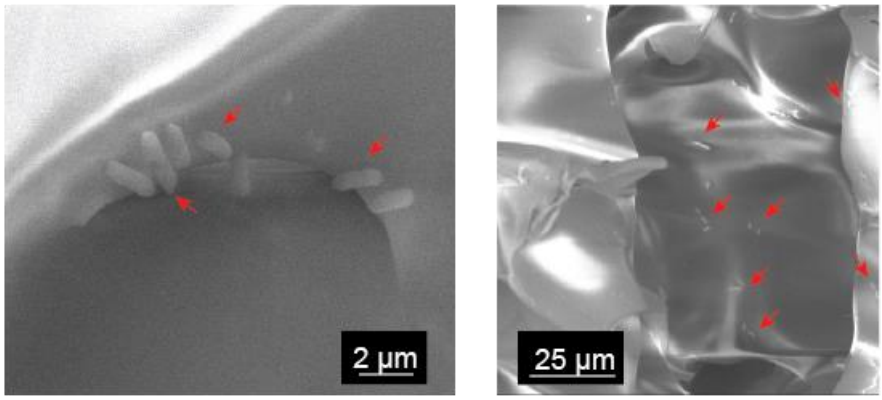

Figure A5.3. Representative ESEM images of cryogel C after incubation with *E. coli* for 1 h, followed by vigorous flushing and agitation with saline buffer (0.9% NaCl solution). Note the red arrows indicate the *E. coli* cells.

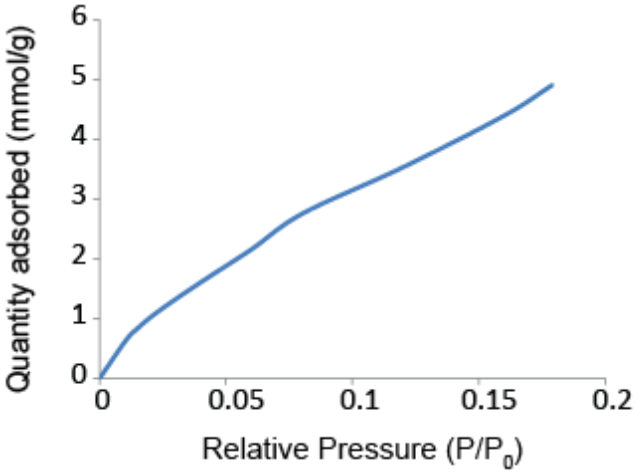

Figure A5.4. Carbon dioxide adsorption isotherm of freeze-dried cryogel C.

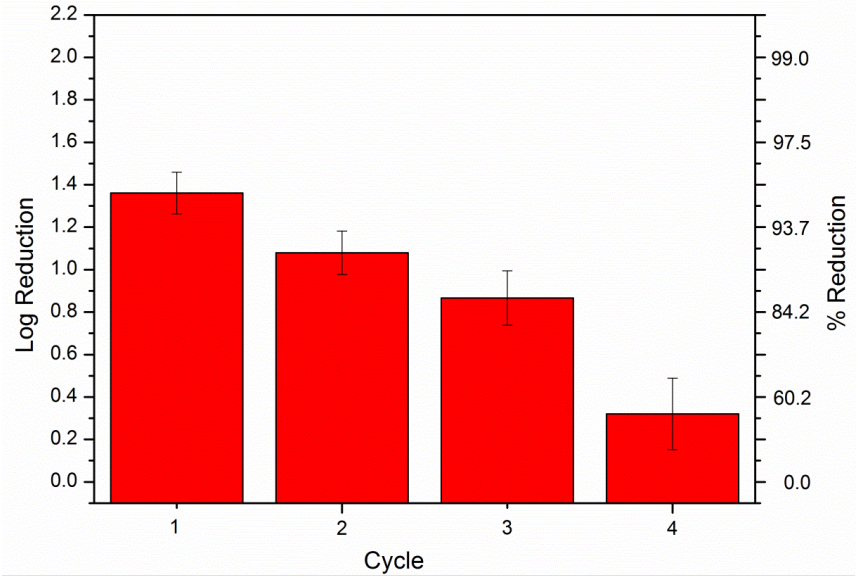

Figure A5.5. Log reduction and % kill of *E. coli* on polypeptide cryogel C after each cycle of use. Error bars represent the standard deviation from the mean ($n \geq 4$).

Article

pubs.acs.org/Biomac

Cisplatin-Induced Formation of Biocompatible and Biodegradable Polypeptide-Based Vesicles for Targeted Anticancer Drug Delivery

Steven J. Shirbin,[†] Katharina Ladewig,[†] Qiang Fu,[†] Molly Klimak,[†] Xiaoqing Zhang,[‡] Wei Duan,[§] and Greg G. Qiao*[,†]

[†]Polymer Science Group, Department of Chemical and Biomolecular Engineering, University of Melbourne, Parkville, Melbourne, Victoria 3010, Australia

[‡]CSIRO Manufacturing Flagship, Clayton South, Victoria 3169, Australia

[§]School of Medicine, Deakin University, Geelong, Victoria 3216, Australia

Supporting Information

ABSTRACT: Novel cisplatin (CDDP)-loaded, polypeptide-based vesicles for the targeted delivery of cisplatin to cancer cells have been prepared. These vesicles were formed from biocompatible and biodegradable maleimide-poly(ethylene oxide)$_{114}$-*b*-poly($_L$-glutamic acid)$_{12}$ (Mal-PEG$_{114}$-*b*-PLG$_{12}$) block copolymers upon conjugation with the drug itself. CDDP conjugation forms a short, rigid, cross-linked, drug-loaded, hydrophobic block in the copolymer, and subsequently induces self-assembly into hollow vesicle structures with average hydrodynamic diameters (D_h) of ∼270 nm. CDDP conjugation is critical to the formation of the vesicles. The reactive maleimide-PEG moieties that form the corona and inner layer of the vesicles were protected via formation of a reversible Diels−Alder (DA) adduct throughout the block copolymer synthesis so as to maintain their integrity. Drug release studies demonstrated a low and sustained drug release profile in systemic conditions (pH = 7.4, [Cl$^-$] = 140 mM) with a higher "burst-like" release rate being observed under late endosomal/lysosomal conditions (pH = 5.2, [Cl$^-$] = 35 mM). Further, the peripheral maleimide functionalities on the vesicle corona were conjugated to thiol-functionalized folic acid (FA) (via in situ reduction of a novel bis-FA disulfide, FA-SS-FA) to form an active targeting drug delivery system. These targeting vesicles exhibited significantly higher cellular binding/uptake into and dose-dependent cytotoxicity toward cancer cells (HeLa) compared to noncancerous cells (NIH-3T3), which show high and low folic acid receptor (FR) expression, respectively. This work thus demonstrates a novel approach to polypeptide-based vesicle assembly and a promising strategy for targeted, effective CDDP anticancer drug delivery.

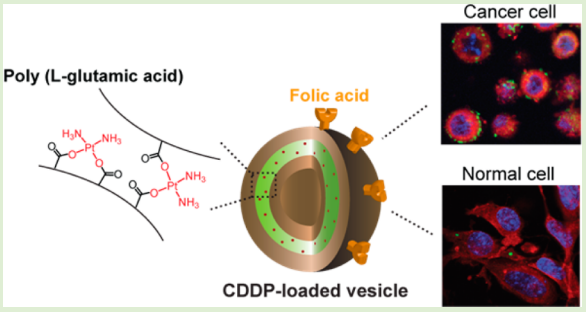

INTRODUCTION

Cisplatin (CDDP), a hydrophobic chemotherapeutic agent used extensively to treat a wide range of cancers,[1,2] has for many years had a limited efficacy due to solubility and toxicity issues that have affected its cancer therapy effect.[3,4] Its incorporation into polymer nanoparticles has been studied for many years as a means to improve its poor water solubility, alleviate the systemic cytotoxicity associated with the free drug, and improve drug loading at the tumor site.[5] Nanoscale assemblies for CDDP delivery has for many years largely involved matrix (micelle) systems, demonstrating effective delivery profiles and reduced CDDP associated toxicity,[6−8] with a focus on the use of biodegradable and biocompatible polymer systems in recent times.[9−14] Most notable has been the widespread use of self-assembling poly(ethylene glycol)-*b*-poly($_L$-glutamic acid) (PEG-*b*-PLG) block copolymers into micellar delivery systems upon conjugation with platinum drugs.[15−19] Poly(ethylene glycol), a hydrophilic biocompatible polymer, acts as a stealth coating that improves the circulation time of the nanoparticles in the bloodstream.[20,21] Poly($_L$-glutamic acid), possesses unique biodegradability properties,[22,23] and a free acid moiety that allows for effective conjugation of the platinum drug to the γ-COOH group of the peptide side chain, rendering the peptide block hydrophobic and leading to drug-induced self-assembly.[16] Cisplatin, with its two coordination sites, is typically able to bind to two carboxylate residues, often leading to intra/inter polymer cross-linking (in principle, similar to its antitumor mechanism of disrupting the DNA structure in cell nuclei through the formation of intra- and interstrand cross-links[24]), which can help stabilize the core of these CDDP-loaded micellar assemblies.[17,25]

Vesicles, large bioinspired nanoscale assemblies,[26] have been of interest in CDDP delivery systems mainly in the form of drug-loaded, self-assembling, lipid-based vesicles (liposomes).[27−29] In contrast to micelles, vesicles contain a

Received: May 25, 2015
Revised: July 8, 2015
Published: July 13, 2015

DOI: 10.1021/acs.biomac.5b00692
Biomacromolecules 2015, 16, 2463−2474

hydrophobic membrane and an aqueous cavity that allow for versatile drug transport properties and—due to their larger structure−encapsulation of a larger amount of drugs compared to micelles, thus allowing for smaller amounts of drug delivery vehicles to be administered while achieving similar drug doses.[30]

Vesicles, like other nanoparticle systems, are able to passively target tumor cells by exploiting the leaky vasculature at tumor sites, commonly known as the enhanced permeability retention (EPR) effect.[31,32] Cell uptake can be further enhanced by modifying the surface of the vesicle with active targeting ligands such as antibodies, aptamers, or folic acid (FA) that bind to cell receptors that are overexpressed in tumor cells; thus allowing for more localized drug release profiles at the tumor sites.[33−35]

We recently developed a vesicle system for CDDP drug delivery via the use of self-assembling synthetic polymers.[36,37] Although, we—similarly to others—demonstrated high drug loading and effective cancer toxicity in this work, the lack of biodegradability limits the practicality of applying such materials clinically. It would thus be desirable to establish a CDDP-loaded vesicle delivery system using naturally occurring precursors in order to further improve on these existing delivery systems.

In the early 2000s, Lecommandoux et al.[38] and Deming et al.[39−41] reported on the successful preparation of vesicles from self-assembling, amphiphilic, polypeptide-based block copolymers. Vesicle formation was attributed to the presence of small, rigid (α-helical), hydrophobic peptide blocks that favor the formation of a densely packed, hydrophobic membrane. The stability of the secondary conformation requires that the hydrophilic segment be sufficiently large to sterically stabilize as well as solubilize these dense, hydrophobic domains.[40,42] Deming and co-workers demonstrated that successful vesicle formation of a poly(ethylene glycol)-modified polypeptide (hydrophilic) and poly($_L$-leucine) (hydrophobic) block copolymer required a hydrophilic block range of 100−150 repeating units with a hydrophobic segment of ∼20 repeat units (∼10−20 mol %).[39] Other reported works, including those from our group, demonstrated the use of long, hydrophilic and short, rigid, hydrophobic segments to promote tight packing of the polymers into spherical vesicles.[43,44]

In these cases, vesicle formation can be attributed to the hydrophobic segment of the polymer itself. However, herein we postulate that the formation of polypeptide-based (PEG-*b*-PLG) block copolymer vesicles may also be directed by the drug itself, whereby the intrinsic cross-linking capabilities of cisplatin are used to form a short, rigid, cross-linked hydrophobic segment, which subsequently induces self-assembly.

Herein we report on the facile preparation of cisplatin (CDDP)-loaded vesicles composed of a biocompatible and biodegradable poly(ethylene oxide)$_{114}$-*b*-poly($_L$-glutamic acid)$_{12}$ block copolymer. The rationally designed block copolymer consists of a hydrophilic PEG block of 114 repeat units with a short PLG block of 12 repeat units to achieve a hydrophobic component of ∼10 mol %. The copolymer itself exists in a unimolecular state in aqueous, physiological environments. CDDP conjugation to the polypeptide block induces the self-assembly of the copolymer into vesicles in water through the formation of a dense, cross-linked, hydrophobic domain. Maleimide functionalities on the vesicle surface/outer corona allow for conjugation of folic acid (FA) thiol, resulting in presentation of this cancer targeting ligand on the vesicle periphery. HeLa (cervical cancer cells) and NIH-3T3 (non-cancerous fibroblasts) cell lines with respectively high and low FA receptor (FR) expression are used for in vitro cytotoxicity and cellular uptake studies to demonstrate the specificity of the cancer targeting capabilities of the resulting drug delivery vehicle.

EXPERIMENTAL SECTION

Materials. Furan (≥99%, Aldrich) cystamine dihydrochloride (96%, Aldrich), cis-dichlorodiamineoplatinum(II) (CDDP) (Aldrich), folic acid (≥97%, Aldrich), trifluoroacetic acid (TFA) (99%, Aldrich), fluorescein isothiocyante isomer 1 (FITC) (≥90% HPLC, Aldrich), phosphate buffered saline (PBS) (tablets, Aldrich), 4-(dimethylamino)pyridine, (DMAP) (99%, Aldrich), tris (2-carboxyethyl)phosphine hydrochloride (TCEP) (≥98%, Aldrich), 3-mercaptopropionic acid (≥99%, Aldrich), *o*-phenylenediamine (99.5%, Aldrich), triphosgene (98%, Aldrich), pyridine (AR, Scharlau), hydrochloric acid (37%, Scharlau), triethylamine (TEA) (99%, Ajax Fine Chemicals), *N*-(3-(dimethylamino)propyl)-*N*′-ethylcarbodiimide hydrochloride (EDCI) (≥98%, Acros), H-Glu(OtBu)−OH (Bachem), Mal-PEG-NH_2·TFA 5 kDa (Jenkem Technology), silver nitrate (AR, Chem-Supply), sodium bicarbonate (AR, Chem-Supply), platinum standard for ICP (100 mg/L Pt in HCl, Aldrich), sodium chloride (AR, Chem-Supply), acetic acid (Glacial AR, Chem-Supply), sodium acetate (anhydrous, Chem-Supply), lithium bromide (99.9%, Aldrich), and sodium hydroxide (AR, Chem-Supply) were used as received. Pentane (anhydrous ≥99%, Aldrich), methanol (AR, Chem-Supply), chloroform (AR, Chem-Supply), dichloromethane (AR, Chem-Supply), chlorotrimetylsilane (≥99%, Aldrich), hydrogen peroxide (30%, AR, Chem-Supply), sulfuric acid (98%, ACI labscan), diethyl ether (AR, Chem-Supply), dimethylformamide (DMF) (extra dry, 99.8%, Acros), and toluene (AR, Ajax Fine Chemicals) were used as received. Tetrahydrofuran (THF)(AR, Chem-Supply) was distilled from benzophenone and sodium metal under argon. Dimethyl sulfoxide (DMSO) (≥99%, Aldrich) was stored under 3 Å molecular sieves. DMSO-d_6 (99.9%) was purchased from Cambridge Isotope Laboratories and Aldrich and stored under 3 Å molecular sieves. Dialysis tubing (Snakeskin 3.5 kDa cutoff) was purchased from ThermoScientific. Cell culture supplies (DMEM, FBS, 100 × GlutaMax, 100 × antibiotic-antimycotic), AlamarBlue(R) assay reagent, paraformaldehyde, and CellMask Deep Red Plasma Membrane Stain were purchased from Life Technologies and used as received. DAPI Fluoromount G was purchased from ProSciTech and used as received. Culture plates, microscope slides and glass coverslips were purchased from Corning.

Instrumentation. ^{1}H NMR analysis was performed using a Varian unity Plus 400 MHz NMR spectrometer using the deuterated solvent as reference. Dynamic light scattering (DLS) measurements were performed on a Wyatt DynaPro NanoStar fitted with a 120 mW Ga−As laser operating at 658 nm; 100 mW was delivered to the sample cell. Analysis was performed at an angle of 90° at a constant temperature of 25 ± 0.01 °C. All sample concentrations were 1 mg mL^{-1} and measurements were performed in triplicate. Zeta potential was measured on a Malvern Zetasizer Nano ZS with 4.0 mW HeNe laser operating at 632.8 nm. Analysis was performed at an angle of 173° and a constant temperature of 25 ± 0.1 °C. Platinum loading content was determined using thermogravimetric analysis (TGA) and inductively coupled plasma optical emission spectroscopy (ICP-OES). TGA was performed on a PerkinElmer Pyris-1 thermogravimetric analyzer, and the samples were heated from 30 to 700 °C at a heating rate of 10 °C/min under an atmosphere flow (20 mL/min). ICP-OES was performed on an Agilent 720-ES ICP-OES at a detected wavelength of 203.646 nm. Samples were dissolved up in 6 M HCl. A three-point standard curve was plotted between intensity versus a serial dilution of a certified Pt reference standard ranging from 1 to 10 ppm. UV−vis spectrometry was performed on a Shimadzu UV-1800 spectrometer using quartz cuvettes with a 1 cm path length, and a Nanodrop 1000 Spectrophotometer (Thermo Scientific) using 2 μL samples with 1 mm path length. FT-IR was performed on a Bruker

DOI: 10.1021/acs.biomac.5b00692
Biomacromolecules 2015, 16, 2463−2474

Tensor 27 with mid-infrared range (400−4000 cm^{-1}). The instrument was equipped with OPUS 6.5 Software. Typically, 0.1 mg of sample were ground with dry potassium bromide (KBr) at approximately 1 wt % and the resulting powder was pressed into a transparent pellet using Specac 10 ton Hydraulic Press. For each sample, 100 scans were taken in transmittance mode at a resolution of 2 cm^{-1}. GPC analysis was performed on a Shimadzu liquid chromatography system fitted with a PostNova Analytics MALS detector (λ = 658 nm), a Shimadzu RID-10 refractometer (λ = 633 nm), and a Shimadzu SPD-20A UV−vis detector, using three phenogel columns (Phenomenex, 5 μm) in series and HPLC grade DMF with 0.05 M LiBr as the mobile phase (1 mL/min). The oven temperature was set to 50 °C to maintain an acceptable pressure across the system, and the detectors were temperature controlled to 25 °C. Nova MALS software (PostNova) was used to determine the molecular weights and PDI using poly(ethylene glycol) standards. All GPC samples filtered through 0.45 μm filters. Fluorescent microscopy images were taken using a Leica TCS SP2 AOBS confocal microscope (Leica, Germany) equipped with an argon laser (λ = 488 nm), using a 63× oil immersion objective (Leica, Germany). DAPI was excited at λ = 405 nm, FITC at λ = 488 nm, and CellMask Deep Red at λ = 633 nm. The emission filters were set at λ = 414−478 nm for DAPI, λ = 500−561 nm for FITC, and λ = 646−726 nm for CellMask Deep Red. Images were recorded at a depth of 10−20 μm from the surface of the glass coverslip. Leica confocal software was used to acquire images of 512 × 512 pixels. Images were recorded from a glass coverslip. Flow cytometry was conducted on an A50-Micro flow cytometer (Apogee) using a 488 laser and three light scattering detectors. At least 10000 cells were analyzed in each experiment. Transition electron microscopy (TEM) was performed on a Tecnai 12 Transmission Electron Microscope (FEI, Eindhoven, The Netherlands) equipped with a Gatan 626 cryoholder (Gatan,Pleasanton, CA, USA) at an operating voltage of 120 kV, and an LVEM5 Transition Electron Low Voltage Microscope (DeLonge America) operating at a voltage of 5 kV. For cryoTEM, 300-mesh copper grids coated with perforated carbon film (Lacey carbon film: ProSciTech, Qld, Australia) were first glow discharged in nitrogen to render them hydrophilic. Four-microliter aliquots of the sample (1.5 $mgml^{-1}$) were pipet onto each grid prior to plunging. After 30 s adsorption time grids were blotted manually using Whatman 541 filter paper, for approximately 2 s. Grids were then plunged into liquid ethane cooled by liquid nitrogen while in a laboratory-built humidity controlled vitrification system (ambient 22 °C). Frozen grids were stored in liquid nitrogen until required. For standard TEM, samples were prepared on carbon coated grids as per cryoTEM, followed by staining with 2% aqueous uranyl acetate at pH7.2 for 10 s then blotted with Whatman 541 blotting paper and air-dried for 2 min. For LVEM, samples were prepared by casting the solution (1 $mgml^{-1}$) onto carbon coated copper grids for ∼30 s then dried under low vacuum for 15 min. No staining was applied. Atomic force microscopy (AFM) analysis was performed on 0.5 $mgml^{-1}$ polymer samples drop casted (20 μL) on silicon wafers washed in piranha solution and allowed to air-dry for 48 h. Images were acquired with an MFP-3D Asylum Research instrument. Typical scans were conducted in AC (tapping) mode with ultrasharp SiN gold-coated cantilevers (MikroMasch, Bulgaria). Image processing and surface roughness analysis were performed using the Nanoscope and Igor Pro software programs, respectively.

*Synthesis of Furan-Protected Mal-PEG-NH_2HCl (**P1**).* Furan-protected Mal-PEG-NH_2HCl (5.3 kDa) was synthesized through general Diels−Alder (DA) cycloaddition conditions, followed by counterion exchange of the trifluoroacetate anion with chloride anions. A mixture of Mal-PEG(5 kDa)-NH_2TFA (150 mg, 0.283 μmol), furan (2.5 mL), and deionized (DI) water (8.5 mL) was gently stirred at 35 °C for 15 h. Excess furan was removed under low vacuum followed by extraction in an ether wash (3 × 5 mL). The aqueous phase was then collected and place under low vacuum to remove excess ether. 1 M HCl (3.2 mL) was then added ($[HCl]_{final}$ = 0.2M), and the clear solution was stirred at room temperature (RT) for 6.5 h. Water was removed under high vacuum and toluene azeotrope to afford a light yellow powder, which was then dissolved in minimal chloroform and precipitated in chilled ether. Precipitate was then centrifuged and dried under low vacuum for 48 h to obtain a white yellow powder (**P1**) (Yield: 130 mg, 86%). ^{19}F NMR was used to determine complete removal of the TFA peak at δ_F = −77 ppm after counterion exchange (refer to the Supporting Information (SI), Figure S1). ^{1}H NMR (400 MHz, $CDCl_3$) δ_H (ppm): 2.35 (t, 1H, J = 7.2 Hz, $-CH_2-CH_2-$), 2.47 (t, 1H, J = 7.2 Hz, $-CH_2-CH_2-$), 2.85 (s, DA c_{exo}), 3.18 (brs, $CH_2-CH_2-NH_2$), 3.40 (m, 2H, $-CH_2-CH_2-$) 3.46 (t, 2H, J = 5.2 Hz, $-CH_2-CH_2-$), 3.63 (s, 455H, CH_2-CH_2-O−), 3.80 (t, 2H, J = 5.2 Hz, CH_2-CH_2-N(Mal)), 5.25 (s, DA b_{exo}), 5.30 (m, DA b_{endo}), 6.4 (s, DA a_{exo}), 6.5 (s, DA a_{endo}), 7.92 (s, CONH) (refer to SI, Figure S2 for DA adduct stereochemistry assignments).

*Synthesis of Furan-Protected Mal-PEG-b-PLG(γ-tBu)-NH_2 (**P2**).* *N*-Carboxyanhydride γ-*tert*-butyl-$_L$-glutamate (γ-tBu Glu NCA) was synthesized according to reported synthetic protocols on similar poly($_L$-glutamic acid) NCA monomers.[45,46] To an oven-dried RBF was added γ-tBu Glu NCA (55 mg, 0.24 mmol) under N_2 followed by anhydrous DMF (0.8 mL) and stirred to dissolve for 5 min. Furan protected Mal-PEG-NH_2HCl (**P1**) (120 mg, 22.6 μmol, M/I = 11) dissolved in anhydrous DMF (1.1 mL) was then added to the flask under N_2. The yellow-brown reaction mixture was then stirred for 3 days under N_2 at 40 °C with a needle bleed to allow for removal of HCl byproduct. Furan (0.5 mL) was then added to flask, stoppered and stirred for a further 7 h. DMF was then removed under high vacuum, with product residue dissolved up in minimal chloroform, precipitated in chilled ether and dried to afford a white-cream powder (**P2**) (Yield: 120 mg, 70%). ^{1}H NMR (400 MHz, d_6-DMSO) δ_H (ppm): 1.40 (s, γ-**tBu**), 1.73−1.90 (m, CH_2-CH_2-COO), 2.19−2.29 (m, CH_2-CH_2-COO), 2.91(s, DA c_{exo}), 3.51 (s, 455H, CH_2-CH_2-O−), 4.24 (m, −N−CH−CO), 5.11 (s, DA b_{exo}), 5.30 (m, DA b_{endo}), 6.38 (s, DA a_{exo}), 6.54 (s, DA a_{endo}), 7.98 (m, CONH).

*Synthesis of Mal-PEG-b-PLG-NH_2 (**P3**).* *t*-Butyl deprotection and retro DA was conducted in a one pot procedure. Protected block copolymer (**P2**) (50 mg, 78.9 μmol Glu units), DCM (3.5 mL), and TFA (3.5 mL) were stirred vigorously for 1 h, followed by the addition of toluene (8 mL). DCM and TFA were then removed under low vacuum with excess TFA removed through DCM azeotrope. The contents were then refluxed at 120 °C for 6 h, concentrated, dissolved in minimal methanol, and precipitated in chilled ether. Precipitate was isolated and dried under vacuum to give a white powder **P3** (Yield: 45 mg, 100%). ^{1}H NMR (400 MHz, d_6-DMSO) δ_H (ppm): 1.75−1.90 (m, CH_2-CH_2-COO), 2.10−2.33 (m, CH_2-CH_2-COO), 3.51 (s, 456H, CH_2-CH_2-O-), 4.21 (s, −N−CH-CO), 7.00 (s, mal −CH═CH-), 8.01 (m, CONH).

Chemical Modification of Mal-PEG-b-PLG-NH_2 for SEC Analysis. For better refractive index (RI) detection after GPC, carboxylic acid groups of Mal-PEG-*b*-PLG-NH_2 polymers were modified into methyl ester units using chlorotrimethylsilane as a methylating agent. Sample (3.5 mg) was dissolved in 250 μL methanol in a 2 mL eppendorf tube. Chlorotrimethylsilane (TMSCl, 9.5 μL, ∼10 equiv to carboxylic acid groups) was then added, and the contents were stirred for 20 h at 21 °C. The solvent and excess TMSCl were then removed under reduced pressure, and the methylated polymer was analyzed by size exclusion chromatography (DMF).

*Fluorescent Tagging of Mal-PEG-b-PLG-NH_2 (**P4**).* FITC (2.17 mg, 5.58 μmol) dissolved in anhydrous DMSO (285 μL) was added to Mal-PEG-*b*-PLG-NH_2 (**P3**) (30 mg, 4.41 μmol), followed by addition of triethylamine (TEA, 0.2 μL, 1.43 μmol, 0.3equiv) as catalyst. The yellow-brown solution was stirred in the dark at 21 °C, 1050 rpm for 14 h. The reaction was then quenched with a few drops of 1 M HCl, and transferred to a 3.5 kDa dialysis cutoff for dialysis against methanol over 48 h. Contents were then concentrated, precipitated in chilled ether, centrifuged, and dried to afford a light yellow solid (Yield: 25 mg, 80%). ^{1}H NMR (400 MHz, d_6-DMSO) δ_H (ppm): 1.75−1.90 (m, CH_2-CH_2-COO), 2.10−2.33 (m, CH_2-CH_2-COO), 3.51 (s, 455H, CH_2-CH_2-O-), 4.20 (s, −N−CH-CO), 6.60 (m, FITC ArH), 7.00 (s, mal −CH═CH−), 7.17 (m, FITC ArH), 7.78−8.04 (m, CONH, FITC ArH), 10.10 (s, FITC COOH). UV−vis analysis determined tagging efficiency to be ∼50%. The integrity of the maleimide double bond was determined to be ∼60% (SI, Figure S4).

DOI: 10.1021/acs.biomac.5b00692
Biomacromolecules 2015, 16, 2463−2474

Preparation of CDDP-Loaded Mal-PEG-b-PLG-FITC Vesicles. The conjugation of *cis*-platinum to block polymer **P4** was performed through the formation of a *cis*-diaminediaqua platinum(II) complex intermediate using modified published procedures.[7,47] CDDP (12 mg, 40 μmol) and $AgNO_3$ (13.3 mg, 80 μmol) ([$AgNO_3$]/[CDDP] = 2) was suspended in 14 mL DI water, and stirred vigorously in the dark at room temperature for 4 h. Silver chloride white precipitate was then removed by centrifuge at 4400 rpm for 1 h and the *cis*-diaminediaqua platinum(II) complex then filtered through a 0.44 μm syringe filter into an RBF containing Mal-PEG-*b*-PLG-FITC **P4** (20 mg, 34 μmol glutamic acid units, [CDDP]/[Glu] = 1.2). The contents were then left to gently stir in the dark at 37 °C for 15 h. The cloudy yellow-orange solution (indicative of self-assembly) was then added to 3.5 kDa dialysis tubing and dialyzed against DI water over 30 h, after which time the solution turned slightly less cloudy due to dilution effects. The dialysis contents were lyophilized to an orange powder with TGA and ICP-OES used for quantitative determination of platinum loading. Refer to Supporting Information for TGA analysis (SI, Figure S3), calculation of drug loading content (DLC) and drug conjugation efficiency (DCE).

In Vitro Drug Release from CDDP-Loaded Vesicles. The in vitro release of CDDP from the drug-loaded vesicles was evaluated by the dialysis method. The CDDP-loaded vesicles (2.4 mg) were dissolved up in the release buffer and added to 3.5 kDa dialysis tubing. The conjugate was dialyzed against the release buffer (50 mL) at 37 °C with 2 mL aliquots withdrawn at time intervals and replaced with fresh buffer. The withdrawn samples were analyzed by the *o*-phenylenediamine (o-PDA) colorimetric assay according to previously published procedures.[48,49] Aliquot samples (2 mL) were added to 2 mL of o-PDA (2 mg/mL DMF) and heated at 100 °C for 15 min. The amount of platinum in the sample was determined by measuring the UV−vis absorbance at 703 nm using cisplatin as a standard curve. The concentration of CDDP released from the conjugate was expressed as a ratio of the amount of platinum in the released solution and that in the initial sample using the following equation:[7]

$$\%\text{CDDP released} = \frac{V_{\text{total}}(t) \times C + Y}{Z}$$

where $V_{\text{total}(t)}$ is the remaining volume in the releasing container at time t (mL); C is the concentration of platinum determined from UV−vis measurements (μg/mL); Y is the amount of platinum that has already been collected (μg); and Z is the total amount of platinum at t = 0 present in the dialysis bag (μg).

Synthesis of FA-SS-FA. FA (80 mg, 0.181 mmol) was first dissolved in anhydrous DMSO (3 mL) using extensive sonication (2 h), then added to an oven-dried flask containing EDCI (84 mg, 0.44 mmol) and DMAP (4.4 mg, 36 μmol) under N_2 and stirred to dissolve. Pyridine (1.5 mL, 18.5 mmol) was then added, followed by the dropwise addition of cystamine·2HCl (21 mg, 93.2 μmol, 0.5 equiv) dissolved in anhydrous DMSO (0.5 mL). The clear solution was stirred at RT in the dark under N_2 for 3 days then precipitated in acetone (45 mL). The precipitate was subsequently washed with 1 M HCl (2 × 30 mL), DI H_2O (2 × 25 mL), acetone (3 × 20 mL) then dried under vacuum to afford a yellow solid (Yield: 55 mg, 60%). ^{1}H NMR (400 MHz, d_6-DMSO) δ_H (ppm): 1.87−2.30 (m, 8H, −C**H**$_2$−C**H**$_2$−CONH− of FA), 2.75 (m, 4H, −C**H**$_2$S−), 4.34 (m, 2H, −C**H**−), 4.48 (s, 4H, Ar−C**H**$_2$−NH−Ar), 6.63 (dd, 4H, J = 8.6, 1.8 Hz, −C**H**− of phenyl ring), 6.92 (br s, −N**H**−), 7.65 (dd, 4H, J = 8.6, 3.0 Hz −C**H**− of phenyl ring), 8.02 (m, 4H, −CON**H**−), 8.64 (s, 2H, C**H** of pyrazine), 11.4 (br s, COOH) (see SI, Figure S5).

Synthesis of FA-Conjugated CDDP-Loaded Vesicles. Synthesis of FA-conjugated drug-loaded vesicles was performed using thiol-maleimide coupling chemistry after in situ reduction of the FA-SS-FA precursor. FA-SS-FA (1.95 mg, 3.9 μmol FA) dissolved in DMSO (750 μL) was added to a suspension containing FITC tagged vesicles (13.1 mg, 1.0 μmol maleimide groups) and degassed 20 mM $NaHCO_3$ solution (750 μL, pH 7.5). TCEP (0.1 M, 5.7 μL, 0.57 μmol) was then added and the contents sealed and stirred in the dark at 22 °C, 1200 rpm for 4 h. The reaction was quenched with 3-mercaptopropionic acid (1 μL) and stirred for an additional 3 h with the contents then transferred to a 3.5 kDa dialysis cassette and dialyzed against DI water for 24 h (3 × 1.8 L). The dialyzed product was lyophilized as a yellow powder. ^{1}H NMR (400 MHz, d_6-DMSO) δ_H (ppm): 1.75−1.90 (m, glutamic C**H**$_2$−CH$_2$−COO), 2.10−2.33 (m, glutamic CH$_2$−C**H**$_2$−COO), 3.50 (s, 455H, PEG C**H**$_2$−C**H**$_2$−O−), 4.25 (brs, glutamic −N−C**H**−CO), 4.48 (s, Ar−C**H**$_2$−NH−Ar), 6.60 (m, FITC Ar**H**), 6.62 (m, FA −C**H**− of phenyl ring), 6.91 (m, FA −N**H**−), 7.64 (m, 4H, FA −C**H**− of phenyl ring), 8.02 (m, FA −CON**H**−), 8.63 (s, FA C**H** of pyrazine) (see SI, Figure S6).

Cell Culture. HeLa and NIH-3T3 cells were maintained in "complete" DMEM (supplemented with 10% FBS, 1× GlutaMAXTM, and 1× antibiotic-antimycotic) in a humidified atmosphere containing 5% CO2 at 37 °C. Usually, cells were seeded in a T175 flask (ca. 3 × 10^6 cells/mL) and passaged twice a week prior to the performance of the subsequent cell viability or cellular uptake imaging studies

Cell Viability Assay. Cytotoxicity of the vesicles was assessed using Invitrogen's alamarBlue cell viability reagent following the manufacturer's instructions. Briefly, cells were plated into 96 well plates at a concentration of ca. 10 000 cells/well except for the "medium blanks" in which the same amount of medium was added instead. Experimental wells received the vesicles, free polymer and CDDP at the indicated ratios/concentrations and the plate was subsequently incubated in a humidified atmosphere containing 5% CO_2 at 37 °C. After 72 h, 10 μL of alamarBlue cell viability reagent was added to each well (except for three wells containing medium only). After 3−3.5 h of incubation under the same growth conditions, the absorbance at 570 and 600 nm of each well was measured using a Varian Cary 50 Bio UV−visible spectrophotometer. The absorbance of each well was corrected against the medium-only wells without alamarBlue reagent, and then expressed as a percentage of the growth control. Note that all experiments were conducted in triplicate, and error bars shown represent the standard error of independent experiments.

Cellular Uptake Test (Confocal Laser Scanning Microscopy CLSM). On Day −1, sterile round glass coverslips (Φ 15 mm) were placed in the wells of a 12 well plate and HeLa and NIH-3T3 cells were seeded in "complete DMEM" medium at a cell density of 200 000 cells per well in 0.5 mL seeding volume before the plate was placed in a humidified incubator (95−100% humidity, 5% CO_2) overnight. On Day 0, the seeding medium was removed from each well and cells were gently washed with 1 mL sterile PBS. Approx. 0.5 mL of fresh "complete DMEM" medium and the FITC-labeled vesicles were added at a ratio of 500:1. The plate was returned to the incubator for 24 h. On Day 1, the medium was removed from each well, and cells were gently washed with PBS. Samples were fixed using paraformaldehyde before being stained with Deep Red Plasma stain and subsequently mounted onto microscopy slides using DAPI Fluoromount G for confocal microscope observation using a Leica TCS SP2 confocal microscope.

Cellular Uptake Test (Flow Cytometry). Again, on Day −1 cells were seeded in "complete DMEM" at a cell density of 200 000 cells per well in 0.5 mL seeding volume before the plate was placed in a humidified incubator (95−100% humidity, 5% CO_2) overnight. On Day 0, the seeding medium was removed from each well and cells were gently washed with 1 mL sterile PBS. Approx. 0.5 mL fresh "complete DMEM" medium and the FITC-labeled vesicles were added at a mass ratio of 500:1. The plate was returned to the incubator for 24 h. On Day 1, the medium was removed from each well, and cells were gently washed with PBS, trypsinised, fixed with paraformaldehyde, and resuspended into PBS. Cell suspensions were subsequently analyzed using an Apogee A-50 Micro Flow cytometer.

RESULTS AND DISCUSSION

Synthesis of Block Copolymer. To prepare the polypeptide-based vesicles suitable for targeted drug delivery to cancer cells, maleimide functionalized PEG-*b*-PLG-NH_2 (Mal-PEG-*b*-PLG-NH_2) **P3** block copolymer was first synthesized by controlled ring-opening polymerization (ROP) of γ-*tert*-butyl-$_L$-glutamate *N*-carboxyanhydride (γ-tBu Glu NCA)

DOI: 10.1021/acs.biomac.5b00692
Biomacromolecules 2015, 16, 2463−2474

Scheme 1. Synthetic Scheme of Folic Acid-Conjugated CDDP-Loaded Mal-PEG-*b*-PLG-FITC Vesicles

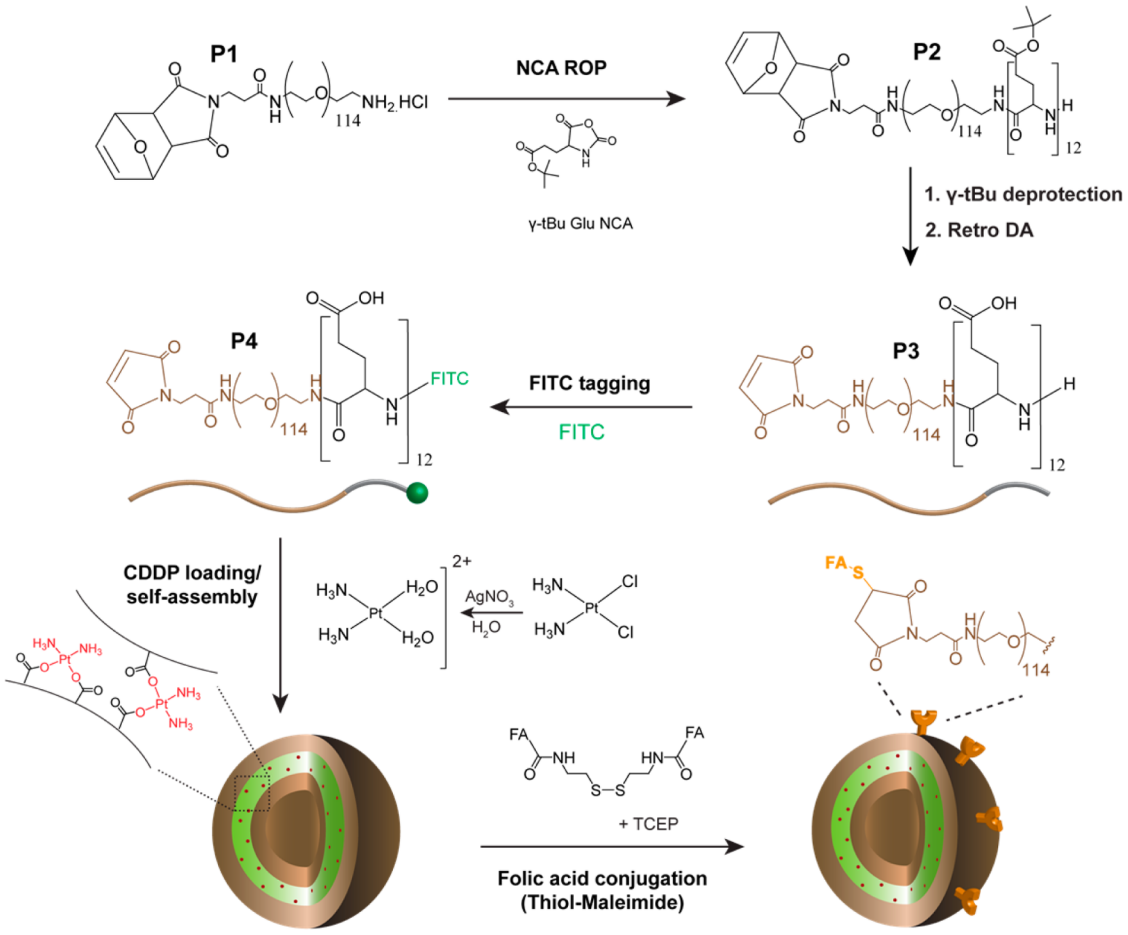

monomer using furan protected Mal-PEG(5 kDa)-NH_2HCl **P1** as macroinitiator (MI) (Scheme 1).

The maleimide group is susceptible to nucleophilic attack by amines.[50] Preliminary NMR and GPC analysis after polymerization using unprotected MI confirmed the presence of higher molecular weight species and a noticeable reduction in maleimide vinyl proton intensities as a result of self-coupling between the terminal maleimide and the amine of the living block copolymer chain. This observation was particularly obvious after repetitive isolation and concentration of the unprotected MI copolymer. A thermally reversible Diels–Alder (DA) reaction between furan and maleimide MI was therefore adopted for the protection of the reactive maleimide double bond in **P1** (~95% protection based on maleimide vinyl proton integration δ = 7.00 ppm, ^{1}H NMR d_6-DMSO) throughout the polymerization process.[51−54]

The use of an amine hydrochloride salt initiator allows for the controlled polymerization of γ-*t*Bu Glu NCA monomer by ensuring a controlled concentration of reactive free amine species in an associate-dissociate equilibrium.[55] For block copolymer synthesis a monomer to macroinitiator ratio ([M]:[I]) of 11 was used to obtain a future hydrophobic (drug conjugated) glutamic acid block of ~10 mol %, with ^{1}H NMR analysis used to confirm block copolymer synthesis with a degree of polymerization (DP) of 12 (Figure 1B, see SI Figure S4 for polypeptide block ^{1}H integration).^{1}H NMR analysis of the block copolymer **P2** in Figure 1A shows the characteristic signals of the poly($_L$-glutamic acid) side chain methylene protons (c and c', CH−C**H**$_2$−C**H**$_2$−CO−O−tBu) at δ = 1.7−2.3 ppm with the γ-*tert*-butyl protecting group (d, CH−CH_2−CH_2−CO−O−**tBu**) proton resonances at δ = 1.4 ppm. Resonances from δ = 5.0−6.5 ppm were assigned to the protected maleimide DA cycloadduct which exists as both endo/exo stereoisomers as reported in literature (see Supporting Information).[54,56]

Traditionally, γ-benzyl protected $_L$-glutamic acid NCA (BLG-NCA) has been employed for the ROP synthesis of PLG. Subsequent deprotection conditions typically involve strong acid (HBr) or bases (NaOH), which have been found to cause both poly(ethylene glycol) and polypeptide backbone chain cleavage.[57] Strong acids have also been found to promote retro DA at low temperatures[58] and readily react with the resulting free maleimide. To avoid any unwanted chain cleavage or maleimide hydrolysis, γ-*t*Bu Glu NCA monomer was employed with the protecting group readily removed under mild conditions (TFA in DCM) after polymerization. Retro DA was performed under reflux to afford the free maleimide copolymer (**P3**) with ^{1}H NMR analysis in Figure 1A confirming the disappearance of the *t*-butyl and DA cycloadduct protons, with an increase in the free maleimide double bond vinyl protons at (δ = 7.00 ppm ^{1}H, d_6-DMSO) to ~97% integrity as calculated by ^{1}H NMR integration. SEC analysis in Figure 1B shows unimodal distribution with a relatively narrow polydispersity (~1.3) maintained throughout the polymerization and deprotection of the block copolymer, indicating the

DOI: 10.1021/acs.biomac.5b00692
Biomacromolecules 2015, 16, 2463−2474

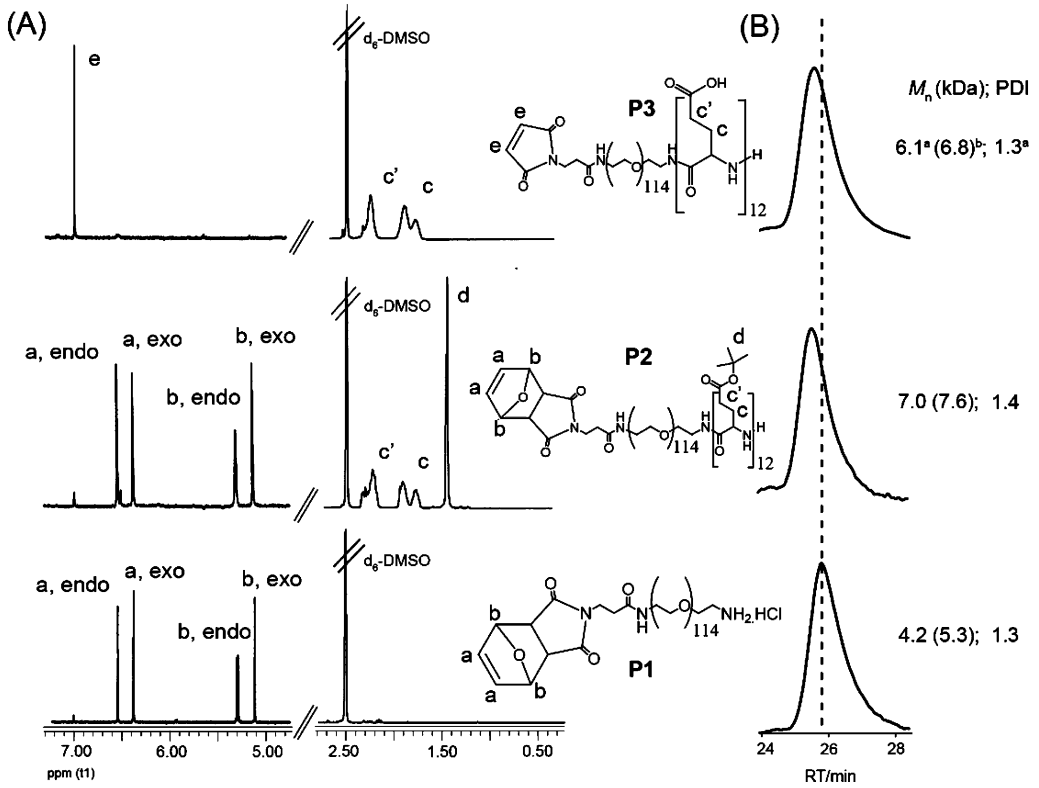

Figure 1. (A) ^{1}H NMR (d_6-DMSO) spectra and (B) GPC (DMF) RI chromatograms of polymers **P1**−**P3**. (a) M_n and PDI determined by GPC using MeO-PEG−OH standards; (b) M_n determined by ^{1}H NMR analysis using PEG (CH_2−CH_2−O) proton integrations as reference.

absence of any unwanted higher MW self-coupled bock copolymer or cleaved species.

The resulting block copolymer **P3** contains a terminal maleimide and amine group suitable for conjugation of a thiol targeting ligand and fluorescent FITC tag, respectively. Conjugation of the FITC tag was performed through a conventional amine-isothiocyanate coupling procedure (Scheme 1) using triethylamine as catalyst to prepare block copolymer **P4**. FITC tagging efficiency was determined to be ∼50% through UV−vis analysis and ^{1}H NMR analysis.

CDDP Loading of Block Copolymer/Vesicle Formation. Cisplatin was conjugated to the carboxylic acid side chain of the PLG block via a *cis*-diaminediaqua platinum(II) complex using previously reported procedures[7] (Scheme 1). Conjugation of platinum to the carboxylic acid side chain was verified through FT-IR (see SI Figure S7). A reduction in absorbance of the carbonyl (C═O) stretch of COOH at 1709 cm^{-1} and the presence of new COO−Pt stretch at 1384 cm^{-1} is consistent with reports of Pt binding to PLG acid groups.[59,60] Additionally, small shifts in the amide I (1670−1660 cm^{-1}) and amide II (1546−1551 cm^{-1}) frequencies indicate a secondary conformation change of the polypeptide block after CDDP conjugation, possibly due to cross-linking by the drug.

ICP-OES was used to determine a drug loading content (DLC) of 7.4 wt % (see SI Figure S3 for comparative DLC based on TGA). Assuming that each platinum drug is bound to two carboxylate groups, this DLC value was used to determine a drug conjugation efficiency (DCE) of 50% (see SI for DCE calculations), indicating a strong drug loading capacity where half of the carboxylate side chains of the polymer are complexed with drug. Table 1 summarizes the Pt (II) loading properties of vesicles, all of which are lipid-based (liposomes) where the Pt(II) drug is encapsulated through physical interactions, currently in clinical trials.[27] The drug loading capacity in this work is comparable, and even higher than SPI-077 and Aroplatin liposomal systems. The added benefit of a biodegradable polypeptide component in this work is also likely to have an improved toxicity and drug release profile to these Pt (II)-loaded liposomes. The drug loading also compares well with cisplatin-conjugated nonbiodegradable synthetic polymer (HPMA) micelles (AP5280) currently in clinical trials (8.5 wt %).[61] In the case of polypeptide-based PEG-*b*-PLG micelles (NC-6004) currently in clinical trials, where CDDP is conjugated to the PLG backbone, the drug loading is much higher (39 wt %).[15,19] In NC-6004, the PLG block consists of ∼40 repeat units[15] and so the lower DLC in this work is expected due to the shorter peptide segment employed (DP = 12) and therefore lower number of $_L$-glutamic acid units available for metal conjugation. However, due to the much larger size of vesicles compared to these micelles, far fewer delivery vectors can be administered for the same therapeutic dose.[30]

Table 1. Platinum(II)-Loaded Vesical (Liposomal) Nanocarriers Currently in Clinical Trials[27]

compound	Pt (II)	carrier	DLC (wt %)	ref
Lipoplatin	cisplatin	liposome	10	62
Lipoxal	oxaliplatin	liposome	10	63
SPI-077	cisplatin	liposome	6.7	64
Aroplatin	oxaliplatin	liposome	6	65
PEG-*b*-PLG	cisplatin	polypeptide-based vesicle	7.4	this work

Analysis of the nanoparticle size and structure was conducted by DLS, TEM, and AFM. DLS data in Figure 2 reveals an

DOI: 10.1021/acs.biomac.5b00692
Biomacromolecules 2015, 16, 2463−2474

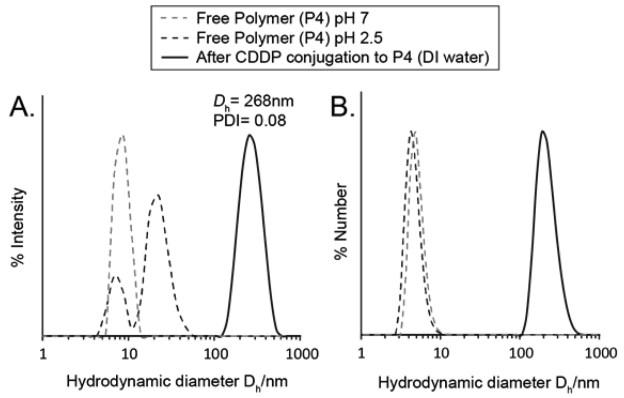

Figure 2. DLS hydrodynamic diameter analysis of free polymer (**P4**) at different pH and free polymer after CDDP conjugation. (A) % Intensity profile; (B) %Number profile. Polymer concentration 1 mg mL^{-1}.

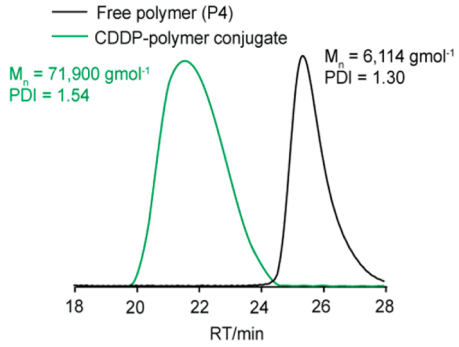

Figure 3. GPC (DMF) SEC chromatograms of free polymer (P4) before and after CDDP conjugation. M_n and PDI determined by GPC using MeO−PEG−OH standards.

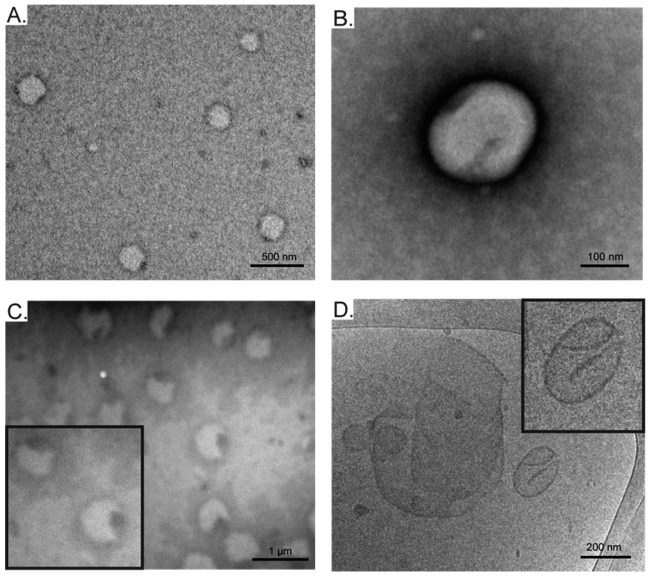

Figure 4. TEM analysis of CDDP-loaded block copolymer vesicles. (A,B) Negative stain, air-dried sample. (C) No stain, vacuum-dried sample. (D) Cryo-TEM sample. Samples at 1 mg mL^{-1} polymer concentration.

average hydrodynamic diameter (D_h) of 268 nm (intensity) after CDDP conjugation, well within the size range of vesicle assemblies. A low PDI of 0.08 was recorded, with number distribution data in Figure 2B indicating an absence of any smaller sized assemblies, e.g., micelles.

To determine whether these vesicle size assemblies could be achieved without CDDP conjugation, self-assembly analysis was performed on the free polymer (**P4**) before CDDP conjugation at pH 7 and at pH 2.5 (Figure 2). As expected no self-assembly of **P4** at pH 7 is observed, with only unimolecular species (<10 nm) present due to the charged (hydrophilic) PLG block. The pK_a of poly($_L$-glutamic acid) is reported to lie between 4 and 5,[66,67] and at pH values <4, PLG groups are predominantly neutralized to form hydrophobic α-helical segments.[68,69] DLS intensity distribution data of neutralized **P4** at pH 2.5 also shows no vesicle size formation, with only small assemblies (~25 nm) and unimolecular species (<10 nm) observed and number distribution data showing entirely unimolecular species. The data indicates that in this case, hydrophobicity of the polypeptide block alone is not enough to form vesicle size assemblies. The formation of well-defined vesicle size assemblies is due to the CDDP conjugation/self-assembly process. We suspect that it involves the conjugation of CDDP to the polymer chains, with intrachain cross-linking forming a short rigid block that self-assembles into tight regularly packed vesicle structures. To determine whether any interstrand cross-linking of the assembled vesicles by CDDP takes place due to the close proximity of the polymer chains in the tightly packed vesicle membrane, SEC analysis of the CDDP conjugated block copolymer was performed in DMF, a good solvent for both PEG and CDDP conjugated PLG blocks. Figure 3 shows a large shift in retention time of the polymer after CDDP conjugation corresponding to a MW increase to ~72 kDa. Such a large increase in MW strongly indicates the presence of interchain cross-linking of polymer chains by CDDP within the vesicle membrane.

In order to observe the physical morphology of the resulting vesicle self-assemblies, TEM and AFM analysis was performed. TEM analysis is shown in Figure 4. Under standard TEM and cryo-TEM conditions, Figure 4A, B and D shows spherical structures with thin membranes and diameters of around 250 nm, in good agreement with the DLS data. Slight structural deformations/indentations are observed on the membranes of the assemblies, typical of vesicles, and is suggestive of a hollow vesicle assembly, e.g., Figure 4D.

Vesicles, unlike micelles, are prone to partial core collapse and membrane deformations due to their intrinsic hollow structure.[70−72] Drying of TEM samples cast onto copper grids by freeze-drying or under direct vacuum has been reported to promote these deformations.[72] Using this method as an aid in further determining whether the self-assembly structures were indeed hollow structures suggestive of vesicles, TEM image of vacuum-dried samples is presented in Figure 4C. The particles show what are suspected to be a ruptured vesicle wall exposing a hollow core. The increase in observed particle size (~500 nm) is due to the flattening of the ruptured vesicle when absorbed onto the TEM grid. Also, it has been reported that vacuum drying of vesicles on TEM grid can result in a 2-fold increase in vesicle wall thickness,[72] which could be another cause for the larger observed size in Figure 4C. Therefore, despite Figure 4C not being representative of the true size of the vesicle, it clearly shows the presence of hollow vesicle structures. The air-dried samples in Figure 4A,B shows only minor shrinkage/core collapse of the vesicle structures after air drying, and still maintain vesicle wall integrity, with sizes (~250

DOI: 10.1021/acs.biomac.5b00692
Biomacromolecules 2015, 16, 2463−2474

nm) slightly lower than those obtained in DLS where the vesicles are in a hydrated state, a commonly reported observation.[73,74] The vacuum-dried sample in Figure 4C was analyzed without staining so that any dense platinum regions could be visualized. The dense (darker) holes in the structures, suggests an exposure of a platinum packed membrane, consistent with the proposed vesicle structure in Figure 5A. It

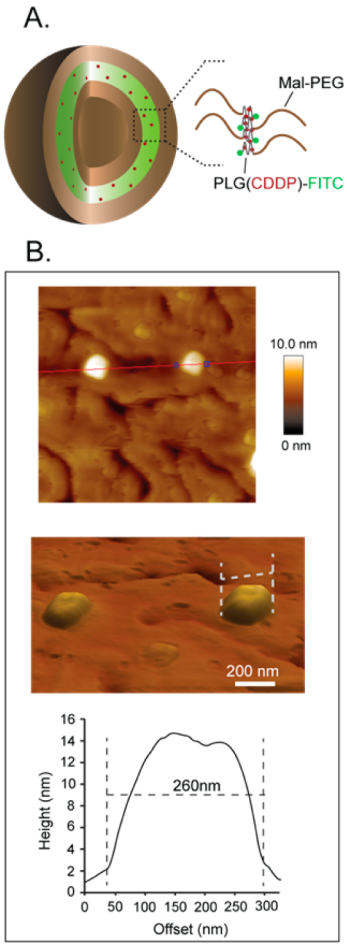

Figure 5. (A) The proposed self-assembly vesicle structure with PEG assemblies on the outer vesicle surface/corona and inner core with dense CDDP cross-linked PLG forming the hydrophobic membrane. (B) AFM analysis of vesicles on silicon wafer (polymer concentrations 0.5 mg mL^{-1}) including 3D AFM image and z-profile analysis showing cross-sectional diameter of vesicle structure marked with a white dashed line.

is important to note that a small number of vesicles of roughly the same size with an anomalous shape were also observed under TEM analysis. Incomplete vesicle assembly in these cases can be explained by the cross-linking of the polypeptide chains inhibiting the regular packing of polymer chains into a uniform vesicle structure.

The formation of hollow vesicle structures is further supported by the AFM data in Figure 5B. The 3D AFM image shows a partial collapse of the particles with z-profile analysis showing a clear indentation in the structure where the collapse occurred predominantly during AFM tapping mode. The cross-sectional diameter of the structure of 260 nm is in good agreement with the other air-dried samples used in TEM analysis (Figure 4A,B) and DLS data.

Zeta potential of the vesicle was measured to be −3.93 ± 0.5 mV, relatively low due to the conjugation of the carboxylate anion with the Pt metal of CDDP. The slight negative charge is likely to be due to the remaining unconjugated carboxylate groups, and is quite suitable for in vivo use, which can effectively reduce protein absorbance during blood circulation.[75]

CDDP Release. In vitro release of the CDDP incorporated vesicles was performed using the *o*-phenylenediamine colorimetric assay (o-PDA) carried out according to a previously published protocol.[7,76] The release of cisplatin is initiated in the presence of chloride ions, which results in a ligand exchange from the metal−polymer back to its original metal−chloride complex (Figure 6A).[7,15] To mimic the pH/chloride concentrations in the plasma and late endosomal/lysosomal environment, release was performed in PBS (pH = 7.4, [Cl^-] = 140 mM) and in sodium acetate buffer (pH = 5.2, [Cl^-] = 35 mM), respectively (Figure 6B). It is commonly misreported that a release in PBS/0.9% NaCl ([Cl^-] = ∼137−150 mM) at pH 5 is representative of the intracellular environment. Rather, the intracellular chloride concentration is reported to lie between 4 and 60 mM, with an average of around 35−40 mM.[77,78] While release at pH 5/([Cl^-] = ∼137−150 mM) often has the result of an improved drug release profile over standard PBS due to the protonation of the carboxylic acid after drug removal to promote its release, it is not representative of the intracellular chloride concentration.

CDDP release data in Figure 6B shows that in pH 7.4 PBS, a slow and sustained release profile is observed with no burst release of drug. This controlled release of CDDP from the vesicles in pH 7.4 PBS is considerably slower than other cisplatin drug delivery systems in the literature[16,47,76] and presents an opportunity for alleviating the systemic drug release/acute toxicity issues that have hampered the use of high cisplatin dosages in cancer therapy.[79] The slow release of drug is likely to be explained by stable secondary structures/CDDP cross-linking in the vesicle membrane which is helping to stabilize the vesicle structure and slow the rate of metal−ligand exchange.[25,80] In fact, this vesicle stability was further supported by DLS analysis, which showed that vesicle size was maintained even after 6 days of release. Release in pH 5.2/35 mM [Cl^-], representative of the late endosomal/lysosomal environment, is twice as fast (∼35% over 24 h), which is suggestive of a faster "burst-like" release profile of the drug from the vesicles once inside the target cancer cell. It is important to note that accelerated intracellular CDDP release is likely to occur inside malignant cells due to overexpression of lysosomal proteases such as cathepsin B (known for its high activity in metabolizing PLG acid resides), which will promote breakdown of the vesicle structure;[81,82] however, this will be the subject of further study. Drug release from the vesicles in pH 5.2 at the higher chloride concentrations of PBS shows a similar release profile to the 35 mM [Cl^-] sample with a slightly higher total release after 76 h. This indicates that chloride concentrations above those present intracellularly only have a marginal effect on the release rate from the vesicles. In this case, pH appears to dominate the rate of drug release.

Cell Cytotoxicity Studies. The in vitro cytotoxicity of the CDDP-loaded vesicles was assessed using an alamarBlue assay on cervical cancer-originating (HeLa) cells following incubation for 72 h. Free block copolymer precursor and free CDDP were employed as controls. As Figure 7 shows, the free polymer (**P4**) demonstrates good biocompatibility, with no cytotoxicity

DOI: 10.1021/acs.biomac.5b00692
Biomacromolecules 2015, 16, 2463−2474

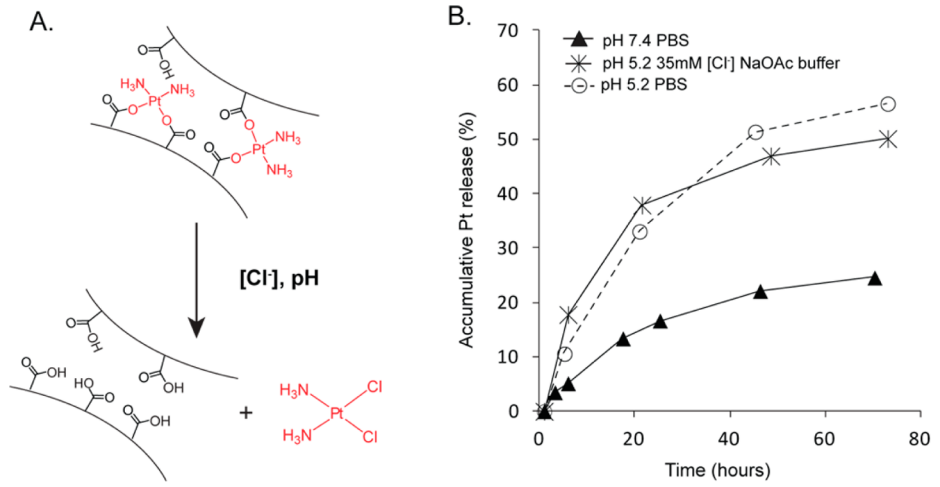

Figure 6. (A) Release mechanism of CDDP from drug-loaded vesicles. (B) Release profile of cisplatin from drug-loaded vesicles. Average error for release ±1.2%.

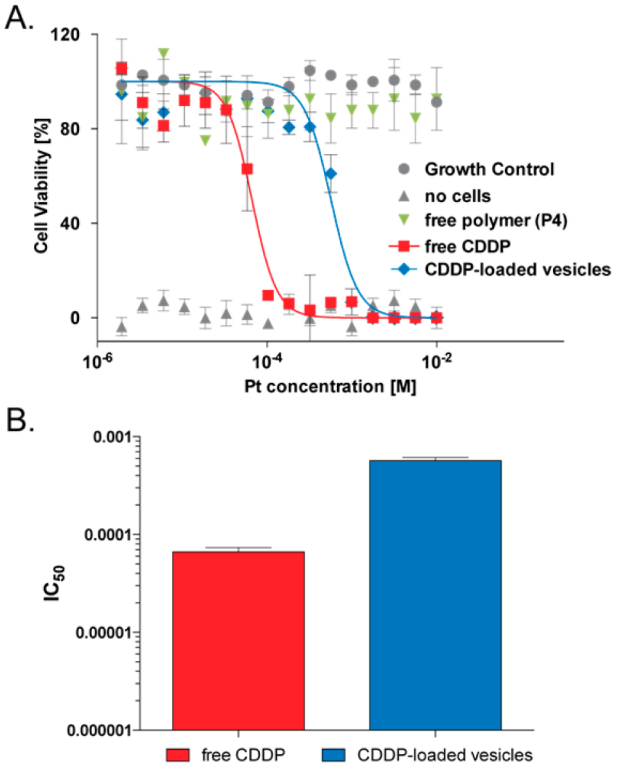

Figure 7. (A) Cytotoxicity of CDDP-loaded vesicles toward HeLa cells incubated for 72 h. (B) IC_{50} values for free drug and CDDP-loaded vesicles. Data shown represents mean ± standard error.

observed over the concentrations tested, supporting its potential as an effective precursor to these drug delivery vesicles. The CDDP-loaded vesicles show a dose dependent inhibition of HeLa cell proliferation (IC_{50} = 0.60 mmol/L). The viability difference of the free CDDP (IC_{50} = 0.065 mmol/L) and that of the CDDP-loaded vesicles at equivalent drug dosages is a commonly reported observation in nanoparticle delivery of CDDP,[8,17,83] and can be attributed to the different drug formats. CDDP is only toxic once dissociated from the vesicle, thus the CDDP-incorporated vesicles with a controlled CDDP release profile would take a longer time to reach similar cytotoxicity than the free CDDP. This reduced toxicity would allow for higher drug dosages to be applied for a more sustained drug effect. As well, any passive and active targeting capabilities of these vesicles is likely to improve cisplatin delivery to the cancer cell and reduce acute cisplatin toxicities very commonly reported with free cisplatin therapy.[5]

The exposed maleimide groups on the vesicle corona present an opportunity to conjugate thiol targeting ligands to form active targeting vesicles. The conjugation of a thiol-modified folic acid (FA) targeting ligand to the vesicle would be expected to facilitate the active targeting of the vesicle to cancerous cells through folate receptor-mediated endocytosis.[84] To determine whether this would result in a higher toxicity to cancer cells compared to noncancerous cells, NIH-3T3 and HeLa cells were selected as noncancerous and cancerous cells, respectively. NIH-3T3 cells lack overexpressed folic acid receptors (FR),[85] while HeLa cells, typical of many cancer cells, greatly overexpress FR.[86]

Folic acid was conjugated to the maleimide moieties on the corona of the FITC-labeled CDDP-loaded vesicle through thiol-maleimide coupling (Scheme 1). A novel FA precursor using cystamine as a disulfide linker was synthesized through standard EDCI/DMAP coupling procedures and confirmed through ^{1}H NMR analysis (SI, Figure S5). The precursor was then reduced in situ in the presence of TCEP to reveal the free reactive thiol for coupling to the vesicle. Normalized UV−vis spectra of the folic acid-decorated vesicle (FA-conj. vesicle) in Figure 8, reveals an absorbance profile matching that of free FA. The absorbance peak at λ = 495 nm corresponds to the FITC-tag absorbance. The extent of FA decoration was deemed to be ∼60% by ^{1}H NMR analysis based on the maleimide double bond proton intensity before conjugation and its subsequent disappearance after the reaction (SI, Figure S6). The zeta potential of the resulting FA conjugated vesicle decreased from an initial value before FA conjugation (−3.93 ± 0.5 mV) to −5.88 ± 0.5 mV, as a result of the contributed negative charge from the free acid group of FA.

Cytotoxicity studies in Figure 9 show that the FA-conjugated, CDDP-loaded vesicles are statistically significantly more toxic to HeLa than NIH-3T3 cells (Figure 9A, B) with IC_{50} values of 0.28 mmol/L and 1.3 mmol/L, respectively. The free drug showed no difference in IC_{50} values for the two cell lines used (Figure 9C), indicating that the higher toxicity of the FA

DOI: 10.1021/acs.biomac.5b00692
Biomacromolecules 2015, 16, 2463−2474

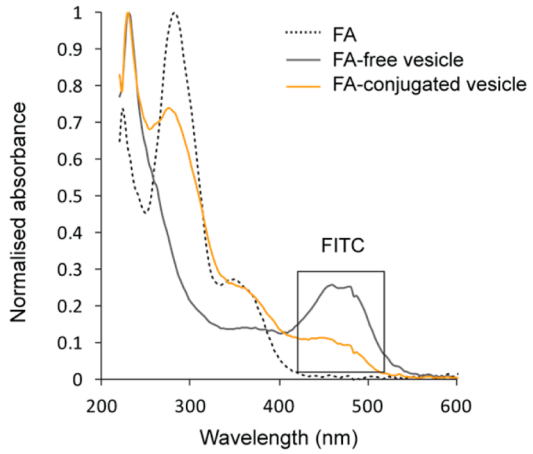

Figure 8. Normalized UV−vis absorbance of FA-conjugated vesicles and FA-free vesicles (DI water).

vesicles to HeLa cells is due to the enhanced cellular uptake attributed to folate receptor-mediated endocytosis.[87]

Cell Uptake Studies. To determine whether the FA targeting ligand improves cell binding and uptake of the vesicles to cancer cells relative to noncancerous cells, both flow cytometry and confocal microscopy analysis were conducted using HeLa and NIH-3T3 cells after incubation with CDDP-loaded vesicles with and without FA for 24 h. Figure 10 shows the mean fluorescence intensity (MFI) of HeLa and NIH-3T3 cells incubated with FA-free and FA-conjugated vesicles bearing FITC-tags, as measured by flow cytometry. The flow cytometry analysis clearly demonstrates a much greater enhancement of vesicle cellular uptake in HeLa cells as a result of the FA targeting ligand (change in MFI of 3462) compared to the NIH-3T3 cells (change in MFI of 193) presumably facilitated by the folate receptor-mediated endocytosis process.

Confocal microscopy analysis was then performed on the same cell uptake samples. As shown in Figure 11, the FITC fluorescence intensity of HeLa cells incubated with FA-conjugated vesicles was significantly higher than cells incubated with FA-free vesicles, which was consistent with the flow cytometry results (Figure 11B,C). Large numbers of FA-conjugated vesicles are clearly seen binding to the HeLa cell membrane, and many are internalized into the cytosol, evidence from the particular patterns of green fluorescence. FITC

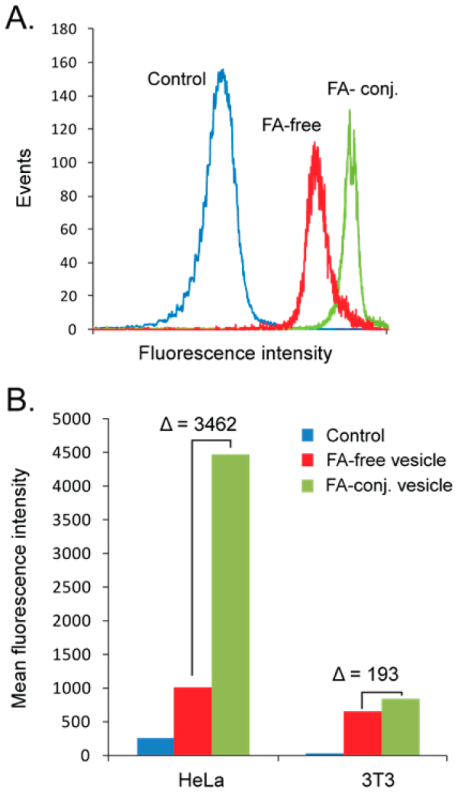

Figure 10. Flow cytometry uptake data of FITC-labeled CDDP-loaded FA-free and FA-conjugated vesicles to HeLa and NIH-3T3 cells after 24 h incubation. (A) Flow cytometry HeLa cell uptake data (B) FITC mean fluorescence intensity (MFI) of HeLa and NIH-3T3 cells. Untreated cells used as controls. Δ represents change in MFI. Data shown represents mean ± standard error.

fluorescence intensity of NIH-3T3 cells incubated with FA-conjugated vesicles was similar to FA-free vesicles (Figure 11E,F) with no observed increase in cell binding. This was again consistent with the flow cytometry results, and confirmed the enhanced binding and uptake of these FA-conjugated vesicles to cancer cells compared to noncancerous cells.

CONCLUSIONS

In summary, CDDP-loaded, PLG-based vesicles were prepared as a novel, biocompatible, and biodegradable architecture for

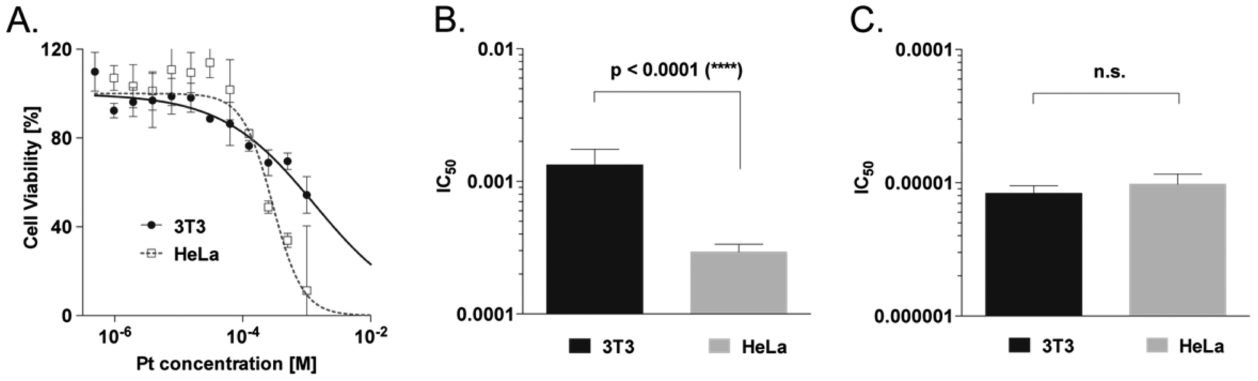

Figure 9. (A) Cytotoxicity of CDDP-loaded, FA-conjugated vesicles toward HeLa (squares) and NIH-3T3 cells (circles) incubated for 72 h. *X*-axis normalized to Pt concentration. Lines show results of nonlinear fit [log(inhibitor) vs normalized response]. (B) Comparison of the IC_{50} values of the FA-conjugated vesicles in NIH-3T3 cells vs HeLa cells. (C) Control experiment comparing the IC_{50} values of free CDDP in the two cell lines. Data shown represents mean ± standard error.

DOI: 10.1021/acs.biomac.5b00692
Biomacromolecules 2015, 16, 2463−2474

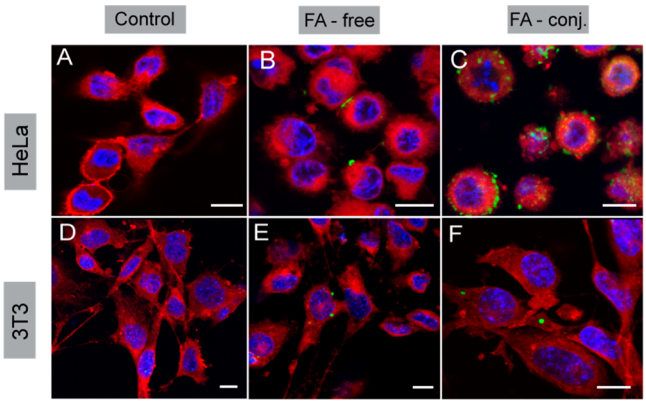

Figure 11. Confocal microscopy images of HeLa (A–C) and NIH-3T3 cells (D–F) incubated with FA-free and FA-conjugated vesicle for 24 h. Untreated cells used as controls. The vesicles were tagged with FITC (green), cell membrane was stained with CellMask Deep Red (red) and the cell nucleus with DAPI (blue) in all images. Scale bar = 10 μm.

targeted CDDP delivery. These vesicles were formed from biocompatible Mal-PEG-*b*-PLG block copolymers with CDDP conjugation forming a short, rigid, cross-linked, drug-loaded, hydrophobic block that induced self-assembly into hollow vesicle structures with average diameters of ~270 nm. The morphologies of these hollow vesicle structures were analyzed and confirmed by a number of analytical techniques including TEM and AFM. Drug loading was comparable to other vesicular assemblies currently in clinical trials for Pt(II) delivery, yet possesses a distinct advantage over these in that its building block (i.e., a polypeptide-based copolymer) is biodegradable. Drug release studies demonstrated a low and controlled drug release profile in systemic conditions with significantly higher release rate observed under intracellular conditions. The exposed maleimide functionalities on the vesicle corona were conjugated to folic acid to form an active targeting delivery system that demonstrated significantly higher cellular uptake and dose-dependent cytotoxicity in cancer cells compared to noncancerous cells. This demonstrates a novel approach to polypeptide-based vesicle assembly and a promising strategy for targeted, effective CDDP anticancer drug delivery.

■ ASSOCIATED CONTENT

Ⓢ Supporting Information

^{1}H NMR spectra, determination of platinum content by TGA, and DLC/DCE calculations. The Supporting Information is available free of charge on the ACS Publications website at DOI: 10.1021/acs.biomac.5b00692.

■ AUTHOR INFORMATION

Corresponding Author

*E-mail: gregghq@unimelb.edu.au. Tel: +61 3 8344 8665. Fax: +61 3 8344 4153.

Notes

The authors declare no competing financial interest.

■ ACKNOWLEDGMENTS

S.J.S would like to thank The University of Melbourne, the Commonwealth Scientific and Industrial Research Organisation (CSIRO), and the Melbourne Materials Institute (MMI) for various scholarships. The authors would like to acknowledge the Australian Research Council (ARC) for funding in the form of a Discovery Project (DP140100002). Q.F and K.L. acknowledges financial support from the ARC in the form of an ARC Super Science Fellowship (FS 110200025). G.G.Q acknowledges the ARC under the Future Fellowship (FT110100411, G.G.Q.) The authors would also like to thank Ms. Lynne Waddington (CSIRO) for help with TEM and Ms. E Nam for help with AFM analysis.

■ REFERENCES

(1) Galanski, M.; Jakupec, M. A.; Keppler, B. K. *Curr. Med. Chem.* **2005**, *12* (18), 2075–2094.
(2) Boulikas, T.; Vougiouka, M. *Oncol. Rep.* **2004**, *11* (3), 559–595.
(3) Stewart, D. J.; Dulberg, C. S.; Mikhael, N. Z.; Redmond, M. D.; Montpetit, V. A. J.; Goel, R. *Cancer Chemother. Pharmacol.* **1997**, *40* (4), 293–308.
(4) Mollman, J. E. *N. Engl. J. Med.* **1990**, *322* (2), 126–127.
(5) Wang, X.; Guo, Z. *Chem. Soc. Rev.* **2013**, *42* (1), 202–224.
(6) Huynh, V. T.; Binauld, S.; de Souza, P. L.; Stenzel, M. H. *Chem. Mater.* **2012**, *24* (16), 3197–3211.
(7) Huynh, V. T.; Chen, G. J.; de Souza, P.; Stenzel, M. H. *Biomacromolecules* **2011**, *12* (5), 1738–1751.
(8) Ahmad, Z.; Tang, Z. H.; Shah, A.; Lv, S. X.; Zhang, D. W.; Zhang, Y.; Chen, X. S. *Macromol. Biosci.* **2014**, *14* (9), 1337–1345.
(9) Duncan, R.; Vicent, M. J. *Adv. Drug Delivery Rev.* **2013**, *65* (1), 60–70.
(10) Croy, S. R.; Kwon, G. S. *Curr. Pharm. Des.* **2006**, *12* (36), 4669–4684.
(11) Hamley, I. W. *Biomacromolecules* **2014**, *15* (5), 1543–1559.
(12) Shi, C.; Yu, H.; Sun, D.; Ma, L.; Tang, Z.; Xiao, Q.; Chen, X. *Acta Biomater.* **2015**, *18*, 68–76.
(13) Yu, H.; Tang, Z.; Zhang, D.; Song, W.; Zhang, Y.; Yang, Y.; Ahmad, Z.; Chen, X. *J. Controlled Release* **2015**, *205*, 89–97.
(14) Song, W.; Tang, Z.; Zhang, D.; Yu, H.; Chen, X. *Small* **2015**, DOI: 10.1002/smll.201500324.
(15) Nishiyama, N.; Okazaki, S.; Cabral, H.; Miyamoto, M.; Kato, Y.; Sugiyama, Y.; Nishio, K.; Matsumura, Y.; Kataoka, K. *Cancer Res.* **2003**, *63* (24), 8977–8983.
(16) Song, W. T.; Li, M. Q.; Tang, Z. H.; Li, Q. S.; Yang, Y.; Liu, H. Y.; Duan, T. C.; Hong, H.; Chen, X. S. *Macromol. Biosci.* **2012**, *12* (11), 1514–1523.
(17) Uchino, H.; Matsumura, Y.; Negishi, T.; Koizumi, F.; Hayashi, T.; Honda, T.; Nishiyama, N.; Kataoka, K.; Naito, S.; Kakizoe, T. *Br. J. Cancer* **2005**, *93* (6), 678–687.
(18) Miura, Y.; Takenaka, T.; Toh, K.; Wu, S.; Nishihara, H.; Kano, M. R.; Ino, Y.; Nomoto, T.; Matsumoto, Y.; Koyama, H.; Cabral, H.; Nishiyama, N.; Kataoka, K. *ACS Nano* **2013**, *7* (10), 8583–8592.
(19) Plummer, R.; Wilson, R. H.; Calvert, H.; Boddy, A. V.; Griffin, M.; Sludden, J.; Tilby, M. J.; Eatock, M.; Pearson, D. G.; Ottley, C. J.; Matsumura, Y.; Kataoka, K.; Nishiya, T. *Br. J. Cancer* **2011**, *104* (4), 593–598.
(20) Roberts, M. J.; Bentley, M. D.; Harris, J. M. *Adv. Drug Delivery Rev.* **2002**, *54* (4), 459–476.
(21) Duncan, R. *Nat. Rev. Cancer* **2006**, *6* (9), 688–701.
(22) Richard, A.; Margaritis, A. *Crit. Rev. Biotechnol.* **2001**, *21* (4), 219–232.
(23) Li, C. *Adv. Drug Delivery Rev.* **2002**, *54* (5), 695–713.
(24) Wang, D.; Lippard, S. J. *Nat. Rev. Drug Discovery* **2005**, *4* (4), 307–320.
(25) Song, W. T.; Tang, Z. H.; Zhang, D. W.; Zhang, Y.; Yu, H. Y.; Li, M. Q.; Lv, S. X.; Sun, H.; Deng, M. X.; Chen, X. S. *Biomaterials* **2014**, *35* (9), 3005–3014.
(26) Discher, D. E.; Eisenberg, A. *Science* **2002**, *297* (5583), 967–973.
(27) Kieler-Ferguson, H. M.; Frechet, J. M. J.; Szoka, F. C., Jr. *Wiley Interdisciplinary Reviews-Nanomedicine and Nanobiotechnology* **2013**, *5* (2), 130–138.

DOI: 10.1021/acs.biomac.5b00692
Biomacromolecules 2015, 16, 2463–2474

(28) Guo, S.; Wang, Y.; Miao, L.; Xu, Z.; Lin, C. M.; Zhang, Y.; Huang, L. *ACS Nano* **2013**, *7* (11), 9896−9904.
(29) Khiati, S.; Luvino, D.; Oumzil, K.; Chauffert, B.; Camplo, M.; Barthelemy, P. *ACS Nano* **2011**, *5* (11), 8649−8655.
(30) Soussan, E.; Cassel, S.; Blanzat, M.; Rico-Lattes, I. *Angew. Chem., Int. Ed.* **2009**, *48* (2), 274−288.
(31) Maeda, H.; Greish, K.; Fang, J., The EPR effect and polymeric drugs: A paradigm shift for cancer chemotherapy in the 21st century. In *Polymer Therapeutics I: Polymers as Drugs, Conjugates and Gene Delivery Systems*, Satchi-Fainaro, R.; Duncan, R., Eds.; Springer-Verlag: Berlin Heidelberg, 2006; Vol. *193*, pp 103−121.10.1007/12_026
(32) Maeda, H.; Wu, J.; Sawa, T.; Matsumura, Y.; Hori, K. *J. Controlled Release* **2000**, *65* (1−2), 271−284.
(33) Lu, Y. J.; Low, P. S. *Adv. Drug Delivery Rev.* **2002**, *54* (5), 675−693.
(34) Kamaly, N.; Xiao, Z.; Valencia, P. M.; Radovic-Moreno, A. F.; Farokhzad, O. C. *Chem. Soc. Rev.* **2012**, *41* (7), 2971−3010.
(35) Zhong, Y.; Meng, F.; Deng, C.; Zhong, Z. *Biomacromolecules* **2014**, *15* (6), 1955−1969.
(36) Fu, Q.; Xu, J.; Ladewig, K.; Henderson, T. M. A.; Qiao, G. G. *Polym. Chem.* **2015**, *6* (1), 35−43.
(37) Xu, J. T.; Fu, Q.; Ren, J. M.; Bryant, G.; Qiao, G. G. *Chem. Commun.* **2013**, *49* (1), 33−35.
(38) Chécot, F.; Lecommandoux, S.; Gnanou, Y.; Klok, H.-A. *Angew. Chem., Int. Ed.* **2002**, *41* (8), 1339−1343.
(39) Bellomo, E. G.; Wyrsta, M. D.; Pakstis, L.; Pochan, D. J.; Deming, T. J. *Nat. Mater.* **2004**, *3* (4), 244−248.
(40) Holowka, E. P.; Pochan, D. J.; Deming, T. J. *J. Am. Chem. Soc.* **2005**, *127* (35), 12423−12428.
(41) Holowka, E. P.; Deming, T. J. *Macromol. Biosci.* **2010**, *10* (5), 496−502.
(42) Holowka, E. P.; Sun, V. Z.; Kamei, D. T.; Deming, T. J. *Nat. Mater.* **2007**, *6* (1), 52−57.
(43) Xu, J.; Tao, L.; Boyer, C.; Lowe, A. B.; Davis, T. P. *Macromolecules* **2011**, *44* (2), 299−312.
(44) Guo, M.; Jiang, M.; Zhang, G. *Langmuir* **2008**, *24* (19), 10583−10586.
(45) Daly, W. H.; Poche, D. *Tetrahedron Lett.* **1988**, *29* (46), 5859−5862.
(46) Sulistio, A.; Blencowe, A.; Widjaya, A.; Zhang, X. Q.; Qiao, G. *Polym. Chem.* **2012**, *3* (1), 224−234.
(47) Fu, Q.; Xu, J.; Ladewig, K.; Henderson, T. M. A.; Qiao, G. G. *Polym. Chem.* **2014**, *6*, 35−43.
(48) Schlechter, B.; Neumann, A.; Wilchek, M.; Arnon, R. *J. Controlled Release* **1989**, *10* (1), 75−87.
(49) Gianasi, E.; Wasil, M.; Evagorou, E. G.; Keddle, A.; Wilson, G.; Duncan, R. *Eur. J. Cancer* **1999**, *35* (6), 994−1002.
(50) Sharpless, N. E.; Flavin, M. *Biochemistry* **1966**, *5* (9), 2963−2971.
(51) Dispinar, T.; Sanyal, R.; Sanyal, A. *J. Polym. Sci., Part A: Polym. Chem.* **2007**, *45* (20), 4545−4551.
(52) Mantovani, G.; Lecolley, F.; Tao, L.; Haddleton, D. M.; Clerx, J.; Cornelissen, J.; Velonia, K. *J. Am. Chem. Soc.* **2005**, *127* (9), 2966−2973.
(53) Sanyal, A. *Macromol. Chem. Phys.* **2010**, *211* (13), 1417−1425.
(54) Sanchez, A.; Pedroso, E.; Grandas, A. *Org. Lett.* **2011**, *13* (16), 4364−4367.
(55) Dimitrov, I.; Schlaad, H. *Chem. Commun.* **2003**, *23*, 2944−2945.
(56) Cooley, J. H.; Williams, R. V. *J. Chem. Educ.* **1997**, *74* (5), 582−585.
(57) Han, J. D.; Ding, J. X.; Wang, Z. C.; Yan, S. F.; Zhuang, X. L.; Chen, X. S.; Yin, J. B. *Sci. China: Chem.* **2013**, *56* (6), 729−738.
(58) Bunnelle, W. H.; Shangraw, W. R. *Tetrahedron* **1987**, *43* (9), 2005−2011.
(59) Fahmy, K.; Merroun, M.; Pollmann, K.; Raff, J.; Savchuk, O.; Hennig, C.; Selenska-Pobell, S. *Biophys. J.* **2006**, *91* (3), 996−1007.
(60) Gryparis, E. C.; Mattheolabakis, G.; Bikiaris, D.; Avgoustakis, K. *Drug Delivery* **2007**, *14* (6), 371−380.
(61) Rademaker-Lakhai, J. M.; Terret, C.; Howell, S. B.; Baud, C. M.; de Boer, R. F.; Pluim, D.; Beijnen, J. H.; Schellens, J. H. M.; Droz, J. P. *Clin. Cancer Res.* **2004**, *10* (10), 3386−3395.
(62) Wheate, N. J.; Walker, S.; Craig, G. E.; Oun, R. *Dalton Transactions* **2010**, *39* (35), 8113−8127.
(63) Stathopoulos, G. P.; Boulikas, T.; Kourvetaris, A.; Stathopoulos, J. *Anticancer Res.* **2006**, *26* (2B), 1489−1493.
(64) Harrington, K. J.; Lewanski, C. R.; Northcote, A. D.; Whittaker, J.; Wellbank, H.; Vile, R. G.; Peters, A. M.; Stewart, J. S. W. *Ann. Oncol.* **2001**, *12* (4), 493−496.
(65) Dragovich, T.; Mendelson, D.; Kurtin, S.; Richardson, K.; Von Hoff, D.; Hoos, A. *Cancer Chemother. Pharmacol.* **2006**, *58* (6), 759−764.
(66) Sanson, C.; Schatz, C.; Le Meins, J. F.; Brulet, A.; Soum, A.; Lecommandoux, S. *Langmuir* **2010**, *26* (4), 2751−2760.
(67) Cheng, Y. F.; Corn, R. M. *J. Phys. Chem. B* **1999**, *103* (41), 8726−8731.
(68) Nagasawa, M.; Holtzer, A. *J. Am. Chem. Soc.* **1964**, *86* (4), 538−543.
(69) Gooding, E. A.; Sharma, S.; Petty, S. A.; Fouts, E. A.; Palmer, C. J.; Nolan, B. E.; Volk, M. *Chem. Phys.* **2013**, *422*, 115−123.
(70) Liu, F. T.; Eisenberg, A. *J. Am. Chem. Soc.* **2003**, *125* (49), 15059−15064.
(71) Wu, J.; Eisenberg, A. *J. Am. Chem. Soc.* **2006**, *128* (9), 2880−2884.
(72) Azzam, T.; Eisenberg, A. *Langmuir* **2010**, *26* (13), 10513−10523.
(73) Moughton, A. O.; O'Reilly, R. K. *Chem. Commun.* **2010**, *46* (7), 1091−1093.
(74) Sulistio, A.; Blencowe, A.; Wang, J.; Bryant, G.; Zhang, X.; Qiao, G. G. *Macromol. Biosci.* **2012**, *12* (9), 1220−1231.
(75) Xiao, K.; Li, Y. P.; Luo, J. T.; Lee, J. S.; Xiao, W. W.; Gonik, A. M.; Agarwal, R. G.; Lam, K. S. *Biomaterials* **2011**, *32* (13), 3435−3446.
(76) Yan, X. L.; Gemeinhart, R. A. *J. Controlled Release* **2005**, *106* (1−2), 198−208.
(77) Sonawane, N. D.; Verkman, A. S. *J. Cell Biol.* **2003**, *160* (7), 1129−1138.
(78) Faundez, V.; Hartzell, H. C. *Science's STKE: Signal transduction knowledge environment* **2004**, *2004* (233), n/a DOI: 10.1126/stke.2332004re8.
(79) Tsang, R.; Al-Fayea, T.; Au, H.-J. *Drug Saf.* **2009**, *32* (12), 1109−1122.
(80) Mochida, Y.; Cabral, H.; Miura, Y.; Albertini, F.; Fukushima, S.; Osada, K.; Nishiyama, N.; Kataoka, K. *ACS Nano* **2014**, *8* (7), 6724−6738.
(81) Shaffer, S. A.; Baker Lee, C.; Kumar, A.; Singer, J. W. *Eur. J. Cancer* **2002**, *38*, S129−S129, DOI: 10.1016/S0959-8049(02)81079-6.
(82) Shaffer, S. A.; Baker-Lee, C.; Kennedy, J.; Lai, M. S.; de Vries, P.; Buhler, K.; Singer, J. W. *Cancer Chemother. Pharmacol.* **2007**, *59* (4), 537−548.
(83) Feng, Z.; Lai, Y. P.; Ye, H. F.; Huang, J.; Xi, X. G.; Wu, Z. R. *Cancer Sci.* **2010**, *101* (11), 2476−2482.
(84) Vlahov, I. R.; Leamon, C. P. *Bioconjugate Chem.* **2012**, *23* (7), 1357−1369.
(85) Bottero, F.; Tomassetti, A.; Canevari, S.; Miotti, S.; Menard, S.; Colnaghi, M. I. *Cancer Res.* **1993**, *53* (23), 5791−5796.
(86) Song, Y.; Shi, W.; Chen, W.; Li, X.; Ma, H. *J. Mater. Chem.* **2012**, *22* (25), 12568−12573.
(87) Leamon, C. P.; Low, P. S. *Biochem. J.* **1993**, *291*, 855−860.

DOI: 10.1021/acs.biomac.5b00692
Biomacromolecules 2015, 16, 2463−2474

Supporting information

Cisplatin-induced formation of biocompatible and biodegradable polypeptide-based vesicles for targeted anticancer drug delivery

Steven J. Shirbin, [†] *Katharina Ladewig,* [†] *Qiang Fu,* [†] *Molly Klimak,* [†] *Xiaoqing Zhang,* [‡] *Wei Duan,* [♦] *Greg G. Qiao** [†]

[†] Polymer Science Group, Department of Chemical and Biomolecular Engineering, University of Melbourne, Victoria 3010, Australia

[‡] CSIRO Material Science and Engineering, Clayton South, Victoria 3169, Australia

[♦] School of Medicine, Deakin University, Geelong, Victoria 3216, Australia

*Corresponding author: gregghq@unimelb.edu.au

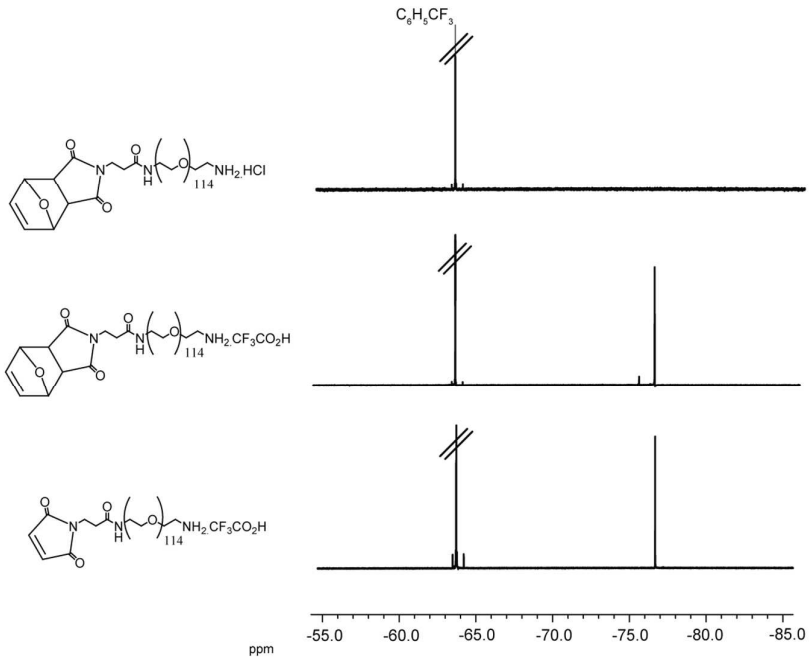

Figure S1. ^{19}F NMR spectra ($CDCl_3$) of furan protected Mal-PEG-NH_2TFA and furan protected Mal-PEG-NH_2HCl (**P1**) after counter ion exchange. Trifluorotoluene used as internal reference.

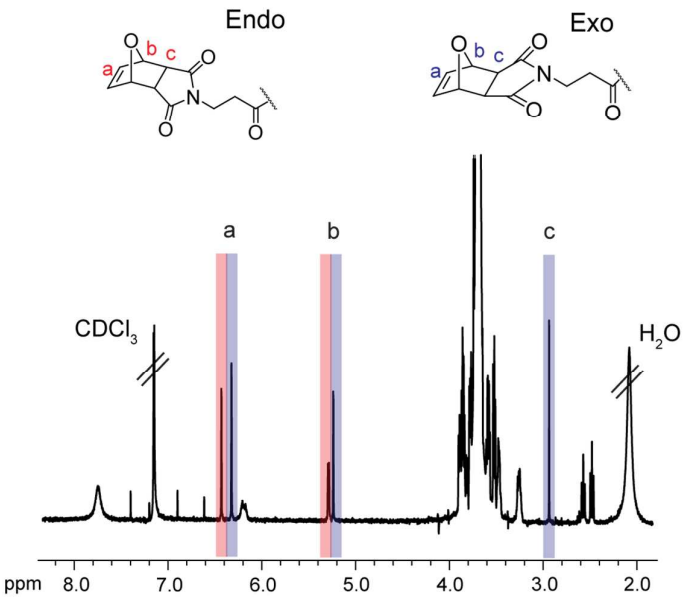

Figure S2. ^{1}H NMR spectra ($CDCl_3$) of **P1** following Diels Alder (DA) reaction between Mal-PEG-NH_2TFA and furan showing the endo and exo isomeric cycloadducts.

Calculations of drug loading content and drug loading efficiency:

Drug loading content (DLC):

TGA data: 8.4 wt%

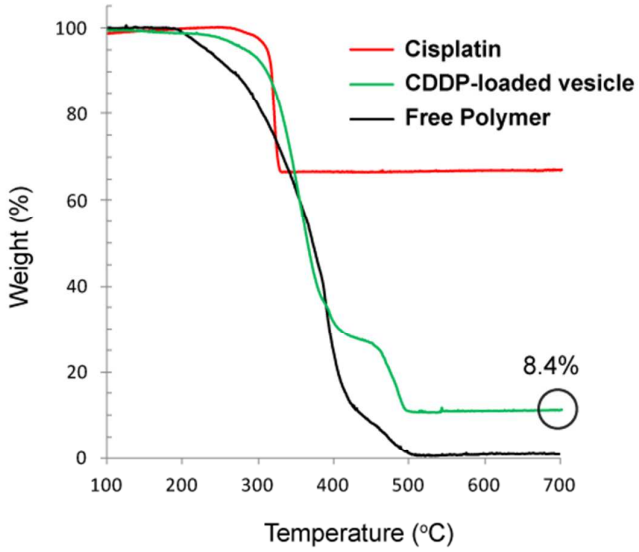

Figure S3. TGA traces for CDDP (red), Mal-PEG-*b*-PLG-FITC free polymer (black) and CDDP-loaded vesicles (green).

ICP data: 7.4 wt%

ICP-OES Pt standard curve λ = 203.646 nm:

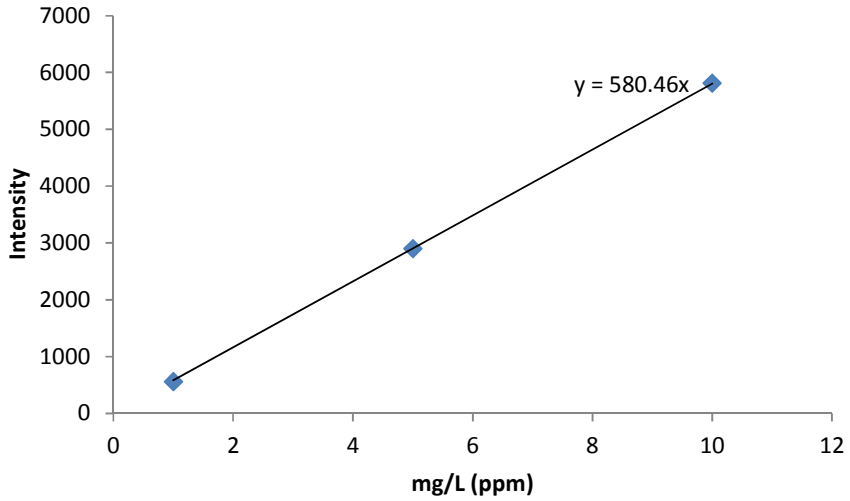

Calculation of drug conjugation efficiency (DCE) based on ICP data (DLC):

$$f = \frac{m_{Pt,exp}}{m_{Pt,theo}} \times 100\% = \frac{W_{Pt}/M_{Pt}}{W_{polymer}/M_{polymer}} \times 100\%$$

$$= \frac{7.4\%/195}{92.6\%/7000} \times 100\%$$

$$= 3\ Pt\ molecules\ per\ diacid\ (6) of\ polymer$$

$$\therefore \sim 50\%\ DCE$$

where $m_{Pt,\ exp}$: the molar amount of Pt determined by experimental data; $m_{Pt,\ theo}$: the theoretical molar amount of Pt in 100% conversion (assume that one Pt molecule forms complex with one di-acid repeating unit); W_{Pt}: weight percent of Pt measured by ICP-OES; M_{Pt}: molecular weight of Pt; $W_{polymer}$: weight percent of polymer determined from 100%-W_{Pt}; $M_{polymer}$: molecular weight of polymer.

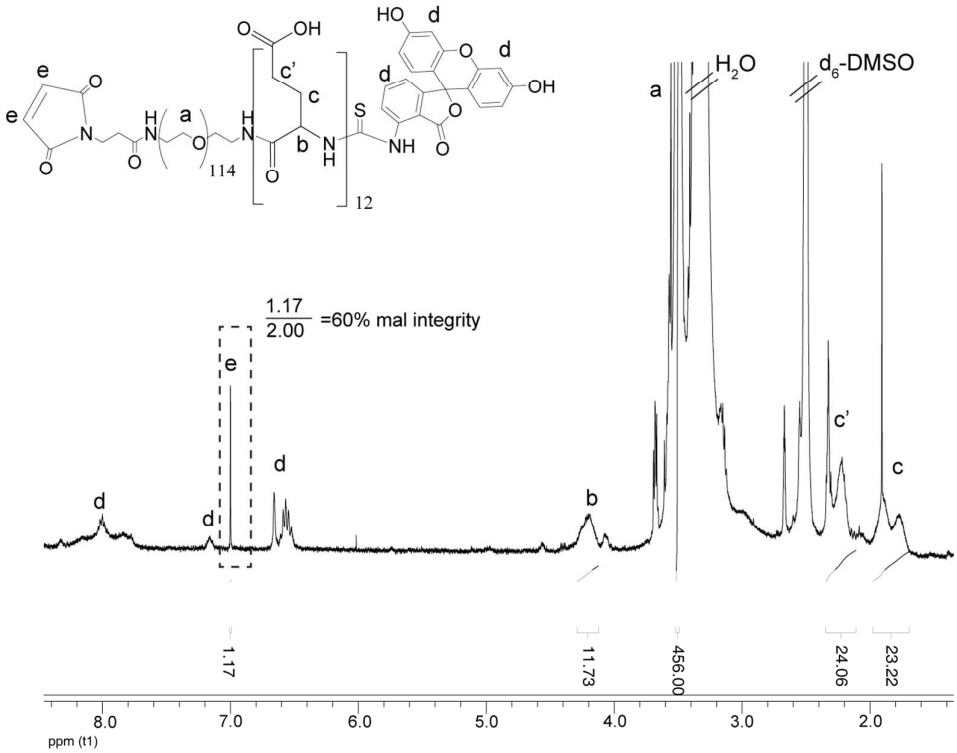

Figure S4. ^{1}H NMR Spectrum (d_6-DMSO) with integrations of FITC tagged block copolymer (**P4**).

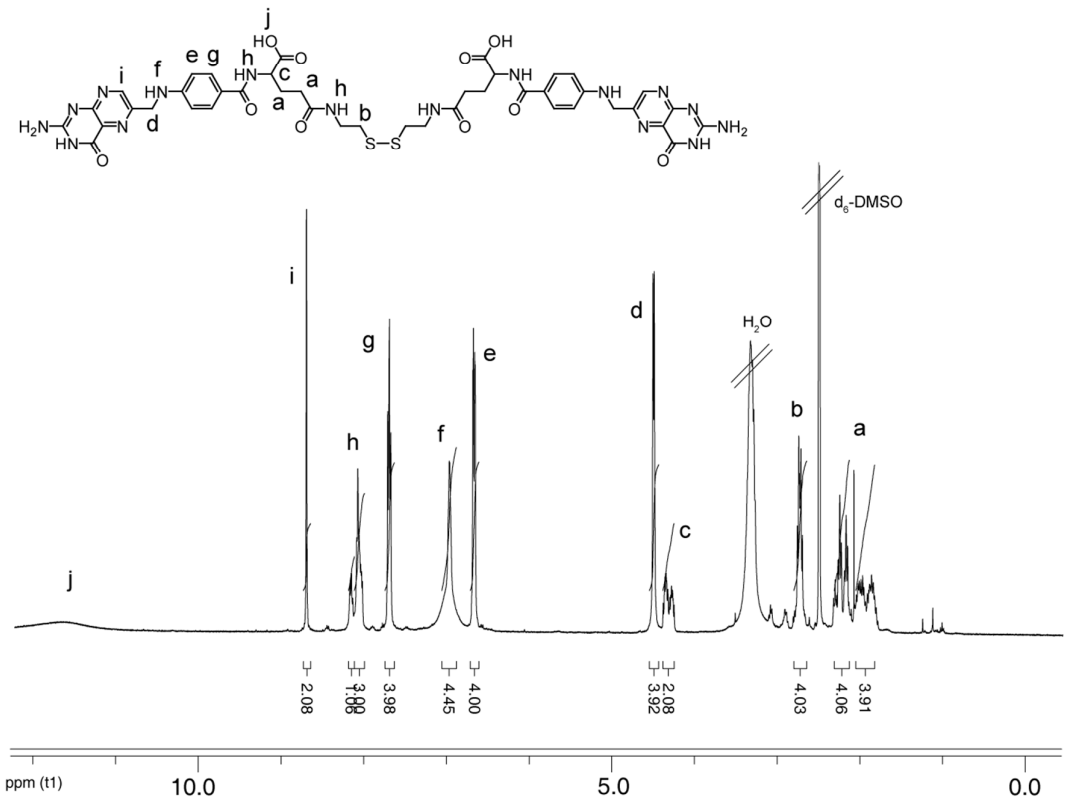

Figure S5. ^{1}H NMR Spectrum (d_6-DMSO) of FA-S-S-FA.

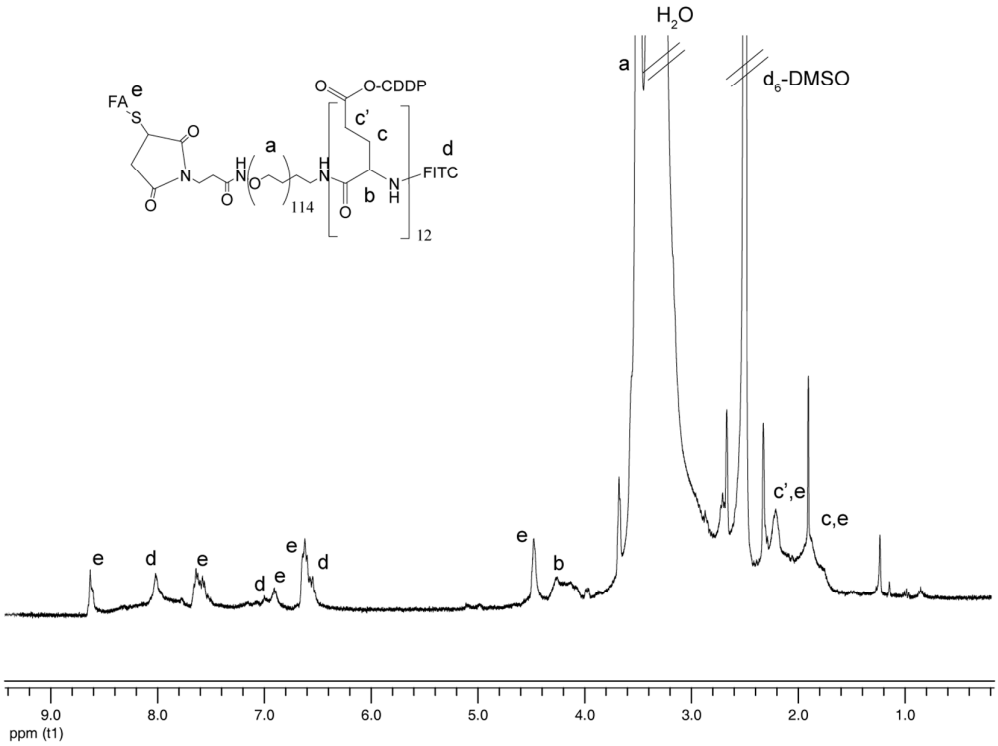

Figure S6. ^{1}H NMR Spectrum (d_6-DMSO) of FITC tagged FA-conjugated CDDP loaded vesicles.

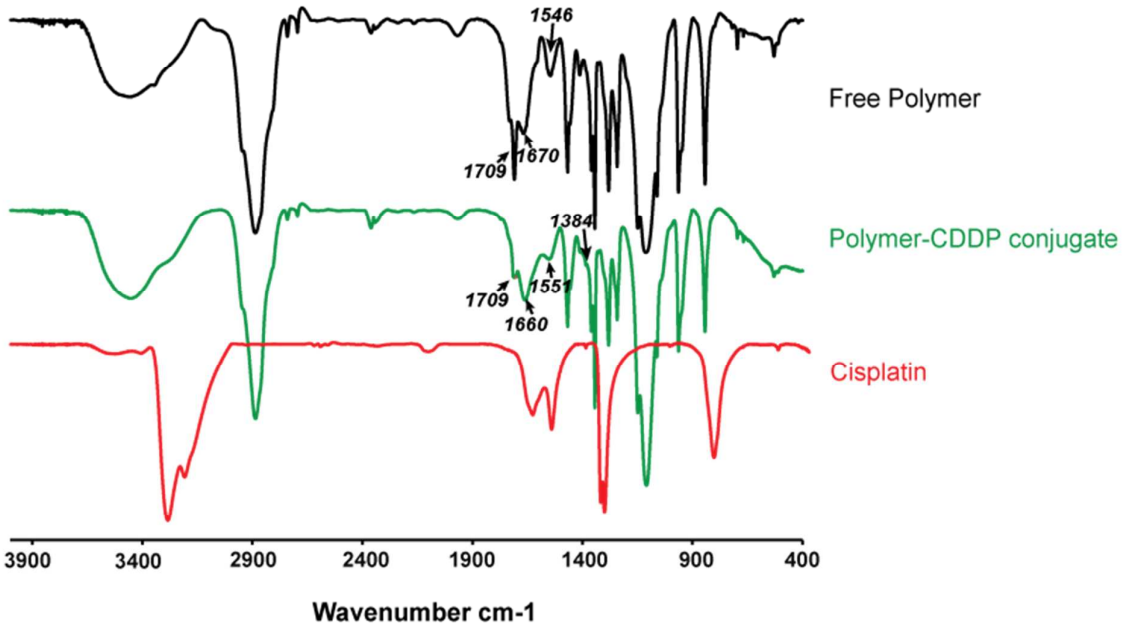

Figure S7. FT-IR spectra of free polymer, polymer-CDDP complex and CDDP. Spectra ran in transmittance mode.

Article

pubs.acs.org/Biomac

Macroporous Hydrogels Composed Entirely of Synthetic Polypeptides: Biocompatible and Enzyme Biodegradable 3D Cellular Scaffolds

Steven J. Shirbin,[†,‡] Fatemeh Karimi,[†,‡] Nicholas Jun-An Chan,[†] Daniel E. Heath,[§] and Greg G. Qiao*[,†]

[†]Polymer Science Group, Department of Chemical and Biomolecular Engineering, and [§]Department of Chemical and Biomolecular Engineering, University of Melbourne, Parkville, Melbourne, Victoria 3010, Australia

Supporting Information

ABSTRACT: Synthetic polypeptides are a class of bioinspired polymers with well demonstrated biocompatibility, enzyme biodegradability, and cell adhesive properties, making them promising materials for the preparation of macroporous hydrogels as 3D cellular scaffolds. Three-dimensional macroporous hydrogels composed entirely of biocompatible and enzyme biodegradable synthetic polypeptides have thus been prepared. Under cryoconditions, macroporous hydrogels in the form of macroporous cryogels were prepared using a single copolymer component through direct EDC/sulfo-NHS zero-length cross-linking between poly(L-glutamic acid) (PLG) and poly(L-lysine) (PLL) residues on a PLG-*r*-PLL random copolypeptide chain. The resulting macroporous cryogels were found to contain large interconnected pores (≥100 μm) highly suitable for tissue engineering applications. Tuning the relative ratios of the amino acid components could result in cryogels with very different pore structures, swelling, and mechanical properties, suitable for developing gels for a range of possible soft tissue engineering applications. These cryogels were shown to be enzymatically biodegradable and demonstrated excellent biocompatibility, cell attachment and cell proliferation profiles with mammalian fibroblast (NIH-3T3) cells, demonstrating the appeal of these novel cryogels as highly suitable cellular scaffolds.

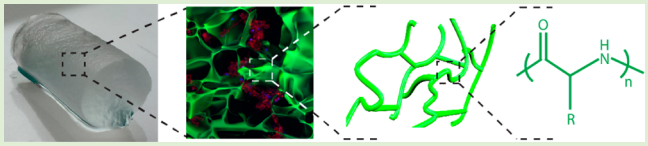

INTRODUCTION

Three-dimensional macroporous polymeric hydrogels have for many years received significant research attention in cell-based therapies[1−3] and tissue engineering applications[4−8] due to their macroporous structure. Compared to conventional non-macroporous hydrogels, the presence of macropores provides superior swelling and mechanical properties to the gel, generating 3D scaffolds highly suitable for in vitro cell culturing by mimicking the physiological function of the extracellular matrix (ECM). The open interconnected porous structure, with pore sizes ≥100 μm allows for effective cell proliferation and vascularization and facilitates the transport of nutrients and metabolites through the scaffold.[4,9] In order to ensure the gel scaffold has suitable biocompatible and bioresponsive properties, the materials used to fabricate the gel must be carefully considered.

Synthetic polypeptides are a class of bioinspired polymers with well demonstrated biocompatibility, enzyme biodegradability, and cell adhesive properties, making them promising materials for the preparation of macroporous hydrogels as 3D cellular scaffolds. Synthetic polypeptides, such as poly(L-glutamic acid) (PLG) have been studied extensively in the drug delivery field as highly biocompatible and enzyme biodegradable drug delivery scaffolds.[10−13] Their effective cell adhesion properties have been demonstrated through the preparation of polyelectrolyte multilayer coatings (PEM) composed of charged synthetic polypeptides such as poly(L-glutamic acid) (PLG) and poly(L-lysine) (PLL) that have shown to enhance the cell adhesion properties of surfaces.[14−16] For these reasons, hydrophilic synthetic polypeptides have been used as partial components of biodegradable macroporous hydrogel scaffolds for tissue engineering applications.[17−21] In all cases, the synthetic polypeptide is one component of the gel, with additional polymers (e.g., chitosan, cellulose) and cross-linkers (e.g., 2-hydroxyethyl methacrylate, HEMA) added and incorporated into the final gel structure. However, additional synthetic steps to modify the polypeptide side chain functionalities are often required for gelation to take place.[19−21] As well, these polypeptide-based gels make it difficult to ascertain the true effect of the synthetic polypeptide on the biocompatibility and biodegradability properties of the gel, and their modifications are likely to alter the characteristics of the gel from their initially intended properties. Therefore, to effectively study the suitability of synthetic polypeptides as a material for 3D cell culture applications and to better utilize the beneficial properties owing to these materials, the preparation of macroporous hydrogels composed entirely of synthetic polypeptides is desirable.

To achieve this, a simple, nontoxic macropore-forming approach must first be considered to fabricate hydrogels with large pore sizes (≥100 μm) suitable for the ingrowth of mammalian cells.[4] Cryogelation through chemical cross-linking

Received: June 4, 2016
Revised: July 27, 2016
Published: July 29, 2016

DOI: 10.1021/acs.biomac.6b00817
Biomacromolecules 2016, 17, 2981−2991

is a simple approach for the introduction of large interconnected pores to a hydrogel structure and avoids the need to remove toxic solutes/gases/solvents from the scaffold,[22−25] as required in other macropore-forming approaches such as gas foaming,[26] phase separation,[18,27] and porogen use.[28,29] In a typical aqueous cryogelation process that is commonly used to prepare cryogels for biomedical applications, an aqueous polymer solution is frozen below 0 °C. Within the concentrated liquid microphase surrounding the ice crystals, gelation or cross-linking of the solution typically occurs to form the dense polymeric pore walls. Thawing of the frozen solution removes the nontoxic ice water crystals to leave behind the macroporous cryogel structure (Scheme 1).

Scheme 1. Formation of Macroporous Cryogels by Direct Zero-Length EDC/(sulfo)-NHS Cross-Linking of a Polypeptide Copolymer

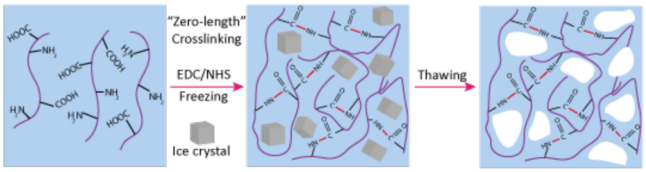

Herein, we report the facile preparation of macroporous hydrogels composed entirely of synthetic polypeptides via the cryogelation process. In fact, this is the first reported case of macroporous hydrogels prepared entirely from synthetic polypeptides. These macroporous hydrogels in the form of macroporous cryogels were prepared through a direct EDC/sulfo-NHS zero-length cross-linking strategy[5,8,30−32] between the carboxylic acid (PLG) and amine (PLL) residues on a PLG-*r*-PLL random copolypeptide chain (Scheme 1). Zero-length cross-linking agents such as EDC and (sulfo)-NHS, activate the reaction of carboxylic acid groups with amines but are not themselves incorporated into the polymer gel structure and are easily removed by washing in water, thus, improving the biocompatibility prospects of the gel.[4,30] For natural/bioinspired polymers,[32] such as polypeptides containing lysine (amine) and glutamic acid (carboxylic acid) amino acid residues, the EDC/(sulfo)-NHS reactive functional groups exist on the same polymer. This offers the prospect of preparing cryogels composed entirely of synthetic polypepides using a single copolymer component (via inter/intra molecular cross-linking) without side chain modification or incorporation of cross-linking agents/additional polymers to the cryogel network (Scheme 1).

The relative ratios of the amine to carboxylic acid (cross-linkable) components on the copolypeptide were varied to determine its effect on the cryogel pore size, pore morphology, porosity, swelling, and mechanical properties. To demonstrate the potential use of these cryogels as 3D cellular scaffolds, enzymatic biodegradability and cytocompatibility of the gels were studied through cell viability, cell attachment, and proliferation tests using mammalian fibroblast (NIH-3T3) cells.

MATERIALS AND METHODS

Materials. H-L-Lys(Z)-OH (Bachem), Z-Glu(OBzl)-OH (Mimotopes), triphosgene (≥98%, Aldrich), dimethylformamide (DMF) (anyhd., 99.8%, Acros), hydrobromic acid (HBr; 33% in acetic acid, Aldrich), *N*-timethylsilyl)allylamine (*N*-TMS allylamine; 95%, Acros), phosphate buffered saline (PBS) tablets (Aldrich), trifluoroacetic acid (TFA; Aldrich), *n*-pentane (anhydrous ≥99%, Aldrich), diethyl ether (AR, Chem-Supply), *N*-(3-(dimethylamino)propyl)-*N*′-ethylcarbodiimide hydrochloride (EDCI; ≥98%, Aldrich), *N*-hydroxysulfosuccinimide sodium salt (sulfo-NHS; ≥98%, Fluka), fluorescein isothiocyanate isomer 1 (FITC; ≥90%, Sigma), dimethyl sulfoxide (DMSO; AR, Ajax Finechem), methanol (MeOH; AR, Chem-Supply), ethanol (EtOH; AR, Chem-Supply), cyclohexane (AR, Ajax Finechem), protease from *Streptomyces griseus* Type XIV (Sigma). Tetrahydrofuran (THF) was distilled from benzophenone and sodium metal under nitrogen.

Instrumentation. ^{1}H NMR analysis was performed using a Varian unity Plus 400 MHz NMR spectrometer using the deuterated solvent as reference. GPC analysis was performed on a Shimadzu liquid chromatography system fitted with a PostNova Analytics MALS detector (λ = 658 nm), a Shimadzu RID-10 refractometer (λ = 633 nm), and a Shimadzu SPD-20A UV−vis detector, using three phenogel columns (Phenomenex, 5 μm) in series and HPLC grade DMF with 0.05 M LiBr as the mobile phase (1 mL/min). The oven temperature was set to 50 °C to maintain an acceptable pressure across the system, and the detectors were temperature controlled to 25 °C. Nova MALS software (PostNova) was used to determine the molecular weights and PDI using poly(ethylene glycol) standards. Attenuated Total Reflectance Fourier Transform Infrared (ATR FT-IR) was performed on dried samples using a Bruker Tensor 27 with mid-infrared range (400−4000 cm^{-1}). The instrument was equipped with OPUS 6.5 software. Measurements were made in transmittance mode. All other instruments are described below in the relevant sections.

Synthesis of Polymeric Precursors. *L-Glutamic Acid and L-Lysine N-Carboxyanhydrides (NCAs).*[33] The amino acid (OBzl)-L-glutamic acid (3 g, 12.64 mmol) or (Z)-L-lysine (3 g, 10.70 mmol) was dissolved in anhydrous THF (75 mL) in a three-necked round bottomed flask under argon. Triphosgene (glu: 1.5 g, 5.05 mmol, 1.2 equiv phosgene; lys: 1.27 g, 4.28 mmol, 1.2 equiv phosgene) was then added, and the mixture was heated at 60 °C for 2 h with continuous stirring. After cooling to room temperature, the reaction mixture was sparged with argon for 45 min into a sat. NaOH solution, then solvent removed in vacuo. The resulting residue was recrystallized from THF (anhydrous) and *n*-pentane (anhydrous) overnight. The resulting crystals were filtered and washed with *n*-pentane (dry), then reprecipitated and washed (×2) with dry *n*-pentane to afford white solids (yields: ∼70%). (Z)-L-lysine NCA ^{1}H NMR (400 MHz, $CDCl_3$): δ_H 1.40−1.60 (m, 4H, -NH-CH_2-CH_2-CH_2-CH_2-), 1.81−1.94 (m, 2H, -NH-CH_2-CH_2-CH_2-CH_2-), 3.18 (m, 2H, -NH-CH_2-CH_2-CH_2-CH_2-), 4.25 (t, 1H, J = 5.6 Hz, C*H*N), 4.97 (s, 1H, side chain NH), 5.09 (s, 2H, CH_2-ArH), 7.04 (s, 1H, ring NH), 7.3−7.4 (m, 5H, ArH). (OBzl)-L-glutamic acid NCA ^{1}H NMR (400 MHz, $CDCl_3$): δ_H 2.09−2.30 (m, 2H, CH_2CH_2CO), 2.60 (t, 2H, J = 6.8 Hz, CH_2CH_2CO), 4.38 (t, 1H, J = 6.0 Hz, C*H*N), 5.14 (s, 2H, CH_2-ArH), 6.58 (s, 1H, ringNH), 7.33−7.38 (m, 5H, ArH).

Synthesis of Protected Random Copolypeptides Poly(OBzl-L-glutamic acid)-*r*-Poly(Z-L-lysine) (PBLG-*r*-PZLL). *Protected Random Copolymer A.* To a dry 25 mL RBF was added both Glu NCA (0.8 g, 3.04 mmol) and Lys NCA (0.233 g, 0.76 mmol) under nitrogen. Dry DMF was then added and stirred to dissolve. To the stirring solution was added *N*-(trimethylsilyl)allylamine (9.12 μL, 54.3 μmol, M/I = 70), and the clear solution was stirred for 72 h under argon with bleed at room temperature. The reaction mixture was then concentrated under high vacuum, dissolved up in minimal DCM, and precipitated in chilled methanol (40 mL), washed in ether (×2), and then dried in vacuo to afford a clear tacky solid (0.83 g, yield: 81%). M_n (GPC) = 7.2 kDa; PDI 1.70. ^{1}H NMR (d_6-DMSO): δ_H 1.20−1.90 (m, Lys -NH-CH_2-CH_2-CH_2-CH_2-), 2.0−2.40 (m, Glu -CH_2-CH_2-CO-), 2.94 (s, Lys -NH-CH_2-CH_2-CH_2-CH_2-), 3.92 (s, C*H*-NH backbone), 4.99 (m, CH_2-ArH), 5.76 (m, CH_2=C*H*-), 7.26 (s, ArH), 8.38 (brs, CO-NH); see Figure S1. Relative ratios of the polypeptides determined from ^{1}H NMR spectra of the fully deprotected products shown in Figure S3.

Protected Random Copolymer B. Identical procedure to above random copolymer A, instead using Glu NCA (0.43 g, 1.63 mmol), Lys NCA (0.5 g, 1.63 mmol), and *N*-(trimethylsilyl)allylamine (43.84 μmol, M/I = 74). After drying, a clear tacky solid was obtained (0.61 g,

DOI: 10.1021/acs.biomac.6b00817
Biomacromolecules 2016, 17, 2981−2991

Yield: 66%). M_n (GPC) = 6.7 kDa; PDI 1.80. ^{1}H NMR (d_6-DMSO): Same peak assignments as protected random copolymer A (see Figure S2). Relative ratios of the polypeptides determined from ^{1}H NMR spectra of the fully deprotected products shown in Figure S4.

Preparation of Deprotected Poly(L-glutamic acid)-*r*-Poly(L-lysine) Random Copolypeptides. Deprotection of the OBzl and CBz (Z) protecting group was achieved through previously reported procedure[33,34] to afford the water-soluble random copolypeptides.

Random Copolymer A. To a 25 mL RBF was added the protected random copolymer A (0.83 g, (0.12 mmol) followed by trifluoroacetic acid (TFA) (5.3 mL). The solution was stirred until the polymer was dissolved, followed by addition of HBr (33% in AcOH, 5.3 mL). The resulting solution was stirred at 35 °C with thick precipitate observed soon after. The reaction mixture was stirred for a total of 2 h at 35 °C, with the suspension then transferred directly into diethyl ether, washed in ether (×2), then dried in vacuo overnight. The solid was then dissolved in DI H_2O and added to 3.5 kDa dialysis tubing for dialysis against 2 L DI water (×3) for 24 h. The polymer precipitated in solution during the dialysis procedure, with the suspension then freeze-dried to obtain a white solid (~300 mg). ^{1}H NMR (D_2O + NaOH): δ_H 1.33−1.72 (m, Lys -NH-CH_2-CH_2-CH_2-CH_2-), 1.89−1.99 (m, Glu -CH_2-CH_2-CO-), 2.23 (m, Glu -CH_2-CH_2-CO-), 2.56 (m, Lys -NH-CH_2-CH_2-CH_2-CH_2-), 4.27 (m, C*H*-NH backbone). Using ^{1}H NMR analysis, selected glutamic acid and lysine side chain methylene protons were integrated to determine a glutamic acid:lysine ratio of 1:0.29 (see Figure S3). Based on this ratio and the calculated M_n from GPC analysis of the protected copolymer, DP is determined to be 31 (24 glutamic, 7 lysine).

Random Copolymer B. Identical procedure to above random copolymer A. During dialysis, no precipitation of the dialysis contents is observed, with the clear solution then freeze-dried to obtain a white powder (~400 mg). ^{1}H NMR (D_2O + HCl): δ_H 1.16−1.65 (m, Lys -NH-CH_2-CH_2-CH_2-CH_2-), 1.88−2.00 (m, Glu -CH_2-CH_2-CO-), 2.25−2.40 (m, Glu -CH_2-CH_2-CO-), 2.69 (s, Lys -NH-CH_2-CH_2-CH_2-CH_2-), 3.81 (s, C*H*-NH backbone). Using ^{1}H NMR analysis, selected glutamic acid and lysine side chain methylene protons were integrated to determine a glutamic acid:lysine ratio of 1:0.73 (see Figure S4). Based on this ratio and the calculated M_n from GPC analysis of the protected copolymer, DP is determined to be 28 (16 glutamic, 12 lysine).

Preparation of Cryogels. Cryogelation reactions were conducted using an EDC/sulfo-NHS cross-linking strategy similar to reported previously.[5]

Cryogel A. A typical procedure for the preparation of cryogel A was as follows: The deprotected random copolymer A (20 mg) was suspended in DI H_2O (400 μL) followed by addition of small amounts of 2 M NaOH to achieve a pH of 5. Brief vortexing resulted in the fully dissolved polymer solution. EDCI and sulfo-NHS (molar ratio of EDCI/sulfo-NHS of 2:1) were then dissolved individually in 100 μL DI water. Based on the amount of NH_2 lysine side chain groups (calculated from the relative ratios on the deprotected polypeptide above) a 2.5-fold excess of EDCI was used. All solutions were kept on ice for 15 min. Subsequently, EDCI and sulfo-NHS solutions were added to polymer solution, mixed briefly by vortexing then withdrawn into cylindrical syringes and placed in freezer.

Cryogel B. A typical procedure for the preparation of cryogel B was as follows: The deprotected random copolymer B (20 mg) was initially suspended in DI H_2O (400 μL) followed by addition of small amounts of 1 M HCl to achieve a pH of 4. Brief vortexing of the solution to dissolve polymer was followed by centrifugation to remove small amounts of insoluble material. The clear polymer solution was then cross-linked through identical EDCI/sulfo-NHS procedure described above.

All cryogelation procedures were conducted at −18 °C for 24 h at a final polymer concentration of 3.33% w/w for all samples. After completion of the cryogelation process, the resulting samples were removed and thawed at room temperature. The cryogels were then immersed in DI water and washed thoroughly with complete replacement of the solution three times (3 × 100 mL). The gels were then washed thoroughly and equilibrated in PBS before use (2 × 100 mL). Cryogels were synthesized shortly before measurements.

Characterization of Cryogels. *Microstructure in the Wet State.* The morphological features of the cryogel scaffolds in the wet state were examined by environmental scanning electron microscopy (ESEM) and confocal laser scanning microscopy (CLSM). ESEM (FEI Quanta 200 ESEM FEG) was performed under low vacuum setting with samples mounted on carbon tape placed on aluminum stubs. CLSM (Nikon A1R+) was performed using both 20× or 40× objectives and an excitation wavelength of 488 nm. All images were generated by optical sectioning in the *z*-direction. Images were stacked in the *z*-direction using ImageJ software. For CLSM measurements, fluorescein isothiocyanate (FITC) was covalently labeled to the cross-linked gels using a previously reported procedure.[7] Gels were incubated with FITC in 0.1 M sodium phosphate buffer (pH 9) overnight followed by extensive washing in buffer to remove unconjugated FITC. CLSM images were analyzed using ImageJ software analysis to determine the pore size and pore wall thickness of the cryogels. Analysis was performed on at least three separate gel cross-section samples with pore size measurements representing the longest pore dimension.

Mechanical Tests. Compression tests on gels were performed using an Instron testing system (Instron 5848). Fully swollen cylindrical gels (cryogel A: ~13 mm diameter, 11 mm height; cryogel B: ~8 mm diameter, 8.5 mm height) were deformed (at constant volume) between two parallel plates, with a strain rate of 60% per minute. Engineering stresses and strains were recorded. The gel cylinders were kept hydrated in PBS solution (pH 7.4) throughout the tests. Young's moduli (compressive) were determined by the average slopes of the stress−strain compression curves over the linear low strain range 0−10%. Runs were performed in triplicate.

Swelling Properties and Gel Fraction of Cryogels. For equilibrium mass swelling ratios, Q_M, cryogel samples (n = 4) fully equilibrated in PBS were first weighed, then freeze-dried. Dried samples were then reweighed. The equilibrium mass swelling ratio, Q_M, was defined as the ratio of the fully swollen cryogel mass to that of its dry mass:

$$Q_M = \frac{m_s}{m_d}$$

where m_s and m_d are the weights of the swollen gel and dried gel, respectively. The swelling data was corrected by subtracting the soluble fraction of salt in PBS from the gel.

Equilibrium volume swelling ratios (Q_v) were calculated as per a previously reported procedure.[35] The diameter of ethanol-dried cryogel samples (n = 3) were first measured, with samples then incubated in PBS for 2 h, followed by measurements of their swollen diameters. The volume swelling ratio was calculated by the following equation:

$$Q_V = \left(\frac{D_s}{D_d}\right)^3$$

where D_s and D_d are the diameters of the swollen gel and dried gel, respectively.

The gel fraction (W_g%) of the cryogels was determined gravimetrically by weighing dried samples (m_d)

$$W_g\% = \frac{m_d}{m_0} \times 100$$

where m_0 is the weight of the polymer components in the initial solution (random copolypeptide).

Porosity. The porosity of the gels was estimated by cyclohexane uptake which determines pore volume.[6,36] Porosity (P) was then calculated as volume fraction (%) of pores in the gel. Gel samples were first dried by gradual dehydration with ethanol (25, 50, 75, and 100%) then dried in a vacuum oven at 55 °C overnight. Preweighed oven-dried gels were immersed in cyclohexane for 1 h, excess liquid was removed, and the samples were weighed. Porosity was calculated as

DOI: 10.1021/acs.biomac.6b00817
Biomacromolecules 2016, 17, 2981−2991

Scheme 2. (a) Synthesis of PLG-*r*-PLL Random Copolypeptides and (b) Their Fabrication into Synthetic Polypeptide Cryogels[a]

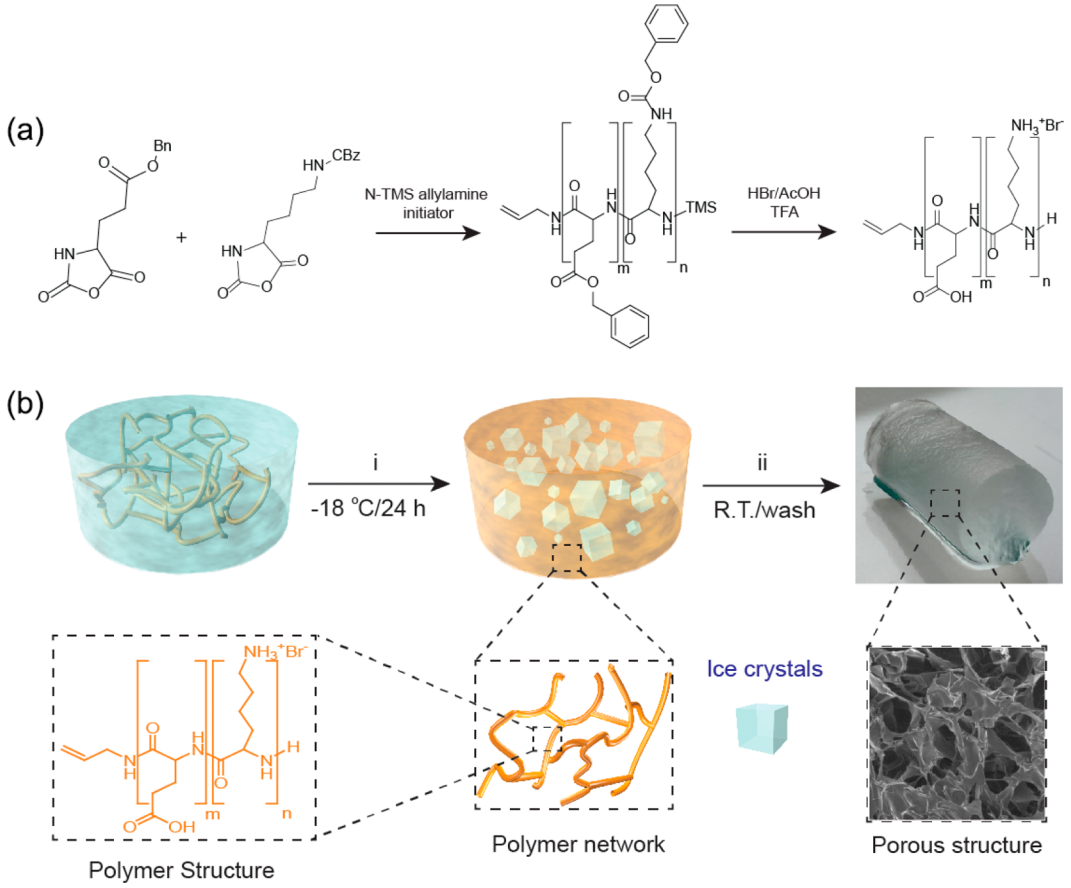

[a]Reagents and conditions: (i) random copolypeptide dissolved in DI H_2O, followed by addition of EDCI/sulfo-NHS then frozen at −18 °C for 24 h; (ii) gel is thawed at RT and washed thoroughly in DI water and PBS (pH = 7.4).

$$P\% = \frac{m_s - m_d}{m_d} \times 100$$

where m_s and m_d are the swollen and dry weights of the gels, respectively. Measurements were made in triplicate for each sample.

Enzymatic Degradation In Vitro. Enzymatic degradation analysis was performed over a period of 14 days using protease (Type XIV from *Streptomyces griseus*). Cryogels were first sterilized and dried through gradual dehydration in EtOH (0−100%) then drying overnight in vacuum oven at 55 °C overnight. Cryogels (∼8 mg dry weight) were then added to 2 mL eppendorf tubes, followed by addition of 1.8 mL of 200 μg/mL protease (PBS) solution, and incubated at 37 °C with gentle mixing. Control samples were prepared through an identical procedure with the addition of PBS only (no enzyme). At designated time points, gels were washed thoroughly in deionized water, sterilized, and dried in EtOH, as per above procedure, and reweighed. Fresh enzyme/buffer addition and drying procedure was used for each time point measurement. The degree of degradation DD(%) was determined by dry weight change at each time point and calculated as

$$DD(\%) = \frac{m_i - m_t}{m_i} \times 100$$

where m_i corresponds to the initial dry weight of sample before degradation, and m_t corresponds to the dry weight of sample after time point of degradation

Cryogels as Cell Scaffolds In Vitro. The potential of synthetic polypeptide cryogels as cell scaffolds was evaluated using mammalian fibroblast (NIH/3T3) cells.

Cell Culture. NIH-3T3 fibroblast cells were obtained from American Type Culture Collection (ATCC). The cells were cultured according to standard procedure. Briefly, Dulbecco's Modified Eagle Medium (DMEM, Gibco, Invitrogen, U.S.A.) was supplemented with 10% Fetal Bovine Serum (FBS, Gibco, Invitrogen, U.S.A.), 2 mM L-glutamine (Gibco, Invitrogen, U.S.A.), 100 units/mL penicillin (Gibco, Invitrogen, U.S.A.), and 100 μg/mL streptomycin (Gibco, Invitrogen, U.S.A.). Cells were passaged every 3−4 days using 0.25% trypsin-EDTA (1×, Gibco, Invitrogen, U.S.A.) at subconfluence and incubated at 37 °C, 5% CO_2, and 90% humidity. Cell passages 5−15 were used for cell experiments.

Cryogel Biocompatibility/Cytotoxicity Studies. Swollen cryogel samples were cut into thin circular disks (cryogel A: ∼6 mm diameter, ∼2 mm thickness; cryogel B: ∼3.5 mm diameter, ∼2 mm thickness). Cryogel A disks were then cut into quarter circles and cryogel B disks into half-circles to cover approximately same interfacial surface area of a 96-well plate. Samples were sterilized in EtOH (50% 1.5 h, 75% 2 h) then thoroughly washed with sterile DI H_2O. Samples were then added to 96-well plates (Corning), washed further with sterile DI H_2O, and then equilibrated in complete DMEM in an incubator overnight (changing solution twice). Cells were first cultured in 96-well culture plates (cell density 3.125×10^3 cells cm^2) and allowed to attach. After 6 h, the medium was aspirated and the cryogel disks were placed inside the wells on top of the attached cells. The fresh culture medium was added into the wells and was changed every alternative day with fresh media during the experiments. The cell viability was probed at 1, 3, 5, and 7 days with the colorimetric CCK-8 assay (Sigma), which is based on the reduction of WST-8 to a formazan dye (orange color) by dehydrogenase activity inside the cells. In order to avoid adsorption of formazan dye by cryogels, they were transferred

DOI: 10.1021/acs.biomac.6b00817
Biomacromolecules 2016, 17, 2981−2991

Table 1. Porosity (P %), Gel Fraction (W_g%), and Young's Modulus (Compressive; E) of Cryogels Synthesized from Their Corresponding Random Copolymers

cryogel	random copolymer	copolymer formula	NH_2/COOH ratio[a] (mol mol^{-1})	c_p% (w/w)	P% (vol)	W_g%	E (kPa)
A	A	PLG_{24}-r-PLL_7	0.29	3.3	85.3 ± 1.0	88.9 ± 2.4	1.6 ± 0.3
B	B	PLG_{16}-r-PLL_{12}	0.73	3.3	82.4 ± 0.9	84.4 ± 1.3	65.8 ± 0.4

[a]Ratio of amine (lysine) to carboxylic acid (glutamic acid) units, as determined by ^{1}H NMR; c_p, concentration of polymer. Values represent mean and standard deviation (n = 3).

into another well before addition of WST-8 solution. The culture medium was changed and 10 μL WST-8 solution was added to the wells, followed by incubation for 4 h. Then, the medium was removed and the absorbance was measured with microplate reader (TECAN M200 infinite Pro) at wavelength of 450 nm. After washing the wells with PBS, the cryogels were transferred back into the wells followed by addition of new medium. The wells were incubated and the same procedure was repeated every alternative day (at 1, 3, 5, and 7 days). At each time point, four control wells cultured without cryogels and four wells cultured in the presence of cryogel were analyzed.

Cell Attachment/Interaction Studies. Swollen FITC-labeled cryogel samples were cut into thin circular disks (cryogel A: ∼6 mm diameter, ∼2 mm thickness; cryogel B: ∼3.5 mm diameter, ∼2 mm thickness). All samples were added directly to 96-well plates and sterilized and washed as per above procedures. The gels were then saturated in complete DMEM medium overnight. The FITC-labeled cryogels were placed in 96-well tissue culture plate and 2.4×10^5 cells were seeded in 50 μL of medium on each cryogel disc. The cryogels were incubated for 4 h with saturated cell suspension to allow cell attachment. Then, 100 μL of culture medium was added and the cryogels were incubated. After 2 and 4 days, the cryogel discs were transferred into new wells and were washed two times with medium. To analyze cell growth in the cryogels, live cell staining and cell nuclear stain were performed using Deep Red and DAPI (4′,6-diamidino-2 phenylindole), respectively. Cells were incubated with Deep Red plasma membrane stain (1:1000, Invitrogen) for 20 min. The samples were then washed three times with PBS and fixed with 4% paraformaldehyde (Aldrich) at room temperature for 10 min. After rinsing the cryogels three times with PBS, the cell nuclei were stained using DAPI (1:1000, Merck Millipore) for 10 min at room temperature. The cryogels were saturated with PBS and imaged on CLSM using excitation wavelengths of 405 nm, 488 and 640 nm. The experiment was repeated at least three times. All images were generated by optical sectioning in the z-direction. Images were stacked in the z-direction using ImageJ software

Cell Proliferation Studies. Swollen cryogel samples were cut into thin circular disks (cryogel A: ∼6 mm diameter, ∼4 mm thickness; cryogel B: ∼3.5 mm diameter, ∼4 mm thickness). Cryogel A disks were then cut into half circles, while cryogel B samples were kept as full circle to ensure comparable swollen gel sizes. Cryogels were sterilized, washed, and equilibrated in medium as per above procedure. Prior to cell seeding, the cryogels were dehydrated by a sterile filter paper for 2 min to remove and expel culture medium from the pores. This procedure facilitates the penetration of the cells into the interior of the cryogel's porous structure. The cryogels were placed into the wells of 24-well tissue culture plates and a cell suspension (10^5 cells in 100 μL) was seeded onto the top of each cryogel disc. The cryogels with the cell suspension were incubated in order for the cells to have time to attach to the pore walls of the cryogels. After 4 h, 500 μL of complete medium were added to each well and the well-plates were returned to the incubator. Every 2 days, the culture medium was changed and the well surfaces were checked to investigate whether migration of cells from the interior of the cryogels onto the well surfaces occurred. Once cells were observed on the well surfaces, the cryogels were carefully transferred to new wells in the well-plate and were incubated further. The step enabled only cells growing on/in the cryogel to be quantified, and not those growing on the underlying tissue culture plastic.

After 1, 4, 7, 10, and 14 days, WST-8 solution was added to each well followed by 4 h of incubation. Then a specific volume of solution was aspirated and transferred to a new well, where the absorbance was measured at 450 nm. Cells cultured on polystyrene tissue culture well-plates were used as control. Measurements were performed in triplicate.

Statistical Analysis. Data are shown as averages and standard deviations. The student's t tests were used to analyze the statistical differences between samples for cytotoxicity and proliferation measurements and were considered significant at $p < 0.05$.

RESULT AND DISCUSSION

Polypeptide Synthesis. Random protected copolypeptides of γ-benzyl-protected poly(L-glutamic acid) (PBLG) and ε-carboxybenzyl-protected poly(L-lysine) (PZLL) were synthesized through α-amino acid *N*-carboxyanhydride (NCA) ring-opening polymerization (ROP) using *N*-(trimethylsilyl)-allylamine (N-TMS allylamine) as initiator (Scheme 2). The polyglutamic and polylysine repeat units contain carboxylic acid and amine side chain functionalities respectively, thereby making it possible for EDC/sulfo-NHS zero-length cross-linking to take place in water using a single random copolypeptide component.

In this system the polypeptide acts as both polymer and cross-linker with both inter and intra molecular cross-linking of the polypeptide expected to take place. To determine the effect of cross-linking on the cryogels, two random copolypeptides with different final ratios of PLG to PLL (PLG:PLL) were prepared. After subsequent side chain deprotection of the protected copolymers in hydrobromic acid (HBr), fully deprotected random copolymer A with a PLG:PLL ratio of 1:0.29 and random copolymer B with a ratio of 1:0.73 (Table 1, see Materials and Methods and Supporting Information ^{1}H NMR for relative ratio determination) were prepared. As can be seen from these ratios, random copolymer B has ∼2.5× more cross-linkable amine groups compared to copolymer A while still remaining within the stoichiometric limits. Based on GPC and ^{1}H NMR analysis, both polypeptides had similar M_n and polydispersity ($Đ$) values (see Materials and Methods). Both fully deprotected polymers demonstrated good water solubility, however this was found to be highly dependent on the solution pH.

Formation of Synthetic Polypeptide Cryogels. Copolymer A was found to be fully water-soluble at pH > 4, whereas copolymer B was found to be soluble at pH values ≤ 4. These observations are consistent with the predicted high net charge (hydrophilicity) of the polypeptides at these respective pH values (calculated using copolymer ratios and side chain pK_a values, not shown). The ability of these polymers to be soluble at these pH values allowed the EDC/sulfo-NHS cross-linking procedure to be performed on either copolymer within the optimum pH range for carboxylic acid/sulfo-NHS activation (pH 4.0−6.0) under cryoconditions. For the preparation of cryogel B, it was found that gelation could occur relatively quickly after addition of sulfo-NHS. Therefore, all reagents were chilled on ice before mixing to reduce the chance of cross-linking occurring before freezing. All cryogels were prepared

DOI: 10.1021/acs.biomac.6b00817
Biomacromolecules 2016, 17, 2981−2991

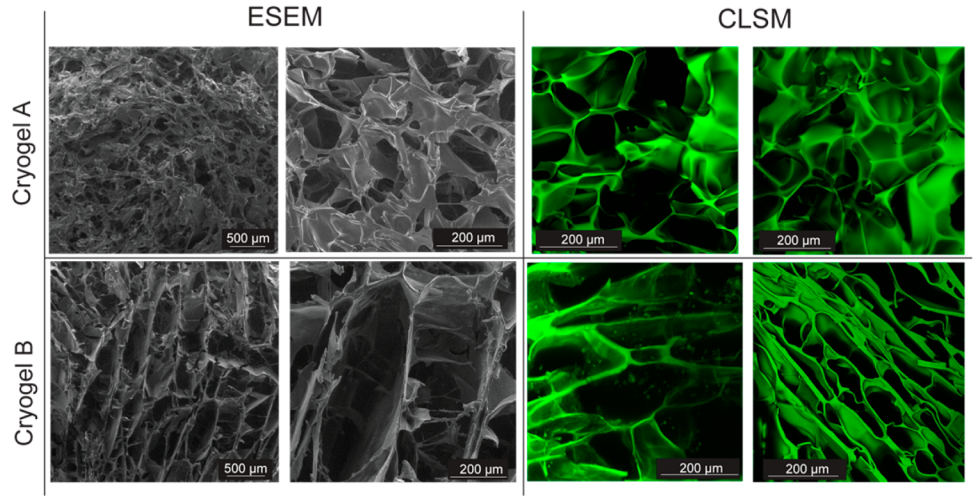

Figure 1. ESEM and CLSM images showing pore morphologies of nonlabeled and FITC-labeled cryogels, respectively. Images are of cross sections in the $x-y$ plane. ESEM images are of swollen cryogels (PBS) under low vacuum. CLSM images of cryogels swollen in PBS and z-stacked.

from their corresponding random copolymer at the same polymer concentration and at a temperature of −18 °C (Scheme 2). To confirm that EDC/sulfo-NHS cross-linking agents were not incorporated into the cryogel network, and their complete removal from the system, FT-IR analysis was performed on the cryogels (see Figures S5 and S6). Almost identical spectra can be seen for the cryogels and their corresponding random copolymer precursors, with no additional peaks in the cryogel spectrum corresponding to EDCI or sulfo-NHS cross-linking agent spectrum profiles.

Morphology of Cryogels. After cryogel preparation, the architecture of the cryogels was determined through E-SEM and CLSM analysis on horizontal cross sections ($x-y$ plane) of nonlabeled gels and FITC-labeled gels (Figure 1, see also Figure S8), respectively. While the E-SEM was performed under low vacuum, the presence of a negative atmosphere and the subsequent partial dehydration of the gels during analysis can give deformed pore structures not truly representative of the gel in the swollen state. Therefore, pore structures of FITC-labeled gels were analyzed on CLSM in their fully hydrated state (PBS). Figure 1 shows both cryogels containing large interconnected pores (≥100 μm) surrounded by pore walls micrometers in thickness, characteristics highly suitable for cell and tissue growth inside hydrogels (see also Figure S8).[4,9,37]

The pore sizes and pore morphologies are distinctively different between the cryogels. The images of cryogel A show a sponge-like morphology with randomly oriented pores ranging in size from 70 to 340 μm and a mean pore size of ∼148 μm as calculated from ImageJ analysis (Figure 2). The pore wall thickness distribution was 2−9 μm, with an average of ∼5 μm. Meanwhile cryogel B have pores that appear columnar in nature,[38] with large defined interconnected closed wall channels running in the z-direction of the gel. The pore sizes in cryogel B are more heterogeneous than cryogel A, ranging in size 50−650 μm with a higher average pore size of ∼213 μm (longest dimension). The pore wall thickness of cryogel B also show higher size distributions to cryogel A with pore wall thicknesses up to 23 μm and a higher average pore thickness of ∼8.5 μm (Figure 2) compared to cryogel A. Discrepancies in size between the E-SEM and CLSM images for cryogel B are likely to be due to both vacuum/preparation defects on the gels during SEM operation and different cross sections of the gel

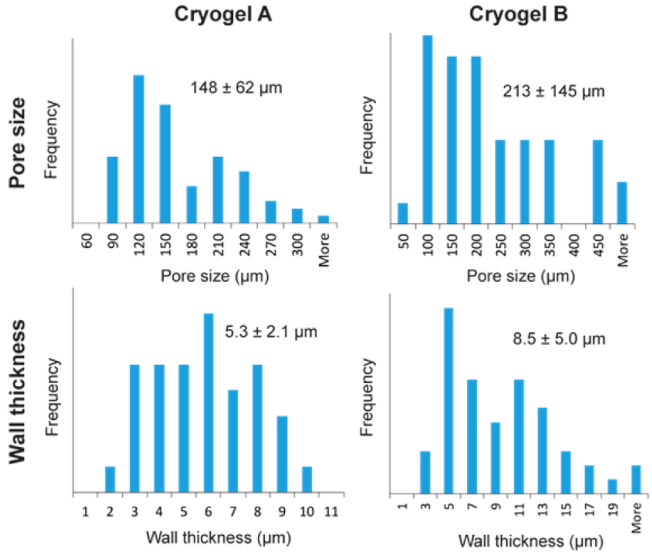

Figure 2. Pore size and pore wall thickness distributions of cryogel A and cryogel B obtained by analysis of CLSM images by ImageJ software.

used for each measurement. Nevertheless, the same large columnar-like channel structure is clearly evident in both.

Changes from sponge-like to columnar-like pore morphology in cryogels (including in polypeptide-based cryogels) have been shown to occur through increases in polymer concentration, resulting in changes to solution viscosities which can affect ice crystal growth during the freezing process.[20,38,39] The difference in pore structure between cryogel A and cryogel B may also be resulting from viscosity changes that affect ice crystal growth due to the different rates of chemical cross-linking in each of the gels. As mentioned previously, gelation of random copolymer B was seen to occur relatively quickly at room temperature compared to copolymer A due to the higher quantity of cross-linkable (amine) groups (Table 1). Despite the chilling of reagents before cryogelation, a small amount of cross-linking may have occurred in cryogel B during the freezing process thereby increasing solution viscosity and affecting ice crystal growth. This increase in viscosity is also likely to affect the cross-linking reaction between the polymer

DOI: 10.1021/acs.biomac.6b00817
Biomacromolecules 2016, 17, 2981−2991

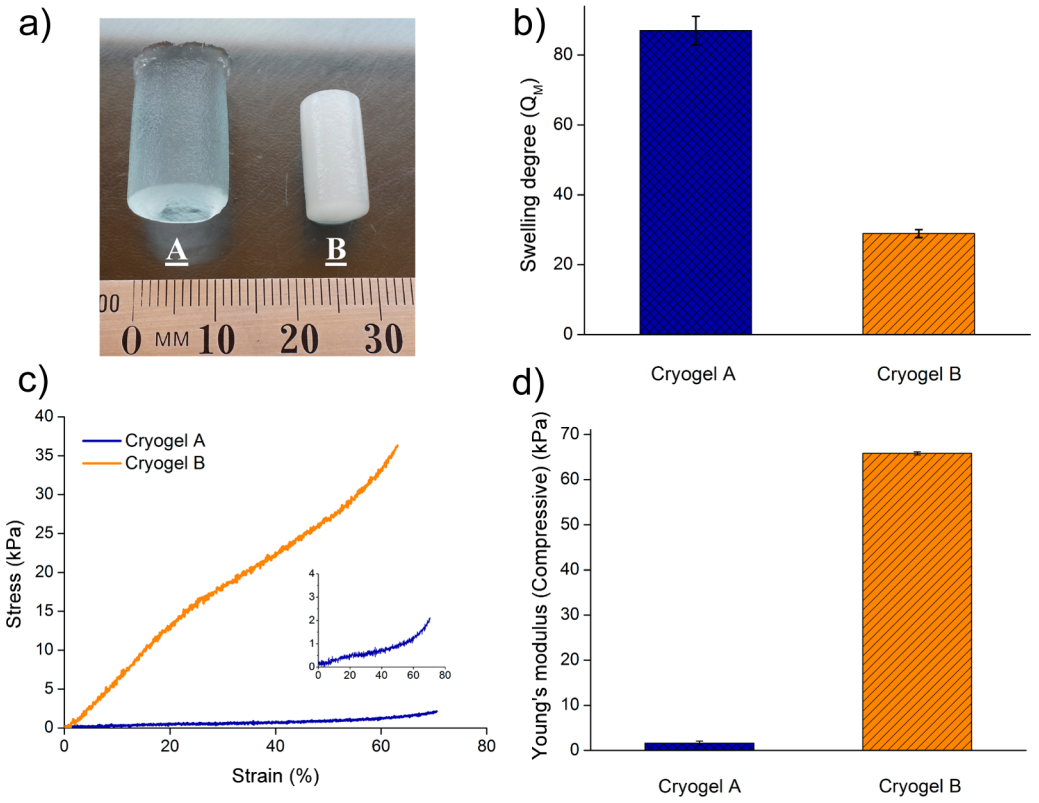

Figure 3. Swelling and mechanical properties of cryogels: (a) Images of cryogels swollen to equilibrium in PBS (left cryogel A, right cryogel B), (b) equilibrium mass swelling ratios, (c) stress vs strain curves from compression tests, and (d) Young's moduli of gels equilibrated in PBS determined from compression tests. Values represent mean and standard deviation (n = 4).

chains due to their decreased diffusivities and may explain the slightly lower gel fraction (yield) observed in cryogel B compared to cryogel A (Table 1).[20,40]

Swelling and Porosity. Due to the macroporous structure and hydrophilic nature of the gels, water can readily enter the pores and inside the pore wall (polymer) regions to effectively swell the cryogels (Figures 3a and S9). The equilibrium swelling ratios of the cryogels has been shown to be influenced by cryogel pore wall thicknesses and cross-linking degrees, with lower wall thicknesses and lower cross-linking degrees resulting in higher swelling ratios due to the flexible pores facilitating the network expansion.[4,5,40,41] Cryogels were swollen to equilibrium in PBS and then freeze-dried, with the results in Figure 3b showing an almost 3× greater mass swelling ratio (Q_M) of cryogel A compared to cryogel B. This mass swelling ratio refers to solvent in both the pores and the pore wall (polymer) regions of the gel. The volume swelling ratios (Q_V), which reflects the solvation of the polymeric walls regions only and therefore the intrinsic swelling capacity of the cryogels,[5,42] was calculated to be 17.94 and 2.52 for cryogel A and cryogel B, respectively. The lower weight and volume swelling ratios of cryogel B compared to cryogel A are consistent with the expected higher cross-linking degree in cryogel B (denser polymeric walls) and its higher pore wall thicknesses compared to cryogel A (Figures 1 and 2). As well, the higher rigidity and reduced flexibility expected from a columnar channel pore morphology (cryogel B) compared to spongy pore morphology (cryogel A) may also impact the swelling nature of the gel. Despite this, only a slight difference in porosity of both gels was determined (Table 1). Using cyclohexane uptake (a nonsolvent commonly used to calculate the pore volume of hydrophilic gels)[43] the porosity (as volume fraction %) of cryogel B (83.4% ± 0.9) was slightly lower than cryogel A (85.3% ± 1.0) suspected to be due to the thicker dense pore walls in cryogel B affecting its overall pore volume.[44] Slight differences in porosity values despite stark differences in pore morphologies and swelling ratios for cryogels has been reported previously in the literature.[32,37]

Mechanical Properties. During tissue regeneration, the gel scaffold provides physical support for the growth and protection of cells and tissue in the presence of internal or external applied forces. The most important mechanical bulk properties of biomaterial scaffolds are the elasticity and stiffness (deformation for a given load). Due to the fact that gel scaffolds as biomaterials are exclusively used in the wet state, mechanical testing was performed on the gels swollen and equilibrated in PBS. For cryogels, buffer solution can flow out from the pores under stress, acting as an efficient energy dissipation mechanism that can prevent crack formation at large deformation ratios.[35] As well, the thin but dense pore walls of the cryogels exhibit a high intrinsic mechanical strength, which provides structural support to the entire highly porous materials.[5]

Uniaxial stress−strain compression tests shown in Figure 3c demonstrate the typical elastic behavior of cryogels, with compression values of up to 70% and beyond (not shown) without deformation or breakage of the gels. After the release of the load, the samples reabsorb the water released during compression and regain their original shape (see Figure S10), with a faster regain observed for cryogel A. This indicates high elasticity and a reversible behavior of the gels. Despite these similarities, the cryogels demonstrated significantly different

DOI: 10.1021/acs.biomac.6b00817
Biomacromolecules 2016, 17, 2981−2991

compression curves, with cryogel B showing a larger slope in the linear elastic region (0−10%) known as the Young's modulus for compression, and a steeper increase in the curve at lower strain values than cryogel A corresponding to material densification (Figure 3c).[5] The Young's modulus of the cryogel is directly related to its bulk stiffness. For tissue engineering applications, it is generally recognized that the stiffness, or Young's modulus of the gel must closely match the tissue being engineered to allow for cells to grow in an environment representative of their natural state.[45] The Young's modulus of soft tissue ranges from <1 kPa (brain tissue) up to ∼600 kPa (cartilage tissue) with strong evidence showing that soft tissue response is dependent upon the mechanical properties of the implanted material.[46−49] Therefore, for any cryogel based-system developed for soft tissue engineering applications in mind, the ability to generate gels with different mechanical properties to suit different tissue properties would be highly beneficial. Shown in Figure 3d, the Young's modulus for cryogel A was calculated to be 1.6 kPa ± 0.4, in the region of brain or skin tissues. Cryogel B on the other hand has a much larger Young's modulus of 65.8 kPa ± 0.3, with stiffness more representative of tendon tissue or nascent bone.[49−51]

An increase in cross-linking degree results in an increase in intrinsic polymer wall stiffness. While this is likely to contribute to an increase in overall (bulk) gel stiffness, the very large increase in bulk stiffness from gel A to gel B is more likely to come from their different porous morphologies discussed previously.[5,44] It has been shown that changing from a spongy to a more closed wall columnar-like structure (including in polypeptide-based systems), can result in large increases in gel strength and stiffness.[20,38] Whereas spongy and fibrillary pore structures consist of thin pore walls randomly distributed throughout the gel network, the columnar channel structure consists of thick polymeric walls spanning the *z*-axis of the gel. These channels therefore generate much more resistance to compression compared to spongy gels particularly along the *z*-axis where the compression tests are performed. Hence the moduli of both cryogels in this study fall within separate regions of soft tissue stiffness thereby demonstrating the ability to generate scaffolds for a range of tissue engineering applications.

Enzymatic Degradation In Vitro. Bioinspired synthetic polypeptides such as poly(L-glutamic acid) can undergo effective enzymatic degradation/cleavage under physiological conditions into soluble fragments, thereby making them suitable biodegradable scaffolds for tissue engineering application.[10,13,15,18,20,52] To test the enzyme biodegradable capabilities of the two cryogels, and to determine their relative degradability profiles, the gels were incubated in the presence of protease XIV, a model enzyme with broad specificity, with degradation measured by the loss of soluble mass (degree of degradation, DD%). Degradation results over a 14 day period in Figure 4 show that the presence of the protease enzyme results in accelerated gel degradation compared to the buffer alone (PBS) due to enzymatic recognition of the polypeptide structure. There was negligible change in the shape of all samples during the degradation process.

Degradation results show a much faster degradation profile for cryogel A compared to cryogel B, with 50% degradation for cryogel A compared to ∼12% degradation for cryogel B after 14 days of incubation. For effective enzymatic degradation and mass loss of the gel to take place, the enzyme must degrade the gel from the surface to the inside of the polymer walls. It must also have conformational access to the relevant inter/intra

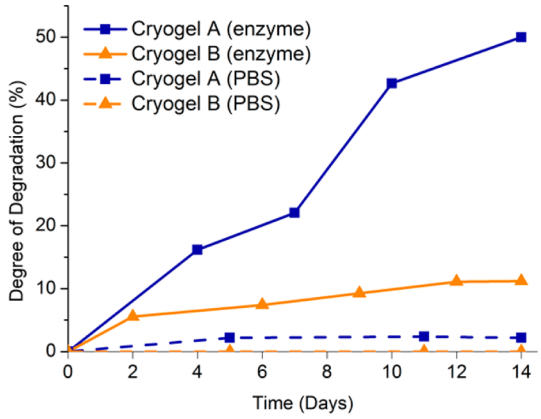

Figure 4. Degree of degradation of cryogels in the presence of enzyme (protease XIV, 200 μg/mL) and in the presence of PBS only (control, dashed line) during 14 days incubation at 37 °C. Degradation rate was determined by change in dry weight. Values are mean values ± (0.5−3%; n = 3).

polypeptide chain bonds within the pore walls. Compared to cryogel A, where greater pore flexibilities and reduced cross-linking densities would give improved access of the enzyme to the relevant bonds for degradation/cleavage to take place, the thicker pore walls and higher cross-linking densities of cryogel B would be expected to make this degradation process slower (Figure 4).

In Vitro Biocompatibility/Cytotoxicity. Recently, the first cryogels partially composed of PLG were prepared for potential tissue engineering applications; however no cell/biological studies were performed on the gels.[20] The use of lingering toxic coupling reagents (e.g. heavy metal copper) used for 'biofunctionalization' of the gels also generated potential biocompatibility issues with the gels. To determine the potential of our synthesized macroporous cryogels as scaffolds for tissue engineering applications, mammalian cell viability tests in the presence of cryogels were performed to test for any cell cytotoxicity.[53] To this end, mammalian NIH-3T3 fibroblast cells, which are commonly used for cell compatibility testing, were seeded on well-plates with cryogels disks placed on top of the culture surface. Cells cultured on the wells without gel were used as controls. The growth of cultured cells were analyzed at days 1, 3, 5, and 7 using CCK-8 assay and presented as absorbance which is proportional to the metabolic activity of the cultured cells (Figure 5). The increasing cellular metabolic activity of the cultured cells with time indicates that cell viability and growth were not hindered by the presence of either of the two cryogels inside the wells. No statistical differences in absorbance were observed between control and cryogels at each time point (P > 0.05) using student t-test. After 5 days of culturing, the cell viability and proliferation on the control wells and the wells containing cryogel did not increase further, suggesting the cells reached confluence inside the wells. The effective growth of fibroblast cells in the presence of the cryogels showed that the cryogels do not exert any soluble or contact cytotoxicity with cells, as the cells maintained their viability and growth in the presence of the gels.

Cell Attachment and Proliferation. The presence of cationic (e.g., amine) and anionic (e.g., acid) species including PLL and PLG sequences has been shown to promote cell attachment to surfaces,[15,16,54,55] without the requirement of biomimetic cell adhesion ligands such as RGD. Reasons for this

DOI: 10.1021/acs.biomac.6b00817
Biomacromolecules 2016, 17, 2981−2991

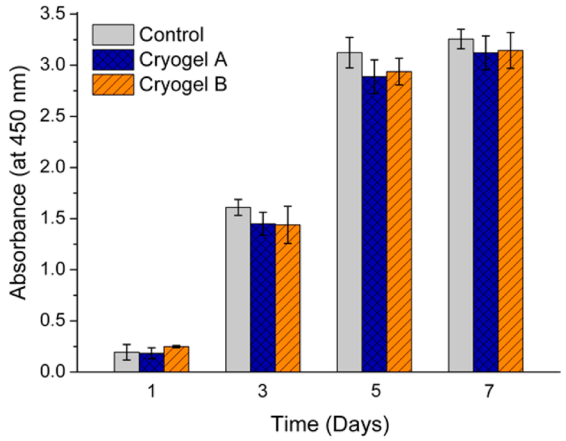

Figure 5. CCK-8 assay of NIH-3T3 fibroblast cells in contact with cryogels during 7 days of culture.

have included the adsorption of proteins to the charged surfaces helping to mediate cell attachment[55−57] and even direct physicochemical interactions of the surface with the cells.[56,57] The presence of residual amine groups in the cryogels can be determined qualitatively through both visual/fluorescent analyses of the cryogels after conjugation to amine-reactive FITC and through FT-IR. Both cryogels show an obvious yellow/red color (Figure S7) and strong green fluorescence under CLSM (Figure 1) due to conjugated FITC, indicating the presence of residual amine groups in the cryogels. In addition, FT-IR analysis of both cryogels (Figures S5 and S6) show peaks at ∼3280 cm^{-1} corresponding to the N−H stretching vibrations of residual free NH_3^+ groups (lysine side chains) after washing/incubation in PBS (pH 7.4).[58,59] The spectrum of both cryogels also show a peak at ∼1540 cm^{-1} characteristic of COO^- side chain stretching bands[60−62] with the absence of any typical COOH carbonyl stretches indicating that the glutamic acid side chains are deprotonated.

To determine the cell attachment and growth capabilities of these multicharged cryogels, CLSM analysis was performed on FITC-labeled cryogels to assess the fibroblast attachment and cell growth. Suspensions of 3T3 fibroblast cells were seeded on top of the cryogel scaffolds and allowed to attach for a brief period of time. Culture medium was then added and the samples then incubated. As shown in Figure 6a, after 2 days of culture, large cell clusters can be seen inside the macroporous structure, indicative of rapid cell adhesion. Cell adhesion and growth closely follows the contours of the pores walls indicating effective cell attachment to the cryogel pore walls. Migration, penetration, and proliferation of the cells from near the site of incubation deeper into the interior of the cryogel can be observed after 4 days of culture as seen with cryogel A in Figure 6b. Despite the different relative ratios of PLL to PLG in the cryogel copolymer precursors, and therefore potentially different surface properties, the images appear to show little difference in the innate cell attachment properties of both cryogels. Determining the effect of surface morphology, protein adsorption, and charge density on the cell attachment properties of these multicharged gels will be a focus of future studies.

To study the proliferation of cells within the gels more closely, a suspension of fibroblast cells were seeded inside the cryogel scaffolds and the cell growth and proliferation evaluated by measuring the cell metabolic activity using CCK-8 assay up to 14 days (Figure 7a). CCK-8 uses reagent WST-8, which is reduced by viable cells extracellularly to form a highly water/media soluble colored formazen in proportion to the number of viable cells. In Figure 7a, the metabolic activity and the number of cells is seen to increase over the culture period, indicating that the cells are able to attach and proliferate inside the cryogel scaffolds. Despite the higher pore size, pore thickness and larger heterogeneities of cryogel B compared to cryogel A, no statistical differences were observed between the two gels during the proliferation measurements. This suggests that although the different pore morphologies of these cryogels have

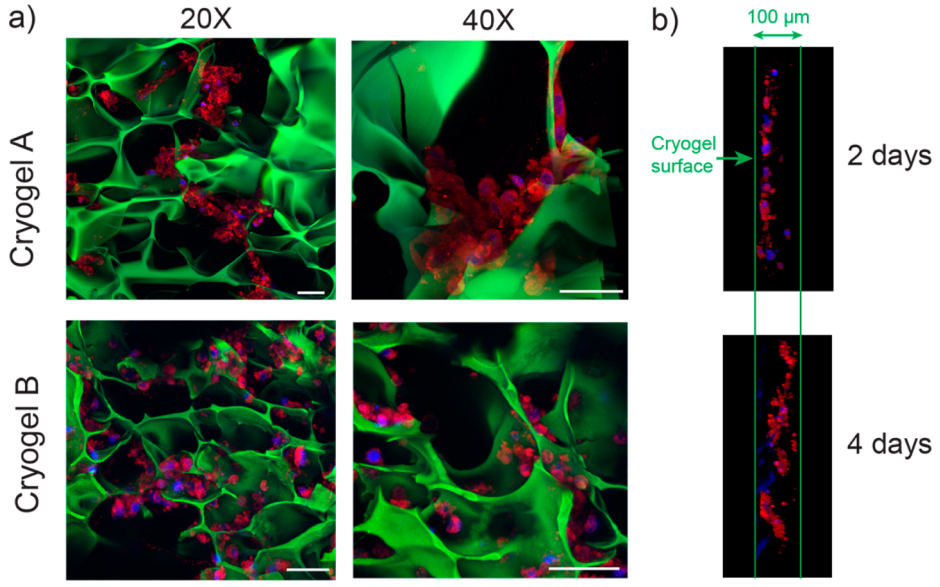

Figure 6. CLSM images of NIH-3T3 cells colonized on cryogels (a) $x-y$ plane images of cryogels after 2 days of culture. 20× and 40× microscope objectives used. Scale bars (white) represent 50 μm. (b) Cross-sectional (z-section) image of cryogel A showing effective cell migration and growth into gel structure from direction of surface incubation (green arrow) after 4 days culture. Boundaries of the cryogel cross-section (100 μm thickness) indicated by green line. Fluorescent cryogel structure (green channel) removed for better visualization of cells.

DOI: 10.1021/acs.biomac.6b00817
Biomacromolecules 2016, 17, 2981−2991

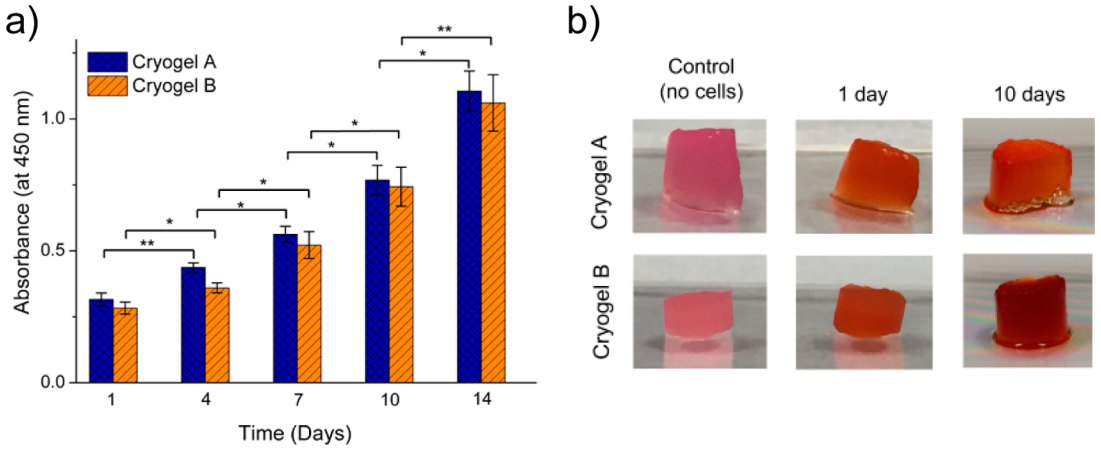

Figure 7. Cell growth of NIH-3T3 fibroblast cells cultured inside cryogel A and B for 14 days. (a) Cell viability determined by CCK-8 assay with absorbance of orange formazan product measured at 450 nm at different time intervals. Statistically significant differences are indicated (*$P < 0.05$ and **$P < 0.01$). (b) Images of gels after CCK-8 staining. Control gels contain CCK-8 stain without cells.

a large effect on their swelling and mechanical properties, they do not appear to have a large effect on cell growth.

Cell proliferation can also be seen visually in Figure 7b with images of cell-cultured cryogels that sequestered the WST-8 dye from solution showing a homogeneous dark orange-red color of the generated formazen due to cell proliferation. This color is seen to darken further after 10 days of culturing as a result of increased cell growth. The cell growth rate of fibroblasts inside the cryogel was seen to be lower than the cell culture on polystyrene well plates. This was likely due to some migration of cells from inside of the gels to the surface of the well during the experiment resulting in a loss of cells from the cryogel samples. Also, the cryogels absorbed and sequestered some of the formazen dye as shown in Figure 7b. Due to this absorption, the concentration of formazen in the solution phase was partially reduced, resulting in a decrease in the measured viability of cells growing on/inside the cryogels. Collectively, the results indicate that these macroporous cryogels provide a supportive scaffold for the attachment, survival, migration, and proliferation of cells.

CONCLUSION

In conclusion, a simple approach to the development of macroporous hydrogels composed entirely of biocompatible and biodegradable synthetic polypeptides has been developed. Through the use of a random copolypeptide containing both PLG and PLL, direct cross-linking of a single polymer chain through EDC/sulfo-NHS cross-linking could be achieved under cryoconditions. The resulting cryogels contain large macroporous structures with pore sizes highly suitable for tissue engineering applications ($\geq$100 μm). By increasing the ratio of lysine relative to glutamic acid in the copolymers, gels with increased pore thicknesses and very different pore morphologies (spongey, columnar-like) could be prepared which had large effects on their swelling and mechanical stiffness properties. The stiffness (Young's modulus) of both cryogels in this study fell within separate regions of soft tissue stiffness thereby demonstrating the ability to generate scaffolds for a range of soft tissue cell culturing. These polypeptide cryogels were shown to be enzymatically biodegradable with a slower degradation profile observed for the stiff, columnar-like cryogel. Both multicharged cryogels demonstrated excellent biocompatibility, cell attachment, and cell proliferation profiles with mammalian fibroblast (NIH-3T3) cells, demonstrating their potential as suitable cellular scaffolds.

ASSOCIATED CONTENT

Supporting Information

The Supporting Information is available free of charge on the ACS Publications website at DOI: 10.1021/acs.biomac.6b00817.

^{1}H NMR spectra of all copolypeptides including the glutamic acid and lysine ratio determinations, FT-IR spectra of cryogels, images of FITC-labeled and dried/swollen cryogels, and mechanical testing images (PDF).

AUTHOR INFORMATION

Corresponding Author

*E-mail: gregghq@unimelb.edu.au. Tel.: +61 3 8344 8665. Fax: +61 3 8344 4153.

Author Contributions

‡These authors contributed equally (S.J.S and F.K).

Notes

The authors declare no competing financial interest.

ACKNOWLEDGMENTS

The authors would like to acknowledge the Australian Research Council (ARC) for funding in the form of a Discovery Project (DP140100002). S.J.S. would like to thank The University of Melbourne, the Commonwealth Scientific and Industrial Research Organization (CSIRO), and the Melbourne Materials Institute (MMI) for various scholarships. F.K. would like to thank the Australian Government and the University of Melbourne for an International Postgraduate Research Scholarship (IPRS).The authors would also like to thank Mr. Dunyin Gu for help with mechanical testing measurements and Mr. Ke Xie for help with ESEM measurements.

REFERENCES

(1) Tibbitt, M. W.; Anseth, K. S. *Biotechnol. Bioeng.* **2009**, *103* (4), 655−663.

(2) Zhao, X.; Kim, J.; Cezar, C. A.; Huebsch, N.; Lee, K.; Bouhadir, K.; Mooney, D. J. *Proc. Natl. Acad. Sci. U. S. A.* **2011**, *108* (1), 67−72.

DOI: 10.1021/acs.biomac.6b00817
Biomacromolecules 2016, 17, 2981−2991

(3) Bencherif, S. A.; Sands, R. W.; Ali, O. A.; Li, W. A.; Lewin, S. A.; Braschler, T. M.; Shih, T.-Y.; Verbeke, C. S.; Bhatta, D.; Dranoff, G.; Mooney, D. J. *Nat. Commun.* **2015**, *6*, 7556.
(4) Henderson, T. M. A.; Ladewig, K.; Haylock, D. N.; McLean, K. M.; O'Connor, A. J. *J. Mater. Chem. B* **2013**, *1* (21), 2682−2695.
(5) Welzel, P. B.; Grimmer, M.; Renneberg, C.; Naujox, L.; Zschoche, S.; Freudenberg, U.; Werner, C. *Biomacromolecules* **2012**, *13* (8), 2349−2358.
(6) Kumari, J.; Karande, A. A.; Kumar, A. *ACS Appl. Mater. Interfaces* **2016**, *8* (1), 264−77.
(7) Dainiak, M. B.; Allan, I. U.; Savina, I. N.; Cornelio, L.; James, E. S.; James, S. L.; Mikhalovsky, S. V.; Jungvid, H.; Galaev, I. Y. *Biomaterials* **2010**, *31* (1), 67−76.
(8) Liu, H. F.; Mao, J. S.; Yao, K. D.; Yang, G. H.; Cui, L.; Cao, Y. L. *J. Biomater. Sci., Polym. Ed.* **2004**, *15* (1), 25−40.
(9) Chiu, Y.-C.; Cheng, M.-H.; Engel, H.; Kao, S.-W.; Larson, J. C.; Gupta, S.; Brey, E. M. *Biomaterials* **2011**, *32* (26), 6045−6051.
(10) Duro-Castano, A.; Conejos-Sanchez, I.; Vicent, M. J. *Polymers* **2014**, *6* (2), 515−551.
(11) Khuphe, M.; Kazlauciunas, A.; Huscroft, M.; Thornton, P. D. *Chem. Commun.* **2015**, *51* (8), 1520−1523.
(12) Shirbin, S. J.; Ladewig, K.; Fu, Q.; Klimak, M.; Zhang, X.; Duan, W.; Qiao, G. G. *Biomacromolecules* **2015**, *16* (8), 2463−2474.
(13) Li, C. *Adv. Drug Delivery Rev.* **2002**, *54* (5), 695−713.
(14) Richert, L.; Arntz, Y.; Schaaf, P.; Voegel, J. C.; Picart, C. *Surf. Sci.* **2004**, *570* (1−2), 13−29.
(15) Cao, B.; Yan, S.; Zhang, K.; Song, Z.; Cao, T.; Chen, X.; Cui, L.; Yin, J. *Macromol. Biosci.* **2011**, *11* (7), 970−977.
(16) Boura, C.; Menu, P.; Payan, E.; Picart, C.; Voegel, J. C.; Muller, S.; Stoltz, J. F. *Biomaterials* **2003**, *24* (20), 3521−3530.
(17) Yan, S.; Zhang, K.; Liu, Z.; Zhang, X.; Gan, L.; Cao, B.; Chen, X.; Cui, L.; Yin, J. *J. Mater. Chem. B* **2013**, *1* (11), 1541−1551.
(18) Cao, B.; Yin, J.; Yan, S.; Cui, L.; Chen, X.; Xie, Y. *Macromol. Biosci.* **2011**, *11* (3), 427−434.
(19) Studenovska, H.; Vodicka, P.; Proks, V.; Hlucilova, J.; Motlik, J.; Rypacek, F. *J. Tissue Eng. Regener. Med.* **2010**, *4* (6), 454−463.
(20) Sedlacik, T.; Proks, V.; Slouf, M.; Duskova-Smrckova, M.; Studenovska, H.; Rypacek, F. *Biomacromolecules* **2015**, *16* (11), 3455−65.
(21) Zhang, Z.; Chen, L.; Deng, M.; Bai, Y.; Chen, X.; Jing, X. *J. Polym. Sci., Part A: Polym. Chem.* **2011**, *49* (13), 2941−2951.
(22) Lozinsky, V. I.; Okay, O. Basic Principles of Cryotropic Gelation. In *Polymeric Cryogels: Macroporous Gels with Remarkable Properties*; Okay, O., Ed.; Springer, 2014; Vol. *263*, pp 49−101.
(23) Lozinsky, V. I. *Russ. Chem. Bull.* **2008**, *57* (5), 1015−1032.
(24) Bencherif, S. A.; Sands, R. W.; Bhatta, D.; Arany, P.; Verbeke, C. S.; Edwards, D. A.; Mooney, D. J. *Proc. Natl. Acad. Sci. U. S. A.* **2012**, *109* (48), 19590−19595.
(25) Koshy, S. T.; Ferrante, T. C.; Lewin, S. A.; Mooney, D. J. *Biomaterials* **2014**, *35* (8), 2477−2487.
(26) Sannino, A.; Netti, P. A.; Madaghiele, M.; Coccoli, V.; Luciani, A.; Maffezzoli, A.; NicolaiS, L. *J. Biomed. Mater. Res., Part A* **2006**, *79A* (2), 229−236.
(27) Levesque, S. G.; Lim, R. M.; Shoichet, M. S. *Biomaterials* **2005**, *26* (35), 7436−7446.
(28) Huang, X.; Zhang, Y.; Donahue, H. J.; Lowe, T. L. *Tissue Eng.* **2007**, *13* (11), 2645−2652.
(29) Murphy, W. L.; Dennis, R. G.; Kileny, J. L.; Mooney, D. J. *Tissue Eng.* **2002**, *8* (1), 43−52.
(30) Van Vlierberghe, S. *J. Mater. Sci.* **2016**, *51* (9), 4349−4357.
(31) Tripathi, A.; Kumar, A. *Macromol. Biosci.* **2011**, *11* (1), 22−35.
(32) Henderson, T. M. A.; Ladewig, K.; Haylock, D. N.; McLean, K. M.; O'Connor, A. J. *J. Biomater. Sci., Polym. Ed.* **2015**, *26* (13), 881−897.
(33) Sulistio, A.; Widjaya, A.; Blencowe, A.; Zhang, X. Q.; Qiao, G. *Chem. Commun.* **2011**, *47* (4), 1151−1153.
(34) Lee, J.; Lee, S. J.; Choi, J. Y.; Yoo, J. Y.; Ahn, C. H. *Eur. J. Pharm. Sci.* **2005**, *24* (5), 441−449.
(35) Ak, F.; Oztoprak, Z.; Karakutuk, I.; Okay, O. *Biomacromolecules* **2013**, *14* (3), 719−727.
(36) Kirsebom, H.; Topgaard, D.; Galaev, I. Y.; Mattiasson, B. *Langmuir* **2010**, *26* (20), 16129−16133.
(37) Phadke, A.; Hwang, Y.; Kim, S. H.; Kim, S. H.; Yamaguchi, T.; Masuda, K.; Varghese, S. *Eur. Cell Mater.* **2013**, *25*, 114−129.
(38) Chau, M.; De France, K. J.; Kopera, B.; Machado, V. R.; Rosenfeldt, S.; Reyes, L.; Chan, K. J. W.; Förster, S.; Cranston, E. D.; Hoare, T.; Kumacheva, E. *Chem. Mater.* **2016**, *28*, 3406−3415.
(39) Strom, A.; Larsson, A.; Okay, O. *J. Appl. Polym. Sci.* **2015**, *132* (29), 42194.
(40) Loo, S.-L.; Krantz, W. B.; Lim, T.-T.; Fane, A. G.; Hu, X. *Soft Matter* **2013**, *9* (1), 224−234.
(41) Oelschlaeger, C.; Bossler, F.; Willenbacher, N. *Biomacromolecules* **2016**, *17* (2), 580−589.
(42) Okay, O. General Properties of Hydrogels. In *Hydrogel Sensors and Actuators: Engineering and Technology*; Gerlach, G., Arndt, K. F., Eds.; Springer, 2009; Vol. *6*, pp 1−14.
(43) Plieva, F. M.; Karlsson, M.; Aguilar, M. R.; Gomez, D.; Mikhalovsky, S.; Galaev, I. Y. *Soft Matter* **2005**, *1* (4), 303−309.
(44) Savina, I. N.; Cnudde, V.; D'Hollander, S.; Van Hoorebeke, L.; Mattiasson, B.; Galaev, I. Y.; Du Prez, F. *Soft Matter* **2007**, *3* (9), 1176−1184.
(45) Liu, J.; Zheng, H.; Poh, P. S. P.; Machens, H.-G.; Schilling, A. F. *Int. J. Mol. Sci.* **2015**, *16* (7), 15997−16016.
(46) Discher, D. E.; Janmey, P.; Wang, Y. L. *Science* **2005**, *310* (5751), 1139−1143.
(47) Wang, B. H.; Campbell, G. *Spine* **2009**, *34* (25), 2745−2753.
(48) Price, G. M.; Wong, K. H. K.; Truslow, J. G.; Leung, A. D.; Acharya, C.; Tien, J. *Biomaterials* **2010**, *31* (24), 6182−6189.
(49) Huang, G.; Wang, L.; Wang, S.; Han, Y.; Wu, J.; Zhang, Q.; Xu, F.; Lu, T. J. *Biofabrication* **2012**, *4* (4), 042001.
(50) Chen, E. J.; Novakofski, J.; Jenkins, W. K.; Obrien, W. D. *IEEE Trans. Ultrason. Ferroelect. Freq. Control* **1996**, *43* (1), 191−194.
(51) Sartori, S.; Chiono, V.; Tonda-Turo, C.; Mattu, C.; Gianluca, C. *J. Mater. Chem. B* **2014**, *2* (32), 5128−5144.
(52) Shen, Y.; Fu, X.; Fu, W.; Li, Z. *Chem. Soc. Rev.* **2015**, *44* (3), 612−622.
(53) Zhou, C.; Heath, D. E.; Sharif, A. R. M.; Rayatpisheh, S.; Oh, B. H. L.; Rong, X.; Beuerman, R.; Chan-Park, M. B. *Macromol. Biosci.* **2013**, *13* (11), 1485−1491.
(54) Lee, J. H.; Jung, H. W.; Kang, I. K.; Lee, H. B. *Biomaterials* **1994**, *15* (9), 705−711.
(55) Omrani, M. M.; Kiaie, N.; Ansari, M.; Kordestani, S. S. *J. Macromol. Sci., Part B: Phys.* **2016**, *55* (6), 617−626.
(56) Qiu, Q.; Sayer, M.; Kawaja, M.; Shen, X.; Davies, J. E. *J. Biomed. Mater. Res.* **1998**, *42* (1), 117−127.
(57) Schneider, G. B.; English, A.; Abraham, M.; Zaharias, R.; Stanford, C.; Keller, J. *Biomaterials* **2004**, *25* (15), 3023−3028.
(58) Shan, C.; Yang, H.; Han, D.; Zhang, Q.; Ivaska, A.; Niu, L. *Langmuir* **2009**, *25* (20), 12030−12033.
(59) Wu, C.; He, Q.; Zhu, A.; Li, D.; Xu, M.; Yang, H.; Liu, Y. *ACS Appl. Mater. Interfaces* **2014**, *6* (23), 21615−21623.
(60) Perry, S. L.; Leon, L.; Hoffmann, K. Q.; Kade, M. J.; Priftis, D.; Black, K. A.; Wong, D.; Klein, R. A.; Pierce, C. F.; Margossian, K. O.; Whitmer, J. K.; Qin, J.; de Pablo, J. J.; Tirrell, M. *Nat. Commun.* **2015**, *6*, 6052.
(61) Dzwolak, W.; Marszalek, P. E. *Chem. Commun.* **2005**, *44*, 5557−5559.
(62) Mendelsohn, J. D.; Yang, S. Y.; Hiller, J.; Hochbaum, A. I.; Rubner, M. F. *Biomacromolecules* **2003**, *4* (1), 96−106.

DOI: 10.1021/acs.biomac.6b00817
Biomacromolecules 2016, 17, 2981−2991

Supporting Information

Macroporous hydrogels composed entirely of synthetic polypeptides: biocompatible and enzyme biodegradable 3D cellular scaffolds

Steven J. Shirbin,[†,‡] Fatemeh Karimi, [†,‡] Nicholas Jun-An Chan, [†] Daniel E. Heath,[§] Greg G. Qiao[†]*

[†] *Polymer Science Group, Department of Chemical and Biomolecular Engineering, University of Melbourne, Parkville, Melbourne, Victoria 3010, Australia*

[§] *Department of Chemical and Biomolecular Engineering, University of Melbourne, Parkville, Melbourne, Victoria 3010, Australia*

[‡] These authors contributed equally (S.J.S and F.K)

*Corresponding author: Greg G.Qiao, Email: gregghq@unimelb.edu.au

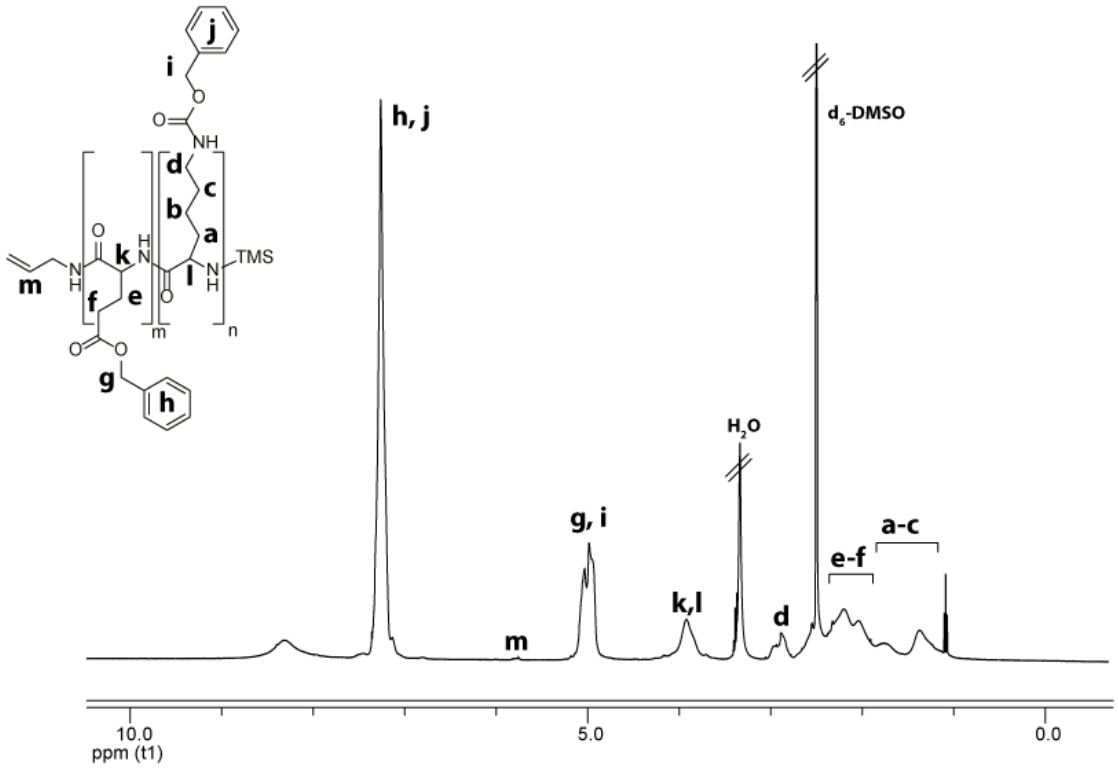

Figure S1: ^{1}H NMR (d_6-DMSO) spectrum of protected random copolymer A.

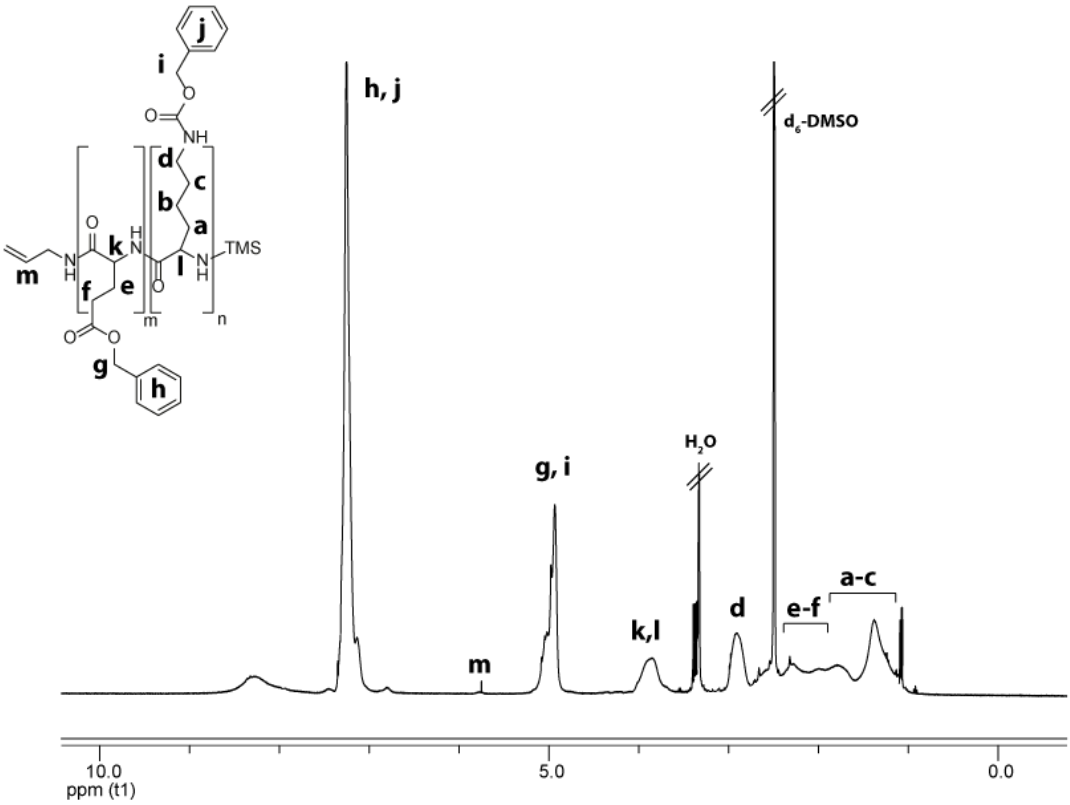

Figure S2: ^{1}H NMR (d_6-DMSO) spectrum of protected random copolymer B.

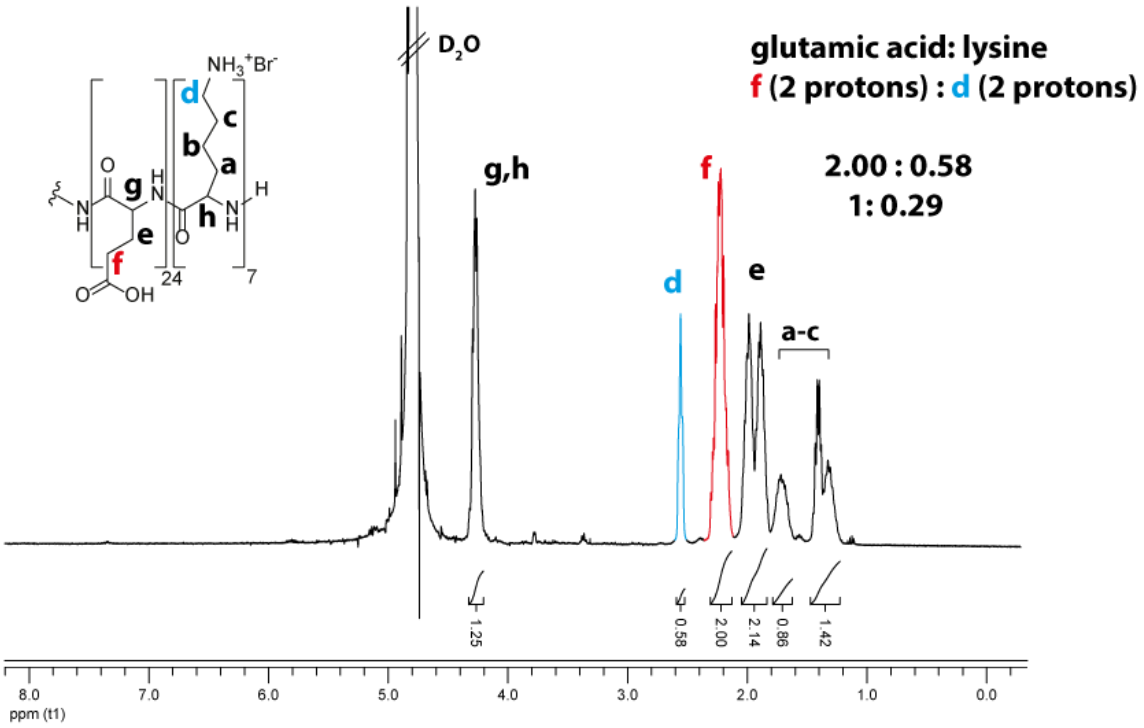

Figure S3: ^{1}H NMR (D_2O/NaOD) spectrum of deprotected random copolymer A including calculations of glutamic acid:lysine ratio based on the relevant integrations.

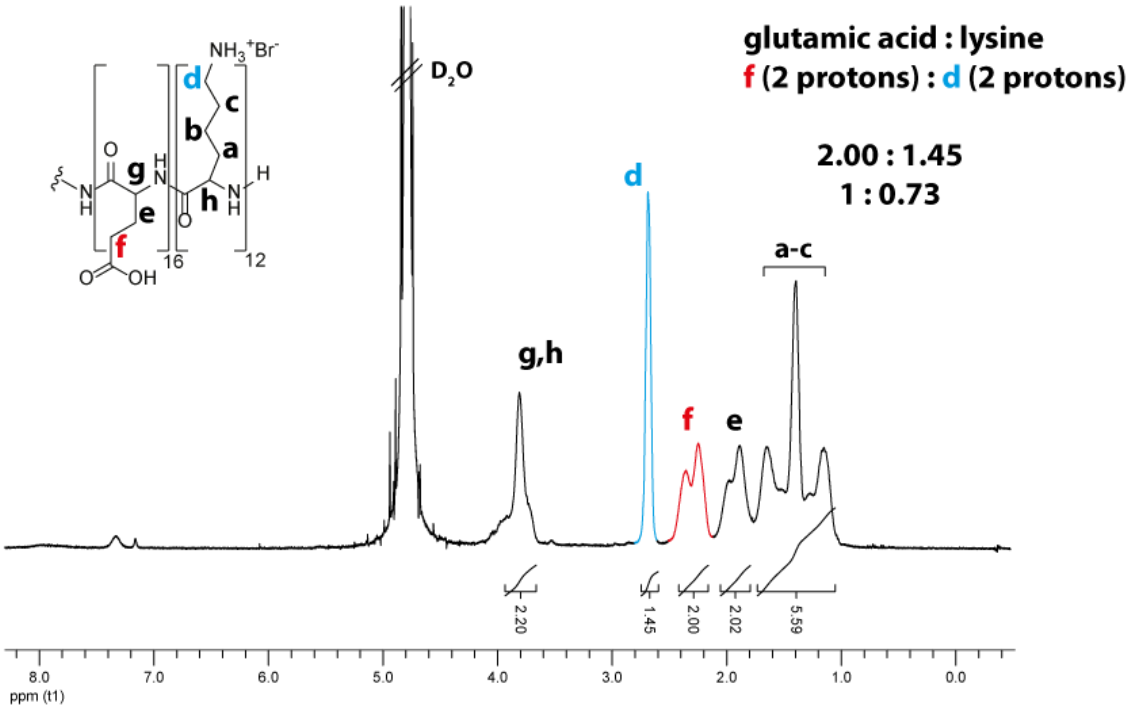

Figure S4: ^{1}H NMR (D_2O/DCl) spectrum of deprotected random copolymer B including calculations of glutamic acid:lysine ratio based on the relevant integrations.

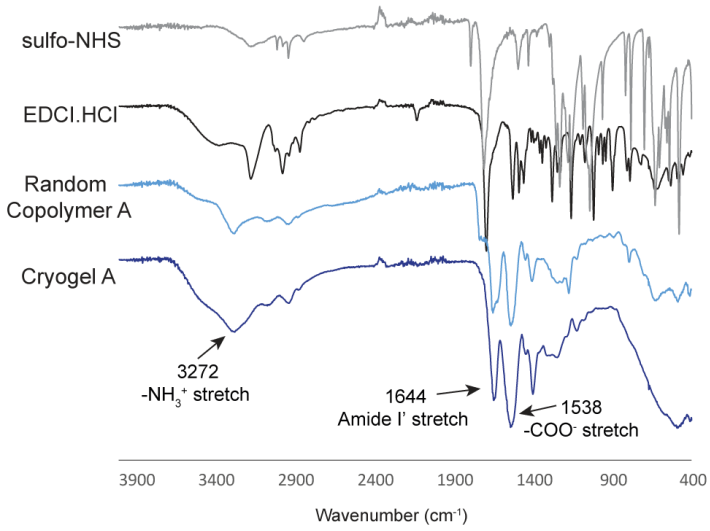

Figure S5: FT-IR spectra of cryogel A, copolymer A, EDCI and sulfo-NHS cross-linking agents. Note: amide I stretch in cryogel corresponding to both copolymer backbone and side chain (amide) cross-links.

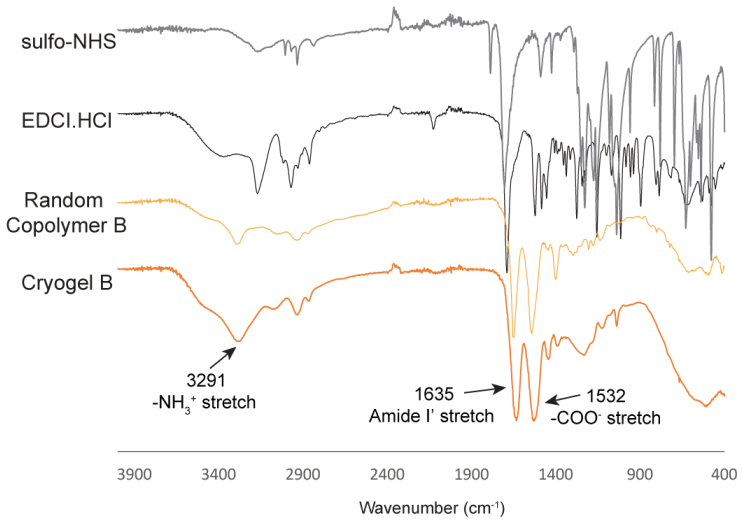

Figure S6: FT-IR spectra of cryogel B, copolymer B, EDCI and sulfo-NHS cross-linking agents. Note: amide I stretch in cryogel corresponding to both copolymer backbone and side chain (amide) cross-links.

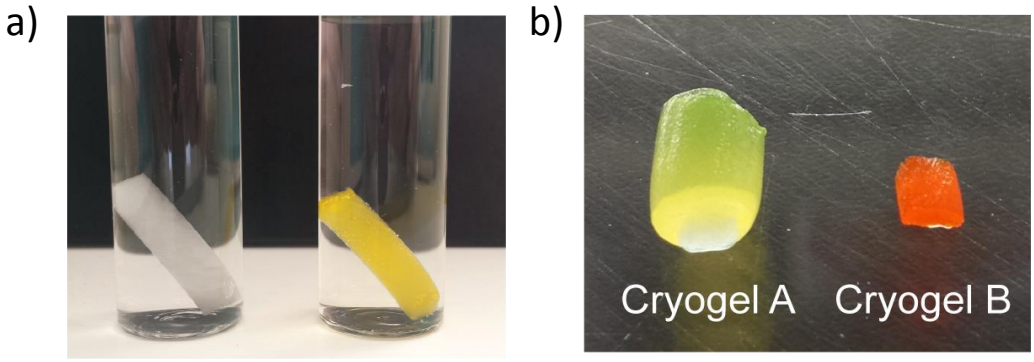

Figure S7: (a) Non-labeled and FITC-labeled cryogel A samples (b) FITC-labeled cryogel A and cryogel B samples

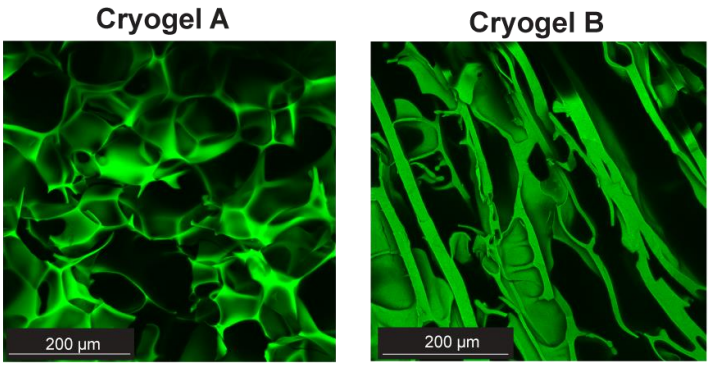

Figure S8: CLSM images showing pore morphologies of FITC-labeled cryogels swollen in PBS. Images are of cross-sections in the x-y plane and z-stacked.

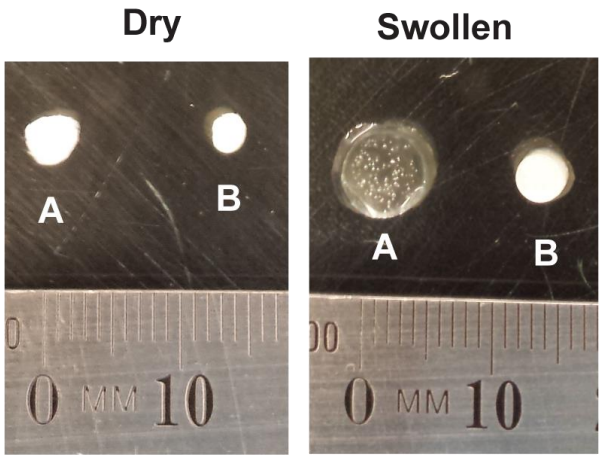

Figure S9: Images of dry and swollen cryogel A and B samples (PBS)

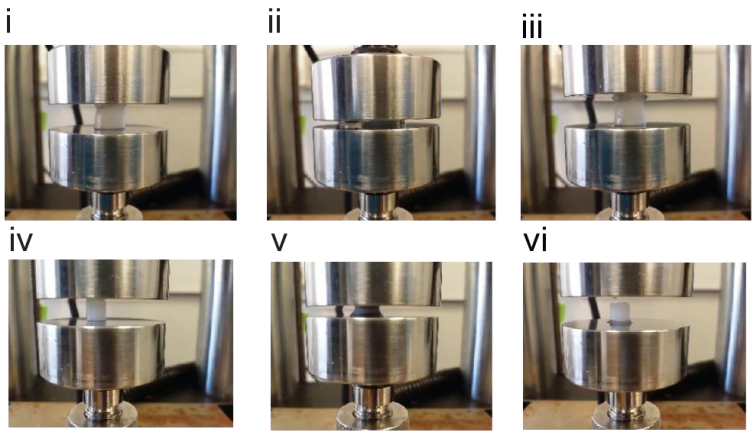

Figure S10: Images of cryogel A (i-iii) and cryogel B (iv-vi) during mechanical testing.

ACS Macro Letters

Letter

pubs.acs.org/macroletters

Polypeptide-Based Macroporous Cryogels with Inherent Antimicrobial Properties: The Importance of a Macroporous Structure

Steven J. Shirbin,[†,‡] Shu J. Lam,[†,‡] Nicholas Jun-An Chan,[†] Mehmet Murat Ozmen,[†,§] Qiang Fu,[†] Neil O'Brien-Simpson,[∥] Eric C. Reynolds,[∥] and Greg G. Qiao*[,†]

[†]Polymer Science Group, Department of Chemical and Biomolecular Engineering, University of Melbourne, Parkville, Melbourne, Victoria 3010, Australia

[§]Department of Bioengineering, Yildiz Technical University, Esenler, 34220, Istanbul, Turkey

[∥]Melbourne Dental School and The Bio21 Institute of Molecular Science and Biotechnology, Oral Health CRC, The University of Melbourne, Parkville, VIC 3010, Australia

Supporting Information

ABSTRACT: Synthetic polypeptide-based macroporous cryogels with inherent antimicrobial properties were prepared for potential water purification applications. Gels were chemically cross-linked through the amine residue of a polycationic polylysine-*b*-polyvaline block copolymer with glutaraldehyde as cross-linker under cryogenic conditions. These cryogels exhibited excellent water swelling and highly compressible mechanical properties owing to their macroporous structure. The antibacterial performance was evaluated based on *E. coli* viability, with cryogels exhibiting up to 95.6% reduction in viable *E. coli* after a brief 1 h incubation. In comparison to the hydrogel control, the presence of macropores is shown to be vital to the antimicrobial effect of the gels. The confined environment and increased antimicrobial surface area of the macropores is believed to result in a "trap and kill" mechanism. Mechanical strength and pore integrity of cryogels were also found to be determinants for antibacterial activity. Along with the lack of toxic leaching, these cryogels with inherent antimicrobial properties pose as potential candidates for use in biological and environmentally friendly water purification applications.

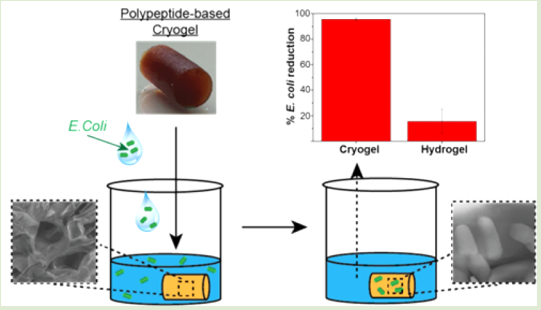

Peptide-based antimicrobial hydrogels have demonstrated significant potential over the years due to their inherent antimicrobial activity upon physical contact between the gel and the bacteria.[1−5] These gels often consist of a polycationic-rich surface (i.e., polylysine), which is suspected to result in bacteria membrane disruption. However, being rigid in nature, the physical properties of such hydrogels limits their range of applications. Cryogels, often termed macroporous hydrogels, have for many years shown significant advantages over their conventional hydrogel counterparts through superior swelling and mechanical (e.g., elasticity, toughness) properties as a result of their interconnected macroporous structure.[6−11] Antimicrobial cryogels, an emerging and exciting field, have looked to exploit the unique mechanical and swelling properties of these systems for biomedical and water purification applications. For water purification, in particular, the presence of a large number of pores allows for faster and larger water absorption properties that are unmatched with conventional hydrogels.[12−14]

Within the limited amount of research into antimicrobial cryogels, including those for water purification, the antimicrobial activity of these gels comes from the incorporation of known antimicrobial agents rather than from the polymer itself. These include heavy metals (e.g., silver or copper),[15,16] ionic liquids,[17] or drugs.[18] Despite showing high activity, the leaching of toxic components (e.g., heavy metals, drugs) in these systems is reported, which could result in (biological and environmental) toxic components leaching into the treated water. Therefore, despite the generation of inherently antimicrobial active hydrogels in the literature, this has yet to be demonstrated in a cryogel system.

Recent studies have revealed that hydrogels consisting of both cationic and hydrophobic polypeptide components have high antimicrobial potency through suspected bacteria membrane disruption.[2,3] Building upon this concept, we decided to synthesize novel polypeptide-based cryogels with similar precursors in order to test for their inherent antimicrobial effect. Herein, we describe our efforts toward the facile preparation of a synthetic polypeptide-based cryogel with inherent antimicrobial properties for potential water

Received: March 1, 2016
Accepted: April 7, 2016
Published: April 11, 2016

DOI: 10.1021/acsmacrolett.6b00174
ACS Macro Lett. 2016, 5, 552−557

Scheme 1. (a) Synthesis of PLL-*b*-PDLV Block Copolypeptide (P1) and (b) Its Fabrication into Cryogels[a]

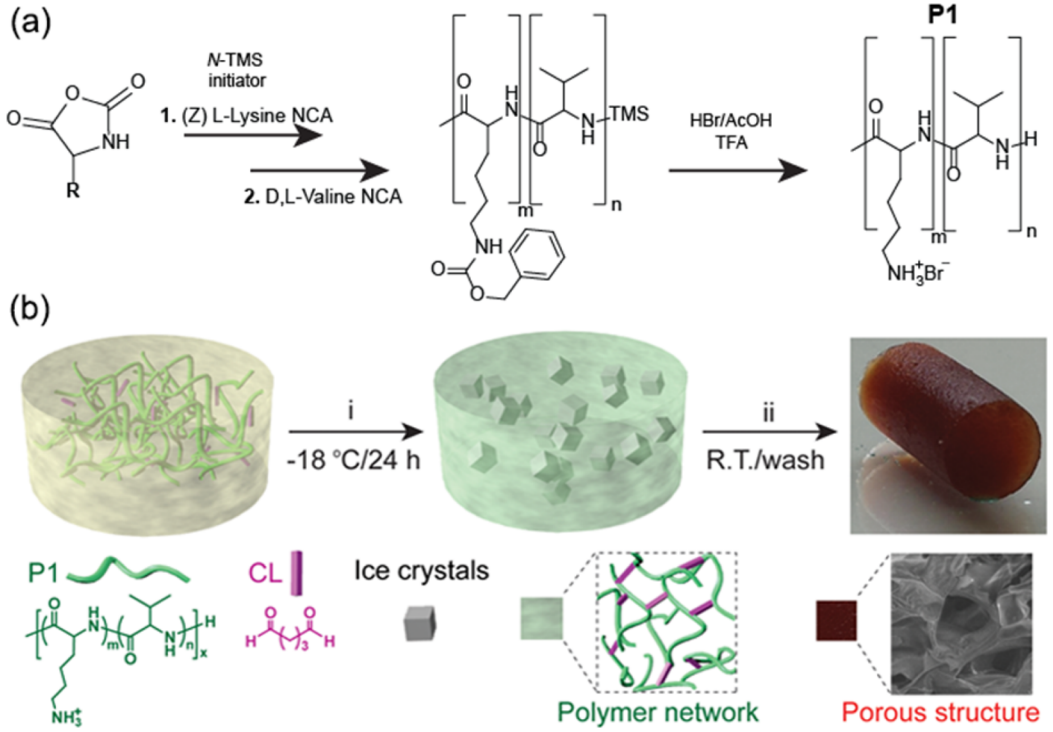

[a]Reagents and conditions: (i) block copolypeptide (P1) and glutaraldehyde crosslinker (CL) dissolved in PBS, then frozen at −18 °C for 24 h; (ii) gel is thawed at RT and washed thoroughly in DI water, $NaBH_4$ 0.1% w/v PBS (pH = 9.4), and PBS (pH= 7.4).

purification applications. As far as we are aware, this appears to be the first cryogel with inherent antimicrobial properties.

Cryogels were chemically cross-linked at subzero temperatures through the amine residue of a polylysine-*b*-polyvaline copolymer with glutaraldehyde as cross-linker. In comparison to a hydrogel control prepared at above zero temperatures, the presence and integrity of macropores is shown to be vital to the antimicrobial effect of the gels. A "trap and kill effect" due to the increased surface area and confinement of the bacteria to the antimicrobial gel is proposed.

The block copolypeptide used in this study was synthesized through *N*-Carboxyanhydride ring-opening polymerization (NCA ROP) using *N*-trimethylsilylallylamine as initiator (Scheme 1a).[19] To ensure good water solubility of the final block copolypeptide, a larger polylysine block relative to hydrophobic polyvaline block was deemed appropriate. An *N*-protected CBz(Z) poly(L-lysine) block was first synthesized, followed by the shorter poly(D,L-valine) block with GPC analysis determining a M_n of 9.9 kDa with a dispersity ($Đ$) of 1.70. Upon isolation, the protected block copolymer was insoluble in a range of organic solvents, owing to the polyvaline block, which is known to exhibit insoluble secondary structures.[20,21] Therefore, characterization of the block copolymer (etc. relative ratios) through ^{1}H NMR analysis could only be achieved upon deprotection of the CBz-lysine side chain of the polymer.

Deprotection of the copolymer polylysine block by hydrobromic acid (HBr) generated an amphiphilic poly(L-lysine)-*b*-poly(D,L-valine) (PLL-*b*-PDLV) copolypeptide (P1) with the cationic polylysine block instilling high water solubility to the copolymer. ^{1}H NMR analysis confirmed the complete deprotection of the copolymer with integration determining a poly(L-lysine) to poly(D,L-valine) ratio of 7:2 (see Figure S1 for ^{1}H NMR analysis). Based on the M_n value above, the repeat units of PLL and PDLV were determined to be 35 and 10 units, respectively.

The amine residues were chosen as the point of cross-linking with the widely used and highly amine-reactive dialdehyde cross-linker (CL), glutaraldehyde.[22−24] The polypeptide and cross-linker in different molar ratios were dissolved in PBS (pH = 7.4) and the mixture was stored at −18 °C for 24 h. During the cryogelation process, the highly interconnected (covalent) polymeric network exists in a semifrozen system in which the solvent (water) crystals act as porogens. Thawing of the frozen solution removes the ice crystals to leave behind the macroporous structure (Scheme 1b). The gels were washed thoroughly and any remaining reactive aldehyde CL groups quenched by washing in a sodium borohydride reducing solution (see Figure S3 for ATR FT-IR analysis of quenched cryogels). Initial studies showed that a polymer concentration of 10 wt % with low cross-linking concentration resulted in immediate gelation of the solution before cryo storage. Therefore, a 5 wt % polymer concentration was employed and kept constant while cross-linking amount was varied in order to study the effect on the resultant cryogel properties. Table 1 shows the relative volume and molar (with respect to cross-linkable functional groups) ratios of glutaraldehyde to block polypeptide. A conventional control hydrogel was synthesized at room temperature, however it required a higher CL concentration and longer storage time for gelation to occur compared to the cryogels. This reduced cross-linking efficiency during conventional gelation, as opposed to the relatively faster cryogelation process, is due to significantly higher polymer and cross-linking concentrations existing in the liquid microphase (surrounding the ice crystal porogens) in the cryogelation state.[6,25] The internal morphologies of the cryogels and control

DOI: 10.1021/acsmacrolett.6b00174
ACS Macro Lett. 2016, 5, 552−557

Table 1. Cryogelation Conditions and the Elastic Modulus (E) of PLL_{35}-*b*-$PDLV_{10}$ Block Copolypeptide Cryogels Using Varying Amounts of Glutaraldehyde Crosslinker (CL)

gel ID	CL to polypeptide % (v/w)	aldehyde/NH_2	c_p % (w/w)	gelation	E^b (kPa)
A	4	0.2	5	cryo	[c]
B	8	0.4	5	cryo	1.6
C	20	1	5	cryo	12.4
D	42	2.1	5	cryo	4.4
[a]	67	3.3	5	hydro	21.0

[a]Control hydrogel sample made at room temperature (25 °C), 48 h. c_p, concentration of polymer component. [b]Mean Young's modulus (elastic modulus) values, $n = 3$. [c]Data could not be obtained due to weakness of gel.

hydrogel were investigated by environmental scanning electron microscopy (E-SEM) in the wet state. As evident in Figure 1, while the hydrogel sample has a nonporous structure, the cross sections of all cryogels (A, C, and D) show a macroporous morphology.

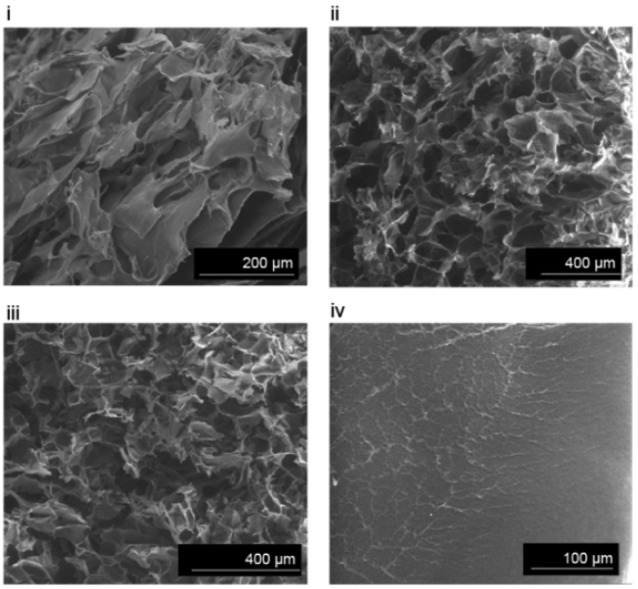

Figure 1. E-SEM characterization on the cross-sectional morphology of (i) cryogel A, (ii) cryogel C, (iii) cryogel D, and (iv) control hydrogel.

Comparisons of the cryogel morphologies show cryogel C (Figure 1ii) with the most intact porous structure (pore sizes between 120 and 150 μm) and cryogel A showing the least, which would be expected to be the case considering the low CL concentration used in cryogel A. Interestingly, cryogel D (Figure 1iii), with a higher CL concentration than cryogel C, displays a less regular pore structure with reduced pore integrity (see also Figure S4).

Compared to the typically low swelling rate of the control hydrogel, cryogel C (typical of the other cryogels, data not shown), demonstrates a far superior swelling rate and degree, due to its macroporous structure. This is demonstrated by the swelling degree (weight swelling ratio) plotted against swelling time in Figure 2a. Uniaxial compression measurements were then performed on the gels in their swollen states. The mechanical stress–strain data in Figure 2b shows the typical elastic behavior of the cryogels in contrast to the brittle and

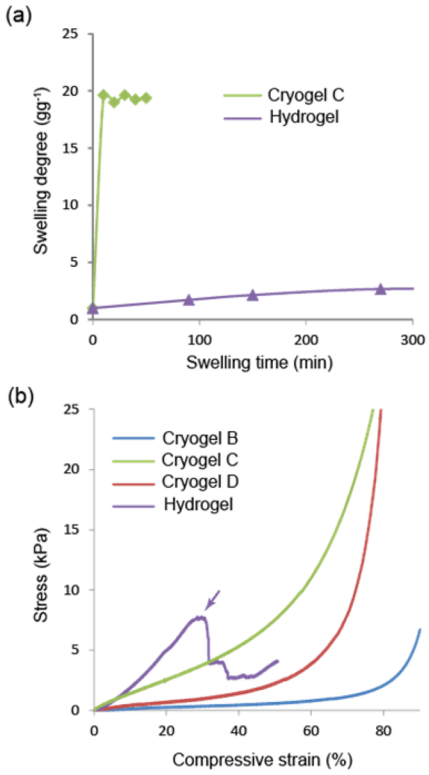

Figure 2. Comparison of physical properties of cryogels and conventional hydrogel. (a) Weight swelling kinetics of dried cryogel and hydrogel in water. (b) Stress vs strain curve of gels subjected to compression tests. Note the purple arrow shows the point at which hydrogel started to fail/deform.

fragile hydrogel. Compared to the cryogels which could be compressed beyond 80% without permanent deformation or failure, the conventional hydrogel suffers irreversible mechanical fracture at ~25% compression due to the lack of interconnected porous structure (see Figure S5). The lack of interconnected porous structure offers low resistance to crack propagation due to the lack of an efficient energy dissipation mechanism in the gel network. For the cryogels, water can flow out from the pore under stress, preventing crack formation at large deformation ratios (see Figure S5).[26] Table 1 shows the Young's modulus (elastic modulus) values of each of the gels, calculated from the stress–strain compression data in Figure 2b. As expected, all the cryogels exhibit a reduced Young's modulus in compression compared to the stiff and brittle control hydrogel. For the cryogels themselves, gel C displayed the highest modulus, with a stress of 7.5 kPa at 50% strain compared to 2.2 and 0.60 kPa for cryogels D and A, respectively.

The higher stiffness of gel C compared to gel D, despite a lower cross-linking concentration, suggests a higher cross-linking density in gel C and appears consistent with the cross-section morphologies observed in the SEM data above. A possible explanation for this may come from the [aldehyde]/[NH_2] cross-linking ratios shown in Table 1. While it is not anticipated that all cross-linking aldehyde groups will react with an equivalent of amine resides during the cryogelation stage, the amount of cross-linker employed with gel D may be reaching a point where oversaturation of the amine residues with just one reactive end of glutaraldehyde is occurring. This

DOI: 10.1021/acsmacrolett.6b00174
ACS Macro Lett. 2016, 5, 552–557

would result in reduced cross-linking density and therefore reduced gel stiffness of gel D compared to gel C.[27]

The absence of any toxic leachate or contaminant is a prerequisite for any material to be used for water disinfection purposes. A preliminary in vitro cytotoxicity study was conducted on the cryogels to evaluate if harmful products were leaching out. Cryogels C and D were selected as representative gels for this study and conditioned mediums were prepared by incubating the cryogels in cell culture medium (i.e., "complete" Dulbecco's Modified Eagle Medium (DMEM)) for 72 h. The conditioned mediums (50 vol %) were then incubated with NIH-3T3 fibroblast cells for another 72 h. Conditioned medium prepared from either cryogel C or D displayed negligible effect on fibroblast cell viability (see Figure S6), indicating that the cryogels did not leach out any substances toxic to mammalian cells. Quantitative removal/reduction of any unreacted glutaraldehyde CL which are toxic to mammalian cells was also confirmed as mentioned previously (see Figure S3).

To test for antimicrobial activity, the cryogels and control hydrogel were challenged with *E. coli*, a model Gram-negative bacterial species, at an initial cell concentration of 1.2×10^8 CFU/mL for 1 h (Figure 3a). A saline-based buffer was then

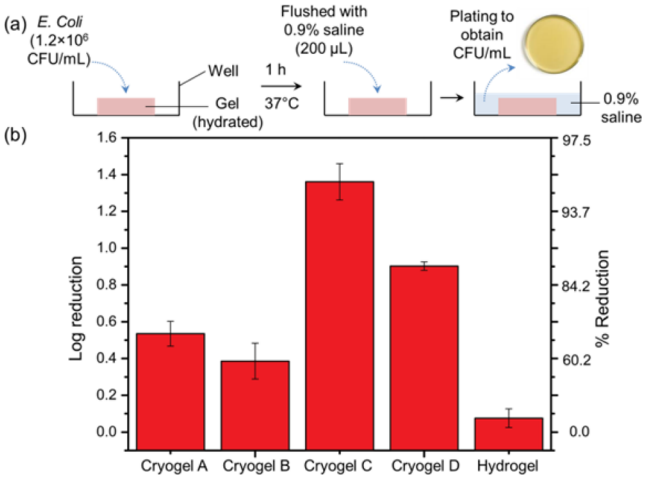

Figure 3. (a) Schematic of method used to investigate the antimicrobial efficacy of peptide gels. (b) Log reduction and % kill of *E. coli* on peptide cryogels A–D, and the control hydrogel. Error bars represent the standard deviation from the mean ($n \geq 4$).

added to wash the gels and capture any remaining viable cells. The viable cell counts in the washing solution were measured and compared to the untreated control (no gel). Note that the number of cells in the untreated control increased by 0.12 log (or 31.6%; averaged for all runs) after 1 h. The cryogels exhibited antimicrobial activity but to differing extents as shown in Figure 3b.

Cryogel C displayed the best efficacy against *E. coli* (1.4-log reduction or 95.6% reduction in cell counts), followed by cryogel D (0.9-log reduction). Cryogels A and B showed lower antimicrobial activities compared to the other cryogels, resulting in only 0.4–0.6-log reductions in cell counts. Compared to cryogels A–D, the control hydrogel possesses negligible activity against *E. coli* (<0.1-log reduction; Figure 3b), suggesting that macropores provided through cryogelation are essential for antimicrobial activity. It is hypothesized that the presence of macropores allows for effective uptake of bacteria into the gels. As well, they provide a large surface area and confined environment (increased time of exposure) for contact with the antimicrobial polymer and effective bacterial killing. A high BET specific surface area of 627 m^2/g was indeed measured for cryogel C (see Supporting Information). The possible link between pore size/surface area and microbial killing efficacy has been suggested in earlier studies;[14,28] however, to the best of our knowledge, this is the first study to elucidate the importance of macropores by comparing the antimicrobial efficacy of macroporous and nonmacroporous gels.

It is noteworthy that the best-performing gel, cryogel C, exhibited the highest stiffness (as indicated by its Young's modulus, Table 1) and pore integrity (based on E-SEM, Figure 1), which suggests that antimicrobial efficacy could also be linked to mechanical strength and pore structure. Cryogels with higher pore integrity, and gel stiffness (e.g., cross-linking densities) would be expected to display higher surface areas and greater confinement of bacteria within the gel pores, thereby increasing their exposure to the antimicrobial surface. The higher antimicrobial efficiency of such cryogels (e.g., cryogel C) in this study appears to support this theory.

A preliminary investigation to gain insight into the antibacterial mechanism of the cryogels was conducted. E-SEM was employed to visualize the cross sections of cryogel C after 1 h of contact with *E. coli* cells. E-SEM was chosen over conventional (high vacuum) SEM to minimize possible introduction of artifacts due to more extensive sample preparation involved in the latter method.[29] Adhesion of bacterial cells (rod-shaped) within the cryogel, especially on the pore walls, was observed (Figures 4a and S7). Note that extensive washing of the gel to flush out any loosely attached bacterial cells (similar to that done in the antimicrobial test above) was performed prior to imaging.

In order to determine if the trapped bacterial cells were viable, an MTS cell viability assay was performed, where cell metabolic is directly proportional to the absorbance at 490 nm.[30,31] After 1 h of gel-bacteria incubation, which was followed by extensive flushing of the gel with saline, the gel was removed from the well and both the gel and the saline washing solution (hereby referred to as "supernatant") were tested for bacterial cell viability. As expected, cell viability in the supernatants of cryogel C, cryogel D, and the control hydrogel (Figure 4b) corresponds to their antimicrobial activity, as shown in Figure 3b. The supernatant of cryogel C (gel with the best antimicrobial efficacy) demonstrated the lowest absorbance at 490 nm compared to the supernatants of cryogel D and the control hydrogel. On the other hand, negligible cell viability (normalized absorbance < 0.02) was shown for all gels tested, indicating that the cells entrapped within (or on the surface of) the gels were nonviable. Based on these results, we hypothesize that cryogels are contact-active (consistent with most antimicrobial gels[2,3,32]) and exert their antimicrobial action through a "trap and kill" mechanism, where bacterial cells are trapped or confined within the macropores and subsequently killed upon contact with the PLL-*b*-PDLV copolypeptide on the pore wall. This postulated mechanism was supported by a gel reusability study, where a modest reduction in activity was observed after each use (see Figure S9). We theorize that as the cryogels are contact-active, the surface area available for bacteria adhesion would be reduced after each use, which indicates that the gel antimicrobial efficacy is surface area-dependent.

DOI: 10.1021/acsmacrolett.6b00174
ACS Macro Lett. 2016, 5, 552–557

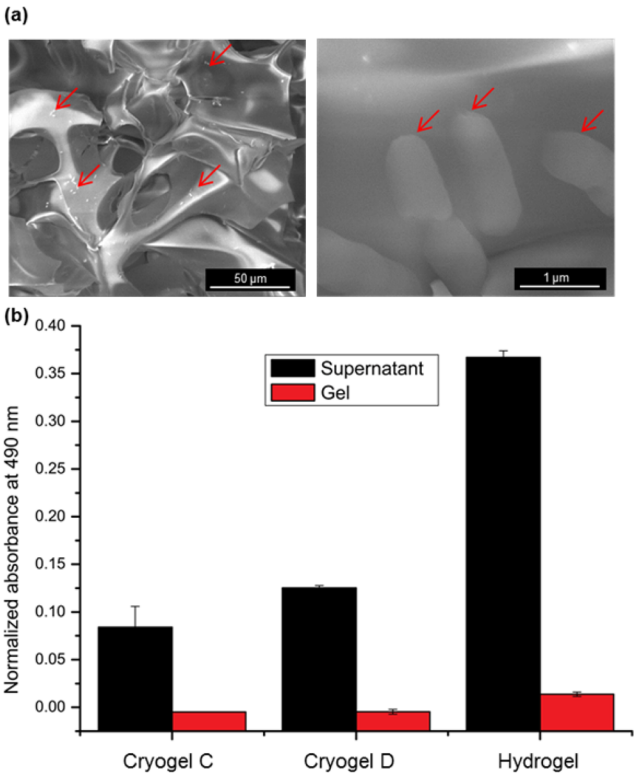

Figure 4. (a) Representative E-SEM images of cryogel C after incubation with *E. coli* for 1 h, followed by vigorous flushing and agitation with saline buffer (0.9% NaCl solution). Note the red arrows indicate the *E. coli* cells. (b) Viability of *E. coli* cells found in the "supernatant" or saline buffer used to flush the gels (black bars) and cells entrapped in the gel (red bars) relative to the positive growth control. Cell viability was measured in terms of the absorbance at 490 nm using an MTS-based assay. Error bars represent the standard deviation from the mean (n = 4).

In summary, we have successfully developed novel peptide-based cryogels by cross-linking the amine residues of PLL-*b*-PDLV copolypeptides with glutaraldehyde. The cryogels exhibited superior swelling properties and mechanical strength compared to their analogous hydrogel due to their macroporous structure. Further, these cryogels displayed inherent antimicrobial activity against *E. coli* with the best performing gel causing a 95.6% reduction in viable cell counts within 1 h incubation. By comparing cryogel antimicrobial efficacy with that of the control hydrogel, macropores were found to be crucial for bactericidal activity. It is believed the presence of macropores allows for effective uptake of bacteria into the gels. E-SEM imaging and cell viability tests suggest that the antimicrobial action of the cryogels involves a "trap and kill" mechanism, where macropores are believed to provide confinement and increased surface area for contact of the bacteria with the antimicrobial polymer. Mechanical strength and pore integrity of cryogels were also found to be determinants for antibacterial activity. Despite showing a reduced antimicrobial potency to existing heavy metal-incorporated cryogel systems, the inherent antimicrobial properties and lack of toxic leaching of the cryogels reported herein show potential for use in biological and environmentally friendly water purification applications. It is hoped that future work will look into investigating different polypeptide compositions to maximize the antimicrobial potencies of these cryogels.

■ ASSOCIATED CONTENT

Supporting Information

The Supporting Information is available free of charge on the ACS Publications website at DOI: 10.1021/acsmacrolett.6b00174.

Experimental procedures and additional characterization data/characterization (PDF).

■ AUTHOR INFORMATION

Corresponding Author

*E-mail: gregghq@unimelb.edu.au.

Author Contributions

‡These authors contributed equally (S.J.S. and S.J.L.).

Notes

The authors declare no competing financial interest.

■ ACKNOWLEDGMENTS

The authors would like to acknowledge the Australian Research Council (ARC) for funding in the form of a Discovery Project (DP140100002). S.J.S. would like to thank The University of Melbourne, the Commonwealth Scientific and Industrial Research Organization (CSIRO), and the Melbourne Materials Institute (MMI) for various scholarships. S.J.L. acknowledges the Australian Government for providing an International Postgraduate Research Scholarship (IPRS) and an Australian Postgraduate Award (APAInt). M.M.O. acknowledges TUBITAK (The Scientific and Technological Research Council of Turkey), 2219-Postdoctorial Fellowship. G.G.Q. acknowledges the ARC under the Future Fellowship (FT110100411, G.G.Q.). The authors would also like to thank Mr. Dunyin Gu for help with mechanical testing measurements and for Mr. Ke Xie for help with surface area BET measurements.

■ REFERENCES

(1) Irwansyah, I.; Li, Y.-Q.; Shi, W.; Qi, D.; Leow, W. R.; Tang, M. B. Y.; Li, S.; Chen, X. *Adv. Mater.* **2015**, *27* (4), 648−654.
(2) Salick, D. A.; Pochan, D. J.; Schneider, J. P. *Adv. Mater.* **2009**, *21* (41), 4120−4123.
(3) Salick, D. A.; Kretsinger, J. K.; Pochan, D. J.; Schneider, J. P. *J. Am. Chem. Soc.* **2007**, *129* (47), 14793−14799.
(4) Jiang, L.; Xu, D.; Sellati, T. J.; Dong, H. *Nanoscale* **2015**, *7* (45), 19160−19169.
(5) Veiga, A. S.; Schneider, J. P. *Biopolymers* **2013**, *100* (6), 637−644.
(6) Henderson, T. M. A.; Ladewig, K.; Haylock, D. N.; McLean, K. M.; O'Connor, A. J. *J. Mater. Chem. B* **2013**, *1* (21), 2682−2695.
(7) Ozmen, M. M.; Fu, Q.; Kim, J.; Qiao, G. G. *Chem. Commun.* **2015**, *51* (98), 17479−17482.
(8) Erturk, G.; Mattiasson, B. *J. Chromatogr. A* **2014**, *1357*, 24−35.
(9) Bencherif, S. A.; Sands, R. W.; Bhatta, D.; Arany, P.; Verbeke, C. S.; Edwards, D. A.; Mooney, D. J. *Proc. Natl. Acad. Sci. U. S. A.* **2012**, *109* (48), 19590−19595.
(10) Lozinsky, V. I.; Okay, O., Basic Principles of Cryotropic Gelation. In *Polymeric Cryogels: Macroporous Gels with Remarkable Properties*; Okay, O., Ed.; Springer, 2014; Vol. *263*, pp 49−101.
(11) Dinu, M. V.; Ozmen, M. M.; Dragan, E. S.; Okay, O. *Polymer* **2007**, *48* (1), 195−204.
(12) Loo, S.-L.; Krantz, W. B.; Lim, T.-T.; Fane, A. G.; Hu, X. *Soft Matter* **2013**, *9* (1), 224−234.
(13) Loo, S.-L.; Krantz, W. B.; Fane, A. G.; Gao, Y.; Lim, T.-T.; Hu, X. *Environ. Sci. Technol.* **2015**, *49* (4), 2310−2318.

DOI: 10.1021/acsmacrolett.6b00174
ACS Macro Lett. 2016, 5, 552−557

(14) Loo, S.-L.; Fane, A. G.; Lim, T.-T.; Krantz, W. B.; Liang, Y.-N.; Liu, X.; Hu, X. *Environ. Sci. Technol.* **2013**, *47* (16), 9363−9371.
(15) Chaturvedi, A.; Bajpai, A. K.; Bajpai, J.; Sharma, A. *Des. Monomers Polym.* **2015**, *18* (4), 385−400.
(16) Chaturvedi, A.; Bajpai, A. K.; Bajpai, J. *Polym. Compos.* **2015**, *36* (11), 1983−1997.
(17) Patachia, S.; Damian, N. *Soft Mater.* **2014**, *12* (4), 371−379.
(18) Martinez, Y. N.; Cavello, I.; Hours, R.; Cavalitto, S.; Castro, G. R. *Bioresour. Technol.* **2013**, *145*, 280−284.
(19) Lu, H.; Cheng, J. J. *J. Am. Chem. Soc.* **2008**, *130* (38), 12562−12563.
(20) Epand, R. F.; Scheraga, H. A. *Biopolymers* **1968**, *6* (11), 1551−1571.
(21) Goh, S. L.; Platt, A. P.; Rutledge, K. E.; Lee, I. *J. Polym. Sci., Part A: Polym. Chem.* **2008**, *46* (16), 5381−5389.
(22) Dainiak, M. B.; Allan, I. U.; Savina, I. N.; Cornelio, L.; James, E. S.; James, S. L.; Mikhalovsky, S. V.; Jungvid, H.; Galaev, I. Y. *Biomaterials* **2010**, *31* (1), 67−76.
(23) Kathuria, N.; Tripathi, A.; Kar, K. K.; Kumar, A. *Acta Biomater.* **2009**, *5* (1), 406−418.
(24) Jurga, M.; Dainiak, M. B.; Sarnowska, A.; Jablonska, A.; Tripathi, A.; Plieva, F. M.; Savina, I. N.; Strojek, L.; Jungvid, H.; Kumar, A.; Lukomska, B.; Domanska-Janik, K.; Forraz, N.; McGuckin, C. P. *Biomaterials* **2011**, *32* (13), 3423−3434.
(25) Lozinsky, V. I.; Plieva, F. M.; Galaev, I. Y.; Mattiasson, B. *Bioseparation* **2001**, *10* (4−5), 163−188.
(26) Ak, F.; Oztoprak, Z.; Karakutuk, I.; Okay, O. *Biomacromolecules* **2013**, *14* (3), 719−727.
(27) Murakami, S.; Aoki, N.; Matsumura, S. *Polym. J.* **2011**, *43* (9), 414−420.
(28) Li, P.; Poon, Y. F.; Li, W.; Zhu, H.-Y.; Yeap, S. H.; Cao, Y.; Qi, X.; Zhou, C.; Lamrani, M.; Beuerman, R. W.; Kang, E.-T.; Mu, Y.; Li, C. M.; Chang, M. W.; Leong, S. S. J.; Chan-Park, M. B. *Nat. Mater.* **2011**, *10* (2), 149−156.
(29) McGregor, J. E.; Staniewicz, L. T. L.; Guthrie Nee Kirk, S. E.; Donald, A. M. *Methods Mol. Biol.* **2012**, *931*, 493−516.
(30) Wang, H. W.; Cheng, H. R.; Wang, F. Q.; Wei, D. Z.; Wang, X. D. *J. Microbiol. Methods* **2010**, *82* (3), 330−333.
(31) Tsukatani, T.; Higuchi, T.; Suenaga, H.; Akao, T.; Ishiyama, M.; Ezoe, T.; Matsumoto, K. *Anal. Biochem.* **2009**, *393* (1), 117−125.
(32) Ng, V. W. L.; Chan, J. M. W.; Sardon, H.; Ono, R. J.; Garcia, J. M.; Yang, Y. Y.; Hedrick, J. L. *Adv. Drug Delivery Rev.* **2014**, *78*, 46−62.

DOI: 10.1021/acsmacrolett.6b00174
ACS Macro Lett. 2016, 5, 552−557

Supporting Information

Polypeptide-based Macroporous Cryogels with Inherent Antimicrobial Properties: The Importance of a Macroporous Structure

Steven J. Shirbin,[§,‡] Shu J. Lam,[§,‡] Nicholas Jun-An Chan,[§] Mehmet Murat Ozmen,[§,φ] Qiang Fu,[§] Neil O'Brien-Simpson,[Ψ] Eric C. Reynolds[Ψ] and Greg G. Qiao[§,]*

[§] *Polymer Science Group, Department of Chemical and Biomolecular Engineering, University of Melbourne, Parkville, Melbourne, Victoria 3010, Australia*

[φ] *Department of Bioengineering, Yildiz Technical University, Esenler, 34220, Istanbul, Turkey*

[Ψ] *Melbourne Dental School and The Bio21 Institute of Molecular Science and Biotechnology, Oral Health CRC, The University of Melbourne, Parkville, VIC 3010, Australia*

[‡] These authors contributed equally (S.J.S and S.J.L)

Corresponding author: Greg G.Qiao, Email: gregghq@unimelb.edu.au

Materials and Methods

Materials

H-$_{L}$-Lys(Z)-OH (Bachem), H-($_{D,L}$)Valine-OH (Bachem), dimethylformamide (DMF) (anyhd., 99.8%, Acros), hydrobromic acid (HBr) (33% in acetic acid, Aldrich), *N*-(trimethylsilyl)allylamine (*N*-TMS allylamine) (95%, Acros), phosphate buffered saline (PBS) tablets (Aldrich), trifluoroacetic acid (TFA) (Aldrich), sodium borohydride ($NaBH_4$) (Ajax chemicals), n-pentane (anhydrous ≥99%, Aldrich), diethyl ether (AR, Chem-Supply), paraformaldehyde (Aldrich), and penillin-streptomycin (Aldrich) were used as received. Tetrahydrofuran (THF) was distilled from benzophenone and sodium metal under nitrogen. Glutaraldehyde was supplied as a 25% aqueous solution (≥98%, Merck). Dulbecco's Modified Eagle Medium (DMEM, GIBCO Cat. No. 11995), fetal bovine serum (FBS, GIBCO Cat. No. 10099), GlutaMAX™ supplement (100x, GIBCO Cat. No. 35050), Dulbecco's Phosphate Buffered Saline (DPBS, GIBCO 14190), 0.05% trypsin-EDTA (1×, GIBCO Cat. No. 25300), SYTO® 9 green fluorescent nucleic acid stain, and propidium iodide (PI) were purchased from Invitrogen and used as received. Defibrinated horse blood (Commonwealth Serum Laboratories (CSL), Melbourne), Mueller-Hinton Broth (CM0405, Oxoid), Blood Agar Base No. 2 (CM0271, Oxoid), Yeast Extract (LP0021, Oxoid), and Bacto™ Tryptone (BD Biosciences) were used as received for bacteria culture. CellTiter 96® Aqueous Non-Radioactive Cell Proliferation assay kit was purchased from Promega and used for cell viability assays following manufacturer's instructions. 96-well cell culture plates and T175 cell culture flasks (Corning) were used for cell culture.

Instrumentation

^{1}H NMR analysis was performed using a Varian unity Plus 400 MHz NMR spectrometer using the deuterated solvent as reference. GPC analysis was performed on a Shimadzu liquid chromatography system fitted with a PostNova Analytics MALS detector (λ = 658 nm), a Shimadzu RID-10 refractometer (λ = 633 nm), and a Shimadzu SPD-20A UV−vis detector, using three phenogel columns (Phenomenex, 5 μm) in series and HPLC grade DMF with 0.05 M LiBr as the mobile phase (1 mL/min). The oven temperature was set to 50 °C to maintain an acceptable pressure across the system, and the detectors were temperature controlled to 25 °C. Nova MALS software (PostNova) was used to determine the molecular weights and PDI using poly(ethylene glycol) standards. Attenuated total reflectance fourier transform infrared (ATR-FTIR) was performed on a Nexus 470 Fourier-Transform Infrared Spectrometer (Thermo Nicolet). Bacterial cell sample analysis was performed using a Cell Lab Quanta SC MPL flow cytometer (Beckman Coulter) equipped with a 100 W stabilized mercury arc lamp with wavelengths of 365, 404, and 435 nm, and a 488 nm diode laser. The fluorescence from SYTO® 9 was measured through a 525-nm band-pass filter (Fluorescent Channel 1, FL-1), and the red emission of PI was measured with a 670-nm long pass filter (Fluorescent Channel 3, FL-3). The multiparametric data were analyzed using the Cell Lab Quanta SC software. Environmental Scanning electron microscope (E-SEM) images were acquired by using a FEI Quanta 200 ESEM FEG. E-SEM gels were placed in wet state with analysis under low vacuum. Mechanical/compression testing measurements of the samples were carried out

using an Instron MicroTester 5848. ESEM images were analysed using ImageJ analysis software to determine the pore size of cryogels (Cryogel C).

Mechanical tests

Young's modulus was determined using an Instron testing system (Instron 5848). Cylindrical gels (~9 mm diameter, 12 mm height) were deformed (at constant volume) between two parallel plates with a strain rate of 60% per minute. Engineering stresses and strains were recorded. The gel cylinders were kept hydrated in PBS solution (pH 7.4) throughout the tests. Young's moduli were determined by the average slopes of the stress–strain compression curves over the strain range 0–10%. Runs were performed in triplicate.

Swelling studies

The weight swelling degree was determined using a conventional gravimetric procedure. The gels were first dried. Cryogels were dried through freeze-drying whilst hydrogels were dried through immersion in increasing (0-100%) acetone solutions followed by vacuum oven drying at 50 ^{o}C overnight. Dried gels were then immersed in DI water with the water uptake measured by the cumulative mass increase at pre-determined time intervals. Excess surface water was wiped away. Degree of swelling at time *t* was calculated by the following equation:

$$\text{Degree of swelling} = \frac{m_t}{m_o}$$

Where m_t and m_o are the masses of the swollen gel at time t and dried gel, respectively

Specific surface area

The specific surface area of a freeze-dried sample of cryogel C was measured by a Micromeritics ASAP 2050 Xtended Pressure Sorption Analyzer with carbon dioxide (CO_2) as adsorbate at 0 ^{o}C. Before the measurements, the samples were degassed at 75 ^{o}C for 16 h. The specific surface area was obtained by the Brunauer, Emmett and Teller (BET) equation. See Figure S8 for isotherm.

Bacterial cell culture

Freeze-dried cultures of *Escherichia coli* (*E. coli*, ATCC 25922) were grown aerobically and maintained by passage at ambient temperature on horse blood agar (10% v/v defibrinated horse blood, 4.4% w/v Oxoid Blood Agar Base No. 2). Overnight cultures were made from transferring a colony (*ca.* half a loop) from the agar plates to culture tubes containing sterilized Luria-Bertani broth (LB, 1% w/v Bacto^{TM} Tryptone, 1% w/v NaCl, 0.5% w/v Oxoid Yeast Extract) (20 mL). Bacterial cultures were incubated overnight at 37 °C with aeration and without agitation. On the next day, aliquots (2 mL) were taken from the culture

tubes, further diluted with LB (20 mL), and incubated for 3-4 h at 37 °C with aeration before use.

Bacterial cell counting

A Cell Lab Quanta SC MPL flow cytometer was used to count the number of bacterial cells prior to use in assays. Cells were diluted with NaCl solution (0.9%) using an appropriate dilution factor and incubated with Syto® 9 and PI (*i.e.*, 1 mL cell suspension to 1 µL of each dye). Syto® 9 stains the nucleic acids in all cells, while PI stains the nucleic acids in cells with damaged membranes. Using the Cell Lab Quanta SC software, the number of viable cells/mL (Syto® 9-positive, PI-negative) was obtained.

Antimicrobial assay

The protocol was adapted from that reported by Chan-Park and co-workers.[1] The gels were soaked and rinsed in sterilized PBS for at least 3 days and then cut into discs of *ca*. 4 mm diameter and 3 mm height. *E. coli* cells which gave an optical density reading of *ca*. 0.7 were diluted to 1.2×10^8 cells/mL in Mueller-Hinton broth and 10 µL of bacterial suspension was spread onto each gel in a 96-well plate. The inoculated gels were incubated for 1 h at 37 °C. NaCl solution (0.9%, 0.2 mL) was then added to each well followed by vigorous agitation and flushing to recover any residual cells. An aliquot (10 µL) of the microbial suspension was then diluted with 0.9% NaCl solution using an appropriate dilution factor and plated out in LB agar (1% w/v Bacto™ Tryptone, 1% w/v NaCl, 0.5% w/v Oxoid Yeast Extract, 15 g/L Oxoid Blood Agar Base No. 2). The plates were incubated overnight at room temperature and counted for colony-forming units (CFU). Positive controls consisting of cell-only wells were used. The results are expressed as:

$$\text{Log reduction} = \log\left(\frac{\text{CFU}}{\text{mL}} \text{ of control after 1 hr}\right) - \log\left(\frac{\text{CFU}}{\text{mL}} \text{ of survivor cells on gel after 1 hr}\right)$$

For the gel reusability study, cryogel C was challenged with *E. coli* cells 4 times successively, where the protocol for each cycle was as described above.

In the same experiment, the viability of the bacterial cells in the microbial suspension outside the gel (obtained through flushing with 0.9% NaCl solution) and in the gel was assessed using Promega's CellTiter 96® Aqueous Non-Radioactive Cell Proliferation assay kit. An aliquot (100 µL) was taken from the remaining microbial suspension and transferred to another 96-well plate. The gels were also transferred to a new 96-well plate and 0.9% NaCl solution (100 µL) was added. MTS/PMS solution (20 µL) was then added to each well (either containing microbial suspension or gel), followed by a 3.5 h incubation. The absorbance at 490 nm was measured with a plate reader (PerkinElmer 1420 Multilabel Counter VICTOR^3). Note that for the gel-containing wells, an aliquot (100 µL) was transferred to unused wells prior to absorbance reading.

Note that a minimum of two independent experiments of the assay were conducted and at least two technical replicates were used in each experiment for each gel type.

Bacteria morphology study

E. coli cells (10 µL, 1.2×10^8 cells/mL in Mueller-Hinton broth) was spread onto cryogel C and incubated for 1 h at 37 °C. NaCl solution (0.9%, 0.2 mL) was added which was then followed by vigorous agitation and flushing. The gel was immediately fixed with paraformaldehyde (4%) solution for 1 h and washed with PBS (1×, 10 min) and DI water (2×, 10 min). The cross-sections of the gel were observed using a FEI Quanta 200 FEG on the low-vacuum setting. Samples were pre-coated with gold using a Dynavac Mini Sputter Coater prior to imaging.

Statistical analysis

Statistical analysis was performed using a one-way classification of ANOVA and student's *t*-test (two-tailed), where differences were regarded as statistically significant with probability $P>0.05$.

Mammalian cell culture

NIH-3T3 cells were cultivated in DMEM medium (supplemented with 10% FBS, 1× GlutaMAX™, and 1× penicillin-streptomycin) in a humidified atmosphere containing 5% CO_2 at 37 °C. Cells were seeded in a T75 flask (*ca.* 3×10^6 cells/ml) and passaged twice a week prior to performing the subsequent cell viability studies.

Mammalian cell viability assay

Cytotoxicity of the cryogels was assessed using Promega's CellTiter 96® Aqueous Non-Radioactive Cell Proliferation assay kit following the manufacturer's instructions. Briefly, the cryogels were incubated in 'complete' DMEM (1 mL) at 37 °C for 72 h. The cryogels were then removed and the conditioned medium was used in subsequent cell viability assays to test for toxic compounds leaching out of the gels and/or toxic degradation products. NIH-3T3 cells were trypsinized using trypsin-EDTA, counted on a cell counter (Coulter Particle Counter Z series, Beckman Coulter), diluted with 'complete' DMEM (conditioned DMEM:fresh DMEM = 1:1), and seeded at 10 000 cells per well on 96-well plates. Subsequently, plates were incubated under standard cell maintenance conditions (37 °C, 5% CO_2). After 72 h, MTS/PMS solution (20 µL per 100 µL cells) was added to each well. Plates were further incubated for 2 h. The absorbance at 490 nm was measured with a plate reader (PerkinElmer 1420 Multilabel Counter VICTOR^3). Note that all experiments were conducted in quadruplicate, and cells that were seeded in 100% fresh and 'complete' DMEM were used as positive growth controls.

Percentage viability of cells was calculated using the following formula:

$$\% \text{ Viability} = \left(\frac{A_{490} \text{ test sample} - A_{490} \text{ background}}{A_{490} \text{ cells alone} - A_{490} \text{ background}} \right) \times 100$$

Experimental Procedures

Synthesis of $_{D,L}$-Valine and (Z)-$_{L}$-Lysine *N*-Carboxyanhydrides (NCAs).[2] The amino acid ((Z)-$_{L}$-Lysine (2 g, 7.14 mmol) or $_{D,L}$-Valine (1 g, 8.53 mmol)) was dissolved in anhydrous THF (50 mL) in a three-necked round bottomed flask under argon. Triphosgene (lys: 0.843 g, 2.84 mmol, 1.2 equiv. phosgene; val: 1.01 g, 3.40 mmol, 1.2 equiv. phosgene) was then added and the mixture was heated at 60 ^{o}C for 2 hr with continuous stirring. After cooling to room temperature, the reaction mixture was sparged with argon for 45 mins into a sat. NaOH solution, then solvent removed *in vacuo*. The resulting residue was recrystallised from THF (anhydrous) and n-pentane (anhydrous) overnight. The resulting crystals were filtered and washed with n-pentane (dry), then re-precipitated and washed (x 2) with dry n-pentane to afford white solids (Yields: ~80 %) ^{1}H NMR ($CDCl_3$): (Z)-$_{L}$-Lysine NCA ^{1}H NMR (400 MHz, CDCl3): δ_H 1.40-1.60 (m, 4H, NH-CH_2-CH_2-CH_2-CH_2-), 1.81-1.94 (m, 2H, NH-CH_2-CH_2-CH_2-CH_2-), 3.18 (m, 2H, NH-CH_2-CH_2-CH_2-CH_2-), 4.25 (t, 1H, C*H*N), 4.97 (s, 1H, side chain NH), 5.09 (s, 2H, CH_2-ArH), 7.04 (s, 1H, ring NH), 7.3-7.4 (m, 5H, ArH). $_{D,L}$-Valine NCA ^{1}H NMR (400 MHz, $CDCl_3$): δ_H 1.02 (d, 3H, *J*= 7.0 Hz, CH_3), 1.08 (d, 3H, *J*= 7.0 Hz, CH_3), 2.25 (m, 1H, C*H*(CH_3)$_2$), 4.22 (d, 1H, *J* = 4.4 Hz, C*H*-NH), 6.95 (s, 1H, CO-N*H*)

Synthesis of poly (Z-$_{L}$-Lysine)-*b*-poly($_{D,L}$-valine) block copolypeptides. To a dry 50 mL RBF was added (Z)-$_{L}$- lysine NCA (1.62 g, 5.3 mmol) under argon. Dry DMF (20 mL) was then added and stirred to dissolve. To the stirring solution was added *N*-(Trimethylsilyl)allylamine (21.2 μL, 0.126 mmol, M/I = 60) and the clear solution stirred for 24 hrs under argon with bleed at room temperature. $_{D,L}$-Valine NCA (0.325 g, 2.27 mmol) was then added to the reaction mixture and the solution stirred for a further 48 hrs. The reaction mixture was then concentrated under high vacuum and precipitated in diethyl ether (40 mL), washed in ether (x 2) then dried *in vacuo* to afford a white solid (0.90 g Yield: 56 %). M_n(GPC)= 9.9 kDa, PDI 1.70. Note: GPC analysis was performed on small sample of reaction mixture. NMR of the protected polypeptide could not be obtained due to the precipitated product being highly insoluble in both aqueous and organic solvents. This is due to polyvaline typically forming insoluble secondary structures as reported previously,[3-5] rendering the block copolypeptide insoluble. See below for ^{1}H NMR of the fully soluble deprotected copolypeptide and resulting Lys : Val molar ratio calculations.

Synthesis of poly ($_{L}$-Lysine)-*b*-poly($_{D,L}$-valine) block copolypeptide (PLL-*b*-PDLV) (P1). Deprotection of the lysine CBz (Z) protecting group was achieved through previously reported procedure[2, 6] to afford the fully water soluble polypeptide. To a 25 mL was added the protected polypeptide (0.90 g, 9.1 μmol) followed by trifluoroacetic acid (4 mL). Brief sonication was employed to dissolve polymer, followed by addition of HBr (33% in AcOH, 4 mL). The resulting solution was stirred at 35 ^{o}C with thick precipitate observed soon after. The reaction mixture stirred for total of 2 hrs at 35 ^{o}C, with the suspension then transferred directly into diethyl ether, washed in ether (x 2), then dried *in vacuo* overnight. The solid was then dissolved in DI H_2O and added to 3.5 kDa dialysis tubing for dialysis against 2 L DI

water (x 3) for 24 hrs followed by freeze drying to obtain a white solid (~340 mg). ^{1}H NMR (d_6-DMSO): δ_H 0.78 (s, 2(C*H*)$_3$), 1.20-1.70 (m, NH-CH$_2$-CH$_2$-C*H*$_2$-C*H*$_2$-), 1.9 (br s, C*H*-NH valine), 2.74 (s, NH-C*H*$_2$-CH$_2$-CH$_2$-CH$_2$-), 4.22 (s, C*H*-NH backbone), 8.00 (s, CO-N*H*). Based on lysine and valine side chain protons, integration determined Lys : Val ratio to be 7:2 (see below). Based on this ratio and the calculated M_n from GPC analysis above, DP is determined to be 45 (35 lysine, 10 valine).

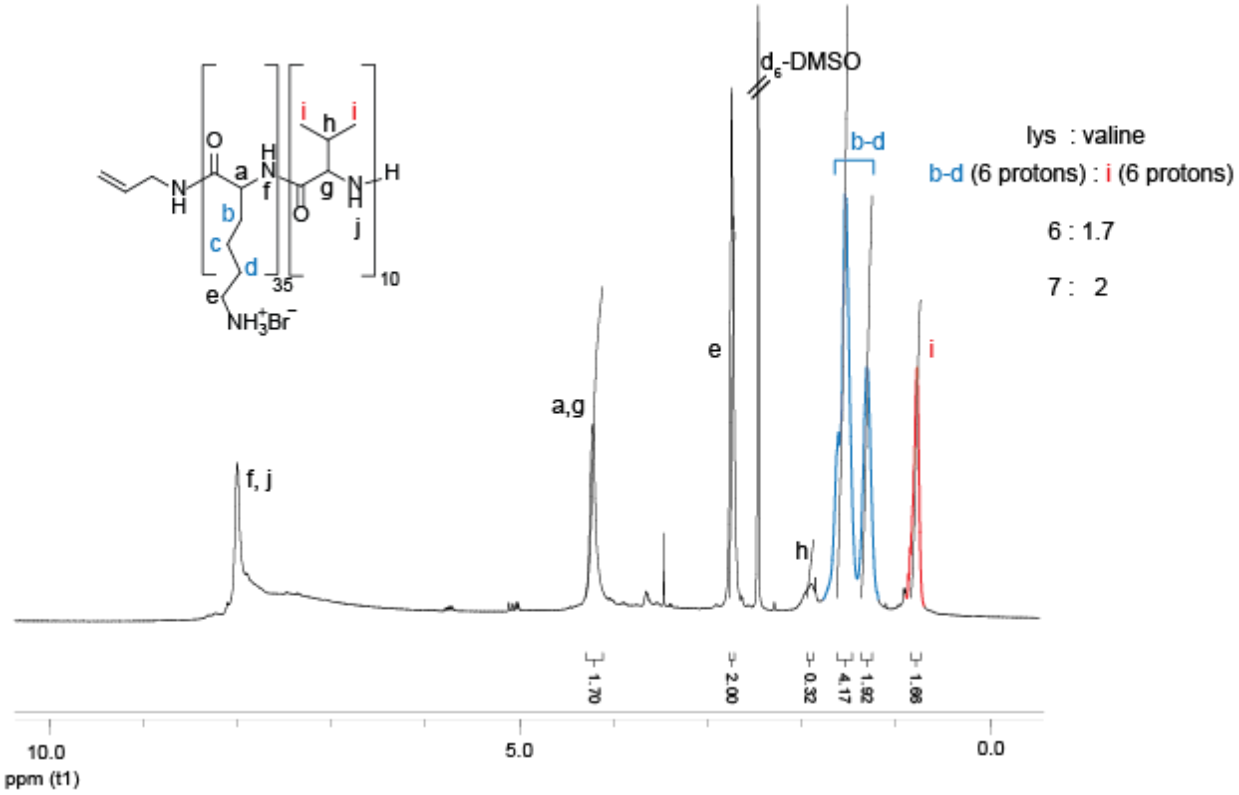

Figure S1: ^{1}H NMR (d_6-DMSO) spectrum of deprotected PLL-*b*-PDLV block copolymer (P1) including calculations of lysine:valine ratio based on the relevant integrations

Cryogel preparation. Cryogelation reactions were conducted at -18 ^{o}C. Hydrogel samples were prepared at room temperature. Deprotected copolypeptide was first dissolved in phosphate buffered saline (PBS, pH 7.4) at a polymer concentration of 5% w/v. Glutaraldehyde solution (25% Aqueous Solution, Merck) at specified crosslinking amounts to polypeptide % (v/w) was then added and vortexed briefly to dissolve. The solution was then withdrawn in plastic syringes and placed directly into freezer at -18 ^{o}C for 24 hrs. For hydrogel formation, plastic syringes containing reagents were kept at room temperature in dark and left for 48 hrs. After completion of the cryogelation process, the resulting samples were removed and thawed at room temperature. The cryogels and hydrogel were then immersed in DI water with complete replacement of the solution three times (3 x 100 mL). The gels were then immersed in a 0.1 % (w/v) sodium borohydride ($NaBH_4$) PBS solution (pH = 9.4, 100 mL) for 3 hrs to reduce unreacted aldehyde groups of crosslinker. Gels were

then washed thoroughly and immersed in DI water (100 mL) then sterile PBS (pH = 7.4) (100 mL, x 2) with complete replacement of solution each time.

Supporting data/characterization:

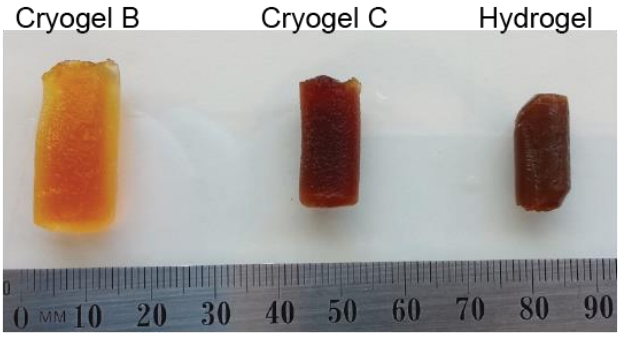

Figure S2. Photographs of swelled cylindrical cryogels/hydrogel made from identical batch volumes. Note increased total swelling of cryogels compared to non-macroporous hydrogel. Distinct brown colour is due to glutaraldehyde cross-linker

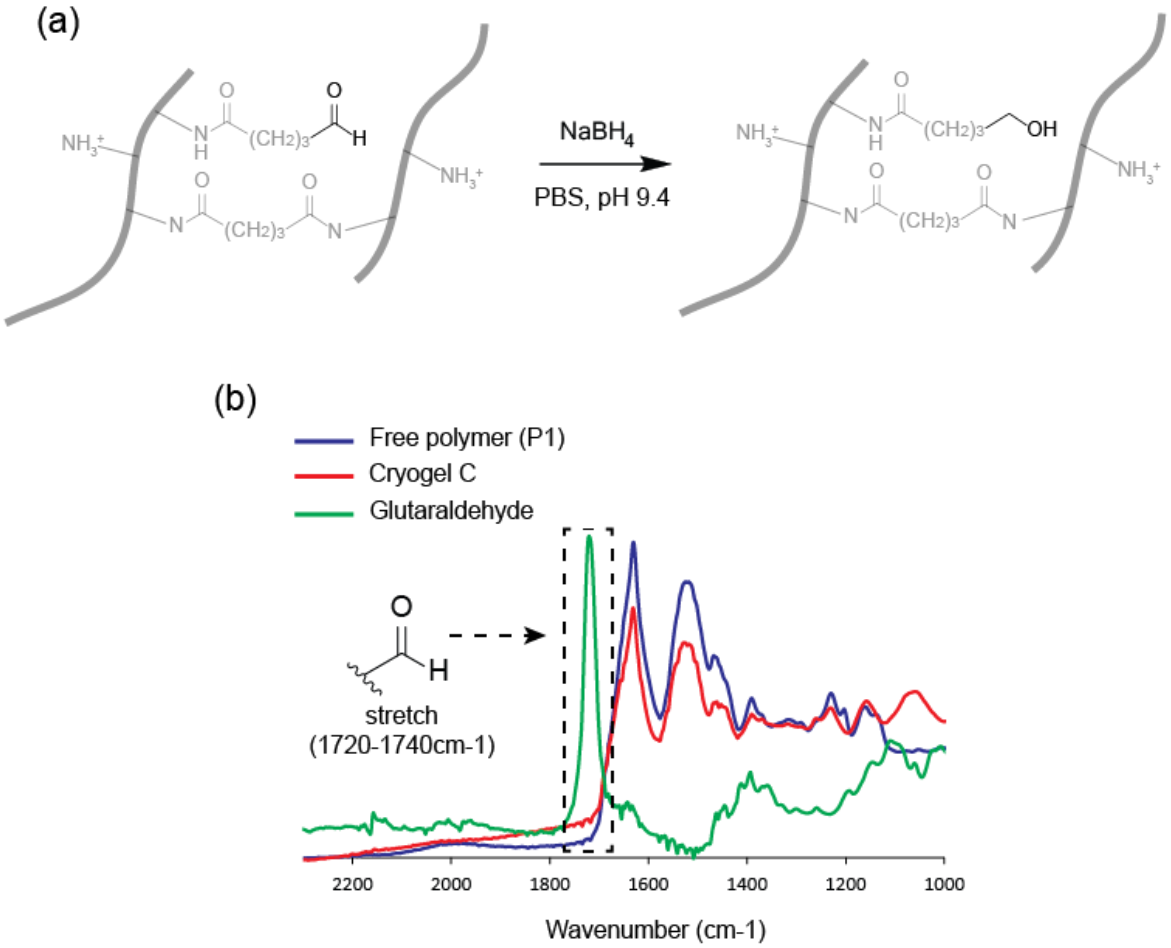

Figure S3. (a) Reduction of excess glutaraldehyde crosslinker with 0.1 % w/v sodium borohydride. (b) ATR FT-IR of cryogel C washed in sodium borohydride showing absence of aldehyde peak

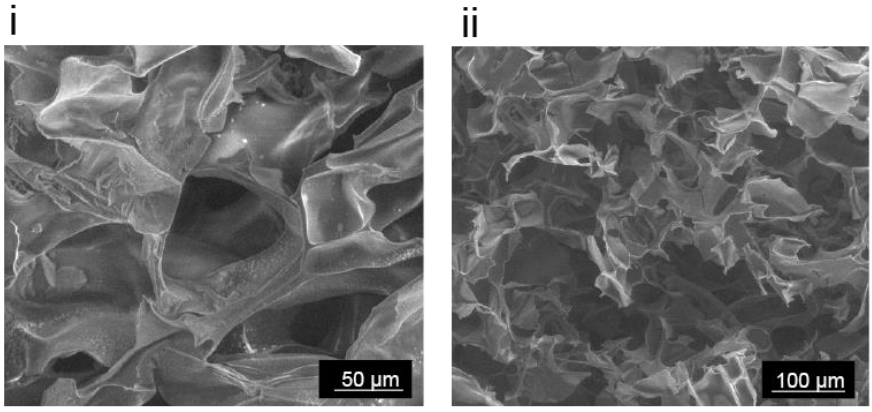

Figure S4. E-SEM close up images on the cross-sectional morphology of (i) Cryogel C and (ii) Cryogel D

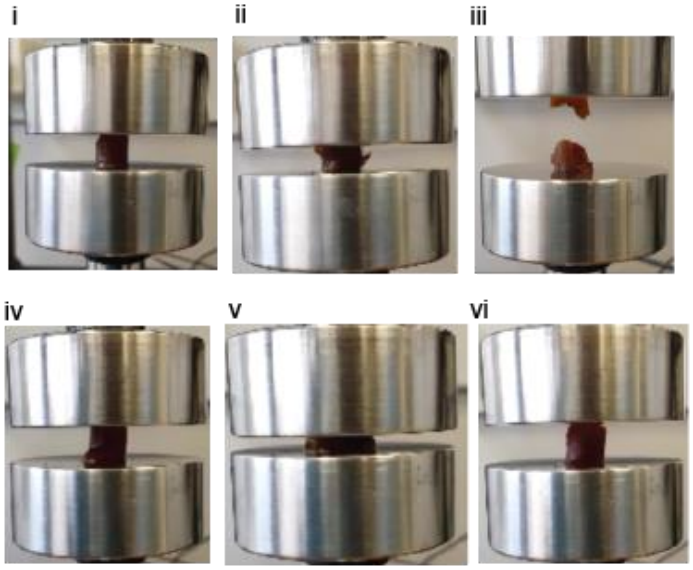

Figure S5. Photographs of hydrogel (i-iii) and cryogel C (iv-vi) during mechanical testing

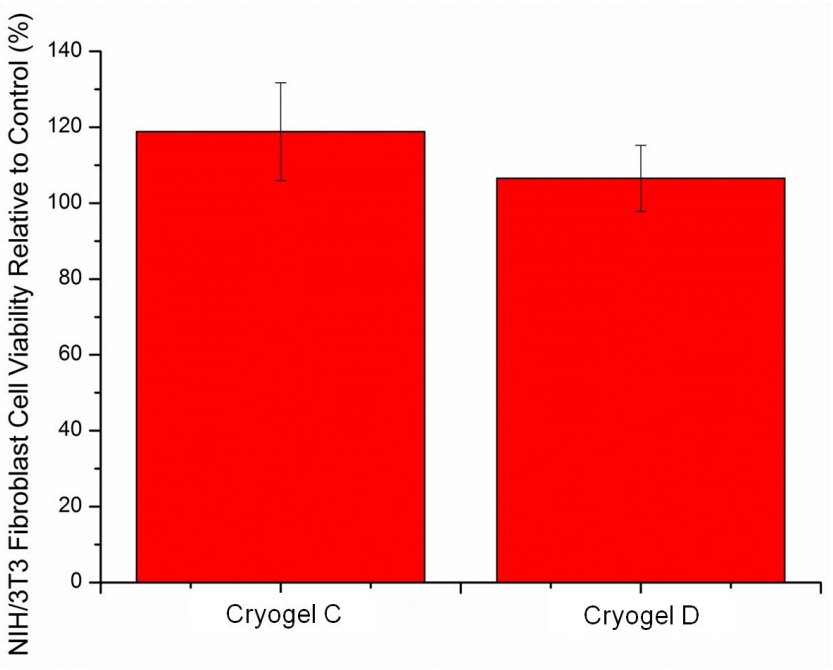

Figure S6. Cytotoxicity evaluation of cryogel-conditioned medium using NIH-3T3 fibroblast cells. Error bars represent the standard deviation from the mean (n = 4).

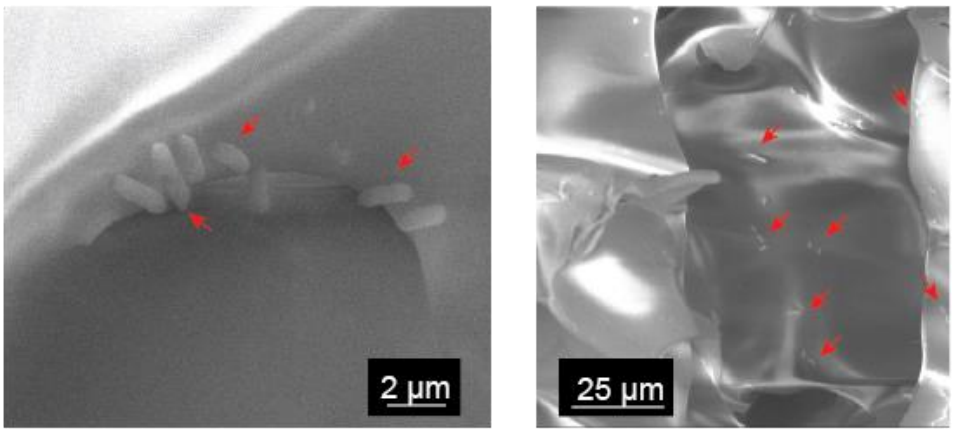

Figure S7. Representative E-SEM images of cryogel C after incubation with *E. coli* for 1 h, followed by vigorous flushing and agitation with saline buffer (0.9% NaCl solution). Note the red arrows indicate the *E. coli* cells.

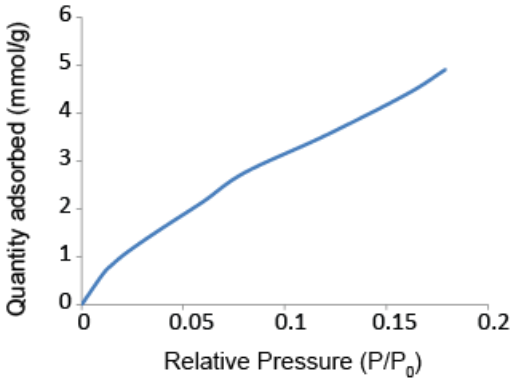

Figure S8. Carbon dioxide adsorption isotherm of freeze-dried cryogel C

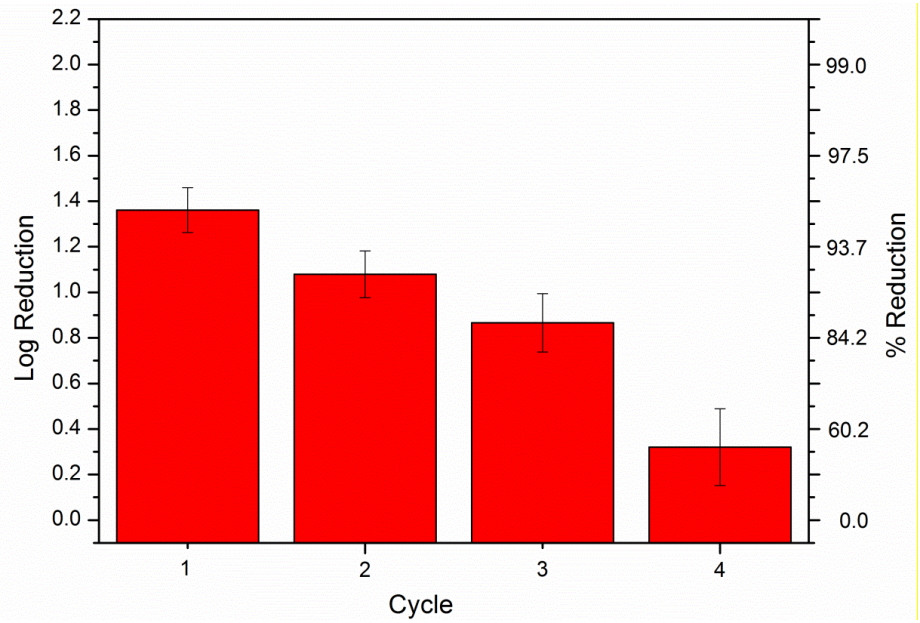

Figure S9. Log reduction and % kill of *E. coli* on peptide cryogel C after each cycle of use. Error bars represent the standard deviation from the mean ($n \geq 4$).

References:

1. Li, P.; Poon, Y. F.; Li, W.; Zhu, H.-Y.; Yeap, S. H.; Cao, Y.; Qi, X.; Zhou, C.; Lamrani, M.; Beuerman, R. W.; Kang, E.-T.; Mu, Y.; Li, C. M.; Chang, M. W.; Leong, S. S. J.; Chan-Park, M. B. *Nat. Mater.* **2011,** 10, (2), 149-156.
2. Sulistio, A.; Widjaya, A.; Blencowe, A.; Zhang, X. Q.; Qiao, G. *Chem. Commun.* **2011,** 47, (4), 1151-1153.
3. Epand, R. F.; Scheraga, H. A. *Biopolymers* **1968,** 6, (11), 1551-1571.
4. Hosia, W.; Johansson, J.; Griffiths, W. J. *Mol. Cell. Proteomics* **2002,** 1, (8), 592-597.
5. Goh, S. L.; Platt, A. P.; Rutledge, K. E.; Lee, I. *J. Polym. Sci., Part A* **2008,** 46, (16), 5381-5389.
6. Lee, J.; Lee, S. J.; Choi, J. Y.; Yoo, J. Y.; Ahn, C. H. *Eur. J. Pharm. Sci.* **2005,** 24, (5), 441-449.